The Influence of Internal Friction on Dilute Polymer Solution Dynamics

Submitted in partial fulfillment of the requirements

for the degree of

Doctor of Philosophy

of the
Indian Institute of Technology Bombay, India
and
Monash University, Australia

by

Ramalingam Kailasham

Supervisors:

Prof. Rajarshi Chakrabarti (IIT Bombay)

Prof. J. Ravi Prakash (Monash University)

Year 2021

Copyright notice

Declaration

This thesis is an original work of my research and contains no material which has been accepted for the award of any other degree or diploma at any university or equivalent institution and that, to the best of my knowledge and belief, this thesis contains no material previously published or written by another person, except where due reference is made in the text of the thesis.

Signature: ……………………

Print Name: RAMALINGAM KAILASHAM

Date: 5th August 2021

Acknowledgements

My foremost and sincere gratitude to my two supervisors, Prof. Rajarshi Chakrabarti of the Department of Chemistry at IIT Bombay, and Prof. J. Ravi Prakash of the Department of Chemical Engineering at Monash University for instilling in me, over the course of this PhD project, a spirit of critical thinking and independent inquiry. This thesis has been made possible by their sage mentorship and advice.

I benefitted greatly from my interactions with Prof. Burkhard Dünweg at the Max Planck Institute for Polymer Research, who was generous with his knowledge about numerical simulations of coarse-grained polymer models. I thank the members of my research progress committee: Profs. P Sunthar and Ranjith Padinhateeri from IIT Bombay and Profs. Mainak Majumder and Rico Tabor from Monash University, for their comments and suggestions.

I was fortunate to have been a part of a scholarly laboratory set-up at both the institutes. I would like to thank all the group members, past and present, of the Statistical Mechanics and Soft Matter Group (at IIT Bombay), and the Molecular Rheology Group (at Monash University) for making the learning experience an enjoyable one. The long discussions with Subhasis Chaki on stochastic thermodynamics are deeply cherished. My sincere thanks also to Kiran Kumari, for cross-checking the derivations during the initial stages of the project and providing insightful tips during code-debugging.

I am grateful to the IIT Bombay-Monash Research Academy for funding and general support, and also to its friendly and professional staff for helping with the logistics and paperwork during various stages of my PhD. CPU time grants from the MonARCH and MASSIVE computational facilities at Monash University, the National Computational Infrastructure (NCI) facility hosted by the Australian National University, and the SpaceTime-2 facility at IIT Bombay are gratefully acknowledged.

Finally, I am ever grateful to the support network comprising my family for their unconditional love and encouragement.

Abstract

Macromolecules in solution experience an additional mode of dissipation or friction due to intramolecular interactions, over and above the solvent drag, which resists their conformational reconfiguration. This additional mode of dissipation termed as "internal friction" or "internal viscosity" (IV), has been known to significantly affect the timescale of protein folding, the mechanical response of macromolecules to stretching, and the rheological properties of polymer solutions. Theoretical and computational investigations into the dynamics of flexible polymer molecules routinely employ the bead-spring-chain model, wherein the beads are massless centres of friction, and the springs model the entropic elasticity of the polymer. This prototypical model may be extended to incorporate the effects of internal friction, by the inclusion of dashpots that provide a rate-dependent restoring force, in parallel with the springs. In principle, the stochastic differential equations governing the motion of beads in this model can be derived using the principles of polymer kinetic theory, and integrated numerically using Brownian dynamics (BD) simulations. However, to date, an exact solution to the bead-spring-dashpot chain has been available only for the case of a dumbbell, which represents two beads ($N_b = 2$) connected by a spring. The key contributions of the thesis are: (a) elucidation and *in silico* validation of an experimentally realisable protocol for the measurement of internal friction; (b) the correct solution of a finitely extensible dumbbell model with internal viscosity and hydrodynamic interactions (HI), in order to examine the effect of HI on the rheological response of models with IV; (c) formulation of an exact solution to the bead-spring-dashpot chain model for the general case of $N_b > 2$ along with the derivation of the appropriate stress tensor expression; and lastly, (d) establishing the importance of fluctuations in the treatment of internal friction, by comparison of the exact solution against a widely used theoretical framework that relies on a preaveraged approximation of the internal friction force.

Key words: internal friction, internal viscosity, bead-spring-dashpot model, simple shear flow, dilute polymer solution, fluctuations

Table of Contents

List of Figures

xi

List of Tables

Notation

Roman Symbols

T Absolute Temperature 4

$\mathcal{D}$ Diffusion tensor 31

$\mathcal{B}$ Square root of the diffusion tensor 32

N_b Number of beads in coarse-grained model 5

N Number of springs in coarse-grained model 7

Greek Symbols

$\boldsymbol{\delta}$ Unit tensor 9

$\boldsymbol{\kappa}$ Flow tensor 8

$\boldsymbol{\Omega}_{\mu\nu}$ Hydrodynamic interaction tensor 9

$\dot{\gamma}$ Shear rate 12

η' Dynamic viscosity, real component of complex viscosity 2

η'' Imaginary component of complex viscosity 3

η_s Solvent viscosity 2

λ_H Characteristic time scale 8

ϕ Total intramolecular potential energy 8

Ψ Normalized configurational distribution function 8

ψ Normalized distribution of internal configurations 8

$\widetilde{\epsilon}$ Strength of excluded volume interactions 11

ζ Bead friction coefficient 8

$\boldsymbol{\tau}_\mathrm{p}$ Stress tensor 67

φ Internal friction parameter, $\varphi = K/\zeta$ 3

ϵ Also internal friction parameter, $\epsilon = 2K/\zeta$ 8

Chapter 1

Introduction

Conformational transitions in polymer molecules are impeded by solvent molecules, and sometimes additionally by intramolecular interactions. The dissipation caused by the latter are termed as *internal friction* or *internal viscosity* (IV) (Kuhn and Kuhn, 1945; de Gennes, 1979; Manke and Williams, 1985; Ansari *et al.*, 1992; Sagnella *et al.*, 2000; Hagen, 2010; Soranno *et al.*, 2012), and examples of such dissipation include the damping of protein folding (Ansari *et al.*, 1992; Qiu and Hagen, 2004a; Cellmer *et al.*, 2008; Wensley *et al.*, 2010; Samanta and Chakrabarti, 2013; Samanta *et al.*, 2014; Samanta and Chakrabarti, 2016; Soranno *et al.*, 2017), the modulation of stretching transitions in polysaccharides (Khatri *et al.*, 2007), and the enhancement of dissipated work in the stretch-relaxation of polymers (Murayama *et al.*, 2007; Alexander-Katz *et al.*, 2009; Schulz *et al.*, 2015a). The discontinuous jump in stress of polymer solutions upon inception or cessation of flow (Liang and Mackay, 1993; Orr and Sridhar, 1996) has also been attributed to internal friction. Given its wide-ranging impact, a careful investigation of the consequences of the presence of internal friction is essential. We choose to study this phenomenon using Brownian dynamics (BD) simulations of coarse-grained polymer models. A brief review of the historical development of micromechanical models for the treatment of internal friction is presented next, before identifying the main objectives of this thesis and specifying the chapterwise organization of material.

The earliest models for polymer chains, proposed by Rouse (1953) and Zimm (1956), modelled macromolecules as massless, phantom beads (which act as centres of friction) connected together by entropic springs. These models, which do not incorporate any internal mode of dissipation, or internal friction, are successful in qualitatively describing several rheological properties of dilute polymer solutions, such as small amplitude oscillatory material functions over a range of frequencies (Bird *et al.*, 1987b; Larson, 1988) and a non-zero first normal stress coefficient in shear flow (Bird *et al.*,

1

1987b). Refined models that account for the finite extensibility of the springs are also able to predict the shear-rate dependence of viscometric functions (Wedgewood and Öttinger, 1988).

The Rouse and Zimm models predict that the dynamic viscosity of polymer solutions, η' approaches the solvent viscosity, η_s, at high frequencies. However, experiments studying the viscoelastic properties of polystyrene solutions (Lamb and Matheson, 1964; Massa *et al.*, 1971) reveal that in the high-frequency regime, η' plateaus at a value higher than η_s. Polymer solutions have also been observed to exhibit a "jump" in stress at the inception of flow (Mackay *et al.*, 1992; Liang and Mackay, 1993), and when flow is switched off. Such a jump was found to be higher than the contribution from the Newtonian solvent. These observations have been predicted by rigid-rod models (Bird *et al.*, 1987b), but not by bead-spring or flexible polymer models extant at that time. The bead-spring chain models described so far assume that the underlying polymer chain is completely flexible at all time scales. In real polymer molecules, however, while the bond angles are usually fixed, there is a distribution of torsional or dihedral angles, due to the *trans* state being thermodynamically favorable compared to the *gauche* state. The two states are, however, separated by an activation energy barrier, which sets a timescale for the hopping between dihedral angle states (Rubinstein and Colby, 2003). Peterlin (1967) and de Gennes (1979) argue that at timescales lower than this transition time, the polymer appears to be frozen, and resists any change in its conformation, in the manner of an "internal" friction. There exist molecular dynamics simulation studies which appear to suggest that such transitions are the source of internal friction (de Sancho *et al.*, 2014; Echeverria *et al.*, 2014).

As suggested by Manke and Williams (1985), if polymer chains are modeled at the monomer level, by considering a full-description of the bond-lengths, bond-angles, and the barriers separating the dihedral states, there would be no need for the concept of internal viscosity. They argue that the necessity to include IV arises only because the coarse-grained description of a polymer chain lumps together several monomer segments into a "bead". In such a picture, a barrier to torsional angle rotation can no longer be defined meaningfully. This is akin to solvent friction that only arises when the solvent degrees of freedom are coarse-grained. To describe the forces acting between the beads at this level of modeling, simple mechanical models have been used. The inclusion of a dashpot (Kuhn and Kuhn, 1945; Booij and van Wiechen, 1970; Bird *et al.*, 1987b), in parallel with the spring connecting adjacent beads, provides a rate-dependent restoring force to any change in the length of the connector vector joining the two beads, and has been found to correctly capture (Manke and Williams, 1988, 1992; Dasbach *et al.*, 1992;

Hua and Schieber, 1995) short-timescale rheological phenomena such as stress jumps and a high-frequency limiting value for the dynamic viscosity that is greater than the solvent viscosity. Interestingly, Gerhardt and Manke (1994) showed subsequently that the stress jump and the high-frequency plateau in dynamic viscosity are identically equal to each other for linear viscoelastic fluids. The internal friction parameter, denoted by φ, and defined as the ratio of the damping coefficient of the dashpot to the bead friction coefficient, is a dimensionless ratio used for quantifying the relative magnitude of the internal friction to the solvent friction.

The correct form of the expression to be used for the force in the connector vector joining the two beads in models with internal viscosity was initially disputed, with most researchers using the linearized rotational velocity (LRV) approximation proposed by Cerf (1951) and Peterlin (1967). Subsequent analytical work by Williams and coworkers (Manke and Williams, 1988; Dasbach et al., 1992) aimed at capturing the stress jump in polymer solutions helped conclusively identify the correct form of the force expression, which was identical to that suggested earlier by Kuhn and Kuhn (1945). The semi-analytical approximation for the stress jump by Williams and coworkers is found to agree with exact BD simulation results by Hua and Schieber (1995), but is different from the LRV prediction. Furthermore, the LRV approximation predicts that the imaginary component of the complex viscosity, η'', vanishes at large values of internal friction parameter (φ) for all frequencies. Dasbach et al. (1992) showed this prediction was shown to be in stark contrast to their semi-analytical approximation which predicts a limiting non-zero value for η'' as $\varphi \to \infty$. The LRV approximation for the treatment of internal viscosity was therefore shown to be incorrect.

A comparison of experimental data on the reconfiguration time of proteins against the predictions of several models of internal friction (Soranno et al., 2018) concludes that it is not only difficult to discriminate between the predictions made by the models but also non-trivial to assign a single mechanism as the source of internal friction. There are studies which argue that internal friction seems to stem from a collection of effects which includes, but is not limited to, dihedral angle rotations (de Sancho et al., 2014; Echeverria et al., 2014), intramolecular interactions (Alexander-Katz et al., 2009), such as hydrodgen bonds (Schulz et al., 2015a) and disulfide linkages (Ameseder et al., 2018), and a coupling of the translational and rotational degrees of freedom to the dihedral angle (Daldrop et al., 2018). While the microscopic origin of internal friction is manyfold (Khatri et al., 2007; Murayama et al., 2007; Alexander-Katz et al., 2009; Schulz et al., 2015a; Echeverria et al., 2014; de Sancho et al., 2014; Sashi et al., 2016; Jain et al., 2016; Ameseder et al., 2018; Jas et al., 2001; Soranno et al., 2017), it has been broadly classified as being either

of the *wet* or *dry* kind (Soranno *et al.*, 2012; Hagen, 2010), depending whether its coupling with the solvent viscosity is multiplicative (wet) or additive (dry). These two categories are explained in brief below.

The transition of a protein from an unfolded to its native folded state is commonly interpreted as a diffusive search process over a rugged energy landscape (Onuchic *et al.*, 1997), and the internal friction associated with landscape roughness is typically considered to be of the wet type (Wensley *et al.*, 2010; Neupane *et al.*, 2017). Such a diffusive motion over a corrugated energy landscape has also been examined in the context of the movement of DNA-binding proteins along the DNA molecule (Yu *et al.*, 2013). An analytical solution for the diffusion coefficient in one dimension was derived by Zwanzig (1988) who observed that the effective friction γ_{eff}, is related purely multiplicatively to the solvent friction γ_s, as $\gamma_{\text{eff}} = \gamma_s \exp\left[(\delta/k_B T)^2\right]$, where k_B is Boltzmann's constant, T is the absolute temperature, and δ^2 is the variance of the heights of the normally distributed undulations. Since $\gamma_s \sim \eta_s$, the effective friction is higher than that expected due to solvent friction alone, at any finite value of η_s. It is also clear that the internal friction would vanish in the extrapolated limit of zero solvent viscosity ($\eta_s \rightarrow 0$), which is a characteristic feature of wet internal friction.

On the other hand, experimental measurements of the dependence of the reconfiguration time of small proteins on η_s find a finite value in the extrapolated limit of $\eta_s \rightarrow 0$, indicating the presence of a solvent-viscosity-independent resistance to folding (Qiu and Hagen, 2004a; Cellmer *et al.*, 2008; Soranno *et al.*, 2012). Hagen (2010) has proposed a heterogeneous reaction friction model with the unfolded and native states separated by two consecutive barriers, one for each mode of friction, as an explanation for the presence of dry internal friction.

One of the main objectives of this thesis is to propose an experimentally realizable protocol that could be used for the measurement and distinction between these two types of internal friction.

The other central goal is to computationally study the dynamics and rheological response of polymer models with internal friction. Our approach to this objective is rather markedly affected by the level of coarse-graining, or the number of beads (N_b) in the polymer model, that we choose. The reasoning is as follows. In the standard, polymer kinetic theory (PKT)-based procedure (Bird *et al.*, 1987b; Öttinger, 1996) for the solution of bead-spring-chain models through Brownian dynamics simulations, the equation of motion for the velocities of the connector vector that connects neighboring beads is combined with an equation of continuity in probability space to obtain a Fokker-Planck equation for the system, and the equivalent stochastic differential equation

is integrated numerically. The inclusion of internal viscosity, however, results in a coupling of connector vector velocities and precludes a trivial application of the usual procedure for all but the case of a dumbbell which has just a single connector vector. The dumbbell model may therefore be solved, after considerable algebra, using the conventional approach. For bead-spring-dashpot chains with more than two beads, however, a methodology for the decoupling of connector vector velocities needs to be formulated before the usual approach can be followed.

The simplicity offered by the dumbbell model makes it an ideal platform to begin our rheological investigations. While the effect of fluctuations in hydrodynamic interactions (HI) on the rheology of dilute polymer solutions is well documented (Larson, 2005; Schroeder, 2018; Prakash, 2019), studies on models that simultaneously incorporate fluctuating hydrodynamic interactions and internal viscosity are scarce (Hua and Schieber, 1996), with the majority including hydrodynamic interactions in a pre-averaged manner (Manke and Williams, 1992; Dasbach *et al.*, 1992). We use Brownian dynamics (BD) simulations to solve a dumbbell model which incorporates finite chain extensibility, fluctuating internal friction and hydrodynamic interactions, in order to study the relative roles played by internal friction and hydrodynamic interactions in determining the dynamics of polymer molecules.

Williams and coworkers have developed a methodology to decouple the connector vector velocities in a bead-spring-dashpot chain with more than two beads, and provide semi-analytical approximate solutions to the stress jump (Manke and Williams, 1988) and linear viscoelastic properties (Dasbach *et al.*, 1992). We aim to expand the scope of their decoupling methodology, and provide an exact solution to the bead-spring-dashpot chain model with fluctuating internal friction that is valid both at equilibrium and in the presence of a flow field.

A commonly used theoretical framework for interpreting the results of experiments and simulations on biopolymers with internal viscosity is the Rouse model with internal friction (RIF) (Khatri and McLeish, 2007), and its variants (Cheng *et al.*, 2013; Samanta *et al.*, 2014; Samanta and Chakrabarti, 2016). While these models remain preferred due to their analytical tractability, their accuracy, from a theoretical standpoint, has so far been unquestioned. We aim to first establish a formal connection between the RIF model and the bead-spring-dashpot model prevalent in the PKT literature, and then compare the RIF model predictions for observables at equilibrium and in flow, against those obtained from simulations on the exact model which incorporates fluctuations in the internal friction force.

This thesis is organized as follows. A brief description of the coarse-grained polymer model used in this thesis, along with an explanation of the various bonded and non-bonded interactions, is given in Chapter 2. The development and validation of a protocol for the measurement of internal friction is described in Chapter 3. In Chapter 4, the rheological consequences of internal friction and hydrodynamic interactions in a finitely extensible dumbbell model are examined in detail. A methodology for obtaining the exact set of governing equations for the bead-spring-dashpot chain model is developed in Chapter 5, and the material functions for a Rouse chain with fluctuating internal friction in simple and small amplitude oscillatory shear flow are presented. The importance of fluctuations in the treatment of internal friction is assessed in Chapter 6, by comparing the analytical predictions of the RIF model against results from simulations of an exact model with fluctuating internal friction. The key contributions of the thesis are summarized in Chapter 7, along with suggestions for future work.

Chapter 2

Materials and Methods

2.1 Model description
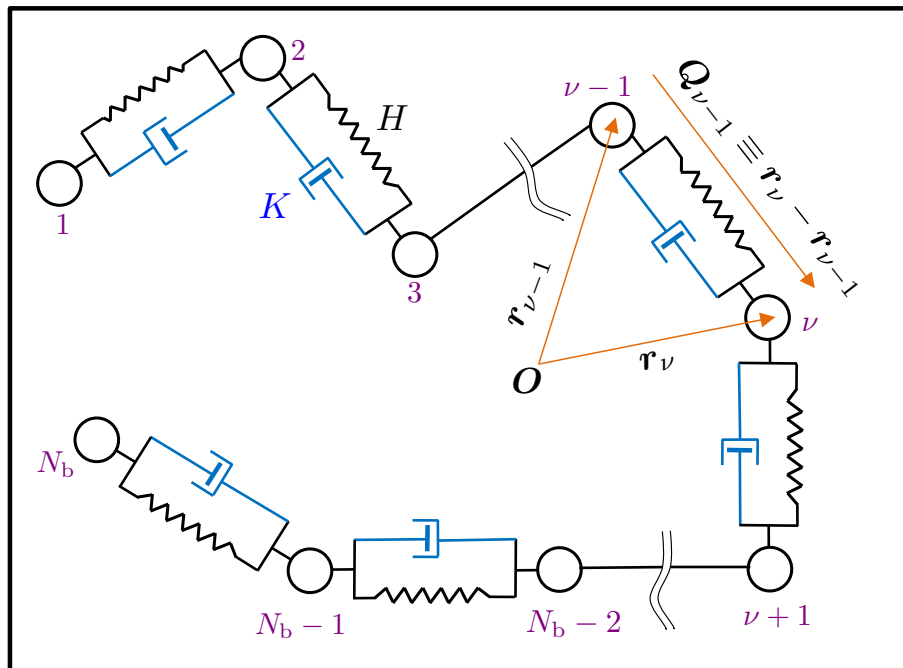
Figure 2.1: Representation of a polymer chain as a sequence of beads connected by spring-dashpots. The stiffness of each spring is H, and the damping coefficient of each dashpot is K.

We consider N_b massless beads, each of radius a, joined by $N \equiv (N_b - 1)$ springs, and a dashpot of damping coefficient K in parallel with each spring, as shown in Fig. 2.1. Hookean springs are completely defined by their stiffness, H, whereas finitely extensible springs with a nonlinear force law require the specification of additional parameters, as discussed later in Section 2.1.2. The position of the νth bead is denoted as r_ν, and the

connector vector joining adjacent beads is represented as $\boldsymbol{Q}_{\nu-1} \equiv \boldsymbol{r}_\nu - \boldsymbol{r}_{\nu-1}$. The centre-of-mass of the chain is denoted by $\boldsymbol{r}_{\mathrm{c}} \equiv (1/N_{\mathrm{b}}) \sum_{\nu=1}^{N_{\mathrm{b}}} \boldsymbol{r}_\nu$. The chain, as shown in Fig. 2.1, is suspended in a Newtonian solvent of viscosity η_{s} where the velocity $\boldsymbol{v}_{\mathrm{f}}$ at any location $\boldsymbol{r}_{\mathrm{f}}$ in the fluid is given by $\boldsymbol{v}_{\mathrm{f}}(\boldsymbol{r}_{\mathrm{f}}, t) \equiv \boldsymbol{v}_0 + \boldsymbol{\kappa}(t) \cdot \boldsymbol{r}_{\mathrm{f}}$, where $\boldsymbol{v}_0$ is a constant vector, and the transpose of the velocity gradient tensor is denoted as $\boldsymbol{\kappa} \equiv (\nabla \boldsymbol{v}_{\mathrm{f}})^T$. The bead friction coefficient is defined as $\zeta := 6\pi\eta_{\mathrm{s}} a$. The chain is assumed to have completely equilibrated in momentum space, and its normalized configurational distribution function at any time t is specified as $\Psi \equiv \Psi(\boldsymbol{r}_1, \boldsymbol{r}_2, ..., \boldsymbol{r}_{N_{\mathrm{b}}}, t) = \Psi(\boldsymbol{r}_{\mathrm{c}}, \boldsymbol{Q}_1, \boldsymbol{Q}_2, ..., \boldsymbol{Q}_N, t) = (1/\mathcal{Z}) \exp[-\phi/k_B T]$, where $\phi \equiv \phi^{\mathrm{S}} + \phi^{\mathrm{EV}}$ denotes the total intramolecular potential energy, which has contributions from the springs joining the beads, ϕ^{S}, and the nonbonded interactions due to excluded volume interactions, ϕ^{EV}. The total intramolecular potential energy depends only on the internal coordinates of the chain $\{\boldsymbol{Q}_i\}$, and not on its centre-of-mass, $\boldsymbol{r}_{\mathrm{c}}$. The partition function which appears as the normalization constant is defined as $\mathcal{Z} = \int \exp[-\phi/k_B T] \, d\boldsymbol{Q}_1 d\boldsymbol{Q}_2 \dots d\boldsymbol{Q}_N$. The expression for the internal viscosity force, $\boldsymbol{F}_k^{\mathrm{IV}}$, in the kth connector vector may be written as $\boldsymbol{F}_k^{\mathrm{IV}} = K\left(\boldsymbol{Q}_k \boldsymbol{Q}_k / Q_k^2\right) \cdot [\![\dot{\boldsymbol{Q}}_k]\!]$, where $[\![\dots]\!]$ denotes an average over momentum-space. The internal friction parameter, $\varphi = K/\zeta$, is defined as the ratio of the dashpot's damping coefficient to the bead friction coefficient. The usage of $\epsilon = 2\varphi$ as the internal friction parameter is also prevalent in the literature. The characteristic length- and time-scales are defined to be $l_H \equiv \sqrt{k_B T/H}$, and $\lambda_H \equiv \zeta/4H$, respectively, and the scaled dimensionless quantities are denoted with an asterisk as superscript.

Within the framework of polymer kinetic theory (Bird *et al.*, 1987b), the Fokker-Planck equation for the configurational distribution function is obtained by combining a force-balance on the beads (or connector vectors) with a continuity equation in probability space. The force-balance mandates that the sum of: (i) the internal friction force due to the dashpot, (ii) the restoring force from the spring, (iii), the force due to excluded volume interactions, (iv) the random Brownian force arising from collisions with solvent molecules, (v) the hydrodynamic force responsible for the solvent-mediated propagation of momentum on each bead, and (vi) external forces, if any, equals zero. It is convenient to work with connector vectors, rather than bead positions. For the general case of bead-spring-chain models with internal friction, excluded volume, and hydrodynamic interaction effects, the following equation has been derived in Prakash (1999) for the momentum-averaged velocity of the kth connector vector

$$[\![\dot{\boldsymbol{Q}}_k]\!] = \boldsymbol{\kappa} \cdot \boldsymbol{Q}_k - \frac{1}{\zeta} \sum_{l=1}^{N} \widetilde{\boldsymbol{A}}_{kl} \cdot \left(k_B T \frac{\partial \ln \Psi}{\partial \boldsymbol{Q}_l} + \frac{\partial \phi}{\partial \boldsymbol{Q}_l} + K \frac{\boldsymbol{Q}_l \boldsymbol{Q}_l}{Q_l^2} \cdot [\![\dot{\boldsymbol{Q}}_l]\!]\right) \tag{2.1}$$

where

$$\tilde{\boldsymbol{A}}_{kl} = \boldsymbol{A}_{kl} + \zeta \left(\boldsymbol{\Omega}_{k,l} + \boldsymbol{\Omega}_{k+1,l+1} + \boldsymbol{\Omega}_{k,l+1} + \boldsymbol{\Omega}_{k+1,l} \right) \tag{2.2}$$

and $\boldsymbol{A}_{kl} = A_{kl}\boldsymbol{\delta}$ where A_{kl} are the elements of the Rouse matrix, given by

$$A_{kl} = \begin{cases} 2; & k = l \\ -1; & |k - l| = 1 \\ 0; & \text{otherwise} \end{cases} \tag{2.3}$$

and $\boldsymbol{\Omega}_{k,l}$ represents the hydrodynamic interaction tensor discussed below. The equation of motion for the connector vector velocity is then substituted into a continuity equation for the configurational distribution function, given by

$$\frac{\partial \Psi}{\partial t} = -\sum_{j=1}^{N} \frac{\partial}{\partial \boldsymbol{Q}_j} \cdot \left\{ [\![\dot{\boldsymbol{Q}}_j]\!] \Psi \right\} \tag{2.4}$$

in order to obtain the Fokker-Planck equation and ultimately the set of governing stochastic differential equations, which are numerically integrated using Brownian dynamics simulations. Note that for homogeneous flow profiles, the continuity equation may be written solely in terms of the relative coordinates, $\boldsymbol{Q}_j$. Under such conditions, the distribution function $\Psi(\boldsymbol{r}_c, \boldsymbol{Q}_1, \boldsymbol{Q}_2, ...\boldsymbol{Q}_N, t)$ can be replaced by $\psi(\boldsymbol{Q}_1, \boldsymbol{Q}_2, ...\boldsymbol{Q}_N, t)$. The exact governing Fokker-Planck and stochastic differential equations (SDE) are specific to the system being studied, and have been presented in the diffferent chapters that follow for the different problems that have been considered here.

A brief explanation about the bonded and non-bonded interactions that appear in Eq (2.1) is given below.

2.1.1   Hydrodynamic interaction tensor

The general form of the hydrodynamic interaction tensor, $\boldsymbol{\Omega}_{\mu\nu}$, is given by

$$\boldsymbol{\Omega}_{\mu\nu} = \frac{3a}{4\zeta \, r_{\mu\nu}} \left\{ \mathscr{A}\boldsymbol{\delta} + \mathscr{B}\frac{\boldsymbol{r}_{\mu\nu}\boldsymbol{r}_{\mu\nu}}{r_{\mu\nu}^2} \right\} \tag{2.5}$$

where $\boldsymbol{r}_{\mu\nu} = \boldsymbol{r}_\nu - \boldsymbol{r}_\mu$ is the interbead separation and the coefficients $\mathscr{A}$ and $\mathscr{B}$, according to the Rotne-Prager-Yamakawa (RPY) definition (Rotne and Prager, 1969; Yamakawa, 1971), are given by

$$\mathscr{A} = \left(1 + \frac{2a^2}{3r_{\mu\nu}^2} \right), \quad \mathscr{B} = \left(1 - \frac{2a^2}{r_{\mu\nu}^2} \right) \quad \text{for} \quad r_{\mu\nu} \geq 2a$$

$$\mathscr{A} = \frac{r_{\mu\nu}}{2a} \left(\frac{8}{3} - \frac{3r_{\mu\nu}}{4a} \right), \quad \mathscr{B} = \frac{1}{8} \left(\frac{r_{\mu\nu}}{a} \right)^2 \quad \text{for} \quad r_{\mu\nu} < 2a \tag{2.6}$$

where $r_{\mu\nu} = |\boldsymbol{r}_{\mu\nu}|$, and the hydrodynamic interaction parameter is defined to be, $h^* = a^*/\sqrt{\pi}$, with $h^* = 0.0$ denoting the free-draining case.

For the special case of dumbbells ($N_b = 2$), there exists an alternative means of describing the hydrodynamic interaction effects between the two beads, given by the Regularized Oseen Burgers (ROB) expression (Zylka and Öttinger, 1989),

$$\boldsymbol{\Omega}\left(\boldsymbol{Q}\right) = \frac{3a}{4\zeta\,Q}\left\{\mathscr{A}\,\boldsymbol{\delta} + \mathscr{B}\frac{\boldsymbol{QQ}}{Q^2}\right\} \tag{2.7}$$

where $\boldsymbol{\Omega}\left(\boldsymbol{Q}\right) \equiv \boldsymbol{\Omega}_{12}$, $\boldsymbol{Q} \equiv \boldsymbol{Q}_1 = \boldsymbol{r}_2 - \boldsymbol{r}_1$, $\bar{p} = 2a/\sqrt{3}$, and

$$\begin{aligned} \mathscr{A} &= \frac{Q^6 + (7/2)\bar{p}^2 Q^4 + (9/2)\bar{p}^4 Q^2}{\left(Q^2 + \bar{p}^2\right)^3} \\ \mathscr{B} &= \frac{Q^6 + (3/2)\bar{p}^2 Q^4 - (3/2)\bar{p}^4 Q^2}{\left(Q^2 + \bar{p}^2\right)^3} \end{aligned} \tag{2.8}$$

In Brownian dynamics simulations, the hydrodynamic interaction tensor must remain positive-definite for all values of the interbead separation. It was found that this regularization of the Oseen-Burgers expression for the HI tensor has a smooth dependence on Q, is positive-definite for all values of Q, and agrees with the RPY tensor to order Q^{-3} (Zylka and Öttinger, 1989).

2.1.2 Spring potential

The simplest form of the potential energy that is stored in a spring connecting neighboring beads is the harmonic potential, which corresponds physically to an infinitely extensible spring, and has the following mathematical representation:

$$\phi_{\mathrm{HK}}^{\mathrm{S}} = \frac{1}{2}HQ^2 \tag{2.9}$$

For finitely extensible springs, with a maximum allowed length of Q_0, given below are two commonly used expressions for the spring potential

$$\phi_{\mathrm{FENE}}^{\mathrm{S}} = -\frac{1}{2}HQ_0^2\ln\left[1 - (Q/Q_0)^2\right] \tag{2.10}$$

$$\phi_{\mathrm{MS}}^{\mathrm{S}} = \frac{HQ_0^2}{3}\left[\left(\frac{Q}{Q_0}\right)^2 + \frac{1}{2\left(1 - Q/Q_0\right)} - \frac{1}{2}\left(\frac{Q}{Q_0}\right)\right] \tag{2.11}$$

The quantity $b = HQ_0^2/k_B T$ is taken to be the finite extensibility parameter.

The force-extension behavior of springs with the FENE potential (Warner, 1972) is qualitatively similar to the inverse Langevin function, and is commonly used in BD simulations (Hua and Schieber, 1995; Prabhakar and Prakash, 2006) due to its simpler functional form.

The elasticity of double-stranded DNA is known to be well approximated by the Marko-Siggia spring potential (Marko and Siggia, 1995), and it is widely employed to model the force-extension relationship in synthetic polymer molecules (Black *et al.*, 2017), as well as biopolymers (Latinwo *et al.*, 2014; Raman *et al.*, 2014; Sunthar and Prakash, 2005; Sasmal *et al.*, 2017).

At small values of the fractional extension, Q/Q_0, both the FENE and the Marko-Siggia potentials mimic the Hookean spring potential. At large values of the fractional extension, the FENE and Marko-Siggia potentials diverge.

2.1.3   Excluded volume interactions

The excluded volume interactions between beads are modelled using the Soddemann-Dünweg-Kremer (SDK) potential (Soddemann *et al.*, 2001), whose functional form is given by

$$
\frac{\phi^{\mathrm{SDK}}(r)}{k_B T} =
\begin{cases}
4\left[\left(\dfrac{\sigma_{\mathrm{s}}}{r}\right)^{12} - \left(\dfrac{\sigma_{\mathrm{s}}}{r}\right)^{6} + \dfrac{1}{4}\right] - \widetilde{\epsilon}; & r \leq 2^{1/6}\sigma_{\mathrm{s}} \\[2ex]
\dfrac{\widetilde{\epsilon}}{2}\left[\cos\left(m_1\left(\dfrac{r}{\sigma_{\mathrm{s}}}\right)^2 + m_2\right) - 1\right]; & 2^{1/6}\sigma_{\mathrm{s}} \leq r \leq r_{\mathrm{cut}} \\[2ex]
0; & r \geq r_{\mathrm{cut}}
\end{cases}
\tag{2.12}
$$

The minimum of the potential occurs at at $r = 2^{1/6}\sigma_{\mathrm{s}}$, and the value of the potential at this location is $\phi^{\mathrm{SDK}} = -\widetilde{\epsilon}\,k_B T$. As seen from Eq. (2.12), the repulsive part of the pair-potential is modeled after the Weeks-Chandler-Andersen (WCA) potential, while the attractive part is constructed using a cosine function which smoothly approaches zero at the cut-off distance, r_{cut}. A detailed comparison of the SDK potential with the Lennard-Jones and the WCA potential has been performed recently (Santra *et al.*, 2019). The parameter values for m_1 and m_2 depend on the choice of r_{cut}. They have been refined by Santra *et al.* (2019) in comparison to the values in the paper by Soddemann *et al.* (2001) in order to be more applicable to BD simulations. Setting $\widetilde{\epsilon} = 0$ in Eq. (2.12) leads to purely repulsive inter-bead interactions, and corresponds to the athermal limit of solvent quality. Increasing the value of $\widetilde{\epsilon}$ beyond zero results in a decrease in the solvent quality. A special feature of the SDK potential (Santra *et al.*, 2019) is that modifying the value of $\widetilde{\epsilon}$ allows one to tune the attractive interactions selectively, without affecting the repulsive branch of the pair-potential. This is in stark contrast to the more commonly used Lennard-Jones (LJ) potential for which changing the well-depth affects both the attractive and the repulsive branches. Furthermore, the exact truncation of the SDK potential at the cutoff distance results in an increased computational efficiency (Soddemann *et al.*,

2001) in comparison to the LJ potential whose long attractive tail approaches zero only asymptotically, at large inter-bead separations.

2.1.4   Flow profile and material functions

The flow tensor, $\boldsymbol{\kappa}$, for simple shear flow has the following form

$$\boldsymbol{\kappa} \equiv \boldsymbol{\kappa}^* \lambda_H^{-1} = \dot{\gamma} \begin{pmatrix} 0 & 1 & 0 \\ 0 & 0 & 0 \\ 0 & 0 & 0 \end{pmatrix} \tag{2.13}$$

and is characterized by the following viscometric functions

$$\eta_{\mathrm{p}} = -\frac{\tau_{\mathrm{p},xy}}{\dot{\gamma}}$$

$$\Psi_1 = -\left[\frac{\tau_{\mathrm{p},xx} - \tau_{\mathrm{p},yy}}{\dot{\gamma}^2} \right] \tag{2.14}$$

$$\Psi_2 = -\left[\frac{\tau_{\mathrm{p},yy} - \tau_{\mathrm{p},zz}}{\dot{\gamma}^2} \right]$$

where $\tau_{\mathrm{p},xy}$ refers to the xy element of the stress tensor, and η_{p}, Ψ_1, and Ψ_2 denote the shear viscosity, the first normal stress coefficient, and the second normal stress coefficient, respectively. In the time dependent period before steady state is reached, in accord with conventional notation, the transient viscometric functions are denoted by η_p^+, Ψ_1^+, and Ψ_2^+.

For small-amplitude oscillatory shear flow, we have

$$\boldsymbol{\kappa} = \dot{\gamma}_0 \cos(\omega t) \begin{pmatrix} 0 & 1 & 0 \\ 0 & 0 & 0 \\ 0 & 0 & 0 \end{pmatrix} \tag{2.15}$$

The material functions relevant to this flow profile, $\eta'(\omega)$ and $\eta''(\omega)$, are given by

$$-\tau_{\mathrm{p},xy} = \eta'(\omega)\dot{\gamma}_0 \cos(\omega t) + \eta''(\omega)\dot{\gamma}_0 \sin(\omega t) \tag{2.16}$$

Where appropriate, the viscometric functions have either been scaled by their respective Rouse chain values, η^{R} and Ψ_1^{R}, in steady shear flow, given by (Bird *et al.*, 1987b)

$$\eta^{\mathrm{R}} = n_{\mathrm{p}} k_B T \lambda_H \left[\frac{N_{\mathrm{b}}^2 - 1}{3} \right] \tag{2.17}$$

$$\Psi_1^{\mathrm{R}} = 2 n_{\mathrm{p}} k_B T \lambda_H^2 \left[\frac{(N_{\mathrm{b}}^2 - 1)(2N_{\mathrm{b}}^2 + 7)}{45} \right] \tag{2.18}$$

or by the Rouse values of the real and imaginary portions of the complex viscosity given by (Bird *et al.*, 1987b)

$$(\eta')^{\mathrm{R}} = n_{\mathrm{p}} k_B T \sum_{j=1}^{N} \frac{\lambda_j}{1 + \left(\lambda_j \omega\right)^2} \tag{2.19}$$

$$(\eta'')^{\mathrm{R}} = n_{\mathrm{p}} k_B T \sum_{j=1}^{N} \frac{\lambda_j^2 \omega}{1 + \left(\lambda_j \omega\right)^2} \tag{2.20}$$

where $\lambda_j = 2\lambda_H/a_j$, and $a_j = 4\sin^2\left[j\pi/2N_{\mathrm{b}}\right]$ are the eigenvalues of the Rouse matrix. Note that the dynamic viscosity, η', has the solvent viscosity contribution subtracted off and the convention is followed throughout this document, wherever data for η' has been reported. Where appropriate, shear rates and angular frequencies are scaled using $\lambda_{\mathrm{p}} \equiv \left(\eta^{\mathrm{R}}/n_{\mathrm{p}} k_B T\right)$, which is the characteristic relaxation time defined using the Rouse viscosity.

In this chapter, we have described the bead-spring-dashpot chain model and the various bonded and non-bonded interactions commonly considered in the theoretical study of such models. The cases considered in the subsequent chapters contain various combinations of the interactions described in the present chapter. Chapter 3 represents a special case which considers coarse-grained models whose terminal beads are subjected to external trapping potentials, and the relevant equations for these external potentials are presented in the next chapter.

Chapter 3

Wet and dry internal friction can be measured with the Jarzynski equality

3.1 Introduction

The existence of two types of internal friction—wet and dry—has been briefly discussed in Chapter 1, where it was pointed out that the classification is made depending upon if the internal friction couples multiplicatively (wet) or additively (dry) with the solvent friction. A brief overview of the extant approaches for the experimental quantification of internal friction is provided below, followed by a description of our proposed protocol for its measurement.

The dynamics of protein reconfiguration is commonly quantified experimentally by tagging the molecule with fluorescent donor-acceptor pairs along their contour length, and extracting a characteristic reconfiguration time from the autocorrelation of the fluorescence signal (Soranno *et al.*, 2017, 2018). In order to isolate the effects of the solvent and internal friction on the dynamics of the molecule, reconfiguration time measurements are first performed at various values of the solvent viscosity (Qiu and Hagen, 2004a; Pabit *et al.*, 2004; Cellmer *et al.*, 2008; Hagen, 2010), followed by a linear extrapolation of these measurements to extract a characteristic timescale in the limit of zero solvent viscosity ($\eta_\mathrm{s} \to 0$). This timescale is taken to represent the resistances to protein reconfiguration that are solely intramolecular in origin, and independent of the solvent viscosity, and is the commonly accepted operational definition for dry internal friction (Qiu and Hagen, 2004a; Avdoshenko *et al.*, 2017; Soranno *et al.*, 2017). This metric, however, does not provide a direct quantitative measure of the internal friction coefficient. The definition also does not apply to the case of wet internal friction (Soranno

et al., 2012; Hagen, 2010), which has a finite contribution at non-zero values of the solvent viscosity, but vanishes in the extrapolated limit of $\eta_s \to 0$.

Advancements in single-molecule-force spectroscopy have enabled an accurate estimation of the conformational diffusion coefficient of small biomolecules hopping between native and unfolded states (Chung and Eaton, 2013; Chung *et al.*, 2015; Neupane *et al.*, 2016, 2018), and an effective friction coefficient could be calculated, in principle, from these diffusivity measurements. For example, the conformational diffusion coefficient of single DNA hairpins (Neupane *et al.*, 2017) is found to depend significantly on the relative number of adenine-thymine (A:T) and cytosine-guanine (C:G) base-pair contacts, with a higher C:G content correlated to an increased diffusion constant. This difference has been suggested to originate from differing barriers to dihedral angle rotation, and consequently differing values of internal friction, for the A:T and G:C contact formation process. Such measurements, however, would not determine if the internal friction were of the wet or the dry type unless they were performed at multiple solvent viscosities, followed by extrapolation to the limit $\eta_s \to 0$. There is clearly a need for a protocol that can directly estimate the internal friction coefficient and distinguish between the two types.

Stretch-relaxation experiments on condensed DNA globules by Murayama *et al.* (2007) have found that the work dissipated in the process is about an order of magnitude higher than the solvent friction contribution estimated from slender-body hydrodynamics, and the internal friction coefficient is estimated to be $\approx 10^{-7}$ kg/s by ignoring the solvent contribution altogether. Netz and coworkers (Alexander-Katz *et al.*, 2009; Schulz *et al.*, 2015a) have proposed a protocol in which the work required to stretch a macromolecule is separated into two parts: reversible free energy increase due to the extension of the molecule, and irreversible work required to overcome rate-dependent restoring forces arising from solvent and internal friction. Within this framework, they show that the average dissipated work in the simulated stretching of polypeptides (Schulz *et al.*, 2015a), in the limit of $\eta_s \to 0$, scales with the number of intramolecular hydrogen bonds, which are considered to be responsible for internal friction. The internal friction coefficient estimated from these simulations is $\approx 10^{-10}$ kg/s. The dissipative signature of internal friction therefore appears to be a viable alternative for its quantification.

Jarzynski (1997) derived, in his landmark communication, a recipe for the estimation of the free-energy difference, ΔA, for a microscopic system transitioning from an initial state to a final state at a finite rate. The work done in a single realization of this transition is denoted as W, and is a stochastic quantity due to thermal fluctuations. The work statistics are related to the free energy difference by the Jarzynski equality (JE)

given by

$$\langle \exp\left[-W/k_B T\right]\rangle = \exp\left[-\Delta A/k_B T\right];$$

$$\langle W_{\text{dis}} \rangle = \langle W \rangle - \Delta A$$

(3.1)

where the $\langle ... \rangle$ in Eq. (3.1) represents an average with respect to the probability distribution of work values. This equality has since been experimentally validated (Liphardt *et al.*, 2002) by measuring the free-energy difference of a single RNA molecule stretched by holding one end of the molecule stationary using a force-measuring optical trap and pulling at the other end using a micropippette.

Here we propose a novel application of the Jarzynski equality (Jarzynski, 1997, 2007) and show that by focussing on measuring the dissipation associated with stretching a macromolecule rather than on obtaining the free-energy difference, a quantitative measure of the internal friction can be obtained. The JE has been routinely employed for reconstructing the free energy landscape of biomolecules from experiments (Harris *et al.*, 2007; Gupta *et al.*, 2011) and simulations (Hummer and Szabo, 2010; Hodges *et al.*, 2016), while dissipation has largely been ignored (except for estimating the accuracy of the free-energy difference (Ritort *et al.*, 2002; Jarzynski, 2006; Yunger Halpern and Jarzynski, 2016)). In the proposed protocol, multiple realizations of the pulling experiment are performed and the JE is used to extract both the free-energy difference and the average dissipated work at finite pulling rates. Prior studies (Murayama *et al.*, 2007; Alexander-Katz *et al.*, 2009; Schulz *et al.*, 2015a) estimate ΔA from the work done in the quasi-static limit (Callen, 1985) and calculate $\langle W_{\text{dis}} \rangle$ at finite pulling rates by subtracting ΔA from the total work done, rather than estimating both components of work simultaneously, as is done here.

In essence, the proposed protocol consists of calculating $\langle W_{\text{dis}} \rangle$ at fixed values of both the pulling velocity v and distance d over which the molecule is stretched, but at various values of η_s. The value in the limit $\eta_s \to 0$, $\langle W_{\text{dis}} \rangle_{\eta_s \to 0}$, is then obtained by extrapolation. By repeating this process for a number of values of v and plotting the ratio $\langle W_{\text{dis}} \rangle_{\eta_s \to 0} /d$ as a function of v, the internal friction coefficient can be determined from the slope of the linear region at sufficiently small velocities. Clearly, dry internal friction corresponds to cases where $\langle W_{\text{dis}} \rangle_{\eta_s \to 0}$ is non-zero, while wet friction is indicated when it is zero. In the latter case, the protocol measures the enhancement in friction at any finite value of η_s.

The validity of the proposed protocol is established for both types of internal friction using coarse-grained polymer models. Additionally, since hydrodynamic interactions (HI) are known to affect the dynamic response of polymers (Prabhakar and Prakash, 2002;

Sunthar and Prakash, 2005; Larson, 2005; Schroeder, 2018; Prakash, 2019), the effect of HI on dissipated work is also examined.

For dry internal friction, a spring-dashpot model (Kuhn and Kuhn, 1945; Manke and Williams, 1985; Khatri and McLeish, 2007; Samanta and Chakrabarti, 2016) is considered where the molecule is represented as massless beads connected by a spring and dashpot in parallel with each other. The spring accounts for entropic elasticity, while dissipative effects due to internal friction are captured by the dashpot (Bird *et al.*, 1987b). The drag on the beads is responsible for solvent friction. By its very construction, this model describes dry internal friction, as the dashpot contributes to dissipation even in the limit of $\eta_s \to 0$. Within this framework, two examples are considered. In the first case, the work distribution for a free-draining Hookean spring-dashpot model subjected to constant-velocity pulling is analytically calculated. In the second case, pulling simulations on a nonlinear-spring-dashpot model with fluctuating HI are performed using Brownian dynamics (BD). In both these cases, it is demonstrated that the internal friction coefficient estimated from $\langle W_{\text{dis}} \rangle$ in the limit $\eta_s \to 0$ is identical to the damping coefficient of the dashpot, which is a model input parameter, thereby establishing the validity of the proposed protocol. It is also shown that HI does not affect $\langle W_{\text{dis}} \rangle$.

For wet internal friction, a bead-spring chain with cohesive interactions between the beads is considered. A similar model was used by Netz and coworkers (Alexander-Katz *et al.*, 2009) to compare simulated values of internal friction with experimental data on force-induced unraveling of collapsed DNA (Murayama *et al.*, 2007). By using Zwanzig's interpretation (Zwanzig, 1988) to estimate energy landscape roughness due to cohesive interactions, they implicitly assume wet internal friction. Using our protocol, it is established directly that the internal friction due to cohesive interactions in this coarse-grained polymer model is wet in nature. Further, it is observed that while HI reduces the total resistance to pulling, the enhancement in the friction coefficient remains unaffected.

The rest of the chapter is organized as follows. In Sec. 3.2, analytical calculations and Brownian dynamics simulations on a spring-dashpot model are presented. Sec. 3.3 covers the application of the protocol to pulling simulations on a single polymer chain with cohesive interactions between the beads. A discussion of the results and concluding remarks are provided in Sec. 3.4.

3.2   Dry internal friction

The work statistics of Rouse chains tethered at one end and subjected to various finite-rate pulling protocols at the other are analytically calculable (Speck and Seifert, 2004, 2005;

[Dhar, 2005; Varghese *et al.*, 2013) owing to the equilibrium configurational distribution function of such chains being a Gaussian. Since the inclusion of internal friction does not affect the configurational distribution of bead positions at equilibrium, we choose the simplest model with internal friction, which is essentially a one-dimensional Hookean spring-dashpot subjected to pulling [in Sec. 3.2.1], as the starting point of our efforts at validating the protocol presented in this chapter for the estimation of the internal friction coefficient. In Sec. 3.2.2, the more general case of a three-dimensional non-linear spring-dashpot with hydrodynamic interactions is considered which does not admit an analytical solution and is therefore solved numerically.

3.2.1   One-dimensional free draining Hookean spring-dashpot

The simple analytically tractable dumbbell model is shown in Fig. 3.1, with one bead, at r_1, fixed at the origin ($r_1 = 0$), and the other bead, at r_2, connected to a bead at χ which is indicative of the cantilever of an atomic force microscope (AFM), or the location of the optical trap. The dumbbell is suspended in an incompressible, Newtonian solvent of viscosity η_s. The bead radius is taken to be a, and its associated friction co-efficient given by $\zeta = 6\pi\eta_s a$. The bead at χ is manipulated using a pre-determined protocol, given by $\chi = \chi(t)$. The derivation presented here holds for arbitrary time-dependent manipulations of the free end of the polymer model, but in this section and for the rest of the chapter, we focus attention on the constant-velocity pulling protocol commonly encountered in single-molecule force spectroscopy (Harris *et al.*, 2007; Gupta *et al.*, 2011). All the springs considered in the present model are Hookean: the spring in parallel with the dashpot has a spring constant of H, whereas the spring connecting the spring-dashpot setup to the driven bead has a spring constant of $c_2 H$, where c_2 is an arbitrary positive constant. The damping coefficient of the dashpot is denoted by K. It is evident that the only degree-of-freedom in the system is r_2, which is allowed to execute stochastic motion. The Hamiltonian of the system is then written as

$$\mathcal{H} = \frac{H}{2}r_2^2 + \frac{c_2 H}{2}\left[r_2 - \chi(t)\right]^2 \tag{3.2}$$

We now present the steps for obtaining a governing equation for the motion of the bead at r_2. As described in Chapter 2, the Fokker-Planck equation for the configurational distribution function $\Psi(r_2, t)$ can be derived by combining a force balance on the beads with an equation of continuity in probability space (Bird *et al.*, 1987b). The force balance essentially states that the (i) the internal friction force due to the dashpot, (ii) the restoring force due to the finitely extensible spring, (iii) external forces (like the force due to the optical traps, in the present case), (iv) the random Brownian force due to bombardment by
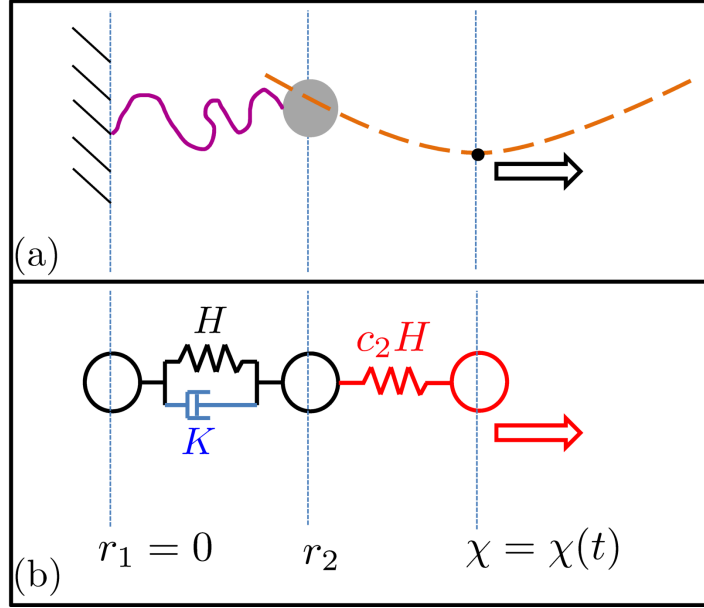
Figure 3.1: Schematic of a one-dimensional polymer model subjected to pulling. (a) A cartoon depicting a single polymer strand that is tethered to a surface at one end, and attached to a bead at the other end. The bead is under the influence of an optical tweezer whose position is varied in time according to a deterministic protocol. (b) Representation of the polymer as a single-mode spring-dashpot, connected to a bead that is manipulated by a predetermined protocol, $\chi(t)$. Internal friction is modeled using the dashpot, whose damping coefficient is K. The Hookean spring constant associated with the spring of the polymer is H, and that associated with the trap is $c_2 H$.

solvent molecules, and (v) the hydrodynamic force responsible for the solvent-mediated propagation of momentum on each bead, must sum up to zero. The force balance over the free bead may then be written as

$$0 = -\zeta [\![\dot{r}_2]\!] - \frac{\partial \mathcal{H}}{\partial r_2} - K [\![\dot{r}_2]\!] - k_B T \left(\frac{\partial \ln \Psi}{\partial r_2} \right) \tag{3.3}$$

Upon simplification,

$$\zeta [\![\dot{r}_2]\!] = -(c_2 + 1) H r_2 + c_2 H \chi(t) - K [\![\dot{r}_2]\!] - k_B T \left(\frac{\partial \ln \Psi}{\partial r_2} \right) \tag{3.4}$$

Grouping together the terms containing $[\![\dot{r}_2]\!]$, and defining $\varrho \equiv [1 + (K/\zeta)] = (1 + \varphi)$,

$$[\![\dot{r}_2]\!] = -\frac{(c_2 + 1) H}{\zeta \varrho} r_2 + \frac{c_2 H}{\zeta \varrho} \chi(t) - \frac{k_B T}{\zeta \varrho} \left(\frac{\partial \ln \Psi}{\partial r_2} \right) \tag{3.5}$$

The equation of continuity for the probability density, $\Psi(r_2, t)$, is written as

$$\frac{\partial \Psi}{\partial t} = -\frac{\partial}{\partial r_2} \left([\![\dot{r}_2]\!] \Psi \right) \tag{3.6}$$

Substituting the expression for $[\![\dot{r}_2]\!]$ from Eq. (3.5) into Eq. (3.6), one obtains

$$\frac{\partial \Psi}{\partial t} = -\frac{\partial}{\partial r_2} \left\{ \left[\frac{-(c_2 + 1) H}{\zeta \varrho} r_2 + \frac{c_2 H}{\zeta \varrho} \chi(t) \right] \Psi \right\} + \frac{1}{2} \left(\frac{2 k_B T}{\zeta \varrho} \right) \frac{\partial^2 \Psi}{\partial r_2^2} \qquad (3.7)$$

The stochastic differential equation corresponding to Eq. (3.7) is given by (Öttinger, 1996)

$$dr_2 = \left[\frac{-(c_2 + 1) H}{\zeta \varrho} r_2 + \frac{c_2 H}{\zeta \varrho} \chi(t) \right] dt + \sqrt{\frac{2 k_B T}{\zeta \varrho}} dW_t \qquad (3.8)$$

where W_t represents a Wiener process, and has dimensions of [time]$^{1/2}$. Eq. (3.8) can be recast in the Langevin form as

$$\frac{dr_2}{dt} = -\frac{(c_2 + 1) H}{\zeta \varrho} r_2 + \frac{c_2 H}{\zeta \varrho} \chi(t) + \sqrt{\frac{2 k_B T}{\zeta \varrho}} f_B(t) \qquad (3.9)$$

where $\langle f_B(t) \rangle = 0$ and $\langle f_B(t) f_B(t') \rangle = \delta(t - t')$, and $f_B(t)$ has dimensions of [time]$^{-1/2}$. For ease of algebra, it is convenient to work with non-dimensional variables until the need for dimensional variables arises. Setting $f_B^*(t^*) = f_B(t) \sqrt{\lambda_H}$, where $\langle f_B^*(t^*) \rangle = 0$ and $\langle f_B^*(t^*) f_B^*(t_1^*) \rangle = \delta(t^* - t_1^*)$, the variables in Eq. (3.9) are cast into their dimensionless form as,

$$\left(\frac{l_H}{\lambda_H} \right) \frac{dr_2^*}{dt^*} = -\frac{(c_2 + 1) H}{\zeta \varrho} r_2^* l_H + \frac{c_2 H}{\zeta \varrho} \chi^*(t^*) l_H + \sqrt{\frac{2 k_B T}{\zeta \varrho}} \left(\frac{f_B^*(t^*)}{\sqrt{\lambda_H}} \right) \qquad (3.10)$$

Multiplying Eq. (3.10) throughout by (λ_H / l_H), and simplifying, the dimensionless Langevin equation is

$$\frac{dr_2^*}{dt^*} = -\frac{(c_2 + 1) H}{4 \varrho} r_2^* + \frac{c_2 \chi^*(t^*)}{4 \varrho} + \frac{1}{\varrho} \sqrt{\frac{\varrho}{2}} f_B^*(t^*) \qquad (3.11)$$

which may be rewritten as

$$\frac{dr_2^*}{dt^*} = -\frac{E r_2^*}{\varrho} + \frac{c_2 \chi^*(t^*)}{4 \varrho} + \frac{1}{\varrho} \xi(t^*) \qquad (3.12)$$

where $E = [(c_2 + 1) / 4]$, and the noise term, $\xi(t^*)$, obeys $\langle \xi(t^*) \rangle = 0$ and

$$\langle \xi(t^*) \xi(t_1^*) \rangle = \frac{\varrho}{2} \delta(t^* - t_1^*) \qquad (3.13)$$

The solution to Eq. (3.12) is given by

$$r_2^*(t^*) = r_2^*(0) G(t^*) + \frac{1}{\varrho} \int_0^{t^*} dt_1^* G(t^* - t_1^*) \left(\frac{c_2 \chi^*(t_1^*)}{4} + \xi(t_1^*) \right) \qquad (3.14)$$

where $G(t^*) = e^{-E t^* / \varrho}$.

The work done during one realization of the pulling performed in the interval $[0, \tau]$ is (Hodges *et al.*, 2016; Chaki and Chakrabarti, 2018)

$$
\begin{aligned}
W &= \int_0^\tau \frac{\partial \mathcal{H}}{\partial t} \, dt = \int_0^\tau \frac{\partial \mathcal{H}}{\partial \chi} \dot{\chi} \, dt \\
&= \int_0^\tau c_2 H \left(\chi(t) - r_2 \right) \dot{\chi}(t) \, dt \\
&= k_B T \left[c_2 \int_0^{\tau^*} \left(\chi^*(t^*) - r_2^* \right) \dot{\chi}^*(t^*) \, dt^* \right]
\end{aligned}
\tag{3.15}
$$

and the dimensionless work, $W^* = W/k_B T$, is then

$$
W^* = \frac{c_2}{2} \left[\chi^{2*}(\tau^*) - \chi^{2*}(0) \right] - c_2 \int_0^{\tau^*} dt^* \dot{\chi}^*(t^*) \, r_2^*
\tag{3.16}
$$

Upon substituting the expression for r_2^* from Eq. (3.14) into Eq. (3.16), one obtains

$$
W^* = \frac{c_2}{2} \left[\chi^{2*}(\tau^*) - \chi^{2*}(0) \right] - c_2 \int_0^{\tau^*} dt^* \dot{\chi}^*(t^*) \left(r_2^*(0) G(t^*) + \frac{c_2}{4\varrho} \int_0^{t^*} dt_1^* G(t^* - t_1^*) \chi^*(t_1^*) \right.
$$
$$
\left. + \frac{1}{\varrho} \int_0^{t^*} dt_1^* G(t^* - t_1^*) \xi(t_1^*) \right)
$$

$$\tag{3.17}$$

It is clear that the distribution of W^* ought also be Gaussian, since W^* is linear in $r_2^*(0)$ and $\xi(t^*)$, both of which are Gaussian variables. It therefore suffices to evaluate the mean and variance of W^* in order to completely determine the distribution. There is only one bead that is allowed to move freely in this problem, and as a result, the dimensionless free-energy, $A^* = -\ln \mathcal{Z}^*$, can be obtained once the dimensionless partition function, $\mathcal{Z}^*$ is known.

The dimensionless partition function of the system can be derived to be,

$$
\mathcal{Z}^* \equiv \int_{-\infty}^{+\infty} \exp \left[-\frac{\mathcal{H}}{k_B T} \right] dr_2^* = \sqrt{\frac{2\pi}{(c_2 + 1)}} \exp \left(-\frac{c_2 \chi^{*2}}{2(c_2 + 1)} \right)
\tag{3.18}
$$

and the dimensionless free-energy, $A^* = -\ln \mathcal{Z}^*$, is then simply

$$
A^*(\chi^*) = \left[\frac{c_2}{2(c_2 + 1)} \right] \chi^{2*},
\tag{3.19}
$$

after ignoring constant prefactors. The probability distribution function for the position of the bead is given by

$$
\Psi^*(r_2^*) \equiv \frac{1}{\mathcal{Z}^*} \exp \left[-\frac{\mathcal{H}}{k_B T} \right] = \left(\frac{c_2 + 1}{2\pi} \right)^{1/2} \exp \left\{ -\frac{1}{2} (c_2 + 1) \left[r_2^* - \left(\frac{c_2 \chi^*}{c_2 + 1} \right) \right]^2 \right\}
\tag{3.20}
$$

and the moments of the distribution are

$$\langle r_2^* \rangle = \frac{c_2 \chi^*}{c_2 + 1} \tag{3.21}$$

$$\left\langle (r_2^* - \langle r_2^* \rangle)^2 \right\rangle = \frac{1}{c_2 + 1} \tag{3.22}$$

The expression for the average work is obtained by taking an ensemble average of Eq. (3.17),

$$\langle W^* \rangle = \frac{c_2}{2} \left[\chi^{2*}(\tau^*) - \chi^{2*}(0) \right] - c_2 \int_0^{\tau^*} dt^* \dot{\chi}^*(t^*) \left[G(t^*) \langle r_2^*(0) \rangle + \frac{c_2}{4\varrho} \int_0^{t^*} dt_1^* G(t^* - t_1^*) \chi^*(t_1^*) \right] \tag{3.23}$$

Substituting Eq. (3.21) into the second term on the RHS of Eq. (3.23),

$$\langle W^* \rangle = \frac{c_2}{2} \left[\chi^{2*}(\tau^*) - \chi^{2*}(0) \right] - \frac{c_2^2}{c_2 + 1} \chi^*(0) \int_0^{\tau^*} dt^* \dot{\chi}^*(t^*) G(t^*)$$

$$- \frac{c_2^2}{4\varrho} \int_0^{\tau^*} dt^* \dot{\chi}^*(t^*) \underline{\int_0^{t^*} dt_1^* G(t^* - t_1^*) \chi^*(t_1^*)} \tag{3.24}$$

The underlined term is simplified as

$$\int_0^{t^*} dt_1^* G(t^* - t_1^*) \chi^*(t_1^*) = \int_0^{t^*} dt_1^* \exp\left[-\frac{E(t^* - t_1^*)}{\varrho} \right] \chi^*(t_1^*)$$

$$= \int_0^{t^*} dt_1^* \chi^*(t_1^*) \frac{d}{dt_1^*} \left(\varrho E^{-1} \exp\left[-\frac{E(t^* - t_1^*)}{\varrho} \right] \right) \tag{3.25}$$

Integrating expression on the RHS of Eq. (3.25) by parts,

$$\int_0^{t^*} dt_1^* G(t^* - t_1^*) \chi^*(t_1^*) = \left[\chi^*(t_1^*) \varrho E^{-1} \exp\left[-\frac{E(t^* - t_1^*)}{\varrho} \right] \right]_0^{t^*}$$

$$- \int_0^{t^*} dt_1^* \dot{\chi}^*(t_1^*) \varrho E^{-1} \exp\left[-\frac{E(t^* - t_1^*)}{\varrho} \right] \tag{3.26}$$

one obtains,

$$\int_0^{t^*} dt_1^* G(t^* - t_1^*) \chi^*(t_1^*) = \left[\chi^*(t^*) \varrho E^{-1} \right] - \left[\chi^*(0) \varrho E^{-1} \exp\left[-\frac{Et^*}{\varrho} \right] \right]$$

$$- \int_0^{t^*} dt_1^* \dot{\chi}^*(t_1^*) \varrho E^{-1} \exp\left[-\frac{E(t^* - t_1^*)}{\varrho} \right] \tag{3.27}$$

which can then be written as

$$\int_0^{t^*} dt_1^* G(t^* - t_1^*) \chi^*(t_1^*) = \varrho E^{-1} \left\{ \chi^*(t^*) - \chi^*(0) G(t^*) - \int_0^{t^*} dt_1^* \dot{\chi}^*(t_1^*) G(t^* - t_1^*) \right\} \tag{3.28}$$

Substituting Eq. (3.28) into Eq. (3.24) and simplifying,

$$\langle W^* \rangle = \frac{c_2}{2}\left[\chi^{2*}(\tau^*) - \chi^{2*}(0)\right] - \frac{c_2^2}{c_2+1}\chi^*(0)\int_0^{\tau^*} dt^*\dot{\chi}^*(t^*)G(t^*) - \frac{c_2^2}{c_2+1}\int_0^{\tau^*} dt^*\dot{\chi}^*(t^*)\chi^*(t^*)$$

(3.29)

$$+ \frac{c_2^2}{c_2+1}\chi^*(0)\int_0^{\tau^*} dt^*\dot{\chi}^*(t^*)G(t^*) + \frac{c_2^2}{c_2+1}\int_0^{\tau^*} dt^*\int_0^{t^*} dt_1^*\dot{\chi}^*(t^*)G(t^*-t_1^*)\dot{\chi}^*(t_1^*)$$

one obtains

$$\langle W^* \rangle = \left(\frac{c_2}{2(c_2+1)}\right)\left[\chi^{2*}(\tau^*) - \chi^{2*}(0)\right] + \frac{c_2^2}{c_2+1}\int_0^{\tau^*} dt^*\int_0^{t^*} dt_1^*\dot{\chi}^*(t^*)G(t^*-t_1^*)\dot{\chi}^*(t_1^*)$$

(3.30)

Recognizing that the first term on the RHS of Eq. (3.30) is the free-energy difference, $\Delta A^* \equiv A^*\left[\chi^*(\tau^*)\right] - A^*\left[\chi^*(0)\right]$, with A given by Eq. (3.19), the expression for the average work can be rewritten as

$$\langle W^* \rangle = \Delta A^* + \frac{c_2^2}{c_2+1}\int_0^{\tau^*} dt^*\int_0^{t^*} dt_1^*\left[\dot{\chi}^*(t^*)G(t^*-t_1^*)\dot{\chi}^*(t_1^*)\right]$$

(3.31)

Using Eqs. (3.17) and (3.23), the variance of the work distribution, $\sigma^2 = \left\langle (W^* - \langle W^* \rangle)^2 \right\rangle$, is written as,

$$\sigma^2 = c_2^2 \int_0^{\tau^*} dt^*\int_0^{\tau^*} dt_1^*\dot{\chi}^*(t^*)G(t^*)\underline{\left[\left\langle (r_2^*(0) - \langle r_2^*(0)\rangle)^2\right\rangle\right]}G(t_1^*)\dot{\chi}^*(t_1^*)$$

(3.32)

$$+ \frac{c_2^2}{\varrho^2}\int_0^{\tau^*} dt_1^*\int_0^{t_1^*} d\widetilde{t_1^*}\int_0^{\tau^*} dt_2^*\int_0^{t_2^*} d\widetilde{t_2^*}\dot{\chi}^*(t_1^*)G(t_1^*-\widetilde{t_1^*})\underline{\left\langle \xi(\widetilde{t_1^*})\xi(\widetilde{t_2^*})\right\rangle}\dot{\chi}^*(t_2^*)G(t_2^*-\widetilde{t_2^*}),$$

Eqs. (3.22) and (3.13) can be used to simplify the underlined terms in Eq. (3.32), and we obtain,

$$\sigma^2 = \frac{c_2^2}{c_1+1}\int_0^{\tau^*} dt^*\int_0^{\tau^*} dt_1^*\dot{\chi}^*(t^*)G(t^*)G(t_1^*)\dot{\chi}^*(t_1^*)$$

(3.33)

$$+ \frac{c_2^2}{2\varrho}\int_0^{\tau^*} dt_1^*\int_0^{t_1^*} d\widetilde{t_1^*}\int_0^{\tau^*} dt_2^*\int_0^{t_2^*} d\widetilde{t_2^*}\dot{\chi}^*(t_1^*)G(t_1^*-\widetilde{t_1^*})\delta\left(\widetilde{t_1^*}-\widetilde{t_2^*}\right)\dot{\chi}^*(t_2^*)G(t_2^*-\widetilde{t_2^*})$$

Subsequent integration over $\widetilde{t_1^*}$ in the second integral yields

$$\sigma^2 = \frac{c_2^2}{c_2+1}\int_0^{\tau^*} dt^*\int_0^{\tau^*} dt_1^*\dot{\chi}^*(t^*)G(t^*)G(t_1^*)\dot{\chi}^*(t_1^*)$$

$$+ \frac{c_2^2}{2\varrho}\int_0^{\tau^*} dt_1^*\int_0^{\tau^*} dt_2^*\int_0^{t_2^*} d\widetilde{t_2^*}\dot{\chi}^*(t_1^*)\dot{\chi}^*(t_2^*)G(t_1^*-\widetilde{t_2^*})G(t_2^*-\widetilde{t_2^*})$$

(3.34)

The following identity

$$\int_0^{t_2^*} d\widetilde{t_2^*}\,G(t_1^*-\widetilde{t_2^*})G(t_2^*-\widetilde{t_2^*}) = \left(\frac{2\varrho}{c_2+1}\right)\left[G(t_1^*-t_2^*) - G(t_1^*)G(t_2^*)\right]$$

(3.35)

can be used used to simplify the second term on the RHS of Eq. (3.34), resulting in the following expression for the variance of the work distribution

$$\sigma^2 = \frac{2c_2^2}{(c_2 + 1)} \int_0^{\tau^*} dt^* \int_0^{t^*} dt_1^* \dot{\chi}^*(t^*) G(t^* - t_1^*) \dot{\chi}^*(t_1^*) \tag{3.36}$$

From Eqs. (3.31) and (3.36), it is readily seen that

$$\langle W^* \rangle = \Delta A^* + \frac{\sigma^2}{2} \tag{3.37}$$

and the average dissipated work is given by

$$\langle W_{\text{dis}}^* \rangle \equiv \langle W^* \rangle - \Delta A^* = \frac{\sigma^2}{2} \tag{3.38}$$

It follows that the probability distribution of work is given by

$$P^*(W^*) = \frac{1}{\sqrt{2\pi\sigma^2}} \exp\left[-\frac{(W^* - \langle W^* \rangle)^2}{2\sigma^2}\right] \tag{3.39}$$

The quantities $\langle W^* \rangle$, ΔA^*, and $\langle W_{\text{dis}}^* \rangle$ have been calculated analytically without explicit recourse to the Jarzynski equality. This is a consequence of the governing equation being linear in the position variable and the noise term, resulting in a Gaussian distribution of the work trajectories. The Jarzynski's equality is satisfied trivially for such systems, since

$$\langle \exp(-W^*) \rangle = \int_{-\infty}^{+\infty} \exp(-W^*) P^*(W^*) dW^*$$

$$= \exp(-\Delta A^*) \tag{3.40}$$

which has also been reported previously (Jarzynski, 1997; Speck and Seifert, 2004).

The development so far is applicable to any arbitrary pulling protocol, $\chi^*(t^*)$. The particular value of the average dissipation is dependent on the protocol used to transition the system between its initial and final states. We now consider the special case of constant velocity pulling. Within this framework, $\chi^*(t^*) = \chi^{(\text{i})*} + (d^* t^*/\tau^*)$, implying that the last bead is moved across a distance d^* over a time τ^*, with a dimensionless pulling velocity given by $\dot{\chi}^*(t^*) = v^* = d^*/\tau^*$. $\chi^{(\text{i})*}$ and $\chi^{(\text{f})*}$ represent the position of the last bead at $t^* = 0$ and $t^* = \tau^*$ respectively. Under this protocol, the free energy difference, ΔA^*, is given by

$$\Delta A^* = \frac{c_2}{2(c_2 + 1)} \left[\left(\chi^{*(\text{f})}\right)^2 - \left(\chi^{*(\text{i})}\right)^2\right], \tag{3.41}$$

and the average dissipated work can be evaluated to be

$$\langle W_{\text{dis}}^* \rangle = 4\left(\frac{c_2}{c_2 + 1}\right)^2 \varrho\, v^* d^* + 16\left(\frac{c_2^2}{(c_2 + 1)^3}\right)\varrho^2 v^{*2}\left[\exp\left(-\frac{(c_2 + 1)d^*}{4v^*\varrho}\right) - 1\right] \tag{3.42}$$

It is now appropriate to obtain the expression for the average dissipated work in the limit of zero solvent friction. Since the solvent friction is absorbed into the definition of the timescale, it is first necessary to convert all quantities in Eq. (3.42) to their dimensional form, before taking the limit. Using the non-dimensionalization scheme discussed previously in Chapter 2, we obtain

$$\langle W \rangle_{\text{dis}} = \left(\frac{c_2}{c_2 + 1} \right)^2 (\zeta + K) \, vd + \frac{c_2^2}{(c_2 + 1)^3} \frac{(\zeta + K)^2 \, v^2}{H} \left[\exp \left(-\frac{H (c_2 + 1) \, d}{(\zeta + K) \, v} \right) - 1 \right] \quad (3.43)$$

In the extrapolated limit of zero solvent friction, $\zeta \to 0$ by definition of the bead-friction coefficient. Upon taking this limit in Eq. (3.43),

$$\langle W \rangle_{\text{dis}, \eta_s \to 0} = \left(\frac{c_2}{c_2 + 1} \right)^2 Kvd + \frac{c_2^2}{(c_2 + 1)^3} \frac{K^2 v^2}{H} \left[\exp \left(-\frac{H (c_2 + 1) \, d}{Kv} \right) - 1 \right] \quad (3.44)$$

In the limit of high pulling trap stiffness ($c_2 \gg 1$), the second term on the RHS of Eq. (3.44) vanishes, and the parenthesized prefactor in the first term asymptotically tends to unity, leading to

$$\frac{\langle W \rangle_{\text{dis}, \eta_s \to 0}}{d} = Kv, \quad (3.45)$$

Clearly, the proposed protocol for determining the internal friction coefficient based on the Jarzynski equality recovers the damping coefficient K, establishing its validity in the case of the simple analytical model considered here.

3.2.2 Non-linear spring-dashpot with hydrodynamic interactions

Model description

In the more general case, a dumbbell model with fluctuating internal friction and hydrodynamic interactions is considered, as shown in Fig. 3.2 (a). The beads, each of radius a, are joined by a spring, with maximum stretchability Q_0 and a Hookean spring constant H, in parallel with a dashpot of damping coefficient K. The entropic elasticity in the dumbbell is described by the Marko-Siggia potential, as given in Equation (2.11) in Chapter 2. The positions of the two beads are r_1 and r_2, the connector vector joining the two beads is denoted by $Q \equiv r_2 - r_1$, and the position of the centre of mass by $r_c \equiv (1/2) (r_1 + r_2)$. Note that while the bead co-ordinates are allowed to sample the entirety of the three-dimensional coordinate space, the pulling is restricted to the x-axis alone. An alternative protocol in which the pulling direction is also in general three-dimensional space can be implemented, but this would not alter the analysis and arguments presented here. The positions of the two beads can be manipulated using
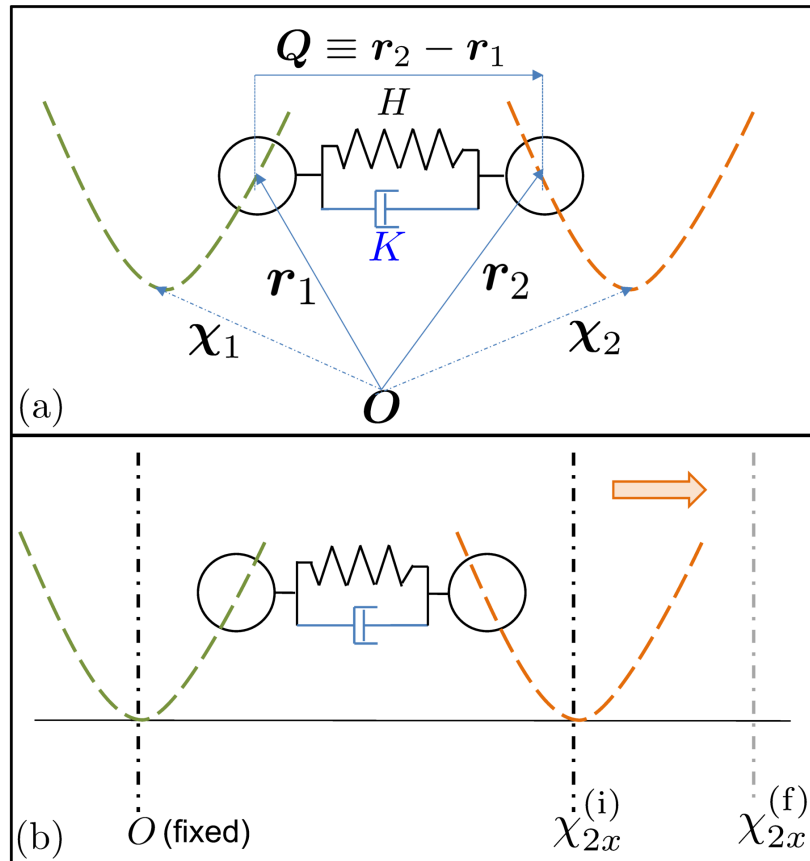
Figure 3.2: Schematic of the proposed simulation/experiment. (a) Schematic diagram of the coarse-grained polymer model entrapped between two optical tweezers. The spring connecting the two beads is finitely extensible, upto a length Q_0. Internal friction is modelled using the dashpot, whose damping coefficient is K. The Hookean spring constant associated with the spring is H. The strengths of the two traps, modelled as Harmonic potential wells, are $H_1 = c_1 H$ and $H_2 = c_2 H$. (b) The one-dimensional pulling protocol : the position of the first trap is taken to be the origin, and remains stationary throughout the experiment. The second trap is moved from its initial position, $\chi_{2x}^{(i)}$ to its final position, $\chi_{2x}^{(f)}$, over a time-interval τ, stretching the spring-dashpot setup in the process. The difference between the initial and the final positions of the mobile trap is d, and the velocity of pulling is v_x.

optical traps, modelled here as harmonic potential wells. The trap stiffnesses are denoted by $H_1 = c_1 H$, and $H_2 = c_2 H$ (in units of the dumbbell spring constant), and the co-ordinates of the minimum of the wells are represented by χ_1 and χ_2, respectively. A temperature of $T = 300\,K$ is considered in all our simulations, as a matter of convenience. The viscosity of the solvent at this temperature is taken to be $\eta_{s,0} = 0.001$ kg/m s, which is close to the viscosity of water at room temperature. In this protocol, values of solvent viscosity which are multiples of $\eta_{s,0}$ will be considered.

In Fig. 3.2 (b), the pulling protocol employed in this study is depicted. Without any loss of generality, χ_1 is chosen as the origin of our frame of reference. In all pulling simulations throughout this work, the first trap is held stationary, and the second trap is moved from its initial position, $\chi_2^{(i)} \equiv (\chi_{2x}^{(i)}, 0, 0)$, to its final position, $\chi_2^{(f)} \equiv (\chi_{2x}^{(f)}, 0, 0)$. The notation "$\chi_{2x}^{(i)} \to \chi_{2x}^{(f)}$" represents such a pulling event. The stretching distance is denoted by $d \equiv \left[\chi_{2x}^{(f)} - \chi_{2x}^{(i)} \right]$, the time interval for stretching by τ, and the pulling velocity by $\boldsymbol{v} \equiv (v_x, 0, 0)$, where $v_x = d/\tau$.

In the more general case, the Hamiltonian, $\mathcal{H}$, of the system for any value of the trap position, χ_2, is given by

$$\mathcal{H} = \phi_{MS}^{S}(\boldsymbol{Q}) + \frac{H_1}{2} r_1^2 + \frac{H_2}{2} (r_2 - \chi_2)^2 \tag{3.46}$$

where $\phi_{MS}^{S}(\boldsymbol{Q})$ represents the potential energy in the Marko-Siggia spring as given by Eq. 2.11 of Chapter 2. The generalized Jarzynski work corresponding to the pulling protocol discussed above is, in this case, given by

$$W = \int_0^\tau \left(\frac{\partial \mathcal{H}}{\partial \chi_2} \right) \cdot \boldsymbol{v}\, dt \tag{3.47}$$

where $\boldsymbol{v} = d\chi_2/dt$. The average dissipation associated with the stretching process is calculated using Jarzynski's equality as shown in Eq. (3.1).

Governing equations

The dumbbell model described in Figure 3.2 is suspended in a fluid where the velocity field at any location $\boldsymbol{r}_f$ is given by $\boldsymbol{v}_f(\boldsymbol{r}, t) \equiv \boldsymbol{v}_0 + \boldsymbol{\kappa}(t) \cdot \boldsymbol{r}_f$, where $\boldsymbol{v}_0$ is a constant vector, and $\boldsymbol{\kappa} \equiv (\nabla \boldsymbol{v}_f)^T$ is the transpose of the velocity gradient tensor. In the present work, both $\boldsymbol{v}_0$ and $\boldsymbol{\kappa}$ are set to $\boldsymbol{0}$ as the pulling experiments are simulated in a quiescent fluid. However, these terms have been included in the governing equations for the sake of generality. The configurational distribution function, $\Psi(\boldsymbol{Q}, \boldsymbol{r}_c, t)$, denotes the probability of finding the centre-of-mass of the dumbbell at a position between $\boldsymbol{r}_c$ and $\boldsymbol{r}_c + d\boldsymbol{r}_c$, with an extension that lies between $\boldsymbol{Q}$ and $\boldsymbol{Q} + d\boldsymbol{Q}$, at any time t.

The force balance on the beads can be solved to obtain the following equations of motion for the position vectors of the beads

$$
[\![\dot{\boldsymbol{r}}_1]\!] = \left[\boldsymbol{\delta} - \frac{\epsilon\beta}{\epsilon\beta + 2}\frac{\boldsymbol{Q}\boldsymbol{Q}}{Q^2}\right] \cdot \left(\boldsymbol{v}_0 + \boldsymbol{\kappa}\cdot\boldsymbol{r}_1 - \frac{1}{\zeta}\left(\boldsymbol{\delta} - \zeta\boldsymbol{\Omega}\right)\cdot\frac{\partial\phi_{\mathrm{MS}}^{\mathrm{S}}}{\partial\boldsymbol{r}_1} - \frac{k_B T}{\zeta}\left(\boldsymbol{\delta} - \zeta\boldsymbol{\Omega}\right)\cdot\frac{\partial\ln\Psi}{\partial\boldsymbol{r}_1}\right.
$$

$$
\left. + \frac{\epsilon}{2}\left(\boldsymbol{\delta} - \zeta\boldsymbol{\Omega}\right)\cdot\frac{\boldsymbol{Q}\boldsymbol{Q}}{Q^2}\cdot[\![\dot{\boldsymbol{r}}_2]\!] - \frac{H_1}{\zeta}\left(\boldsymbol{r}_1 - \boldsymbol{\chi}_1\right) - \boldsymbol{\Omega}\cdot H_2\left(\boldsymbol{r}_2 - \boldsymbol{\chi}_2\right)\right) \tag{3.48}
$$

and

$$
[\![\dot{\boldsymbol{r}}_2]\!] = \left[\boldsymbol{\delta} - \frac{\epsilon\beta}{\epsilon\beta + 2}\frac{\boldsymbol{Q}\boldsymbol{Q}}{Q^2}\right] \cdot \left(\boldsymbol{v}_0 + \boldsymbol{\kappa}\cdot\boldsymbol{r}_2 - \frac{1}{\zeta}\left(\boldsymbol{\delta} - \zeta\boldsymbol{\Omega}\right)\cdot\frac{\partial\phi_{\mathrm{MS}}^{\mathrm{S}}}{\partial\boldsymbol{r}_2} - \frac{k_B T}{\zeta}\left(\boldsymbol{\delta} - \zeta\boldsymbol{\Omega}\right)\cdot\frac{\partial\ln\Psi}{\partial\boldsymbol{r}_2}\right.
$$

$$
\left. + \frac{\epsilon}{2}\left(\boldsymbol{\delta} - \zeta\boldsymbol{\Omega}\right)\cdot\frac{\boldsymbol{Q}\boldsymbol{Q}}{Q^2}\cdot[\![\dot{\boldsymbol{r}}_1]\!] - \frac{H_2}{\zeta}\left(\boldsymbol{r}_2 - \boldsymbol{\chi}_2\right) - \boldsymbol{\Omega}\cdot H_1\left(\boldsymbol{r}_1 - \boldsymbol{\chi}_1\right)\right) \tag{3.49}
$$

where $\boldsymbol{\Omega}$ is the hydrodynamic interaction tensor, defined using the Rotne-Prager-Yamakawa (RPY) expression as described in Section 2.1.1 of Chapter 2. The quantity β that appears in Eqs. (3.48) and (3.49) is defined as

$$
\beta = 1 - \frac{h}{Q}\left(\mathscr{A} + \mathscr{B}\right) \tag{3.50}
$$

where $\mathscr{A}$ and $\mathscr{B}$ take the form given in Eq. (2.6) of Chapter 2. Using $\boldsymbol{r}_1 = \boldsymbol{r}_{\mathrm{c}} - (1/2)\boldsymbol{Q}$; $\boldsymbol{r}_2 = \boldsymbol{r}_{\mathrm{c}} + (1/2)\boldsymbol{Q}$, and the chain-rule for partial differentiation to operate on $\partial\Psi/\partial\boldsymbol{r}_1$ and $\partial\Psi/\partial\boldsymbol{r}_2$, leads to,

$$
[\![\dot{\boldsymbol{r}}_1]\!] = \boldsymbol{v}_0 + \boldsymbol{\kappa}\cdot\left(\boldsymbol{r}_{\mathrm{c}} - \frac{1}{2}\boldsymbol{Q}\right) + \boldsymbol{\Omega}\cdot\left(-k_B T\left[\frac{1}{2}\frac{\partial\ln\Psi}{\partial\boldsymbol{r}_{\mathrm{c}}} + \frac{\partial\ln\Psi}{\partial\boldsymbol{Q}}\right] - \frac{\partial\phi_{\mathrm{MS}}^{\mathrm{S}}}{\partial\boldsymbol{r}_2} - K\frac{\boldsymbol{Q}\boldsymbol{Q}}{Q^2}\cdot[\![\dot{\boldsymbol{Q}}]\!]\right.
$$

$$
\left. - H_2\left(\boldsymbol{r}_{\mathrm{c}} + \frac{1}{2}\boldsymbol{Q} - \boldsymbol{\chi}_2\right)\right) - \frac{k_B T}{\zeta}\left[\frac{1}{2}\frac{\partial\ln\Psi}{\partial\boldsymbol{r}_{\mathrm{c}}} - \frac{\partial\ln\Psi}{\partial\boldsymbol{Q}}\right] - \frac{1}{\zeta}\frac{\partial\phi_{\mathrm{MS}}^{\mathrm{S}}}{\partial\boldsymbol{r}_1} \tag{3.51}
$$

$$
+ \frac{\epsilon}{2}\frac{\boldsymbol{Q}\boldsymbol{Q}}{Q^2}\cdot[\![\dot{\boldsymbol{Q}}]\!] - \frac{H_1}{\zeta}\left(\boldsymbol{r}_{\mathrm{c}} - \frac{1}{2}\boldsymbol{Q} - \boldsymbol{\chi}_1\right)
$$

and

$$
[\![\dot{\boldsymbol{r}}_2]\!] = \boldsymbol{v}_0 + \boldsymbol{\kappa}\cdot\left(\boldsymbol{r}_{\mathrm{c}} + \frac{1}{2}\boldsymbol{Q}\right) + \boldsymbol{\Omega}\cdot\left(-k_B T\left[\frac{1}{2}\frac{\partial\ln\Psi}{\partial\boldsymbol{r}_{\mathrm{c}}} - \frac{\partial\ln\Psi}{\partial\boldsymbol{Q}}\right] - \frac{\partial\phi_{\mathrm{MS}}^{\mathrm{S}}}{\partial\boldsymbol{r}_1} + K\frac{\boldsymbol{Q}\boldsymbol{Q}}{Q^2}\cdot[\![\dot{\boldsymbol{Q}}]\!]\right.
$$

$$
\left. - H_1\left(\boldsymbol{r}_{\mathrm{c}} - \frac{1}{2}\boldsymbol{Q} - \boldsymbol{\chi}_1\right)\right) - \frac{k_B T}{\zeta}\left[\frac{1}{2}\frac{\partial\ln\Psi}{\partial\boldsymbol{r}_{\mathrm{c}}} + \frac{\partial\ln\Psi}{\partial\boldsymbol{Q}}\right] - \frac{1}{\zeta}\frac{\partial\phi_{\mathrm{MS}}^{\mathrm{S}}}{\partial\boldsymbol{r}_2} \tag{3.52}
$$

$$
+ \frac{\epsilon}{2}\frac{\boldsymbol{Q}\boldsymbol{Q}}{Q^2}\cdot[\![\dot{\boldsymbol{Q}}]\!] - \frac{H_2}{\zeta}\left(\boldsymbol{r}_{\mathrm{c}} + \frac{1}{2}\boldsymbol{Q} - \boldsymbol{\chi}_2\right)
$$

By adding and subtracting Eqs. (3.51) and (3.52) suitably, we obtain

$$
[\![\dot{\boldsymbol{r}}_{\mathrm{c}}]\!] = \boldsymbol{v}_0 + \boldsymbol{\kappa}\cdot\boldsymbol{r}_{\mathrm{c}} - \frac{k_B T}{2\zeta}\left(\boldsymbol{\delta} + \zeta\boldsymbol{\Omega}\right)\cdot\frac{\partial\ln\Psi}{\partial\boldsymbol{r}_{\mathrm{c}}} - \frac{1}{2\zeta}\left(\boldsymbol{\delta} + \zeta\boldsymbol{\Omega}\right)\cdot\boldsymbol{X} \tag{3.53}
$$

$$\llbracket \dot{\boldsymbol{Q}} \rrbracket = \left[\boldsymbol{\delta} - \frac{\epsilon\beta}{\epsilon\beta + 1} \frac{\boldsymbol{Q}\boldsymbol{Q}}{Q^2} \right] \cdot \left(\boldsymbol{\kappa} \cdot \boldsymbol{Q} - \frac{2k_BT}{\zeta} (\boldsymbol{\delta} - \zeta\boldsymbol{\Omega}) \cdot \frac{\partial}{\partial \boldsymbol{Q}} \ln \Psi \right.$$

$$\left. - \frac{2}{\zeta} (\boldsymbol{\delta} - \zeta\boldsymbol{\Omega}) \cdot \frac{\partial \phi_{\mathrm{MS}}^{\mathrm{S}}}{\partial \boldsymbol{Q}} - \frac{1}{\zeta} (\boldsymbol{\delta} - \zeta\boldsymbol{\Omega}) \cdot \boldsymbol{Y} \right) \tag{3.54}$$

where

$$\boldsymbol{X} = \boldsymbol{r}_{\mathrm{c}} (H_2 + H_1) + \boldsymbol{Q} \left(\frac{H_2 - H_1}{2} \right) - (H_2 \boldsymbol{\chi}_2 + H_1 \boldsymbol{\chi}_1)$$

and

$$\boldsymbol{Y} = \boldsymbol{r}_{\mathrm{c}} (H_2 - H_1) + \boldsymbol{Q} \left(\frac{H_2 + H_1}{2} \right) - (H_2 \boldsymbol{\chi}_2 - H_1 \boldsymbol{\chi}_1)$$

and both $\boldsymbol{X}$ and $\boldsymbol{Y}$ have dimensions of force.

The equation of continuity in terms of $\boldsymbol{r}_{\mathrm{c}}$ and $\boldsymbol{Q}$ is given by (Bird *et al.*, 1987b),

$$\frac{\partial \Psi}{\partial t} = - \left(\frac{\partial}{\partial \boldsymbol{r}_{\mathrm{c}}} \cdot \llbracket \dot{\boldsymbol{r}}_{\mathrm{c}} \rrbracket \Psi \right) - \left(\frac{\partial}{\partial \boldsymbol{Q}} \cdot \llbracket \dot{\boldsymbol{Q}} \rrbracket \Psi \right) \tag{3.55}$$

Substituting Eqs. (3.53) and (3.54) into the above expression leads to the Fokker-Planck equation that governs the configurational distribution function $\Psi(\boldsymbol{Q}, \boldsymbol{r}_{\mathrm{c}}, t)$,

$$\frac{\partial \Psi}{\partial t} = - \frac{\partial}{\partial \boldsymbol{r}_{\mathrm{c}}} \cdot \left\{ \left[\boldsymbol{v}_0 + \boldsymbol{\kappa} \cdot \boldsymbol{r}_{\mathrm{c}} - \frac{1}{2\zeta} (\boldsymbol{\delta} + \zeta\boldsymbol{\Omega}) \cdot \boldsymbol{X} \right] \Psi \right\} + \frac{k_BT}{2\zeta} \frac{\partial}{\partial \boldsymbol{r}_{\mathrm{c}}} \cdot (\boldsymbol{\delta} + \zeta\boldsymbol{\Omega}) \cdot \frac{\partial \Psi}{\partial \boldsymbol{r}_{\mathrm{c}}}$$

$$- \frac{\partial}{\partial \boldsymbol{Q}} \cdot \left\{ \left[\left[\boldsymbol{\delta} - \frac{\epsilon\beta}{\epsilon\beta + 1} \frac{\boldsymbol{Q}\boldsymbol{Q}}{Q^2} \right] \cdot \left(\boldsymbol{\kappa} \cdot \boldsymbol{Q} - \frac{2}{\zeta} (\boldsymbol{\delta} - \zeta\boldsymbol{\Omega}) \cdot \frac{\partial \phi_{\mathrm{MS}}^{\mathrm{S}}}{\partial \boldsymbol{Q}} - \frac{1}{\zeta} (\boldsymbol{\delta} - \zeta\boldsymbol{\Omega}) \cdot \boldsymbol{Y} \right) \right] \Psi \right\}$$

$$+ \frac{2k_BT}{\zeta} \frac{\partial}{\partial \boldsymbol{Q}} \cdot \left[\left(\boldsymbol{\delta} - \frac{\epsilon\beta}{\epsilon\beta + 1} \frac{\boldsymbol{Q}\boldsymbol{Q}}{Q^2} \right) \cdot (\boldsymbol{\delta} - \zeta\boldsymbol{\Omega}) \right] \cdot \frac{\partial \Psi}{\partial \boldsymbol{Q}} \tag{3.56}$$

We define the following dimensionless quantities,

$$t^* = \frac{t}{\lambda_{\mathrm{H}}}; \ \boldsymbol{Q}^* = \frac{\boldsymbol{Q}}{l_{\mathrm{H}}}; \ b = \frac{Q_0^2}{l_{\mathrm{H}}^2}; \ \boldsymbol{\kappa}^* = \lambda_{\mathrm{H}}\boldsymbol{\kappa}; \ \phi_{\mathrm{MS}}^{*\mathrm{S}} = \frac{\phi_{\mathrm{MS}}^{\mathrm{S}}}{k_BT}; \ \Psi^* = \Psi l_{\mathrm{H}}^3; \ \boldsymbol{X}^* = \frac{\boldsymbol{X}}{\sqrt{k_BTH}} \tag{3.57}$$

In terms of these non-dimensional variables, the Fokker-Planck equation assumes the following form,

$$\frac{\partial \Psi^*}{\partial t^*} = - \frac{\partial}{\partial \boldsymbol{r}_{\mathrm{c}}^*} \cdot \left\{ \left[\boldsymbol{v}_0^* + \boldsymbol{\kappa}^* \cdot \boldsymbol{r}_{\mathrm{c}}^* - \frac{1}{8} (\boldsymbol{\delta} + \zeta\boldsymbol{\Omega}) \cdot \boldsymbol{X}^* \right] \Psi^* \right\} + \frac{1}{8} \frac{\partial}{\partial \boldsymbol{r}_{\mathrm{c}}} \cdot (\boldsymbol{\delta} + \zeta\boldsymbol{\Omega}) \cdot \frac{\partial \Psi^*}{\partial \boldsymbol{r}_{\mathrm{c}}^*}$$

$$- \frac{\partial}{\partial \boldsymbol{Q}^*} \cdot \left\{ \left[\left[\boldsymbol{\delta} - \frac{\epsilon\beta^*}{\epsilon\beta^* + 1} \frac{\boldsymbol{Q}^*\boldsymbol{Q}^*}{Q^{*2}} \right] \cdot \left(\boldsymbol{\kappa}^* \cdot \boldsymbol{Q}^* - \frac{1}{2} (\boldsymbol{\delta} - \zeta\boldsymbol{\Omega}) \cdot \frac{\partial \phi_{\mathrm{MS}}^{*\mathrm{S}}}{\partial \boldsymbol{Q}^*} - \frac{1}{4} (\boldsymbol{\delta} - \zeta\boldsymbol{\Omega}) \cdot \boldsymbol{Y}^* \right) \right] \Psi^* \right\}$$

$$+ \frac{1}{2} \frac{\partial}{\partial \boldsymbol{Q}^*} \cdot \left[\left(\boldsymbol{\delta} - \frac{\epsilon\beta^*}{\epsilon\beta^* + 1} \frac{\boldsymbol{Q}^*\boldsymbol{Q}^*}{Q^{*2}} \right) \cdot (\boldsymbol{\delta} - \zeta\boldsymbol{\Omega}) \right] \cdot \frac{\partial \Psi^*}{\partial \boldsymbol{Q}^*} \tag{3.58}$$

Note that β^* and β are both dimensionless. However,

$$\beta^* = 1 - \frac{\bar{\alpha}}{Q^*}(\mathscr{A}^* + \mathscr{B}^*) \tag{3.59}$$

where $\mathscr{A}^*$ and $\mathscr{B}^*$ can be obtained by recasting all the dimensional quantities in Eq. (2.6) into their non-dimensionalized form, and $\bar{\alpha}$ is given by $\bar{\alpha} = (3/4)\sqrt{\pi}h^*$, where $h^* = a/\left(\sqrt{\pi}l_H\right)$ is the hydrodynamic interaction parameter.

Invoking the identity given in Equation D.38 of Appendix D, we may write the second and fourth terms on the right-hand-side of Eq. (3.58) in a way that renders the Fokker-Planck equation amenable to Itô's interpretation.

Since $\mathbf{\Omega}(\mathbf{Q^*})$ is independent of $\mathbf{r}_c^*$, and

$$\left(\boldsymbol{\delta} - \frac{\epsilon\beta^*}{\epsilon\beta^* + 1}\frac{\mathbf{Q^*Q^*}}{Q^{*2}}\right)\cdot(\boldsymbol{\delta} - \zeta\mathbf{\Omega}) = \left(\frac{Q^* - \mathscr{A}^*\bar{\alpha}}{Q^*}\right)\left(\boldsymbol{\delta} - g_1\frac{\mathbf{Q^*Q^*}}{Q^{*2}}\right) \tag{3.60}$$

the Fokker-Planck equation can be rewritten as follows,

$$\frac{\partial\Psi^*}{\partial t^*} = -\frac{\partial}{\partial\mathbf{r}_c^*}\cdot\left\{\left[\mathbf{v}_0^* + \boldsymbol{\kappa}^*\cdot\mathbf{r}_c^* - \frac{1}{8}(\boldsymbol{\delta} + \zeta\mathbf{\Omega})\cdot\mathbf{X^*}\right]\Psi^*\right\} + \frac{1}{2}\frac{\partial}{\partial\mathbf{r}_c^*}\frac{\partial}{\partial\mathbf{r}_c^*} : \left[\frac{(\boldsymbol{\delta} + \zeta\mathbf{\Omega})}{4}\Psi^*\right]$$

$$- \frac{\partial}{\partial\mathbf{Q^*}}\cdot\left\{\left[\frac{g_2}{2}\frac{\mathbf{Q^*}}{Q^*} + \left[\boldsymbol{\delta} - \frac{\epsilon\beta^*}{\epsilon\beta^* + 1}\frac{\mathbf{Q^*Q^*}}{Q^{*2}}\right]\cdot\left(\boldsymbol{\kappa}^*\cdot\mathbf{Q^*} - \frac{1}{2}(\boldsymbol{\delta} - \zeta\mathbf{\Omega})\cdot\frac{\partial\phi_{\text{MS}}^{*\text{S}}}{\partial\mathbf{Q^*}}\right.\right.$$

$$\left.\left.- \frac{1}{4}(\boldsymbol{\delta} - \zeta\mathbf{\Omega})\cdot\mathbf{Y^*}\right)\right]\Psi^*\right\} + \frac{1}{2}\frac{\partial}{\partial\mathbf{Q^*}}\frac{\partial}{\partial\mathbf{Q^*}} : \left[\left(\frac{Q^* - \mathscr{A}^*\bar{\alpha}}{Q^*}\right)\left(\boldsymbol{\delta} - g_1\frac{\mathbf{Q^*Q^*}}{Q^{*2}}\right)\Psi^*\right] \tag{3.61}$$

where

$$g_1 = \frac{\bar{\alpha}\mathscr{B}^*Q^* + \epsilon(Q^* - \mathscr{A}^*\bar{\alpha})[Q^* - \bar{\alpha}(\mathscr{A}^* + B^*)]}{(Q^* - \mathscr{A}^*\bar{\alpha})\{Q^* + \epsilon[Q^* - \bar{\alpha}(\mathscr{A}^* + \mathscr{B}^*)]\}} \tag{3.62}$$

$$g_2 = \frac{2\bar{\alpha}\mathscr{B}^*}{\{Q^* + \epsilon[Q^* - \bar{\alpha}(\mathscr{A}^* + \mathscr{B}^*)]\}^2} - 2g_1\left(\frac{Q^* - \mathscr{A}^*\bar{\alpha}}{Q^{*2}}\right)$$

The Fokker-Planck equation (Eq. (3.61)) can be written in the following compact form,

$$\frac{\partial\Psi^*}{\partial t^*} = -\frac{\partial}{\partial\mathbf{r}_c^*}\cdot\left\{\mathbf{e}\Psi^*\right\} + \frac{1}{2}\frac{\partial}{\partial\mathbf{r}_c^*}\frac{\partial}{\partial\mathbf{r}_c^*} : [\widetilde{\mathbf{e}}\Psi^*] - \frac{\partial}{\partial\mathbf{Q^*}}\cdot\left\{\mathbf{g}\Psi^*\right\} + \frac{1}{2}\frac{\partial}{\partial\mathbf{Q^*}}\frac{\partial}{\partial\mathbf{Q^*}} : [\widetilde{\mathbf{g}}\Psi^*] \tag{3.63}$$

where the definitions of the quantities $\mathbf{e}, \widetilde{\mathbf{e}}, \mathbf{g}$ and $\widetilde{\mathbf{g}}$ are clear by comparison of Eqs. (3.61) and (3.63).

It is convenient to define a collective variable, $\mathbf{c}$, which is a six-element vector containing the Cartesian components of both $\mathbf{r}_c^*$ and $\mathbf{Q^*}$. Similarly, a six-element vector $\mathbf{j}$ can be defined, containing the components of $\mathbf{e}$ and $\mathbf{g}$, along with the definition of a 2×2 block matrix $\mathcal{D}$, whose off-diagonal elements are $\mathbf{0}$, and the diagonal elements are the matrices $\widetilde{\mathbf{e}}$ and $\widetilde{\mathbf{g}}$ (each of size 3×3). With these definitions, the Fokker-Planck equation in Eq. (3.63) can be written as

$$\frac{\partial\Psi^*}{\partial t^*} = -\frac{\partial}{\partial\mathbf{c}}\cdot\left\{\mathbf{j}\Psi^*\right\} + \frac{1}{2}\frac{\partial}{\partial\mathbf{c}}\frac{\partial}{\partial\mathbf{c}} : [\mathcal{D}\Psi^*] \tag{3.64}$$

The stochastic differential equation (SDE) corresponding to Eq. (3.64) can be obtained using the Itô interpretation, as

$$dc = j dt^* + \boldsymbol{\mathcal{B}} \cdot d\boldsymbol{W}_t^* \tag{3.65}$$

where $\boldsymbol{W}_t^*$ is a Wiener process and $\boldsymbol{\mathcal{B}} \cdot \boldsymbol{\mathcal{B}}^T = \boldsymbol{\mathcal{D}}$. The SDE (Eq. (3.65)) is solved using a semi-implicit predictor-corrector scheme (Öttinger, 1996), as discussed in the following subsection.

Solver details

With reference to Eq. (3.64), $\boldsymbol{\mathcal{D}}$ is a 6×6 matrix, and its square root, $\boldsymbol{\mathcal{B}}_j$, at any time t_j^* is found using Cholesky decomposition (Press *et al.*, 2007). Although Eq. (3.65) is written in terms of the collective variable c, the equation for r_c^* is solved purely explicitly, whereas the equation in $\boldsymbol{Q}^*$ is solved by treating only the spring force term implicitly. For the sake of clarity, the predictor and corrector equations for r_c^* and $\boldsymbol{Q}^*$ are presented separately. It is useful to define another six-element vector, $\Delta \boldsymbol{S}_j$, as

$$\Delta \boldsymbol{S}_j = \boldsymbol{\mathcal{B}}_j \cdot \Delta \boldsymbol{W}_j \tag{3.66}$$

where $\boldsymbol{W}_j$ is a vector of six independent Wiener processes, each of mean zero and variance Δt_j^*. The first three elements of $\Delta \boldsymbol{S}_j$, denoted by $\Delta \boldsymbol{S}_j^{(r_c)}$, contain the noise contribution to r_c^*, and the next three elements, denoted by $\Delta \boldsymbol{S}_j^{(Q)}$, contribute to the noise in $\boldsymbol{Q}^*$. In the following discussion, Eqs. (3.67)—(3.74) are in their dimensionless form, but the asterisk has been dropped from these equations for the sake of notational simplicity.

Predictor step

$$\widetilde{\boldsymbol{r}}_c \left(t_{j+1} \right) = \boldsymbol{r}_c(t_j) + \left[\boldsymbol{v}_0 + \boldsymbol{\kappa}(t_j) \cdot \boldsymbol{r}_c(t_j) - \boldsymbol{X}_a(t_j) \right] \Delta t_j + \Delta \boldsymbol{S}_j^{(r_c)} \tag{3.67}$$

$$
\widetilde{\boldsymbol{Q}} \left(t_{j+1} \right) = \boldsymbol{Q}(t_j) + \left[\boldsymbol{\kappa}(t_j) \cdot \boldsymbol{Q}(t_j) - \left(\frac{\epsilon \beta(t_j)}{\epsilon \beta(t_j) + 1} \right) \left[\boldsymbol{\kappa}(t_j) : \frac{\boldsymbol{Q}(t_j)\boldsymbol{Q}(t_j)}{Q^2(t_j)} \right] \boldsymbol{Q}(t_j) \right.
$$
$$
\left. - \frac{f}{2} \left(\frac{\beta(t_j)}{\epsilon \beta(t_j) + 1} \right) \frac{\boldsymbol{Q}(t_j)}{Q(t_j)} + \frac{g_2(t_j)}{2} \frac{\boldsymbol{Q}(t_j)}{Q(t_j)} - \boldsymbol{Y}_a(t_j) \right] \Delta t_j + \Delta \boldsymbol{S}_j^{(Q)} \tag{3.68}
$$

where

$$\boldsymbol{X}_a(t_j) = \frac{1}{8} \left(\boldsymbol{\delta} + \zeta \boldsymbol{\Omega}(\boldsymbol{Q}_j) \right) \cdot \boldsymbol{X} \left(\boldsymbol{Q}_j, \boldsymbol{r}_c(t_j) \right)$$

$$\boldsymbol{Y}_a(t_j) = \frac{1}{4} \left(\boldsymbol{\delta} - \frac{\epsilon \beta(t_j)}{\epsilon \beta(t_j) + 1} \frac{\boldsymbol{Q}(t_j)\boldsymbol{Q}(t_j)}{Q^2(t_j)} \right) \cdot \left(\boldsymbol{\delta} - \zeta \boldsymbol{\Omega}(\boldsymbol{Q}_j) \right) \cdot \boldsymbol{Y} \left(\boldsymbol{Q}_j, \boldsymbol{r}_c(t_j) \right) \tag{3.69}$$

$$f(t_j) = \frac{\sqrt{b}}{3} \left[\frac{1}{2 \left(1 - Q(t_j)/\sqrt{b} \right)^2} - \frac{1}{2} + 2 \left(\frac{Q(t_j)}{\sqrt{b}} \right) \right]$$

and the notations $\boldsymbol{Q}_j$ and $\boldsymbol{Q}(t_j)$ have been used interchangeably to refer to the same quantity.

Corrector step

$$\boldsymbol{r}_{\text{c}}(t_{j+1}) = \widetilde{\boldsymbol{r}}_{\text{c}}\left(t_{j+1}\right) + \frac{1}{2}\left[\boldsymbol{\kappa}(t_{j+1}) \cdot \widetilde{\boldsymbol{r}}_{\text{c}}\left(t_{j+1}\right) - \boldsymbol{\kappa}(t_j) \cdot \boldsymbol{r}_{\text{c}}\left(t_j\right) - \widetilde{\boldsymbol{X}}_a(t_{j+1}) + \boldsymbol{X}_a(t_j)\right]\Delta t_j \quad (3.70)$$

$$\begin{aligned}
&\left[1 + \frac{f(t_{j+1})}{4Q(t_{j+1})}\left(\frac{\widetilde{\beta}(t_{j+1})}{\epsilon\widetilde{\beta}(t_{j+1}) + 1}\right)\Delta t_j\right]\boldsymbol{Q}(t_{j+1}) = \widetilde{\boldsymbol{Q}}\left(t_{j+1}\right) \\
&\quad + \frac{1}{2}\left[\boldsymbol{\kappa}(t_{j+1}) \cdot \widetilde{\boldsymbol{Q}}_{j+1} - \boldsymbol{\kappa}(t_j) \cdot \boldsymbol{Q}_j + \widetilde{\boldsymbol{q}}(t_{j+1}) - \boldsymbol{q}(t_j) - \widetilde{\boldsymbol{Y}}_a(t_{j+1}) + \boldsymbol{Y}_a(t_j)\right]\Delta t_j
\end{aligned} \quad (3.71)$$

where

$$\widetilde{\boldsymbol{X}}_a(t_{j+1}) = \frac{1}{8}\left(\boldsymbol{\delta} + \zeta\boldsymbol{\Omega}(\widetilde{\boldsymbol{Q}}_{j+1})\right) \cdot \widetilde{\boldsymbol{X}}\left(\widetilde{\boldsymbol{Q}}_{j+1}, \widetilde{\boldsymbol{r}}_{\text{c}}(t_{j+1})\right)$$

$$\widetilde{\boldsymbol{Y}}_a(t_{j+1}) = \frac{1}{4}\left(\boldsymbol{\delta} - \frac{\epsilon\widetilde{\beta}(t_{j+1})}{\epsilon\widetilde{\beta}(t_{j+1}) + 1}\frac{\widetilde{\boldsymbol{Q}}(t_{j+1})\widetilde{\boldsymbol{Q}}(t_{j+1})}{\widetilde{Q}^2(t_{j+1})}\right) \cdot \left(\boldsymbol{\delta} - \zeta\boldsymbol{\Omega}(\widetilde{\boldsymbol{Q}}_{j+1})\right) \cdot \boldsymbol{Y}\left(\widetilde{\boldsymbol{Q}}_{j+1}, \widetilde{\boldsymbol{r}}_{\text{c}}(t_{j+1})\right)$$

$$f(t_{j+1}) = \frac{\sqrt{b}}{3}\left[\frac{1}{2\left(1 - Q(t_{j+1})/\sqrt{b}\right)^2} - \frac{1}{2} + 2\left(\frac{Q(t_{j+1})}{\sqrt{b}}\right)\right] \quad (3.72)$$

$$\boldsymbol{q}(t_j) = \frac{g_2(t_j)}{2}\frac{\boldsymbol{Q}(t_j)}{Q(t_j)} - \left(\frac{\epsilon\beta(t_j)}{\epsilon\beta(t_j) + 1}\right)\left[\boldsymbol{\kappa}(t_j) : \frac{\boldsymbol{Q}(t_j)\boldsymbol{Q}(t_j)}{Q^2(t_j)}\right]\boldsymbol{Q}(t_j)$$

$$\widetilde{\boldsymbol{q}}(t_{j+1}) = \frac{g_2(t_{j+1})}{2}\frac{\widetilde{\boldsymbol{Q}}(t_{j+1})}{\widetilde{Q}(t_{j+1})} - \left(\frac{\epsilon\widetilde{\beta}(t_{j+1})}{\epsilon\widetilde{\beta}(t_{j+1}) + 1}\right)\left[\boldsymbol{\kappa}(t_{j+1}) : \frac{\widetilde{\boldsymbol{Q}}(t_{j+1})\widetilde{\boldsymbol{Q}}(t_{j+1})}{\widetilde{Q}^2(t_{j+1})}\right]\widetilde{\boldsymbol{Q}}(t_{j+1})$$

By setting the length of the vector on the RHS of Eq. (3.71) to be d_{R}, and the length of $\boldsymbol{Q}(t_{j+1})$ to be d_Q, the following cubic equation is obtained:

$$\mathcal{V}^3 - \mathcal{V}^2\left[\frac{3(3\Phi + 4 + 2J)}{2(2\Phi + 3)}\right] + \mathcal{V}\left[\frac{3(1 + \Phi + 2J)}{2\Phi + 3}\right] - \frac{3J}{2\Phi + 3} = 0 \quad (3.73)$$

where

$$\Phi = \left(\frac{\widetilde{\beta}(t_{j+1})}{\epsilon\widetilde{\beta}(t_{j+1}) + 1}\right)\frac{\Delta t_j}{4}; \quad \mathcal{V} = \frac{d_Q}{\sqrt{b}}; \quad J = \frac{d_{\text{R}}}{\sqrt{b}} \quad (3.74)$$

Eq. (3.73) has three roots—two complex and one real—and the real root is obtained using the Newton-Raphson scheme (Press *et al.*, 2007). Note that the equations are solved in their dimensionless form, and the dimensional quantities are obtained by a suitable multiplication with the scaling factors, as explained in the discussion surrounding Eq. (3.57).

Simulation details

To begin with, the initial values of $\boldsymbol{Q}^*$ and $\boldsymbol{r}_c^*$ are picked from a Gaussian distribution of zero mean and unit variance. With the first trap held at the origin, and the second at $\chi_2^{(i)*} = (\chi_{2x}^{(i)*}, 0, 0)$, the dumbbell is equilibrated for a duration of fifty-five dimensionless times. Equilibration is ascertained by checking that $\left\langle Q^{*2} \right\rangle$ has reached a steady value with respect to time. Then, the pulling is commenced (at $t^* = 0$), by varying the position of the second trap linearly, as $\chi_{2x}^* = \chi_{2x}^{(i)*} + v_x^* t^*$, till $t^* = \tau^*$. The window $[0, \tau^*]$ is uniformly divided into N_t intervals, such that $\Delta t_j^* \equiv t_j^* - t_{j-1}^* = \tau^*/N_t$, where $j = 1, 2, ..., (N_t + 1)$.

The dimensionless equivalent of the work done by the mobile trap during one realization of the pulling event is calculated using a simple rectangular quadrature as follows,

$$W^* = c_2 \sum_{j=1}^{N_t} (\chi_{2x}^* - r_{2x}^*)_j \, v_x^* \Delta t_j^* \tag{3.75}$$

where the subscript j on the first term indicates that it is evaluated at time, t_j^*, and r_{2x}^* refers to the x-coordinate of the position of the dumbbell bead subjected to pulling. For representative values of the molecular and control parameters, which are discussed in more detail in the next subsection, the average dissipated work is computed using the time-step widths $\Delta t^* = \left\{ 10^{-5}, 10^{-4}, 10^{-3} \right\}$. The values of the average work calculated at all the time-steps concur within statistical error bars of the simulation, and the largest of the three time-step widths, i.e; $\Delta t^* = 1 \times 10^{-3}$, is used for all the cases where $c_2 = 1000$. For $c_2 = 100$, $\Delta t^* = 1 \times 10^{-2}$ is found to suffice, whereas $c_2 = 10000$ requires $\Delta t^* = 1 \times 10^{-4}$. The choice of the time-step width is also affected by the values of the internal friction and the finite extensibility parameter as higher values of these parameters necessitate the use of smaller time-steps.

The protocol proposed here involves pulling the molecule over a pre-determined distance at the same dimensional velocity but different solvent viscosities. In this context, it is essential to note that the timescale varies linearly with the solvent viscosity, $\lambda_H \propto \eta_s$. In order to maintain the same dimensional pulling time ($\tau = \tau^* \lambda_H$) across simulations with differing solvent viscosity, the dimensionless pulling time (τ^*) is scaled by $1/\eta_s$ as the solvent viscosity is increased.

Code validation for pulling simulations on the dumbbell model

The total Hamiltonian of the dumbbell and trap system is written as

$$\mathcal{H}^* \equiv \frac{\mathcal{H}}{k_B T} = \phi_{\text{MS}}^{*\text{S}} + \frac{c_1}{2} (r_1^* - \chi_1^*)^2 + \frac{c_2}{2} (r_2^* - \chi_2^*)^2 \tag{3.76}$$

Table 3.1:   Parameter values for the two representative cases for which the free energy differences are evaluated using Jarzynski's equality and numerical integration.

	Parameter sets	
	1	2
b	50	80
c_1	20	15
c_2	1	15
$\boldsymbol{\chi^*}_1$	$(0, 0, 0)$	$(0, 0, 0)$
$\boldsymbol{\chi}_2^{(i)*}$	$(1, 0, 0)$	$(4, 0, 0)$
$\boldsymbol{\chi}_2^{(f)*}$	$(3, 0, 0)$	$(5, 0, 0)$

The expression for $\mathcal{H}^*$ can be rewritten in terms of $\boldsymbol{Q}^*$ and $\boldsymbol{r}_c^*$ as,

$$\mathcal{H}^* = \frac{b}{3}\left[\frac{1}{2\left(1 - Q^*/\sqrt{b}\right)} - \frac{1}{2}\left(\frac{Q^*}{\sqrt{b}}\right) + \left(\frac{Q^*}{\sqrt{b}}\right)^2\right] - \boldsymbol{r}_c^* \cdot (c_1\boldsymbol{\chi^*}_1 + c_2\boldsymbol{\chi^*}_2) + \frac{c_1\chi_1^{*2} + c_2\chi_2^{*2}}{2}$$

$$+ \frac{\boldsymbol{Q}^*}{2} \cdot (c_1\boldsymbol{\chi^*}_1 - c_2\boldsymbol{\chi^*}_2) - \left(\frac{c_1 - c_2}{2}\right)\boldsymbol{Q}^* \cdot \boldsymbol{r}_c^* + r_c^{*2}\left(\frac{c_1 + c_2}{2}\right) + \frac{Q^{*2}}{4}\left(\frac{c_1 + c_2}{2}\right)$$

$$(3.77)$$

The steady-state configurational distribution function can be written as

$$\Psi^*(\boldsymbol{Q}^*, \boldsymbol{r}_c^*) = \frac{1}{\mathcal{Z}}\exp[-\mathcal{H}^*] \tag{3.78}$$

where $\mathcal{Z}$ is the partition function of the system, given by

$$\mathcal{Z} = \int\int \exp[-\mathcal{H}^*] d\boldsymbol{r}_c^* d\boldsymbol{Q}^* \tag{3.79}$$

Substituiting the definition of $\mathcal{H}^*$ from Eq. (3.77) into Eq. (3.79) yields the following equation,

$$\mathcal{Z} = \int\left[\int \exp\left[-\bar{c}\left(\boldsymbol{r}_c^* \cdot \boldsymbol{r}_c^*\right) - m\left(\boldsymbol{r}_c^* \cdot \boldsymbol{l}\right)\right]d\boldsymbol{r}_c^*\right]\exp[\varkappa]\,d\boldsymbol{Q}^* \tag{3.80}$$

where

$$\bar{c} = \frac{c_1 + c_2}{2}; \quad m = 1; \boldsymbol{l} = -\left[c_1\boldsymbol{\chi^*}_1 + c_2\boldsymbol{\chi^*}_2 + \left(\frac{c_1 - c_2}{2}\right)\boldsymbol{Q}^*\right];$$

$$\varkappa = -\frac{Q^{*2}}{4}\left(\frac{c_1 + c_2}{2}\right) - \frac{\boldsymbol{Q}^*}{2} \cdot (c_1\boldsymbol{\chi}_1^* - c_2\boldsymbol{\chi}_2^*) - \frac{c_1\chi_1^{*2} + c_2\chi_2^{*2}}{2} - \phi_{\text{MS}}^{*S}$$

$$(3.81)$$

The inner integral in Eq. (3.80) can be evaluated using the following identity (Bird *et al.*, 1987b) for Gaussian integrals,

$$\int \exp\left[-\overline{c}\,(\boldsymbol{u} \cdot \boldsymbol{u}) - m\,(\boldsymbol{u} \cdot \boldsymbol{j})\right] d\boldsymbol{u} = \left(\frac{\pi}{\overline{c}}\right)^{3/2} \exp\left[\frac{m^2}{4\overline{c}}\,(\boldsymbol{j} \cdot \boldsymbol{j})\right] \tag{3.82}$$

resulting in

$$\mathcal{Z} = \left(\frac{2\pi}{c_1 + c_2}\right)^{3/2} \int \exp\left[\frac{\boldsymbol{l} \cdot \boldsymbol{l}}{4\overline{c}} + \varkappa\right] d\boldsymbol{Q}^* \tag{3.83}$$

Upon simplification, one obtains

$$\mathcal{Z} = \left(\frac{2\pi}{c_1 + c_2}\right)^{3/2} \int \exp\left\{-k\,[\boldsymbol{Q}^* - \boldsymbol{s}^*]^2 - \phi_{\mathrm{MS}}^{*\mathrm{S}}\right\} d\boldsymbol{Q}^* \tag{3.84}$$

where $k = (c_1 c_2)/2(c_1 + c_2)$, and $\boldsymbol{s}^* = \chi_2^* - \chi_1^*$. The integral in Eq. (3.84) can be evaluated by converting to spherical co-ordinates, recognising that $Q_x^* = Q^* \sin\theta \cos\phi$, $Q_y^* = Q^* \sin\theta \sin\phi$, $Q_z^* = Q^* \cos\theta$. Therefore,

$$\mathcal{Z} = \left(\frac{2\pi}{c_1 + c_2}\right)^{3/2} \int_{Q^*=0}^{\sqrt{b}} \int_{\theta=0}^{\pi} \int_{\phi=0}^{2\pi} \left[\exp\left(-k\,[Q_x^* - s_x^*]^2\right) \exp\left(-k\,[Q_y^* - s_y^*]^2\right) \exp\left(-k\,[Q_z^* - s_z^*]^2\right)\right.$$

$$\left. \times \exp\left\{\frac{b}{3}\left[\frac{1}{2}\left(\frac{Q^*}{\sqrt{b}}\right) - \frac{1}{2\left(1 - Q^*/\sqrt{b}\right)} - \left(\frac{Q^*}{\sqrt{b}}\right)^2\right]\right\}\right] Q^{*2} dQ^* \sin\theta\, d\theta\, d\phi \tag{3.85}$$

The integral in Eq. (3.85) does not have an analytically closed-form solution, and is evaluated numerically using MATLAB. The free-energy difference in going from the initial state to the final state is then given by,

$$\Delta A_{\mathrm{num}}^* = \ln\left[\frac{\mathcal{Z}(\chi_2^* = \chi_2^{*(\mathrm{i})})}{\mathcal{Z}(\chi_2^* = \chi_2^{*(\mathrm{f})})}\right] \tag{3.86}$$

where the subscript 'num' indicates that the free energy difference has been calculated numerically.

Figure 3.3 shows a comparison between the free energy difference obtained from Brownian dynamics simulations of $N_{\mathrm{ens}} = 1 \times 10^5$ trajectories using Jarzynski's equality, and that obtained from Eq. (3.86), for the two parameter sets indicated in Table 3.1. The data in Fig. 3.3 are presented in tabular format in Table 3.2, where it is observed that the average dissipation, and the error in the estimated free-energy difference, increases with an increase in the pulling velocity. This is because at higher values of the dissipation, the work distribution is broadened [as explained later in Figure 3.6], and a larger number of trajectories are required to accurately estimate the free-energy difference from the rare realizations that occur near the tail of the work distribution.

Table 3.2: A comparison of the free-energy differences calculated using numerical integration [Eq. (3.86)], and BD simulations using Jarzynski's equality [Eq. (3.1)], over $N_{\text{ens}} = 1 \times 10^5$ trajectories. Simulation data reported for freely-draining dumbbells with no internal friction [$h^* = 0.0$, $\epsilon = 0.0$]. The error is quantified as, % error $= 100 \times \left| (\Delta A^* - \Delta A^*_{\text{num}}) / \Delta A^*_{\text{num}} \right|$.

v^*	ΔA^*	% error	$\left\langle W^*_{\text{dis}} \right\rangle$
Parameter set 1 :	$\Delta A^*_{\text{num}} = 2.11504$		
0.001	2.1151 ± 0.0002	0.0006	0.0017 ± 0.0003
0.005	2.1149 ± 0.0004	0.008	0.0084 ± 0.0006
0.01	2.1147 ± 0.0006	0.02	0.0169 ± 0.008
0.02	2.1144 ± 0.0008	0.03	0.033 ± 0.001
0.05	2.116 ± 0.001	0.04	0.081 ± 0.002
0.1	2.114 ± 0.002	0.06	0.155 ± 0.003
0.2	2.116 ± 0.003	0.05	0.281 ± 0.004
0.5	2.116 ± 0.004	0.04	0.508 ± 0.005
1.0	2.115 ± 0.005	0.01	0.673 ± 0.006
Parameter set 2 :	$\Delta A^*_{\text{num}} = 5.55479$		
v^*	ΔA^*	% error	$\left\langle W^*_{\text{dis}} \right\rangle$
0.001	5.5551 ± 0.0002	0.005	0.0031 ± 0.0004
0.005	5.5559 ± 0.0006	0.02	0.0156 ± 0.0008
0.01	5.5546 ± 0.0008	0.003	0.031 ± 0.001
0.02	5.553 ± 0.001	0.02	0.063 ± 0.002
0.05	5.554 ± 0.002	0.01	0.155 ± 0.003
0.1	5.551 ± 0.003	0.07	0.306 ± 0.004
0.2	5.549 ± 0.005	0.08	0.593 ± 0.006
0.5	5.54 ± 0.01	0.26	1.38 ± 0.01
1.0	5.50 ± 0.03	0.95	2.42 ± 0.03
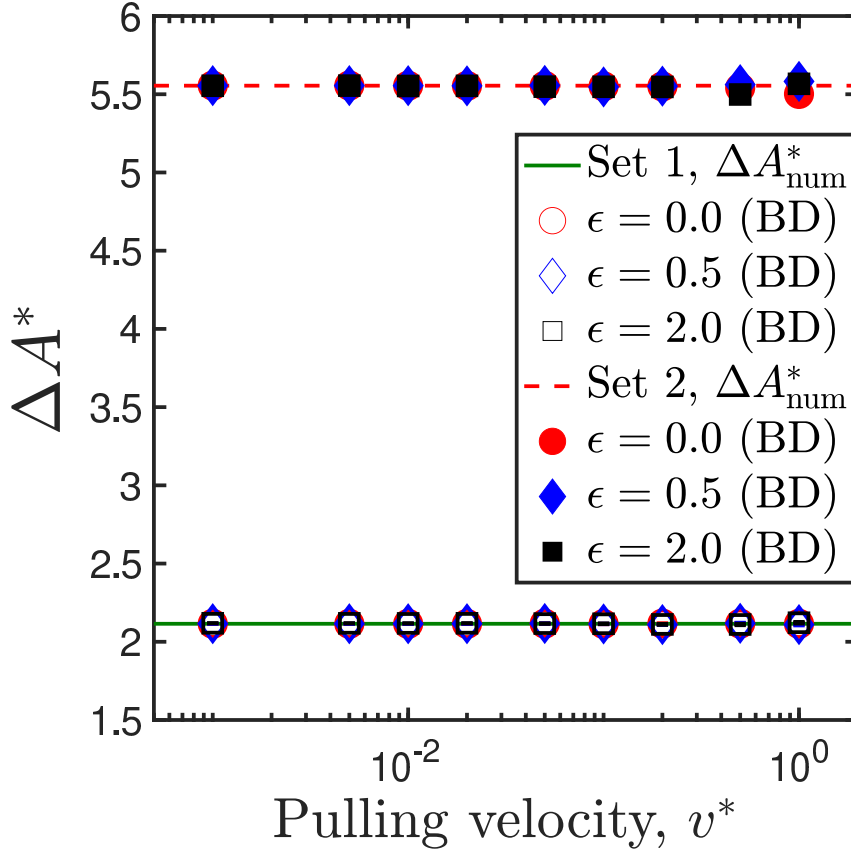
Figure 3.3: Validation of the code for pulling a single-mode spring-dashpot. Comparison of the numerically calculated free energy differences (indicated by horizontal lines) against that calculated using the JE, for two different parameter sets shown in Table 3.1.

Molecular and control parameters

The parameters used in the present work are broadly classified into molecular and control parameters. Molecular parameters pertain to the polymer that is being stretched, whereas control parameters are set by the experiments or the simulations used in the study of stretching the molecule.

The choice of molecular parameters is based on the λ-phage DNA (48.5 kbp) used in Murayama et al.'s (Murayama *et al.*, 2007) work, which has a contour length, L_c, of 16.5 μm, and Kuhn segment length, b_K, of approximately 88 nm. In order to model this molecule as a dumbbell, the model parameters, b, and l_H, are chosen such that the contour length and the radius of gyration of the model and the DNA molecule are the same. Following the procedure for parameter selection described in detail in Sunthar and Prakash (2005), we obtain $b = 811.25$ and $l_H = 580.95$ nm. We round down both these values, and use $b = 800$ and $l_H = 500$ nm as the parameters to model λ-phage DNA.

The Hookean spring constant of the model, *H*, is then found using

$$H = \frac{k_B T}{l_{\mathrm{H}}^2} = \frac{4.142 \text{ pN nm}}{(500)^2 \text{ (nm)}^2} = 1.657 \times 10^{-5} \text{ pN/nm}$$

The choice of the bead radius, *a*, is motivated by Alexander-Katz *et al.*'s (2009) work, where it is suggested that the monomeric radius may be taken as the persistence length of the molecule. We choose $a = 30$ nm, which is identical to the choice made by Alexander-Katz *et al.* (2009) for comparing the results of BD simulations against experiments on DNA.

Other values of *b* and l_{H}, of the same order-of-magnitude as obtained for the λ-phage DNA case, have been used in this study and in addition to $a = 30$ nm, bead radii of 80 nm and 100 nm have also been used.

Fig. 3.4 provides a snapshot of the *x*-*y* projection of the positions of an ensemble of beads of the dumbbell, obtained after an equilibration of fifty-five dimensionless times at the initial trap positions $\chi_1^* = (0,0,0)$, $\chi_2^{(i)*} = (5,0,0)$ and final trap states $\chi_1^* = (0,0,0)$, $\chi_2^{(f)*} = (7,0,0)$, as a function of the optical trap stiffness. It is clearly seen that the strength of the trap (c_1 or c_2) determines its ability to confine the bead near the position of its minimum. Since it is intended to hold the position of the first bead fixed at the origin, a trap strength of $c_1 = 1000$ is used throughout our simulations.

In Figs. 3.5, the effect of the mobile trap stiffness (c_2) on the dissipation is shown for a fixed value of the stationary trap stiffness, for freely-draining dumbbells. In Fig. 3.5 (a), the average dissipation as the dumbbell is pulled at a constant velocity and a fixed pulled distance, is plotted as a function of the mobile trap stiffness. It is seen that the dissipation reaches a plateau at $c_2 \approx 100$. This behavior is in agreement with the dissipation calculated for the analytical model [Eq. (3.42)], which reaches $\sim 98\%$ of its asymptotic value at $c_2 \approx 100$. In all our simulations, we set $c_1 = c_2 = 1000$ (unless specified otherwise), in order to operate in a regime where the dissipation is independent of the trap stiffness.

In Fig. 3.5 (b), the average dissipation is plotted as a function of the pulling velocity, over the same fixed distance, for three different values of the mobile trap stiffness. At lower values of the trap stiffness, the dissipation grows linearly before scaling sub-linearly with the velocity. The onset of the non-linear regime is pushed to higher velocities as the trap stiffness is increased. In the asymptotic limit of high trap stiffness, the non-linear regime vanishes, and a linear scaling of the dissipation with the pulling velocity is observed for over two orders of magnitude in the velocity. There is a good agreement between the trends predicted by the simple analytical model using a Hookean spring-dashpot discussed in Sec. 3.2.1 and BD simulations on a model with a nonlinear force
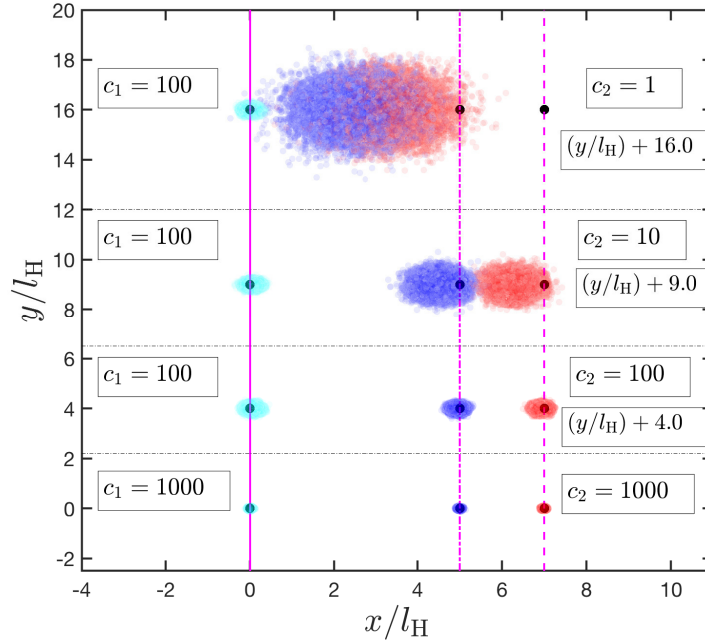
Figure 3.4: Trap stiffness determines the distribution of bead positions. An $x-y$ projection of the equilibrated positions of the beads, for an ensemble of free-draining dumbbells ($N_{\text{ens}} = 1 \times 10^4$), for different values of the trap stiffness. From left to right, the solid vertical line, the dash-dotted vertical line, and the dashed vertical line represent the positions of the first trap (χ_1^*), the initial position of the second trap ($\chi_2^{(i)*}$), and the final position of the second trap ($\chi_2^{(f)*}$), respectively. From left to right, data points in cyan, close to the solid vertical line, correspond to the positions of the first bead with the corresponding trap at the origin, those in blue denote the positions of the second bead when the trap position is at $\chi_2^{(i)} = (5\,l_{\text{H}}, 0, 0)$, and those in red represent the positions of the second bead when the trap is located at $\chi_2^{(f)} = (7\,l_{\text{H}}, 0, 0)$. The data sets have been shifted vertically for clarity, and the offsets for each of the shifted cases are indicated in the figure.

law. Remarkably, the effect of the non-linear force law is more perceptible at lower trap stiffnesses, vanishing as the mobile trap stiffness is increased, until a quantitative agreement is obtained between the simulation and the analytical results.

The Marko-Siggia force expression is linear at low values of the extension of the molecule, and diverges as the fractional extension approaches unity. For initial extensions in the linear regime of the force-extension profile, a trap stiffness of $c_2 = 1000$ is sufficient to make the bead track the position of the trap, as shown in Fig. 3.4. Higher trap stiffnesses are found to be required for operating in the non-linear regime of the force-extension curve.
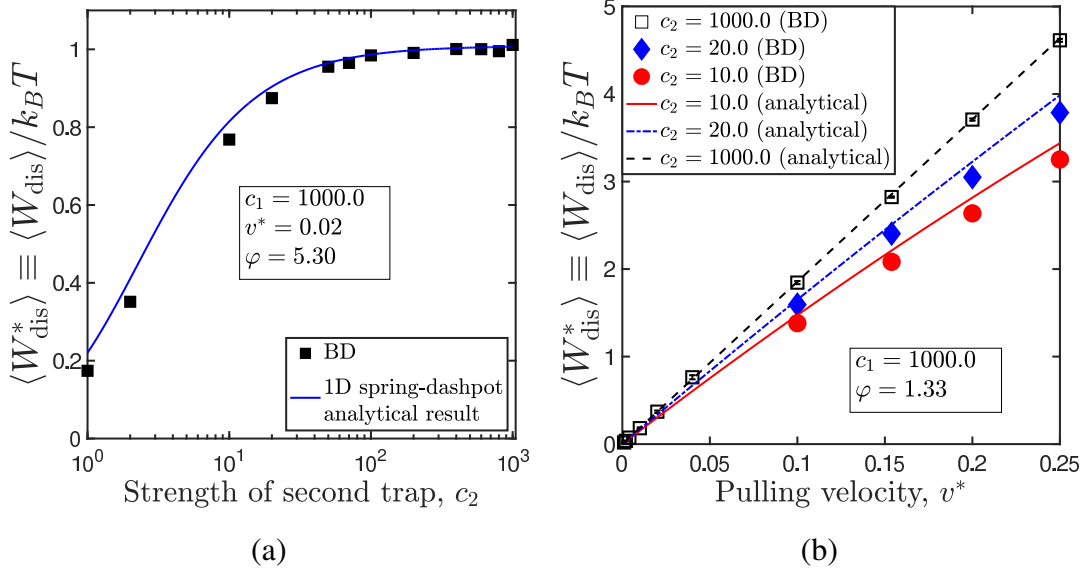
Figure 3.5: Comparison of the average dissipation from BD simulations against analytical results. Plots of the average dissipation for the pulling protocol $5\,l_H \to 7\,l_H$, as a function of (a) mobile trap stiffness, for a fixed value of the pulling velocity, $v^* = 0.02$, and (b) pulling velocity, at three different values of the mobile trap stiffness. The lines indicate analytical value of the average dissipation for a freely draining Hookean spring-dashpot [Eq. (3.42)] plotted for the parameter values indicated in the figure. The symbols are results from BD simulations on a freely draining spring-dashpot with Marko-Siggia force law, and $b = 800$.

The Jarzynski equality is strictly *exact* only in the limit of an infinite number of work trajectories, $N_{ens} \to \infty$. In applications of the JE, the number of trajectories required to accurately recover the free-energy difference increases with average dissipated work in the process, as discussed in Ritort *et al.* (2002); Jarzynski (2006); Yunger Halpern and Jarzynski (2016).

In Figs. 3.6, the effect of internal friction and pulling velocity on the probability distribution of the work trajectories is plotted for freely-draining dumbbells. The vertical green lines in the figures indicate the free-energy difference, ΔA^*, obtained by taking an error-weighted mean of the values of the free energy difference obtained at dimensionless pulling velocities $v^* \leq 0.02$. Interestingly the work-distributions are normally distributed, as seen by the good agreement between the histogram data and the Gaussian fit. That it is so, despite the equations of motion for the system being non-linear, is an observation previously made by Speck and Seifert (2004). The Gaussianity of the distribution is attributed to the slow rate of the driving protocol ($1/\tau$) with respect to the molecular

(a)

(b)
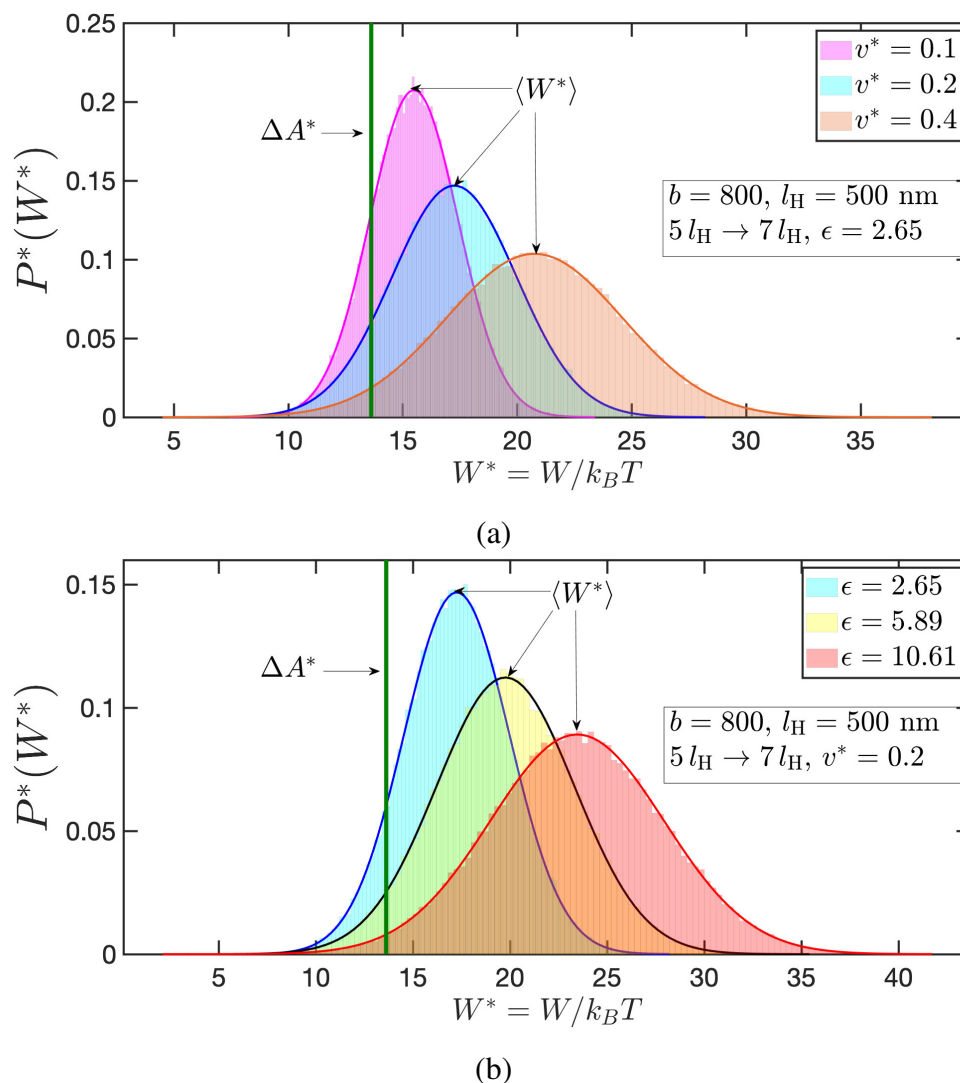
Figure 3.6: Pulling velocity and internal friction broaden the the probability density of work. Probability densities of the work done over 10^5 realizations of the pulling protocol, for: (a) a fixed value of the internal friction parameter, and three different values of the pulling velocity, and (b) a fixed pulling velocity, and three different values of the internal friction parameter. The green vertical line represents the free-energy difference obtained by taking an error-weighted mean of the values of the free energy difference obtained at pulling velocities $v^* \leq 0.02$ using Jarzynski's equality. The solid lines are Gaussian fits to the data.
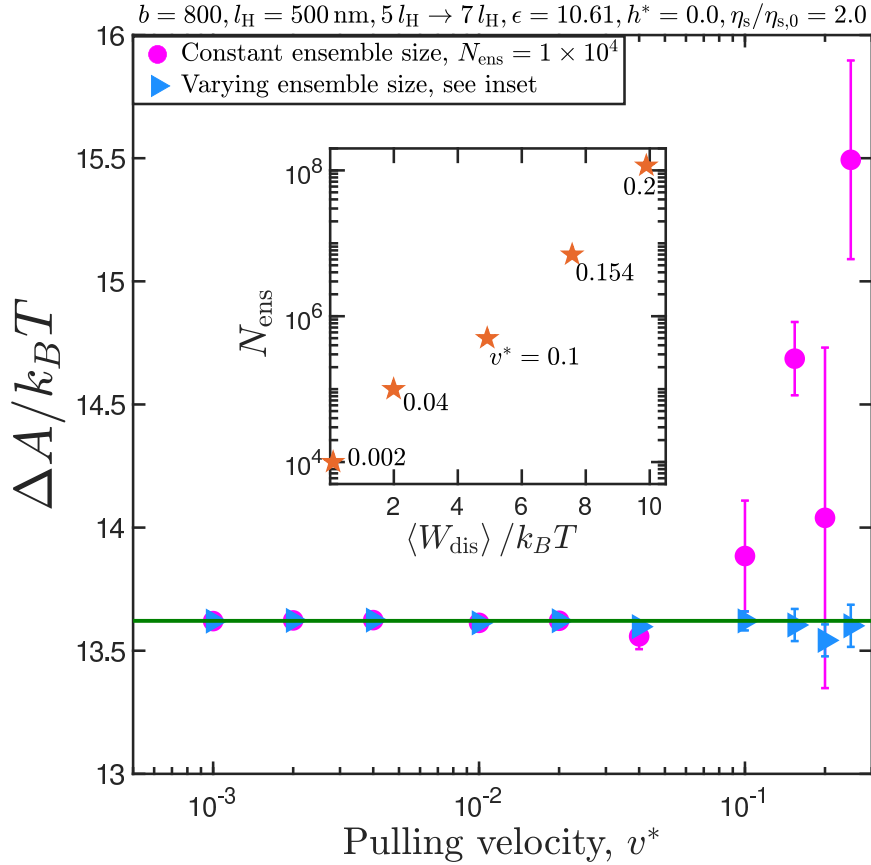
Figure 3.7: Dissipation dictates ensemble size for the application of Jarzynski's equality. Free energy difference as a function of pulling velocity, for a representative case. Inset shows the empirically chosen ensemble size as a function of the average dissipated work. The numbers next to the data points indicate the corresponding values of the dimensionless pulling velocity. Trap stiffness used is $c_1 = c_2 = 1000$.

relaxation rate $(1/\lambda_H)$. For all the data-sets plotted in Figs. 3.6, the driving rate is at least five times slower than the molecular relaxation rate.

From Fig. 3.6 (a), it is seen that increasing the pulling velocity at a fixed value of the internal friction parameter increases the average dissipated work, and the width of the distribution. An identical trend is observed in Fig. 3.6 (b), where an increase in the internal friction parameter at a fixed pulling velocity causes the work distribution to shift rightwards, and results in an increased dissipation. Thus, the dissipation in our model is directly correlated with the pulling velocity, and the internal friction in the system. Under such conditions of high dissipation, the estimates for ΔA are dominated by rare realizations that occur near the tail of the work distribution, necessitating the use of a larger number of trajectories to obtain an accurate estimate of the free energy difference.

In Fig. 3.7, we illustrate the above point using an alternative representation. Without prior knowledge of the ensemble size required for the simulations, an initial guess of

Table 3.3: Typically observed lower and upper bounds on optical tweezer parameters.

Parameter	Lower bound	Upper bound
Trap stiffness (pN/nm)	0.0002 [Black *et al.* (2017)]	0.9 [Gupta *et al.* (2011)]
Pulling velocity (nm/s)	10 [Gupta *et al.* (2011)]	13560 [Trepagnier *et al.* (2004)]
Stretching distance (nm)	10 [Gupta *et al.* (2011)]	8000 [Murayama *et al.* (2007)]

$N_{\text{ens}} = 1 \times 10^4$ was chosen. The green horizontal line represents the free-energy difference obtained by taking an error-weighted mean of the values of the free energy difference obtained at pulling velocities $v^* \leq 0.02$ using Jarzynski's equality. An ensemble size of $N_{\text{ens}} = 1 \times 10^4$ is sufficient for an accurate estimation of the free energy difference at lower velocities (dissipation), but is found to become inadequate at $v^* \geq 0.04$. Upon increasing the ensemble size for the higher velocity cases *empirically*, the accuracy of the estimated free energy difference improves. The ensemble size is plotted as a function of the average dissipated work in the inset of Fig. 3.7, which shows that the choice of the pulling velocity and the ensemble size are mutually related.

In Fig. 3.8, the average dissipated work (scaled by the thermal energy $k_B T$) calculated for a variety of molecular and control parameters is plotted against the magnitude of the dimensionless pulling velocity, v^*. It is seen that the average dissipated work varies linearly over the entire range of the pulling velocity, $v^* = 0.001 - 0.1$. The velocity range in dimensional units would depend on the molecular parameters.

The experimental feasibility of the proposed protocol can be discussed in the context of the molecular parameters used for the dataset represented by filled circles in Fig. 3.8. For these set of parameters, the pulling velocities explored in Fig. 3.8 vary from $v = 29.3\,\text{nm/s}\,(v^* = 0.001)$ to $v = 2.93\,\mu\text{m/s}\,(v^* = 0.1)$. The molecule is stretched over a distance of $1\mu\text{m}$. The stiffness of this molecule is $H = 1.657 \times 10^{-5}$ pN/nm. In order to operate in a regime where the dissipated work is independent of the trap strength, as discussed earlier, the stiffness of the trap must be at least a hundred times that of the molecule, which implies $H_{\text{trap,min}} = 1.657 \times 10^{-3}$ pN/nm.

In Table 3.3, based on a survey of the literature, the range of trap stiffnesses, pulling velocities, and stretching distances typically accessible by optical tweezers is given. Additionally, the position and force resolution limits of optical traps are inversely correlated: stiffer traps improve the spatial resolution but also introduce large fluctuations in the measured force. A rough estimate of these resolution limits may be obtained using
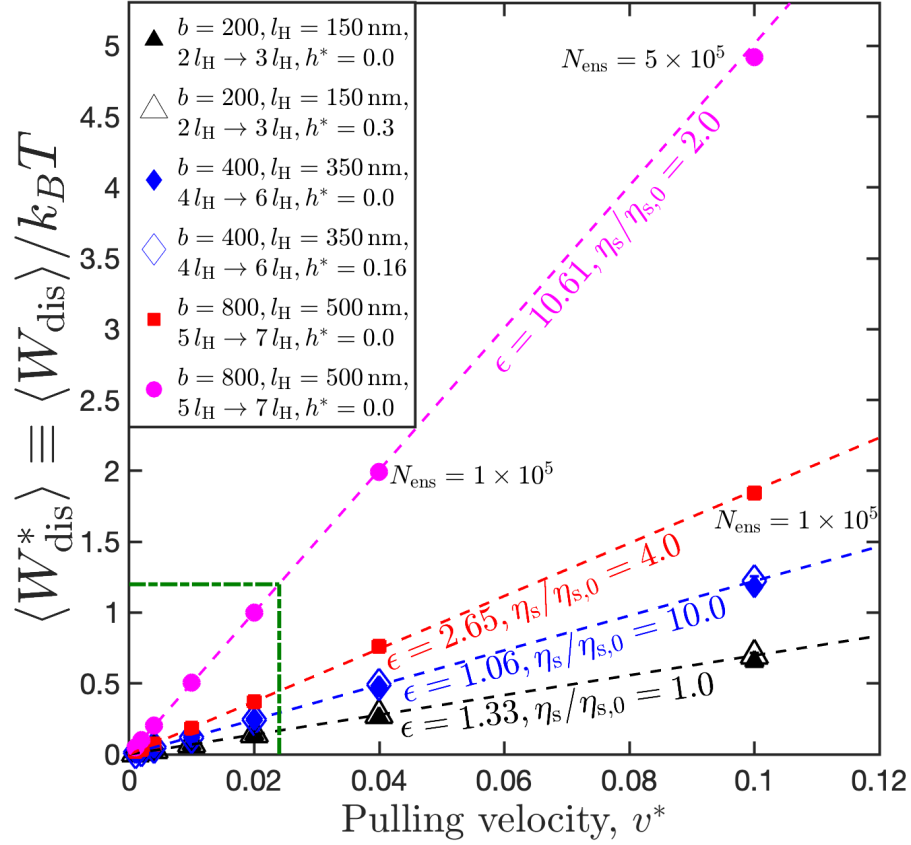
Figure 3.8: Average dissipated work as a function of the dimensionless pulling velocity, for various molecular and control parameters. Except when mentioned otherwise, an ensemble size of $N_{\text{ens}} = 1 \times 10^4$ is used for all the data points. Symbols indicating datasets with fluctuating hydrodynamic interactions have been enlarged for the sake of clarity. The boxed region indicates the regime of operation for the simulation results reported in this section.

the equipartition theorem, as explained in Smith *et al.* (2007); Neuman and Nagy (2008). Most commercial optical tweezer setups are equipped with filtering mechanisms that aid in improving the precision in the measurements, by reducing the resolution limits (Gupta *et al.*, 2011). A detailed discussion of the resolution offered by optical tweezers can be found in Smith *et al.* (2007) and Neuman and Nagy (2008).

From Table 3.3, it is clear that the values of v, d, and $H_{\text{trap,min}}$ for the representative case lie well within the range of values explored experimentally.

Ritort *et al.* (2002) have established from computer simulations of mechanical unfolding that the number of trajectories required to obtain estimates for free energy difference within an error of $O(k_BT)$ increases exponentially with the average dissipation associated with the unfolding process. They predict that for dissipation less than $4k_BT$, around 100 trajectories would suffice, and for a dissipation of $5k_BT$, about 1000

trajectories would be required. These predictions agree well with the average dissipation and ensemble sizes encountered in optical-tweezer-based pulling experiments. For example, Liphardt *et al.* (2002) stretch RNA hairpins using optical tweezers, and estimate $\langle W_{\text{dis}} \rangle = 2 \text{-} 3\, k_B T$ with $N_{\text{ens}} = 47$. Similarly, for pulling experiments on DNA hairpins performed by Gupta et al. Gupta *et al.* (2011), $\langle W_{\text{dis}} \rangle = 1.1 \pm 0.7 k_B T$ for $N_{\text{ens}} = 99$, and $\langle W_{\text{dis}} \rangle = 4.9 \pm 0.3 k_B T$ for $N = 1293$.

For simulations on the single-mode spring dashpot, the statistical error in the free-energy difference is maintained to be $\sim \mathcal{O}(0.01 k_B T)$, in order to obtain a sufficiently accurate estimate of the average dissipated work that enables the internal friction coefficient to be extracted reliably. By restricting the regime of operation to the boxed region in Fig. 3.8, with $v^* \leq 0.02$ and $\langle W_{\text{dis}} \rangle \sim k_B T$, it is found that $N_{\text{ens}} = 1 \times 10^4$ trajectories are sufficient to obtain the free energy difference within the desired error limits. It is possible to operate at higher values of dissipation, outside the boxed regime, provided that the ensemble size is suitably increased, as shown in the inset of Fig. 3.7.

All the results prior to Fig. 3.8 have been presented for the case of freely-draining dumbbells. In Fig. 3.8, it is observed that the inclusion of fluctuating HI does not affect the dissipated work values in a single-mode spring dashpot. Speck (2017) has shown in the context of colloidal suspensions that the inclusion of hydrodynamic interactions does not alter the dissipation along a single trajectory. The effect of fluctuating hydrodynamic interactions on the dissipation is markedly different in the case of wet internal friction, as will be discussed in greater detail in Sec. 3.3.5.

Dry friction in equals dry friction out

The methodology to extract the internal friction coefficient is illustrated using a molecule with parameters: $\left\{ b = 800, l_{\text{H}} = 500\,\text{nm}, K = 3.0 \times 10^{-9}\,\text{kg/s}, h^* = 0.0 \right\}$ as an example. An ensemble of such molecules is pulled from an initial trap position of $\chi_{2x}^{(\text{i})} = 5\, l_{\text{H}}$ to a final trap position of $\chi_{2x}^{(\text{f})} = 7\, l_{\text{H}}$ at different pulling velocities. At each value of the pulling velocity, the average dissipated work is calculated at several values of the solvent viscosity in the range, $\eta_{\text{s}} = \eta_{\text{s},0}$ to $\eta_{\text{s}} = 10\, \eta_{\text{s},0}$. In an experimental setting with water as the solvent, suitable viscogens, such as glucose or sucrose, may be added to the solvent in order to realize an approximately four-fold increase in its viscosity (Jas *et al.*, 2001; Qiu and Hagen, 2004a). In experiments that study the kinetics of intrachain contact formation in polypeptides (Bieri *et al.*, 1999) suspended in a solvent mixture of ethanol and glycerol, the solvent viscosity was varied over two orders of magnitude by adjusting the proportion of glycerol in the mixture.
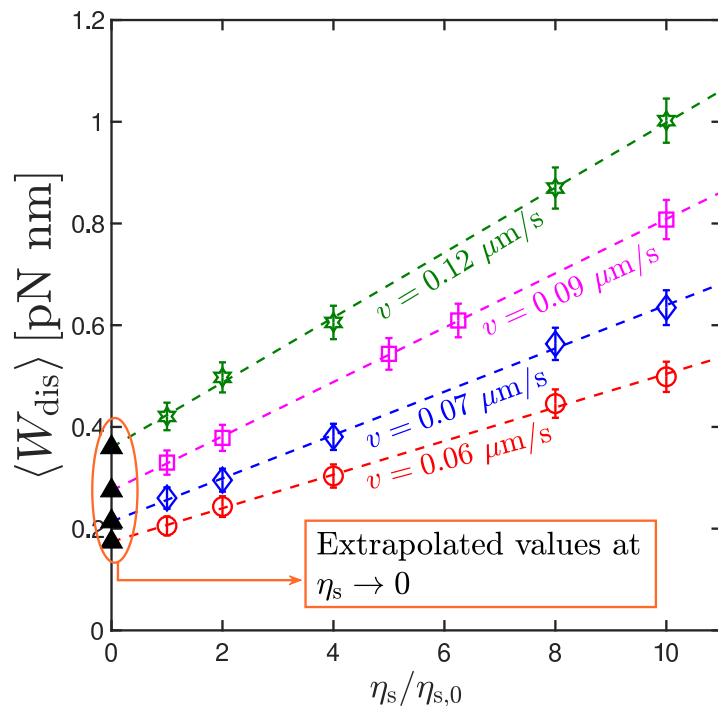
(a)
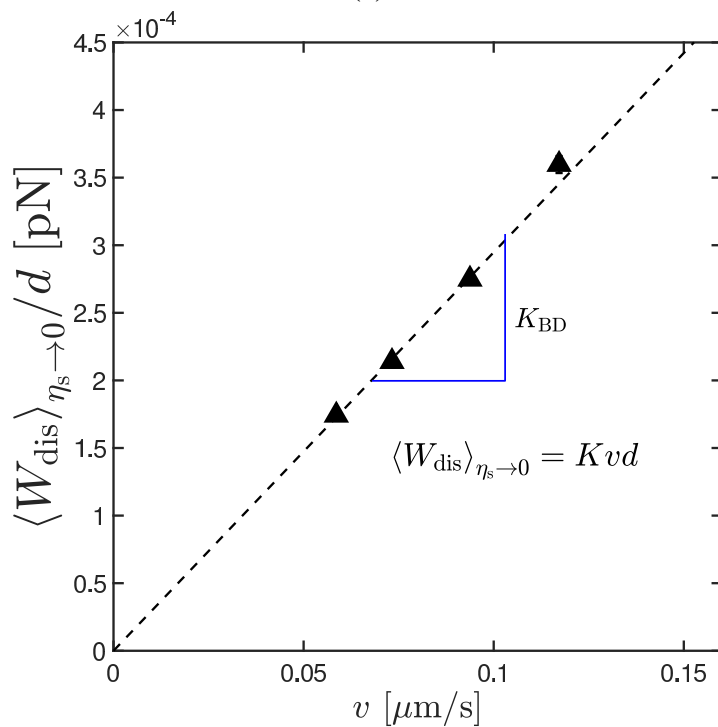
(b)

Figure 3.9: (Protocol for the extraction of the internal friction coefficient: (a) Average dissipated work as a function of the solvent viscosity, for molecules with the parameters: $\{b = 800, l_H = 500\,\text{nm}, K = 3.0 \times 10^{-9}\,\text{kg/s}\}$, subjected to pulling denoted by $5\,l_H \rightarrow 7\,l_H$ at various values of the pulling velocity, v, for an ensemble size, $N = 1 \times 10^4$. (b) The extrapolated values of $\langle W_{\text{dis}} \rangle$ in the hypothetical limit of zero solvent viscosity, divided by the stretching distance, as a function of the pulling velocity. The slope of the graph, K_{BD}, is an estimate of the internal friction coefficient.

Table 3.4: Internal friction coefficients estimated using the protocol described in Fig. 3.9, for various values of the molecular, and control parameters. The error associated with the protocol is calculated as, % error $= 100 \times |(K_{BD} - K)/K|$. An ensemble size of $N = 1 \times 10^4$ and a time-step width of $\Delta t^* = 1 \times 10^{-3}$ was used to obtain the results. For the $K = 100.0 \times 10^{-9}$ kg/s case (Marko-Siggia), a smaller time-step, $\Delta t^* = 1 \times 10^{-4}$, was used. For the $K = 4.0 \times 10^{-9}$ kg/s case (FENE), a larger ensemble, $N = 1 \times 10^5$, was used.

Spring force law:	Input,	Marko-Siggia $h^* = 0.0$		$h^* > 0.0$		
Parameters	$K\,[\times 10^9$ kg/s]	$K_{BD}\,[\times 10^9$ kg/s]	% error	h^*	$K_{BD}\,[\times 10^9$ kg/s]	% error
$b = 200$, $l_H = 150\,\mathrm{nm}$, $2\,l_H \rightarrow 3\,l_H$	1.0	1.04 ± 0.01	4.42	0.3	0.97 ± 0.02	3.11
$b = 400$, $l_H = 350\,\mathrm{nm}$, $4\,l_H \rightarrow 6\,l_H$	1.0	0.99 ± 0.03	1.36	0.16	1.04 ± 0.02	4.29
$b = 200$, $l_H = 150\,\mathrm{nm}$, $2\,l_H \rightarrow 3\,l_H$	10.0	10.04 ± 0.05	0.47	0.3	9.87 ± 0.09	1.24
$b = 400$, $l_H = 350\,\mathrm{nm}$, $4\,l_H \rightarrow 6\,l_H$	10.0	9.922 ± 0.008	0.78	0.16	9.95 ± 0.09	0.52
$b = 800$, $l_H = 500\,\mathrm{nm}$, $5\,l_H \rightarrow 7\,l_H$	3.0	2.95 ± 0.02	1.74	–	–	–
$b = 800$, $l_H = 500\,\mathrm{nm}$, $5\,l_H \rightarrow 7\,l_H$	6.0	6.00 ± 0.07	0.11	–	–	–
$b = 800$, $l_H = 500\,\mathrm{nm}$, $5\,l_H \rightarrow 7\,l_H$	100.0	97.4 ± 1.4	2.56	–	–	–

Spring force law:	Input,	FENE $h^* = 0.0$		$h^* > 0.0$		
Parameters	$K\,[\times 10^9$ kg/s]	$K_{BD}\,[\times 10^9$ kg/s]	% error	h^*	$K_{BD}\,[\times 10^9$ kg/s]	% error
$b = 400$, $l_H = 350\,\mathrm{nm}$, $2\,l_H \rightarrow 3\,l_H$	2.0	–	–	0.23	1.993 ± 0.009	0.35
$b = 600$, $l_H = 250\,\mathrm{nm}$, $3\,l_H \rightarrow 4\,l_H$	3.0	–	–	0.09	2.985 ± 0.009	0.50
$b = 800$, $l_H = 500\,\mathrm{nm}$, $3\,l_H \rightarrow 5\,l_H$	4.0	3.992 ± 0.007	0.18	–	–	–
$b = 800$, $l_H = 500\,\mathrm{nm}$, $3\,l_H \rightarrow 5\,l_H$	6.0	6.02 ± 0.02	0.23	–	–	–

As shown in Fig. 3.9 (a), for each value of the pulling velocity used, the average dissipated work in the hypothetical limit of zero solvent viscosity, $\langle W_{\text{dis}} \rangle_{\eta_{\text{s}} \to 0}$, is obtained from a linear fit to the average dissipated work at finite solvent viscosities. Since the extrapolated value is finite, it is clear signature of the presence of dry internal friction. In Fig. 3.9 (b), the extrapolated values of the average dissipated work in the limit of zero solvent viscosity (divided by the stretching distance d), is plotted against the pulling velocity. The slope of the graph (K_{BD}) represents the internal friction coefficient extracted from simulations.

Table 3.4 shows a comparison between the value of the internal friction coefficient used as an input parameter in the Brownian dynamics simulations, and the corresponding value extracted from the dissipated work using the protocol proposed here, for various molecular and control parameters. Our protocol recovers the input internal friction coefficient to within 5% accuracy, and is insensitive to the choice of the spring-force law, as shown for the Marko-Siggia and the FENE force laws in Table 3.4. Further, values of K_{BD}, for models with and without HI, lie close to each other, indicating that HI does not affect the dissipated work due to dry internal friction.

The validity of the proposed protocol for the extraction of the dry internal friction coefficient has thus been established. In the next section, the application of the protocol to a model with wet internal friction is discussed, in the context of a coarse-grained polymer model with cohesive intra-chain interactions.

3.3   Wet internal friction

In this section, the case of wet internal friction is investigated in the context of the force-induced unraveling of a coiled globule which has previously been studied experimentally by Murayama *et al.* (2007) and with simulations by Alexander-Katz *et al.* (2009). The problem is revisited here with the goal of understanding the role of solvent viscosity and HI, both of which have not been considered previously.

3.3.1   Model description

A bead-spring model with N_{b} beads connected by FENE springs, each stretchable up to a maximum length of Q_0, is considered. The excluded volume interactions between beads are modelled using the Soddemann-Dünweg-Kremer (SDK) potential (2001), whose functional form is given by Eq. 2.12 in Chapter 2.
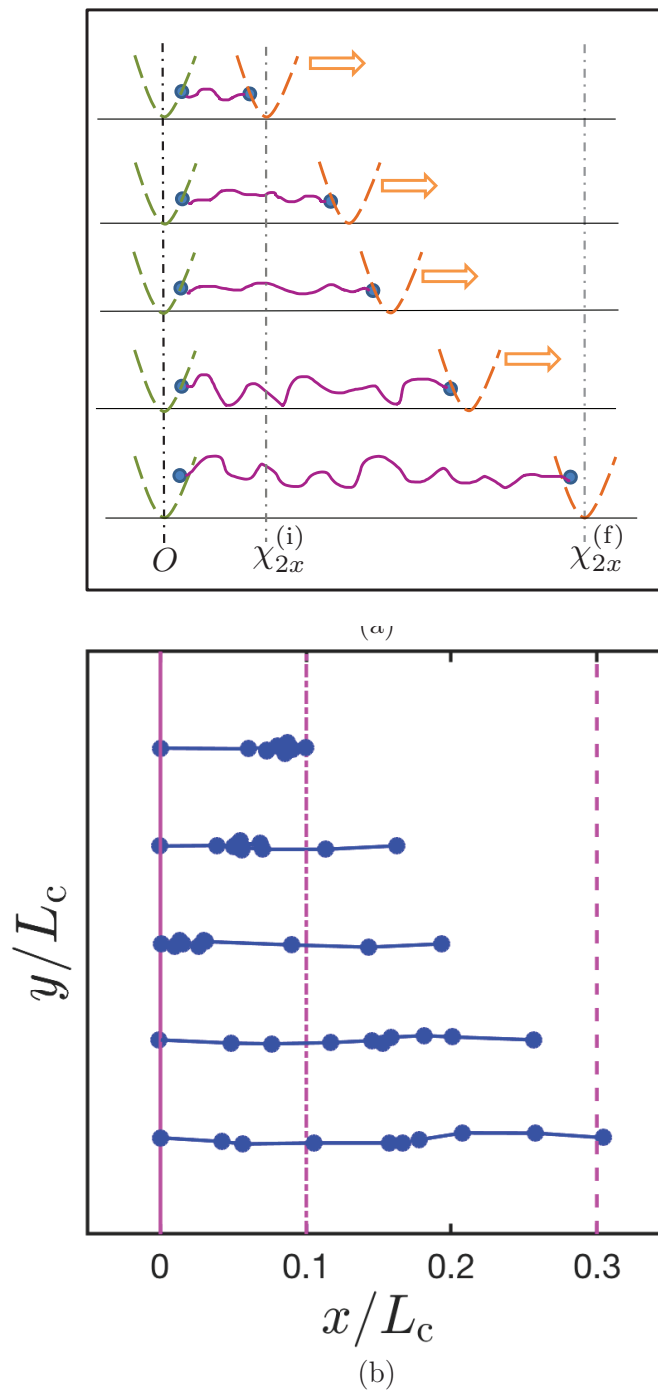
Figure 3.10: Schematic and snapshot of single chain polymer model subjected to pulling (a) Schematic representation of a polymer chain subjected to pulling, (b) snapshots from the BD simulations of a chain with $N_{\mathrm{b}} = 10$ and $\widetilde{\epsilon} = 3.45$, pulled with a constant velocity of $v^* = 0.01$. From left to right, the solid vertical line, the dash-dotted vertical line, and the dashed vertical line represent the positions of the first trap (χ_1^*), the initial position of the second trap ($\chi_2^{(i)*}$), and the final position of the second trap ($\chi_2^{(f)*}$), respectively.

As discussed previously, the terminal beads of the chain are subjected to harmonic trap potentials. One of the traps is held fixed at $\chi_1 = (0, 0, 0)$, and the other is moved from $\chi_2^{(i)} \equiv (\chi_{2x}^{(i)}, 0, 0)$, to $\chi_2^{(f)} \equiv (\chi_{2x}^{(f)}, 0, 0)$ at a constant velocity, $\boldsymbol{v} \equiv (v_x, 0, 0)$.

The force on the μth bead due to bonded and non-bonded interactions is denoted by $\boldsymbol{F}_\mu^\phi$. The hydrodynamic interaction between any pair of beads μ and ν is accounted for by defining the diffusion tensor $\widehat{\boldsymbol{\Upsilon}}_{\mu\nu} = \delta_{\mu\nu}\boldsymbol{\delta} + \zeta\boldsymbol{\Omega}_{\mu\nu}$, where $\delta_{\mu\nu}$ is the Kroenecker delta, and the hydrodynamic interaction tensor, $\boldsymbol{\Omega}_{\mu\nu}$, is approximated using the Rotne-Prager-Yamakawa expression. For notational convenience, we define $\mathcal{D}$, a block matrix of size $N_b \times N_b$, whose each element is the 3×3 matrix, $\widehat{\boldsymbol{\Upsilon}}_{\mu\nu}$. Additionally, the block matrix $\mathcal{B}$ is defined as $\mathcal{B} \cdot \mathcal{B}^T = \mathcal{D}$.

The stochastic differential equation describing the time-evolution of the position of the μth bead is given by

$$\boldsymbol{r}^*_\mu(t^* + \Delta t^*) = \boldsymbol{r}^*_\mu(t^*) + \frac{1}{4}\sum_{\nu=1}^{N_b}\left[\widehat{\boldsymbol{\Upsilon}}^*_{\mu\nu} \cdot \boldsymbol{F}^{*(\phi)}_\nu - \widehat{\boldsymbol{\Upsilon}}^*_{1\nu} \cdot [c_1(\boldsymbol{r}^*_1 - \chi^*_1)]\right.$$

$$\left. - \widehat{\boldsymbol{\Upsilon}}^*_{N_b\nu} \cdot [c_2(\boldsymbol{r}^*_{N_b} - \chi^*_2)]\right]\Delta t^* + \frac{1}{\sqrt{2}}\sum_{\nu=1}^{N_b}\boldsymbol{B}^*_{\mu\nu} \cdot \Delta \boldsymbol{W}^*_\nu \qquad (3.87)$$

where $\boldsymbol{B}^*_{\mu\nu}$ is the (μ, ν)−th element of $\mathcal{B}^*$, and $\Delta\boldsymbol{W}^*$ is a dimensionless Wiener process of zero mean and variance Δt^*. In Fig. 3.10 (a), a schematic representation of the pulling is shown, and in Fig. 3.10 (b), snapshots from BD simulations on a ten-bead chain is presented.

3.3.2   Simulation details

The stochastic differential equation governing the pulling of a single polymer chain [Eq. (3.87)] is solved numerically using Brownian dynamics simulations. The initial bead positions are picked from the equilibrium distribution function corresponding to the FENE force law. The chain is then equilibrated at the initial state, with $\chi^*_{2x} = \chi^{*(i)}_{2x}$, for fifty Rouse times. Equilibration is ascertained by checking that the mean-squared value of the dimensionless radius of gyration, $\langle R_g^{2*}\rangle$, has reached a steady value with respect to time. Pulling is then commenced at $t^* = 0$, by changing the position of the mobile trap linearly in time, as $\chi^*_{2x} = \chi^{*(i)}_{2x} + v^*_x t^*$, till $t^* = \tau^*$. The work done in one realization of the pulling event is given by Eq. (3.75), with r^*_{2x} replaced with $r^*_{N_b x}$, where $r^*_{N_b x}$ refers to the x-coordinate of the last bead in the chain, and the remaining symbols retain their original meaning as defined in Sec. 3.2.2. A timestep width of $\Delta t^* = 1.0 \times 10^{-4}$ is used after ascertaining, for a ten-bead chain with representative parameter values, that the average work obtained for the $\Delta t^* = 1.0 \times 10^{-4}$ and $\Delta t^* = 1.0 \times 10^{-5}$ cases agree within error bars.
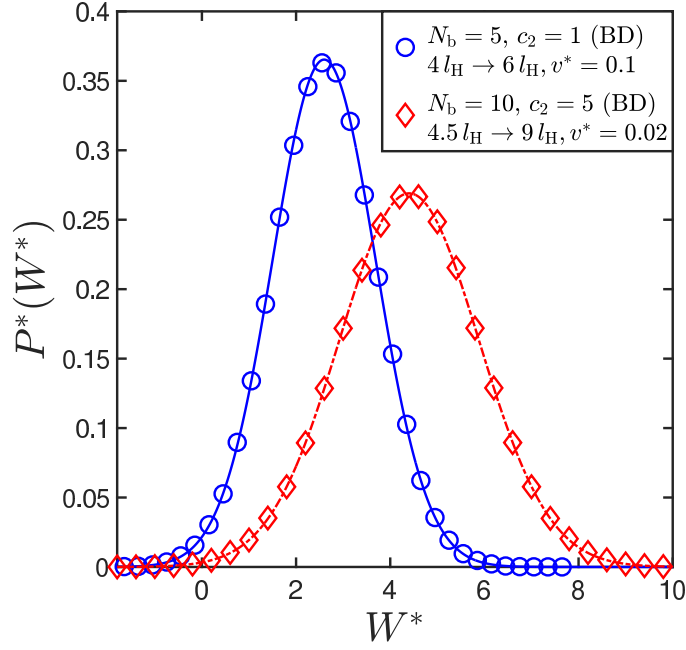
Figure 3.11: Validation of the code for single chain pulling. Comparison of the analytical probability distribution function of the work trajectories, against that computed by binning the work trajectories obtained in pulling simulations on Hookean chains. The lines correspond to the Gaussian probability distribution given by Eq. (3.89), with variance and mean defined in Eqs. (3.90) and (3.91), respectively.

The calculated work is then used to estimate the free-energy difference and the average dissipation as shown in Eq. (3.1).

3.3.3   Code validation for the single chain case

The probability of the work distribution for a one-dimensional Rouse chain tethered at one end and subjected to constant velocity pulling may be analytically calculated, as shown by Dhar (2005). A chain of N_b beads connected by N springs is considered, with the stiffness of each spring denoted by H. The first bead is held fixed at the origin, and the last bead is subjected to a harmonic trap of stiffness $c_2 H$. The trap is moved from an initial position of $\chi^{(i)}$ to a final position of $\chi^{(f)}$, over a time τ. The distance traveled by the trap is denoted by $d \equiv \chi^{(f)} - \chi^{(i)}$, and the pulling velocity, v, given by $v = d/\tau$.

Following the procedure proposed by Dhar (2005), and using the standard non-dimensionalization scheme [see Eq. (3.57), for example], the free energy difference associated with the stretching process is evaluated to be

$$\Delta A^* = \frac{c_2}{2\,(c_2 N + 1)}\left[\left(\chi^{(f)*}\right)^2 - \left(\chi^{(i)*}\right)^2\right], \tag{3.88}$$

and $P^*(W^*)$ is found to be a Gaussian of the form,

$$P^*(W^*) = \frac{1}{\sqrt{2\pi\sigma^2}} \exp\left[-\frac{(W^* - \langle W^*\rangle)^2}{2\sigma^2}\right], \tag{3.89}$$

whose variance and mean are given by

$$\sigma^2 = \frac{c_2^2 v^* d^*}{2\tau^*}\left\{\boldsymbol{E}^{-2} + \frac{1}{\tau^*}\boldsymbol{E}^{-3}\left(e^{-\boldsymbol{E}\tau^*} - 1\right)\right\}_{NN} \equiv 2\langle W_{\text{dis}}^*\rangle \tag{3.90}$$

$$\langle W^*\rangle = \Delta A^* + \frac{\sigma^2}{2} \tag{3.91}$$

where the notation $\{...\}_{ij}$ refers to the $(ij)^{\text{th}}$ matrix element, and $\boldsymbol{E}$ is a symmetric, tridiagonal $N \times N$ matrix of the following form

$$E_{ij} = \begin{cases} \dfrac{1}{2}; & i = j \neq N \\[2ex] -\dfrac{1}{4}; & |i - j| = 1 \\[2ex] \dfrac{(c_2 + 1)}{4}; & i = j = N \\[2ex] 0; & \text{otherwise} \end{cases} \tag{3.92}$$

The pulling of Rouse chains was simulated using Brownian dynamics, and the work statistics calculated over an ensemble size of $O(10^5)$, by numerically integrating Eq. (3.87). The first bead was held fixed at the origin by means of a stiff harmonic trap of strength $c_1 = 1000$, and two different values for the pulling trap stiffness, c_2 have been considered. In Fig. 3.11, the probability distribution of work values obtained from BD simulations is compared against the analytical solution for two sample cases. The good agreement between the two suggests the validity of the code used to perform pulling simulations on polymer chains.

3.3.4   Parameter space specification

A value of $b = 50$ is used throughout this section for the dimensionless FENE parameter. For a free chain (without confining potentials acting on the terminal beads), with this particular value of b, the choice of $r_{\text{cut}} = 1.82\sigma$, $m_1 = 1.5306333121$, and $m_2 = 1.213115524$ have been shown to lead to the correct scaling predictions in poor, θ, and good solvent conditions for the radius of gyration with the number of beads in the chain, as described in detail in Santra *et al.* (2019), and hence have been used for all simulations on single chains discussed in this section. The θ-temperature for this system
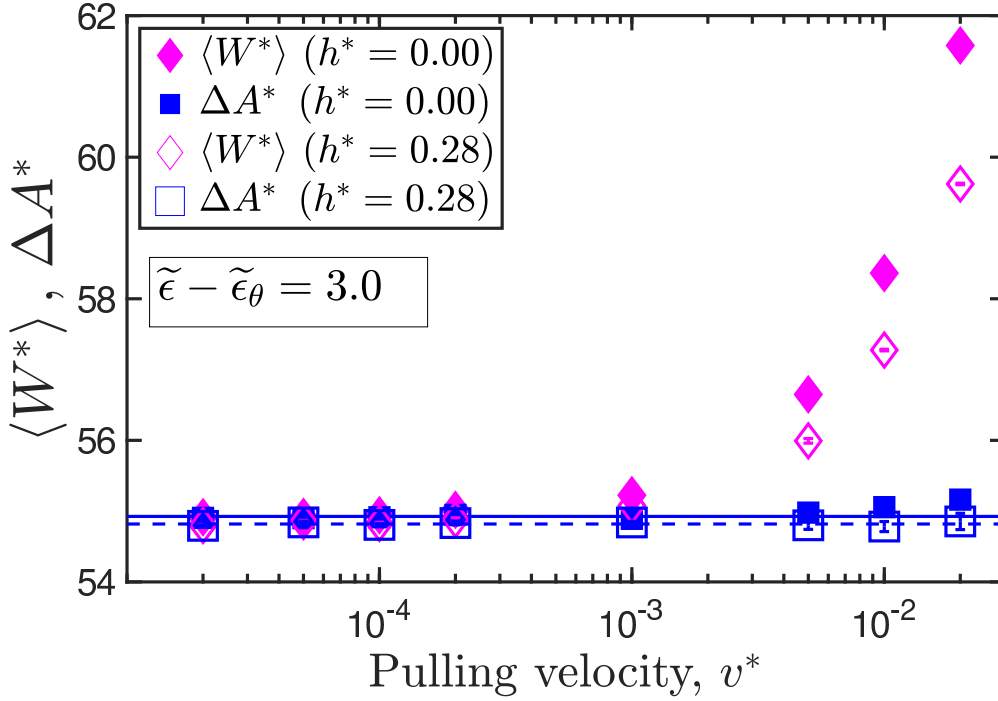
Figure 3.12: Equivalence between the free energy difference estimated using the Jarzynski equality and the classical definition. Total work done as a function of the pulling velocity, for a well-depth of $\widetilde{\epsilon} = 3.45$ and a chain size of ten beads. The open and filled square symbols indicate the Jarzynski estimate of the free-energy difference evaluated for models with and without the inclusion of fluctuating hydrodynamic interactions, respectively.

is observed to be at $\widetilde{\epsilon} \approx 0.45$, where $\left\langle R_{\mathrm{g}}^{2} \right\rangle \sim (N_{\mathrm{b}} - 1)$ and the second virial coefficient, $B_2 = 0$ (Santra *et al.*, 2019). This value of cohesive strength is denoted as $\widetilde{\epsilon}_\theta$. Poor solvent scaling, namely, $\left\langle R_{\mathrm{g}}^{2} \right\rangle \sim (N_{\mathrm{b}} - 1)^{0.67}$, is observed for $\widetilde{\epsilon} \geq 0.55$. The bead radius, a, is defined on the basis of σ_{s}, as $a = 0.5\sigma_{\mathrm{s}}$. We set $\sigma_{\mathrm{s}} = l_{\mathrm{H}}$ in all our simulations.

A trap stiffness of $c_1 = c_2 = 1000$ is used for both the stationary and the mobile traps. The initial and final positions of the mobile traps are chosen as $\chi_{2x}^{(\mathrm{i})} = 0.1 \, L_{\mathrm{c}}$ and $\chi_{2x}^{(\mathrm{f})} = 0.3 \, L_{\mathrm{c}}$, respectively, where $L_{\mathrm{c}} \equiv (N_{\mathrm{b}} - 1) Q_0$ is the contour length of the chain. A chain size of $N_{\mathrm{b}} = 10$ has been used for all the simulation results reported in this section.

3.3.5 Globule unraveling is wet

Netz and coworkers (Alexander-Katz *et al.*, 2009) have measured the internal friction associated with collapsed homopolymers by measuring the work dissipated in the force-induced unfolding of a single polymer chain. As mentioned previously, they estimate the free energy difference, denoted by W_{eq}, as the work done in the quasi-static pulling limit, that is, $W_{\mathrm{eq}}(\widetilde{\epsilon}) \equiv W(\widetilde{\epsilon}, v \to 0)$. The dissipated work at any finite pulling velocity is then calculated as the difference between the average work done at that
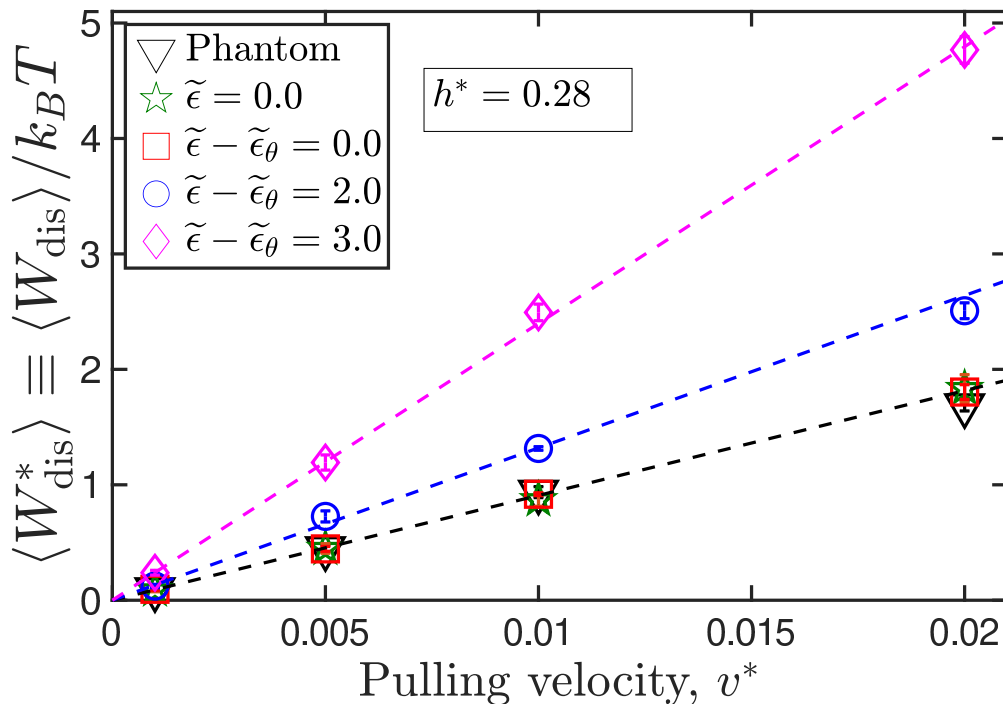
Figure 3.13: Regime of linear dependence between average dissipation and pulling velocity determined by strength of cohesive interactions. Average dimensionless dissipation, as a function of the dimensionless pulling velocity. The dashed lines are linear fits to the data.

velocity, and the reversible work. This is exactly the definition of dissipation that we have adopted throughout this chapter, as indicated in Eq. (3.1). However, rather than using the work done in the quasi-static limit to estimate the free-energy difference, we use the Jarzynski equality to evaluate the same quantity.

In Fig. 3.12, the total dimensionless work done in pulling a ten-bead chain with a representative set of parameters is plotted as a function of the dimensionless pulling velocity, for cases with and without hydrodynamic interactions. Horizontal lines represent the error-weighted mean of the total work at the lowest four values of the pulling velocity, and is therefore a measure of the free-energy difference in the classical sense. Solid lines correspond to the freely-draining case, while dashed lines indicate the case with hydrodynamic interactions. It is seen that the free-energy differences for cases with and without HI concur within $\sim 10^{-1} k_B T$, in agreement with the expectation that the free-energy difference, a static equilibrium property, remains unaffected by hydrodynamic fluctuations. Furthermore, it is also seen from the figure that the work done in the quasi-static limit agrees, within error bars, with the free-energy difference estimated using the Jarzynski equality (square symbols), thus establishing the validity of our approach for the estimation of the free-energy difference and the dissipation.
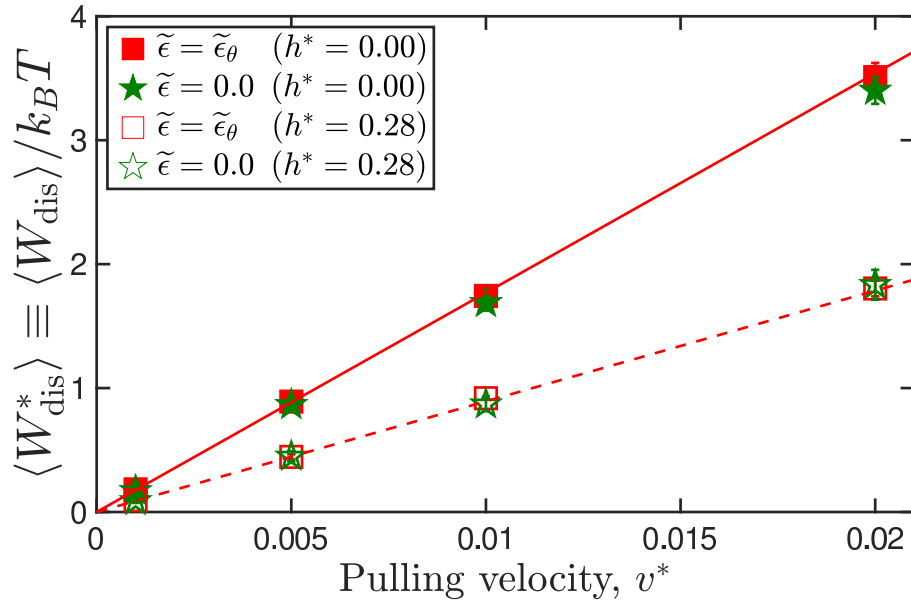
(a)
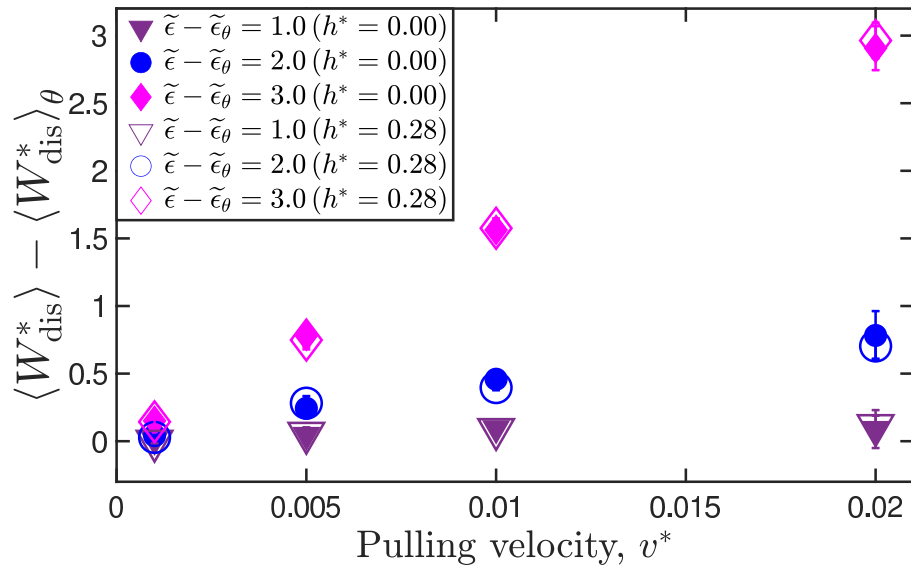
(b)

Figure 3.14: Effect of hydrodynamic interactions on the dissipated work: (a) the average dissipation, and (b) the enhancement in the average dissipation (with respect to the dissipation due to solvent) due to cohesive interactions, plotted as a function of the dimensionless pulling velocity. Symbols representing the enhancement values for cases with HI have been enlarged for clarity.

In Fig. 3.13, the dimensionless average dissipation is plotted as a function of the dimensionless pulling velocity. It is seen that the data for the phantom chain (no excluded volume interactions), athermal chain (purely repulsive interactions) and the chain under θ−conditions superimpose. This indicates that for uncollapsed chains, the work dissipated during pulling is expended entirely against the solvent friction, and there is no internal friction associated with these cases. Furthermore, increasing the well-depth beyond the θ−point results in an increased dissipation at a fixed value of the pulling velocity, which is due to the additional work needed to unravel the globule as the polymer chain is stretched. The average dissipation scales linearly with the pulling velocity over the entire range of the latter quantity.

In the linear regime, for a collapsed globule ($\widetilde{\epsilon} > \widetilde{\epsilon}_\theta$), the following relationship for the dissipation can be written,

$$\langle W_{\text{dis}} \rangle = \gamma_{\text{G}} v d \tag{3.93}$$

where γ_{G} is the globule friction coefficient. The same expression is valid in the uncollapsed case, with γ_{G} replaced with γ_{s}, the solvent friction coefficient. As $\widetilde{\epsilon} \to \widetilde{\epsilon}_\theta$, the dissipation is entirely due to the solvent, and $\gamma_{\text{G}} \to \gamma_{\text{s}}$.

Fig. 3.14 elucidates the effect of hydrodynamic interactions on the dissipation more clearly. As shown in Fig. 3.14 (a), for chains under both θ and athermal conditions, the dissipation due to the solvent decreases identically upon the inclusion of fluctuating hydrodynamic interactions. In Fig. 3.14 (b), it is seen that the enhancement in the dissipation due to cohesive interactions, measured as the difference between the total dissipation and the dissipation due to solvent alone, remains practically unaffected by hydrodynamic interactions.

In Fig. 3.15, the average dissipated work is plotted for two values of the well-depth, for one value of the dimensional pulling velocity, as a function of the solvent viscosity. At any finite value of the solvent viscosity, the work dissipated for the collapsed globule case is greater than that for that in θ−condition. However, in the extrapolated limit $\eta_{\text{s}} \to 0$, the dissipated work goes to zero. Clearly, this suggest that the additional dissipation due to cohesive interactions between the beads corresponds to the case of wet internal friction, which is not clear a priori, and can only be established following the protocol proposed here.

In Figs. 3.16, the friction coefficients calculated using Eq. (3.93) have been plotted as a function of the solvent viscosity. From Fig. 3.16 (a), it is seen that friction coefficient due to the solvent scales linearly with the solvent viscosity, and that hydrodynamic interactions reduce the friction coefficient in comparison to the freely draining case.
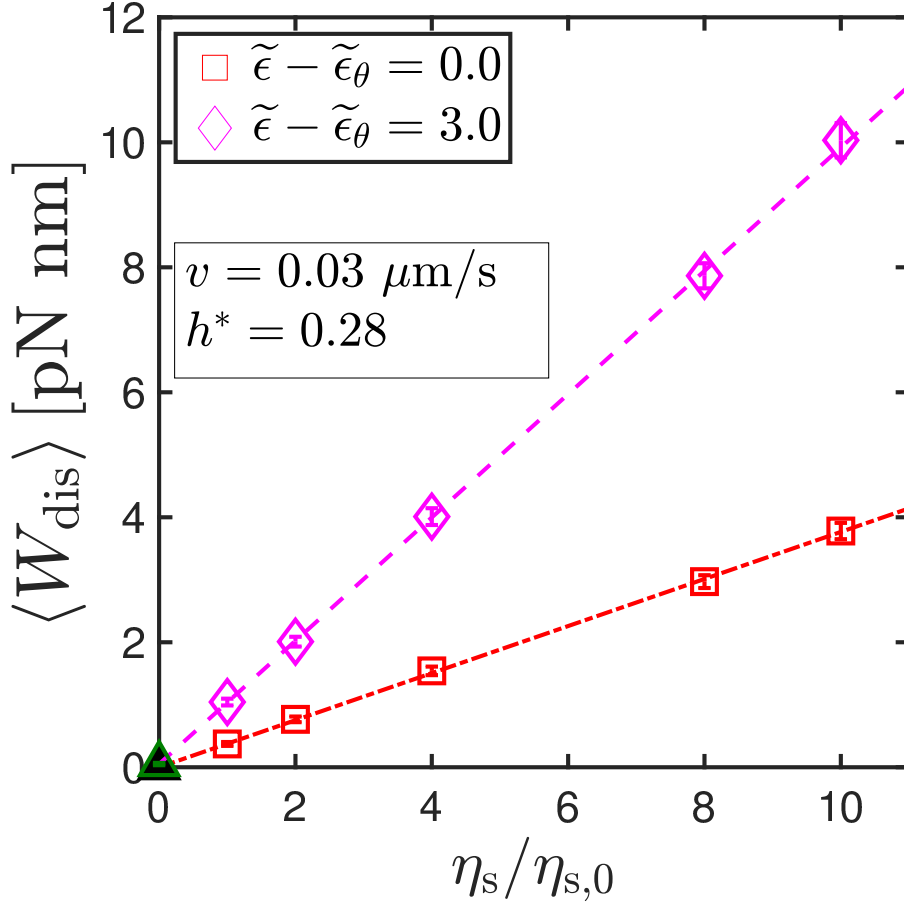
Figure 3.15: Protocol establishes the presence of wet friction. Average dissipation as a function of the solvent viscosity for two different well-depths. The extrapolated value in the limit of zero solvent viscosity is indicated by an upright triangle, and the extrapolated values for both the cases are found to coincide within error bars of the simulation.

From Fig. 3.16 (b), it is seen that the inclusion of cohesive interactions results in an enhancement in the friction coefficient at all finite values of the solvent viscosity. In the extrapolated limit of zero solvent viscosity, however, the friction coefficient is also seen to tend to zero, as is typical of wet friction.

By taking a ratio of the slopes of the dissipation versus pulling velocity for the collapsed and the uncollpased states, for identical pulling distances in the linear regime, one gets

$$\frac{\langle W_{\text{dis}} \rangle}{\langle W_{\text{dis}} \rangle_\theta} - 1 = \frac{\gamma_G - \gamma_s}{\gamma_s} \qquad (3.94)$$

This quantity represents the rescaled excess contribution to the dissipation due to internal friction, and enables an investigation of the relationship between γ_G and γ_s, and comparison with Zwanzig's (1988) prediction, as was done previously by Alexander-Katz *et al.* (2009) in the absence of hydrodynamic interactions. For a Brownian particle moving
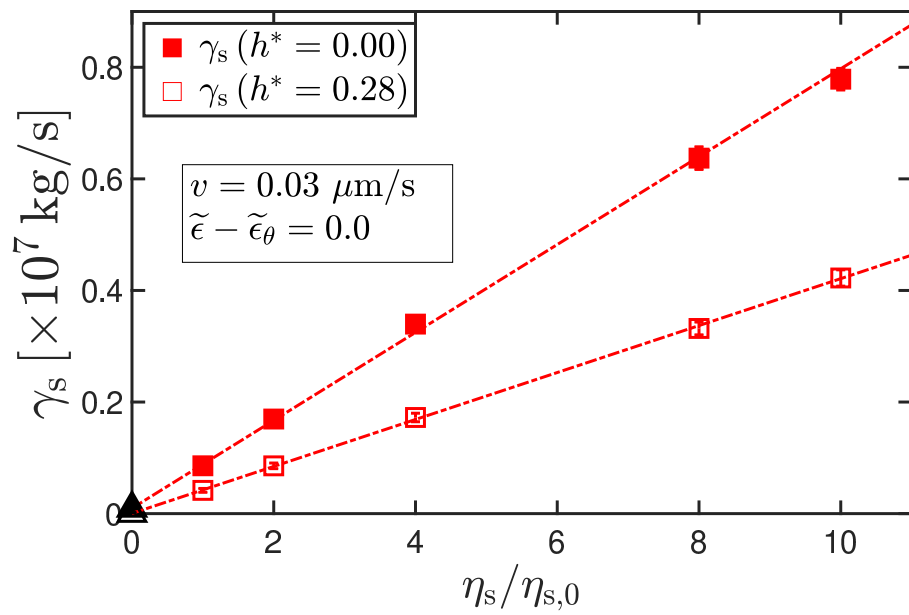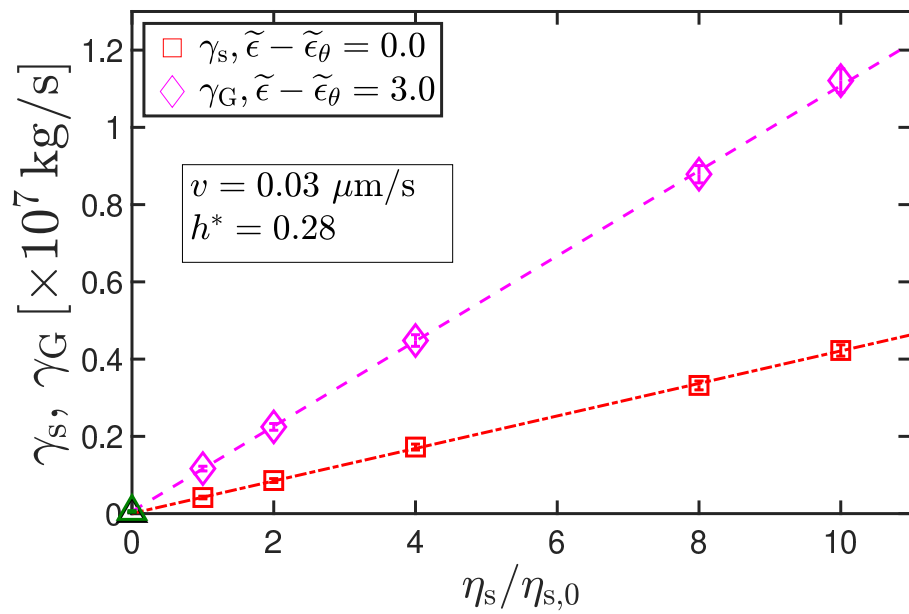
Figure 3.16: Effect of hydrodynamic interactions on the friction coefficient: (a) Solvent friction, with and without hydrodynamic interactions and (b) a comparison between the solvent and globule friction coefficient, with hydrodynamic interactions, plotted as a function of solvent viscosity.
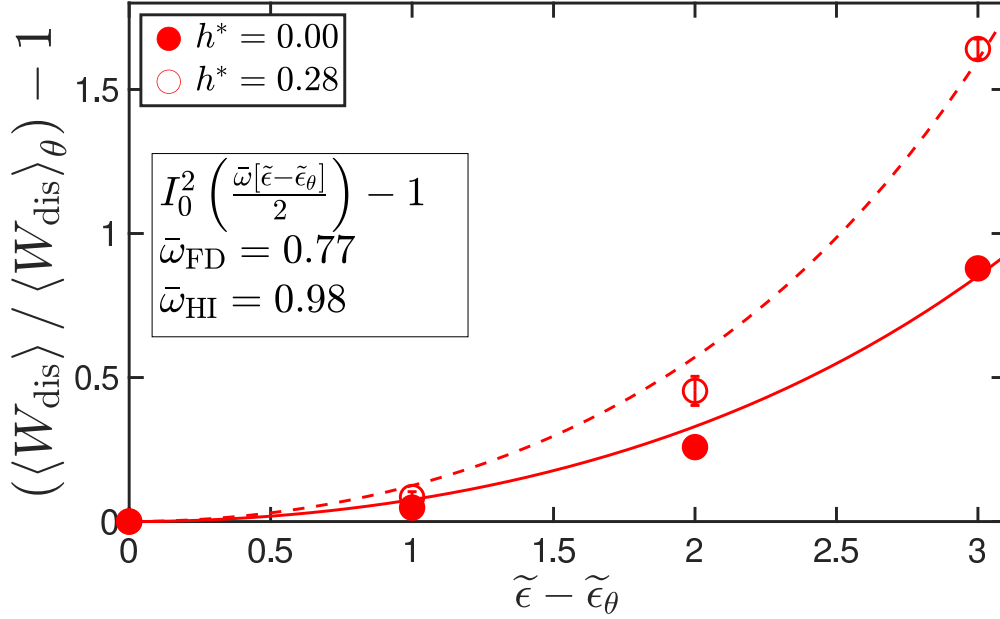
Figure 3.17: Magnification of internal friction due to cohesive interactions. Rescaled excess contribution to dissipation as a function of the effective well-depth. Solid and dashed lines are used to fit the data points obtained for cases without and with HI, respectively, and correspond to Eq. (3.95) with fitting parameters $\bar{\omega}_{\mathrm{FD}} = 0.77$ and $\bar{\omega}_{\mathrm{HI}} = 0.98$.

in a corrugated one-dimensional potential of the form $U(x) = (\bar{\omega}/2)(\widetilde{\epsilon} - \widetilde{\epsilon}_{\theta})\sin(\pi x/a)$, the effective friction and the solvent friction are related by (Alexander-Katz *et al.*, 2009; Zwanzig, 1988)

$$\frac{\gamma_{\mathrm{G}} - \gamma_{\mathrm{s}}}{\gamma_{\mathrm{s}}} = I_0^2\left(\frac{\bar{\omega}(\widetilde{\epsilon} - \widetilde{\epsilon}_{\theta})}{2}\right) - 1 \tag{3.95}$$

where $I_0(..)$ is the modified Bessel function of zeroth order, and $\bar{\omega}$ is a fitting parameter.

In Fig. 3.17, the rescaled excess dissipation due to internal friction, for models with and without fluctuating hydrodynamic interactions, is plotted as a function of the well-depth relative to the θ−condition. It is seen from the figure that a good qualitative agreement is observed between the simulation results and Eq. (3.95), but with a fitting parameter that depends on whether hydrodynamic interactions are incorporated in the simulations. This agreement between simulations and theory, also observed by Alexander-Katz *et al.* (2009), suggests that Zwanzig's formulation, albeit based on a one-dimensional energy landscape, satisfactorily captures the scaling of internal friction with the strength of cohesive interactions in force-spectroscopy simulations on single molecules. The subject of diffusion on rugged energy landscapes of dimension higher than one has been treated rigorously in Seki and Bagchi (2015) and Seki *et al.* (2016).

3.4   Conclusions

In summary, we have introduced a simple and novel protocol based on the Jarzynski equality for determining both dry and wet internal friction coefficients of macromolecules that can be implemented experimentally using optical tweezers.   Using Brownian dynamics simulations on a spring-dashpot model for a polymer, we establish proof-of-principle by recovering the dry internal friction coefficient which is used as a model input, and show that a bead-spring chain with cohesive interactions is an example of wet friction. It is conceivable that some real polymer chains might possess both wet and dry internal friction, and modeling such molecules would require the use of multi-bead-spring-dashpots with cohesive interactions. We envisage that the scheme proposed here may be applicable to a variety of macromolecules, and would enable a succinct characterization of the dissipative properties of the molecule. The results presented in this chapter have been published in Kailasham *et al.* (2020).

The rheology of coarse-grained models with internal friction is discussed in the subsequent two chapters, and Chapter 4 is dedicated to the study of finitely extensible dumbbells with fluctuating internal viscosity and hydrodynamic interactions.

Chapter 4

Rheological consequences of internal friction and hydrodynamic interactions in a dumbbell model

4.1   Introduction

The effects of internal friction on the dynamic response of polymer chains, and the rheological response of dilute polymer solutions has been briefly surveyed in Chapter 1. There is a wealth of literature on the rheological properties of dumbbell models with internal viscosity (Booij and van Wiechen, 1970; Schieber, 1993; Wedgewood, 1993; Sureshkumar and Beris, 1995; Hua and Schieber, 1995; Hua *et al.*, 1996). In a parallel development, recent advances in modelling the non-equilibrium behaviour of polymer solutions have revealed the crucial role played by fluctuating hydrodynamic interactions in determining the dynamics of polymer chains (Prabhakar and Prakash, 2002; Sunthar and Prakash, 2005; Larson, 2005; Schroeder, 2018; Prakash, 2019). Coarse-grained polymer models that include both fluctuating internal friction and hydrodynamic interactions, however, are rare (Hua and Schieber, 1996), with the majority including hydrodynamic interactions in a pre-averaged manner (Manke and Williams, 1992; Dasbach *et al.*, 1992). In this chapter, we use Brownian dynamics simulations to solve a dumbbell model of the polymer with a finitely extensible spring, and fluctuating internal friction and hydrodynamic interactions, and examine its properties at equilibrium, and in the presence of flow, in order to study the relative roles played by internal friction and hydrodynamic interactions in determining the dynamics of polymer molecules.

Analytical studies by Manke and Williams (1992) predict that the stress jump of a model with IV and pre-averaged HI would be higher than that for a model with IV alone.

A prior BD simulation study of a dumbbell model with fluctuating internal viscosity and hydrodynamic interactions, which examined the stress and velocity fields during startup of shear-flow using the CONFESSIT approach (Hua and Schieber, 1996), concludes that hydrodynamic interactions have a negligible effect on the stress field. Here, we re-examine the accuracy of this prediction, with particular attention to the magnitude of the stress jump in the presence of fluctuating hydrodynamic interactions.

The Gaussian approximation for internal viscosity (Schieber, 1993) concludes that it has no effect on zero-shear rate viscometric functions. The validity of this prediction is scrutinized using exact BD simulations, particularly in the presence of both fluctuating HI and IV. Building upon prior work (Gerhardt and Manke, 1994; Hua *et al.*, 1996), we also present what we consider to be a hitherto unexplored relationship between zero-shear rate properties, the relaxation modulus and the stress jump.

Polymer solutions and melts are commonly observed to exhibit an "overshoot" in their rheological properties(Bird *et al.*, 1987a) when subjected to shear flow. The effect of fluctuating internal viscosity and hydrodynamic interactions on the magnitude, and the time of occurrence of the overshoot is analyzed in this work, and compared to prior observations.

It is well known that dumbbell models which limit the extensibility of the spring predict the shear-thinning of viscometric functions (Warner, 1972; Christiansen and Bird, 1977). The effect of internal viscosity on such shear-thinning has already been studied (Hua and Schieber, 1995). Here, the combined effect of fluctuating internal viscosity and hydrodynamic interactions on this phenomenon is quantitatively analyzed by comparing shear-thinning exponents for the various cases.

Manke and Williams have analytically examined the relationship between rigid dumbbells and dumbbell models with an infinite value of the internal viscosity parameter (Manke and Williams, 1986, 1989, 1991, 1993), and predict that an ensemble of Hookean dumbbells with an infinite value of the internal viscosity parameter would resemble the viscometric functions of an ensemble of rigid dumbbells, at least qualitatively. Hua *et al.* (1996) have compared the linear viscoelastic properties of Hookean dumbbells with IV to that of rigid dumbbells, and find that the relaxation modulus of dumbbells with a high value of the IV parameter agrees remarkably well with that of rigid dumbbells with a Gaussian distribution of lengths. We use exact BD simulations to calculate the linear viscoelastic and viscometric properties of dumbbells with a high value of the IV parameter, and compare the results against prior observations. We find that the nature of the spring force law qualitatively influences the predicted viscometric functions.

The chapter is structured as follows. In Section 4.2 we present the governing equations for the FENE dumbbell model for a polymer with internal viscosity and hydrodynamic interactions, its solution methodology and the simulation details. Section 4.3, which summarises our results and the relevant discussions, is subdivided into four sections; Sec. 4.3.1 deals with code validation, Sec. 4.3.2 discusses the transient response of dumbbells subjected to shear-flow, Sec. 4.3.3 presents the steady-state results of viscometric functions, and Sec. 4.3.4 the results for models with a high value of the internal viscosity parameter against that of rigid dumbbells. The key findings of this chapter are summarised in the Sec. 4.4. The detailed steps for the derivation of the governing equations, starting from a force balance on the beads, is given in Appendix A.

4.2   Governing Equations and Simulation Details

For a FENE dumbbell with internal viscosity and hydrodynamic interactions and no excluded volume interactions in a homogeneous flow field, the equation for the connector vector velocity given by Eq. 2.1 in Chapter 2 reduces to

$$\llbracket \dot{\boldsymbol{Q}} \rrbracket = \left[\boldsymbol{\delta} - \frac{\epsilon\beta}{\epsilon\beta + 1} \frac{\boldsymbol{Q}\boldsymbol{Q}}{Q^2} \right] \cdot \left([\boldsymbol{\kappa} \cdot \boldsymbol{Q}] - \frac{2k_BT}{\zeta} (\boldsymbol{\delta} - \zeta\boldsymbol{\Omega}) \cdot \frac{\partial}{\partial \boldsymbol{Q}} \ln \psi - \frac{2}{\zeta} (\boldsymbol{\delta} - \zeta\boldsymbol{\Omega}) \cdot \frac{\partial \phi}{\partial \boldsymbol{Q}} \right) \quad (4.1)$$

where $\phi \equiv \phi_{\text{FENE}}^{\text{S}}$ [as defined in Eq. 2.10] throughout this chapter. By substituting Eq. (4.1) into the equation of continuity, the Fokker-Planck equation for a FENE dumbbell with HI and IV is obtained as

$$\begin{aligned}
\frac{\partial \psi}{\partial t} = & - \frac{\partial}{\partial \boldsymbol{Q}} \cdot \left\{ \left(\boldsymbol{\delta} - \frac{\epsilon\beta}{\epsilon\beta + 1} \frac{\boldsymbol{Q}\boldsymbol{Q}}{Q^2} \right) \cdot \left(\boldsymbol{\kappa} \cdot \boldsymbol{Q} - \frac{2}{\zeta} (\boldsymbol{\delta} - \zeta\boldsymbol{\Omega}) \cdot \frac{\partial \phi}{\partial \boldsymbol{Q}} \right) \psi \right\} \\
& + \frac{2k_BT}{\zeta} \frac{\partial}{\partial \boldsymbol{Q}} \cdot \left\{ \left[\left(\boldsymbol{\delta} - \frac{\epsilon\beta}{\epsilon\beta + 1} \frac{\boldsymbol{Q}\boldsymbol{Q}}{Q^2} \right) \cdot (\boldsymbol{\delta} - \zeta\boldsymbol{\Omega}) \right] \cdot \frac{\partial \psi}{\partial \boldsymbol{Q}} \right\}
\end{aligned} \quad (4.2)$$

Using the following dimensionless variables,

$$t^* = \frac{t}{\lambda_{\text{H}}}; \; \boldsymbol{Q}^* = \frac{\boldsymbol{Q}}{l_H}; \; \boldsymbol{\kappa}^* = \lambda_{\text{H}}\boldsymbol{\kappa}; \; \phi^* = \frac{\phi}{k_BT}; \; \psi^* = \psi l_H^3 \quad (4.3)$$

the Fokker-Planck equation in its dimensionless form may be written as follows.

$$\begin{aligned}
\frac{\partial \psi^*}{\partial t^*} = & - \frac{\partial}{\partial \boldsymbol{Q}^*} \cdot \left\{ \left(\boldsymbol{\delta} - \frac{\epsilon\beta^*}{\epsilon\beta^* + 1} \frac{\boldsymbol{Q}^*\boldsymbol{Q}^*}{Q^{*2}} \right) \cdot \left(\boldsymbol{\kappa}^* \cdot \boldsymbol{Q}^* - (\boldsymbol{\delta} - \zeta\boldsymbol{\Omega}) \cdot \frac{\frac{1}{2}\boldsymbol{Q}^*}{1 - Q^{*2}/b} \right) \psi^* \right\} \\
& + \frac{1}{2} \frac{\partial}{\partial \boldsymbol{Q}^*} \cdot \left\{ \left[\left(\boldsymbol{\delta} - \frac{\epsilon\beta^*}{\epsilon\beta^* + 1} \frac{\boldsymbol{Q}^*\boldsymbol{Q}^*}{Q^{*2}} \right) \cdot (\boldsymbol{\delta} - \zeta\boldsymbol{\Omega}) \right] \cdot \frac{\partial \psi^*}{\partial \boldsymbol{Q}^*} \right\}
\end{aligned} \quad (4.4)$$

Note that β^* and β are both dimensionless. However,

$$\beta^* = 1 - \frac{\bar{\alpha}}{Q^*} (\mathscr{A}^* + \mathscr{B}^*) \quad (4.5)$$

where $\mathscr{A}^*$ and $\mathscr{B}^*$ can be obtained by recasting all the dimensional quantities in Eq. (2.6) into their non-dimensionalized form, and $\bar{\alpha}$ is given by $\bar{\alpha} = (3/4)\sqrt{\pi}h^*$, where $h^* = a/\left(\sqrt{\pi}l_H\right)$ is the hydrodynamic interaction parameter.

As shown in Appendix A, the stochastic differential equation (SDE) equivalent to Eq. (4.4) can be derived using the Itô interpretation as,

$$
d\boldsymbol{Q}^* = \left[\boldsymbol{\kappa}^* \cdot \boldsymbol{Q}^* + \frac{g_2}{2}\frac{\boldsymbol{Q}^*}{Q^*} - \left(\frac{Q^* - \mathscr{A}^*\bar{\alpha}}{Q^*}\right)\left(\boldsymbol{\delta} - g_1\frac{\boldsymbol{Q}^*\boldsymbol{Q}^*}{Q^{*2}}\right) \cdot \left(\frac{\frac{1}{2}\boldsymbol{Q}^*}{1 - Q^{*2}/b} + \epsilon\frac{\boldsymbol{Q}^*\boldsymbol{Q}^*}{Q^{*2}} \cdot \boldsymbol{\kappa}^* \cdot \boldsymbol{Q}^*\right)\right]dt^*
$$

$$
+ \sqrt{\frac{Q^* - \mathscr{A}^*\bar{\alpha}}{Q^*}}\left[\boldsymbol{\delta} - \left(1 - \sqrt{1 - g_1}\right)\frac{\boldsymbol{Q}^*\boldsymbol{Q}^*}{Q^{*2}}\right] \cdot d\boldsymbol{W}_t
$$

(4.6)

In the second term of the above equation, the prefactor that multiplies $d\boldsymbol{W}_t$ is the diffusion tensor. It is worth noting that the functional form of the SDE remains the same, irrespective of the choice of the HI tensor. The definitions of g_1 and g_2 are as follows

$$
g_1 = \frac{\bar{\alpha}\mathscr{B}^*Q^* + \epsilon(Q^* - \mathscr{A}^*\bar{\alpha})[Q^* - \bar{\alpha}(\mathscr{A}^* + \mathscr{B}^*)]}{(Q^* - A^*\bar{\alpha})\{Q^* + \epsilon[Q^* - \bar{\alpha}(A^* + B^*)]\}}
$$

(4.7)

$$
g_2 = \frac{2\bar{\alpha}\mathscr{B}^*}{\{Q^* + \epsilon[Q^* - \alpha(\mathscr{A}^* + \mathscr{B}^*)]\}^2} - 2g_1\left(\frac{Q^* - \mathscr{A}^*\bar{\alpha}}{Q^{*2}}\right)
$$

(4.8)

$$
- \bar{\rho}\frac{2\epsilon\bar{\alpha}[Q^* - \bar{\alpha}(\mathscr{A}^* + \mathscr{B}^*)]\,[2Q^* + \epsilon[Q^* - \bar{\alpha}(\mathscr{A}^* + \mathscr{B}^*)]]}{Q^{*2}\{Q^* + \epsilon[Q^* - \bar{\alpha}(\mathscr{A}^* + \mathscr{B}^*)]\}^2}
$$

where

$$
\bar{\rho} = (s - \mathscr{B}^*), \quad s = \frac{1}{2}\left[(\mathscr{A}^* + \mathscr{B}^*) - Q^*\frac{\partial}{\partial Q^*}(\mathscr{A}^* + \mathscr{B}^*)\right]
$$

(4.9)

Interestingly, for the RPY tensor, the following property holds for both its branches.

$$
(\mathscr{A}^* + \mathscr{B}^*) - Q^*\frac{\partial}{\partial Q^*}(\mathscr{A}^* + \mathscr{B}^*) = 2\mathscr{B}^*
$$

(4.10)

This results in a simplification and we have

$$
g_2^{\text{RPY}} = \frac{2\bar{\alpha}\mathscr{B}^*}{\{Q^* + \epsilon[Q^* - \bar{\alpha}(\mathscr{A}^* + \mathscr{B}^*)]\}^2} - 2g_1\left(\frac{Q^* - \mathscr{A}^*\bar{\alpha}}{Q^{*2}}\right)
$$

(4.11)

Eq. (4.6) is solved using a semi-implicit predictor-corrector algorithm, as outlined below. Note that, while Eqs. (4.12) to (4.16) below are in their non-dimensionalized form, the asterisk superscript has been dropped from these equations for notational simplicity.

Predictor Step

$$
\widetilde{\boldsymbol{Q}}(t_{j+1}) = \boldsymbol{Q}(t_j) + \left[\boldsymbol{\kappa}(t_j) \cdot \boldsymbol{Q}(t_j) - \left(\frac{\epsilon\beta(t_j)}{\epsilon\beta(t_j) + 1}\right)\frac{\boldsymbol{Q}(t_j)\boldsymbol{Q}(t_j)}{Q^2(t_j)} \cdot \left(\boldsymbol{\kappa}(t_j) \cdot \boldsymbol{Q}(t_j)\right)\right.
$$

$$
\left. - \frac{1}{2\left(1 - Q^2(t_j)/b\right)}\left(\frac{\beta(t_j)}{\epsilon\beta(t_j) + 1}\right)\boldsymbol{Q}(t_j) + \frac{g_2(t_j)}{2}\frac{\boldsymbol{Q}(t_j)}{Q(t_j)}\right]\Delta t_j + \Delta\boldsymbol{S}_j
$$

(4.12)

where

$$\Delta S_j = b_j \cdot \Delta W_j \tag{4.13}$$

and

$$b_j = \sqrt{\frac{Q(t_j) - \mathscr{A}(t_j)\bar{\alpha}}{Q(t_j)}} \left[\delta - \left(1 - \sqrt{1 - g_1(t_j)} \right) \frac{Q(t_j)Q(t_j)}{Q^2(t_j)} \right] \tag{4.14}$$

ΔW_j is a vector of three independent Wiener processes, each of mean zero and variance Δt_j.

Corrector Step

$$\left[1 + \frac{1}{4}\left(\frac{\widetilde{\beta}(t_{j+1})}{\epsilon\widetilde{\beta}(t_{j+1}) + 1} \right) \frac{\Delta t_j}{1 - Q^2(t_{j+1})/b} \right] Q(t_{j+1}) = Q(t_j)\left[1 - \frac{1}{4}\left(\frac{\beta(t_j)}{\epsilon\beta(t_j) + 1} \right)\left(\frac{1}{1 - Q^2(t_j)/b} \right) \right.$$

$$+ \frac{g_2(t_j)}{4Q(t_j)} \right] \Delta t_j + \widetilde{Q}(t_{j+1})\left[\frac{\widetilde{g_2}(t_{j+1})}{4\widetilde{Q}(t_{j+1})} \right] \Delta t_j + \frac{1}{2}\left[\kappa(t_j) \cdot Q(t_j) + \kappa(t_{j+1}) \cdot \widetilde{Q}(t_{j+1}) \right.$$

$$- \left(\frac{\epsilon\beta(t_j)}{\epsilon\beta(t_j) + 1} \right) \frac{Q(t_j)Q(t_j)}{Q^2(t_j)} \cdot \left(\kappa(t_j) \cdot Q(t_j) \right)$$

$$- \left. \left(\frac{\epsilon\widetilde{\beta}(t_{j+1})}{\epsilon\widetilde{\beta}(t_{j+1}) + 1} \right) \frac{\widetilde{Q}(t_{j+1})\widetilde{Q}(t_{j+1})}{\widetilde{Q}^2(t_{j+1})} \cdot \left(\kappa(t_{j+1}) \cdot \widetilde{Q}(t_{j+1}) \right) \right] \Delta t_j + \Delta S_j \tag{4.15}$$

Here, $\widetilde{Q}(t_{j+1})$ is the value of Q after the predictor step, evaluated in Eq. (4.12).

Note that only the FENE spring force term is treated implicitly in the corrector step. By setting the length of the vector on the RHS of Eqn. (4.15) to be *L*, and the length of $Q(t_{j+1})$ to be *x*, we get the following cubic equation in *x*

$$x^3 - x^2 L - xb\left[1 + \frac{\Delta t_j}{4}\left(\frac{\widetilde{\beta}(t_{j+1})}{\epsilon\widetilde{\beta}(t_{j+1}) + 1} \right) \right] + Lb = 0 \tag{4.16}$$

Eq. (3.73) can be solved exactly using trigonometric functions (Öttinger, 1996) and only one root lies in the interval $\left[0, \sqrt{b} \right]$, which is chosen as the physically relevant solution for *x*. The Kramers expression for the stress-tensor is not thermodynamically consistent for dumbbells with internal viscosity (Schieber and Öttinger, 1994), and the Giesekus expression cannot be used when hydrodynamic interactions are included (Bird *et al.*, 1987b). For the general case considered here, with both IV and HI, Hua and Schieber (1996) suggest that the Kramers-Kirkwood expression can be used, since it is thermodynamically consistent (Schieber and Öttinger, 1994),

$$\tau_p = -n_p \sum_\nu \left\langle R_\nu F_\nu^{(h)} \right\rangle \tag{4.17}$$

where n_p is the number of polymer molecules per unit volume, and $\boldsymbol{R}_\nu$ is the position of the νth bead with respect to the centre-of-mass, $\boldsymbol{r}_\mathrm{c}$. $\boldsymbol{F}_\nu^{(h)}$ is the hydrodynamic force acting on bead ν. We thus have

$$\boldsymbol{R}_\nu = \boldsymbol{r}_\nu - \boldsymbol{r}_c \,; \quad \boldsymbol{r}_c = \frac{\boldsymbol{r}_1 + \boldsymbol{r}_2}{2} \tag{4.18}$$

and

$$\boldsymbol{F}_\nu^{(h)} = \zeta \widehat{\boldsymbol{C}} \cdot \left[[\![\dot{\boldsymbol{r}}_\mu]\!] - \boldsymbol{v}_o - \boldsymbol{\kappa} \cdot \boldsymbol{r}_\mu \right] \tag{4.19}$$

with

$$\widehat{\boldsymbol{C}} = \left(\frac{Q}{Q - \mathscr{A}h} \right) \left[\boldsymbol{\delta} + \frac{h\mathscr{B}}{Q\beta} \frac{\boldsymbol{QQ}}{Q^2} \right] \tag{4.20}$$

In terms of the connector vector $\boldsymbol{Q}$, the stress tensor expression is as follows

$$\boldsymbol{\tau}_\mathrm{p} = -\frac{n_\mathrm{p}}{2} \left\langle \boldsymbol{Q} \left[\zeta \widehat{\boldsymbol{C}} \cdot \left[\boldsymbol{\kappa} \cdot \boldsymbol{Q} - [\![\dot{\boldsymbol{Q}}]\!] \right] \right] \right\rangle \tag{4.21}$$

On substituting the expression for $[\![\dot{\boldsymbol{Q}}]\!]$ from Eq.(4.1) into Eq.(4.21) and simplifying,

$$\begin{aligned}
\boldsymbol{\tau}_\mathrm{p} = &-\frac{n_\mathrm{p}\zeta\epsilon}{2} \left\langle g_3 \boldsymbol{\kappa} : \frac{\boldsymbol{QQQQ}}{Q^2} \right\rangle - n_\mathrm{p} H \left\langle g_3 \frac{\boldsymbol{QQ}}{1 - (Q/Q_0)^2} \right\rangle \\
&+ \frac{n_\mathrm{p}\zeta}{2} \left\langle \left(\frac{Q}{Q - \mathscr{A}h} \right) \left[\left(\boldsymbol{\delta} - \vartheta \frac{\boldsymbol{QQ}}{Q^2} \right) \cdot \left(-\frac{2k_B T}{\zeta} (\boldsymbol{\delta} - \zeta\boldsymbol{\Omega}) \cdot \frac{\partial}{\partial \boldsymbol{Q}} \ln \psi \right) \right] \right\rangle
\end{aligned} \tag{4.22}$$

where

$$\vartheta = \frac{\epsilon\beta}{\epsilon\beta + 1} - \frac{hB}{Q\beta(\epsilon\beta + 1)} \tag{4.23}$$

Using the following identity

$$\frac{\partial}{\partial Q} \left(\frac{\epsilon\beta}{\epsilon\beta + 1} \right) = \frac{\epsilon h}{\{Q + \epsilon[Q - h(\mathscr{A} + \mathscr{B})]\}^2} \left[(\mathscr{A} + \mathscr{B}) - Q \frac{\partial}{\partial Q} (\mathscr{A} + \mathscr{B}) \right] \tag{4.24}$$

to simplify Eq. (4.22), the dimensionless equation for the stress tensor may be written as

$$\boldsymbol{\tau}^*_\mathrm{p} = \frac{\boldsymbol{\tau}_\mathrm{p}}{n_\mathrm{p} k_B T} = \boldsymbol{\delta} - \left\langle g_3 \frac{\boldsymbol{Q}^*\boldsymbol{Q}^*}{1 - Q^{*2}/b} \right\rangle - \epsilon \left\langle g_4 \frac{\boldsymbol{Q}^*\boldsymbol{Q}^*}{Q^{*2}} \right\rangle - 2\epsilon \left\langle g_3 \boldsymbol{\kappa}^* : \frac{\boldsymbol{Q}^*\boldsymbol{Q}^*\boldsymbol{Q}^*\boldsymbol{Q}^*}{Q^{*2}} \right\rangle, \tag{4.25}$$

where g_3 and g_4 in Eq. (4.25) are defined as follows,

$$g_3 = \frac{1}{\epsilon\beta^* + 1} = \frac{Q^*}{Q^* + \epsilon[Q^* - \bar{\alpha}(\mathscr{A}^* + \mathscr{B}^*)]} \tag{4.26}$$

and

$$g_4 = \frac{2s\bar{\alpha}Q^*}{\{Q^* + \epsilon[Q^* - \bar{\alpha}(\mathscr{A}^* + \mathscr{B}^*)]\}^2} + \frac{3[Q^* - \bar{\alpha}(\mathscr{A}^* + \mathscr{B}^*)]}{\{Q^* + \epsilon[Q^* - \bar{\alpha}(\mathscr{A}^* + \mathscr{B}^*)]\}} \tag{4.27}$$

where s has already been defined in Eq. (4.9).

While the second term on the right hand side of the stress tensor expression [Eq. (4.25)] represents the elastic contribution to the stress tensor due to the presence

of the FENE spring, the third and fourth terms arise due to the presence of IV. The last term on the right hand side is the viscous or dissipative component of the stress tensor, which disappears (appears) instantaneously when the flow is turned off (on). The jump in viscosity at the inception of shear flow is due to this last term, because none of the other terms in the equation contribute to the shear component of the stress tensor, $\tau_{p,yx}$, as the other averages are isotropic at equilibrium, i.e, $\left\langle Q_x Q_y \right\rangle_{\text{eq}} = 0$. Interestingly, bead-rod models and bead-rod chains also have a viscous contribution to stress (Bird *et al.*, 1987b). Flexible polymer models, with only an entropic spring connecting the beads, do not have this viscous contribution to the shear stress, and only the inclusion of a dashpot in parallel with the spring, through the incorporation of internal viscosity into such models, results in a stress jump.

4.3 Results and Discussion

4.3.1 Code validation

To test the validity of the code, an ensemble of 2×10^5 FENE dumbbells, with a dimensionless maximum allowable length of $b = 100$ and internal viscosity parameter of $\epsilon = 0.1$, is subjected to shear flow at a dimensionless shear rate of $\lambda_H \dot{\gamma} = 1.0$. In Fig. 4.1, the predicted shear viscosity of this ensemble is plotted against dimensionless time, and compared against data from the work by Hua and Schieber (1995). The good agreement between the two results indicates the reliability of the current code.

Hua *et al.* (1996) have previously simulated a dumbbell model with internal viscosity and hydrodynamic interactions in startup of shear flow, using the CONFESSIT method. They conclude that hydrodynamic interactions have a negligible effect on the stress field. However, as shown in Appendix A, one of the functions in their governing stochastic differential equations is incorrect, and leads to erroneous predictions. As a consequence, there are no published results in the literature with which our simulations (which incorporate both internal viscosity and hydrodynamic interactions) can be compared. Nevertheless, as will be seen in Section. 4.3.2, our simulations agree with the analytical results of Manke and Williams (1992) (who used pre-averaged hydrodynamic interactions) for the stress jump at the onset of shear flow over a range of values of ϵ and h^*, providing some validation for our code in its most general form.

Simulations which incorporate hydrodynamic interactions using the ROB expression take nearly twice as long to complete, for the same set of parameter values, as when the RPY expression is used. Though the two treatments yield results that are indistinguishable within error bars, the calculation of the shear viscosity of an ensemble of 2×10^5 FENE
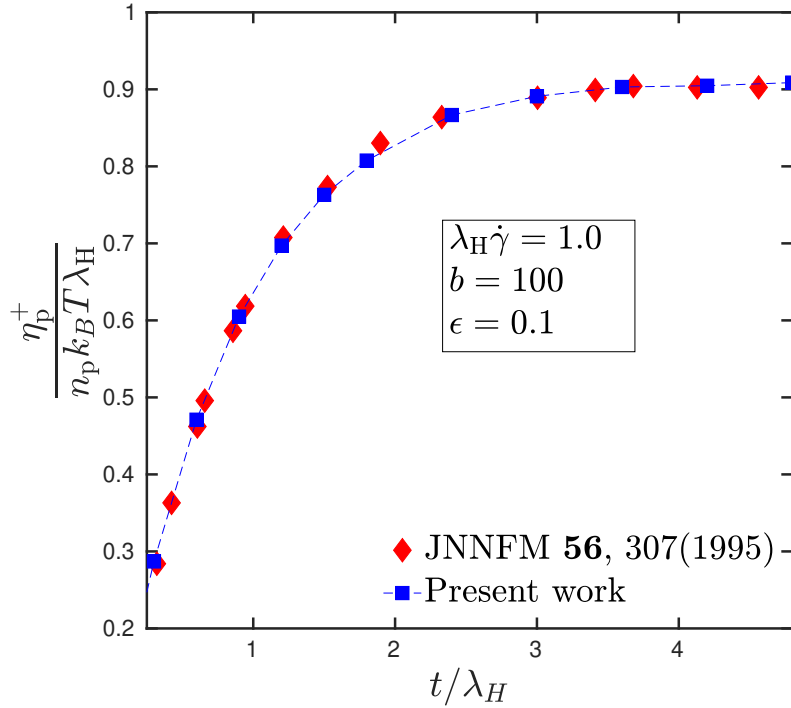
Figure 4.1: Polymer contribution to shear viscosity, $\eta_p^+/n_p k_B T \lambda_H$, as a function of dimensionless time at a dimensionless shear rate of 1.0. Error bars are smaller than symbol size.

dumbbells with both internal viscosity and hydrodynamic interactions, on an Intel Core i7-6700 CPU, takes about 379 seconds for the RPY case, as opposed to nearly 768 seconds for the ROB case. As a consequence, all simulations which involve HI have been performed using the RPY tensor. The RPY tensor has two branches and the terms $\mathscr{A}$ and $\mathscr{B}$ have to be evaluated separately for the two branches, as seen from Equation (2.6) in Chapter 2. Nevertheless, its implementation is faster due to the higher number of function evaluations required for the ROB tensor, as can be seen from Eqs. (4.9) and (4.10). Essentially, the definitions of functions g_1 and g_3 are the same for both RPY and ROB, while the functions g_2 and g_4 entail more calculations for the ROB case.

4.3.2   Transient response to shear flow

To calculate the viscometric functions, an initial equilibrium ensemble of $O(10^6)$ FENE dumbbells, picked from the equilibrated database as described in Section. II, have been used in all the simulations. The transient response of the ensemble-averaged rheological properties recorded as a function of time, are presented in this section.
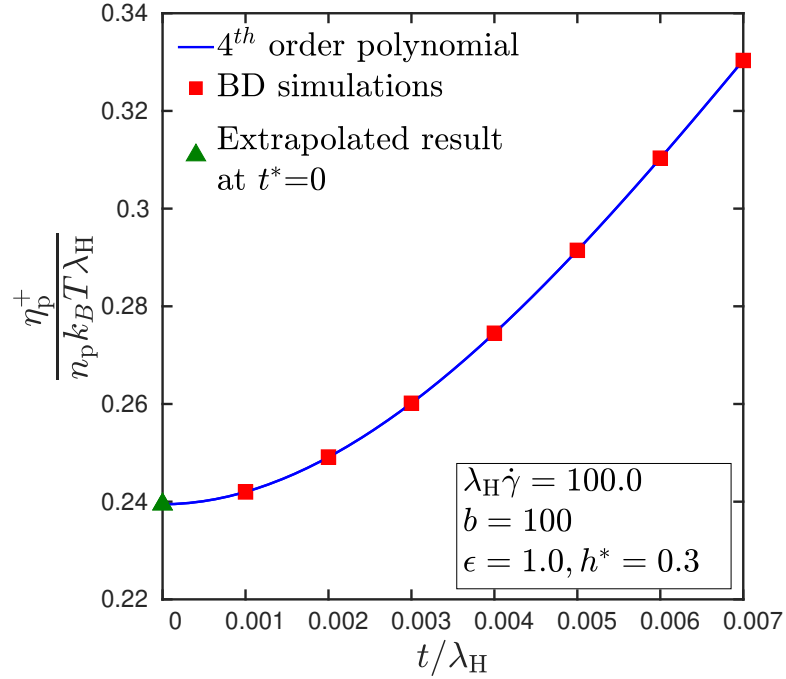
(a)
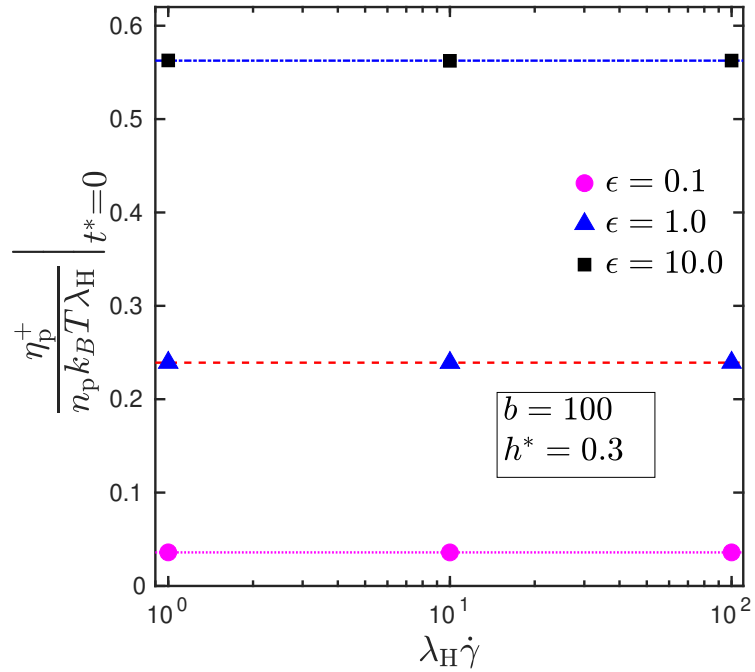
(b)

Figure 4.2: (a) Methodology to find the stress jump by extrapolating to $t^* = 0$ using a fourth order polynomial. (b) Shear rate independence of stress jump for various values of ϵ and a fixed value of $h^* = 0.3$. Dotted horizontal lines are error-weighted averages of the data points they traverse. Error bars are smaller than symbol size.

The stress jump

The "stress jump" refers to the discontinuous jump in viscosity at the inception of flow, i.e, at time, $t^* = 0$. The methodology to find this quantity has been illustrated in Fig. 4.2 (a) for a sample case where an ensemble of dumbbells with IV and HI is subjected to a dimensionless shear rate of 100. The viscosity is recorded as a function of time, and a fourth order polynomial is then fitted to this data (using the "fit" functionality of gnuplot, as described by Young (2015)), so as to find the stress jump by extrapolation to time $t^* = 0$. Analytical predictions (Manke and Williams, 1992; Dasbach *et al.*, 1992; Gerhardt and Manke, 1994) indicate that the stress jump must be independent of shear rate. To test this prediction, FENE dumbbells with $b = 100$ and various values of ϵ and h^* are subjected to three different shear rates, and their corresponding stress jumps are calculated using the method outlined above. In Fig. 4.2 (b), stress jumps for such dumbbells with varying values of ϵ and a fixed value of $h^* = 0.3$ are plotted against the respective shear rates, and it is seen that the jump is indeed independent of shear rate, thereby confirming the analytical predictions. A similar shear-rate independence is observed when the hydrodynamic interaction parameter is varied.

Manke and Williams (1988) derived an analytical result for the stress jump exhibited by a Hookean dumbbell with IV. Schieber calculated the same quantity for a FENE dumbbell with IV and obtained the following formula (Hua and Schieber, 1995), for the free-draining (FD) case,

$$\left.\frac{\eta_{\mathrm{p}}^+}{n_{\mathrm{p}} k_B T \lambda_{\mathrm{H}}}\right|_{t^*=0,\mathrm{FD}} = \left(\frac{b}{b+5}\right)\frac{2\epsilon}{5(1+\epsilon)} \tag{4.28}$$

Manke and Williams (1992) have also derived a similar formula for the stress jump exhibited by a Hookean dumbbell with IV and pre-averaged HI. By following a procedure analogous to Schieber's, the analytical result of Manke and Williams can be extended to find the stress jump for a FENE dumbbell with IV and pre-averaged HI, and can be shown to be

$$\left.\frac{\eta_{\mathrm{p}}^+}{n_{\mathrm{p}} k_B T \lambda_{\mathrm{H}}}\right|_{t^*=0,\mathrm{HI}} = \left(\frac{b}{b+5}\right)\frac{2\epsilon}{5(1+\epsilon(1-\sqrt{2}h^*))} \tag{4.29}$$

Recognizing that $\sigma(0) = -\eta_{\mathrm{p}}^+(0)\dot{\gamma}$, the stress jump ratio is then given by taking a ratio of the above two equations.

$$\frac{\sigma_{\mathrm{HI}}(0)}{\sigma_{\mathrm{FD}}(0)} = \frac{1+\epsilon}{1+\epsilon(1-\sqrt{2}h^*)} \tag{4.30}$$

This equation has been represented as lines in Fig. 4.3, for various values of the internal viscosity parameter. The prediction from analytical theory is that the stress jump in the presence of hydrodynamic interactions and internal viscosity is higher than that due
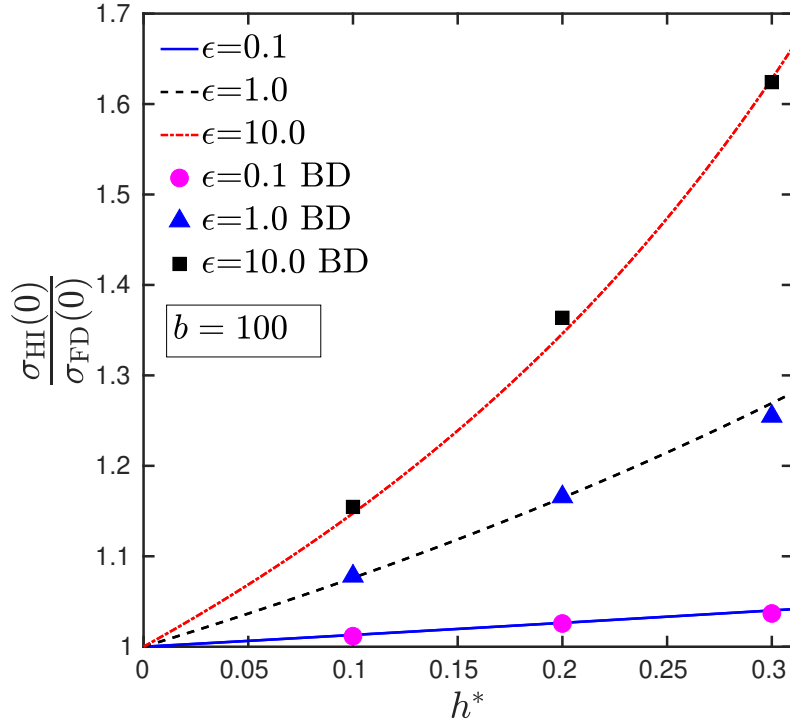
Figure 4.3: Stress jump ratio calculations for FENE dumbbells with $b = 100$ for various values of ϵ, h^*. Each data point in the figure is obtained as an error-weighted average of the stress jump measured at the different shear rates as shown in Fig. 4.2 (b). Lines represent Eq. (4.30). Error bars are smaller than symbol size.

to IV alone. The stress jump ratio for the case with HI to the free draining case, obtained from BD simulations for various combinations of ϵ and h^*, is plotted in Fig. 4.3. The simulations results agree well with the theoretical prediction, suggesting that fluctuations in HI do not play a significant role in determining the magnitude of the stress jump.

Such a result also seems correct intuitively. In the absence of IV or HI, the diffusion tensor in the stochastic differential equation is diagonal, i.e, there is no correlation between the motion of the two beads of the dumbbell. Introduction of IV adds off-diagonal terms to the diffusion tensor, introducing a coupling between the motion of the two beads. Hydrodynamic interactions also contribute to a coupling and this appears to enhance the effect brought on by IV. In a physical sense, the phenomenon of stress jump arises solely due to internal viscosity, as the "dashpot" connecting the two beads responds instantaneously to a change in the displacement between the two beads. Hydrodynamic interactions add to this effect because it enhances the strength of the correlation between the motion of the two beads.

Interestingly, our BD simulations indicate that there is no jump in either Ψ_1 or Ψ_2 [defined in Eq. (2.14) of Chapter 2] at $t^* = 0$ for models with internal viscosity. This is in line with prior observations on Hookean dumbbells that employed a Gaussian approximation (Schieber, 1993) for internal viscosity. The absence of jumps in Ψ_1 and Ψ_2 is explained in Appendix F using the Hookean dumbbell model with IV as an example.

Transient viscosity

As observed in various experiments on polymer solutions and melts (Bird *et al.*, 1987a), simulations indicate that during the startup of shear flow, the viscosity shows a transient rise, above its steady-state value, commonly termed the "overshoot", with the highest point of positive deviation from the steady-state value denoted as the magnitude of overshoot. To analyze this phenomenon, the viscosity of dumbbells (normalized by the steady-state value, $\eta_p^+(t \rightarrow \infty)$) is plotted as a function of strain units in Fig. 4.4. It is important to note that the phenomenon of overshoot is observed even for the case of FENE dumbbells, without the incorporation of internal viscosity or hydrodynamic interaction effects.

Throughout the analysis in this section and the next, it must be noted that an "overshoot" is said to occur only when the normalized quantity attains a value greater than one. Local peaks in the normalized quantity, such as the one observed for the $\epsilon = 10$ case in Fig. 4.4 (b), are only considered as "maxima" and not categorized as an "overshoot".

In Fig. 4.4 (a), the overshoot behavior in FENE dumbbells with $b = 100$ is recorded for various shear rates. At low shear rates, there is no overshoot, and viscosity reaches its steady-state value asymptotically. At a certain threshold shear rate, overshoot is first observed. From there on, the magnitude of the overshoot increases as the shear rate is increased. Interestingly, however, the location of the overshoot, i.e; the strain at which overshoot occurs ($\gamma_{\max}$), is roughly constant over the entire range of shear rates examined in this work, in agreement with the experimentally observed trend for a range of different polymer solutions and melts (Bird *et al.*, 1987a).

In Fig. 4.4 (b), the effect of internal viscosity and hydrodynamic interactions on the magnitude and location of overshoot is examined at a fixed dimensionless shear rate of 100. It is seen that a low value of ϵ (=0.1) dampens the magnitude of overshoot, but does not change $\gamma_{\max}$ significantly. At higher values of the internal viscosity parameter, the overshoot occurs at a lower strain, and its magnitude is significantly decreased. The inclusion of hydrodynamic interactions increases the magnitude of overshoot in comparison to the free-draining case ($h^* = 0$) but does not affect $\gamma_{\max}$ perceptibly. For a given value of the hydrodynamic interaction parameter, the coupling between IV and

(a)

(b)
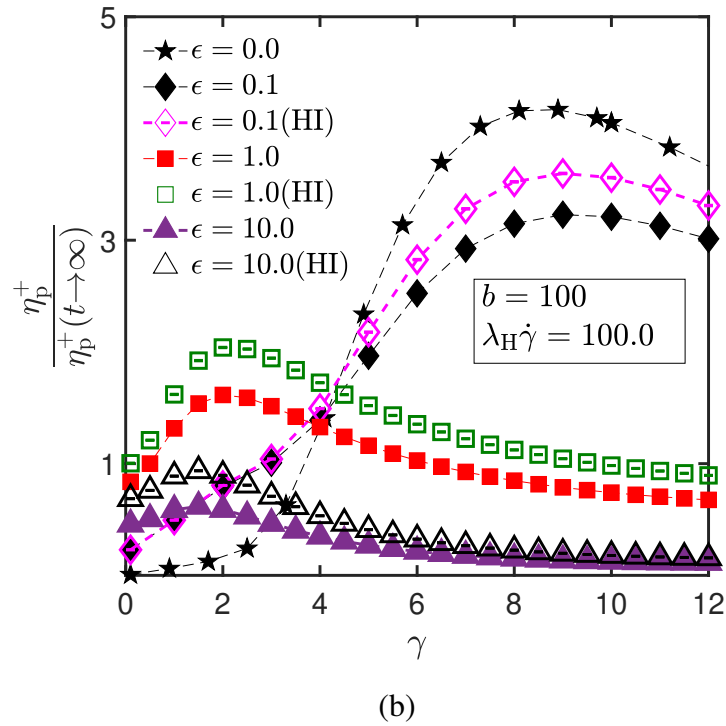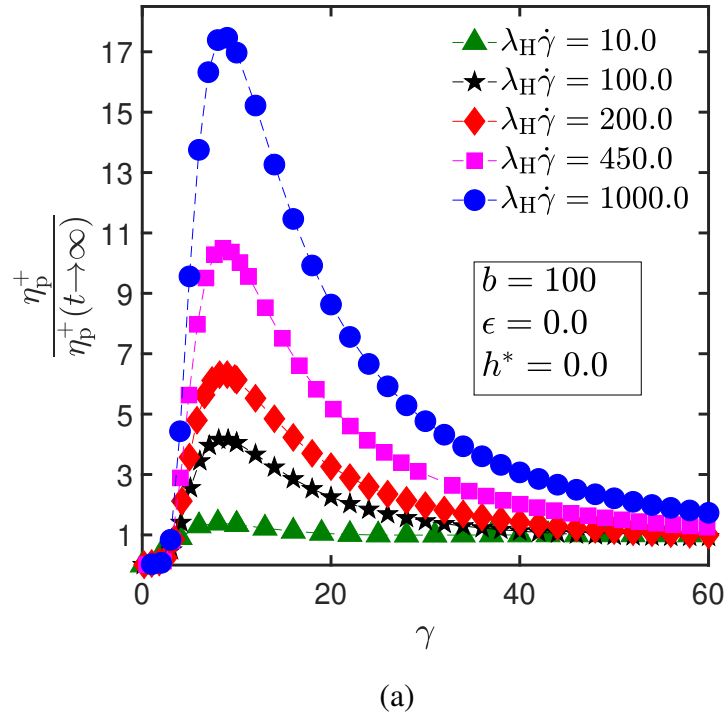
Figure 4.4: Transient behavior of shear viscosity for FENE dumbbells with $b = 100$ and various values of ϵ and h^*, as a function of strain units: (a) overshoot behavior for the pure FENE model, (b) effect of ϵ and h^* on overshoot at a dimensionless shear rate of 100. In each case, η_p^+ is normalized by the steady-state value, $\eta_p^+(t \to \infty)$, obtained at the same shear rate, and ϵ and h^*, as the transient data themselves. The hydrodynamic interaction parameter in these simulations is $h^* = 0.3$. Error bars are smaller than symbol size.

HI is enhanced at higher values of the IV parameter, at early times (or strains). At later times, the nature of the coupling is non-trivial. While it appears that the $\epsilon = 1.0$ and $\epsilon = 10.0$ curves (with and without HI) settle to a value lower than 1 at the highest values of strain in the figure, as a matter of fact they do approach 1 at much larger strains, when the transient viscosity η_p^+ attains its steady-state value, as can be seen from Fig. 4.6 (a).

It is observed that the dumbbell model with only FENE effects and that with a small value of ϵ show nearly identical behaviour, qualitatively. The onset of overshoot occurs at roughly the same shear rate, $\lambda_H \dot{\gamma} \sim 10.0$, for both the cases. However, as the IV parameter is increased to higher values, say $\epsilon = 1$ or $\epsilon = 10$, there is a marked change in the transient response. This is clearly seen from Fig. 4.4 (b), where a shear rate of $\lambda_H \dot{\gamma} \sim 100.0$ triggers an overshoot in a system with a lower value of ϵ, but only causes a long wavelength oscillation in the shear viscosity for a system with $\epsilon = 10$. The occurrence of oscillations is discussed further in the context of Figs. 4.6 below.

Transient first normal stress coefficient

Overshoots in Ψ_1 [defined in Eq. (2.14)] can also be analyzed using the framework developed in the previous section. The first normal stress coefficient (normalized by the steady-state value, $\Psi_1^+(t \to \infty)$) is plotted as a function of strain in Fig. 4.5.

In Fig. 4.5 (a), the overshoot in Ψ_1 for FENE dumbbells with $b = 100$ is plotted for various shear rates. The strain at which the overshoot occurs is slightly higher than that for the viscosity, in agreement with experiments (Bird *et al.*, 1987a). Nonetheless, γ_{max} remains roughly constant over shear rates that span two orders of magnitude. However, the size of the overshoot in Ψ_1 is lower than that in η_p. This is in accordance with the predictions of the FENE-P dumbbell model (Mochimaru, 1981), and BD simulation results for a twenty-bead chain with FENE springs (Prabhakar and Prakash, 2006). These simulation results and model predictions, are, however, in direct contrast with experimental observations (Huppler *et al.*, 1967) which predict that the overshoot in the first normal stress coefficient is greater than that observed in the viscosity.

In Fig. 4.5 (b), the effect of internal viscosity and hydrodynamic interactions on the Ψ_1 overshoot is studied at a dimensionless shear rate of 1000. The addition of hydrodynamic interactions enhances the magnitude of overshoot but leaves γ_{max} largely unperturbed. Similar to the trend observed in the transient behavior of viscosity, the time-variation of Ψ_1 for the pure FENE case and the case with low IV parameter are qualitatively comparable. A low value of ϵ reduces the magnitude of the overshoot slightly, but high values of the IV parameter, say $\epsilon = 10$, induce an overshoot only at the highest shear rate examined in this work ($\lambda_H \dot{\gamma} = 1000$), and that too, due to the
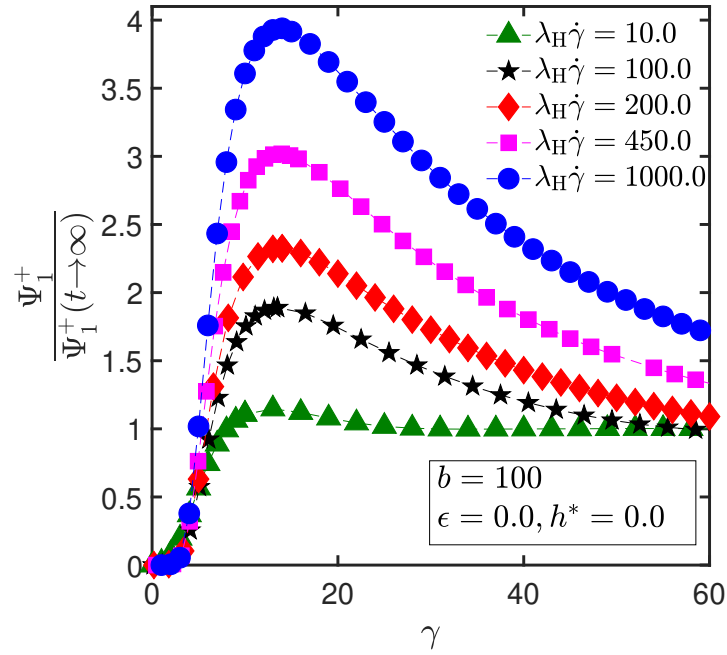
(a)
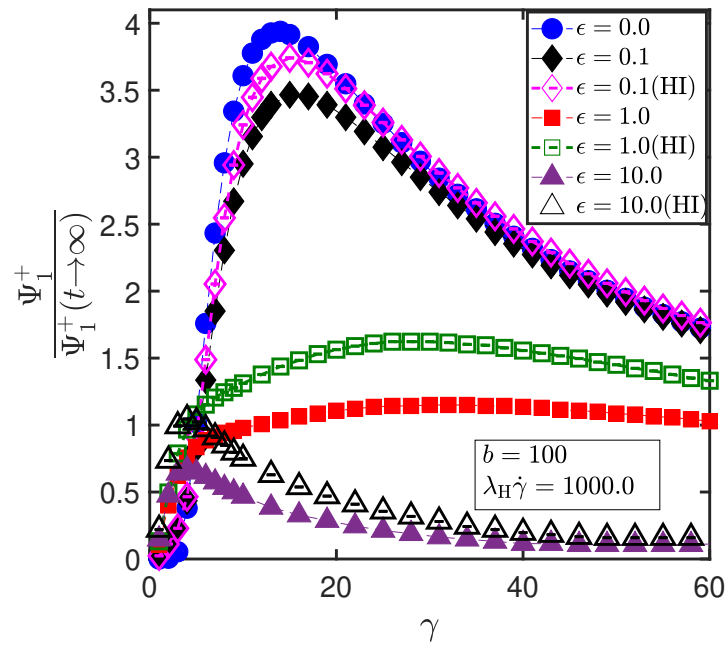
(b)

Figure 4.5: Transient behavior of the first normal stress coefficient for FENE dumbbells with $b = 100$ and various values of ϵ and h^*, as a function of strain units: (a) overshoot behavior for the pure FENE model, (b) effect of ϵ and h^* on overshoot at a dimensionless shear rate of 1000. In each case, Ψ_1^+ is normalized by the steady-state value, $\Psi_1^+(t \to \infty)$, obtained at the same shear rate, and ϵ and h^*, as the transient data themselves. The hydrodynamic interaction parameter in these simulations is $h^* = 0.3$. Error bars are smaller than symbol size.
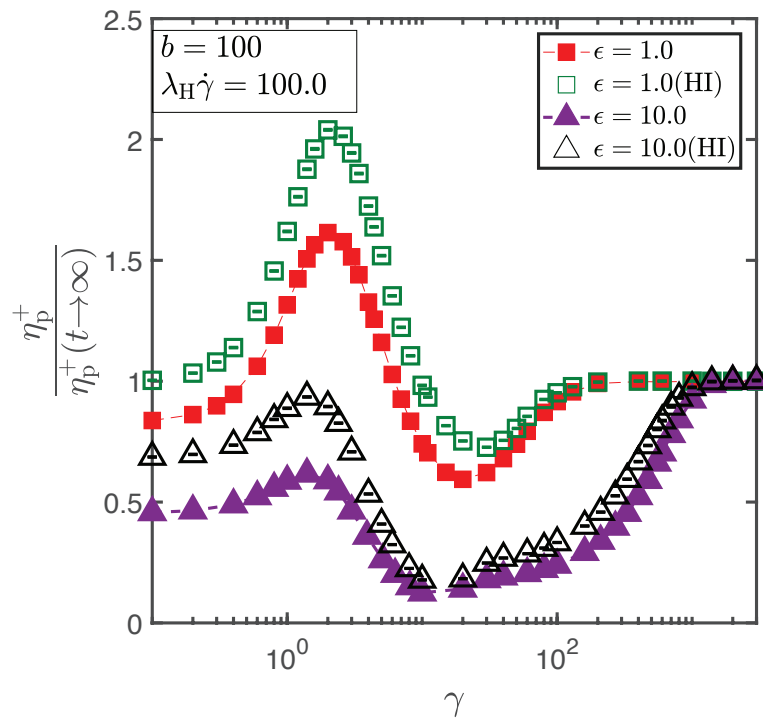
(a)
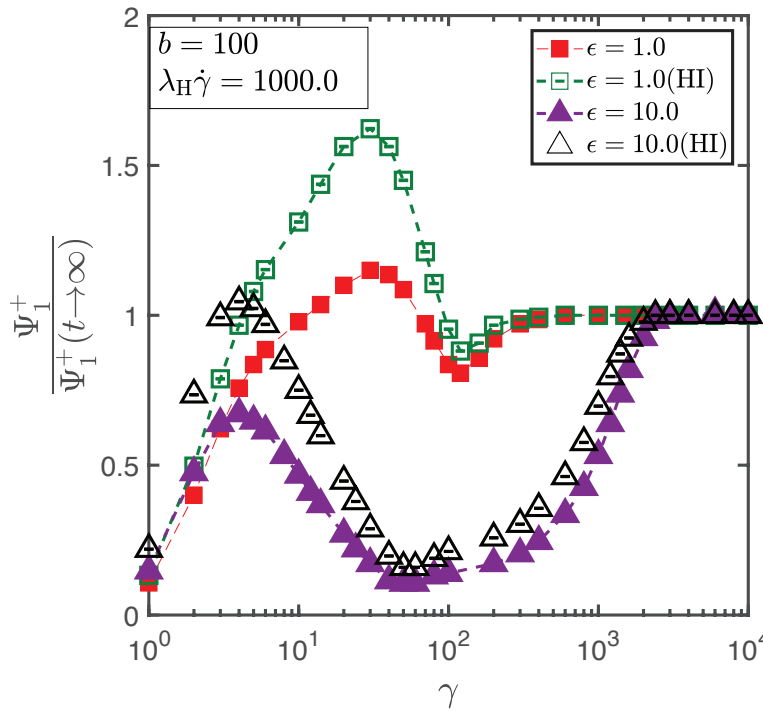
(b)

Figure 4.6: Transient (a) viscosity, η_{p} and (b) first normal stress coefficient, Ψ_1, normalized by the steady-value of the respective viscometric functions obtained at the same values of shear rate, and ϵ and h^*, as the transient data themselves, as a function of strain units. The hydrodynamic interaction parameter used in these simulations is $h^* = 0.3$. Error bars are smaller than symbol size.

enhancing effect of the hydrodynamic interactions mentioned above. In general, however, the inclusion of HI does not alter the shear rate at which overshoot is first observed. More simulations at higher shear rates need to be performed, in order to comment conclusively about the constancy of γ_{max} for the high-ϵ cases. The Gaussian approximation developed by Schieber (1993) for the treatment of internal viscosity indicates that for $\epsilon = 10$ and $\lambda_H \dot{\gamma} = 100$, high-frequency oscillations are observed in η_{p} and Ψ_1 (see Figs. 5 and 7 in Schieber (1993)). For the same set of parameters studied by BD simulations, however, no such high-frequency oscillations are observed, as can be seen from Figs. 4.6, where the normalized transient viscosity and first normal stress coefficients of FENE dumbbells with $\epsilon = 1$ and $\epsilon = 10$ (with and without HI) have been plotted for a larger range of strain units Figs. 4.4 and 4.5. Both viscometric functions go through a local maximum and minimum before gradually attaining their steady state values. The inclusion of HI does not qualitatively alter this trend, and only slightly increases the maximum observed for the case with IV alone. Neither does the inclusion of HI affect the shear rate at which overshoot is first observed. While both η_{p} and Ψ_1 exhibit an overshoot for the $\epsilon = 1$ case, these observables vary differently for the higher value of the internal viscosity parameter. As seen from Fig. 4.6 (a), η_{p} for the $\epsilon = 10$ case (with and without HI) does not show any overshoot (the ordinate never crossing 1), but rather oscillates once, i.e, goes through a local maximum and a minimum, before a gradual approach to steady state. From Fig. 4.6 (b), it is seen that Ψ_1 for $\epsilon = 10$ exhibits a slight overshoot only in the presence of HI, whereas for the free-draining case at the same value of the IV parameter, Ψ_1 goes through a single oscillation before attaining steady-state. While the Gaussian approximation includes fluctuations in the internal viscosity, it is an 'uncontrolled' approximation (Prakash and Öttinger, 1999), in the sense that though it is exact to first order in the perturbation parameter, it includes infinitely many unspecified higher order terms. The results of BD simulations, on the other hand, are an exact solution of the governing equation.

Transient second normal stress coefficient

In Fig. 4.7, the second normal stress coefficient [defined in Eq. (2.14)] is plotted as a function of strain. It is observed that Ψ_2 evolves non-monotonically, and settles to zero as its steady-state value, within statistical error bars of the simulation. Therefore, Ψ_2 has been scaled using the steady-state value of the first normal stress coefficient, $\Psi_1^+(t \to \infty)$. Increasing the value of the IV parameter increases the amplitude of oscillations in Ψ_2. Furthermore, it is seen that the effect of HI on Ψ_2 is minimal, becoming stronger as the value of the internal viscosity parameter is increased.
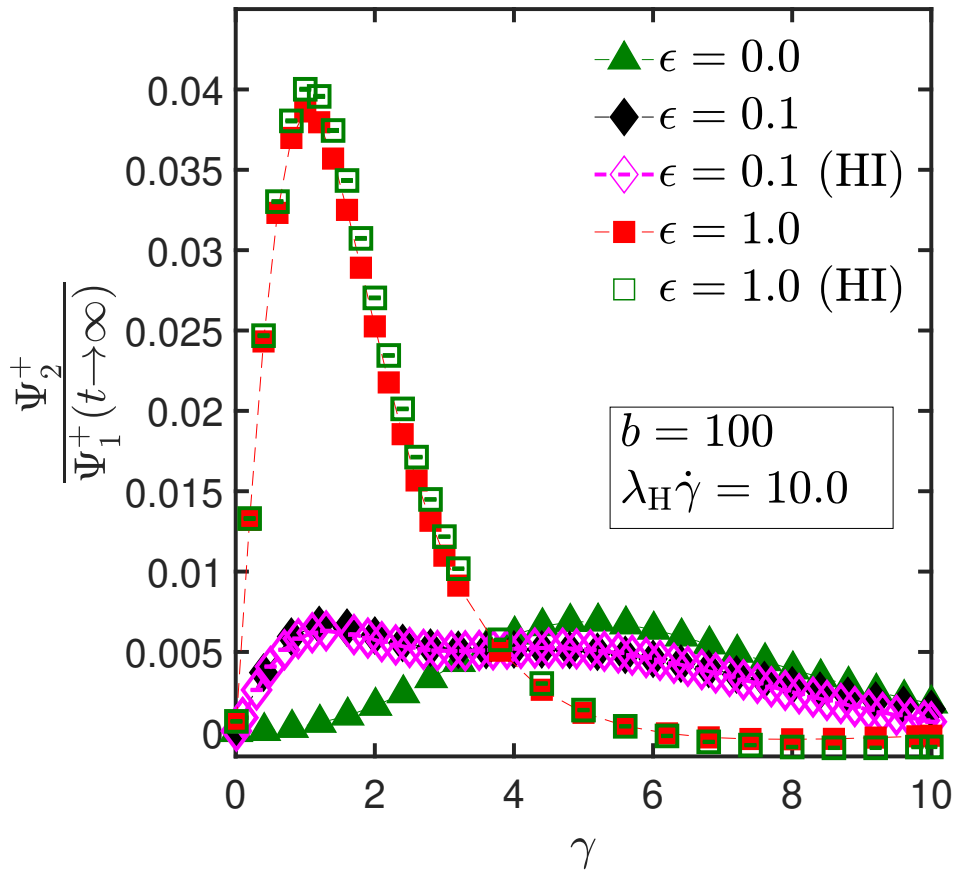
Figure 4.7: Influence of h^* and ϵ on the second normal stress coefficient of FENE dumbbells with $b = 100$. The hydrodynamic interaction parameter in these simulations is $h^* = 0.3$. In each case, Ψ_2^+ is normalized by the steady-state value of the first normal stress coefficient, $\Psi_1^+(t \to \infty)$, obtained at the same shear rate, and ϵ and h^*, as the transient data themselves. Error bars are smaller than symbol size.

4.3.3 Steady-shear results

Zero-shear rate properties

The dimensionless zero-shear rate viscosity, $\eta_{p,0}^*$, is obtained from BD simulations by taking an error-weighted mean of the viscosity at the four lowest shear-rates that were simulated, i.e, 0.01, 0.03, 0.05 and 0.07, after verifying that shear-thinning had not set in at these shear-rates.

Using a Gaussian approximation (GA) analysis on Hookean dumbbells with internal viscosity, Schieber (1993) has shown that zero-shear rate properties are unaffected by internal viscosity. To test this prediction for the case of FENE dumbbells, the viscosity and first normal stress coefficient are plotted as a function of dimensionless shear rate, in Fig. 4.8, for various values of ϵ and h^*. From Fig. 4.8 (a) it can be seen that for cases with internal viscosity alone, the zero-shear rate viscosity remains unaffected by ϵ. However, in the presence of internal viscosity and hydrodynamic interactions, the zero-shear rate viscosity no longer remains independent of ϵ. Even though h^* is constant, the coupling of HI and IV induces an internal viscosity dependence on $\eta_{p,0}^*$. A plot for the first normal stress coefficient, as shown in Fig. 4.8 (b), seems to reveal a similar trend regarding the constancy of the zero-shear rate value in the presence of internal viscosity alone. With the inclusion of hydrodynamic interactions, however, $\Psi_{1,0}^*$ ceases to be independent of ϵ. The coupling of HI and IV seems to lead to a more dramatic dependence of $\Psi_{1,0}^*$ on ϵ, than that observed for $\eta_{p,0}^*$. It is worth noting that the fluctuations in Ψ_1^* at $\lambda_H \dot{\gamma} < 0.1$ necessitate a time-averaging algorithm for calculating the ensemble average at low shear rates, as detailed below.

For a dimensionless shear rate of 0.05 and representative values of ϵ and h^*, the transient behavior of the viscosity and the first normal stress coefficient is compared in Fig. 4.9(a). It can be seen that the standard deviation of the first normal stress coefficient is significantly higher than that for viscosity. Additionally, it was observed that the fluctuations in Ψ_1^* are noticeable at both low and high values of the IV parameter. In Fig. 4.9 (b), the first normal stress coefficient calculated for the same conditions as in part (a) are compared for two different sizes of the ensemble. It is seen that even as the ensemble size is increased ten-fold, fluctuations in Ψ_1^* persist. To obtain a reliable estimate of the steady-state value of Ψ_1^*, a time-averaging of the data points was carried out, after the stationary state is reached (the threshold value is 15 dimensionless time units for the case considered in Fig. 4.9 (b)). The horizontal line in Fig. 4.9 (b) represents the mean value obtained from such an averaging procedure, and the thickness of the line indicates the error in the mean. The steady-state value of the first normal stress coefficient for
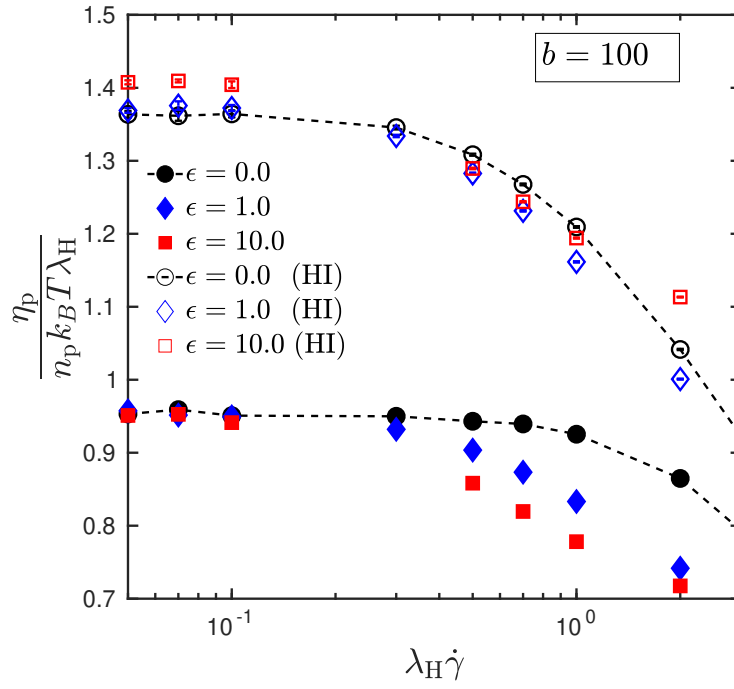
(a)
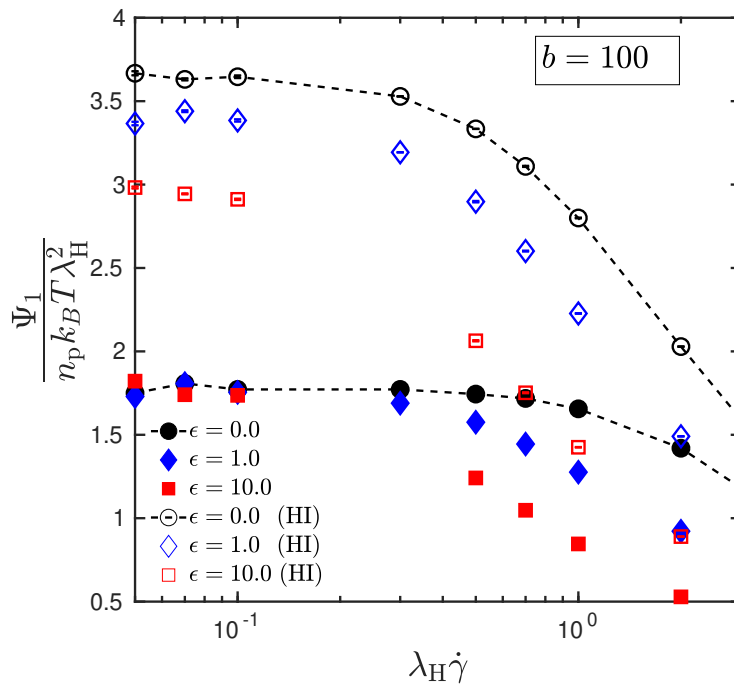
(b)

Figure 4.8: (a) Polymer contribution to viscosity at low shear rates. (b) First normal stress coefficient at low shear rates. The hydrodynamic interaction parameter in these simulations is $h^* = 0.3$. Error bars are smaller than symbol size.

(a)

(b)
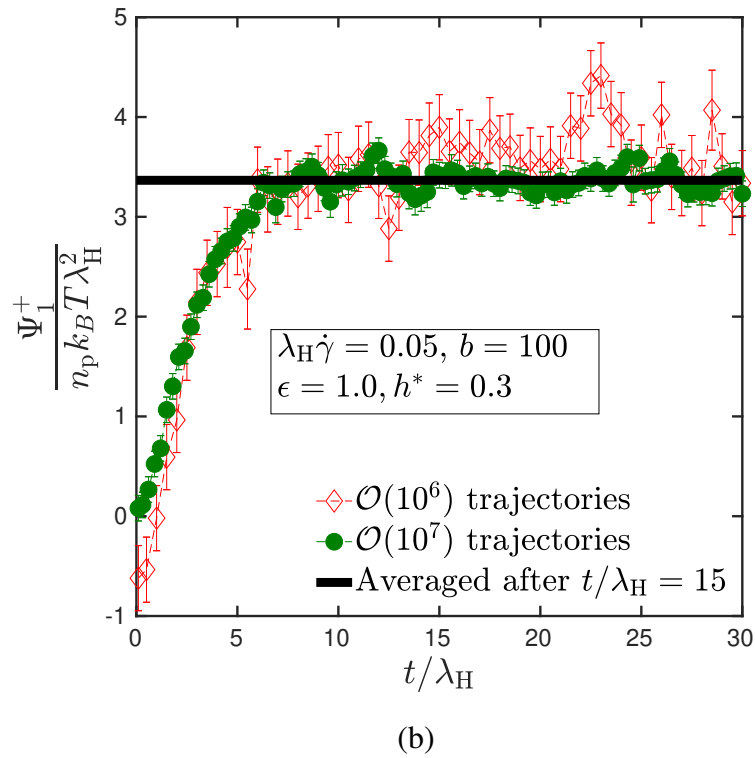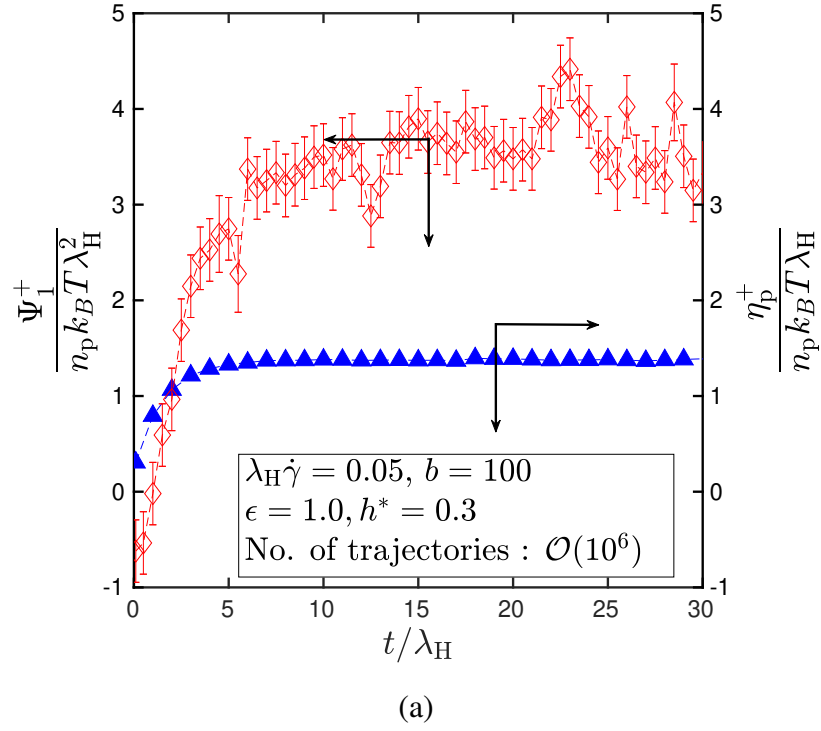
Figure 4.9: (a) Transient viscosity and first normal stress coefficient estimated from an ensemble of approximately 1 million data points. (b) Time-averaging procedure to estimate the steady-state value of the first normal stress coefficient.

dimensionless shear rates lower than 0.1 was calculated in this manner, with an ensemble size of $O(10^7)$. For the viscosity, there is no statistically discernible difference between data sampled from an ensemble of the order of one million or ten million data points.

The steady-state value of the second normal stress coefficient is zero within statistical error bars of the simulation, for free-draining dumbbells with and without the inclusion of internal viscosity, as observed from the transient simulations at large times. With the inclusion of hydrodynamic interactions, however, small negative values for Ψ_2 are obtained at low shear rates, for cases with and without internal viscosity. At higher shear rates, Ψ_2 is zero for all the different parameters considered in this work. A similar trend in the variation of Ψ_2 with the shear rate, for models with fluctuating hydrodynamic interactions, has been noticed by Zylka (1991) in his work on bead-spring chains.

Calculation of zero-shear rate viscosity from the relaxation modulus and the stress jump

It is known from linear viscoelastic fluid theory that the zero-shear rate viscosity can be calculated by integrating the relaxation modulus, $G(t)$, with respect to time (Rubinstein and Colby, 2003). That is,

$$\eta_0 = \int_0^\infty G(t)dt \tag{4.31}$$

The general form of the relaxation modulus of a polymer solution can be expressed as the sum of an elastic part, $G_{el}(t)$ (corresponding to a slow decay in stress), and a singular part (accounting for the viscous portion) that captures the instantaneous response of the solution to a stress (Bird *et al.*, 1987a; Hua *et al.*, 1996),

$$G(t) = G_{el}(t) + 2\eta_v \, \delta(t) \tag{4.32}$$

For models without internal viscosity, $\eta_v = \eta_s$, but as will be discussed later in this section, $\eta_v > \eta_s$ for models that incorporate IV.

Schieber and coworkers (Hua *et al.*, 1996) have used BD simulations to estimate the relaxation modulus of Hookean dumbbells with IV, from the stress relaxation that follows from an instantaneous step-strain in shear (Hua and Schieber, 1995). They find excellent agreement between the $G(t)$ obtained using such a procedure and that obtained from linear-response theory, and observe that the latter method is computationally more efficient and accurate. It is worth noting, however, that both the approaches are unable to capture the singular portion in $G(t)$. In our simulations, $G_{el}^*(t^*)$ is obtained using linear response theory, i.e, the Green-Kubo relationship, which is based on the stress-autocorrelation of an ensemble of dumbbells at equilibrium,

$$G_{el}^*(t^*) = \frac{G_{el}(t^*)}{n_p k_B T} = \left\langle \tau_{p,yx}^*(t^*)\tau_{p,yx}^*(0) \right\rangle_{eq} \tag{4.33}$$
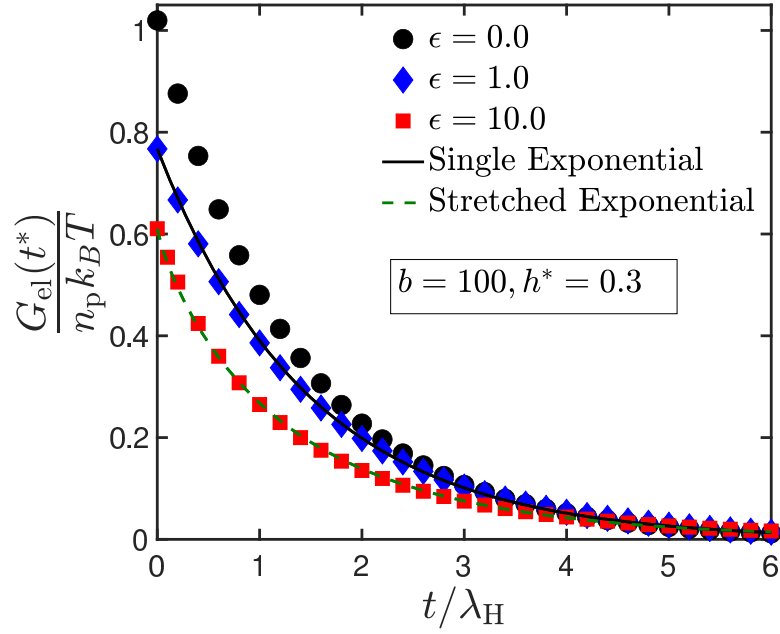
(a)
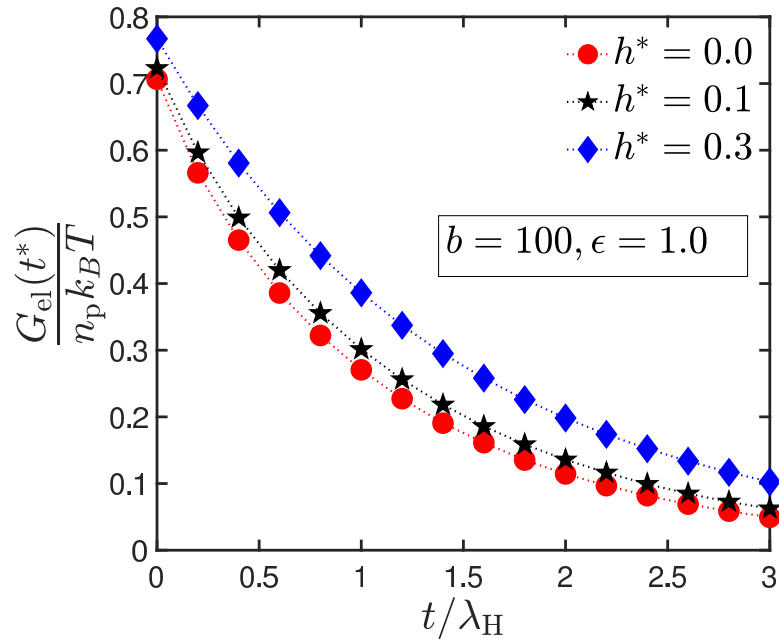
(b)

Figure 4.10: Elastic component of the relaxation modulus as a function of dimensionless time. (a) Effect of internal viscosity at a fixed value of the hydrodynamic interaction parameter, h^*. The solid line is a single exponential fit [see Eq. (4.34)] with $\tau = 1.48$. The dashed line is a stretched exponential [see Eq. (4.35)] with $\tau_k = 1.26$ and $m = 0.85$. (b) Effect of hydrodynamic interactions at a fixed value of the internal viscosity parameter, ϵ. Dotted lines are drawn to guide the eye. Error bars are smaller than symbol size.

In Fig. 4.10, the elastic component of the relaxation modulus calculated in this manner has been plotted against dimensionless time, for various values of ϵ and h^*. The area under the curve represents $\eta_{p,0}^{*,el}$, the dimensionless elastic contribution to the zero shear viscosity. In Fig. 4.10 (a), the effect of varying ϵ on $G_{el}^*(t^*)$ at a fixed value of h^* has been captured. As the internal viscosity is increased, it is seen that the area under the curve decreases, and the relaxation slows down. On the other hand, increasing the strength of hydrodynamic interactions while keeping ϵ constant also slows the decay of $G_{el}^*(t^*)$, but increases $\eta_{p,0}^{*,el}$, as seen from Fig. 4.10 (b). The integration of the relaxation modulus required in Eq. (4.31) is simplified if an analytical fit can be obtained to the $G_{el}^*(t^*)$ data. For small values of ϵ, a single exponential of the form

$$G_{el}^*(t^*) = \frac{G_{el}(0)}{n_p k_B T} \exp(-t^*/\tau) \tag{4.34}$$

where τ is an adjustable parameter, produces a good fit, as seen in Fig. 4.10 (a) for $\epsilon = 1.0$. For large values of ϵ, it is found that a stretched exponential of the form,

$$G_{el}^*(t^*) = \frac{G_{el}(0)}{n_p k_B T} \exp\left[(-t^*/\tau_k)^m\right] \tag{4.35}$$

provides a more accurate fit to the data than does the single exponential. Here, τ_k and m are fitting parameters. This is seen from Fig. 4.10 (b) for $\epsilon = 10.0$.

Gerhardt and Manke (1994) have shown analytically that the instantaneous stress-jump observed as a polymer solution is subject to the start up of shear flow is identically equal to the singular portion in Eq. (4.32), for linear viscoelastic fluids. As noted previously, since models with IV show a stress jump in η_p^+, it follows from Gerhardt and Manke's work that the numerical prefactor, η_v, to the Dirac delta function in $G(t)$ must be greater than η_s, and in fact, the polymer contribution to the stress jump, η_{jump}, is given by

$$\eta_{jump} = \eta_v - \eta_s \tag{4.36}$$

The polymer-contribution to zero-shear rate viscosity, $\eta_{p,0}$, can then be written as

$$\begin{aligned}
\eta_{p,0} \equiv \eta_0 - \eta_s &= \left[\int_0^\infty G(t)dt\right] - \eta_s \\
&= \int_{0^+}^\infty G_{el}(t)dt + 2\int_0^\infty \eta_v\,\delta(t)dt - \eta_s \\
&= \eta_{p,0}^{el} + \eta_{jump}
\end{aligned} \tag{4.37}$$

where $\eta_{p,0}^{el} = \int_{0^+}^\infty G_{el}(t)dt$, and $2\int_0^\infty \eta_v\,\delta(t)dt = \eta_v$.

The zero-shear rate viscosity calculated in this manner is compared against the value obtained from direct BD simulations in Table 4.1, for various values of the internal

Table 4.1: Zero-shear rate viscosity of FENE dumbbells with $b = 100$ for various values of the internal viscosity parameter, ϵ and the hydrodynamic interaction parameter, h^*, calculated from Eq. (4.37) and BD simulations. Dimensionless quantities are denoted with an asterisk as a superscript.

		$h^* = 0$		
ϵ	$\eta_{\mathrm{p},0}^{*,\mathrm{el}}$	η_{jump}^*	$\eta_{\mathrm{p},0}^* = \eta_{\mathrm{p},0}^{*,\mathrm{el}} + \eta_{\mathrm{jump}}^*$	$\eta_{\mathrm{p},0}^*$ from BD
0.0	0.951 ± 0.003	0	0.951 ± 0.003	0.954 ± 0.003
0.1	0.918 ± 0.001	0.0346 ± 0.0006	0.952 ± 0.001	0.956 ± 0.003
0.5	0.8275 ± 0.0009	0.1270 ± 0.0003	0.954 ± 0.001	0.953 ± 0.003
1.0	0.7580 ± 0.0009	0.1905 ± 0.0002	0.9485 ± 0.0009	0.956 ± 0.002
10.0	0.5982 ± 0.0005	0.3464 ± 0.0003	0.9445 ± 0.0006	0.952 ± 0.001
		$h^* = 0.3$		
ϵ	$\eta_{\mathrm{p},0}^{*,\mathrm{el}}$	η_{jump}^*	$\eta_{\mathrm{p},0}^* = \eta_{\mathrm{p},0}^{*,\mathrm{el}} + \eta_{\mathrm{jump}}^*$	$\eta_{\mathrm{p},0}^*$ from BD
0.0	1.358 ± 0.002	0	1.358 ± 0.002	1.363 ± 0.003
0.1	1.326 ± 0.002	0.0359 ± 0.0001	1.362 ± 0.002	1.363 ± 0.003
0.5	1.223 ± 0.002	0.1466 ± 0.0002	1.369 ± 0.002	1.371 ± 0.002
1.0	1.137 ± 0.001	0.2391 ± 0.0002	1.376 ± 0.001	1.373 ± 0.002
10.0	0.8353 ± 0.0006	0.5626 ± 0.0004	1.3979 ± 0.0007	1.409 ± 0.001

viscosity and the hydrodynamic interaction parameter. We see that there is a good agreement between the values obtained by these two different approaches, and in some sense validates both the estimation of the zero-shear rate viscosity from BD simulations, and the estimation of the relaxation modulus.

Stress tensor components

Even away from the linear viscoelastic regime, there exist separate contributions to the stress tensor for models with internal viscosity. As briefly discussed in Section 4.2, the second and third terms on the right hand side of Eq. (4.25) together represent the elastic contribution to the stress tensor, while the last term represents the viscous (dissipative) contribution. Mackay *et al.* (1992) have devised experimental techniques involving the cessation of flow to separately identify elastic and dissipative contributions to the total polymer shear stress, and present results for semidilute xanthan gum solutions (Liang and Mackay, 1993). The predictions of our model, however, are valid only for dilute

polymer solutions, and hence cannot be compared directly with their experimental results. Nonetheless, it is worthwhile examining the two contributions, as they provide interesting insights into the roles played by internal viscosity and hydrodynamic interactions in affecting the steady-shear stress field of dilute polymer solutions.

In Fig. 4.11 (a), the steady-state dissipative contribution to the shear-component of the stress tensor $\left(\tau_{\mathrm{p},yx}^{\mathrm{d}}\right)$ is plotted as a function of shear rate. For a fixed value of h^*, it is seen that an increase in the internal viscosity parameter from $\epsilon = 0.1$ to $\epsilon = 10.0$ results in a significant increase in the dissipative contribution to shear stress.

The effect of hydrodynamic interactions on $\tau_{\mathrm{p},yx}^{\mathrm{d}}$, however, is less pronounced. At a constant value of ϵ, an increase in h^* (from 0 to 0.3) increases the stress marginally at lower shear rates, and ceases to affect the stress field significantly at higher shear rates. The reason for this behavior is well established (Zylka and Öttinger, 1989; Zylka, 1991) and can be understood by examining the role of hydrodynamic interactions at low and high shear rates. At low shear rates, the beads of the dumbbell are closer to each other, and there is a significant contribution to the hydrodynamic interaction force, as is clear from the form of the HI tensor given by Eq. (2.7) of Chapter 2. At higher shear rates, the connector between the beads is expanded, resulting in lower contributions to the HI tensor, and the viscometric functions tend to approach their free-draining values. This trend for the effect of HI is also true for the other steady-shear observables measured in our work, as will be seen in the following sections.

In Fig. 4.11 (b), the variation of the steady-state elastic contribution to the shear-component of the stress tensor $\left(\tau_{\mathrm{p},yx}^{\mathrm{e}}\right)$ is plotted as a function of shear rate. When the value of h^* is fixed, and ϵ is increased from 0.1 to 10, the elastic contribution to shear stress decreases markedly. The inclusion of hydrodynamic interactions, at a constant value of the IV parameter, has a less perceptible effect on $\tau_{\mathrm{p},yx}^{\mathrm{e}}$.

Fig. 4.12 shows the variation of the total shear stress, which is a sum of the elastic and dissipative components examined in Fig. 4.11, with the shear rate. At low shear rates, the total stress for $\epsilon = 0.1$ slightly exceeds that for $\epsilon = 10.0$. There is a crossover region at approximately $\lambda_{\mathrm{H}}\dot{\gamma} \approx 4$, after which the total stress for a higher value of ϵ exceeds that for lower ϵ. Such a crossover appears to indicate that the predominant contribution to the total stress at lower shear rates arises from the elastic component (which is higher for low values of ϵ), whereas at higher shear rates, the dissipative component (which is higher for higher values of ϵ) contributes more significantly to the total stress. The inset in Fig. 4.12 shows the effect of hydrodynamic interactions (with $h^* = 0.3$) on the total stress, at $\epsilon = 10.0$. The trend is similar to that observed for the effect of HI on $\tau_{\mathrm{p},yx}^{\mathrm{d}}$ and
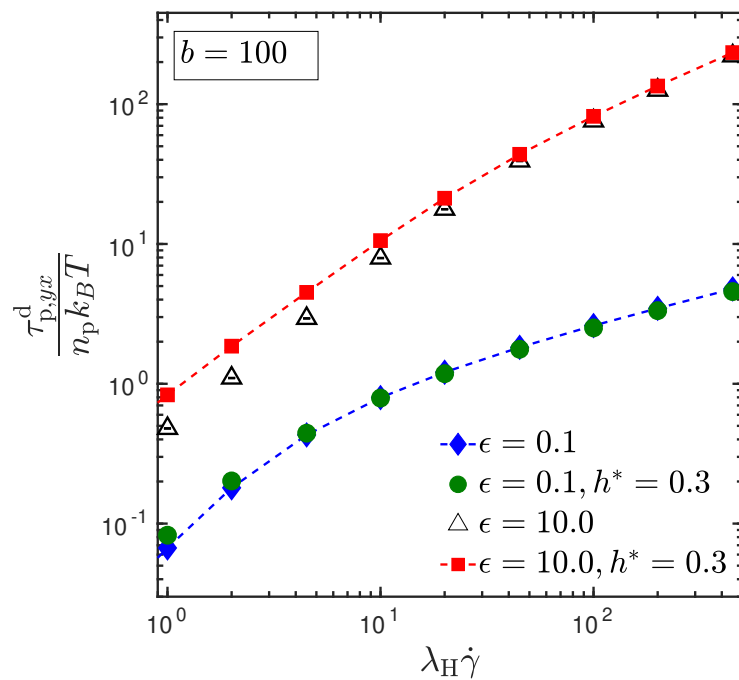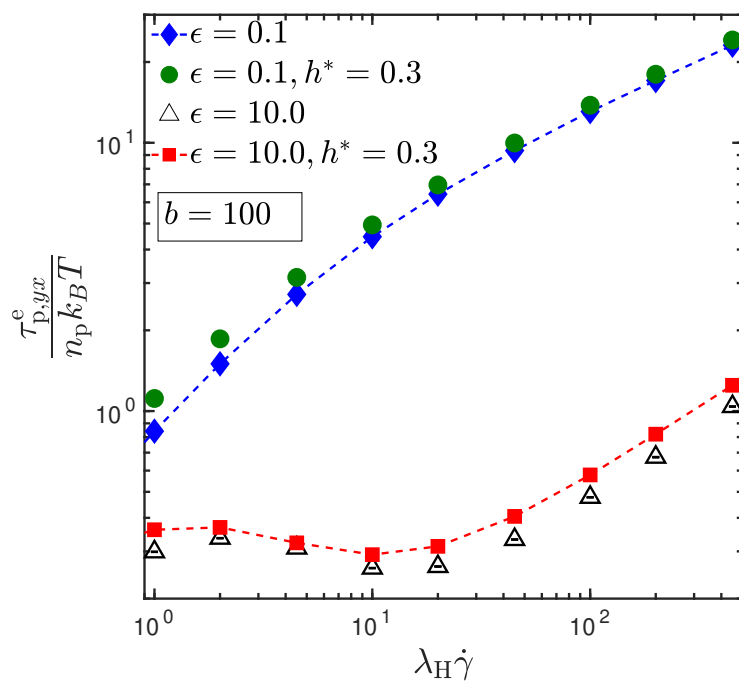
Figure 4.11: Effect of internal viscosity and hydrodynamic interactions on (a) dissipative and (b) elastic portions of the *yx*-component of the polymer contribution to the stress tensor, as a function of shear-rate. Error bars are smaller than symbol size.
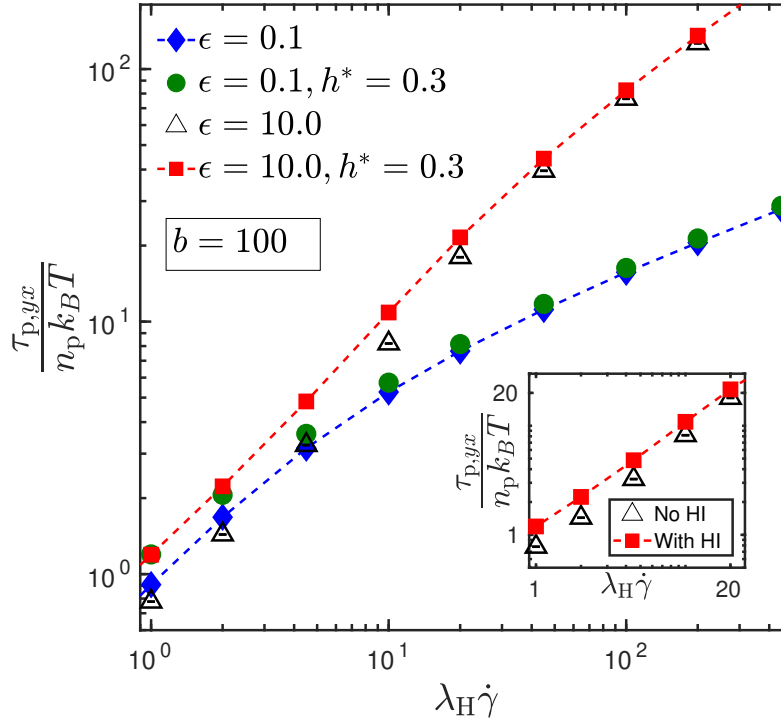
Figure 4.12: Total shear stress, $\tau_{\text{p},yx}$, as a function of shear rate for various values of ϵ and h^*. Error bars are smaller than symbol size.

$\tau_{\text{p},yx}^{\text{e}}$, with HI contributing to a small increase in stress compared to the free-draining case at lower shear rates, and weakening in effect at higher shear rates.

Shear-thinning of η_p and Ψ_1

To examine the steady-state behavior of the viscosity and first normal stress coefficient, both these quantities are plotted as a function of dimensionless shear rate in Figs. 4.13 and 4.14, respectively, for various values of ϵ and h^*.

Figure 4.13 (a) shows that hydrodynamic interactions enhance the zero-shear rate viscosity and push the onset of shear-thinning to lower shear rates. At higher shear rates, however, hydrodynamic interactions do not have a significant effect on the viscosity. Internal viscosity, on the other hand, leaves the zero-shear rate viscosity unperturbed, but quickens the onset of shear-thinning to low shear rates. At higher shear rates, however, internal viscosity is seen to slow down shear-thinning, as evidenced by the crossover between the $\epsilon = 1$ and the pure FENE case.

In Fig. 4.13 (b), the viscosity at high shear rates is plotted for three values of the internal viscosity parameter, to quantify the rates of shear thinning for the various cases. The FENE-P model predicts that the shear-thinning of viscosity follows a power law
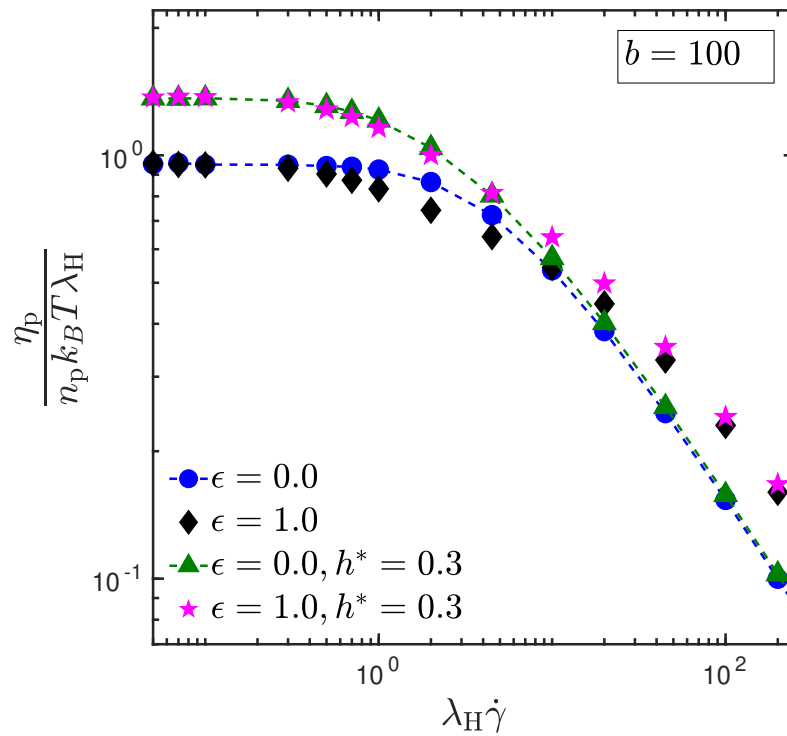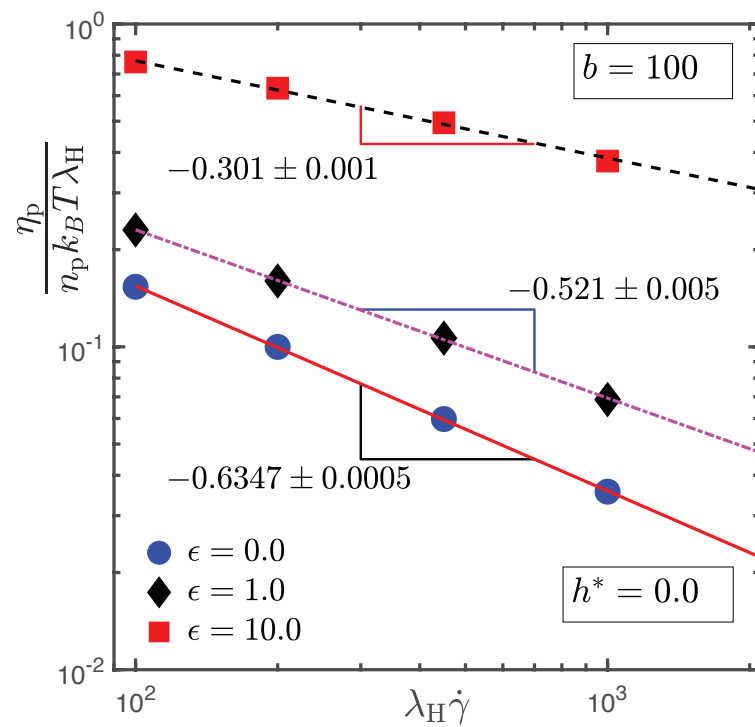
Figure 4.13: Plots of steady-shear viscosity for FENE dumbbells with $b = 100$. (a) Effect of IV and HI on shear-thinning and zero-shear rate viscosity at low and moderate shear rates. (b) Effect of IV on the shear-thinning exponent, at high shear rate. Errorbars are smaller than symbol size.

(a)

(b)
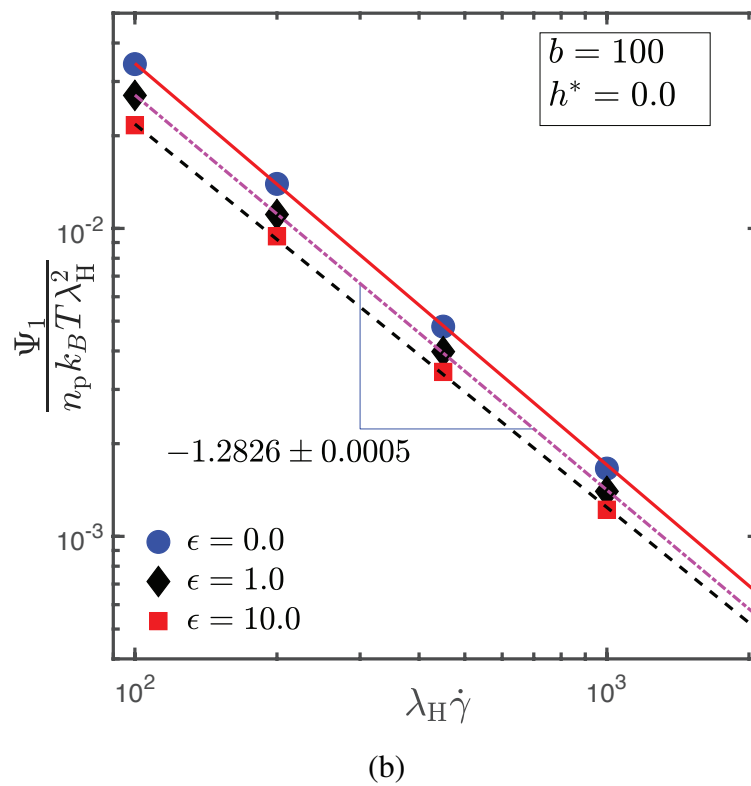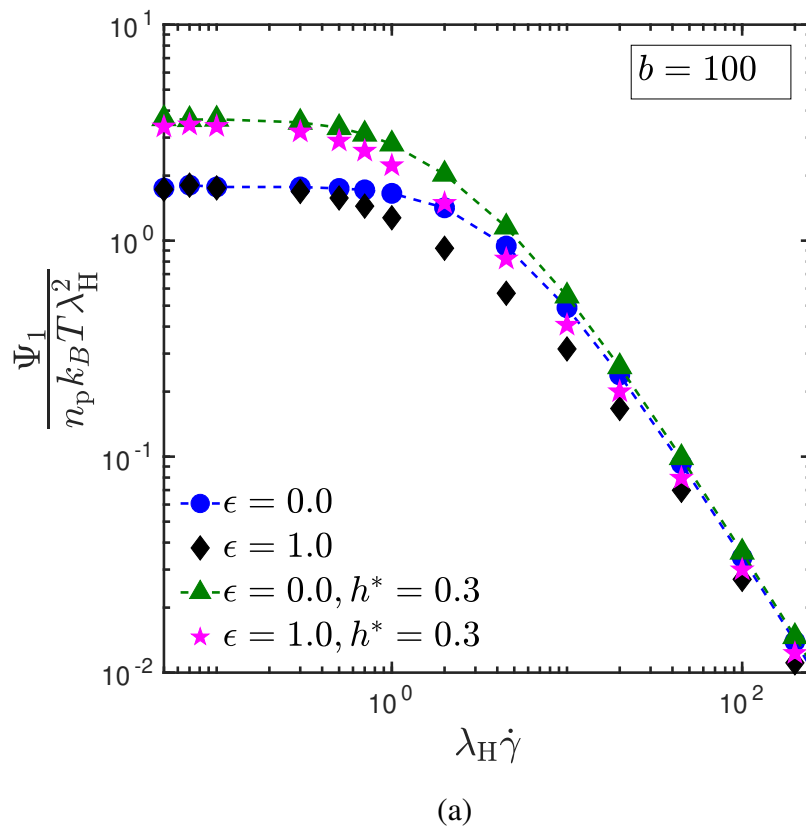
Figure 4.14: Plots for steady-shear first normal stress coefficient. (a) Effect of IV and HI on the zero-shear rate value, and shear-thinning at low and moderate shear rates. (b) Effect of IV on the shear-thinning exponent, at high shear rates. Error bars are smaller than symbol size.

behavior (Bird *et al.*, 1987b), with an exponent of $-(2/3)$. Exact BD simulations of a FENE dumbbell lead to an exponent of $-0.634(7)$, as seen from Fig. 4.13(b). As the IV parameter is increased, viscosity decreases less steeply with the shear rate, and the magnitude of the shear-thinning exponent decreases. A coupling between internal viscosity and finite extensibility appears to determine the rate at which the viscosity decreases with shear rate in the asymptotic limit. The inclusion of hydrodynamic interactions does not significantly change the shear-thinning exponent (not shown in figure). The shear-thinning exponent for the $\epsilon = 10$ case is roughly $-1/3$, which corresponds to the exponent for the rigid dumbbell model. It is worth noting that the $-1/3$ exponent is observed at sufficiently high shear rates, even for larger values of the FENE parameter. Section 4.3.4 contains a more detailed comparison between the FENE dumbbells with high IV and the rigid dumbbell model.

Similar to the trend observed for the polymer contribution to the viscosity, we see from Fig. 4.14 (a) that hydrodynamic interactions increase the zero-shear rate first normal stress coefficient and quicken the onset of shear-thinning. Also, the effect of hydrodynamic interactions becomes less perceptible at higher shear rates. In a deviation from the trend observed for viscosity, the first normal stress coefficient for the cases with and without internal viscosity scale identically with shear rate at higher shear rates, as observed from the lack of a crossover between the $\epsilon = 1$ and the pure FENE case. The asymptotic scaling of Ψ_1 with shear rate is captured more clearly in Fig. 4.14 (b), where the shear-thinning at high shear rates has been quantified using the slope of the curve. It is seen that there is no significant effect of the IV parameter on the shear thinning exponent for Ψ_1, in stark contrast to the dependence of the shear-thinning exponent on IV for viscosity. The FENE-P model predicts a shear-thinning exponent (Bird *et al.*, 1987b) of $-(4/3)$ for Ψ_1, which is twice the shear-thinning exponent for the viscosity. As seen from the figure, a slope of $-1.282(6)$ is obtained for the $\epsilon = 1.0$ case, which is also roughly the slope for the FENE dumbbell without internal viscosity, and twice the value of the shear-thinning exponent for the viscosity of the FENE dumbbell. Furthermore, the inclusion of hydrodynamic interactions is not seen to distinctly affect the shear-thinning exponent. Figures 4.15, which examine the shear rate-dependence of both the viscosity and the first normal stress coefficient on the FENE parameter (for free-draining dumbbells), display significant differences in the behavior of both viscometric functions. The steady-shear values of these two viscometric functions are plotted for various values of the FENE parameter, at a fixed value of the internal viscosity parameter ($\epsilon = 10$). Two limiting conditions arise in this discussion, that of the high shear rate limit ($\dot{\gamma} \rightarrow \infty$), and the Hookean limit ($b \rightarrow \infty$). Since the $b \rightarrow \infty$ limit is a singular one, the order in which
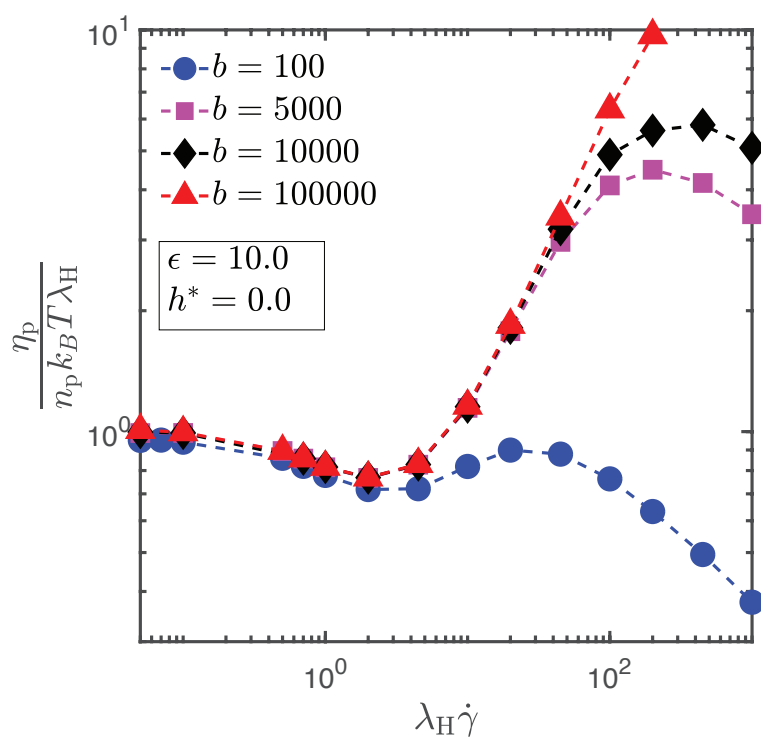
(a)
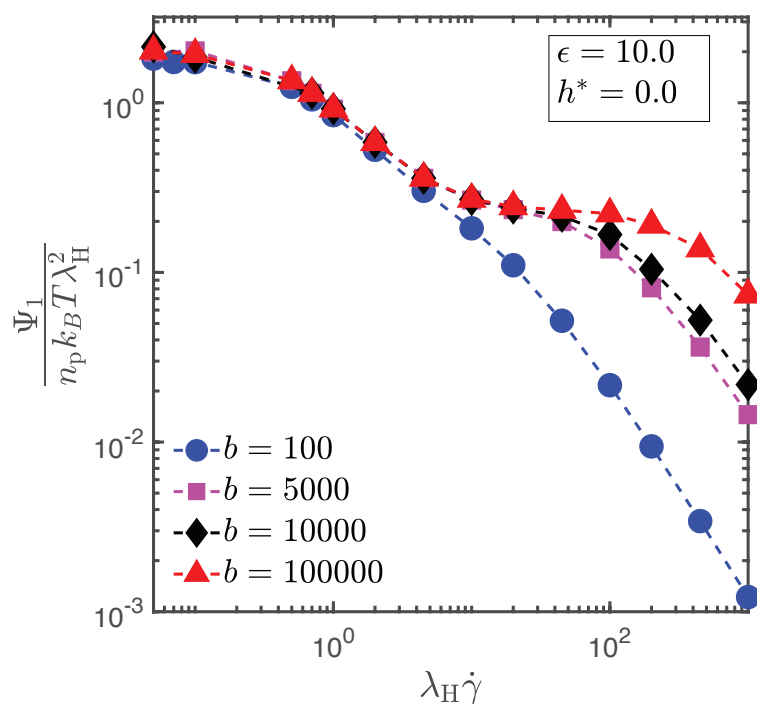
(b)

Figure 4.15: Effect of FENE parameter on the steady-shear viscometric functions for free-draining dumbbells with $\epsilon = 10$: (a) dimensionless viscosity as a function of dimensionless shear rate, (b) dimensionless first normal stress coefficient as a function of dimensionless shear rate. Error bars are smaller than symbol size.

these limits are taken matters. Note that the averaging technique described in Fig. 4.9 (b) has been used to obtain the steady-state value for the first normal stress coefficient at $\lambda_H\dot\gamma < 0.1$ for all the values of the FENE parameter plotted in Fig. 4.15 (b). For the lowest value of the FENE parameter ($b = 100$) examined in Fig. 15 (a), two shear-thinning regimes are observed for the viscosity, separated by a shear-thickening regime. Since any finite value of the FENE parameter, no matter how large, is indicative of a nonlinear spring, its finite extensibility will cause both η_p and Ψ_1 to eventually shear thin at large enough shear rates. This can be seen in Fig. 15 (a), where it is clear that increasing the value of b causes the power law region to be pushed to larger $\dot\gamma$. It appears that the shear-thinning exponent at sufficiently large $\dot\gamma$ is likely to be independent of b. If the FENE dumbbell is allowed to approach the Hookean limit, i.e; $b \to \infty$ (which, as noted is singular), we anticipate that there would be no shear-thinning at high shear rates, but only shear-thickening. Internal viscosity-induced shear thickening has also been observed by Hua and Schieber (1995), who noticed that the inclusion of internal viscosity for Hookean dumbbells results in shear-thinning at lower shear rates followed by shear-thickening at higher shear rates. They do not observe a second shear thinning regime, as expected for Hookean dumbbells. They also observe that an increase in the IV parameter shifts the onset of shear-thickening to lower shear rates.

The pattern of shear-thinning-thickening-thinning is strikingly similar to that previously reported by Kishbaugh and McHugh (1990) and Prabhakar and Prakash (2006) in their work on multi-bead chains with finitely extensible springs in the presence of hydrodynamic interactions. In the Hookean limit, and in the presence of hydrodynamic interactions, they also observe an indefinite shear-thickening of viscosity which follows the initial shear-thinning. The thinning of viscosity at high shear rates has been attributed by these authors to the finite extensibility of the spring. It is known that the inclusion of hydrodynamic interactions results in a shear-thinning for Hookean dumbbells (Zylka and Öttinger, 1989), and only induces a shear-thickening in bead-spring chains which have six or greater beads (Zylka, 1991). As discussed in section 4.3.3, for models with HI, the viscometric functions at high shear rates tend towards their values in the free-draining limit. For dumbbells ($N = 2$), the Rouse viscosity (free-draining) is lower than the Zimm viscosity (pre-averaged hydrodynamic interactions), and hence there is a shear-thinning when hydrodynamic interactions are included. For $N \geq 6$, the Rouse viscosity is higher than the Zimm viscosity, and consequently, the viscosity tends towards the higher Rouse value at higher shear rates, resulting in shear-thickening.

In contrast, internal viscosity is seen to cause shear-thickening even for the dumbbell case. The physical mechanism behind internal viscosity-induced shear thickening remains

unclear. Manke and Williams have analyzed the transient stress response of multi-bead models with internal viscosity (Manke and Williams, 1989) using the LRV approximation, in the low ϵ regime. However, they do not present the steady-shear viscosity of these dumbbells as a function of shear rate, and we are currently unable to comment on the existence of shear-thickening of viscosity in multi-bead chains with internal viscosity. Furthermore, the failings of the LRV approximation are well-documented (Manke and Williams, 1988; Dasbach *et al.*, 1992), and a rigorous treatment of the multi-bead model with internal viscosity is needed to draw meaningful conclusions about its steady-shear response. In Fig. 4.15 (b), for the lowest value of the FENE parameter ($b = 100$), it is seen that the first normal stress coefficient exhibits a continuous shear-thinning. An increase in the extensibility of the spring results in the appearance of a plateau in Ψ_1, followed by a second shear-thinning regime. Higher values of the FENE parameter pushes the onset of the second shear-thinning regime to higher shear rates, while widening the range of shear-rates over which the plateau is observed. In the Hookean limit, i.e; $b \to \infty$, we expect the second shear-thinning regime to vanish completely. This is in accord with the results of Hua and Schieber (1995), who observe a plateauing in Ψ_1 for Hookean dumbbells with internal viscosity. They also notice that an increase in the IV parameter causes the plateau to appear at lower shear rates.

4.3.4 Comparison of a model with large IV parameter with a rigid dumbbell model

There has been significant interest in the literature, Manke and Williams (1986, 1989, 1991, 1993) in approximating rheological properties—such as shear and complex viscosity —of rigid dumbbells with flexible polymer models using an infinitely high value of the IV parameter. Manke and Williams (1986) argue that with an increase in the value of the IV parameter, the timescale for the stretching of the dumbbell also increases. As $\epsilon \to \infty$, the dumbbells rotate and orient themselves much quicker than the time needed for their stretching. Essentially, such a high value of ϵ "freezes" the stretching of the dumbbell's connector vector, so their lengths retain the original distribution they were sampled from.

In this section, predictions by a FENE dumbbell model with a high value of the IV parameter ($\epsilon = 10$) is compared against that by a rigid dumbbell for three observables, namely, the relaxation modulus, the stress jump, and the steady-shear viscosity. For a monodisperse ensemble of rigid dumbbells of length L, the relaxation modulus, $G^{\text{uni}}(L, t)$,
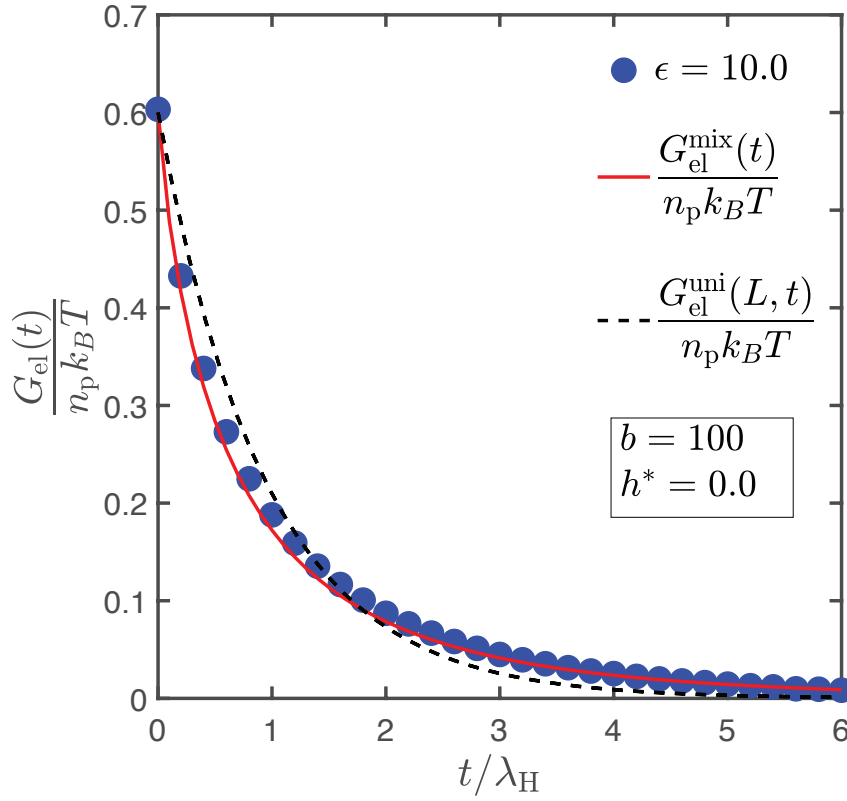
Figure 4.16:   Elastic component of the relaxation modulus for free-draining FENE dumbbells with $b = 100$ and $\epsilon = 10$. The dotted line corresponds to Eq. (4.38) with $L = \sqrt{<Q^2>_{\text{eq}}}$, without the singularity. The solid line is a plot of Eq. (4.40), without the singularity. Error bars are smaller than symbol size.

is given by (Bird *et al.*, 1987a)

$$\frac{G^{\text{uni}}(L,t)}{n_{\text{p}}k_BT} = 2\left(\frac{\eta_{\text{s}}}{n_{\text{p}}k_BT} + \frac{2}{5}\lambda_R\right)\delta(t) + \frac{3}{5}\exp\left(-t/\lambda_R\right) \qquad (4.38)$$

where the rod relaxation time, $\lambda_R = \zeta L^2/12k_BT$. Hua *et al.* (1996) showed that the relaxation modulus of a Hookean dumbbell model with a large value of the IV parameter ($\epsilon = 10$) is well approximated by $G^{\text{H,mix}}(t)$, which is the relaxation modulus of a rigid dumbbell model with a mixture of lengths. $G^{\text{H,mix}}(t)$ is calculated by convolving $G^{\text{uni}}(L,t)$ with the equilibrium distribution function for Hookean dumbbells.

Following the approach of Hua *et al.* (1996), the relaxation modulus for a system of rigid dumbbells whose lengths are sampled from a FENE distribution, $G^{\text{mix}}(t)$, is given by the following expression

$$\frac{G^{\text{mix}}(t)}{n_{\text{p}}k_BT} = \int \frac{G^{\text{uni}}(L,t)}{n_{\text{p}}k_BT}\psi^*_{\text{eq}}(\boldsymbol{Q}^*)d\boldsymbol{Q}^* \qquad (4.39)$$

where $\psi^*_{\text{eq}}(\boldsymbol{Q}^*) \equiv \left(1/J^*_{\text{eq}}\right)\left[1 - \left(Q^{*2}/b\right)\right]^{b/2}$ is the equilibrium configurational distribution function for an ensemble of FENE dumbbells, with the normalization constant given by

$J^*_{\text{eq}} = 2\pi b^{3/2} B(3/2, ((b+2)/2))$ where $B(.., ..)$ is the beta function (Abramowitz and Stegun, 1972). The integral in Eq. (4.39) can be evaluated by converting to spherical co-ordinates, as shown below

$$
\frac{G^{\text{mix}}(t)}{n_{\text{p}}k_B T} = 4\pi \int_0^\infty \frac{G^{\text{uni}}(L,t)}{n_{\text{p}}k_B T} \psi^*_{\text{eq}}(\boldsymbol{Q}^*) Q^{*2} dQ^*
$$

$$
= 2\left[\left(\frac{\eta_{\text{s}}}{n_{\text{p}}k_B T}\right) + \frac{2}{5}\left(\frac{b}{b+5}\right)\lambda_{\text{H}}\right]\delta(t) + \frac{3}{5}\left[y_1(t) + c_2 q^{3/2}(t)y_2(t)\right]
$$

$$
= 2\left(\frac{\eta_{\text{s}} + \eta_{\text{jump,rigid}}}{n_{\text{p}}k_B T}\right)\delta(t) + \frac{G^{\text{mix}}_{\text{el}}(t)}{n_{\text{p}}k_B T} \tag{4.40}
$$

where $q(t) = 3t/\lambda_{\text{H}}b$ and

$$
y_1(t) = {}_1F_1\left(-\left(\frac{b+3}{2}\right); -0.5; -q(t)\right)
$$

$$
y_2(t) = {}_1F_1\left(-\frac{b}{2}; 2.5; -q(t)\right) \tag{4.41}
$$

$$
c_2 = \frac{4\sqrt{\pi}}{3B(3/2, ((b+2)/2))}
$$

${}_1F_1$ is the confluent hypergeometric function of the first kind, defined by

$$
{}_1F_1(c; d; x) = \sum_{k=0}^\infty \frac{(c)_k}{(d)_k}\frac{x^k}{k!} \tag{4.42}
$$

$(c)_k$ and $(d)_k$ are Pochhammer symbols defined by

$$
(y)_m = \frac{\Gamma(y+m)}{\Gamma(y)} \tag{4.43}
$$

where $\Gamma(.)$ is the gamma function (Abramowitz and Stegun, 1972).

In Fig. 4.16, the elastic component of the relaxation modulus for free-draining FENE dumbbells with an internal viscosity parameter of $\epsilon = 10$ is plotted as a function of dimensionless time. There appears to be good agreement with the elastic component of $G^{\text{mix}}(t)$. Furthermore, it is observed that an attempt to fit the elastic portion of $G^{\text{uni}}(L,t)$, with L equal to the equilibrium length of the FENE dumbbells with $\epsilon = 10$, does not produce a good fit. Thus, at equilibrium, an internal viscosity parameter $\epsilon = 10$ appears to be sufficient to capture rigid dumbbell behavior. In the presence of flow, however, the dumbbell lengths are not completely frozen when an IV parameter of $\epsilon = 10$ is used, and a comparison with rigid dumbbell models is harder to draw. From Eq. (4.37) and (4.40), the stress jump for a rigid dumbbell system, with a FENE distribution of lengths, is given by

$$
\frac{\eta_{\text{jump,rigid}}}{n_{\text{p}}k_B T \lambda_{\text{H}}} = \frac{2}{5}\left(\frac{b}{b+5}\right) \tag{4.44}
$$

The analytical prediction of the same quantity for an ensemble of FENE dumbbells with IV is given by Eq. (4.28). Comparing the two equations shows that the stress jump predictions will be identical for the two models only in the limit of $\epsilon \gg 1$. Using $\epsilon = 10$, the stress jump prediction for the model with IV [$\eta^*_{\text{jump,IV}} = 0.346(3)$] is within 10% of that predicted by the rigid dumbbell model [$\eta^*_{\text{jump,rigid}} = 0.381$], for $b = 100$. Using an approximate analytical model, Manke and Williams (1986) establish a rheological equivalence between a rigid dumbbell system and an ensemble of monodisperse dumbbells with an infinite value of the IV parameter, and argue that an ensemble of Hookean dumbbells with an infinite value of the internal viscosity parameter should resemble the viscometric functions of an ensemble of rigid dumbbells, at least qualitatively. Exact BD simulations on dumbbells with a high value of the IV parameter undergoing shear flow, however, paint a different picture (Hua and Schieber, 1995).
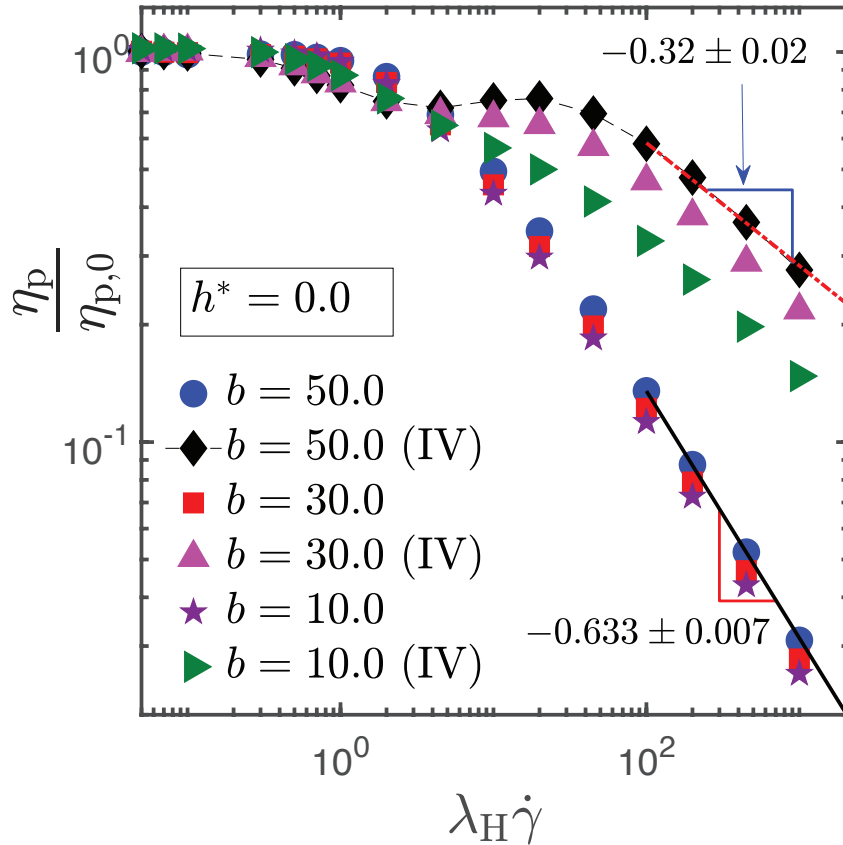
Figure 4.17: Normalized shear viscosity as a function of dimensionless shear rate, for different values of the FENE parameter, for free-draining dumbbells with and without internal viscosity. The internal viscosity parameter used in these simulations is $\epsilon = 10$. Error bars are smaller than symbol size.

We know from the work of Stewart and Sorensen (1972) that the steady-shear viscosity profile of rigid dumbbells has an initial Newtonian plateau followed by shear-

thinning with an exponent of $-(1/3)$. Hookean dumbbells with a high value of the IV parameter, on the other hand, display shear-thickening at high shear rates, as shown in Fig. 4.15 (a). Therefore, we do not have sufficient reason to believe that increasing the value of the IV parameter to higher values for a Hookean dumbbell model would bring a qualitative similarity with rigid dumbbell behavior.

With reference to the discussion surrounding Fig. 4.15 (a), Kishbaugh and McHugh (1990) and Prabhakar and Prakash (2006) observe for multi-bead chains (with finitely extensible springs and hydrodynamic interactions) that as the FENE parameter is decreased below a threshold value, the inflection point in the curve is seen to vanish, and only a continuous shear-thinning regime is observed, after an initial Newtonian plateau at low shear rates. The similarity between their system and that of a FENE dumbbell model with IV in the limit of a high value of b suggests that a similar trend would be observed in the low b limit as well.

In Fig. 4.17, the polymer contribution to shear viscosity (normalized by the zero-shear rate value) is plotted against the dimensionless shear rate, for various values of the FENE parameter, for free-draining dumbbells with and without internal viscosity. It is observed that at high shear rates, the viscosity of FENE dumbbells without internal viscosity scales roughly as $-0.63(3)$ with respect to the shear rate, for the three values of the FENE parameter considered here. As noted previously in the discussion surrounding Fig. 4.13 (b), this is in agreement with the FENE-P model prediction (Bird *et al.*, 1987b), which assigns a shear-thinning exponent of $-(2/3)$ at high shear rates, irrespective of the value of the FENE parameter. For models with internal viscosity ($\epsilon = 10$), the shear-thinning exponent for viscosity in all the three cases is roughly $-0.3(2)$. Interestingly, decreasing the value of the FENE parameter from $b = 50$ to $b = 10$ leads to the disappearance of the inflection point, and a smooth shear-thinning of viscosity is observed in the asymptotic limit of high shear rates. While sufficiently decreasing the value of the FENE b parameter, and increasing the IV parameter ϵ, leads to the disappearance of the shear thickening regime, and to a power law shear thinning exponent that is the same as that for a bead-rod model, it is not clear however, if the entire curve for the FENE dumbbell model coincides with that for the bead-rod model over all values of shear rate. Bead-rod results cannot be reported in Fig. 4.17 since the relaxation time $\lambda_{\rm H}$ is not appropriate for non-dimensionalizing the shear rate in that case. The relevant relaxation time is the bead-rod relaxation time $\lambda_{\rm R} (= \zeta Q_0^2/12 k_B T)$, introduced previously in Eq. (4.38), but defined here for a rod of length Q_0 in place of L. Using $\lambda_{\rm R}$ to non-dimensionalize FENE dumbbell results does not pose a problem, and as a result, the viscosity ratio for the FENE dumbbell model for various values of b and ϵ can be

(a)

(b)
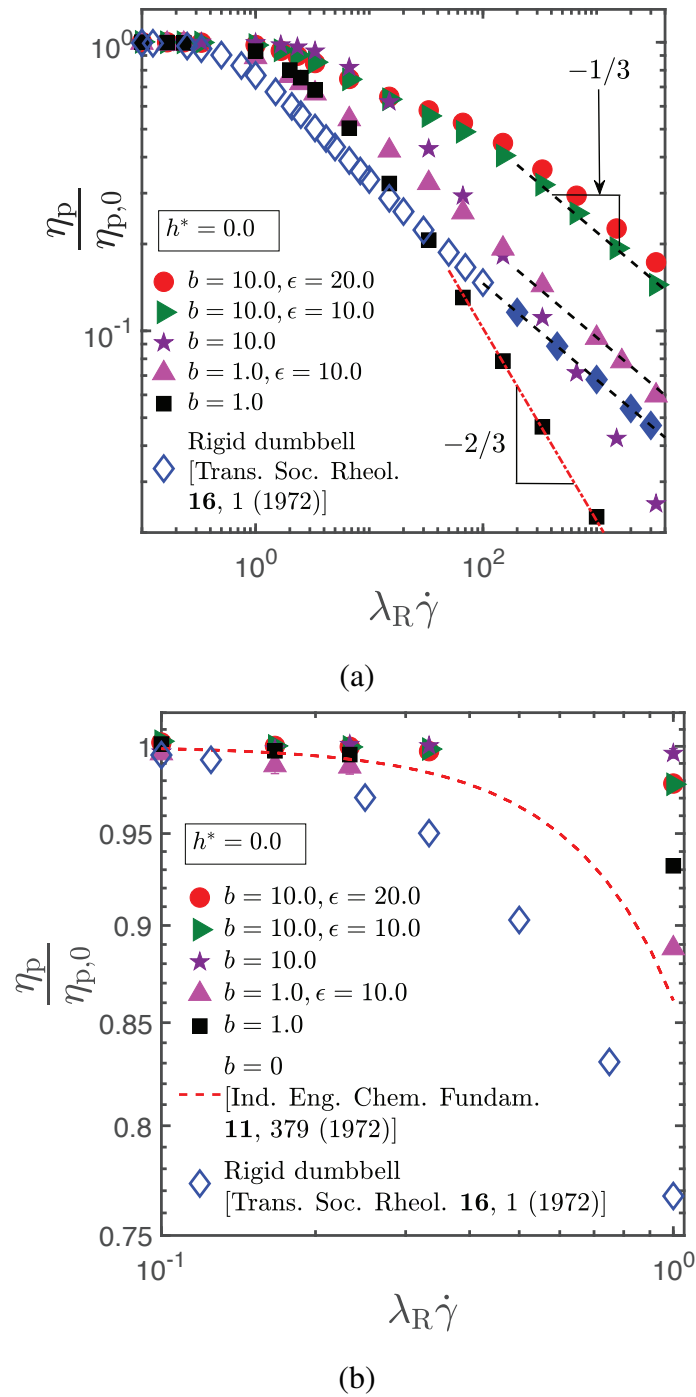
Figure 4.18: Normalised shear viscosity as a function of dimensionless shear rate (non-dimensionlised with the bead-rod relaxation time), for free-draining FENE dumbbells with $b = 1$ and $b = 10$, with and without internal viscosity. (a) Comparison with rigid dumbbell results reported in Stewart and Sorensen (1972). Data corresponding to the empty diamonds ($\diamond$) have been taken from Table II of Stewart and Sorensen (1972), while the filled diamonds ($\blacklozenge$) have been obtained the expression for the asymptotic values of the viscosity ratio at high shear rates (Eq. (17) of Stewart and Sorensen (1972)). (b) Comparison with the results of the bead-string model ($b = 0$) reported in Warner (1972), at small values of shear rate. Error bars are smaller than symbol size.

compared with bead-rod results over a wide range of shear rates, as shown in Figs. 4.18. The values of the viscosity ratio for the bead-rod model are taken from Stewart and Sorensen (1972) who report data in the form of a Table for $\lambda_R\dot\gamma \lesssim 100$ (see Table II in Stewart and Sorensen (1972)) and as an analytical expression for asymptotic values of the ratio at high shear rates (see Eq. (17) in Stewart and Sorensen (1972)).

There are several points that are worth noting in Fig. 4.18 (a), and they are discussed in turn. Both the $b = 10$ and $b = 1$ curves have the same asymptotic shear thinning slope of $-(1/3)$ as the bead-rod model for $\epsilon \geq 10$ (as noted previously), but they lie above the bead-rod curve at all values of the shear rate. When ϵ is set equal to zero, the asymptotic shear thinning exponent for the FENE dumbbell model becomes $-(2/3)$, and as a result, curves for both $b = 10$ and $b = 1$ cross the bead-rod curve at large enough shear rates due to the enhanced shear thinning. An important point to note here is that the notion of the FENE dumbbell model as a coarse-grained representation of a bead-rod chain is no longer tenable for small values of b (Underhill and Doyle, 2004; Pham *et al.*, 2008), and their use here should be viewed as merely an examination of a phenomenological model that could serve as a substitute for the bead-rod model. A problem with decreasing values of b is, however, that accurate results require smaller and smaller values of the time step.

In his early investigation of FENE dumbbell models, Warner (1972) introduced the notion of a *bead-string* model that corresponds to the limit $b = 0$, in which the force is negligible until a finite length. This is clearly as small a value as b can take, and in this limit Warner (1972) derived a power series expansion for the polymer contribution to viscosity up to second order in the non-dimensional shear rate (see Eq. (23) in Warner (1972)). Fig. 4.18 (b) compares the viscosity ratio predicted by the bead-string, bead-rod and FENE dumbbell models for small values of shear rate. It is apparent that the extent of shear thinning is nearly independent of the value of b at very small shear rates, and that the bead-rod model shear thins more rapidly than the FENE dumbbell model at any value of b. One can consequently conclude that while the asymptotic shear thinning exponent is identical for bead-rod and FENE dumbbell models for small values of b and large values of ϵ, the onset of shear thinning occurs at smaller shear rates for the bead-rod model, causing the viscosity curves for the two models to diverge.

The rigid dumbbell model (Stewart and Sorensen, 1972) predicts a shear-thinning exponent of $-(4/3)$ for Ψ_1, which is four times the shear-thinning exponent for the viscosity. From the variation in the first normal stress coefficient as a function of shear rate (not plotted here), a shear-thinning exponent of approximately $-1.2(6)$ is obtained for the entire parameter set used in Fig. 4.17, which is roughly four times the shear-thinning exponent for viscosity.

4.4 Conclusions

Using a dumbbell model of a polymer that accounts for the finite extensibility of the spring, we have examined the effect of fluctuating internal viscosity and hydrodynamic interactions on a range of rheological properties. This model may be viewed as a preliminary pedagogical tool for capturing the influence of these phenomena on key rheological observables. The results presented in this chapter have been published in Kailasham *et al.* (2018). The important results of our study are summarised below.

1. The most significant effect of hydrodynamic interactions is the magnification of the stress jump in dilute polymer solutions in comparison to the free-draining case, a finding that concurs with analytical predictions.

2. The zero-shear rate viscosity can be expressed as the sum of an elastic component (the integral of the relaxation modulus) and a viscous component (the stress jump). Values calculated in this manner have been compared against BD simulations and are in good agreement.

3. The zero-shear rate viscometric functions are practically independent of the internal viscosity parameter, for free-draining dumbbells. The inclusion of hydrodynamic interactions, however, induces a non-trivial coupling with internal viscosity, and consequently, the zero-shear rate properties display a dependence on both the HI and the IV parameter.

4. Hydrodynamic interactions alter the transient viscometric functions perceptibly. However, their effect on the steady-shear properties are less marked, with the effect of HI weakening at higher shear rates.

5. Overshoots in viscosity and the first normal stress coefficient occur at progressively earlier times as the shear rate is increased, yet the strain at which overshoot occurs remains roughly constant over a wide range of shear rates, in agreement with experimental observations on polymer solutions and melts.

6. In the asymptotic limit of high shear rates, internal viscosity significantly affects the shear-thinning exponent in viscosity, with the magnitude of the slope decreasing with an increase in the magnitude of the internal viscosity parameter. The shear-thinning exponent for the first normal stress coefficient, however, remains practically unaffected by the inclusion of internal viscosity.

7. There is a remarkable, but unexplained, similarity in the steady-shear viscosity profiles of FENE-IV dumbbells and multi-bead chains with finitely extensible springs and hydrodynamic interactions.

8. The relaxation modulus of an ensemble of FENE dumbbells with $\epsilon = 10$ is identical to that of a mixture of rigid dumbbells. For the stress jump, increasing values of the IV parameter give results that are in closer agreement with the rigid dumbbell case. In steady shear flow, the asymptotic shear thinning exponent is identical for bead-rod and FENE dumbbell models with small values of b and large values of ϵ. However, the onset of shear thinning occurs at smaller shear rates for the bead-rod model than for FENE dumbbells with any value of b, no matter how small.

A comparison with biophysical experiments that determine the reconfiguration time of proteins, or the energy landscape of polysaccharides, would necessitate the use of a multi-bead spring chain that incorporates IV and HI. Dasbach *et al.* (1992) have obtained an approximate analytical solution for such a chain model. The use of BD simulations to solve the bead-spring-dashpot chain model exactly is rendered difficult by the fact that formulating the correct Fokker-Planck equation for such a system, and finding the equivalent set of stochastic differential equations, is non-trivial, and is the subject of Chapter 5.

Chapter 5

Rouse model with fluctuating internal friction

5.1 Introduction

The machinery for the solution of coarse-grained polymer models through Brownian dynamics (BD) simulations is well-established (Bird *et al.*, 1987b; Öttinger, 1996): the equation of motion for the connector vector velocities is combined with an equation of continuity in probability space to obtain a Fokker-Planck equation for the system, and the equivalent stochastic differential equation is integrated numerically. The inclusion of internal viscosity, however, results in a coupling of connector vector velocities and precludes a trivial application of the usual procedure for all but the simplest case of a dumbbell. By expanding the scope of an existing methodology for velocity-decoupling (Manke and Williams, 1988), the exact set of governing stochastic differential equations for a bead-spring-dashpot chain with N_b beads, and its numerical solution using BD simulations is presented here. The thermodynamically consistent (Schieber and Öttinger, 1994) stress tensor expression for this model is derived, and material functions in simple shear and oscillatory shear flows have been calculated.

It is instructive to first briefly survey the methods employed in the past, before turning our attention to the solution proposed in the present work. Booij and van Wiechen (1970) used perturbation analysis to expand the configurational distribution function of a Hookean spring-dashpot in terms of the internal friction parameter, $\varphi = K/\zeta$, which is the ratio of the dashpot's damping coefficient, K, to the bead friction coefficient, ζ, and predicted optical and rheological properties in the presence of steady shear flow. On the other hand, Williams and coworkers offered a semi-analytical approximate solution for the stress-jump (Manke and Williams, 1988) of bead-spring-dashpot-chains

with an arbitrary number of beads, using a decoupling procedure which is discussed at length later in this chapter. They also obtained predictions for the complex viscosity of such chains by writing the configurational distribution function as a series expansion in strain Dasbach *et al.* (1992). While the approach of Booij and van Wiechen (1970) is restricted to small values of the internal friction parameter, the solutions proposed by Williams and coworkers (Manke and Williams, 1988; Dasbach *et al.*, 1992) are applicable only in the linear viscoelastic regime. The transient variation and steady-state values of viscometric functions of bead-spring-dashpot chains with arbitrary chain-length in shear flow have been predicted (Bazúa and Williams, 1974; Manke and Williams, 1989) using the linearized rotational velocity (Cerf, 1957; R. Cerf, 1969; Peterlin, 1967) (LRV) approximation for the internal viscosity force. The LRV approximation, however, was shown to be incorrect (Booij and van Wiechen, 1970; Manke and Williams, 1988; Dasbach *et al.*, 1992) and its use was subsequently discarded. For the simplest case of a single-mode dumbbell-dashpot, it is straightforward to formulate the governing Fokker-Planck equation and obtain its equivalent stochastic differential equation. Both linear viscoelastic properties (Hua and Schieber, 1995) and viscometric functions in steady-shear flow (Hua *et al.*, 1996) have been calculated for this model using Brownian dynamics (BD) simulations, for arbitrary values of the internal friction parameter, as discussed previously in Chapter 4. The single-mode spring-dashpot model has also been solved using a Gaussian approximation for the distribution function (Schieber, 1993; Sureshkumar and Beris, 1995). Upon comparison against exact BD simulation results, it was found that the Gaussian approximation (GA) offers accurate predictions of linear viscoelastic properties, but is unable to predict the shear-thickening of viscosity (Hua and Schieber, 1995) predicted by the exact model. Furthermore, the predictions for the stress jump in the start up of shear flow, obtained from BD simulations on the exact model, the Gaussian approximation, and the semi-analytical treatment of Manke and Williams agree with one another (Hua and Schieber, 1995).

Fixman (1988) has shown that the effects of bond length and bond angle constraints in stiff polymer models may be sufficiently mimicked by a Rouse/Zimm-like chain with internal friction. A preaveraged form of the internal friction force was chosen for analytical tractability, and this simplified model yields predictions for equilibrium and linear viscoelastic properties, such as the bond-vector correlations and storage and loss moduli, that are in reasonable agreement with that of stiff polymer chains. McLeish and coworkers developed the Rouse model with internal friction (Khatri and McLeish, 2007) (RIF), wherein the standard continuum Rouse model is modified to include a rate-dependent dissipative force that resists changes in the curvature of the space-curve

representing the polymer molecule. As will be shown in the next chapter, the RIF model represents a preaveraged treatment of internal friction, while, in this work, we have developed an exact model which accounts for fluctuations in the internal friction force. A thorough test of the accuracy of the preaveraging approximation, by comparing model predictions for observables at equilibrium and in flow, against exact BD simulations which account for fluctuations in internal friction, is presented in Chapter 6.

There currently exists no methodology that is able to predict both linear viscoelastic properties and viscometric functions in shear flow for bead-spring-dashpot chains with arbitrary number of beads and magnitude of internal friction parameter. We address this deficiency by solving the bead-spring-dashpot chain problem exactly. We compare BD simulation results for the stress jump and complex viscosity against approximate analytical predictions given in Manke and Williams (1988) and Dasbach *et al.* (1992), respectively, and present steady-state results for viscometric functions in simple shear flow for the general case of $N_\text{b} > 2$, for the first time.

A crucial step in our methodology is the decoupling of the connector vector velocities of neighboring beads. Stripping away all physical detail, the decoupling problem may be stated as follows: given a "generating equation" for some $\mathcal{S}_j$ which is of the form

$$\mathcal{S}_j = d_{j-1}\mathcal{S}_{j-1} + e_{j+1}\mathcal{S}_{j+1} + \xi(X_1, X_2, \ldots, X_N) \tag{5.1}$$

where $j \in [1, N]$, and the X_i do not depend on the $\mathcal{S}_j$, with $\left\{\xi, d_j, e_j\right\}$ being some arbitrary functions of the X_i, is it possible to write an expression for $\mathcal{S}_j$ solely in terms of the X_i that does not explicitly depend on any other $\mathcal{S}_i$? Manke and Williams (1988) have proposed a three-step procedure for the solution of this problem. As the first step, the equation for $\mathcal{S}_j$ is successively substituted into $\mathcal{S}_{j+1}$, starting from $j = 1$. At the end of this forward substitution step, an equation for $\mathcal{S}_j$ is obtained that only depends explicitly on $\mathcal{S}_{j+1}$ and X_i with $1 \leq i \leq j$. The second step is a backward substitution, where the equation for $\mathcal{S}_j$ is successively substituted into $\mathcal{S}_{j-1}$, starting from $j = N$. This results in an expression for $\mathcal{S}_j$ that only depends explicitly on $\mathcal{S}_{j-1}$ and X_i with $j \leq i \leq N$. Finally, upon combining the results from the forward and backward substitution procedures, the decoupling procedure is completed, resulting in $\mathcal{S}_j = \mathcal{A}_j \xi(X_1, X_2, \ldots, X_N)$ where $\mathcal{A}_j$ is defined recursively in terms of d and e. While the decoupling methodology developed by Manke and Williams has been adopted in the present work, we differ significantly in the generating equation which is subjected to the decoupling procedure, as discussed below. A schematic representation of the decoupling methodology is displayed in Fig. 5.1.

The rest of this chapter is structured as follows. Section 5.2 presents the governing stochastic differential equations and the stress tensor expression for a free-draining

Decoupling Methodology	
Given $\mathcal{S}_j = d_{j-1}\mathcal{S}_{j-1} + e_{j+1}\mathcal{S}_{j+1} + \xi$, the following procedure leads to an expression for $\mathcal{S}_j$ that does not depend explicitly on any other $\mathcal{S}_i$	
Step	**Output**
(1) Forward Substitution $\boxed{\mathcal{S}_1} \implies \boxed{\mathcal{S}_2} \implies \cdots \boxed{\mathcal{S}_j} \cdots \implies \boxed{\mathcal{S}_{N-1}} \implies \boxed{\mathcal{S}_N}$	$\mathcal{S}_j \equiv f\left(\mathcal{S}_{j+1}, \xi\right)$
(2) Backward Substitution $\boxed{\mathcal{S}_N} \implies \boxed{\mathcal{S}_{N-1}} \implies \cdots \boxed{\mathcal{S}_j} \cdots \implies \boxed{\mathcal{S}_2} \implies \boxed{\mathcal{S}_1}$	$\mathcal{S}_j \equiv g\left(\mathcal{S}_{j-1}, \xi\right)$
(3) Combine expressions from (1) and (2) to get decoupled expression for $\mathcal{S}_j$	$\mathcal{S}_j \equiv \mathcal{A}_j \xi$ $\mathcal{A}_j \equiv \hat{h}\left(\{d, e\}\right)$

Figure 5.1: Schematic of three-step decoupling methodology introduced in Manke and Williams (1988).

bead-spring-dashpot chain, and contains simulation details pertaining to the numerical integration of the governing equations. Sec. 5.3, which is a compilation of our results and the relevant discussion, is divided into three sections; Sec. 5.3.1 deals with code validation, Sec. 5.3.2 presents results for the complex viscosity calculated from oscillatory shear flow simulations, and Sec. 5.3.3 contains results for steady shear viscometric functions.We conclude in Sec. 5.4.

In Appendix B, the first few iterations of the forward and backward substitution steps are explicitly shown, from which the general expressions may be discerned by induction. The detailed steps for the derivation of the stress tensor expression are provided in Appendix C. As described later in detail, the governing stochastic differential equation and the stress tensor expression require the evaluation of a divergence term which does not appear in conventional bead-spring-chain models. Appendix D outlines a procedure for evaluating these terms analytically.

5.2 Governing Equation and simulation details

As will be seen shortly, in the absence of hydrodynamic interactions, the inclusion of internal viscosity results in an explicit coupling of the connector vector velocities between nearest neighbors, and these velocities may be decoupled using the procedure suggested by Manke and Williams (1988). The simultaneous inclusion of fluctuating

hydrodynamic interactions and internal viscosity, however, results in a one-to-all coupling of the connector vector velocities, which renders the problem intractable using the approach suggested by Manke and Williams (1988). As shown in Chapter 4, in dumbbell models with internal viscosity, hydrodynamic interactions significantly magnify the stress jump and perceptibly affect the transient viscometric functions. Coarse-grained polymer models which incorporate both fluctuating hydrodynamic interactions and internal viscosity are currently unsolved for the $N_b > 2$ case. In this chapter, we restrict our attention to freely-draining bead-spring-dashpot chains.

In the absence of excluded volume and hydrodynamic interaction effects, the governing equation given by Eq. (2.1) reduces to

$$\llbracket \dot{\boldsymbol{Q}}_k \rrbracket = \boldsymbol{\kappa} \cdot \boldsymbol{Q}_k - \frac{1}{\zeta} \sum_{l=1}^{N} \boldsymbol{A}_{kl} \cdot \left(k_B T \frac{\partial \ln \Psi}{\partial \boldsymbol{Q}_l} + \frac{\partial \phi}{\partial \boldsymbol{Q}_l} + K \frac{\boldsymbol{Q}_l \boldsymbol{Q}_l}{\boldsymbol{Q}_l^2} \cdot \llbracket \dot{\boldsymbol{Q}}_l \rrbracket \right) \tag{5.2}$$

with $\widetilde{\boldsymbol{A}}_{kl}$ in Eq. (2.1) replaced by $\boldsymbol{A}_{kl}$ as given in Eq. (2.3), and $\phi \equiv \phi_{\mathrm{HK}}^{\mathrm{S}}$ [as defined in Eq. 2.9] throughout this chapter. The solid and dashed underlined terms on the RHS of Eq. (5.2) represent the Brownian and spring force contributions, respectively. Since Manke and Williams (1988) were concerned only with the evaluation of the stress-jump, which occurs instantaneously upon the inception of flow, they assumed that the configurational distribution function may be reasonably approximated by its equilibrium value. Since the Brownian and spring forces exactly balance each other at equilibrium, i.e., $k_B T (\partial \ln \Psi_{\mathrm{eq}} / \partial \boldsymbol{Q}_l) + (\partial \phi / \partial \boldsymbol{Q}_l) = 0$, Manke and Williams (1988) ignore both these forces in their equation of motion. Here, however, we aim to find the exact governing equation that is valid both near and far away from equilibrium, and have consequently retained both the underlined terms in the force-balance equation.

As seen from Eq. (5.2), there is an explicit coupling between the velocity of the kth connector vector and its nearest neighbors which precludes a straightforward substitution into the equation of continuity for the configurational distribution function. This velocity-coupling may be removed by applying the decoupling scheme described in Fig. 5.1, as shown below. We first define the quantity

$$C_k = \frac{\boldsymbol{Q}_k \cdot \llbracket \dot{\boldsymbol{Q}}_k \rrbracket}{Q_k^2}; \quad k = 1, 2, \cdots, N \tag{5.3}$$

Upon taking a dot-product on both the sides of Eq. (5.2) with $\boldsymbol{Q}_k/Q_k^2$, an equation for C_k is obtained as

$$C_k = \left(\frac{\boldsymbol{Q}_k}{Q_k^2}\right) \cdot \boldsymbol{\kappa} \cdot \boldsymbol{Q}_k - \left(\frac{k_BT}{\zeta}\right)\left(\frac{\boldsymbol{Q}_k}{Q_k^2}\right) \cdot \left[-\frac{\partial \ln \Psi}{\partial \boldsymbol{Q}_{k-1}} + 2\frac{\partial \ln \Psi}{\partial \boldsymbol{Q}_k} - \frac{\partial \ln \Psi}{\partial \boldsymbol{Q}_{k+1}}\right]$$

$$-\frac{1}{\zeta}\left(\frac{\boldsymbol{Q}_k}{Q_k^2}\right) \cdot \left[-\frac{\partial \phi}{\partial \boldsymbol{Q}_{k-1}} + 2\frac{\partial \phi}{\partial \boldsymbol{Q}_k} - \frac{\partial \phi}{\partial \boldsymbol{Q}_{k+1}}\right]$$

$$+\left(\frac{K}{\zeta}\right)C_{k-1}L_{k-1}\left(\frac{Q_{k-1}}{Q_k}\right) - \left(\frac{2K}{\zeta}\right)C_k + \left(\frac{K}{\zeta}\right)C_{k+1}L_k\left(\frac{Q_{k+1}}{Q_k}\right) \qquad (5.4)$$

where

$$L_k \equiv \cos \theta_k = \frac{\boldsymbol{Q}_k \cdot \boldsymbol{Q}_{k+1}}{Q_k Q_{k+1}} \qquad (5.5)$$

Upon grouping together terms containing C_k on the RHS and simplifying, the generating equation is obtained as

$$C_k = \left(\frac{\zeta}{\zeta + 2K}\right)\left(\frac{\boldsymbol{Q}_k}{Q_k^2}\right) \cdot (\boldsymbol{\kappa} \cdot \boldsymbol{Q}_k) - \left(\frac{k_BT}{\zeta + 2K}\right)\left(\frac{\boldsymbol{Q}_k}{Q_k^2}\right) \cdot \left[-\frac{\partial \ln \Psi}{\partial \boldsymbol{Q}_{k-1}} + 2\frac{\partial \ln \Psi}{\partial \boldsymbol{Q}_k} - \frac{\partial \ln \Psi}{\partial \boldsymbol{Q}_{k+1}}\right]$$

$$-\left(\frac{1}{\zeta + 2K}\right)\left(\frac{\boldsymbol{Q}_k}{Q_k^2}\right) \cdot \left[-\frac{\partial \phi}{\partial \boldsymbol{Q}_{k-1}} + 2\frac{\partial \phi}{\partial \boldsymbol{Q}_k} - \frac{\partial \phi}{\partial \boldsymbol{Q}_{k+1}}\right] \qquad (5.6)$$

$$+\left(\frac{K}{\zeta + 2K}\right)\left[C_{k-1}L_{k-1}\left(\frac{Q_{k-1}}{Q_k}\right) + C_{k+1}L_k\left(\frac{Q_{k+1}}{Q_k}\right)\right]$$

Eq. (5.6) is then subjected to the forward and backward substitution schema discussed previously, to obtain a decoupled expression for C_k. In the forward substitution step, the equation for C_k is substituted into that for C_{k+1}, iteratively, starting from $k = 1$ until $k = (N-1)$. The first few steps of the iteration are explicitly illustrated in Sec. B.1 of Appendix B, following which, the general expression may be written, by induction, to be

$$C_k(1 - M_k) = \left(\frac{K}{\zeta + 2K}\right)C_{k+1}L_k\left(\frac{Q_{k+1}}{Q_k}\right) + \left(\frac{\zeta}{\zeta + 2K}\right)\left(\frac{1}{Q_k}\right)\sum_{l=1}^{k}\boldsymbol{\Gamma}_l^{(k)} \cdot (\boldsymbol{\kappa} \cdot \boldsymbol{Q}_l)$$

$$+ (1 - \delta_{kN})\left(\frac{k_BT}{\zeta + 2K}\right)\left(\frac{1}{Q_k}\right)\left(\frac{\boldsymbol{Q}_k}{Q_k}\right) \cdot \left(\frac{\partial \ln \Psi}{\partial \boldsymbol{Q}_{k+1}}\right) + (1 - \delta_{kN})\left(\frac{1}{\zeta + 2K}\right)\left(\frac{1}{Q_k}\right)\left(\frac{\boldsymbol{Q}_k}{Q_k}\right) \cdot \left(\frac{\partial \phi}{\partial \boldsymbol{Q}_{k+1}}\right)$$

$$- \left(\frac{k_BT}{\zeta + 2K}\right)\left(\frac{1}{Q_k}\right)\sum_{l=1}^{k}\boldsymbol{E}_l^{(k)} \cdot \left(\frac{\partial \ln \Psi}{\partial \boldsymbol{Q}_l}\right) - \left(\frac{1}{\zeta + 2K}\right)\left(\frac{1}{Q_k}\right)\sum_{l=1}^{k}\boldsymbol{E}_l^{(k)} \cdot \left(\frac{\partial \phi}{\partial \boldsymbol{Q}_l}\right) \qquad (5.7)$$

where

$$M_k = \left(\frac{K}{\zeta + 2K}\right)^2\left(\frac{L_{k-1}^2}{1 - M_{k-1}}\right); \quad \text{with} \quad M_1 = 0, \qquad (5.8)$$

$$\boldsymbol{\Gamma}_l^{(k)} = \left(\frac{K}{\zeta + 2K}\right)^{k-l} \left[\prod_{i=l}^{k-1} \left(\frac{1}{1 - M_i}\right) L_i\right] \left(\frac{\boldsymbol{Q}_l}{Q_l}\right), \tag{5.9}$$

and

$$\boldsymbol{E}_l^{(k)} = 2\boldsymbol{\Gamma}_l^{(k)} - \boldsymbol{\Gamma}_{l-1}^{(k)} - \boldsymbol{\Gamma}_{l+1}^{(k)} \tag{5.10}$$

Here, $\boldsymbol{\Gamma}_l^{(k)}$ is defined only for $0 < l \le k \le N$, and is set to zero otherwise.

The backward substitution step involves plugging in the equation for C_k into C_{k-1}, iteratively, starting from $k = N$ until $k = 2$. The first few steps of the iteration are explicitly illustrated in Sec. B.2 of Appendix B, following which, the general expression may be written, by induction, to be

$$C_k L_{k-1} \left(\frac{Q_k}{Q_{k-1}}\right) = \left(\frac{K}{\zeta + 2K}\right)\left(\frac{1}{1 - P_k}\right) C_{k-1} L_{k-1}^2 + \left(\frac{\zeta}{\zeta + 2K}\right)\left(\frac{1}{Q_{k-1}}\right) \sum_{l=k}^{N} \widetilde{\boldsymbol{\rho}}_l^{(k)} \cdot (\boldsymbol{\kappa} \cdot \boldsymbol{Q}_l)$$

$$+ \left(\frac{k_B T}{\zeta + 2K}\right)\left(\frac{1}{1 - P_k}\right) L_{k-1} \left(\frac{1}{Q_{k-1}}\right)\left(\frac{\boldsymbol{Q}_k}{Q_k}\right) \cdot \left(\frac{\partial \ln \Psi}{\partial \boldsymbol{Q}_{k-1}}\right)$$

$$+ \left(\frac{1}{\zeta + 2K}\right)\left(\frac{1}{1 - P_k}\right) L_{k-1} \left(\frac{1}{Q_{k-1}}\right)\left(\frac{\boldsymbol{Q}_k}{Q_k}\right) \cdot \left(\frac{\partial \phi}{\partial \boldsymbol{Q}_{k-1}}\right)$$

$$- \left(\frac{k_B T}{\zeta + 2K}\right)\left(\frac{1}{Q_{k-1}}\right) \sum_{l=k}^{N} \widetilde{\boldsymbol{G}}_l^{(k)} \cdot \left(\frac{\partial \ln \Psi}{\partial \boldsymbol{Q}_l}\right) - \left(\frac{1}{\zeta + 2K}\right)\left(\frac{1}{Q_{k-1}}\right) \sum_{l=k}^{N} \widetilde{\boldsymbol{G}}_l^{(k)} \cdot \left(\frac{\partial \phi}{\partial \boldsymbol{Q}_l}\right) \tag{5.11}$$

where

$$P_k = \left(\frac{K}{\zeta + 2K}\right)^2 \left(\frac{L_k^2}{1 - P_{k+1}}\right); \quad \text{with} \quad P_N = 0, \tag{5.12}$$

and

$$\widetilde{\boldsymbol{\rho}}_l^{(k)} = \left(\frac{K}{\zeta + 2K}\right)^{l-k} \left[\prod_{i=k}^{l} \left(\frac{1}{1 - P_i}\right) L_{i-1}\right] \left(\frac{\boldsymbol{Q}_l}{Q_l}\right) \tag{5.13}$$

The vector $\widetilde{\boldsymbol{G}}_l^{(k)}$ appearing in Eq. (5.11) is constructed using a slightly elaborate procedure. It is useful to first consider a block Rouse matrix, $\widehat{\boldsymbol{R}}$, of size $\Upsilon \times \Upsilon$, where $\Upsilon = (N - k) + 1$, whose each element is a 3×3 matrix, and has the following structure,

$$\widehat{\boldsymbol{R}} = \begin{pmatrix} 2\delta & -\delta & \boldsymbol{0} & \cdots & \\ -\delta & 2\delta & -\delta & \boldsymbol{0} & \cdots \\ \boldsymbol{0} & -\delta & 2\delta & -\delta & \cdots \\ \vdots & \vdots & \vdots & & \\ \boldsymbol{0} & \boldsymbol{0} & \cdots & & -\delta & 2\delta \end{pmatrix} \tag{5.14}$$

and define the intermediate quantity,

$$\widetilde{\boldsymbol{Y}}_s^{(k)} = \left(\frac{K}{\zeta + 2K}\right)^{s-1} \left[\prod_{i=k}^{k+s-1} \left(\frac{1}{1 - P_i}\right) L_{i-1}\right] \left(\frac{\boldsymbol{Q}_{s+k-1}}{Q_{s+k-1}}\right) \tag{5.15}$$

which is then used to populate a block matrix, $\widehat{\boldsymbol{\Theta}}^{(k)}$, of size $\Upsilon \times \Upsilon$ that has the following structure

$$
\widehat{\boldsymbol{\Theta}}^{(k)} = \begin{pmatrix}
\widetilde{\boldsymbol{Y}}_1^{(k)} & \widetilde{\boldsymbol{Y}}_1^{(k)} & \mathbf{0} & \cdots & & \\
\widetilde{\boldsymbol{Y}}_2^{(k)} & \widetilde{\boldsymbol{Y}}_2^{(k)} & \widetilde{\boldsymbol{Y}}_2^{(k)} & \mathbf{0} & \cdots & \\
\mathbf{0} & \widetilde{\boldsymbol{Y}}_3^{(k)} & \widetilde{\boldsymbol{Y}}_3^{(k)} & \widetilde{\boldsymbol{Y}}_3^{(k)} & \cdots & \\
\vdots & \vdots & \vdots & & & \\
\mathbf{0} & \mathbf{0} & \cdots & & \widetilde{\boldsymbol{Y}}_\Upsilon^{(k)} & \widetilde{\boldsymbol{Y}}_\Upsilon^{(k)}
\end{pmatrix} \tag{5.16}
$$

We next consider the block matrix $\boldsymbol{Z}^{(k)}$ constructed from $\widehat{\boldsymbol{R}}$ and $\widehat{\boldsymbol{\Theta}}^{(k)}$, such that $\boldsymbol{Z}^{(k)} = \widehat{\boldsymbol{R}} \cdot \widehat{\boldsymbol{\Theta}}^{(k)}$. Now, $\widetilde{\boldsymbol{G}}_{k+m}^{(k)} = \boldsymbol{Z}_{m+1,m+1}^{(k)}$, which is the $(m+1)^{\text{th}}$ diagonal element of $\boldsymbol{Z}^{(k)}$. A change of variable, $k \to (k+1)$, in Eq. (5.11) permits us to write

$$
C_{k+1} L_k \left(\frac{Q_{k+1}}{Q_k} \right) = \left(\frac{K}{\zeta + 2K} \right) \left(\frac{1}{1 - P_{k+1}} \right) C_k L_k^2 + \left(\frac{\zeta}{\zeta + 2K} \right) \left(\frac{1}{Q_k} \right) \sum_{l=k+1}^{N} \widetilde{\boldsymbol{\rho}}_l^{(k+1)} \cdot (\boldsymbol{\kappa} \cdot \boldsymbol{Q}_l)
$$

$$
+ (1 - \delta_{kN}) \left(\frac{1}{1 - P_{k+1}} \right) L_k \left(\frac{1}{Q_k} \right) \left[\left(\frac{k_B T}{\zeta + 2K} \right) \left(\frac{\boldsymbol{Q}_{k+1}}{Q_{k+1}} \right) \cdot \left(\frac{\partial \ln \Psi}{\partial \boldsymbol{Q}_k} \right) + \left(\frac{1}{\zeta + 2K} \right) \left(\frac{\boldsymbol{Q}_{k+1}}{Q_{k+1}} \right) \cdot \left(\frac{\partial \phi}{\partial \boldsymbol{Q}_k} \right) \right]
$$

$$
- \left(\frac{k_B T}{\zeta + 2K} \right) \left(\frac{1}{Q_k} \right) \sum_{l=k+1}^{N} \widetilde{\boldsymbol{G}}_l^{(k+1)} \cdot \left(\frac{\partial \ln \Psi}{\partial \boldsymbol{Q}_k} \right) - \left(\frac{1}{\zeta + 2K} \right) \left(\frac{1}{Q_k} \right) \sum_{l=k+1}^{N} \widetilde{\boldsymbol{G}}_l^{(k+1)} \cdot \left(\frac{\partial \phi}{\partial \boldsymbol{Q}_k} \right) \tag{5.17}
$$

Lastly, by inserting the backward substitution result, Eq. (5.17), into the equation obtained from forward substitution, Eq. (5.7), the decoupled expression is obtained as

$$
C_k \left(1 - M_k - P_k \right) = \left(\frac{\zeta}{\zeta + 2K} \right) \left(\frac{1}{Q_k} \right) \sum_{l=1}^{N} \widehat{\boldsymbol{\Lambda}}_l^{(k)} \cdot (\boldsymbol{\kappa} \cdot \boldsymbol{Q}_l)
$$

$$
- \left(\frac{1}{Q_k} \right) \left[\left(\frac{k_B T}{\zeta + 2K} \right) \sum_{l=1}^{N} \widehat{\boldsymbol{J}}_l^{(k)} \cdot \left(\frac{\partial \ln \Psi}{\partial \boldsymbol{Q}_l} \right) + \left(\frac{1}{\zeta + 2K} \right) \sum_{l=1}^{N} \widehat{\boldsymbol{J}}_l^{(k)} \cdot \left(\frac{\partial \phi}{\partial \boldsymbol{Q}_l} \right) \right] \tag{5.18}
$$

with

$$
\widehat{\boldsymbol{\Lambda}}_l^{(k)} = \begin{cases}
\boldsymbol{\Gamma}_l^{(k)}; & l < k \\[2ex]
\left(\dfrac{\boldsymbol{Q}_k}{Q_k} \right); & l = k \\[2ex]
\left(\dfrac{K}{\zeta + 2K} \right) \widetilde{\boldsymbol{\rho}}_l^{(k+1)}; & l > k
\end{cases} \tag{5.19}
$$

and

$$
\widehat{\boldsymbol{J}}_l^{(k)} =
\begin{cases}
\boldsymbol{E}_l^{(k)}; & l < k \\[2ex]
\boldsymbol{E}_l^{(k)} - (1 - \delta_{kN})\left(\dfrac{1}{1 - P_{k+1}}\right)\left(\dfrac{K}{\zeta + 2K}\right) L_k\left(\dfrac{\boldsymbol{Q}_{k+1}}{Q_{k+1}}\right); & l = k \\[2ex]
(1 - \delta_{kN})\left[\left(\dfrac{K}{\zeta + 2K}\right)\widetilde{\boldsymbol{G}}_l^{(k+1)} - \left(\dfrac{\boldsymbol{Q}_k}{Q_k}\right)\right]; & l = k + 1 \\[2ex]
\left(\dfrac{K}{\zeta + 2K}\right)\widetilde{\boldsymbol{G}}_l^{(k+1)}; & l > (k+1)
\end{cases}
\tag{5.20}
$$

The procedure for the construction of $\widetilde{\boldsymbol{G}}_l^{(k+1)}$ which appears in Eq. (5.20) is fairly similar to that described in Eqs. (5.14)–(5.16) for the construction of $\widetilde{\boldsymbol{G}}_l^{(k)}$, with the only caveat that the size of the block matrices, $\widehat{\boldsymbol{R}}$ and the $\widehat{\boldsymbol{\Theta}}^{(k+1)}$, remain $\Upsilon \times \Upsilon$, where $\Upsilon = (N - k) + 1$. This procedure for the construction of $\widetilde{\boldsymbol{G}}_l^{(k+1)}$ allows for an easier mathematical description. The implementation of this calculation in the computer code, however, follows the formula:

$$
\widetilde{\boldsymbol{G}}_{k+1+m}^{(k+1)} = 2\widetilde{\boldsymbol{Y}}_{m+1}^{(k+1)} - \widetilde{\boldsymbol{Y}}_m^{(k+1)} - \widetilde{\boldsymbol{Y}}_{m+2}^{(k+1)}; \quad 1 \le k \le N
\tag{5.21}
$$

While Eq. (5.21) appears to be relatively simple in comparison to the detailed procedure described above, its implementation requires a cascade of "if-else" statements to ensure a valid value for each term on its RHS. For example, we see from Eq. (5.15) that $\widetilde{\boldsymbol{Y}}_m^{(k+1)}$ has a non-zero value only if: (a) $m \ge 1$, and (b) $1 \le (m + k) \le N$, and is set to zero otherwise. Defining

$$
\begin{aligned}
\boldsymbol{\Lambda}_l^{(k)} &= \left(\frac{1}{1 - M_k - P_k}\right)\widehat{\boldsymbol{\Lambda}}_l^{(k)} \\[2ex]
\boldsymbol{J}_l^{(k)} &= \left(\frac{1}{1 - M_k - P_k}\right)\widehat{\boldsymbol{J}}_l^{(k)}
\end{aligned}
\tag{5.22}
$$

Eq. (6.41) may be rewritten as

$$
\begin{aligned}
C_k &= \left(\frac{1}{1 + 2\varphi}\right)\left(\frac{1}{Q_k}\right)\sum_{l=1}^{N}\boldsymbol{\Lambda}_l^{(k)} \cdot (\boldsymbol{\kappa} \cdot \boldsymbol{Q}_l) - \left(\frac{1}{1 + 2\varphi}\right)\left(\frac{1}{Q_k}\right)\left[\left(\frac{k_B T}{\zeta}\right)\sum_{l=1}^{N}\boldsymbol{J}_l^{(k)} \cdot \left(\frac{\partial \ln \Psi}{\partial \boldsymbol{Q}_l}\right)\right. \\[2ex]
&\quad + \left.\left(\frac{1}{\zeta}\right)\sum_{l=1}^{N}\boldsymbol{J}_l^{(k)} \cdot \left(\frac{\partial \phi}{\partial \boldsymbol{Q}_l}\right)\right]
\end{aligned}
\tag{5.23}
$$

to give the decoupled expression for C_k. Noting that the equation for the momentum-averaged velocity of the jth connector vector in a freely-draining chain is given by

$$
[\![\dot{\boldsymbol{Q}}_j]\!] = \boldsymbol{\kappa} \cdot \boldsymbol{Q}_j - \sum_{k=1}^{N}\boldsymbol{A}_{jk} \cdot \left(\frac{k_B T}{\zeta}\frac{\partial \ln \Psi}{\partial \boldsymbol{Q}_k} + \frac{1}{\zeta}\frac{\partial \phi}{\partial \boldsymbol{Q}_k}\right) - \varphi \sum_{k=1}^{N}\boldsymbol{A}_{jk} \cdot \boldsymbol{Q}_k C_k
\tag{5.24}
$$

and substituting the expression for C_k from Eq. (5.23) into Eq. (5.24),

$$
[\![\dot{\boldsymbol{Q}}_j]\!] = \boldsymbol{\kappa} \cdot \boldsymbol{Q}_j - \sum_{k=1}^{N} \boldsymbol{A}_{jk} \cdot \left(\frac{k_B T}{\zeta} \frac{\partial \ln \Psi}{\partial \boldsymbol{Q}_k} + \frac{1}{\zeta} \frac{\partial \phi}{\partial \boldsymbol{Q}_k} \right) - \left(\frac{\varphi}{1 + 2\varphi} \right) \sum_{k,l=1}^{N} \boldsymbol{A}_{jk} \cdot \left(\frac{\boldsymbol{Q}_k}{Q_k} \right) \boldsymbol{\Lambda}_l^{(k)} \cdot (\boldsymbol{\kappa} \cdot \boldsymbol{Q}_l)
$$

$$
+ \left(\frac{k_B T}{\zeta} \right) \left(\frac{\varphi}{1 + 2\varphi} \right) \sum_{k,l=1}^{N} \boldsymbol{A}_{jk} \cdot \left(\frac{\boldsymbol{Q}_k}{Q_k} \right) \boldsymbol{J}_l^{(k)} \cdot \left(\frac{\partial \ln \Psi}{\partial \boldsymbol{Q}_l} \right)
$$

$$
+ \left(\frac{1}{\zeta} \right) \left(\frac{\varphi}{1 + 2\varphi} \right) \sum_{k,l=1}^{N} \boldsymbol{A}_{jk} \cdot \left(\frac{\boldsymbol{Q}_k}{Q_k} \right) \boldsymbol{J}_l^{(k)} \cdot \left(\frac{\partial \phi}{\partial \boldsymbol{Q}_l} \right)
$$

$$(5.25)$$

The dashed and dotted underlined terms in Eq. (5.25) are denoted by the tensors $\boldsymbol{\alpha}_{kl}$ and $\boldsymbol{\mu}_{kl}$, respectively. The following simplifications in notation are introduced before proceeding to the next step:

$$
\boldsymbol{\alpha}_{kl} = \left(\frac{\boldsymbol{Q}_k}{Q_k} \right) \boldsymbol{\Lambda}_l^{(k)}; \quad \boldsymbol{\mu}_{kl} = \left(\frac{\boldsymbol{Q}_k}{Q_k} \right) \boldsymbol{J}_l^{(k)}
$$

$$
\boldsymbol{U}_{jl} = \sum_{k=1}^{N} \boldsymbol{A}_{jk} \cdot \boldsymbol{\alpha}_{kl}; \quad \boldsymbol{V}_{jl} = \sum_{k=1}^{N} \boldsymbol{A}_{jk} \cdot \boldsymbol{\mu}_{kl}
$$

$$(5.26)$$

Using Eqs. (5.19) and (5.22), an alternate definition for $\boldsymbol{\alpha}_{kl}$ that is more convenient for the construction of the stress tensor expression, may be constructed as,

$$
\boldsymbol{\alpha}_{kl} = \chi_l^{(k)} \left(\frac{\boldsymbol{Q}_k \boldsymbol{Q}_l}{Q_k Q_l} \right)
$$

$$(5.27)$$

where

$$
\chi_l^{(k)} = \begin{cases}
\left(\dfrac{1}{1 - M_k - P_k} \right) \left(\dfrac{K}{\zeta + 2K} \right)^{k-l} \left[\Pi_{i=l}^{k-1} \left(\dfrac{1}{1 - M_i} \right) L_i \right]; & l < k \\[3ex]
\left(\dfrac{1}{1 - M_k - P_k} \right); & l = k \\[3ex]
\left(\dfrac{1}{1 - M_k - P_k} \right) \left(\dfrac{K}{\zeta + 2K} \right)^{l-k} \left[\Pi_{i=k+1}^{l} \left(\dfrac{1}{1 - P_i} \right) L_{i-1} \right]; & l > k
\end{cases}
$$

$$(5.28)$$

The equation for $[\![\dot{\boldsymbol{Q}}_j]\!]$ then becomes

$$
[\![\dot{\boldsymbol{Q}}_j]\!] = \boldsymbol{\kappa} \cdot \boldsymbol{Q}_j - \sum_{k=1}^{N} \boldsymbol{A}_{jk} \cdot \left(\frac{k_B T}{\zeta} \frac{\partial \ln \Psi}{\partial \boldsymbol{Q}_k} + \frac{1}{\zeta} \frac{\partial \phi}{\partial \boldsymbol{Q}_k} \right) - \left(\frac{\varphi}{1 + 2\varphi} \right) \left[\sum_{l=1}^{N} \boldsymbol{U}_{jl} \cdot (\boldsymbol{\kappa} \cdot \boldsymbol{Q}_l) \right.
$$

$$
\left. - \left(\frac{k_B T}{\zeta} \right) \sum_{l=1}^{N} \boldsymbol{V}_{jl} \cdot \left(\frac{\partial \ln \Psi}{\partial \boldsymbol{Q}_l} \right) + \left(\frac{1}{\zeta} \right) \sum_{l=1}^{N} \boldsymbol{V}_{jl} \cdot \left(\frac{\partial \phi}{\partial \boldsymbol{Q}_l} \right) \right]
$$

$$(5.29)$$

which is simplified to

$$\llbracket \dot{\boldsymbol{Q}}_j \rrbracket = \left[\boldsymbol{\kappa} \cdot \boldsymbol{Q}_j - \left(\frac{\varphi}{1+2\varphi} \right) \sum_{k=1}^{N} \boldsymbol{U}_{jk} \cdot (\boldsymbol{\kappa} \cdot \boldsymbol{Q}_k) \right] - \frac{1}{\zeta} \sum_{k=1}^{N} \left(\boldsymbol{A}_{jk} - \frac{\varphi}{1+2\varphi} \boldsymbol{V}_{jk} \right) \cdot \left(\frac{\partial \phi}{\partial \boldsymbol{Q}_k} \right)$$
$$- \frac{k_B T}{\zeta} \sum_{k=1}^{N} \left(\boldsymbol{A}_{jk} - \frac{\varphi}{1+2\varphi} \boldsymbol{V}_{jk} \right) \cdot \left(\frac{\partial \ln \Psi}{\partial \boldsymbol{Q}_k} \right) \tag{5.30}$$

As the next step, the expression for $\llbracket \dot{\boldsymbol{Q}}_j \rrbracket$ will be substituted into the equation of continuity, recognizing that the homogeneous flow profile allows one to write the continuity equation solely in terms of the relative coordinates, $\boldsymbol{Q}_j$. This means that the distribution function $\Psi(\boldsymbol{r}_c, \boldsymbol{Q}_1, \boldsymbol{Q}_2, ... \boldsymbol{Q}_N)$ can be replaced by $\psi(\boldsymbol{Q}_1, \boldsymbol{Q}_2, ... \boldsymbol{Q}_N)$, and we have

$$\frac{\partial \psi}{\partial t} = - \sum_{j=1}^{N} \frac{\partial}{\partial \boldsymbol{Q}_j} \cdot \left\{ \llbracket \dot{\boldsymbol{Q}}_j \rrbracket \psi \right\} = - \sum_{j=1}^{N} \frac{\partial}{\partial \boldsymbol{Q}_j} \cdot \left\{ \left[\boldsymbol{\kappa} \cdot \boldsymbol{Q}_j - \left(\frac{\varphi}{1+2\varphi} \right) \sum_{k=1}^{N} \boldsymbol{U}_{jk} \cdot (\boldsymbol{\kappa} \cdot \boldsymbol{Q}_k) \right. \right. \tag{5.31}$$
$$\left. \left. - \frac{1}{\zeta} \sum_{k=1}^{N} \left(\boldsymbol{A}_{jk} - \frac{\varphi}{1+2\varphi} \boldsymbol{V}_{jk} \right) \cdot \left(\frac{\partial \phi}{\partial \boldsymbol{Q}_k} \right) \right] \psi \right\} + \frac{k_B T}{\zeta} \sum_{j,k=1}^{N} \frac{\partial}{\partial \boldsymbol{Q}_j} \cdot \left(\boldsymbol{A}_{jk} - \frac{\varphi}{1+2\varphi} \boldsymbol{V}_{jk} \right) \cdot \frac{\partial \psi}{\partial \boldsymbol{Q}_k}$$

The last term on the RHS of Eq. (5.31) must be processed further, in order to render the Fokker-Planck equation amenable to the Itô interpretation (Öttinger, 1996). Invoking the identity given in Equation D.38 of Appendix D, we may write

$$\frac{\partial}{\partial \boldsymbol{Q}_j} \cdot \left(\boldsymbol{A}_{jk} - \frac{\varphi}{1+2\varphi} \boldsymbol{V}_{jk} \right) \cdot \frac{\partial \psi}{\partial \boldsymbol{Q}_k} = \frac{\partial}{\partial \boldsymbol{Q}_j} \frac{\partial}{\partial \boldsymbol{Q}_k} : \left[\left(\boldsymbol{A}_{jk} - \frac{\varphi}{1+2\varphi} \boldsymbol{V}_{jk} \right)^T \psi \right]$$
$$- \frac{\partial}{\partial \boldsymbol{Q}_j} \cdot \left\{ \psi \frac{\partial}{\partial \boldsymbol{Q}_k} \cdot \left(\boldsymbol{A}_{jk} - \frac{\varphi}{1+2\varphi} \boldsymbol{V}_{jk} \right)^T \right\} \tag{5.32}$$

Recognizing that the Rouse matrix, $\boldsymbol{A}_{jk}$, is composed only of constant values independent of the chain connector vectors, we have $(\partial/\partial \boldsymbol{Q}_k) \cdot \boldsymbol{A}_{jk}^T = 0$, and can simplify Eq. (5.32) to the form

$$\frac{\partial}{\partial \boldsymbol{Q}_j} \cdot \left(\boldsymbol{A}_{jk} - \frac{\varphi}{1+2\varphi} \boldsymbol{V}_{jk} \right) \cdot \frac{\partial \psi}{\partial \boldsymbol{Q}_k} = \frac{\partial}{\partial \boldsymbol{Q}_j} \frac{\partial}{\partial \boldsymbol{Q}_k} : \left[\left(\boldsymbol{A}_{jk} - \frac{\varphi}{1+2\varphi} \boldsymbol{V}_{jk} \right)^T \psi \right]$$
$$+ \left(\frac{\varphi}{1+2\varphi} \right) \frac{\partial}{\partial \boldsymbol{Q}_j} \cdot \left\{ \psi \frac{\partial}{\partial \boldsymbol{Q}_k} \cdot \boldsymbol{V}_{jk}^T \right\},$$

which, upon substitution into Eq. (5.31), results in

$$\frac{\partial \psi}{\partial t} = - \sum_{j=1}^{N} \frac{\partial}{\partial \boldsymbol{Q}_j} \cdot \left\{ \left[\boldsymbol{\kappa} \cdot \boldsymbol{Q}_j - \left(\frac{\varphi}{1+2\varphi} \right) \sum_{k=1}^{N} \boldsymbol{U}_{jk} \cdot (\boldsymbol{\kappa} \cdot \boldsymbol{Q}_k) - \frac{1}{\zeta} \sum_{k=1}^{N} \left(\boldsymbol{A}_{jk} - \frac{\varphi}{1+2\varphi} \boldsymbol{V}_{jk} \right) \cdot \left(\frac{\partial \phi}{\partial \boldsymbol{Q}_k} \right) \right. \right. \tag{5.33}$$
$$\left. \left. - \left(\frac{k_B T}{\zeta} \right) \left(\frac{\varphi}{1+2\varphi} \right) \sum_{k=1}^{N} \frac{\partial}{\partial \boldsymbol{Q}_k} \cdot \boldsymbol{V}_{jk}^T \right] \psi \right\} + \frac{k_B T}{\zeta} \sum_{j,k=1}^{N} \frac{\partial}{\partial \boldsymbol{Q}_j} \frac{\partial}{\partial \boldsymbol{Q}_k} : \left[\left(\boldsymbol{A}_{jk} - \frac{\varphi}{1+2\varphi} \boldsymbol{V}_{jk} \right)^T \psi \right]$$

Defining

$$\widehat{A}_{jk} = A_{jk} - \frac{\varphi}{1 + 2\varphi} V_{jk}; \quad j, k = 1, 2, \cdots, N$$

$$\widehat{\boldsymbol{v}}_j = \sum_{k=1}^{N} \frac{\partial}{\partial \boldsymbol{Q}_k} \cdot V_{jk}^T; \quad j = 1, 2, \cdots, N \tag{5.34}$$

$$\boldsymbol{F}_k^{\mathrm{s}} = \frac{\partial \phi}{\partial \boldsymbol{Q}_k}; \quad k = 1, 2, \cdots, N$$

the Fokker-Planck equation is rewritten as

$$\frac{\partial \psi}{\partial t} = -\sum_{j=1}^{N} \frac{\partial}{\partial \boldsymbol{Q}_j} \cdot \left\{ \left[\boldsymbol{\kappa} \cdot \boldsymbol{Q}_j - \left(\frac{\varphi}{1 + 2\varphi} \right) \sum_{k=1}^{N} U_{jk} \cdot (\boldsymbol{\kappa} \cdot \boldsymbol{Q}_k) - \frac{1}{\zeta} \sum_{k=1}^{N} \widehat{A}_{jk} \cdot \boldsymbol{F}_k^{\mathrm{s}} \right. \right. \tag{5.35}$$

$$\left. \left. - \left(\frac{k_B T}{\zeta} \right) \left(\frac{\varphi}{1 + 2\varphi} \right) \widehat{\boldsymbol{v}}_j \right] \psi \right\} + \frac{k_B T}{\zeta} \sum_{j,k=1}^{N} \frac{\partial}{\partial \boldsymbol{Q}_j} \frac{\partial}{\partial \boldsymbol{Q}_k} : \left[\widehat{A}_{jk}^T \psi \right]$$

and its dimensionless equivalent is given by

$$\frac{\partial \psi^*}{\partial t^*} = -\sum_{j=1}^{N} \frac{\partial}{\partial \boldsymbol{Q}_j^*} \cdot \left\{ \left[\boldsymbol{\kappa}^* \cdot \boldsymbol{Q}_j^* - \left(\frac{\varphi}{1 + 2\varphi} \right) \sum_{k=1}^{N} U_{jk} \cdot (\boldsymbol{\kappa}^* \cdot \boldsymbol{Q}_k^*) - \frac{1}{4} \sum_{k=1}^{N} \widehat{A}_{jk} \cdot \boldsymbol{F}_k^{*\,\mathrm{s}} \right. \right. \tag{5.36}$$

$$\left. \left. - \frac{1}{4} \left(\frac{\varphi}{1 + 2\varphi} \right) \sum_{k=1}^{N} \frac{\partial}{\partial \boldsymbol{Q}_k^*} \cdot V_{jk}^T \right] \psi^* \right\} + \frac{1}{4} \sum_{j,k=1}^{N} \frac{\partial}{\partial \boldsymbol{Q}_j^*} \frac{\partial}{\partial \boldsymbol{Q}_k^*} : \left[\widehat{A}_{jk}^T \psi^* \right]$$

In the absence of internal friction, both U_{jk}, and V_{jk} reduce to $\mathbf{0}$, and $\widehat{A}_{jk}$ becomes A_{jk}. In order to simplify the notation, it is convenient to rewrite the Fokker-Planck equation in terms of collective coordinates. We define

$$\widetilde{\boldsymbol{Q}}^* \equiv [\boldsymbol{Q}_1^*, \boldsymbol{Q}_2^*, ..., \boldsymbol{Q}_N^*] \equiv \left[Q_1^{*1}, Q_1^{*2}, Q_1^{*3}, Q_2^{*1}, Q_2^{*2}, ..., Q_N^{*3} \right]$$

and write $\widetilde{Q}^*{}_i = Q_k^{*\beta}$, where $k = 1, 2, ..., N$ and $\beta = 1, 2, 3$ (represent Cartesian components in the x, y, z directions, respectively), with i related to k and β as $i = 3(k-1) + \beta$. Similarly, $\widetilde{\boldsymbol{F}}^{*\,\mathrm{s}} \equiv [\boldsymbol{F}_1^{*\,\mathrm{s}}, \boldsymbol{F}_2^{*\,\mathrm{s}}, ..., \boldsymbol{F}_N^{*\,\mathrm{s}}]$, and $\widetilde{\boldsymbol{v}}^* \equiv \left[\widehat{\boldsymbol{v}^*}_1, \widehat{\boldsymbol{v}^*}_2 ..., \widehat{\boldsymbol{v}^*}_N \right]$. The diffusion matrix $\mathcal{D}$ of size $N \times N$ is defined, whose elements are the tensors $\widehat{A}_{jk}$. The block matrix $\mathcal{K}^*$ is defined such that its diagonal elements are given by the 3×3 matrix $\boldsymbol{\kappa}^*$, and its off-diagonal blocks are $\mathbf{0}$. Lastly, the block matrix $\mathcal{U}$ consists of the tensors U_{jk}. In terms of these collective variables, the stochastic differential equation equivalent to Eq. (5.36), using Itô's interpretation (Öttinger, 1996), is given by

$$d\widetilde{\boldsymbol{Q}}^* = \left[\mathcal{K}^* \cdot \widetilde{\boldsymbol{Q}}^* - \left(\frac{\varphi}{1 + 2\varphi} \right) \mathcal{U} \cdot \left(\mathcal{K}^* \cdot \widetilde{\boldsymbol{Q}}^* \right) - \frac{1}{4} \mathcal{D} \cdot \widetilde{\boldsymbol{F}}^{*\,\mathrm{s}} - \frac{1}{4} \left(\frac{\varphi}{1 + 2\varphi} \right) \widetilde{\boldsymbol{v}}^* \right] dt^* + \frac{1}{\sqrt{2}} \mathcal{B} \cdot d\widetilde{\boldsymbol{W}}^* \tag{5.37}$$

where $\widetilde{\boldsymbol{W}}^*$ is a $3N-$dimensional Wiener process, and $\boldsymbol{\mathcal{B}} \cdot \boldsymbol{\mathcal{B}}^T = \boldsymbol{\mathcal{D}}$. The symmetricity and positive-definiteness of the diffusion matrix is established empirically in Section D.2 of Appendix D. The square-root of the diffusion matrix is found using Cholesky decomposition (Press *et al.*, 2007). Equation (5.37) is solved numerically using a simple explicit Euler method, as follows

$$\widetilde{\boldsymbol{Q}}^*(t_{n+1}) = \widetilde{\boldsymbol{Q}}^*_n + \left[\boldsymbol{\mathcal{K}}^*(t_n) \cdot \widetilde{\boldsymbol{Q}}^*(t_n) - \left(\frac{\varphi}{1+2\varphi} \right) \boldsymbol{\mathcal{U}}(t_n) \cdot \left(\boldsymbol{\mathcal{K}}^*(t_n) \cdot \widetilde{\boldsymbol{Q}}^*(t_n) \right) - \frac{1}{4} \boldsymbol{\mathcal{D}}^*(t_n) \cdot \widetilde{\boldsymbol{F}}^{*\,\text{s}}(t_n) \right.$$
$$\left. - \left(\frac{1}{4} \right) \left(\frac{\varphi}{1+2\varphi} \right) \widetilde{\boldsymbol{v}}^*(t_n) \right] \Delta t_n + \frac{1}{\sqrt{2}} \Delta \widetilde{\boldsymbol{S}}^*_n \qquad (5.38)$$

where $\Delta \widetilde{\boldsymbol{S}}^*_n = \boldsymbol{\mathcal{B}} \cdot \Delta \widetilde{\boldsymbol{W}}^*_n$.

In Fig. 5.2, the scaling of the execution time as a function of the chain length is presented for a code written using the simple explicit Euler method for solving the SDE. The time taken for simulation of simple Rouse chains scales with an exponent of 1.7 with respect to the chain length, whereas chains with internal friction scale with an exponent of 2.7. Moreover, running simulations on chains with internal friction after dropping the noise term from the governing equation does not seem to significantly affect the execution time, indicating that the calculation of the square root of the diffusion tensor, using Cholesky decomposition, represents only a minor portion of the total workload. Furthermore, the execution time and scaling for chains with internal friction is practically unaffected by the value of the internal friction parameter.

The code is written in a way that the simulation of chains without internal friction involves neither the construction of the $\boldsymbol{\mathcal{U}}$ and $\boldsymbol{\mathcal{D}}$ matrices, nor the evaluation of the divergence terms or the square-root of the diffusion tensor. In fact, the Rouse case is simulated exactly as given in Eq. (4.4) of Öttinger (1996), which is a significant simplification over the case with internal friction turned on.

In absolute numbers, the execution time for one trajectory of a ten-bead Rouse chain is 0.07 seconds, whereas that for a ten-bead Rouse chain with internal friction ($\varphi = 1.0$) is 49.6 seconds, representing an increase that is nearly three-orders in magnitude.

In order to relate the time-evolution of the connector vectors to macroscopically observable rheological properties, it is necessary to specify an appropriate stress tensor expression for the model discussed above. The formal, thermodynamically consistent stress tensor expression for free-draining models with internal friction may be obtained
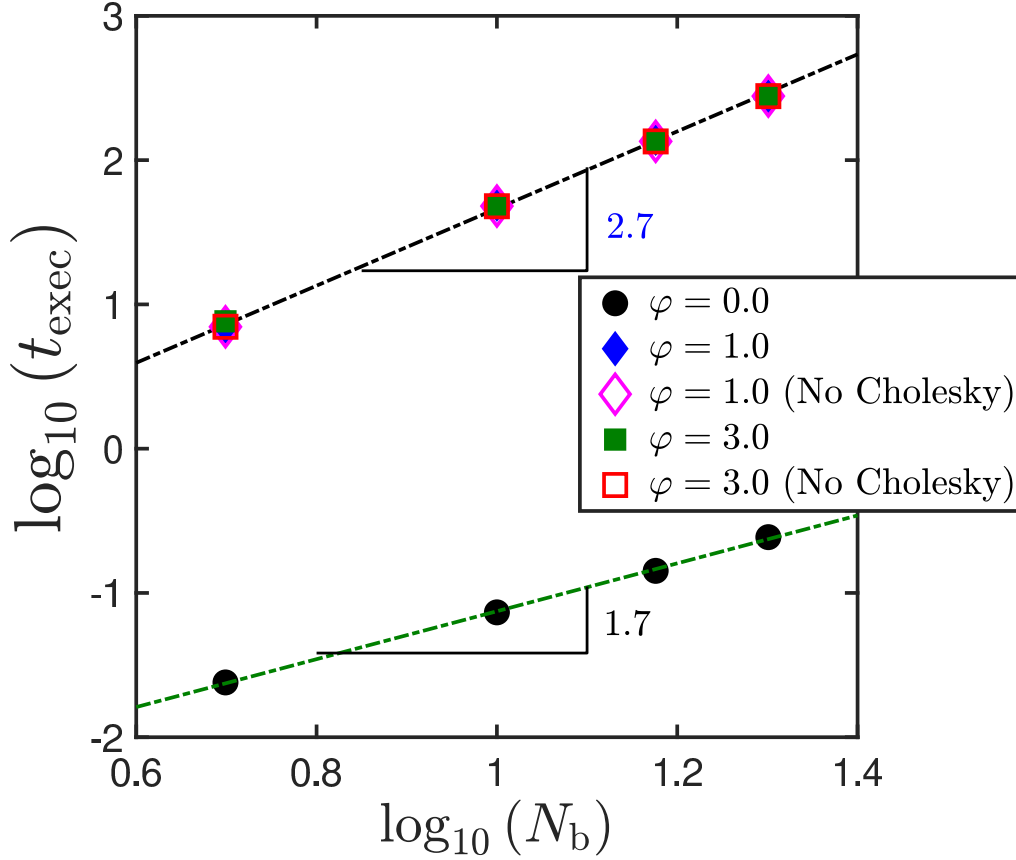
Figure 5.2: Scaling of simulation time as a function of number of beads in the chain. Execution time is calculated as an average over one hundred trajectories at each value of N_b. Each trajectory is 100 dimensionless times (λ_H) long. Simulations performed on MonARCH, the HPC hosted at Monash University, with all the runs executed on the same type of processor [16 core Xeon-E5-2667-v3 @ 3.20GHz servers with 100550MB usable memory]. A step size of $\Delta t^* = 10^{-2}$ is used for all the simulation runs in this plot.

using the Giesekus expression (Schieber and Öttinger, 1994), as follows

$$\boldsymbol{\tau}_{\mathrm{p}} = \frac{n_{\mathrm{p}}\zeta}{2} \left\langle \sum_{j=1}^{N} \sum_{k=1}^{N} \mathscr{C}_{jk} \boldsymbol{Q}_j \boldsymbol{Q}_k \right\rangle_{(1)} = \frac{n_{\mathrm{p}}\zeta}{2} \left[\frac{d}{dt} \left\langle \sum_{j,k} \mathscr{C}_{jk} \boldsymbol{Q}_j \boldsymbol{Q}_k \right\rangle - \boldsymbol{\kappa} \cdot \left\langle \sum_{j,k} \mathscr{C}_{jk} \boldsymbol{Q}_j \boldsymbol{Q}_k \right\rangle \right.$$

$$\left. - \left\langle \sum_{j,k} \mathscr{C}_{jk} \boldsymbol{Q}_j \boldsymbol{Q}_k \right\rangle \cdot \boldsymbol{\kappa}^T \right] \tag{5.39}$$

where $\mathscr{C}_{jk}$ is the Kramers matrix (Bird *et al.*, 1987b). Upon simplification, as detailed in Appendix C,

$$\boldsymbol{\tau}_{\mathrm{p}} = n_{\mathrm{p}} k_B T (N_b - 1) \boldsymbol{\delta} - n_{\mathrm{p}} \left\langle \sum_{k=1}^{N_b-1} \boldsymbol{Q}_k \boldsymbol{F}_k^c \right\rangle \tag{5.40}$$

which is formally similar to the Kramers expression (Bird *et al.*, 1987b), except that the force in the connector vector, $\boldsymbol{F}_k^c$, is redefined to include contributions from both the spring

and the dashpot (also noted by Wedgewood (1993); Schieber and Öttinger (1994); Hua *et al.* (1996) for Hookean dumbbells with IV), as follows,

$$\boldsymbol{F}_k^{\mathrm{c}} = \boldsymbol{F}_k^{\mathrm{s}} + KC_k\boldsymbol{Q}_k \tag{5.41}$$

where $C_k = \left(\boldsymbol{Q}_k \cdot [\![\dot{\boldsymbol{Q}}_k]\!]/Q_k^2\right)$. Substituting Eq. (5.41) into Eq. (5.40) and using the closed-form expression for C_k as given by Eq. (5.23), the dimensionless stress tensor expression is obtained as

$$
\begin{aligned}
\frac{\boldsymbol{\tau}_{\mathrm{p}}}{n_{\mathrm{p}}k_B T} &= (N_{\mathrm{b}} - 1)\boldsymbol{\delta} - \left\langle \sum_k \boldsymbol{Q}_k^* \boldsymbol{F}_k^{*\mathrm{s}} \right\rangle - \frac{1}{2}\left(\frac{\epsilon}{1+\epsilon}\right)\left[\left\langle \sum_{k,l} (\boldsymbol{Q}_k^* \boldsymbol{F}_l^{*\mathrm{s}}) \cdot \boldsymbol{\mu}_{kl}^T \right\rangle + \left\langle \sum_k \boldsymbol{\mu}_{kk}^T \right\rangle \right. \\
&\quad + \left. \left\langle \sum_{k,l} \boldsymbol{Q}_k^* \frac{\partial}{\partial \boldsymbol{Q}_l^*} \cdot \boldsymbol{\mu}_{kl}^T \right\rangle \right] - \left(\frac{2\epsilon}{1+\epsilon}\right)\boldsymbol{\kappa}^* : \left\langle \sum_{k,l} \frac{\chi_l^{(k)} \boldsymbol{Q}_l^* \boldsymbol{Q}_l^* \boldsymbol{Q}_k^* \boldsymbol{Q}_k^*}{Q_l^* Q_k^*} \right\rangle
\end{aligned}
\tag{5.42}
$$

where $\epsilon = 2\varphi$, and the definitions of $\boldsymbol{\mu}_{kl}$ and $\chi_l^{(k)}$ are provided in Eqs. (5.26) and (5.28).

Variance reduction (Öttinger, 1996; Wagner and Öttinger, 1997) has been used in the evaluation of steady-shear viscometric functions at low shear rates ($\lambda_H \dot{\gamma} < 1.0$), and for the calculation of oscillatory shear material functions at all frequencies reported in this work. In Fig. 5.3, the effectiveness of variance reduction in oscillatory shear flow has been illustrated by comparison against data obtained from control simulations without variance reduction, for the same ensemble size of 10^4 trajectories and a step-size of $\Delta t^* = 10^{-3}$.

The underlined terms in Eqs. (5.38) and (5.42) may be calculated by two routes: analytically, using recursive functions as explained in Appendix D, or they can be calculated numerically. The connector vectors appearing in Eqs. (5.43)–(5.44) below are in their dimensionless form, with the asterisks omitted for the sake of clarity. The numerical route for the calculation of divergence is described below. Consider the general divergence,

$$\frac{\partial}{\partial \boldsymbol{Q}_k} \cdot \boldsymbol{\mathcal{G}}_{jk} = \sum_{\beta=1}^3 \sum_{\gamma=1}^3 \frac{\partial}{\partial Q_k^\beta}\left(\mathcal{G}_{jk}^{\beta\gamma}\right)\boldsymbol{e}_\gamma \tag{5.43}$$

where β and γ run over the three Cartesian indices, $\boldsymbol{\mathcal{G}}_{jk}$ is a configuration-dependent tensor, and $\boldsymbol{e}_\gamma$ is a unit vector. The computation of the divergence requires the calculation of nine gradient terms, which are evaluated using the central-difference approximation. One such evaluation is shown here as an example:

$$\frac{\partial}{\partial Q_k^1}\left(\mathcal{G}_{jk}^{12}\right) = \frac{1}{2\Delta_1}\left[\mathcal{G}_{jk}^{12}\left(Q_k^1 + \Delta_1, Q_k^2, Q_k^3\right) - \mathcal{G}_{jk}^{12}\left(Q_k^1 - \Delta_1, Q_k^2, Q_k^3\right)\right] \tag{5.44}$$

where Δ_1 is the spatial discretization width along one Cartesian direction, representing the infinitesimal change in Q_k^1. The error in the evaluation of the gradient using this approximation scales as $O\left(\Delta_1^2\right)$. We have validated that the divergences calculated
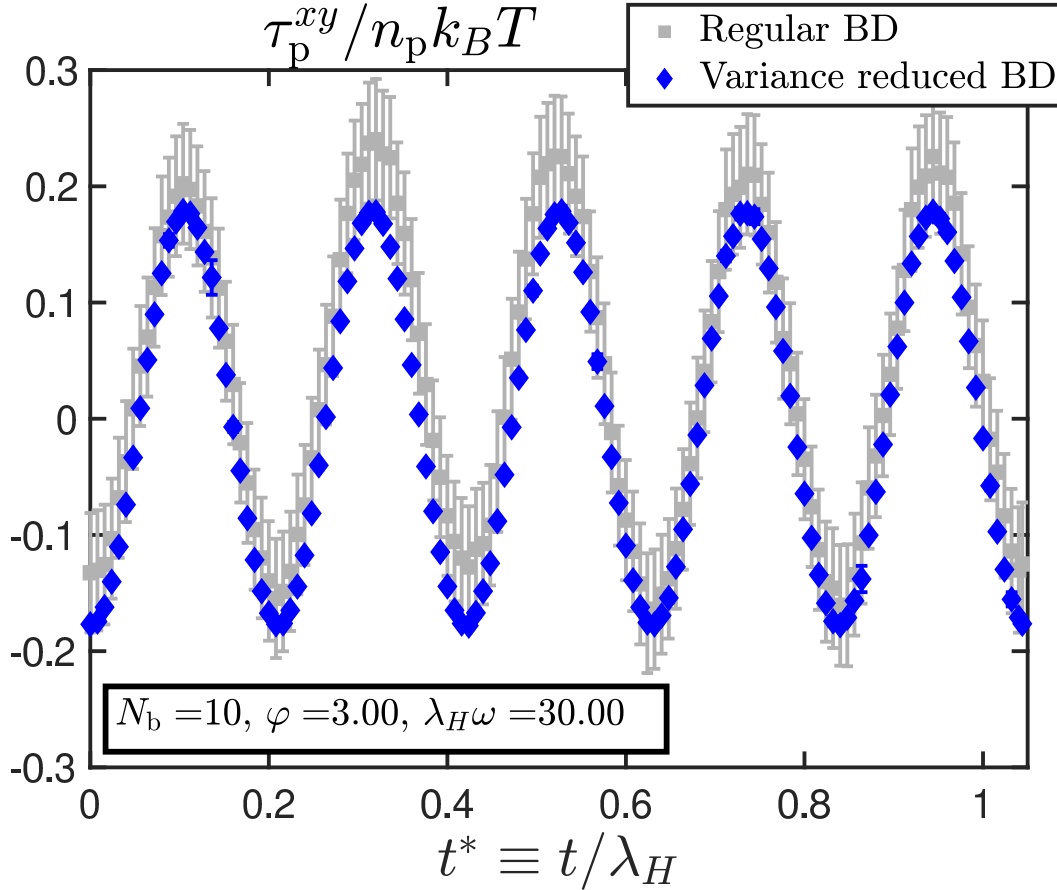
Figure 5.3: Illustration of the efficacy of variance reduction for a ten-bead chain with internal friction in small amplitude oscillatory shear flow.

numerically agrees with that obtained using recursive functions [see Figure D.4 in Appendix D], and have chosen the numerical route in view of its faster execution time that is largely invariant with chain length. In numerical computations, we set $\Delta_1 = \Delta_2 = \Delta_3 = \Delta_d = 10^{-5}$, unless noted otherwise.

5.3   Results

5.3.1   Code Validation

In Fig. 5.4, the methodology for the estimation of the shear stress jump from BD simulations is illustrated for a three-bead chain with an internal friction parameter of unity, subjected to a dimensionless shear rate of $\lambda_H \dot{\gamma} = 50$. The shear viscosity is recorded as a function of time, and a fourth order polynomial is fit through the data points, to obtain its extrapolated value at $t^* = 0$, which represents the stress-jump, as indicated by the triangle.

In Fig. 5.5, the stress-jump calculated for different chain lengths using the procedure described above is plotted as a function of the dimensionless shear rate. It is observed
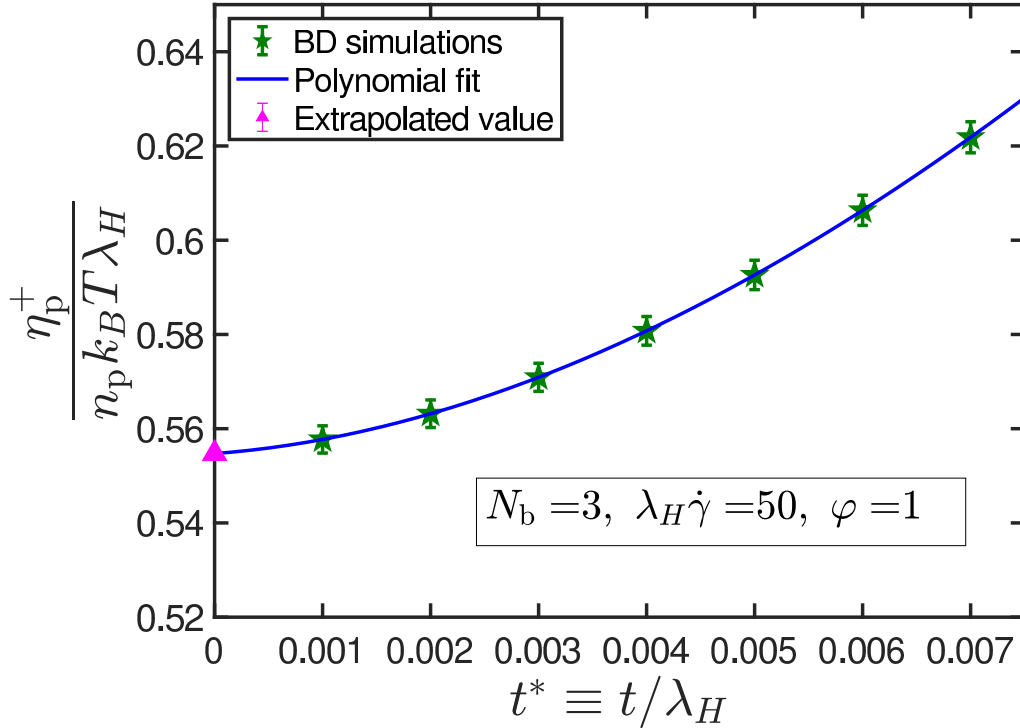
Figure 5.4: Procedure for estimation of stress jump illustrated for a three-bead chain with $\varphi = 1.0$, subjected to steady-shear flow at $\lambda_H \dot{\gamma} = 50$. A fourth order polynomial is fit to the transient shear viscosity data, to obtain the extrapolated value at $t^* = 0.0$.

that the stress jump is independent of the shear rate, in agreement with the theoretically expected trend (Gerhardt and Manke, 1994). The horizontal lines in the figure represent the approximate analytical values for the stress jump evaluated by Manke and Williams (1988), and very good agreement is observed between the values estimated using the two approaches.

In Fig. 5.6 (a), the stress jump evaluated from BD simulations for two different values of the internal friction parameter is plotted as a function of the number of springs in the chain. The semi-analytical approximation of Manke and Williams Manke and Williams (1988) is found to compare favourably against the exact simulation result. Furthermore, it is observed that the stress jump scales linearly with number of springs in the chain, with the slope of the line dependent on the internal friction parameter. It is instructive to first understand the two simplifying assumptions made in Manke and Williams Manke and Williams (1988) before interpreting the data in Fig. 5.6 (b) where the percentage difference between the analytical and simulation results is plotted as a function of chain length at a fixed value of the internal friction parameter. The first assumption is that the configurational distribution function at the inception of flow may be approximated by its equilibrium value, as mentioned in the discussion surrounding Eq. (6.31). Secondly,
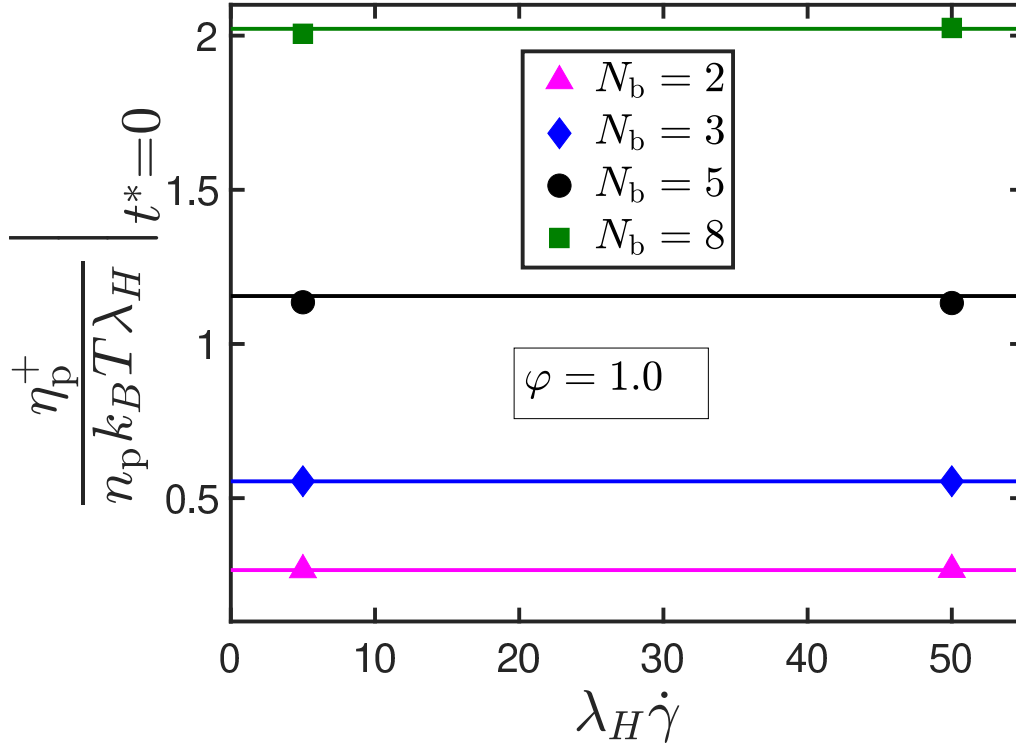
Figure 5.5: Stress jump as a function of dimensionless shear rate for various chain lengths and a fixed internal friction parameter of $\varphi = 1.0$. Lines are approximate solutions by Manke and Williams (1988). Error bars are smaller than symbol size.

it is assumed that the terminal connector vectors and interior connector vectors contribute equally towards the stress jump. This assumption is necessary only for chains with $N > 2$, because there is no distinction between a terminal and interior connector vector for a dumbbell ($N = 1$), and the two connector vectors for the $N = 2$ case are shown by Manke and Williams (1988), using the first assumption, to contribute identically to the total stress jump. It is anticipated that the second assumption would be most severely tested in chains with fewer number of springs, where the terminal springs represent a larger fraction of the overall chain, and becomes progressively better with an increase in the number of springs. The expected trend is clearly borne out by Fig. 5.6 (b), where the deviation between the exact simulation result and the analytical value first increases (beyond $N = 1$) and later decreases with the number of springs in the chain.

5.3.2   Complex viscosity from oscillatory shear flow

In Figures 5.7 and 5.8 , the material functions in oscillatory shear flow are plotted for a fixed value of the internal friction parameter, and varying number of beads in the chain. The exact BD simulation results, indicated by symbols, are compared against the the approximate prediction given by Dasbach *et al.* (1992), shown as solid lines.
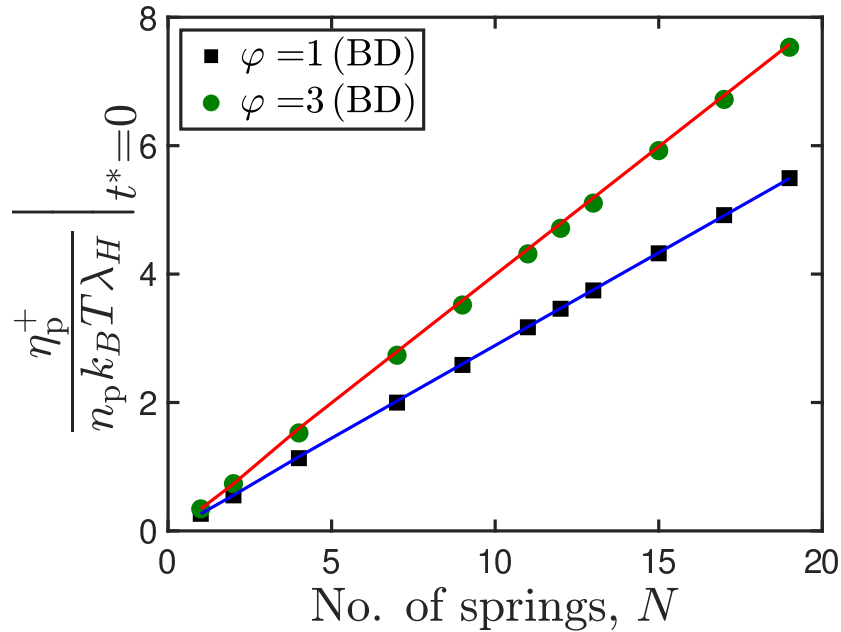
(a)
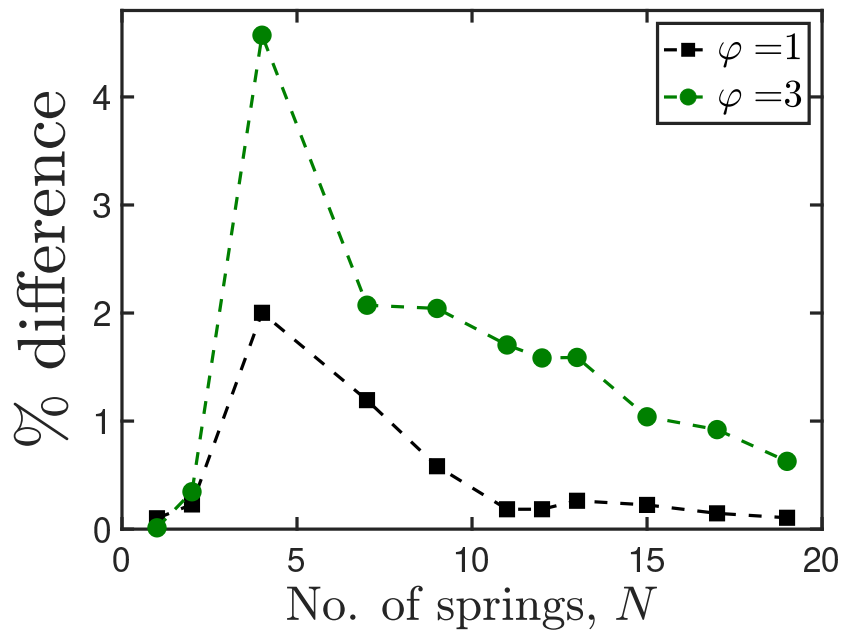
(b)

Figure 5.6: (a) Comparison of stress jump obtained using extrapolation of BD simulation data, and approximate solutions by Manke and Williams (1988) indicated by solid lines. (b) Percentage difference between stress jump obtained using the two approaches, as a function of chain length. Dashed lines are drawn to guide the eye. Error bars are smaller than symbol size.

Schieber Schieber (1993) has obtained predictions for η' and η'' for Hookean dumbbells ($N_b = 2$) with internal viscosity, using a Gaussian approximation (GA), and these predictions have been shown using dash-dotted lines. The high-frequency-limiting value of η' obtained by GA agrees with that derived by Dasbach *et al.* (1992). Furthermore, while the functional form of η'' obtained by GA matches with the expression given by Dasbach *et al.* (1992), they differ in the sense that the GA predicts a φ-dependent rescaling of the frequency which is absent in the latter work.

As seen from Fig. 5.7 (a), the inclusion of internal friction into the Rouse model introduces a qualitative change in the variation of the dynamic viscosity, η', with the appearance of a plateau in the high-frequency regime, in contrast to the Rouse model where $\eta' \rightarrow 0$ in the high-frequency limit. The numerical value of the plateau is equal to the stress jump, as seen from our simulations, which is in agreement with the theoretical prediction of Gerhardt and Manke (1994). Since the stress jump scales linearly with the number of beads in the chain[Fig. 5.6 (a)], and the Rouse viscosity, η^R, scales as N^2 [Eq. (2.17)], the height of the high-frequency plateau decreases with an increase in the number of beads in the chain. The difference in the dynamic viscosity for the three different cases are less perceptible in the low frequency regime, where they are all seen to approach the respective Rouse viscosity. The GA prediction (Schieber, 1993) is seen to perform marginally better than the Dasbach *et al.* (1992) prediction at low frequencies. With the increase in the number of beads, the Dasbach *et al.* (1992) approximation compares satisfactorily against BD simulation results.

In Fig. 5.7 (b), the dynamic viscosity for chains with internal friction is scaled by its corresponding values for a Rouse chain and plotted as a function of scaled frequency. It is seen that the departure from Rouse prediction is pushed to higher values of the scaled frequency with an increase in the number of beads. Furthermore, since models with internal friction predict a saturation of the dynamic viscosity at high frequencies, and since the Rouse model prediction in the high frequency regime decays asymptotically as $\sim \omega^{-2}$ [Eq. 2.19], the scaled dynamic viscosity is expected to vary as $\sim \omega^2$ at high frequencies. This scaling is observed for all three cases examined in Fig. 5.7 (b). The long-chain ($N_b = 100$) result predicted by the Dasbach *et al.* (1992) approximation plotted on the same graph, further enunciates that for a fixed value of φ, the effect of internal friction decays with an increase in chain length.

A similar weakening of internal friction effects has also been predicted by the RIF model (Khatri and McLeish, 2007), where the relaxation time of a mode q is simply the sum of a mode-number-dependent Rouse contribution ($\tau_q^R \equiv \tau^R/q^2$), and an internal friction contribution (τ_{int}) that is independent of mode-number. Here, $\tau^R = \left(N_b^2 \zeta/\pi^2 H\right)$ is

(a)

(b)
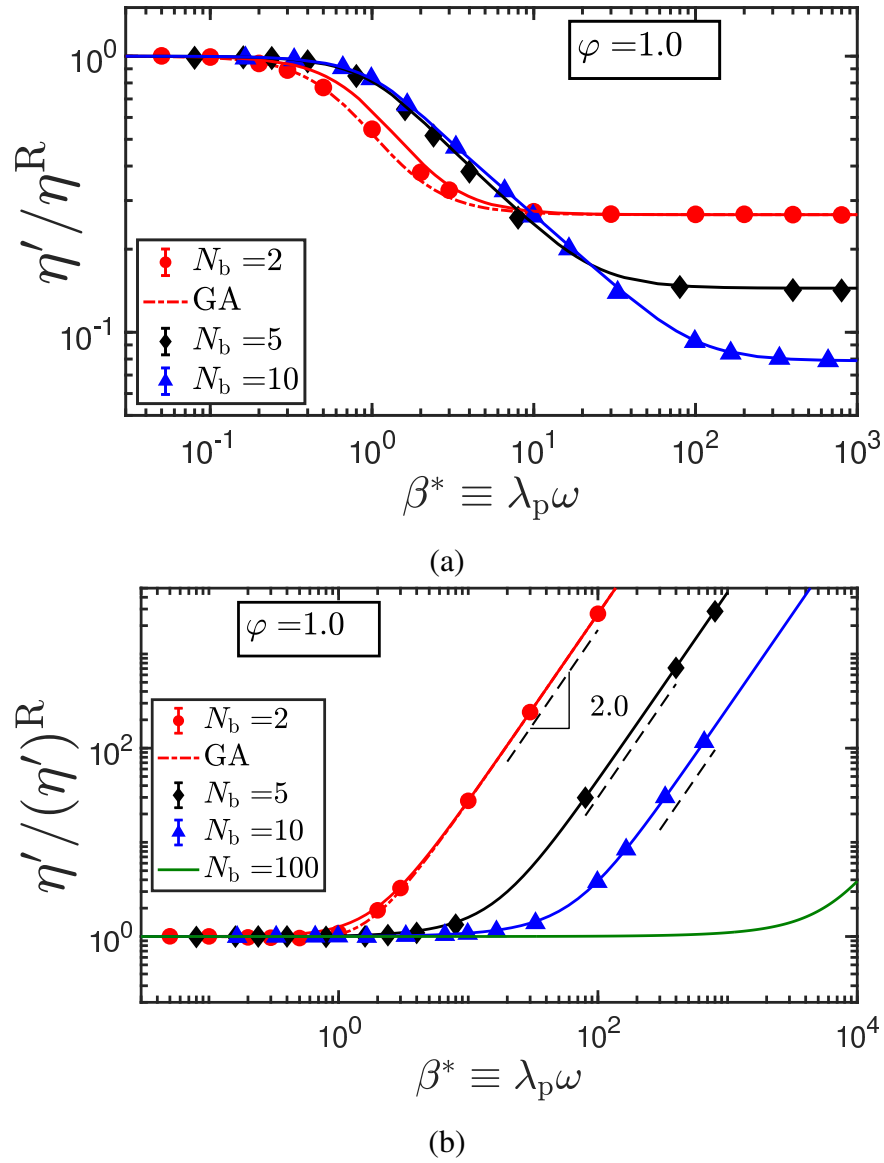
Figure 5.7: Plots of the real (η') component of the complex viscosity, as a function of the scaled frequency, for a fixed value of the internal friction parameter and three different values for the number of beads in the chain, scaled by (a) the Rouse viscosity and (b) the real component of the complex viscosity of a Rouse chain. The solid lines are approximate solutions given in Dasbach *et al.* (1992). The dash-dotted lines represent predictions obtained using the Gaussian approximation (Schieber, 1993). Error bars are smaller than symbol size.
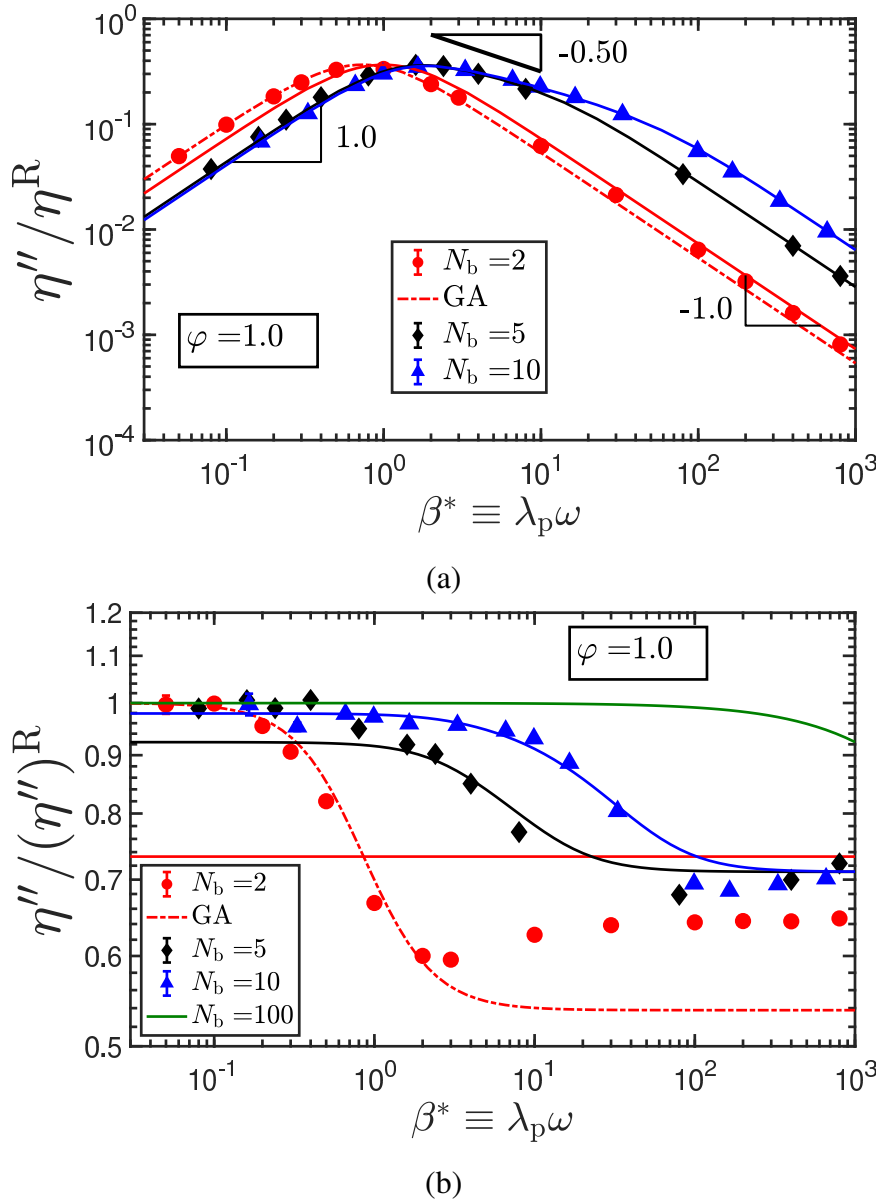
Figure 5.8: Plots of the imaginary component (η'') of the complex viscosity, as a function of the scaled frequency, for a fixed value of the internal friction parameter and three different values for the number of beads in the chain, scaled by (a) the Rouse viscosity and (b) the imaginary component of the complex viscosity of a Rouse chain. The solid lines are approximate solutions given in Dasbach *et al.* (1992). The dash-dotted lines represent predictions obtained using the Gaussian approximation (Schieber, 1993). Error bars are smaller than symbol size.

the Rouse relaxation time, and $\tau_{\text{int}} = K/H$ is a characteristic timescale defined on the basis of the damping coefficient of the dashpot. The relative magnitude of the two timescales is then

$$\frac{\tau_{\text{int}}}{\tau_q^{\text{R}}} = \left(\frac{\pi q}{N_{\text{b}}}\right)^2 \varphi \tag{5.45}$$

Two aspects are clear from the pre-averaged model predictions, for a fixed value of φ: Firstly, for a fixed chain length, the effects of internal friction are most pronounced at the higher mode numbers, i.e., at short time scales, and has the least impact on the global relaxation time, corresponding to the $q = 1$ case. This aspect is qualitatively evident from Fig. 5.7 (b): at low frequencies, where long wavelength motions (low mode numbers) are perturbed, the dynamic viscosity for chains with internal friction is indistinguishable from the Rouse value. At higher frequencies, where short wavelength motions (large mode numbers) are probed, a clear departure from the Rouse value is observed, and one could consider that the deviation occurs at some critical mode number for a given chain length. Secondly, for a given mode number, the effect of internal friction diminishes with an increase in the chain length. This trend is also evident from Fig. 5.7 (b), where it is observed that the onset of deviation from the Rouse prediction is pushed to higher frequencies with an increase in chain length. Hagen and coworkers (Qiu and Hagen, 2004b; Pabit *et al.*, 2004; Hagen, 2010) predict, based on experimental reconfiguration time measurements on proteins, that the effect of internal friction is most easily discernible in short molecules that fold on microsecond-timescales, and could scarcely be detected in longer molecules whose folding times are in the millisecond range.

In Fig. 5.8 (a), the imaginary component of the complex viscosity, η'', is normalized by the Rouse viscosity and plotted as a function of the scaled frequency. The Rouse scaling exponents at the low, intermediate and high frequency regimes are indicated in the figure. It is seen that inclusion of internal friction does not affect the Rouse scaling at low and high frequencies. In the intermediate frequency regime, a power law region appears with an increase in the number of beads, with an exponent not exactly identical to the Rouse value. However, it is anticipated that the Rouse exponent in the intermediate frequency regime would be attained for chains with greater number of beads. As observed in the case of η', the accuracy of the Dasbach *et al.* (1992) prediction is seen to improve with an increase in the number of beads. Notably, for the two-bead case, the GA prediction for η'' is closer to the BD results at low frequencies, but a slight deviation is observed at values of the scaled frequency, $\beta^* > 2$.

In Fig. 5.8 (b), η'' is normalized by its corresponding value for a Rouse chain and plotted as a function of frequency. At the coarsest level of discretization ($N_{\text{b}} = 2$), there is a striking, qualitative difference between the Dasbach *et al.* (1992) approximation

and exact BD simulation results, in that the former predicts a frequency-independent response, while the latter exhibits a frequency-dependent variation which is also seen in models with higher number of beads. The GA prediction, however, captures the frequency dependence at the $N_b = 2$ level, but is unable to account for the slight increase observed at $\beta^* > 2$, and underestimates the magnitude of the high-frequency plateau. Furthermore, the low-frequency plateau for all the three values of the chain lengths (N_b) simulated is seen to approach unity, which is also the value predicted by the Dasbach *et al.* (1992) approximation in the long-chain ($N_b = 100$) limit. Additionally, the onset of decrease in $\eta'' / (\eta'')^R$ is pushed to higher frequencies as the number of beads in the chain is increased.

In Figures 5.9 and 5.10 , the effect of the internal friction parameter on material functions in oscillatory shear flow is examined for a five-bead chain. The exact BD simulation results, indicated by symbols, are compared against the the approximate prediction given by Dasbach *et al.* (1992), shown as lines.

As seen from Fig. 5.9 (a), the height of the high-frequency plateau in the dynamic viscosity varies directly with the magnitude of the internal friction parameter. The low frequency, or long wavelength, response of the chain is unaffected by a variation in the internal friction parameter. In Fig. 5.9 (b), the dynamic viscosity normalized by its corresponding value for a Rouse chain and plotted as a function of the scaled frequency. This quantity is seen to increase as the square of the frequency, for the same reasons elaborated in connection with Fig. 5.7 (b).

In Fig. 5.10 (c), the imaginary component of the complex viscosity is scaled by the Rouse viscosity and plotted as a function of frequency. The effect of the variation in the internal friction parameter is almost negligible in the low frequency regime and is weak in the high frequency regime.

The difference between the approximate model predictions and the exact BD simulation results are most starkly visible in Fig. 5.10 (d), where the imaginary component of the complex viscosity is scaled by its corresponding value for a Rouse chain and plotted as a function of the scaled frequency. Firstly, the approximate model predicts a low-frequency plateau that is dependent on the internal friction parameter. The simulation results, however, appear to converge on a low-frequency plateau value that is almost independent of the IV parameter. Secondly, the difference between the two predictions is seen to increase with the internal friction parameter.

In addition to the assumptions made in connection with the calculation of the stress jump, the Dasbach *et al.* (1992) approximation also relies on a normal-coordinate transformation, using the eigenvectors of the Rouse matrix, which allows the writing of a separate diffusion equation for each of the normal modes, and the subsequent evaluation of

(a)

(b)
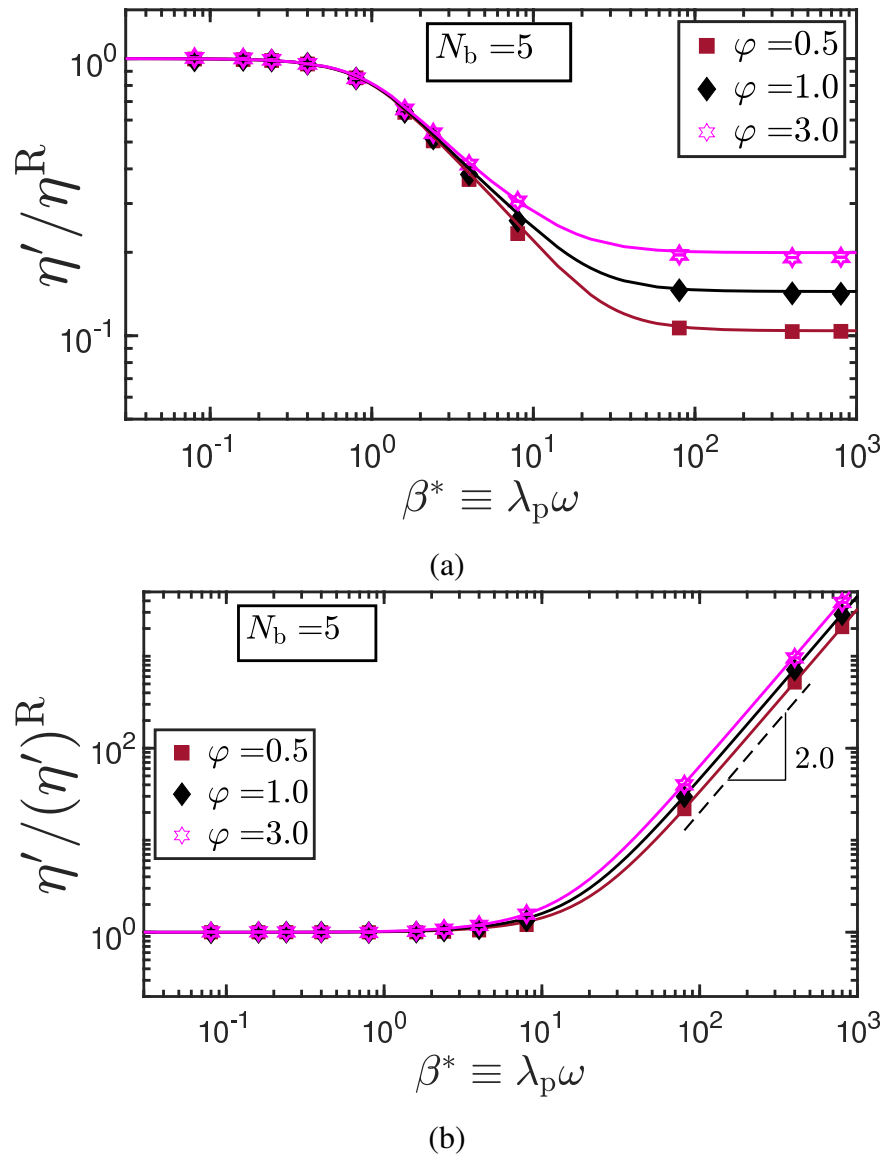
Figure 5.9: Plots of the real (η') component of the complex viscosity, as a function of the scaled frequency, for a five-bead chain at three different values for the number of beads in the chain, scaled by (a) the Rouse viscosity and (b) the real component of the complex viscosity of a Rouse chain. The lines are approximate solutions given in Dasbach *et al.* (1992). Error bars are smaller than symbol size.
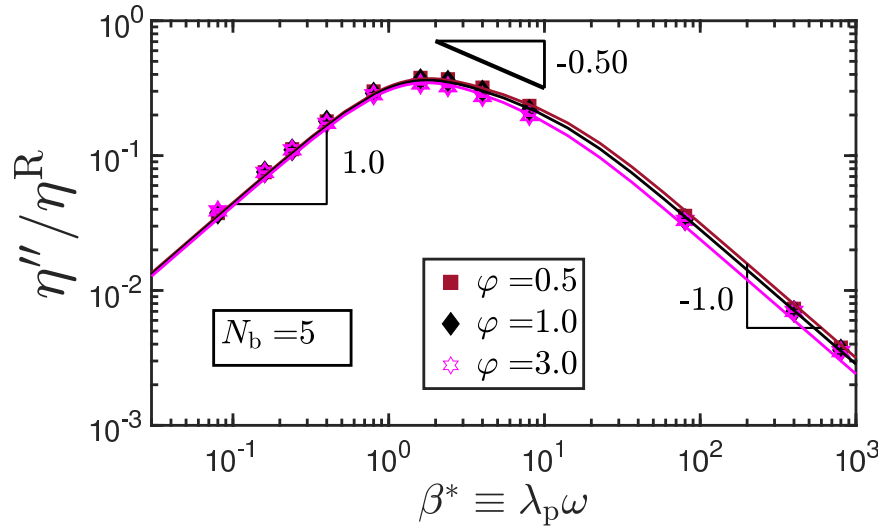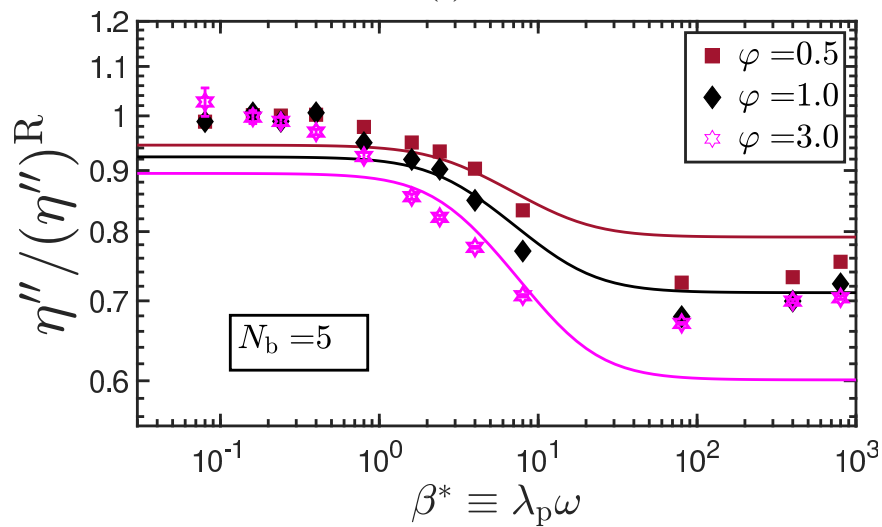
Figure 5.10: Plots of the imaginary component (η'') of the complex viscosity, as a function of the scaled frequency, for a five-bead chain at three different values for the number of beads in the chain, scaled by (a) the Rouse viscosity and (b) the imaginary component of the complex viscosity of a Rouse chain. The lines are approximate solutions given in Dasbach *et al.* (1992). Error bars are smaller than symbol size.

the material functions. Based on the comparison of this approximation against exact BD simulations and the GA prediction, it appears that this route for coordinate transformation is justified for longer chains, but might not be prudent for the two-bead case. Furthermore, as explained in detail by Schieber and coworkers Hua *et al.* (1996), the evaluation of the stress tensor in the Dasbach *et al.* (1992) approach relies on approximating an average of the ratio, $\left\langle QQ/Q^2 \right\rangle$, by the ratio of averages, $\langle QQ \rangle / \left\langle Q^2 \right\rangle$. This could be another probable source of discrepancy between the approximation and the exact BD simulation results observed in Figs. 5.7 - 5.10.

A major motivation for the inclusion of internal friction in early theoretical models for polymeric solutions (Peterlin, 1967; Peterlin and Reinhold, 1967; Bazúa and Williams, 1974) was to explain the high-frequency limiting value of the dynamic viscosity, $\eta'(\omega \rightarrow \infty) \equiv \eta'_\infty$, observed in experiments (Lamb and Matheson, 1964; Philippoff, 1964; Massa *et al.*, 1971). An improvement to the Rouse/Zimm models was sought since they predict that the dynamic viscosity vanishes in the limit of high frequency, in contrast with experimental observations which in most instances indicate a positive limiting value (Lamb and Matheson, 1964; Philippoff, 1964; Massa *et al.*, 1971). Models with internal friction, however, are able to successfully predict this plateau. There do exist systems, however, where the limiting value of the dynamic viscosity in the high frequency limit is *negative* (Morris *et al.*, 1988). A detailed experimental investigation of the solvent molecule and polymer segment relaxation dynamics in such systems has been conducted by Lodge and coworkers (Morris *et al.*, 1988; Lodge, 1993). They conclude that such negative values of η'_∞ cannot be explained within the existing polymer kinetic theory framework. Suggested modifications to the framework comprise the inclusion of an additional term in the stress tensor expression that accounts for coupling effects between the polymer molecules and the solvent (Bird, 1989). It is not clear what factors determine when internal friction may be invoked to explain high frequency oscillatory shear data, and when additional physics needs to be considered. This is an important question that awaits theoretical and experimental investigation, but is beyond the scope of the present work.

An alternative explanation offered by Lodge and coworkers (Lodge, 1993) for the $\eta'_\infty > 0$ observed, for example, in a dilute solution of polystyrene in Aroclor is that the polymer molecules, possessing a lower glass transition temperature (T_g) than the solvent, retard the rotational mobility of the solvent molecules and increase the viscosity of the solution, thereby resulting in a positive value for η'_∞. The opposite effect is observed in the case of polyisoprene in Arocolor, wherein the polymer molecules accelerate the solvent mobility, resulting in $\eta'_\infty < 0$.
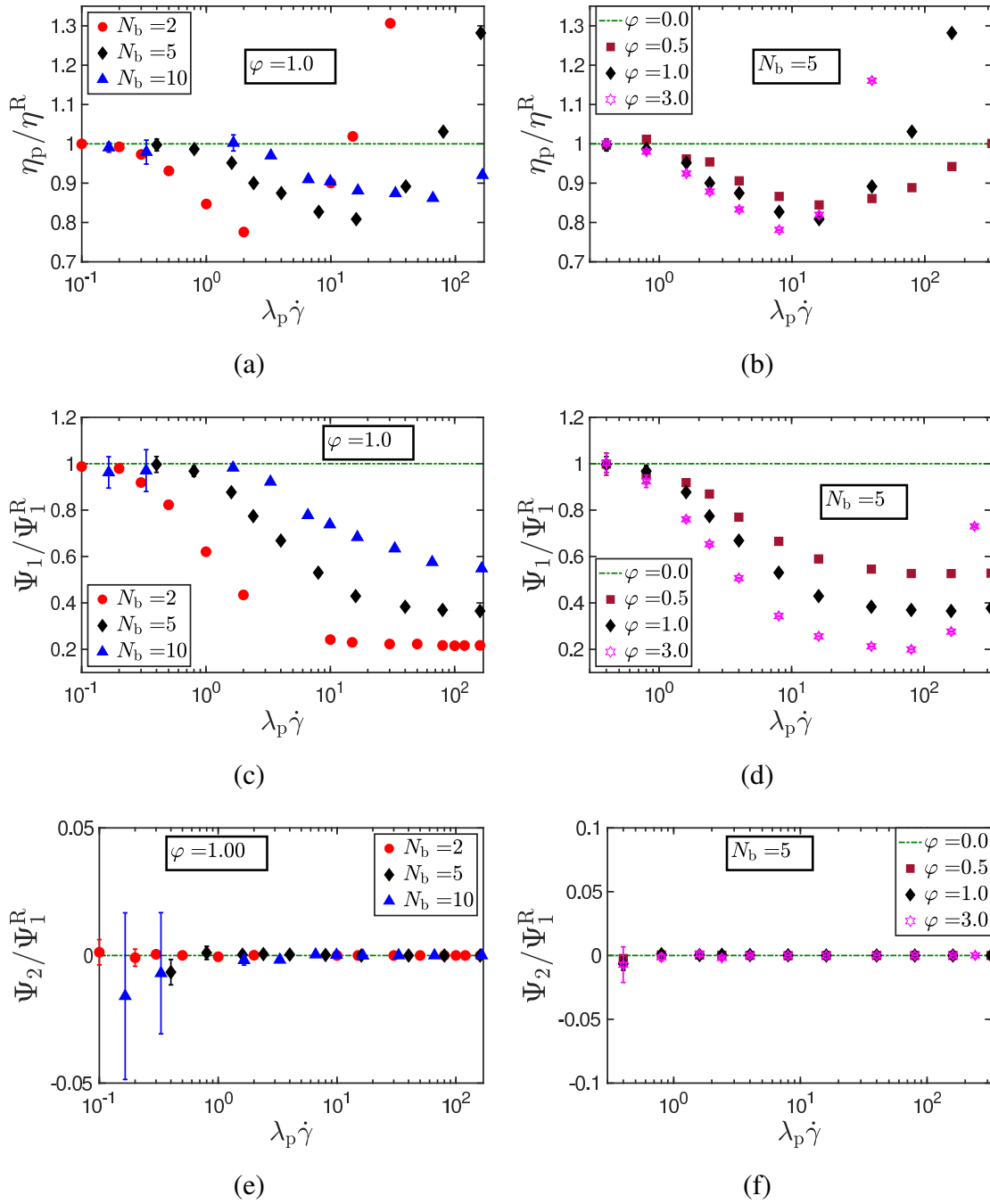
Figure 5.11: Steady-shear viscometric functions for bead-spring-dashpot chains with varying number of beads in the chain and values of the internal friction parameter. The horizontal lines in the figures indicate the material functions for a Rouse chain.

5.3.3   Steady-shear viscometric functions

In Fig. 5.11, the steady-shear values of the material functions are scaled by the corresponding values for a Rouse chain and plotted as a function of the characteristic shear rate. Schieber (1993) has shown, using the Gaussian approximation for dumbbells, that the zero-shear rate viscometric functions are unaffected by internal viscosity. The simulation data is found to concur with this prediction for all the three material functions. It is found that Ψ_2 is practically zero across the range of shear rates examined for all the cases.

As observed from Figs. 5.11 (a) and (b), there is a striking similarity in the steady-shear variation of viscosity between Rouse chains with internal viscosity, and Rouse chains with hydrodynamic interactions (Zylka, 1991; Prabhakar and Prakash, 2006), in that there is shear-thinning followed by shear-thickening. For bead-spring-dashpot chains with a fixed number of beads, it is observed that the characteristic shear rate at which the minimum in the viscosity occurs is largely unaffected by the internal friction parameter. At shear rates larger than this critical value, the viscosity is found to increase with an increase in the IV parameter. For Rouse chains with hydrodynamic interactions, not only is the zero-shear-rate viscosity different from the free-draining case, the shear-dependence of viscosity is markedly dependent on the number of beads in the chain (Zylka, 1991): for $N_b < 6$, the Rouse viscosity is lower than the Zimm viscosity, and at large shear rates, where the effect of HI weakens, the viscosity values tend towards the Rouse value, and a shear-thinning is observed, following the Newtonian plateau at low shear rates. For $N_b \geq 6$, however, the Rouse viscosity is greater than the Zimm viscosity, and at higher shear rates, the weakening of hydrodynamic interactions result in an upturn in the viscosity, causing it to approach the Rouse limit. An analogous explanation for the shear-thickening observed in Rouse chains with internal friction does not seem possible, since not only does the internal friction parameter result in a pronounced increase in shear thickening at high shear rates, but the viscosity is also seen to *exceed* the Rouse value, clearly ruling out any weakening of the internal friction effects at high shear rates.

As seen from Figs. 5.11 (c), the onset of shear-thinning in the first normal stress coefficient is pushed to higher shear rates, and the extent of shear-thinning reduced, with an increase in the number of beads at a fixed value of the internal friction parameter. For an internal friction parameter value of $\varphi = 1.0$, and the range of shear rates examined in the present work, there doesn't appear to be a shear-thickening in the first normal stress coefficient. BD simulations for Hookean dumbbells with internal friction by Hua and Schieber (1995) show a similar plateauing in the first normal stress coefficient, as seen

in the present work. There appears to be a suggestion, but no clear evidence of shear-thickening of Ψ_1, in their work(Hua and Schieber, 1995).

It is anticipated that a shear-thickening in Ψ_1 would be observed at higher values of the internal friction parameter, as evidenced by Fig. 5.11 (d), where the effect of the internal friction parameter on the first normal stress coefficient is examined for a five-bead chain. At lower values of φ, there is no pronounced shear-thickening in Ψ_1, but a value of $\varphi = 3.0$ results in the onset of a pronounced shear-thickening at $\lambda_p \dot{\gamma} \approx 100.0$. Furthermore, this critical shear rate for the onset of shear-thickening in Ψ_1 is about an order-of-magnitude larger than that in the case of viscosity.

It appears plausible that the shear-thickening in the viscosity and the first normal stress coefficient involves an interplay of internal friction and the number of beads in the chain.

A prevalent notion in the literature (Manke and Williams, 1986, 1989, 1991, 1993) is that the $\varphi \rightarrow \infty$ corresponds to the rigid-rod limit. This is supported by the following observation. The stress jump for rigid dumbbells with a Gaussian distribution of lengths is given by Hua *et al.* (1996) $\eta_{\text{jump,rigid}} = 0.4 \, n_p k_B T \lambda_H$; while the stress jump for Hookean dumbbells with IV has the following form given by Manke and Williams (1988), $\eta_{\text{jump,IV}} = 0.4 \left[2\varphi/(1 + 2\varphi) \right] n_p k_B T \lambda_H$. Clearly, taking the $\varphi \rightarrow \infty$ limit for Hookean spring-dashpots gives the rigid-rod result. The similarity between the two models, however, ceases here, and their steady-shear viscometric functions look markedly different: while bead-rod-chains are known to display a plateau in viscosity at high shear-rates (Petera and Muthukumar, 1999), preceded by a shear-thinning regime, there is a pronounced increase in shear-thickening as φ is increased for flexible chains with internal friction. Furthermore, while the first normal stress coefficient for bead-rod chains shear-thins continuously (Petera and Muthukumar, 1999), chains with IV exhibit a slight shear-thickening at high shear rates, as discussed previously.

A detailed comparison of the rheological properties of FENE dumbbells with IV and rigid dumbbells is given in Chapter 4 where it is concluded that a combination of finite extensibility and a high value of the internal friction parameter ($\varphi \geq 5$) is required to qualitatively mimic the steady-shear rheological response of rigid-rod models.

5.4 Conclusions

The exact set of stochastic differential equations, and a thermodynamically consistent stress tensor expression for a Rouse chain with fluctuating internal friction has been derived. The BD simulation algorithm for the solution of these equations has been

validated by comparison against approximate predictions available in the literature for the stress jump, and material functions in oscillatory and steady simple shear flows have been calculated. Semi-analytical predictions (Dasbach *et al.*, 1992) for the dynamic viscosity are in near-quantitative agreement with the exact simulation results, with the accuracy improving with an increase in the number of beads in the chain. The difference between the predictions and the simulation results are more pronounced for the case of the imaginary component of the complex viscosity. The approximation by Dasbach *et al.* (1992) fails to capture the frequency dependence of η'' for the dumbbell case observed in exact BD simulations and predicted by the Gaussian approximation (Schieber, 1993).

The approach developed by Williams and coworkers (Manke and Williams, 1988; Dasbach *et al.*, 1992), however, is valid only in the linear viscoelastic regime, and cannot be used to obtain steady-shear viscometric predictions. The Gaussian approximation (Schieber, 1993) solution is only available for Hookean dumbbells with internal friction, and is unable to predict the shear-thickening in viscosity observed in exact Brownian dynamics simulations.

Bead-spring-dashpot chains exhibit a non-monotonous variation in the viscosity with respect to the shear rate, with shear-thinning followed by shear-thickening. At a fixed value of the internal friction parameter, the shear-thickening effect is seen to weaken with an increase in the number of beads in the chain. Increasing the internal friction parameter at a fixed value of the number of beads in the chain leads to an increase in shear-thickening. The inclusion of internal friction results in a slight shear-thickening of the first normal stress coefficient, with the onset of thickening pushed to lower shear rates with an in increase in the internal friction parameter. The results of the present chapter have been written up as a manuscript, and is available in Kailasham *et al.* (2021b).

The importance of hydrodynamic interactions in describing the dynamics of dilute polymer solutions is well-documented (Prabhakar and Prakash, 2002; Sunthar and Prakash, 2005; Larson, 2005; Schroeder, 2018; Prakash, 2019), with Chapters 3 and 4 and describing particularly the consequences of including HI in models with internal viscosity. However HI has not been considered in the present chapter, because its inclusion introduces an explicit coupling between all bead-pairs, and the procedure developed here is not applicable for the decoupling of the connector vector velocities. The solution of bead-spring-dashpot chains with hydrodynamic and excluded volume interactions is a subject for future study.

In the next chapter, the importance of fluctuations in the treatment of internal friction is examined, by comparing data obtained obtained from simulating the exact stochastic

differential equations derived in the present chapter, against the analytical predictions of a preaveraged internal friction model.

Chapter 6

How important are fluctuations in the treatment of internal friction in polymers?

6.1 Introduction

The most widely used theoretical framework for the interpretation of internal friction effects (Soranno *et al.*, 2012; Schulz *et al.*, 2012; Ameseder *et al.*, 2018; Soranno *et al.*, 2018) is the Rouse model with internal friction (Khatri and McLeish, 2007) (RIF) and its variants (Cheng *et al.*, 2013; Samanta *et al.*, 2014; Samanta and Chakrabarti, 2016), which modify the standard continuum Rouse model to include an additional frictional force that resists changes in the curvature of the space-curve representing the polymer molecule. While these models remain preferred due to their analytical tractability, their accuracy, from a theoretical standpoint, has so far been unquestioned. We first show that the RIF model represents an approximation that ignores fluctuations in the internal friction force and is rather a preaveraged treatment. As discussed in Chapter 5, we have developed an exact numerical solution to the Rouse model with fluctuating internal friction, and used it to estimate linear-viscoelastic and steady-shear viscometric functions using Brownian dynamics (BD) simulations. In this chapter, the exact model is used to test the accuracy of the RIF model, by comparing their predictions for quantities both at and away from equilibrium.

The effect of internal friction on the dynamics of protein reconfiguration is commonly quantified experimentally by tagging the molecule with fluorescent donor-acceptor pairs along their contour length, and extracting a characteristic reconfiguration time from the autocorrelation of the fluorescence signal (Soranno *et al.*, 2017, 2018).

Analytical and simulation estimates of the reconfiguration time are based on the autocorrelation of the vector that connects the tagged monomers along the chain (Cheng *et al.*, 2013; Samanta *et al.*, 2014; Samanta and Chakrabarti, 2016). We examine this property, which represents an equilibrium situation, where the molecule is suspended in a quiescent fluid. In order to examine the importance of fluctuations away from equilibrium, a polymer molecule subjected to simple shear flow is considered as a prototypical out-of-equilibrium process. Several biological processes, such as ciliary and flagellar oscillations in microorganisms (Poirier and Marko, 2002; Mondal *et al.*, 2020; Nandagiri *et al.*, 2020), are driven by the hydrolysis of ATP molecules, and the contribution from internal friction in these far-from-equilibrium processes is seen to outweigh hydrodynamic drag by nearly an order of magnitude. Protein molecules such as hormones and antibodies are commonly subjected to shear flow during various stages of bioprocessing (Bekard *et al.*, 2011). The conformational dynamics of these molecules in flow directly affects their structure and function, which further adds relevance to the study of the dynamic response of polymers to shear flow.

We find that the equilibrium predictions made by the preaveraged model and the one with fluctuations differ at small separations between the tagged monomers along the polymer backbone, with the difference diminishing with an increase in the inter-tag separation. However, in the presence of shear flow, the two model predictions differ starkly and qualitatively: the preaveraged model predicts values for the chain extension and viscosity that are identical to the standard Rouse model, with the internal friction parameter only affecting the transient phase that precedes the attainment of steady state. Contrarily, as seen from Chapter 5, exact BD simulations which account for fluctuations in IV establish that both the transients and the steady-state values are modified by internal friction.

The rest of this chapter is organized as follows. In Section 6.2, the discrete version of the RIF model is presented and solved using normal-mode analysis. The derivation of the governing set of stochastic differential equations for a bead-spring-dashpot chain with preaveraged internal friction is presented in Sec. 6.3. Results on the effect of fluctuations at equilibrium [Sec. 6.4] and in flow [Sec. 6.5] are presented next, followed by concluding remarks in Sec. 6.7. The application of the normal mode analysis for obtaining an analytical expression for the mean-squared end-to-end distance of coarse-grained models in shear flow, and the detailed steps for the derivation of the appropriate stress tensor expression for chains with preaveraged internal friction have been presented in Appendix E.

6.2   Solution of discrete RIF model

The standard RIF model is in the continuous chain limit, but it is convenient to work with a discrete model for ease of comparison with simulations. The solution of the discrete model is presented below, following which it will be established that it is identical to the continuous chain RIF model as the number of beads, $N_b \gg 1$. In the discrete RIF model, the beads, each of radius a and suspended in a solvent of viscosity η_s, are located at positions $\{r_1, r_2, \cdots, r_{N_b}\}$, and connected by Hookean springs of stiffness H in parallel with dashpots that have a damping coefficient $(K/3)$. The factor of 3 is explained below. The dashpots provide a resistive force that is proportional to the relative velocity between adjacent beads, and the force due to internal friction on a bead μ not at the chain ends is given by (Khatri and McLeish, 2007)

$$
\begin{aligned}
F_\mu^{(IV),RIF} &= (K/3)\left(\dot{r}_{\mu+1} - \dot{r}_\mu\right) - (K/3)\left(\dot{r}_\mu - \dot{r}_{\mu-1}\right) \\
&= (K/3)\left[\dot{r}_{\mu+1} - 2\dot{r}_\mu - \dot{r}_{\mu-1}\right]
\end{aligned}
\tag{6.1}
$$

where $\dot{r}_\mu = dr_\mu/dt$. The overdamped Langevin equation for the time evolution of r_μ, is given as (Khatri and McLeish, 2007)

$$
\frac{dr_\mu}{dt} = -\left(\frac{H}{\zeta} + \frac{K}{3\zeta}\frac{d}{dt}\right)\sum_{\nu=1}^{N_b} A_{\mu\nu}^{(R)} r_\nu + \kappa \cdot r_\mu + \xi_\mu(t)
\tag{6.2}
$$

where $\zeta = 6\pi\eta_s a$ is the bead friction coefficient, $A_{\mu\nu}^{(R)}$ are elements of the Rouse matrix (Bird *et al.*, 1987b) defined as

$$
A^{(R)} = \begin{pmatrix}
1 & -1 & 0 & \cdots & & 0 \\
-1 & 2 & -1 & 0 & \cdots & 0 \\
0 & -1 & 2 & -1 & \cdots & \\
\vdots & \vdots & \vdots & & & \\
0 & 0 & \cdots & -1 & 2 & -1 \\
0 & 0 & \cdots & 0 & -1 & 1
\end{pmatrix}
\tag{6.3}
$$

and κ represents the flow-field, which is **0** in the absence of flow, and takes the form given by Eq. (2.13) of Chapter 2 for simple shear flow. The internal friction parameter, $\varphi \equiv K/\zeta$, is taken to be the ratio of the damping coefficient of the dashpot to the bead friction coefficient. The moments of the noise term, $\xi_\mu(t)$, are not specified in real space, but rather in normal-mode space. Essentially, Eq. (6.2) is solved by first using the eigenvectors of the Rouse matrix for projecting the bead positions into normal-mode space, followed by the assumption that the noise term in normal mode space is white, so as to satisfy the requirements of equipartition. This treatment results in a solution which is similar to the

standard Rouse model, with a renormalization of the mode relaxation times. The detailed steps are given below. The elements of the orthogonal matrix $\boldsymbol{\Omega}$ which project the bead-positions into normal-mode space are given by (Verdier, 1966; Kopf *et al.*, 1997)

$$\Omega_{\mu n} = \left(\frac{2 - \delta_{n0}}{N_{\mathrm{b}}}\right)^{1/2} \cos\left[\left(\mu - \frac{1}{2}\right)\frac{n\pi}{N_{\mathrm{b}}}\right] \tag{6.4}$$

where $\mu = 1, 2, 3, ...N_{\mathrm{b}}$ and $n = 0, 1, 2, ...(N_{\mathrm{b}} - 1)$. The columns of $\boldsymbol{\Omega}$ are eigenvectors of $\boldsymbol{A}^{(\mathrm{R})}$, which means

$$\sum_{\mu} \Omega_{\mu m}\Omega_{\mu n} = \delta_{mn}$$

$$\sum_{n} \Omega_{\mu n}\Omega_{\nu n} = \delta_{\mu\nu} \tag{6.5}$$

$$\sum_{\mu}\sum_{\nu} \Omega_{\mu n}A_{\mu\nu}\Omega_{\nu m} = a_m\delta_{nm}$$

where a_m refers to the eigenvalues of $\boldsymbol{A}^{(\mathrm{R})}$, given by

$$a_m = 4\sin^2\left(\frac{m\pi}{2N_{\mathrm{b}}}\right); \quad m = 0, 1, 2, ..., (N_{\mathrm{b}} - 1) \tag{6.6}$$

We additionally define $\theta = (K/3\zeta) = \varphi/3$ for notational convenience. It is desired to first calculate the autocorrelation of the interbead connector vector, $\boldsymbol{R}_{\mu\nu} \equiv \boldsymbol{r}_{\nu} - \boldsymbol{r}_{\mu}$, at equilibrium. Setting $\boldsymbol{\kappa} = 0$ in Eq. (6.2) and transforming to normal co-ordinates, $\boldsymbol{X}_j$ (Verdier, 1966; Kopf *et al.*, 1997) using $\boldsymbol{X}_j = \sum_{\mu} \Omega_{\mu j}\boldsymbol{r}_{\mu}$, the governing equation becomes

$$\frac{d\boldsymbol{X}_p}{dt} = -\frac{H_p}{\zeta_p}\boldsymbol{X}_p + \boldsymbol{g}_p(t) \tag{6.7}$$

where the moments of the noise vector, $\boldsymbol{g}_p(t)$, are given as follows

$$\left\langle g_p^{\alpha} \right\rangle = 0; \quad \left\langle g_p^{\alpha}(t)g_q^{\beta}(t') \right\rangle = \frac{2k_BT}{\zeta_p}\delta_{pq}\delta^{\alpha\beta}\delta(t - t') \tag{6.8}$$

with $H_p = Ha_p$, and $\zeta_p = \zeta\left(1 + \theta a_p\right)$. The indices α and β in Eq. (6.8) run from 1 to d, where d denotes the dimensionality of the system. For the rest of this appendix, we shall concern ourselves with the $d = 3$ case. Eq. (6.7) represents the equation of motion of a Brownian harmonic oscillator moving in a potential of stiffness H_p and experiencing a friction coefficient ζ_p. For such an oscillator, it is known that (Verdier, 1966; Doi and Edwards, 1986; Kopf *et al.*, 1997)

$$\left\langle \boldsymbol{X}_p(0) \cdot \boldsymbol{X}_q(t) \right\rangle = \frac{3k_BT}{H_p}\delta_{pq}e^{-t/\tau_p} \tag{6.9}$$

where

$$\tau_p = \zeta_p/H_p = (\zeta/4H)\sin^{-2}(p\pi/2N_{\mathrm{b}}) + (K/3H) \tag{6.10}$$

The expressions for the bead position vectors in terms of the normal coordinates is given as

$$r_\mu = \sum_{j=0}^{N_b-1} \Omega_{\mu j} X_j(t) \tag{6.11}$$

and the vector joining beads μ and ν is written as

$$\boldsymbol{R}_{\mu\nu}(t) \equiv \boldsymbol{r}_\nu(t) - \boldsymbol{r}_\mu(t) = \sqrt{\frac{2}{N_b}} \sum_{q=1}^{N_b-1} \left\{ \cos\left[\left(\nu - \frac{1}{2}\right)\frac{q\pi}{N_b}\right] - \cos\left[\left(\mu - \frac{1}{2}\right)\frac{q\pi}{N_b}\right] \right\} X_q(t) \tag{6.12}$$

from which the expression for its autocorrelation may be written as

$$\left\langle \boldsymbol{R}_{\mu\nu}(0) \cdot \boldsymbol{R}_{\mu\nu}(t) \right\rangle = \left(\frac{2}{N_b}\right) \sum_{q=1}^{N_b-1} \sum_{p=1}^{N_b-1} \left\{ \cos\left[\left(\nu - \frac{1}{2}\right)\frac{q\pi}{N_b}\right] - \cos\left[\left(\mu - \frac{1}{2}\right)\frac{q\pi}{N_b}\right] \right\}$$

$$\times \left\{ \cos\left[\left(\nu - \frac{1}{2}\right)\frac{p\pi}{N_b}\right] - \cos\left[\left(\mu - \frac{1}{2}\right)\frac{p\pi}{N_b}\right] \right\} \left\langle X_p(0) \cdot X_q(t) \right\rangle \tag{6.13}$$

The choice of the noise term in normal mode space [Eq. (6.8)] ensures that the mean-squared value of the segmental vector $\boldsymbol{R}_{\mu\nu}$ at equilibrium is given by $\left\langle \boldsymbol{R}_{\mu\nu}^2 \right\rangle_{\text{eq}} \equiv \left\langle \boldsymbol{R}_{\mu\nu}^2(0) \right\rangle = 3|\nu - \mu|(k_B T/H)$. Using Eqs. (6.9) and (6.13), the normalized autocorrelation for the discrete RIF model may be written as follows

$$\frac{\left\langle \boldsymbol{R}_{\mu\nu}(0) \cdot \boldsymbol{R}_{\mu\nu}(t) \right\rangle}{\left\langle \boldsymbol{R}_{\mu\nu}^2(0) \right\rangle} = \left[\frac{2}{N_b(N_b-1)}\right] \left[\sum_{p=1}^{N_b-1} \left\{ \cos\left[\left(\nu - \frac{1}{2}\right)\frac{p\pi}{N_b}\right] - \cos\left[\left(\mu - \frac{1}{2}\right)\frac{p\pi}{N_b}\right] \right\}^2 \right.$$

$$\left. \times \left(\frac{1}{a_p}\right) e^{-t/\tau_p} \right] \tag{6.14}$$

For the special case of the end-to-end vector, $\boldsymbol{R}_E(t) \equiv \boldsymbol{R}_{1N_b}(t)$, the normalized autocorrelation is given by

$$\frac{\left\langle \boldsymbol{R}_E(0) \cdot \boldsymbol{R}_E(t) \right\rangle}{\left\langle \boldsymbol{R}_E^2(0) \right\rangle} = \left[\frac{8}{N_b(N_b-1)}\right] \left[\sum_{p:\text{odd}}^{N_b-1} \cos^2\left(\frac{p\pi}{2N_b}\right)\left(\frac{1}{a_p}\right) e^{-t/\tau_p} \right] \tag{6.15}$$

Using Eq. (6.10), we may write

$$\frac{t}{\tau_p} \equiv \frac{H_p t}{\zeta_p} = \left(\frac{Ha_p t}{\zeta(1+\theta a_p)}\right) = \left(\frac{Ha_p t}{4H\lambda_H(1+\theta a_p)}\right) = \left(\frac{1}{4}\right)\left(\frac{a_p}{1+\theta a_p}\right)\left(\frac{t}{\lambda_H}\right) = \left(\frac{a_p}{1+\theta a_p}\right)\frac{t^*}{4} \tag{6.16}$$

and

$$\frac{t}{\tau_p} \equiv \left(\frac{1+\theta a_1}{1+\theta a_p}\right)\left(\frac{a_p}{a_1}\right)\left(\frac{t}{\tau_1}\right), \tag{6.17}$$

The expression for the normalized dimensionless autocorrelation of the interbead connector vector is then

$$\frac{\langle \boldsymbol{R}_{\mu\nu}^*(0) \cdot \boldsymbol{R}_{\mu\nu}^*(t^*) \rangle}{\langle \boldsymbol{R}_{\mu\nu}^{*2}(0) \rangle} = \left[\frac{2}{N_\mathrm{b}|\nu - \mu|} \right] \sum_{p=1}^{N_\mathrm{b}-1} \left\{ \cos\left[\left(\nu - \frac{1}{2}\right)\frac{p\pi}{N_\mathrm{b}} \right] - \cos\left[\left(\mu - \frac{1}{2}\right)\frac{p\pi}{N_\mathrm{b}} \right] \right\}^2$$
$$\times \left(\frac{1}{a_p}\right) \exp\left[-\left(\frac{a_p}{1 + \theta a_p}\right)\frac{t^*}{4} \right]$$
(6.18)

and the dimensionless, normalized autocorrelation of the end-to-end vector may therefore be rewritten as

$$\frac{\langle \boldsymbol{R}_\mathrm{E}^*(0) \cdot \boldsymbol{R}_\mathrm{E}^*(t^*) \rangle}{\langle \boldsymbol{R}_\mathrm{E}^{*2}(0) \rangle} = \left[\frac{8}{N_\mathrm{b}(N_\mathrm{b} - 1)} \right] \sum_{p:\mathrm{odd}}^{N_\mathrm{b}-1} \cos^2\left(\frac{p\pi}{2N_\mathrm{b}}\right)\left(\frac{1}{a_p}\right)\exp\left[-\left(\frac{a_p}{1 + \theta a_p}\right)\frac{t^*}{4} \right] \quad (6.19)$$

In terms of t/τ_1, the autocorrelation is given to be

$$\frac{\langle \boldsymbol{R}_\mathrm{E}^*(0) \cdot \boldsymbol{R}_\mathrm{E}^*(t/\tau_1) \rangle}{\langle \boldsymbol{R}_\mathrm{E}^{*2}(0) \rangle} = \left[\frac{8}{N_\mathrm{b}(N_\mathrm{b} - 1)} \right] \sum_{p:\mathrm{odd}}^{N_\mathrm{b}-1} \cos^2\left(\frac{p\pi}{2N_\mathrm{b}}\right)\left(\frac{1}{a_p}\right)\exp\left[-\left(\frac{1 + \theta a_1}{1 + \theta a_p}\right)\left(\frac{a_p}{a_1}\right)\left(\frac{t}{\tau_1}\right) \right]$$
(6.20)

The normalized autocorrelation for the continuum model is as follows (Khatri and McLeish, 2007; Doi and Edwards, 1986)

$$\frac{\langle \boldsymbol{R}_\mathrm{E}^*(0) \cdot \boldsymbol{R}_\mathrm{E}^*(t) \rangle}{\langle \boldsymbol{R}_\mathrm{E}^{*2}(0) \rangle} = \left(\frac{8}{\pi^2}\right) \sum_{p:\mathrm{odd}}^{\infty} \left(\frac{1}{p^2}\right)\exp\left[-\frac{t}{\widetilde{\tau}_p} \right], \quad (6.21)$$

where

$$\widetilde{\tau}_p = \left(N_\mathrm{b}^2 \zeta / p^2 \pi^2 H \right) + (K/3H), \quad (6.22)$$

and the dimensionless mean-squared end-to-end distance at equilibrium is given by $\langle \boldsymbol{R}_\mathrm{E}^{*2}(0) \rangle \equiv \langle \boldsymbol{R}_\mathrm{E}^{*2} \rangle_\mathrm{eq} = 3N_\mathrm{b}$. The above expression may be rewritten in terms of $t/\widetilde{\tau}_1$ as

$$\frac{\langle \boldsymbol{R}_\mathrm{E}^*(0) \cdot \boldsymbol{R}_\mathrm{E}^*(t/\widetilde{\tau}_1) \rangle}{\langle \boldsymbol{R}_\mathrm{E}^{*2}(0) \rangle} = \left(\frac{8}{\pi^2}\right) \sum_{p:\mathrm{odd}}^{\infty} \left(\frac{1}{p^2}\right)\exp\left\{ -p^2 \left[\frac{(N_\mathrm{b}/\pi)^2 + \theta}{(N_\mathrm{b}/\pi)^2 + p^2\theta} \right]\left(\frac{t}{\widetilde{\tau}_1}\right) \right\} \quad (6.23)$$

From Eqs. (6.10) and (6.22), and recognizing that $\sin(x) \approx x$ as $x \to 0$, it is observed that $\tau_p \to \widetilde{\tau}_p$ as $N_\mathrm{b} \to \infty$.

The infinite summation in Eq. (6.23) runs over all positive odd integers. We define a related quantity $S(N_\mathrm{b}, N_\mathrm{t}, t/\widetilde{\tau}_1)$, as

$$S(N_\mathrm{b}, N_\mathrm{t}, t/\widetilde{\tau}_1) = \sum_{p=1,3,5,\ldots}^{2N_\mathrm{t}-1} \left(\frac{1}{p^2}\right)\exp\left\{ -p^2 \left[\frac{(N_\mathrm{b}/\pi)^2 + \theta}{(N_\mathrm{b}/\pi)^2 + p^2\theta} \right]\left(\frac{t}{\widetilde{\tau}_1}\right) \right\} \quad (6.24)$$

In Fig. 6.1, the variation of S as function of the number of terms included in the summation, N_t, for two different chain lengths, at two values of the dimensionless time
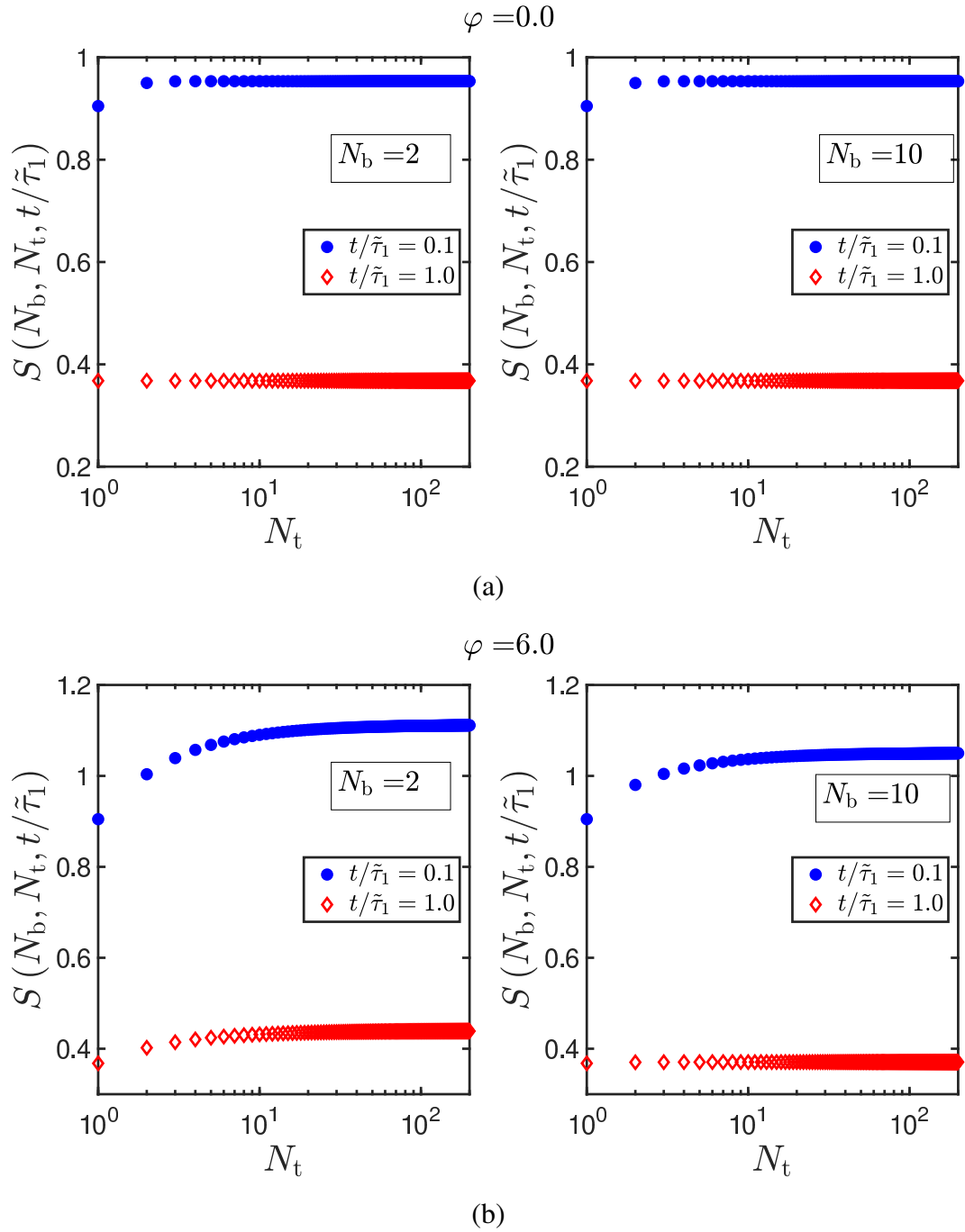
Figure 6.1: Plot of number of terms required for convergence of summation indicated by Eq. (6.24) for two different chain lengths, for models without [(a)] and with [(b)] internal friction, at different values of the scaled time.
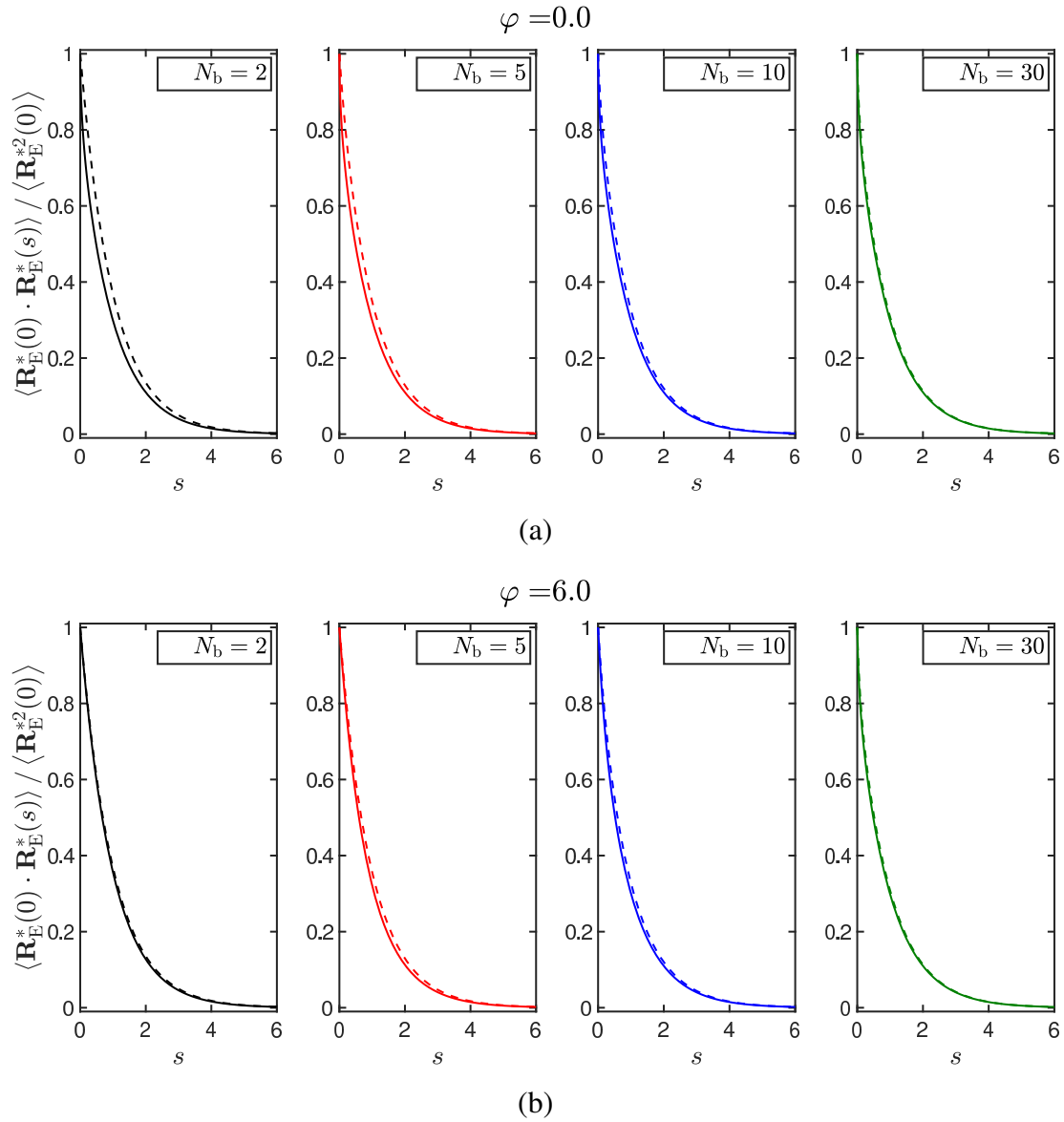
Figure 6.2: Comparison of the normalized autocorrelation expressions for the discrete [dashed line, Eq. (6.20)] and continuum [solid line, Eq. (6.23)] RIF models, for various chain lengths, for models without [(a)] and with [(b)] internal friction. Note that $s \equiv t/\tau_1$ for the discrete model and $s \equiv t/\widetilde{\tau}_1$ for the continuum model.

and the internal friction parameter are displayed. In Fig. 6.1 (a), the case without internal friction is presented, and it is clearly seen that the summation requires fewer than ten terms for convergence at both early and later values of time. The summation at later times converges more quickly than the convergence at earlier times, for both two-bead and ten-bead chains. In Fig. 6.1 (b), the case with internal friction is presented. It is seen that nearly two hundred terms are required for the convergence of the sum for the two-bead chain at early times, and the corresponding number for the ten-bead chain at the same value of scaled time is marginally lower. As seen in (a), the summation at later times require fewer terms for convergence as compared to early times. We henceforth use two hundred terms in the numerical calculation of the infinite sum indicated in Eq. (6.23).

In Fig. 6.2, it is seen that the normalized autocorrelation for the discrete model approaches the continuum result as the chain length is increased, for cases with and without internal friction. The difference is larger at early times, and lesser at later times, for all the values of chain length examined in the figure. In this figure, the normalized autocorrelation for the discrete chain is plotted as a function of time scaled by the longest relaxation time of the discrete chain [t/τ_1], whereas the autocorrelation for the continuum model is plotted as a function of $t/\widetilde{\tau}_1$. The variable s is used to refer to the scaled time, and its exact definition is context-dependent. For the case without internal friction [Fig. 6.2 (a)], it is clearly seen that the difference between the discrete and continuum result decreases with an increase in the chain length. However, for the case with internal friction [Fig. 6.2 (b)], the difference appears to be non-monotonic in the chain length.

Fig. 6.3 examines the variation of the difference between the discrete and continuum result as a function of chain length, at three different instances of the scaled time s, for different values of the internal friction parameter. Note that the difference between the two models is taken at the same value of s. The magnitude of the difference is seen to be larger at shorter times, and smaller at later times, as previously seen in Fig. 6.2, for models with and without internal friction. However, the nature of the variation of the difference with the chain length is significantly impacted by the presence of internal friction. For cases without internal friction, the difference decreases monotonically with the chain length. With the inclusion of internal friction, however, the difference hits a peak before decreasing monotonically with the chain length. The height of the peak is seen to be diminished at later times.

A solution for the continuum RIF chain subjected to shear flow is not available in the literature. As detailed in Section E.1 of Appendix E, we have derived an expression for the transient evolution of the dimensionless mean-squared end-to-end vector in shear
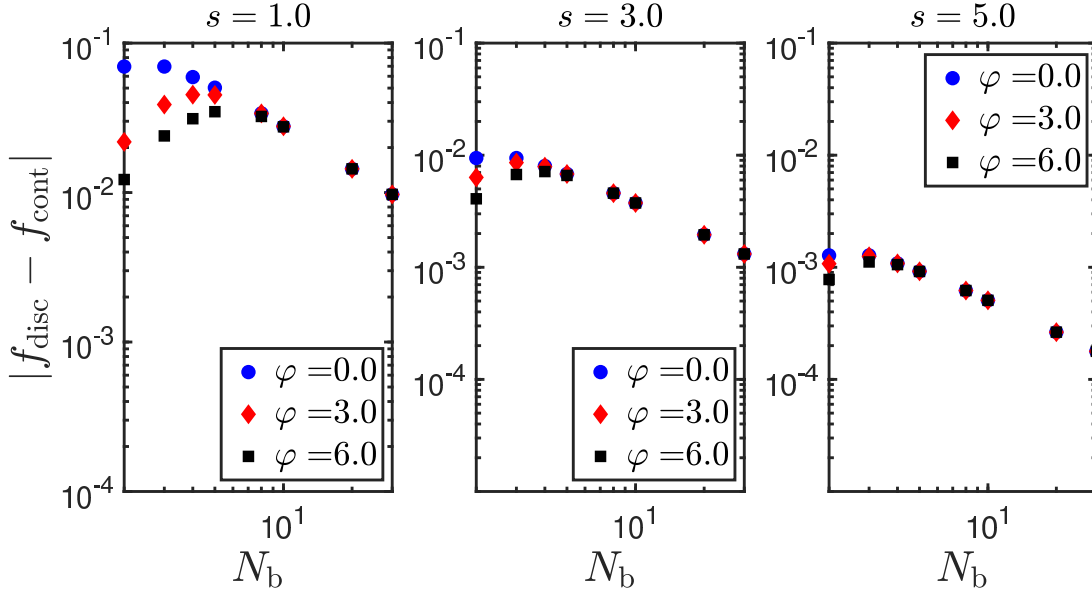
Figure 6.3: The absolute value of the difference between the discrete and continuum models at various instances of scaled time, plotted as a function of the chain length, for varying values of the internal friction parameter. Here, f_{disc} represents the normalized autocorrelation for the discrete model at the indicated value of s, and f_{cont} represents the normalized autocorrelation for the continuum model at the same value of s.

flow scaled by its equilibrium value, $\left\langle \boldsymbol{R}_{\text{E}}^{*2}(t^*) \right\rangle / \left\langle \boldsymbol{R}_{\text{E}}^{*2} \right\rangle_{\text{eq}}$, for the discrete RIF model, as

$$
\frac{\left\langle \boldsymbol{R}_{\text{E}}^{*2}(t^*) \right\rangle}{\left\langle \boldsymbol{R}_{\text{E}}^{*2} \right\rangle_{\text{eq}}} = \left[\frac{8}{N_{\text{b}}(N_{\text{b}} - 1)} \right] \sum_{p:\text{odd}}^{N_{\text{b}}-1} \left(\frac{1}{a_p} \right) \cos^2\left(\frac{p\pi}{2N_{\text{b}}} \right)
$$
$$
\times \left\{ 1 + \frac{8\,(\lambda_{\text{H}}\dot{\gamma})^2}{3a_p^2} \left[1 - \left(\exp\left[-\left(\frac{3a_p}{3 + \varphi a_p} \right) \frac{t^*}{2} \right] \left[1 + \left(\frac{3a_p}{3 + \varphi a_p} \right) \frac{t^*}{2} \right] \right) \right] \right\}
$$

(6.25)

where $\left\langle \boldsymbol{R}_{\text{E}}^{*2} \right\rangle_{\text{eq}} = 3\,(N_{\text{b}} - 1)$ is the mean-squared value for the end-to-end vector at equilibrium. The steady state value is obtained by taking the limit $t^* \to \infty$ in Eq. (6.25) to give

$$
\frac{\left\langle \boldsymbol{R}_{\text{E}}^{*2} \right\rangle}{\left\langle \boldsymbol{R}_{\text{E}}^{*2} \right\rangle_{\text{eq}}} = \left[\frac{8}{N_{\text{b}}(N_{\text{b}} - 1)} \right] \sum_{p:\text{odd}}^{N_{\text{b}}-1} \left(\frac{1}{a_p} \right) \cos^2\left(\frac{p\pi}{2N_{\text{b}}} \right) \left\{ 1 + \frac{8\,(\lambda_{\text{H}}\dot{\gamma})^2}{3a_p^2} \right\}
$$

(6.26)

6.3 Bead-spring-dashpot chain with preaveraged internal friction

We show next that a Rouse model with preaveraged internal friction, constructed using the principles of polymer kinetic theory (Bird *et al.*, 1987b; Öttinger, 1996) (PKT), is
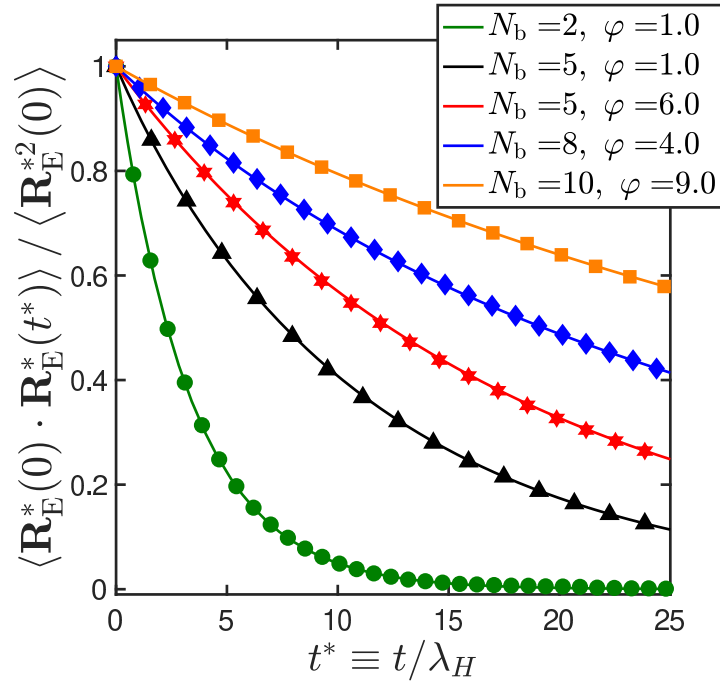
(a)
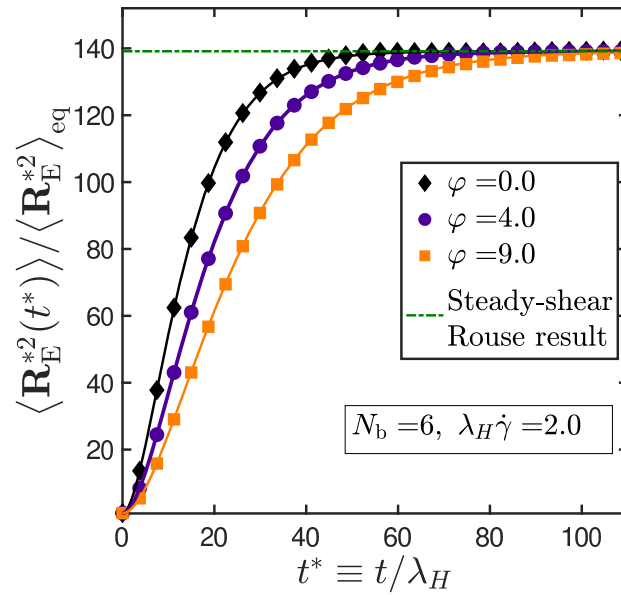
(b)

Figure 6.4: BD simulation results of the preaveraged internal friction model, for: (a) Normalized autocorrelation of the end-to-end vector at equilibrium, and (b) transient evolution of the mean-squared end-to-end vector in shear flow, obtained by numerically integrating Eq. (6.49). The lines in (a) and (b) represent discrete RIF results given by Eq. (6.19) and Eq. (6.25), respectively. Error bars, which represent standard error of the mean, are roughly of the same size or smaller than the symbols used.

formally identical to the RIF model. A Hookean bead-spring-dashpot chain is considered, similar to the RIF model, except the dashpot coefficient is taken to be K. The total force on a bead μ (not at the chain ends) due to internal viscosity is given by (Prakash, 1999)

$$\boldsymbol{F}_\mu^{(\text{IV})} = K\left(\frac{\boldsymbol{Q}_\mu \boldsymbol{Q}_\mu}{Q_\mu^2}\right) \cdot [\![\dot{\boldsymbol{r}}_{\mu+1} - \dot{\boldsymbol{r}}_\mu]\!] - K\left(\frac{\boldsymbol{Q}_{\mu-1} \boldsymbol{Q}_{\mu-1}}{Q_{\mu-1}^2}\right) \cdot [\![\dot{\boldsymbol{r}}_\mu - \dot{\boldsymbol{r}}_{\mu-1}]\!] \tag{6.27}$$

where $\boldsymbol{Q}_\mu \equiv \boldsymbol{r}_{\mu+1} - \boldsymbol{r}_\mu$ is the connector vector joining the μth and the $(\mu + 1)^{\text{th}}$ bead, and $[\![\cdots]\!]$ represents an average over the distribution of velocities in the phase space. The equilibrium configurational distribution function for the model is unaltered by the presence of internal viscosity, and is simply given by the Gaussian distribution function for a Rouse chain. The preaveraging approximation entails a replacement of the underlined projection operators in Eq. (6.27) by their average taken with respect to the equilibrium distribution function, which may be evaluated to be $(\boldsymbol{\delta}/3)$ (Doi and Edwards, 1986). The resultant internal friction force is then

$$\boldsymbol{F}_\mu^{(\text{IV}),\text{preav.}} = \left(\frac{K}{3}\right)[\![\dot{\boldsymbol{r}}_{\mu+1} - 2\dot{\boldsymbol{r}}_\mu - \dot{\boldsymbol{r}}_{\mu-1}]\!] \tag{6.28}$$

which is identical to the RIF description of the same force as given by Eq. (6.1). Notably, the use of the preaveraging approximation as a means to make flexible polymer models with internal friction analytically tractable was also suggested by Fixman (1988) several decades ago.

The equation of motion for the momentum-averaged velocity of the jth connector vector in a free-draining bead-spring-dashpot chain may be written as [Chapter 5]

$$[\![\dot{\boldsymbol{Q}}_j]\!] = \boldsymbol{\kappa} \cdot \boldsymbol{Q}_j - \frac{1}{\zeta} \sum_k A_{jk}\left(k_B T \frac{\partial \ln \Psi}{\partial \boldsymbol{Q}_k} + \frac{\partial \phi}{\partial \boldsymbol{Q}_k} + K \frac{\boldsymbol{Q}_k \boldsymbol{Q}_k}{\boldsymbol{Q}_k^2} \cdot [\![\dot{\boldsymbol{Q}}_k]\!]\right) \tag{6.29}$$

where A_{jk} is the Rouse matrix as defined as in Eq. (2.3) of Chapter 2.

Clearly, the equation for the jth connector-vector velocity is coupled to that of its nearest neighbors, which precludes not only the naive substitution of Eq. (6.29) into an equation of continuity in Ψ, but also the derivation of the Fokker-Planck equation and the governing set of stochastic differential equations for the system, for all but the simplest case of a dumbbell ($N = 1$). This velocity coupling is removed using the three-step iterative substitution methodology described in Chapter 5, to obtain the governing set of exact stochastic differential equations for a Rouse chain with fluctuating internal viscosity that are valid both at equilibrium and in the presence of a flow profile. The same methodology is applied here to solve for the governing stochastic differential equations of a Rouse chain with preaveraged internal viscosity.

As detailed in the discussion surrounding Eq. (6.27) in Chapter 6, the preaveraging approximation entails a replacement of the underlined term in Eq. (6.29) by its average evaluated with respect to the equilibrium distribution function of a Rouse chain, which is $(\delta/3)$. Therefore, for a chain with preaveraged internal viscosity, Eq. (6.29) reduces to

$$\llbracket \dot{\boldsymbol{Q}}_j \rrbracket = \boldsymbol{\kappa} \cdot \boldsymbol{Q}_j - \frac{1}{\zeta} \sum_k A_{jk} \left(k_B T \frac{\partial \ln \Psi}{\partial \boldsymbol{Q}_k} + \frac{\partial \phi}{\partial \boldsymbol{Q}_k} + \frac{K}{3} \llbracket \dot{\boldsymbol{Q}}_k \rrbracket \right) \tag{6.30}$$

which may be simplified to give

$$\llbracket \dot{\boldsymbol{Q}}_j \rrbracket = \left(\frac{1}{1+2\theta} \right) (\boldsymbol{\kappa} \cdot \boldsymbol{Q}_k) - \left(\frac{k_B T}{\zeta} \right) \left(\frac{1}{1+2\theta} \right) \left[-\frac{\partial \ln \Psi}{\partial \boldsymbol{Q}_{k-1}} + 2 \frac{\partial \ln \Psi}{\partial \boldsymbol{Q}_k} - \frac{\partial \ln \Psi}{\partial \boldsymbol{Q}_{k+1}} \right]$$
$$- \left(\frac{1}{\zeta} \right) \left(\frac{1}{1+2\theta} \right) \left[-\frac{\partial \phi}{\partial \boldsymbol{Q}_{k-1}} + 2 \frac{\partial \phi}{\partial \boldsymbol{Q}_k} - \frac{\partial \phi}{\partial \boldsymbol{Q}_{k+1}} \right] + \left(\frac{\theta}{1+2\theta} \right) \llbracket \dot{\boldsymbol{Q}}_{j-1} \rrbracket + \left(\frac{\theta}{1+2\theta} \right) \llbracket \dot{\boldsymbol{Q}}_{j+1} \rrbracket \tag{6.31}$$

An ensuing simplicity of the preaveraging approximation is that Eq. (6.31) may directly be subjected to the iterative-substitution-based decoupling methodology, unlike the case with fluctuations where the expression for $C_k \equiv \boldsymbol{Q}_k \cdot \llbracket \dot{\boldsymbol{Q}}_k \rrbracket / Q_k^2$ must first be decoupled before obtaining the desired expression for $\llbracket \dot{\boldsymbol{Q}}_k \rrbracket$.

Firstly, in the forward substitution step, the expression for $\llbracket \dot{\boldsymbol{Q}}_j \rrbracket$ is substituted into that for $\llbracket \dot{\boldsymbol{Q}}_{j+1} \rrbracket$, iteratively, starting from $j = 1$ until $j = (N-1)$. This results in the following general expression,

$$(1 - M_k) \llbracket \dot{\boldsymbol{Q}}_k \rrbracket = \left(\frac{\theta}{1+2\theta} \right) \llbracket \dot{\boldsymbol{Q}}_{k+1} \rrbracket + \left(\frac{1}{1+2\theta} \right) \sum_{l=1}^{k} \Gamma_l^{(k)} (\boldsymbol{\kappa} \cdot \boldsymbol{Q}_l)$$
$$+ (1 - \delta_{kN}) \left(\frac{k_B T}{\zeta} \right) \left(\frac{1}{1+2\theta} \right) \left(\frac{\partial \ln \Psi}{\partial \boldsymbol{Q}_{k+1}} \right) + (1 - \delta_{kN}) \left(\frac{1}{\zeta} \right) \left(\frac{1}{1+2\theta} \right) \left(\frac{\partial \phi}{\partial \boldsymbol{Q}_{k+1}} \right) \tag{6.32}$$
$$- \left(\frac{k_B T}{\zeta} \right) \left(\frac{1}{1+2\theta} \right) \sum_{l=1}^{k} E_l^{(k)} \left(\frac{\partial \ln \Psi}{\partial \boldsymbol{Q}_l} \right) - \left(\frac{1}{\zeta} \right) \left(\frac{1}{1+2\theta} \right) \sum_{l=1}^{k} E_l^{(k)} \left(\frac{\partial \phi}{\partial \boldsymbol{Q}_l} \right)$$

where the explicit dependence of $\llbracket \dot{\boldsymbol{Q}}_k \rrbracket$ on $\llbracket \dot{\boldsymbol{Q}}_{k-1} \rrbracket$ has been removed and the following definitions apply

$$M_k = \left(\frac{\theta}{1+2\theta} \right)^2 \left(\frac{1}{1 - M_{k-1}} \right); \quad \text{with} \quad M_1 = 0 \tag{6.33}$$

$$\Gamma_l^{(k)} = \left(\frac{\theta}{1+2\theta} \right)^{k-l} \prod_{i=l}^{k-1} \left(\frac{1}{1 - M_i} \right) \tag{6.34}$$

$$E_l^{(k)} = 2\Gamma_l^{(k)} - \Gamma_{l-1}^{(k)} - \Gamma_{l+1}^{(k)} \tag{6.35}$$

Next, in the backward substitution step, the expression for $[\![\dot{\mathbf{Q}}_j]\!]$ is substituted into that for $[\![\dot{\mathbf{Q}}_{j-1}]\!]$, iteratively, starting from $j = N$ until $j = 2$. This results in the following general expression,

$$
\begin{aligned}
[\![\dot{\mathbf{Q}}_k]\!] &= \left(\frac{\theta}{1+2\theta}\right)\left(\frac{1}{1-P_k}\right)[\![\dot{\mathbf{Q}}_{k-1}]\!] + \left(\frac{1}{1+2\theta}\right)\sum_{l=k}^{N} \widetilde{\rho}_l^{(k)}\left(\boldsymbol{\kappa}\cdot\mathbf{Q}_l\right) \\
&+ \left(\frac{k_B T}{\zeta}\right)\left(\frac{1}{1+2\theta}\right)\left(\frac{1}{1-P_k}\right)\left(\frac{\partial \ln \Psi}{\partial \mathbf{Q}_{k-1}}\right) + \left(\frac{1}{\zeta}\right)\left(\frac{1}{1+2\theta}\right)\left(\frac{1}{1-P_k}\right)\left(\frac{\partial \phi}{\partial \mathbf{Q}_{k-1}}\right) \\
&- \left(\frac{k_B T}{\zeta}\right)\left(\frac{1}{1+2\theta}\right)\sum_{l=k}^{N} \widetilde{G}_l^{(k)}\left(\frac{\partial \ln \Psi}{\partial \mathbf{Q}_l}\right) - \left(\frac{1}{\zeta}\right)\left(\frac{1}{1+2\theta}\right)\sum_{l=k}^{N} \widetilde{G}_l^{(k)}\left(\frac{\partial \phi}{\partial \mathbf{Q}_l}\right)
\end{aligned}
\tag{6.36}
$$

where the explicit dependence of $[\![\dot{\mathbf{Q}}_k]\!]$ on $[\![\dot{\mathbf{Q}}_{k+1}]\!]$ has been removed and the following definitions apply

$$
P_k = \left(\frac{\theta}{1+2\theta}\right)^2\left(\frac{1}{1-P_{k+1}}\right); \quad \text{with} \quad P_N = 0.
\tag{6.37}
$$

$$
\widetilde{\rho}_l^{(k)} = \left(\frac{\theta}{1+2\theta}\right)^{l-k} \prod_{i=k}^{l}\left(\frac{1}{1-P_i}\right)
\tag{6.38}
$$

The quantity $\widetilde{G}_l^{(k)}$ appearing in Eq. (6.36) is constructed using a slightly elaborate procedure. It is useful to first consider the Rouse matrix, $\mathbf{A}$ [defined as in Eq. (2.3)], of size $\Upsilon \times \Upsilon$, where $\Upsilon = (N-k) + 1$, and the intermediate quantity,

$$
\widetilde{Y}_s^{(k)} = \left(\frac{\theta}{1+2\theta}\right)^{s-1}\left[\prod_{i=k}^{k+s-1}\left(\frac{1}{1-P_i}\right)\right]
\tag{6.39}
$$

which is then used to populate a matrix, $\widehat{\boldsymbol{\Theta}}^{(k)}$, of size $\Upsilon \times \Upsilon$ that has the following structure

$$
\widehat{\boldsymbol{\Theta}}^{(k)} = \begin{pmatrix}
\widetilde{Y}_1^{(k)} & \widetilde{Y}_1^{(k)} & 0 & \cdots & & \\
\widetilde{Y}_2^{(k)} & \widetilde{Y}_2^{(k)} & \widetilde{Y}_2^{(k)} & 0 & \cdots & \\
0 & \widetilde{Y}_3^{(k)} & \widetilde{Y}_3^{(k)} & \widetilde{Y}_3^{(k)} & \cdots & \\
\vdots & \vdots & \vdots & & & \\
0 & 0 & \cdots & & \widetilde{Y}_\Upsilon^{(k)} & \widetilde{Y}_\Upsilon^{(k)}
\end{pmatrix}
\tag{6.40}
$$

We next consider the matrix $\mathbf{Z}^{(k)}$ constructed from $\mathbf{A}$ [see Eq. (2.3)] and $\widehat{\boldsymbol{\Theta}}^{(k)}$, such that $\mathbf{Z}^{(k)} = \mathbf{A}\cdot\widehat{\boldsymbol{\Theta}}^{(k)}$. Now, $\widetilde{G}_{k+m}^{(k)}$ is defined as the $(m+1)^{\text{th}}$ diagonal element of $\mathbf{Z}^{(k)}$. As the final step of the decoupling procedure, a change of variable, $k \to (k+1)$, is performed in Eq. (6.36), and the resulting expression is substituted into the equation derived from the forward substitution step [Eq. (6.32)]. The decoupled expression for $[\![\dot{\mathbf{Q}}_k]\!]$ is finally

obtained as

$$\llbracket\dot{\boldsymbol{Q}}_k\rrbracket = \left(\frac{1}{1+2\theta}\right)\sum_{l=1}^{N}\Lambda_{kl}\left(\boldsymbol{\kappa}\cdot\boldsymbol{Q}_l\right) - \left(\frac{1}{\zeta}\right)\left(\frac{1}{1+2\theta}\right)\sum_{l=1}^{N}J_{kl}\left(\frac{\partial\phi}{\partial\boldsymbol{Q}_l}\right)$$

$$- \left(\frac{k_BT}{\zeta}\right)\left(\frac{1}{1+2\theta}\right)\sum_{l=1}^{N}J_{kl}\left(\frac{\partial\ln\Psi}{\partial\boldsymbol{Q}_l}\right) \tag{6.41}$$

In defining Eqs. (6.34), (6.38), and (6.39), we have adopted the convention $0^0 = 1$, i.e., when $\theta = 0$, $\Gamma_k^{(k)} = \widetilde{\rho}_k^{(k)} = \widetilde{Y}_1^{(k)} = 1$. The matrix elements, Λ_{kl}, and J_{kl}, each of size $N\times N$, are defined as

$$\Lambda_{kl} = \left(\frac{1}{1-M_k-P_k}\right)\widehat{\Lambda}_{kl}; \quad J_{kl} = \left(\frac{1}{1-M_k-P_k}\right)\widehat{J}_{kl} \tag{6.42}$$

with

$$\widehat{\Lambda}_{kl} = \begin{cases} \Gamma_l^{(k)}; & l < k \\[2mm] 1; & l = k \\[2mm] \left(\dfrac{\theta}{1+2\theta}\right)\widetilde{\rho}_l^{(k+1)}; & l > k \end{cases} \tag{6.43}$$

and

$$\widehat{J}_{kl} = \begin{cases} E_l^{(k)}; & l < k \\[3mm] E_l^{(k)} - (1-\delta_{kN})\left(\dfrac{1}{1-P_{k+1}}\right)\left(\dfrac{\theta}{1+2\theta}\right); & l = k \\[3mm] (1-\delta_{kN})\left[\left(\dfrac{\theta}{1+2\theta}\right)\widetilde{G}_l^{(k+1)} - 1\right]; & l = k+1 \\[3mm] \left(\dfrac{\theta}{1+2\theta}\right)\widetilde{G}_l^{(k+1)}; & l > (k+1) \end{cases} \tag{6.44}$$

The procedure for the construction of $\widetilde{G}_l^{(k+1)}$ which appears in Eq. (6.44) is fairly similar to that described in Eq. (6.40) for the construction of $\widetilde{G}_l^{(k)}$, with the only caveat that the size of the block matrices, A and the $\widehat{\Theta}^{(k+1)}$, remain $\Upsilon\times\Upsilon$, where $\Upsilon = (N-k)+1$.

Another point of difference between the preaveraged IV model and the fluctuating IV one is that for the former, the quantities $\{M_k, P_k, \Gamma_l^{(k)}, E_l^{(k)}, \widetilde{\rho}_l^{(k)}, \widetilde{Y}_s^{(k)}, \widetilde{G}_l^{(k)}, \Lambda_{kl}, J_{kl}\}$ are functions only of the internal friction parameter θ, and not dependent on the chain configuration or the flow strength. In the fluctuating IV model, however, these quantities are functions of both the internal friction parameter, and the chain configuration.

As the next step, the expression for $\llbracket\dot{\boldsymbol{Q}}_k\rrbracket$ will be substituted into the equation of continuity, recognizing that the homogeneous flow profile allows one to write the

continuity equation solely in terms of the relative coordinates, $\mathbf{Q}_k$. This means that the distribution function $\Psi(\mathbf{r}_c, \mathbf{Q}_1, \mathbf{Q}_2, ...\mathbf{Q}_N)$ can be replaced by $\psi(\mathbf{Q}_1, \mathbf{Q}_2, ...\mathbf{Q}_N)$, and we have

$$
\begin{aligned}
\frac{\partial \psi}{\partial t} =& -\sum_{k=1}^{N} \frac{\partial}{\partial \mathbf{Q}_k} \cdot \left\{ \llbracket \dot{\mathbf{Q}}_k \rrbracket \psi \right\} \\
=& -\sum_{k=1}^{N} \frac{\partial}{\partial \mathbf{Q}_k} \cdot \left\{ \left[\left(\frac{1}{1+2\theta} \right) \sum_{l=1}^{N} \mathbf{\Lambda}_{kl} \cdot (\boldsymbol{\kappa} \cdot \mathbf{Q}_l) \right. \right. \\
& \left. \left. -\left(\frac{1}{\zeta} \right)\left(\frac{1}{1+2\theta} \right) \sum_{l=1}^{N} \mathbf{J}_{kl} \cdot \left(\frac{\partial \phi}{\partial \mathbf{Q}_l} \right) \right] \psi \right\} \\
& +\left(\frac{k_B T}{\zeta} \right)\left(\frac{1}{1+2\theta} \right) \sum_{k=1}^{N} \sum_{l=1}^{N} \frac{\partial}{\partial \mathbf{Q}_k} \cdot \left[\mathbf{J}_{kl} \cdot \frac{\partial \psi}{\partial \mathbf{Q}_l} \right]
\end{aligned}
\tag{6.45}
$$

where $\mathbf{J}_{kl} = J_{kl}\boldsymbol{\delta}$, and $\mathbf{\Lambda}_{kl} = \Lambda_{kl}\boldsymbol{\delta}$. Since $\mathbf{J}_{kl}$ is composed entirely of constant coefficients that are independent of the stochastic variables $\mathbf{Q}_k$, it is divergence-free, and the noise term may be rewritten, giving the following Fokker-Planck equation

$$
\begin{aligned}
\frac{\partial \psi}{\partial t} =& -\sum_{k=1}^{N} \frac{\partial}{\partial \mathbf{Q}_k} \cdot \left\{ \left[\left(\frac{1}{1+2\theta} \right) \sum_{l=1}^{N} \mathbf{\Lambda}_{kl} \cdot (\boldsymbol{\kappa} \cdot \mathbf{Q}_l) - \left(\frac{1}{\zeta} \right)\left(\frac{1}{1+2\theta} \right) \sum_{l=1}^{N} \mathbf{J}_{kl} \cdot \left(\frac{\partial \phi}{\partial \mathbf{Q}_l} \right) \right] \psi \right\} \\
& +\left(\frac{k_B T}{\zeta} \right)\left(\frac{1}{1+2\theta} \right) \sum_{k=1}^{N} \sum_{l=1}^{N} \frac{\partial}{\partial \mathbf{Q}_k} \frac{\partial}{\partial \mathbf{Q}_l} : [\mathbf{J}_{kl}\psi]
\end{aligned}
\tag{6.46}
$$

where we have implicitly used the fact that $\mathbf{J}_{kl}^T = J_{kl}\boldsymbol{\delta}^T = \mathbf{J}_{kl}$, and note that $J_{kl} = J_{lk}$, and $\Lambda_{kl} = \Lambda_{lk}$. Noting that $\mathbf{F}_l^{(\phi)} \equiv (\partial \phi / \partial \mathbf{Q}_l) = H\mathbf{Q}_l$ for Hookean springs, the stochastic differential equation may be written, using the Itô interpretation (Öttinger, 1996) of Eq. (6.46), as

$$
d\mathbf{Q}_k = \left(\frac{1}{1+2\theta} \right)\left[\sum_{l=1}^{N} \Lambda_{kl}(\boldsymbol{\kappa} \cdot \mathbf{Q}_l) - \left(\frac{H}{\zeta} \right) \sum_{l=1}^{N} J_{kl}\mathbf{Q}_l \right] dt + \sqrt{\frac{2k_B T}{\zeta(1+2\theta)}} \sum_{l=1}^{N} B_{kl}\, d\mathbf{W}_l \tag{6.47}
$$

where $d\mathbf{W}_l$ is three-dimensional Wiener process, and

$$
\sum_{j=1}^{N} B_{kj}B_{lj} = J_{kl} \tag{6.48}
$$

The dimensionless form of Eq. (6.47) is presented as

$$
d\mathbf{Q}_k^* = \left(\frac{1}{1+2\theta} \right)\left[\sum_{l=1}^{N} \Lambda_{kl}(\boldsymbol{\kappa}^* \cdot \mathbf{Q}_l^*) - \left(\frac{1}{4} \right) \sum_{l=1}^{N} J_{kl}\mathbf{Q}_l^* \right] dt^* + \sqrt{\frac{1}{2(1+2\theta)}} \sum_{l=1}^{N} B_{kl}\, d\mathbf{W}_l^*, \tag{6.49}
$$

which is integrated numerically using the simple Euler discretization (Öttinger, 1996) method, with a time-step width of $\Delta t^* = 10^{-3}$. Averages are evaluated over an ensemble of $O(10^5)$ trajectories.

In Fig. 6.4, simulation results at equilibrium and in shear flow, obtained by numerically integrating the stochastic differential equation for the preaveraged IV model using BD simulations (shown as symbols) have been compared against discrete RIF predictions (indicated by lines), for several parameter values. The excellent agreement between the two model predictions establishes their equivalence. Furthermore, the preaveraged treatment predicts that internal friction only affects the time-evolution of the mean-squared end-to-end vector in shear flow, but not its steady-state value which is identical to the standard Rouse model prediction.

6.4   Effect of fluctuations at equilibrium

As the next step, the accuracy of the preaveraging approximation is compared against the exact numerical solution [see Chapter 5] we have derived recently, in which the original non-preaveraged form of the internal friction force given by Eq. (6.27) is used. BD simulations of the Rouse model with fluctuating internal friction were performed with a time-step width of $\Delta t^* = 10^{-3}$. Averages are evaluated over an ensemble of $\approx 10^4 - 10^5$ trajectories.

In Fig. 6.5, the normalized autocorrelation of $\boldsymbol{R}_{\mu\nu}^* \equiv \boldsymbol{r}_\nu^* - \boldsymbol{r}_\mu^*$ in a chain with N_b beads predicted by the discrete RIF model (indicated by lines) is compared against exact BD simulation results of a model with fluctuating internal friction (shown as symbols). The notation $\{\mu, \nu, N_b\}$ uniquely identifies the vector originating at the bead index μ and terminating at ν in a chain of N_b beads. The parameter space specified by $\{\mu, \nu, N_b\}$ may broadly be classified into three topological classes (Des Cloizeaux, 1980; Toan *et al.*, 2008; Samanta *et al.*, 2014; Kumari *et al.*, 2021), and these categories have been considered in Fig. 6.5 (a)-(c). In Fig. 6.5 (a), the end-to-end case is considered, where μ and ν are taken to be the terminal beads in a chain. Fig. 6.5 (b) represents the end-to-interior topology class, where ν is taken to be a terminal bead, and μ is chosen from the interior set of beads, while Fig. 6.5 (c) represents the interior-to-interior case wherein both μ and ν are taken to be interior beads. In all the three cases, the difference between the fluctuating IV model and the preaveraged one is seen to diminish with an increase in $\nu - \mu$, i.e., the number of beads between the μ and ν positions. A similar qualitative trend was observed for other values of φ, and consequently, $\varphi = 3.0$, has been used for all the cases considered in Fig. 6.5. In Fig. 6.5 (d), the root-mean-squared difference (RMSD, Δ) between the two model results are plotted against the bead number μ, at two different values of the interbead separation, $\nu - \mu$. It is observed that the RMSD decreases with an increase in the interbead separation, and is fairly insensitive to the specific choice of the
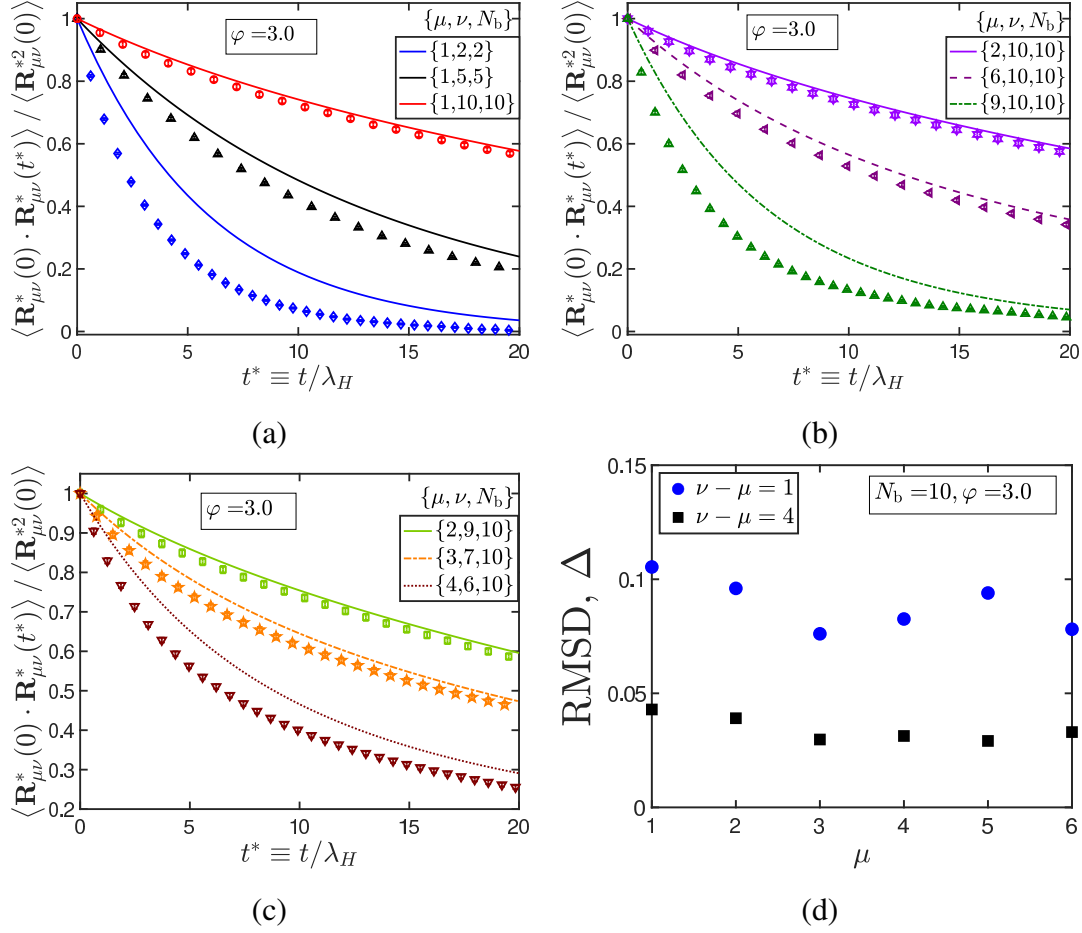
Figure 6.5: Normalized autocorrelation of $\boldsymbol{R}^*_{\mu\nu}$, the vector connecting the μth and ν^{th} bead in a chain with N_{b} beads, for (a) end-to-end, (b) end-to-interior, and (c) interior-to-interior cases. The notation $\{\mu, \nu, N_{\text{b}}\}$ is used to completely specify the vector originating at the bead index μ and terminating at ν in a chain with N_{b} beads. Lines represent preaveraged model results, given by Eq. (6.18). Symbols are BD simulation results on the Rouse model with fluctuating internal friction. An internal friction parameter of $\varphi = 3.0$ has been used for all the cases. Subfigure (d) represents the root-mean-squared difference between the two model results for various values of the interbead separation $\nu - \mu$, quantified as $\Delta = \sqrt{\frac{1}{N_{\text{points}}} \sum_{i=1}^{N_{\text{points}}} \left[y_i^{\text{(BD)}} - y_i^{\text{(analytical)}} \right]^2}$, where $y_i^{\text{(BD/analytical)}}$ refers to the simulation/analytical result at the ith datapoint, with N_{points} the number of time-instances at which the simulation results have been obtained.

bead number μ. This implies that the end-to-interior, and the interior-to-interior topology classes may be considered equivalent with regards to the measured deviation between the preaveraged and fluctuating IV results.

There are two implications to the trend observed in Fig. 6.5: firstly, the preaveraged model is sufficiently accurate for characterizing the bead connector vector correlations of longer segments, as compared to local correlations corresponding to shorter chain segments, and secondly, the preaveraged model may satisfactorily be used for end-to-end vector reconfiguration time calculations provided that a sufficiently fine enough level of discretization (i.e., large enough N_b) is chosen. Note, however, that the choice of N_b is not arbitrary, and its largest permitted value is the number of Kuhn segments in the underlying polymer molecule. For example, the preaveraged IV model (Samanta and Chakrabarti, 2016; Soranno *et al.*, 2017, 2018) has been used for studying internal friction effects in the sixty-seven amino-acid residue cold shock protein at various concentrations of the denaturant, guanindinium chloride (GdmCl). The protein has a Kuhn segment length of about five residues at 6M GdmCl, which implies that the number of Kuhn segments in the molecule, and consequently the finest level of discretization, N_b, is $(67/5) \approx 13$. From Fig. 6.5, it would appear that at such values of N_b, the use of the preaveraged IV model for the calculation of the reconfiguration time would be justified for an internal friction parameter of $\varphi = 3.0$. The discrepancy between the two model predictions, however, is expected to increase with the internal friction parameter. Furthermore, internal friction has also been observed in a synthetic tryptophan cage molecule (Qiu *et al.*, 2002; Qiu and Hagen, 2004a) with twenty-residues, whose Kuhn segment length has not been reported, and it would appear that fluctuations in internal friction should be included for modeling such small molecules, given the constraint on the level of discretization.

6.5   Effect of fluctuations in shear flow

In Fig. 6.6, the normalized, steady-state mean-squared end-to-end distance of a chain in simple shear flow is plotted as a function of the dimensionless shear rate. The lines, which represent the preaveraged model results, coincide with the simple Rouse model predictions implying that the steady-shear values are unaffected by the internal friction parameter, as also evident from Fig. (6.4) (b). The model with fluctuating internal friction, however, predicts that the extension in shear-flow is a function of the internal friction parameter.

There exist no prior studies of the viscometric functions predicted by the Rouse model with preaveraged internal friction. We have derived an expression for the stress
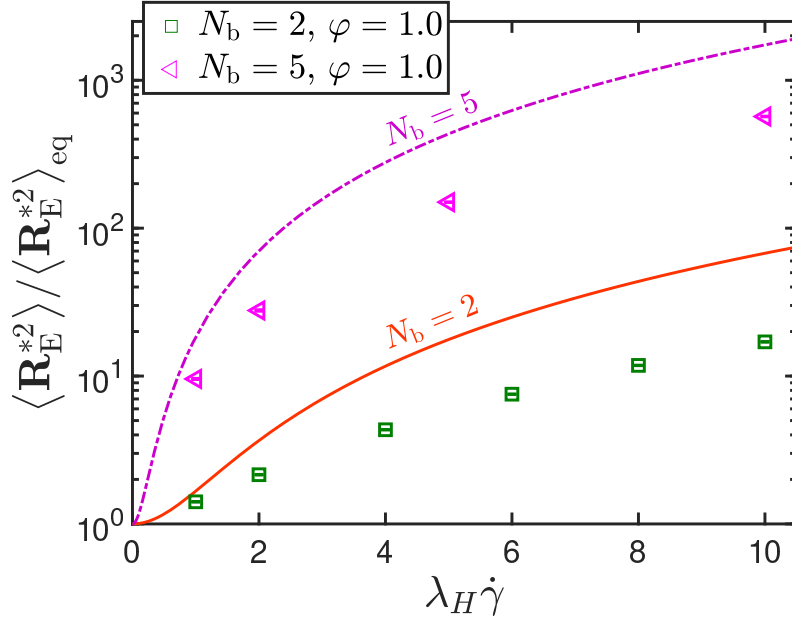
Figure 6.6:   Normalized steady-state mean-squared distance as a function of dimensionless shear rate for chains in shear flow. Lines correspond to preaveraged model results given by Eq. (6.26). Symbols are BD simulation results on the Rouse model with fluctuating internal friction.

tensor [see Section E.2.3 in Appendix E for details] by using the Giesekus formula (Bird *et al.*, 1987b), since this choice has been shown to lead to thermodynamically consistent results for models with fluctuating IV (Schieber and Öttinger, 1994). An analytical expression for the time-evolution of the shear viscosity may be obtained, using normal-mode analysis, as follows

$$\frac{\eta_{\mathrm{p}}(t^*)}{n_{\mathrm{p}} k_B T \lambda_H} = \left(\frac{1}{1+2\theta}\right) \sum_{m,n,q=1}^{N} \Pi_{mq} \mathcal{L}_{mn} \Pi_{nq} I_q(t^*) + 2\,\mathrm{tr}\left[C - \frac{1}{1+2\theta}\mathcal{S}\right]; \qquad (6.50)$$

with

$$I_q(t^*) = 2\left(\frac{\widetilde{b}_q}{\widetilde{a}_q}\right)\left\{1 - \exp\left[-\left(\frac{\widetilde{a}_q}{1+2\theta}\right)\frac{t^*}{2}\right]\right\} \qquad (6.51)$$

where C denotes the Kramers matrix (Bird *et al.*, 1987b), $\mathcal{L} = J \cdot C$, $\mathcal{S} = \Lambda \cdot C$, and $\widetilde{a}_q$ and $\widetilde{b}_q$ represent the eigenvalues of J and Λ, respectively. The matrix Π diagonalizes J, as $\sum_{l,n=1}^{N} \Pi_{lj} J_{ln} \Pi_{nk} = \widetilde{a}_j \delta_{jk}$. The validity of Eq. (6.50) has been established by comparison against BD simulations on the model with preaveraged IV, as shown in Fig. E.2 of Appendix E. An important rheological consequence of internal friction is the appearance of a discontinuous, shear-rate-independent, jump in viscosity at the inception of flow (Manke and Williams, 1988; Hua and Schieber, 1995), as discussed in Chapter 4. This phenomenon, called "stress jump" is not predicted by other bead-spring-

(a)

(b)

(c)
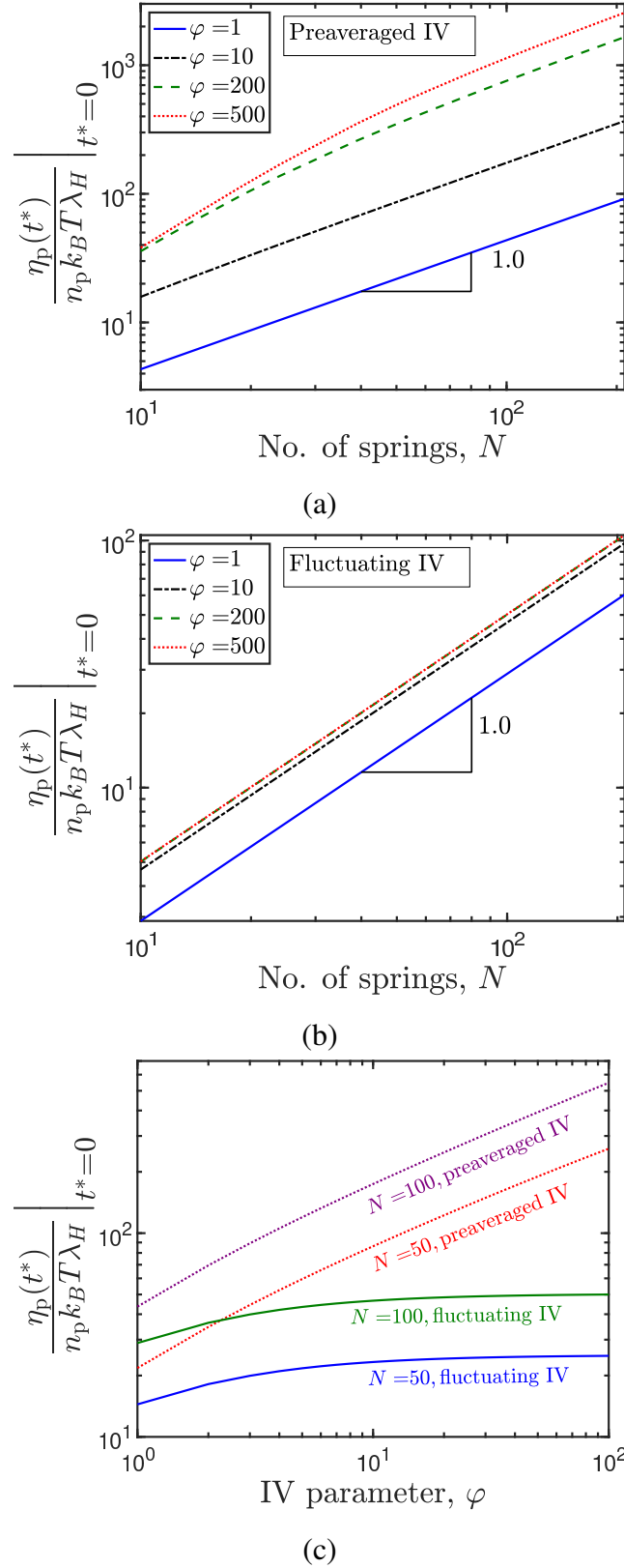
Figure 6.7: Stress jump as a function of chain length for (a) preaveraged IV and (b) fluctuating IV models. In (c) the stress jump is plotted as a function of the internal friction parameter, for two different chain lengths. Preaveraged model results are given by Eq. (6.52), while the fluctuating IV predictions are obtained using the semi-analytical approximation given by Manke and Williams (1988).

chain models. The stress jump predicted by the preaveraged IV model is given by

$$\left.\frac{\eta_{\mathrm{p}}(t^*)}{n_{\mathrm{p}}k_BT\lambda_H}\right|_{t^*=0} = 2\operatorname{tr}\left[C - \frac{1}{1+2\theta}\mathcal{S}\right] \tag{6.52}$$

which follows from Eq. (6.50) upon recognizing that the function $I_q(t^*)$ in Eq. (6.51) vanishes as $t^* \to 0$.

In Fig. 6.7, the stress jumps predicted by the preaveraged and the fluctuating IV models are plotted as a function of the chain lengths and the internal friction parameter. A semi-analytical approximation for the stress jump in Rouse chains with fluctuating IV has been derived by Manke and Williams (1988), and compares excellently against exact BD simulation results [see Figure 5.6 in Chapter 5], with the accuracy of the approximation observed to improve with an increase in the number of beads. This approximate solution has therefore been used to plot Fig. 6.7 (b). From Figs. 6.7 (a) and 6.7 (b), it is observed that while the fluctuating IV model predicts that the stress jump scales linearly with the chain length for values of the internal friction parameter spanning two orders of magnitude, a similar linear dependence in the preaveraged model predictions is pushed to larger values of the number of springs, N, as the internal friction parameter is increased. From Fig. 6.7 (c), it is observed that for a given value of the internal friction parameter, φ, and chain length, the stress jump predicted by the fluctuating IV model is lower than that predicted by the preaveraged model. Furthermore, for a given value of the chain length, the stress jump predicted by the fluctuating IV model saturates with an increase in the internal friction parameter. No such saturation, however, is predicted by the preaveraged IV model.

In Fig. 6.8, the transient evolution of shear-viscosity for models with preaveraged and fluctuating IV are compared for a five-bead chain. As seen from Fig. 6.8 (a), at a fixed value of the shear rate, there is a qualitative difference in the transient evolution of viscosity as predicted by the two models for two different values of the internal friction parameter. In Fig. 6.8 (b), the transient response is plotted for a fixed value of the internal friction parameter and two different shear rates. The preaveraged model prediction is independent of the shear rate, and grows monotonously, while the viscosity predicted by the model with fluctuations is shear-rate-dependent, going through a local maximum for larger shear rates, as seen clearly for the $\lambda_H\dot{\gamma} = 20.0$ case.

Furthermore, in the long-time limit, the preaveraged IV model predicts a shear-rate independent, constant value of the viscosity, equal to the Rouse viscosity for a given chain length, independent of the internal friction parameter. As seen from Fig. 5.11 of Chapter 5, however, Rouse chains with fluctuating IV exhibit a shear-thinning followed by a shear-thickening of the steady-state viscosity with respect to the shear rate, with
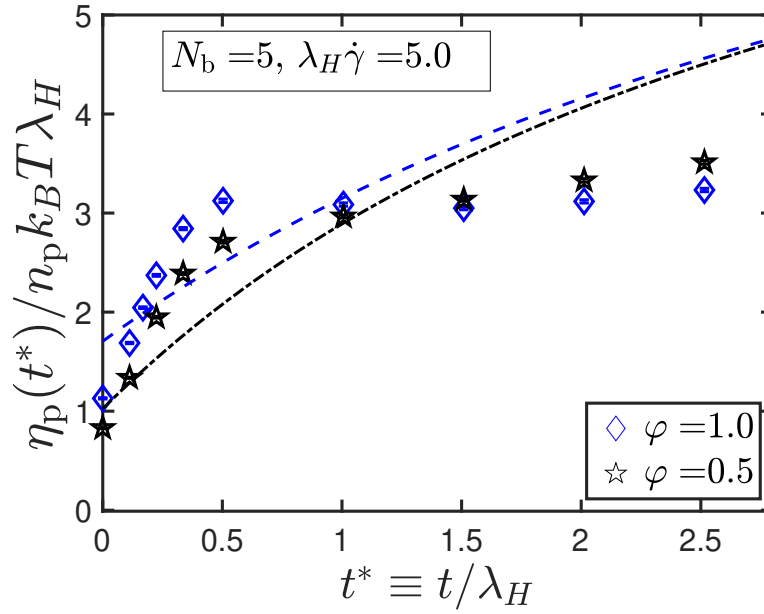
(a)
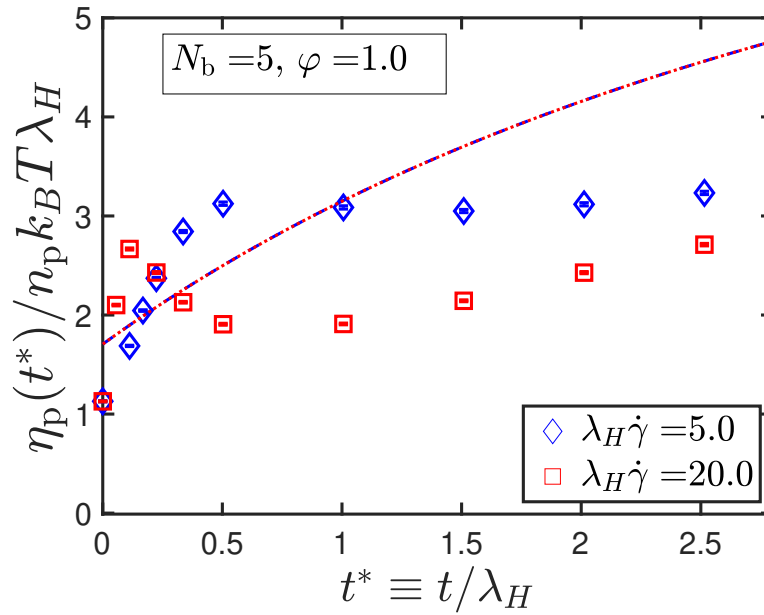
(b)

Figure 6.8: The effect of (a) internal friction parameter, and (b) shear rate on the time evolution of the dimensionless shear viscosity for a five-bead Rouse chain with internal friction. Lines correspond to preaveraged model predictions given by Eq. (6.50). Symbols are BD simulation results on the Rouse model with fluctuating internal friction.
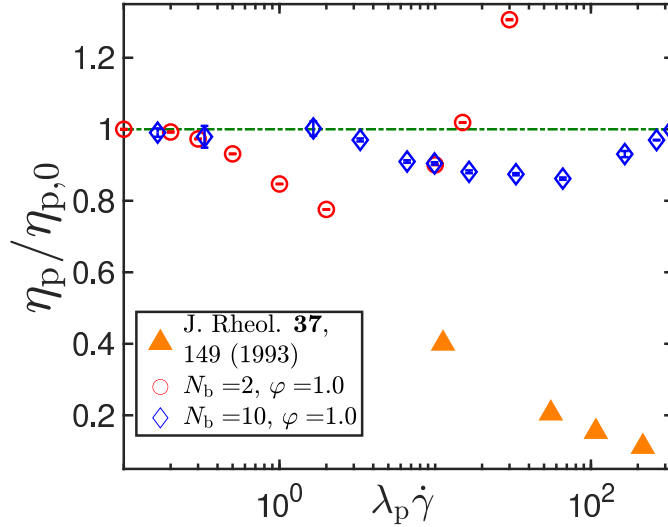
Figure 6.9: Steady-shear viscosity as a function of the dimensionless shear rate. The broken horizontal line corresponds to the preaveraged model result [Eq. (E.69) with $t^* \to \infty$]. Hollow symbols are BD simulation results on the Rouse model with fluctuating internal friction. Filled symbols indicate viscosity data for 0.01 wt% xanthan gum solution, taken from the work of Liang and Mackay (1993). Error bars are roughly of the same size or smaller than the symbols used.

the internal friction parameter governing the onset and extent of the observed shear-thickening.

6.6   Comparison with experimental data

There is a dearth of experimental data that attempt to examine the influence of IV on the steady shear rheology of dilute polymer solutions. An exception is the work by Liang and Mackay (1993) who have performed cessation of shear-flow experiments on sem-dilute xanthan gum solutions to specifically identify the elastic and viscous contributions to the total shear stress. Schieber and coworkers (Hua and Schieber, 1995) have previously compared BD simulation results for dumbbell models with IV against Liang and Mackay (1993)'s data. The same data is used here in order to establish the significance of internal friction in capturing the dissipative or viscous contribution to the total stress in the context of the two models considered in this work. In Fig. 6.9, the steady-shear viscosity of Rouse chains with fluctuating internal friction (indicated by hollow symbols) is plotted against the shear rate non-dimensionalized by the timescale obtained from the Rouse zero shear viscosity $\lambda_p = \eta^R / n_p k_B T$. The experimental value of the zero-shear-rate viscosity is used for plotting the Liang and Mackay (1993) data. The preaveraged IV result, indicated by the broken horizontal line, is independent of the internal friction parameter and the shear rate. While Rouse chains with fluctuating IV
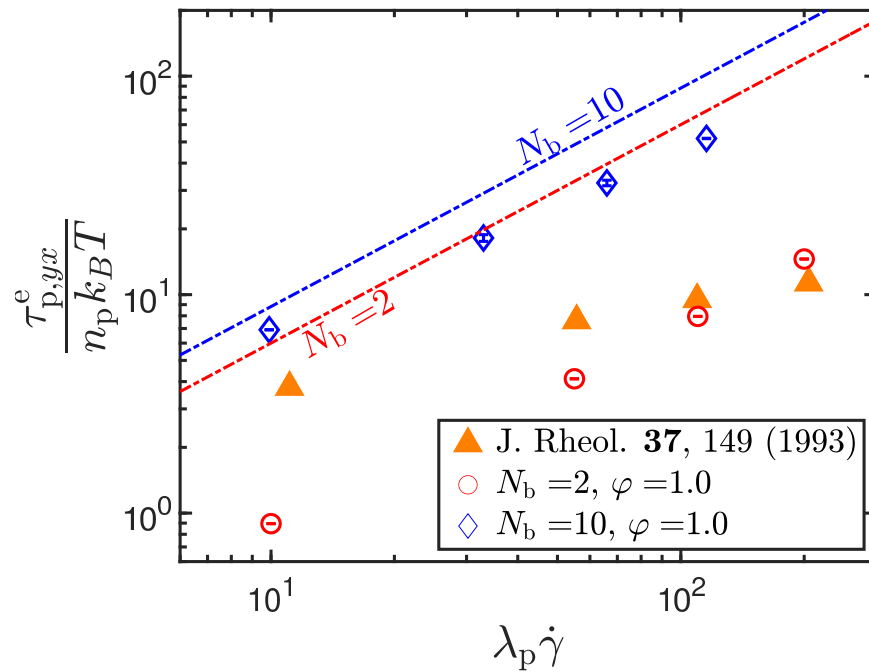
(a)
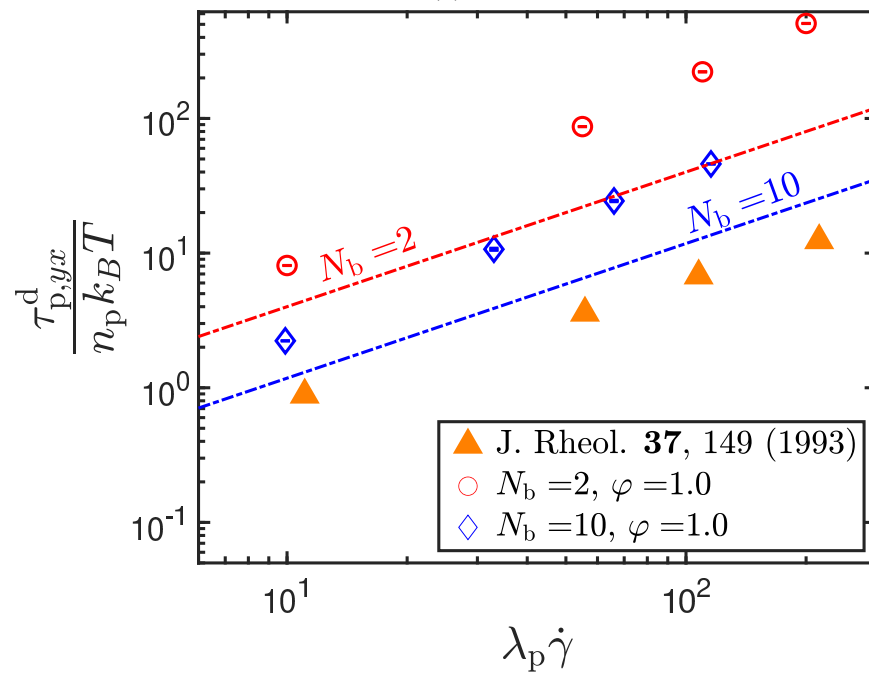
(b)

Figure 6.10: (a) Elastic and (b) viscous components of the steady state stress as a function of the dimensionless shear rate. Lines represent preaveraged IV results [Eq. (E.67) with $t^* \to \infty$]. Hollow symbols are BD simulation results on the Rouse model with fluctuating internal friction. Filled symbols indicate viscosity data for 0.01 wt% xanthan gum solution, taken from the work of Liang and Mackay (1993). Error bars are roughly of the same size or smaller than the symbols used.

display both shear-thinning and thickening, as discussed in greater detail in Kailasham *et al.* (2021b), the xanthan gum solution only exhibits shear-thinning. It is known from Hua and Schieber (1995); Kailasham *et al.* (2018) that the shear-thickening effect may be suppressed by the use of finitely extensible (FE) springs. It is essential that other nonlinear effects, such as excluded volume (EV) and hydrodynamic interactions (HI) are considered, before qualitative or quantitative agreement can be obtained with experiments (Sunthar and Prakash, 2005; Sasmal *et al.*, 2017; Prakash, 2019). The effect of interchain interactions would also need to be accounted for before comparison with semi-dilute solution data. The development of molecular models that account for all these phenomena is still work in progress.

In Fig. 6.10, the elastic and viscous contributions to the steady-state stress are plotted as a function of the dimensionless shear rate. The value of the internal friction parameter for xanthan gum solution is unknown, and we use $\varphi = 1$ for the purposes of a qualitative comparison of predictions with experiments. The filled symbols are obtained from cessation of shear-flow experiments (Liang and Mackay, 1993), while the hollow symbols and broken lines represent the fluctuating and preaveraged IV results, respectively. While polymer models with rigid connectors also predict a dissipative contribution to the total stress, the inclusion of internal friction is essential for capturing the viscous component of the total stress in flexible chain models. As discussed above, agreement with experimental data cannot be expected by including the physics of internal friction alone. Nevertheless, the existence of a viscous contribution to the shear stress demonstrates the importance of accounting for IV.

6.7   Conclusions

The results of this chapter clearly indicate that fluctuations significantly affect the dynamics of polymer molecules away from equilibrium. While a majority of experiments and simulations (Wensley *et al.*, 2010; Soranno *et al.*, 2012; Schulz *et al.*, 2012; Cheng *et al.*, 2013; Ameseder *et al.*, 2018) over the last two decades on understanding the effects of internal friction on biomolecule dynamics have focused on equilibrium measurements, such as reconfiguration and folding times, the effect of this phenomenon on the probability distribution of polymer extensions in coil-stretch transitions during turbulent flow has recently garnered attention (Vincenzi, 2021). We anticipate that the present work will provide a theoretical framework for discerning the effects of internal friction in out-of-equilibrium systems. The results of this chapter have been written up as a manuscript, and is available in Kailasham *et al.* (2021a).

Quantitative comparisons against experiments would require the incorporation of hydrodynamic interaction effects (Sasmal *et al.*, 2017; Prakash, 2019). However, the solution of coarse-grained models which account for fluctuations in both internal viscosity and hydrodynamic interactions (with more than two beads), have additional challenges, as discussed in Chapter 5, that have not been addressed so far.

Chapter 7

Conclusions and Future Work

7.1 Conclusions

The broad objective of this work has been the theoretical and computational investigation of the effects of internal friction on the dynamics of polymer solutions, using Brownian dynamics simulations of bead-spring-dashpot models. The following is a brief list of the key contributions of this thesis:

1. The existence of two types of internal friction—wet and dry—is revisited, and a simple protocol is proposed (Chapter 3) for distinguishing between the two types and extracting the appropriate internal friction coefficient. The scheme requires repeatedly stretching a polymer molecule and measuring the average work dissipated in the process by applying the Jarzynski equality. The internal friction coefficient is then estimated from the average dissipated work in the extrapolated limit of zero solvent viscosity.

2. A detailed characterization of the rheological consequences of internal friction and hydrodynamic interactions in a finitely extensible dumbbell model is provided (Chapter 4), examining the effects of these nonlinear phenomena on the stress relaxation modulus at equilibrium, and on the transient and steady-state material functions in the presence of simple shear flow.

3. The conventional machinery for the numerical solution of bead-spring-chain models is not readily applicable to systems with internal friction, due to a coupling between the connector vector velocities. We have proposed a method (Chapter 5) to overcome this inadequacy, by expanding the scope of an existing decoupling methodology (Manke and Williams, 1988), and obtained exact rheological predictions for linear viscoelastic properties and steady-shear material functions.

165

We have validated our algorithm by comparison against available approximate solutions in the linear viscoelastic regime. Steady-shear viscometric predictions for models with internal viscosity were hitherto unavailable for chains with greater than two beads, and are presented here for the first time, to the best of our knowledge.

4. The effects of internal friction on polymer dynamics have been observed in both biophysical and rheological contexts. The most commonly used theoretical framework for the interpretation of internal friction effects in the biological context is the Rouse model with internal friction (RIF) (Khatri and McLeish, 2007), while rheological investigations have relied on the polymer-kinetic-theory (PKT) based approach. We have established (Chapter 6) a formal connection between these two treatments of internal friction, by showing that the RIF model is essentially a preaveraged treatment of the internal friction force appearing in the PKT-based approach. While the preaveraged and the fluctuating IV models predict intrachain autocorrelations that approach each other for long enough chain segments, they differ in their predictions for shorter segments. Furthermore, the two models differ qualitatively in their predictions for the chain extension and viscosity in shear flow, which is taken to represent a prototypical out-of-equilibrium condition.

The choice of the resolution level for the modeling of internal friction would ultimately be decided by the amount of information that is needed. For example, investigations into the molecular origins of internal friction (de Sancho *et al.*, 2014; Zheng *et al.*, 2018), or the correlation between the magnitude of the internal friction coefficient and parameters on an atomistic scale (Schulz *et al.*, 2015b) would necessitate the use of highly resolved models that accurately specify the energetics of the various intramolecular interactions and solvent friction. On the other hand, the effect of internal friction on a large length/time-scale property such as the viscosity may be studied using coarse-grained models of the type discussed in this thesis, and an estimate of the internal friction parameter can be obtained using the protocol described in Chapter 3.

The ideas of wet and dry internal friction are briefly reviewed below, in order to chiefly emphasize the connection between internal friction effects observed in experiments/all-atom simulations and coarse-grained, micromechanical models of the type described in Chapter 2 of this thesis.

Netz and coworkers Schulz *et al.* (2015b) have studied the force-induced unfolding of α-helices and β-hairpins using all-atom, explicit solvent molecular dynamics (MD) simulations, with equilibration performed in an NPT ensemble, and production runs in an NVT ensemble. This represents the highest level of resolution possible in the classical

(Newtonian) sense, one that does not invoke quantum mechanical degrees of freedom. In order to meaningfully define a free energy, they have identified the protein being pulled as the "system", and the solvent molecules as the "bath". The free-energy change associated with taking the protein from its initial state to a final stretched state is defined as the quasi-static work to be done on the system for realizing this change. At faster than quasi-static pulling rates, the work expended in the process is greater than the free-energy difference, and the difference is defined as the dissipation associated with the process. This dissipation is hypothesized to have two sources: one arising from having to pull the protein through the bath of solvent molecules, and the other being resistive elements from within the protein itself. Under identical solvent conditions, it is found that the work dissipated in stretching a protein correlates with the number of intramolecular hydrogen bonds ruptured in the process. By repeating the pulling in solvents of varying viscosity (realized by changing the mass of the solvent molecules Schulz *et al.* (2012)), and extrapolating to the $\eta_s \to 0$ limit, it is possible to extract an internal friction coefficient for the protein molecule under investigation. Central to this exercise for finding the internal friction coefficient is the heuristic assumption about the additive coupling between the friction contributions from the solvent and the molecule. Coarse-grained simulations for modeling such systems would be well-served by the use of the spring-dashpot model, since it is known that there is a finite source of dissipation over and above that due to the solvent viscosity. This type of internal friction has been classified to be of the "dry" type, and is consistently non-zero, independent of the solvent viscosity, at both the levels of resolution considered.

Soranno *et al.* (2012) find, based on reconfiguration/folding time studies on a cold shock protein, that the internal friction in the molecule is of the dry type and argue that this is due to the exclusion of the solvent from the regions of the protein that contribute to internal friction.

On the other hand, Soranno *et al.* (2012) highlight the study by Waldauer *et al.* (2010) to explain wet internal friction. Waldauer *et al.* (2010) have experimentally studied the intramolecular contact formation in the B1 domain of protein L, and find that the rate of contact formation is 500 times slower than under high concentrations of denaturant, which affirms the presence of internal friction. On a plot of the contact formation time against the solvent viscosity, however, the extrapolated value of the contact formation time in the $\eta_s \to 0$ limit is zero within experimental error, which is a signature of wet internal friction. Soranno *et al.* (2012) suggest that the occurrence of wet internal friction is due to the complete solvation of the chemical groups on the protein responsible for internal friction. Building upon the work of Alexander-Katz *et al.* (2009), we show

in Chapter 3 that wet internal friction can be faithfully incorporated in coarse-grained models by the inclusion of cohesive, non-bonded interactions. This treatment results in the occurrence of a friction component that is larger than the solvent contribution at finite values of the solvent viscosity, and one that vanishes in the $\eta_s \to 0$ limit.

From the above discussion, it is clear that the choice of dashpots or cohesive interactions for modeling internal friction effects depends on the nature of the internal friction present in the molecule (dry/wet). It is quite possible for a polymer to possess both wet and dry internal friction simultaneously, and such molecules may be modeled by bead-spring-dashpot chains with cohesive forces and hydrodynamic interactions. The development of a single-chain model that simultaneously accounts for internal friction, excluded volume, and hydrodynamic interaction effects remains work in progress.

7.2 Future Work

A few directions in which the current work may be taken further are listed below.

1. As discussed in Chapter 5, in coarse-grained models with more than two beads, and which account for fluctuations in both internal viscosity and hydrodynamic interactions, there is a one-to-all coupling between the connector vector velocities, which precludes the use of the decoupling machinery proposed by Manke and Williams (1988). The development of an alternate decoupling methodology would expand the predictive capabilities of the current model, since quantitative comparisons against experiments would require the incorporation of hydrodynamic interaction effects (Sasmal *et al.*, 2017; Prakash, 2019).

2. In Chapter 3, the protocol for the measurement of dry internal friction considered a single-mode spring-dashpot subjected to constant velocity pulling, and it was shown through analytical calculations and simulations that the work dissipated in the zero-solvent-viscosity limit is linearly related to the damping coefficient of the dashpot, as

$$\langle W_{\text{dis}} \rangle_{\eta_s \to 0} = K \, v d \tag{7.1}$$

For a bead-spring-dashpot chain whose all springs have the Hookean spring constant H and dashpots have an associated damping coefficient K subjected to similar treatment, as shown in Fig. 7.1, one might anticipate a relationship similar to Eq. 7.1 for the dissipation, with the single-mode damping coefficient replaced by an effective internal friction coefficient, K_{eff}, but it is not immediately obvious how this effective coefficient is related to the damping coefficient of the individual dashpots
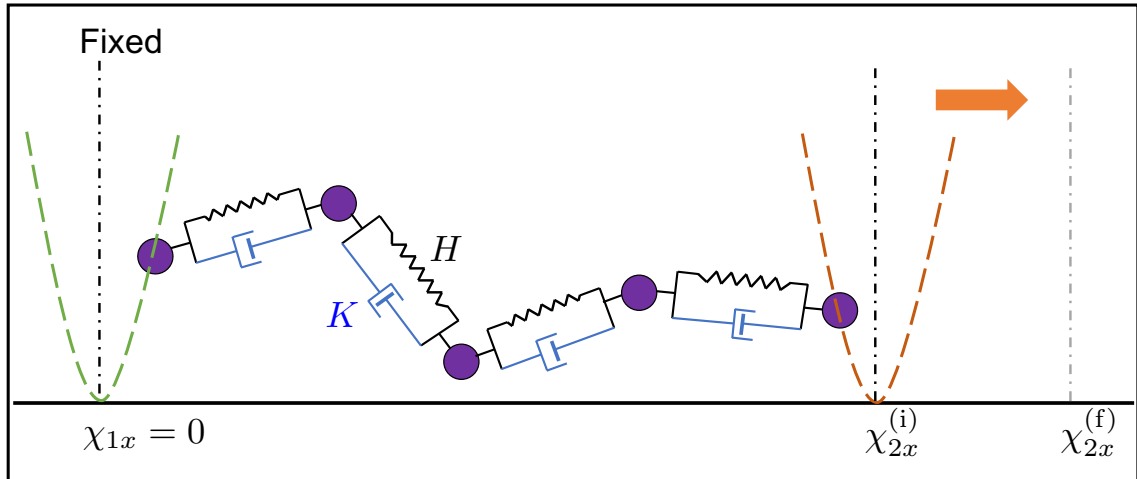
Figure 7.1: Proposed schematic for pulling simulations on a bead-spring-dashpot chain.

and the number of beads in the chain. In other words, if the effective internal friction coefficient is represented as $K_{\text{eff}} = \mathcal{F}(K, N_{\text{b}})$, it is presently known that for $N_{\text{b}} = 2$, $K_{\text{eff}} = \mathcal{F}(K, 2) = K$, but the functional form of $\mathcal{F}(\cdots)$ is unknown for the general case of $N_{\text{b}} > 2$. A knowledge of this relationship would permit a greater flexibility in the comparisons against experimental data on the dissipation observed in single-molecule stretching, since it would specify the choice of the damping coefficient value for a given level of discretization (N_{b}), and a fixed value of the effective internal friction coefficient. It is possible that a combination of analytical calculations on a one-dimensional model and BD simulations as discussed in Chapter 3 may be used to answer this question. The governing equations for a bead-spring-dashpot chain subjected to pulling would first have to be derived.

3. In the bead-spring-dashpot model considered in this work, an identical value of the damping coefficient is chosen for all the dashpots in the chain, in line with the common practice in the literature. Studies have revealed the influence of internal friction on the dynamics of chromatin (Poirier and Marko, 2002; Socol *et al.*, 2019), which has been shown to form topologically associated domains (Lesage *et al.*, 2019; Kumari *et al.*, 2020, 2021). Depending on their spatial compactness, it is probable that the different domains might have different values of internal friction. A coarse-grained representation of the polymer, therefore, would perhaps be better served by the incorporation of "heterogeneous internal friction", by allowing for a different damping coefficient (say K_1, K_2, $\cdots$) for each dashpot in the chain.

4. Brownian   dynamics   simulations   on   chains   with   hydrodynamic interactions[see Prabhakar and Prakash (2004),   Jendrejack *et al.* (2000), for

example] commonly employ Fixman's suggestion (Fixman, 1986) for the evaluation of the noise term in the governing stochastic differential equation, by using a Chebyshev polynomial expansion to calculate the square root of the diffusion matrix. The number of Chebyshev polynomials required in the expansion depends on the ratio of the maximum eigenvalue of the diffusion tensor to its minimum value. Analytical estimates for the eigenvalues of the diffusion tensor of the Zimm model (preaveraged HI) are available in Thurston and Morrison (1969); Kröger *et al.* (2000). An extension of the Fixman (1986) method for calculating the noise term for chains with fluctuating internal friction would be simplified if the maximum and minimum eigenvalues of the diffusion tensor are known. To the best of our knowledge, analytical estimates are not available. In this regard, Figure D.6 in Appendix D presents an interesting observation. The smallest eigenvalue of the diffusion tensor, for a hundred different initial configurations of a forty-five-spring chain, is found to be a constant that depends only on the internal friction parameter. It therefore appears plausible that the extremal eigenvalues of the diffusion tensor may be calculated analytically. Even though Figure 5.2 in Chapter 5 suggests that the total simulation time for chains with fluctuating internal friction remains largely unaffected if the noise term calculation is turned off, implying that using the Fixman (1986) method for the noise-term calculation would not translate to a significant computational advantage, a careful investigation into the spectral properties of the diffusion tensor in systems with internal friction still appears interesting.

Appendices

Appendix A

Derivation of Fokker-Planck and stochastic differential equations for a FENE dumbbell with IV and HI

A force balance on the νth bead of a multi-bead chain with internal viscosity, hydrodynamic interactions, and a FENE spring can be written as follows,

$$\boldsymbol{F} = m\mathbf{a} = \boldsymbol{F}_\nu^{(h)} + \boldsymbol{F}_\nu^{(b)} + \boldsymbol{F}_\nu^{(c)} \tag{A.1}$$

where $\boldsymbol{F}_\nu^{(h)}$ is the hydrodynamic force, $\boldsymbol{F}_\nu^{(b)}$ is the Brownian force, and $\boldsymbol{F}_\nu^{(c)}$ is the force due to the spring-dashpot system for any arbitrary spring force. Expressions for each of these forces are given in Bird *et al.* (1987b) On substituting the expressions, and neglecting the masses of the beads, the force balance can be recast as

$$-\zeta\left[[\![\dot{\boldsymbol{r}}_\nu]\!] - \boldsymbol{v}_0 - \boldsymbol{\kappa}\cdot\boldsymbol{r}_\nu + \sum_\mu \boldsymbol{\Omega}_{\nu\mu}\cdot\boldsymbol{F}_\mu^{(h)}\right] - k_BT\frac{\partial\ln\psi}{\partial\boldsymbol{r}_\nu} - \frac{\partial\phi}{\partial\boldsymbol{r}_\nu}$$

$$+ K\left(\frac{(\boldsymbol{r}_{\nu+1} - \boldsymbol{r}_\nu)(\boldsymbol{r}_{\nu+1} - \boldsymbol{r}_\nu)}{|\boldsymbol{r}_{\nu+1} - \boldsymbol{r}_\nu|^2}\right)\cdot[\![\dot{\boldsymbol{r}}_{\nu+1} - \dot{\boldsymbol{r}}_\nu]\!] \tag{A.2}$$

$$- K\left(\frac{(\boldsymbol{r}_\nu - \boldsymbol{r}_{\nu-1})(\boldsymbol{r}_\nu - \boldsymbol{r}_{\nu-1})}{|\boldsymbol{r}_\nu - \boldsymbol{r}_{\nu-1}|^2}\right)\cdot[\![\dot{\boldsymbol{r}}_\nu - \dot{\boldsymbol{r}}_{\nu-1}]\!] = 0$$

where $\phi \equiv \phi_{\text{FENE}}^{\text{S}}$ [as defined in Eq. 2.10] throughout this appendix.

For a dumbbell, the time-rate of change of the position vectors of the two beads can then be written as

$$[\![\dot{\boldsymbol{r}}_1]\!] = \boldsymbol{v}_0 + \boldsymbol{\kappa}\cdot\boldsymbol{r}_1 + \boldsymbol{\Omega}\cdot\left(-k_BT\frac{\partial\ln\psi}{\partial\boldsymbol{r}_2} - \frac{\partial\phi}{\partial\boldsymbol{r}_2} - K\frac{\boldsymbol{QQ}}{Q^2}\cdot[\![\dot{\boldsymbol{Q}}]\!]\right)$$

$$- \frac{k_BT}{\zeta}\frac{\partial\ln\psi}{\partial\boldsymbol{r}_1} - \frac{1}{\zeta}\frac{\partial\phi}{\partial\boldsymbol{r}_1} + \frac{\epsilon}{2}\frac{\boldsymbol{QQ}}{Q^2}\cdot[\![\dot{\boldsymbol{Q}}]\!] \tag{A.3}$$

and

$$\llbracket \dot{r}_2 \rrbracket = v_0 + \kappa \cdot r_2 + \Omega \cdot \left(-k_B T \frac{\partial \ln \psi}{\partial r_1} - \frac{\partial \phi}{\partial r_1} + K \frac{QQ}{Q^2} \cdot \llbracket \dot{Q} \rrbracket \right)$$

$$- \frac{k_B T}{\zeta} \frac{\partial \ln \psi}{\partial r_2} - \frac{1}{\zeta} \frac{\partial \phi}{\partial r_2} - \frac{\epsilon}{2} \frac{QQ}{Q^2} \cdot \llbracket \dot{Q} \rrbracket \tag{A.4}$$

Subtracting Eq. (A.4) from Eq. (A.3) yields the following equation for the time-rate of change of the connector vector, $\llbracket \dot{Q} \rrbracket$,

$$\llbracket \dot{Q} \rrbracket = [\kappa \cdot Q] - \frac{2k_B T}{\zeta} (\delta - \zeta \Omega) \cdot \frac{\partial}{\partial Q} \ln \psi - \frac{2}{\zeta} (\delta - \zeta \Omega) \cdot \frac{\partial \phi}{\partial Q} - \epsilon (\delta - \zeta \Omega) \cdot \frac{QQ}{Q^2} \cdot \llbracket \dot{Q} \rrbracket \tag{A.5}$$

Grouping together the terms containing $\llbracket \dot{Q} \rrbracket$, the equation can be rewritten as

$$\llbracket \dot{Q} \rrbracket = \left[\delta + \epsilon \beta \frac{QQ}{Q^2} \right]^{-1} \cdot \left([\kappa \cdot Q] - \frac{2k_B T}{\zeta} (\delta - \zeta \Omega) \cdot \frac{\partial}{\partial Q} \ln \psi - \frac{2}{\zeta} (\delta - \zeta \Omega) \cdot \frac{\partial \phi}{\partial Q} \right) \tag{A.6}$$

One can find the inverse of the first bracketed term on the RHS of Eq. (A.6) analytically with the Sherman-Morrison formula (Press *et al.*, 2007), which states that for a matrix $\mathbb{Z}$ whose inverse $\mathbb{Z}^{-1}$ is known,

$$[\mathbb{Z} + uv]^{-1} = \mathbb{Z}^{-1} - \frac{(\mathbb{Z}^{-1} \cdot u)(\mathbb{Z}^{-1} \cdot v)}{1 + v \cdot \mathbb{Z}^{-1} \cdot u} \tag{A.7}$$

where u and v are vectors. Identifying δ as $\mathbb{Z}$, $\sqrt{\epsilon \beta} (Q/Q)$ as u, and $\sqrt{\epsilon \beta} (Q/Q)$ as v, we get

$$\left[\delta + \epsilon \beta \frac{QQ}{Q^2} \right]^{-1} = \delta - \frac{\epsilon \beta}{\epsilon \beta + 1} \frac{QQ}{Q^2} \tag{A.8}$$

Once the inverse has been found in this manner, the equation for $\llbracket \dot{Q} \rrbracket$ can be written as shown in Eq. (4.1) of Chapter 4. Substituting the expression for the time-rate of change of the connector vector into the equation of continuity yields the appropriate Fokker-Planck equation for the system, as given by Eq. (4.2). The dimensionless form of the same has been given in Eq. (4.4).

Using Itô's interpretation, any Fokker-Planck equation of the following form

$$\frac{\partial \psi}{\partial t} = -\frac{\partial}{\partial Q} \cdot (a\psi) + \frac{1}{2} \frac{\partial}{\partial Q} \frac{\partial}{\partial Q} : [D\psi] \tag{A.9}$$

has its equivalent SDE (Öttinger, 1996) given by

$$dQ = a \, dt + b \cdot dW_t \tag{A.10}$$

where W_t is a Wiener process and $b \cdot b^T = D$. Invoking the identity given in Equation D.38 of Appendix D, the second term on the RHS of Eq. (4.4) can be written as

$$\frac{1}{2} \frac{\partial}{\partial Q^*} \cdot \left\{ \left[\left(\delta - \frac{\epsilon \beta^*}{\epsilon \beta^* + 1} \frac{Q^* Q^*}{Q^{*2}} \right) \cdot (\delta - \zeta \Omega) \right] \cdot \frac{\partial \psi^*}{\partial Q^*} \right\}$$

$$= \frac{1}{2} \frac{\partial}{\partial Q^*} \frac{\partial}{\partial Q^*} : \left[\left(\delta - \frac{\epsilon \beta^*}{\epsilon \beta^* + 1} \frac{Q^* Q^*}{Q^{*2}} \right) \cdot (\delta - \zeta \Omega) \psi^* \right] - \frac{\partial}{\partial Q^*} \cdot \left[\frac{g_2}{2} \frac{Q^*}{Q^*} \psi^* \right] \tag{A.11}$$
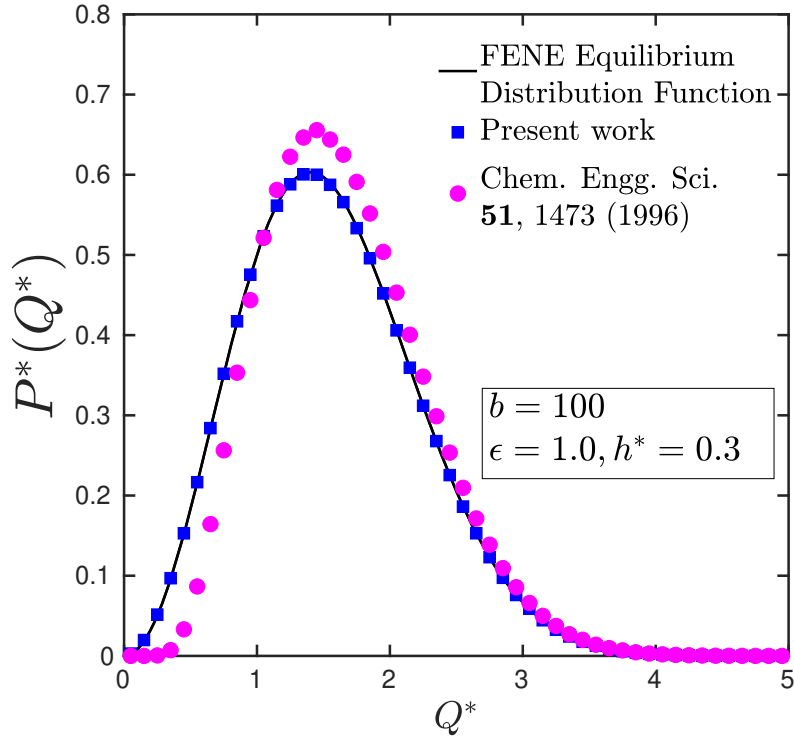
Figure A.1: Probability distribution of Q^*, the dimensionless length of the connector vector. Solid line corresponds to the analytical function given by Eq. (A.14) for $b = 100$. Error bars are smaller than symbol size.

With the above conversion, the Fokker-Planck can be rewritten in a form that is amenable for applying the Itô interpretation, as shown below,

$$\frac{\partial \psi^*}{\partial t^*} = -\frac{\partial}{\partial \boldsymbol{Q}^*} \cdot \left\{ \frac{g_2}{2} \frac{\boldsymbol{Q}^*}{Q^*} + \left(\boldsymbol{\delta} - \frac{\epsilon\beta^*}{\epsilon\beta^* + 1} \frac{\boldsymbol{Q}^*\boldsymbol{Q}^*}{Q^{*2}} \right) \cdot \left(\boldsymbol{\kappa}^* \cdot \boldsymbol{Q}^* - (\boldsymbol{\delta} - \zeta\boldsymbol{\Omega}) \cdot \frac{\frac{1}{2}\boldsymbol{Q}^*}{1 - Q^{*2}/b} \right) \psi^* \right\}$$

$$+ \frac{1}{4} \frac{\partial}{\partial \boldsymbol{Q}^*} \frac{\partial}{\partial \boldsymbol{Q}^*} : \left[\left(\boldsymbol{\delta} - \frac{\epsilon\beta^*}{\epsilon\beta^* + 1} \frac{\boldsymbol{Q}^*\boldsymbol{Q}^*}{Q^{*2}} \right) \cdot (\boldsymbol{\delta} - \zeta\boldsymbol{\Omega}) \psi^* \right]$$

$$(A.12)$$

The SDE corresponding to this Fokker-Planck equation has been given in Eq. (4.6), and has the same functional form, irrespective of whether the hydrodynamic interaction tensor is described using the RPY expression or the Regularized Oseen Burgers expression. Though the SDE obtained in this work is identical to the one derived by Hua and Schieber (1996) , the definition of g_2 [see Eq. 4.8 in Chapter 4] in our work is different from that obtained in theirs. Since it is known that IV and HI do not affect the equilibrium probability distribution of the dumbbell configurations, we can test the correctness of the SDE by comparing the probability distribution of the lengths of the connector vector obtained from simulations against its analytically known expression for FENE dumbbells.

The equilibrium configurational distribution function for an ensemble of FENE dumbbells has the following form (Hua and Schieber, 1995),

$$\psi_{\text{eq}}^*(\boldsymbol{Q}^*) = \frac{1}{J_{\text{eq}}^*}\left(1 - \frac{Q^{*2}}{b}\right)^{b/2} \tag{A.13}$$

where $J_{\text{eq}}^* = 2\pi b^{3/2} B(3/2, ((b+2)/2))$. By averaging over the orientations of the dumbbells in spherical coordinates, the probability distribution of the *lengths* of the connector vector can be obtained as

$$P^*(Q^*) = 4\pi Q^{*2}\psi_{\text{eq}}^*(\boldsymbol{Q}^*) \tag{A.14}$$

In Fig. A.1, the probability distribution generated by our code and that which results when the SDE from the work by Hua and Schieber (1996) is used, are plotted alongside the function given by Eq. (A.14) for $b = 100$. The good agreement between the simulation results obtained by our code with the analytical result establishes the validity of our SDE.

Appendix B

Illustration of the iterative forward and backward substitution procedures

In this appendix, the first few iterations of the forward and backward substitution steps for obtaining the decoupled equation for the connector vector velocity in a freely-draining bead-spring-dashpot chain are presented. The generating equation is given below, reproduced from Equation (5.6) of Chapter 5.

$$
\begin{aligned}
C_k = \frac{\boldsymbol{Q}_k \cdot [\![\dot{\boldsymbol{Q}}_k]\!]}{Q_k^2} = {} & \left(\frac{\zeta}{\zeta + 2K}\right)\left(\frac{\boldsymbol{Q}_k}{Q_k^2}\right) \cdot (\boldsymbol{\kappa} \cdot \boldsymbol{Q}_k) - \left(\frac{k_B T}{\zeta + 2K}\right)\left(\frac{\boldsymbol{Q}_k}{Q_k^2}\right) \cdot \left[-\frac{\partial \ln \Psi}{\partial \boldsymbol{Q}_{k-1}} + 2\frac{\partial \ln \Psi}{\partial \boldsymbol{Q}_k}\right. \\
& \left. -\frac{\partial \ln \Psi}{\partial \boldsymbol{Q}_{k+1}}\right] - \left(\frac{1}{\zeta + 2K}\right)\left(\frac{\boldsymbol{Q}_k}{Q_k^2}\right) \cdot \left[-\frac{\partial \phi}{\partial \boldsymbol{Q}_{k-1}} + 2\frac{\partial \phi}{\partial \boldsymbol{Q}_k} - \frac{\partial \phi}{\partial \boldsymbol{Q}_{k+1}}\right] \\
& + \left(\frac{K}{\zeta + 2K}\right)\left[C_{k-1} L_{k-1}\left(\frac{Q_{k-1}}{Q_k}\right) + C_{k+1} L_k\left(\frac{Q_{k+1}}{Q_k}\right)\right]
\end{aligned}
\tag{B.1}
$$

where

$$
L_k \equiv \cos \theta_k = \frac{\boldsymbol{Q}_k \cdot \boldsymbol{Q}_{k+1}}{Q_k Q_{k+1}}
\tag{B.2}
$$

and $\phi \equiv \phi_{\text{HK}}^{\text{S}}$ [as defined in Eq. 2.9] throughout this appendix. Eq. (B.1) is then subjected to forward and backward substitution schema to obtain a decoupled expression for C_k.

B.1 Sample iterations from the forward substitution step

In the forward substitution scheme, the equation for C_k is plugged in to that for C_{k+1}, starting with $k = 1$. The step is illustrated for a series of k values, as shown below.

Forward substitution expression for $k = 1$:

From Eq. (B.1), we have

$$
C_1 = \left(\frac{\zeta}{\zeta + 2K}\right)\left(\frac{\boldsymbol{Q}_1}{Q_1^2}\right) \cdot (\boldsymbol{\kappa} \cdot \boldsymbol{Q}_1) - \left(\frac{k_B T}{\zeta + 2K}\right)\left(\frac{\boldsymbol{Q}_1}{Q_1^2}\right) \cdot \left[2\frac{\partial \ln \Psi}{\partial \boldsymbol{Q}_1} - \frac{\partial \ln \Psi}{\partial \boldsymbol{Q}_2}\right] \tag{B.3}
$$

$$
- \left(\frac{1}{\zeta + 2K}\right)\left(\frac{\boldsymbol{Q}_1}{Q_1^2}\right) \cdot \left[2\frac{\partial \phi}{\partial \boldsymbol{Q}_1} - \frac{\partial \phi}{\partial \boldsymbol{Q}_2}\right] + \left(\frac{K}{\zeta + 2K}\right)\left[C_2 L_1\left(\frac{Q_2}{Q_1}\right)\right]
$$

which may be recast as

$$
C_1 = \left(\frac{\zeta}{\zeta + 2K}\right)\left(\frac{\boldsymbol{Q}_1}{Q_1^2}\right) \cdot (\boldsymbol{\kappa} \cdot \boldsymbol{Q}_1) + \left(\frac{K}{\zeta + 2K}\right)\left[C_2 L_1\left(\frac{Q_2}{Q_1}\right)\right] \tag{B.4}
$$

$$
+ \left(\frac{k_B T}{\zeta + 2K}\right)\left(\frac{1}{Q_1}\right)\left(\frac{\boldsymbol{Q}_1}{Q_1}\right) \cdot \left[\frac{\partial \ln \Psi}{\partial \boldsymbol{Q}_2}\right] + \left(\frac{1}{\zeta + 2K}\right)\left(\frac{1}{Q_1}\right)\left(\frac{\boldsymbol{Q}_1}{Q_1}\right) \cdot \left[\frac{\partial \phi}{\partial \boldsymbol{Q}_2}\right]
$$

$$
- \left(\frac{k_B T}{\zeta + 2K}\right)\left(\frac{2}{Q_1}\right)\left(\frac{\boldsymbol{Q}_1}{Q_1}\right) \cdot \left[\frac{\partial \ln \Psi}{\partial \boldsymbol{Q}_1}\right] - \left(\frac{1}{\zeta + 2K}\right)\left(\frac{2}{Q_1}\right)\left(\frac{\boldsymbol{Q}_1}{Q_1}\right) \cdot \left[\frac{\partial \phi}{\partial \boldsymbol{Q}_1}\right]
$$

Forward substitution expression for $k = 2$:

From Eq. (B.1), we have

$$
C_2 = \left(\frac{\zeta}{\zeta + 2K}\right)\left(\frac{\boldsymbol{Q}_2}{Q_2^2}\right) \cdot (\boldsymbol{\kappa} \cdot \boldsymbol{Q}_2) - \left(\frac{k_B T}{\zeta + 2K}\right)\left(\frac{\boldsymbol{Q}_2}{Q_2^2}\right) \cdot \left[-\frac{\partial \ln \Psi}{\partial \boldsymbol{Q}_1} + 2\frac{\partial \ln \Psi}{\partial \boldsymbol{Q}_2} - \frac{\partial \ln \Psi}{\partial \boldsymbol{Q}_3}\right]
$$

$$
- \left(\frac{1}{\zeta + 2K}\right)\left(\frac{\boldsymbol{Q}_2}{Q_2^2}\right) \cdot \left[-\frac{\partial \phi}{\partial \boldsymbol{Q}_1} + 2\frac{\partial \phi}{\partial \boldsymbol{Q}_2} - \frac{\partial \phi}{\partial \boldsymbol{Q}_3}\right] \tag{B.5}
$$

$$
+ \left(\frac{K}{\zeta + 2K}\right)\left[C_1 L_1\left(\frac{Q_1}{Q_2}\right) + C_3 L_2\left(\frac{Q_3}{Q_2}\right)\right]
$$

Multiplying Eq. (B.3) by $L_1(Q_1/Q_2)$, we obtain

$$
C_1 L_1\left(\frac{Q_1}{Q_2}\right) = L_1\left(\frac{\zeta}{\zeta + 2K}\right)\left(\frac{1}{Q_2}\right)\left(\frac{\boldsymbol{Q}_1}{Q_1}\right) \cdot (\boldsymbol{\kappa} \cdot \boldsymbol{Q}_1) - \left(\frac{k_B T}{\zeta + 2K}\right)\left(\frac{L_1}{Q_2}\right)\left(\frac{\boldsymbol{Q}_1}{Q_1}\right) \cdot \left[2\frac{\partial \ln \Psi}{\partial \boldsymbol{Q}_1} - \frac{\partial \ln \Psi}{\partial \boldsymbol{Q}_2}\right]
$$

$$
- \left(\frac{1}{\zeta + 2K}\right)\left(\frac{L_1}{Q_2}\right)\left(\frac{\boldsymbol{Q}_1}{Q_1}\right) \cdot \left[2\frac{\partial \phi}{\partial \boldsymbol{Q}_1} - \frac{\partial \phi}{\partial \boldsymbol{Q}_2}\right] + \left(\frac{K}{\zeta + 2K}\right)C_2 L_1^2 \tag{B.6}
$$

Substituting Eq. (B.6) into Eq. (B.5),

$$C_2 = \left(\frac{K}{\zeta + 2K}\right) C_3 L_2 \left(\frac{Q_3}{Q_2}\right) + \left(\frac{\zeta}{\zeta + 2K}\right)\left(\frac{\boldsymbol{Q}_2}{Q_2^2}\right) \cdot (\boldsymbol{\kappa} \cdot \boldsymbol{Q}_2)$$

$$+ \left(\frac{k_B T}{\zeta + 2K}\right)\left(\frac{\boldsymbol{Q}_2}{Q_2^2}\right) \cdot \left[\frac{\partial \ln \Psi}{\partial \boldsymbol{Q}_1}\right] - 2\left(\frac{k_B T}{\zeta + 2K}\right)\left(\frac{\boldsymbol{Q}_2}{Q_2^2}\right) \cdot \left[\frac{\partial \ln \Psi}{\partial \boldsymbol{Q}_2}\right] + \left(\frac{k_B T}{\zeta + 2K}\right)\left(\frac{\boldsymbol{Q}_2}{Q_2^2}\right) \cdot \left[\frac{\partial \ln \Psi}{\partial \boldsymbol{Q}_3}\right]$$

$$+ \left(\frac{1}{\zeta + 2K}\right)\left(\frac{\boldsymbol{Q}_2}{Q_2^2}\right) \cdot \left[\frac{\partial \phi}{\partial \boldsymbol{Q}_1}\right] - 2\left(\frac{1}{\zeta + 2K}\right)\left(\frac{\boldsymbol{Q}_2}{Q_2^2}\right) \cdot \left[\frac{\partial \phi}{\partial \boldsymbol{Q}_2}\right] + \left(\frac{1}{\zeta + 2K}\right)\left(\frac{\boldsymbol{Q}_2}{Q_2^2}\right) \cdot \left[\frac{\partial \phi}{\partial \boldsymbol{Q}_3}\right]$$

$$+ \left(\frac{K}{\zeta + 2K}\right)^2 C_2 L_1^2 \tag{B.7}$$

$$+ L_1 \left(\frac{K}{\zeta + 2K}\right)\left(\frac{\zeta}{\zeta + 2K}\right)\left(\frac{1}{Q_2}\right)\left(\frac{\boldsymbol{Q}_1}{Q_1}\right) \cdot (\boldsymbol{\kappa} \cdot \boldsymbol{Q}_1)$$

$$+ \left(\frac{K}{\zeta + 2K}\right)\left\{\left(\frac{k_B T}{\zeta + 2K}\right)\left(\frac{L_1}{Q_2}\right)\left(\frac{\boldsymbol{Q}_1}{Q_1}\right) \cdot \left[\frac{\partial \ln \Psi}{\partial \boldsymbol{Q}_2}\right] - 2\left(\frac{k_B T}{\zeta + 2K}\right)\left(\frac{L_1}{Q_2}\right)\left(\frac{\boldsymbol{Q}_1}{Q_1}\right) \cdot \left[\frac{\partial \ln \Psi}{\partial \boldsymbol{Q}_1}\right]\right.$$

$$+ \left(\frac{1}{\zeta + 2K}\right)\left(\frac{L_1}{Q_2}\right)\left(\frac{\boldsymbol{Q}_1}{Q_1}\right) \cdot \left[\frac{\partial \phi}{\partial \boldsymbol{Q}_2}\right] - 2\left(\frac{1}{\zeta + 2K}\right)\left(\frac{L_1}{Q_2}\right)\left(\frac{\boldsymbol{Q}_1}{Q_1}\right) \cdot \left[\frac{\partial \phi}{\partial \boldsymbol{Q}_1}\right]\right\}$$

Defining

$$M_2 = \left(\frac{K}{\zeta + 2K}\right)^2 L_1^2 \tag{B.8}$$

and grouping like terms together,

$$C_2 (1 - M_2) = \left(\frac{K}{\zeta + 2K}\right) C_3 L_2 \left(\frac{Q_3}{Q_2}\right) \tag{B.9}$$

$$+ \left(\frac{\zeta}{\zeta + 2K}\right)\left(\frac{1}{Q_2}\right)\left[\left(\frac{\boldsymbol{Q}_2}{Q_2}\right) \cdot (\boldsymbol{\kappa} \cdot \boldsymbol{Q}_2) + L_1 \left(\frac{K}{\zeta + 2K}\right)\left(\frac{K}{\zeta + 2K}\right)\left(\frac{\boldsymbol{Q}_1}{Q_1}\right) \cdot (\boldsymbol{\kappa} \cdot \boldsymbol{Q}_1)\right]$$

$$+ \left(\frac{k_B T}{\zeta + 2K}\right)\left(\frac{\boldsymbol{Q}_2}{Q_2^2}\right) \cdot \left[\frac{\partial \ln \Psi}{\partial \boldsymbol{Q}_3}\right] + \left(\frac{1}{\zeta + 2K}\right)\left(\frac{\boldsymbol{Q}_2}{Q_2^2}\right) \cdot \left[\frac{\partial \phi}{\partial \boldsymbol{Q}_3}\right]$$

$$- \left(\frac{k_B T}{\zeta + 2K}\right)\left(\frac{1}{Q_2}\right)\left[-\left(\frac{K}{\zeta + 2K}\right) L_1 \left(\frac{\boldsymbol{Q}_1}{Q_1}\right) + 2\left(\frac{\boldsymbol{Q}_2}{Q_2}\right)\right] \cdot \left(\frac{\partial \ln \Psi}{\partial \boldsymbol{Q}_2}\right)$$

$$- \left(\frac{k_B T}{\zeta + 2K}\right)\left(\frac{1}{Q_2}\right)\left[2\left(\frac{K}{\zeta + 2K}\right) L_1 \left(\frac{\boldsymbol{Q}_1}{Q_1}\right) - \left(\frac{\boldsymbol{Q}_2}{Q_2}\right)\right] \cdot \left(\frac{\partial \ln \Psi}{\partial \boldsymbol{Q}_1}\right)$$

$$- \left(\frac{1}{\zeta + 2K}\right)\left(\frac{1}{Q_2}\right)\left[-\left(\frac{K}{\zeta + 2K}\right) L_1 \left(\frac{\boldsymbol{Q}_1}{Q_1}\right) + 2\left(\frac{\boldsymbol{Q}_2}{Q_2}\right)\right] \cdot \left(\frac{\partial \phi}{\partial \boldsymbol{Q}_2}\right)$$

$$- \left(\frac{1}{\zeta + 2K}\right)\left(\frac{1}{Q_2}\right)\left[2\left(\frac{K}{\zeta + 2K}\right) L_1 \left(\frac{\boldsymbol{Q}_1}{Q_1}\right) - \left(\frac{\boldsymbol{Q}_2}{Q_2}\right)\right] \cdot \left(\frac{\partial \phi}{\partial \boldsymbol{Q}_1}\right)$$

It is clear from the underlined terms in Eq. (B.4) and Eq. (B.9) that the coefficients for the spring force and the Brownian force terms are identical. In the forthcoming steps, therefore, only the spring force term shall be indicated for the sake of brevity. Once a general pattern has been identified, the final expression would contain both the Brownian and the spring force terms, multiplied by the same prefactor.

We thus have the following final expression for C_2,

$$
\begin{aligned}
C_2 = {} & \left(\frac{1}{1-M_2}\right)\left(\frac{K}{\zeta+2K}\right)C_3 L_2\left(\frac{Q_3}{Q_2}\right) \\
& + \left(\frac{1}{1-M_2}\right)\left(\frac{\zeta}{\zeta+2K}\right)\left(\frac{1}{Q_2}\right)\left[\left(\frac{\boldsymbol{Q}_2}{Q_2}\right)\cdot(\boldsymbol{\kappa}\cdot\boldsymbol{Q}_2)+L_1\left(\frac{\boldsymbol{Q}_1}{Q_1}\right)\cdot(\boldsymbol{\kappa}\cdot\boldsymbol{Q}_1)\right] \\
& + \left(\frac{1}{1-M_2}\right)\left(\frac{1}{\zeta+2K}\right)\left(\frac{\boldsymbol{Q}_2}{Q_2^2}\right)\cdot\left[\frac{\partial\phi}{\partial\boldsymbol{Q}_3}\right] \\
& - \left(\frac{1}{1-M_2}\right)\left(\frac{1}{\zeta+2K}\right)\left(\frac{1}{Q_2}\right)\left[-\left(\frac{K}{\zeta+2K}\right)L_1\left(\frac{\boldsymbol{Q}_1}{Q_1}\right)+2\left(\frac{\boldsymbol{Q}_2}{Q_2}\right)\right]\cdot\left(\frac{\partial\phi}{\partial\boldsymbol{Q}_2}\right) \\
& - \left(\frac{1}{1-M_2}\right)\left(\frac{1}{\zeta+2K}\right)\left(\frac{1}{Q_2}\right)\left[2\left(\frac{K}{\zeta+2K}\right)L_1\left(\frac{\boldsymbol{Q}_1}{Q_1}\right)-\left(\frac{\boldsymbol{Q}_2}{Q_2}\right)\right]\cdot\left(\frac{\partial\phi}{\partial\boldsymbol{Q}_1}\right)
\end{aligned} \tag{B.10}
$$

Forward substitution expression for $k = 3$:

From Eq. (B.1), we have

$$
\begin{aligned}
C_3 = {} & \left(\frac{\zeta}{\zeta+2K}\right)\left(\frac{\boldsymbol{Q}_3}{Q_3^2}\right)\cdot(\boldsymbol{\kappa}\cdot\boldsymbol{Q}_3)-\left(\frac{1}{\zeta+2K}\right)\left(\frac{\boldsymbol{Q}_3}{Q_3^2}\right)\cdot\left[-\frac{\partial\phi}{\partial\boldsymbol{Q}_2}+2\frac{\partial\phi}{\partial\boldsymbol{Q}_3}-\frac{\partial\phi}{\partial\boldsymbol{Q}_4}\right] \\
& + \left(\frac{K}{\zeta+2K}\right)\left[C_2 L_2\left(\frac{Q_2}{Q_3}\right)+C_4 L_3\left(\frac{Q_4}{Q_3}\right)\right]
\end{aligned} \tag{B.11}
$$

Multiplying Eq. (B.10) by $L_2(Q_2/Q_3)$, we obtain

$$
\begin{aligned}
C_2 L_2\left(\frac{Q_2}{Q_3}\right) = {} & \left(\frac{1}{1-M_2}\right)\left(\frac{K}{\zeta+2K}\right)C_3 L_2^2 \\
& + \left(\frac{1}{1-M_2}\right)\left(\frac{\zeta}{\zeta+2K}\right)\left(\frac{L_2}{Q_3}\right)\left[\left(\frac{\boldsymbol{Q}_2}{Q_2}\right)\cdot(\boldsymbol{\kappa}\cdot\boldsymbol{Q}_2)+L_1\left(\frac{K}{\zeta+2K}\right)\left(\frac{\boldsymbol{Q}_1}{Q_1}\right)\cdot(\boldsymbol{\kappa}\cdot\boldsymbol{Q}_1)\right] \\
& + \left(\frac{1}{1-M_2}\right)\left(\frac{1}{\zeta+2K}\right)\left(\frac{L_2}{Q_3}\right)\left(\frac{\boldsymbol{Q}_2}{Q_2}\right)\cdot\left[\frac{\partial\phi}{\partial\boldsymbol{Q}_3}\right] \\
& - \left(\frac{1}{1-M_2}\right)\left(\frac{1}{\zeta+2K}\right)\left(\frac{L_2}{Q_3}\right)\left[-\left(\frac{K}{\zeta+2K}\right)L_1\left(\frac{\boldsymbol{Q}_1}{Q_1}\right)+2\left(\frac{\boldsymbol{Q}_2}{Q_2}\right)\right]\cdot\left(\frac{\partial\phi}{\partial\boldsymbol{Q}_2}\right) \\
& - \left(\frac{1}{1-M_2}\right)\left(\frac{1}{\zeta+2K}\right)\left(\frac{L_2}{Q_3}\right)\left[2\left(\frac{K}{\zeta+2K}\right)L_1\left(\frac{\boldsymbol{Q}_1}{Q_1}\right)-\left(\frac{\boldsymbol{Q}_2}{Q_2}\right)\right]\cdot\left(\frac{\partial\phi}{\partial\boldsymbol{Q}_1}\right)
\end{aligned} \tag{B.12}
$$

Substituting Eq. (B.12) into Eq. (B.11), we obtain

$$
C_3 = \left(\frac{K}{\zeta + 2K}\right) C_4 L_3 \left(\frac{Q_4}{Q_3}\right) + \left(\frac{\zeta}{\zeta + 2K}\right)\left(\frac{\boldsymbol{Q}_3}{Q_3^2}\right) \cdot (\boldsymbol{\kappa} \cdot \boldsymbol{Q}_3) \tag{B.13}
$$

$$
+ \left(\frac{1}{\zeta + 2K}\right)\left(\frac{\boldsymbol{Q}_3}{Q_3^2}\right) \cdot \left(\frac{\partial \phi}{\partial \boldsymbol{Q}_2}\right) - 2\left(\frac{1}{\zeta + 2K}\right)\left(\frac{\boldsymbol{Q}_3}{Q_3^2}\right) \cdot \left(\frac{\partial \phi}{\partial \boldsymbol{Q}_3}\right) + \left(\frac{1}{\zeta + 2K}\right)\left(\frac{\boldsymbol{Q}_3}{Q_3^2}\right) \cdot \left(\frac{\partial \phi}{\partial \boldsymbol{Q}_4}\right)
$$

$$
+ \left(\frac{K}{\zeta + 2K}\right)^2 \left(\frac{1}{1 - M_2}\right) C_3 L_2^2
$$

$$
+ \left(\frac{1}{1 - M_2}\right)\left(\frac{K}{\zeta + 2K}\right)\left(\frac{\zeta}{\zeta + 2K}\right)\left(\frac{L_2}{Q_3}\right)\left[\left(\frac{\boldsymbol{Q}_2}{Q_2}\right) \cdot (\boldsymbol{\kappa} \cdot \boldsymbol{Q}_2) + L_1\left(\frac{K}{\zeta + 2K}\right)\left(\frac{\boldsymbol{Q}_1}{Q_1}\right) \cdot (\boldsymbol{\kappa} \cdot \boldsymbol{Q}_1)\right]
$$

$$
+ \left(\frac{1}{1 - M_2}\right)\left(\frac{K}{\zeta + 2K}\right)\left(\frac{1}{\zeta + 2K}\right)\left(\frac{L_2}{Q_3}\right)\left(\frac{\boldsymbol{Q}_2}{Q_2}\right) \cdot \left[\frac{\partial \phi}{\partial \boldsymbol{Q}_3}\right]
$$

$$
- \left(\frac{1}{1 - M_2}\right)\left(\frac{1}{\zeta + 2K}\right)\left(\frac{L_2}{Q_3}\right)\left[-\left(\frac{K}{\zeta + 2K}\right)^2 L_1\left(\frac{\boldsymbol{Q}_1}{Q_1}\right) + 2\left(\frac{K}{\zeta + 2K}\right)\left(\frac{\boldsymbol{Q}_2}{Q_2}\right)\right] \cdot \left(\frac{\partial \phi}{\partial \boldsymbol{Q}_2}\right)
$$

$$
- \left(\frac{1}{1 - M_2}\right)\left(\frac{1}{\zeta + 2K}\right)\left(\frac{L_2}{Q_3}\right)\left[2\left(\frac{K}{\zeta + 2K}\right)^2 L_1\left(\frac{\boldsymbol{Q}_1}{Q_1}\right) - \left(\frac{K}{\zeta + 2K}\right)\left(\frac{\boldsymbol{Q}_2}{Q_2}\right)\right] \cdot \left(\frac{\partial \phi}{\partial \boldsymbol{Q}_1}\right)
$$

Defining

$$
M_3 = \left(\frac{K}{\zeta + 2K}\right)^2 \left(\frac{1}{1 - M_2}\right) L_2^2 \tag{B.14}
$$

and grouping like terms together,

$$
C_3 (1 - M_3) = \left(\frac{K}{\zeta + 2K}\right) C_4 L_3 \left(\frac{Q_4}{Q_3}\right) \tag{B.15}
$$

$$
+ \left(\frac{\zeta}{\zeta + 2K}\right)\left(\frac{1}{Q_3}\right)\left[\left(\frac{\boldsymbol{Q}_3}{Q_3}\right) \cdot (\boldsymbol{\kappa} \cdot \boldsymbol{Q}_3) + \left(\frac{1}{1 - M_2}\right)\left(\frac{K}{\zeta + 2K}\right) L_2 \left(\frac{\boldsymbol{Q}_2}{Q_2}\right) \cdot (\boldsymbol{\kappa} \cdot \boldsymbol{Q}_2)\right.
$$

$$
\left. + \left(\frac{1}{1 - M_2}\right) L_2 L_1 \left(\frac{K}{\zeta + 2K}\right)^2 \left(\frac{\boldsymbol{Q}_1}{Q_1}\right) \cdot (\boldsymbol{\kappa} \cdot \boldsymbol{Q}_1)\right]
$$

$$
+ \left(\frac{1}{\zeta + 2K}\right)\left(\frac{\boldsymbol{Q}_3}{Q_3^2}\right) \cdot \left(\frac{\partial \phi}{\partial \boldsymbol{Q}_4}\right)
$$

$$
- \left(\frac{1}{\zeta + 2K}\right)\left(\frac{1}{Q_3}\right)\left[-\left(\frac{1}{1 - M_2}\right)\left(\frac{K}{\zeta + 2K}\right) L_2 \left(\frac{\boldsymbol{Q}_2}{Q_2}\right) + 2 \left(\frac{\boldsymbol{Q}_3}{Q_3}\right)\right] \cdot \left(\frac{\partial \phi}{\partial \boldsymbol{Q}_3}\right)
$$

$$
- \left(\frac{1}{\zeta + 2K}\right)\left(\frac{1}{Q_3}\right)\left[-\left(\frac{1}{1 - M_2}\right)\left(\frac{K}{\zeta + 2K}\right)^2 L_2 L_1 \left(\frac{\boldsymbol{Q}_1}{Q_1}\right)\right.
$$

$$
\left. + 2 \left(\frac{1}{1 - M_2}\right)\left(\frac{K}{\zeta + 2K}\right) L_2 \left(\frac{\boldsymbol{Q}_2}{Q_2}\right) - \left(\frac{\boldsymbol{Q}_3}{Q_3}\right)\right] \cdot \left(\frac{\partial \phi}{\partial \boldsymbol{Q}_2}\right)
$$

$$
- \left(\frac{1}{\zeta + 2K}\right)\left(\frac{1}{Q_3}\right)\left[2 \left(\frac{K}{\zeta + 2K}\right)^2 \left(\frac{1}{1 - M_2}\right) L_2 L_1 \left(\frac{\boldsymbol{Q}_1}{Q_1}\right)\right.
$$

$$
\left. - \left(\frac{K}{\zeta + 2K}\right)\left(\frac{1}{1 - M_2}\right) L_2 \left(\frac{\boldsymbol{Q}_2}{Q_2}\right)\right] \cdot \left(\frac{\partial \phi}{\partial \boldsymbol{Q}_1}\right)
$$

We thus have the following final expression for C_3

$$C_3 = \left(\frac{1}{1-M_3}\right)\left(\frac{K}{\zeta+2K}\right)C_4 L_3\left(\frac{Q_4}{Q_3}\right) \tag{B.16}$$

$$+ \left(\frac{\zeta}{\zeta+2K}\right)\left(\frac{1}{Q_3}\right)\left[\left(\frac{1}{1-M_3}\right)\left(\frac{\boldsymbol{Q}_3}{Q_3}\right)\cdot(\boldsymbol{\kappa}\cdot\boldsymbol{Q}_3)\right.$$

$$+ \left(\frac{1}{1-M_3}\right)\left(\frac{1}{1-M_2}\right)\left(\frac{K}{\zeta+2K}\right)L_2\left(\frac{\boldsymbol{Q}_2}{Q_2}\right)\cdot(\boldsymbol{\kappa}\cdot\boldsymbol{Q}_2)$$

$$+ \left(\frac{1}{1-M_3}\right)\left(\frac{1}{1-M_2}\right)\left(\frac{K}{\zeta+2K}\right)^2 L_2 L_1\left(\frac{\boldsymbol{Q}_1}{Q_1}\right)\cdot(\boldsymbol{\kappa}\cdot\boldsymbol{Q}_1)\right]$$

$$+ \left(\frac{1}{\zeta+2K}\right)\left(\frac{\boldsymbol{Q}_3}{Q_3^2}\right)\cdot\left(\frac{\partial\phi}{\partial\boldsymbol{Q}_4}\right)$$

$$- \left(\frac{1}{\zeta+2K}\right)\left(\frac{1}{Q_3}\right)\left[-\left(\frac{1}{1-M_3}\right)\left(\frac{1}{1-M_2}\right)\left(\frac{K}{\zeta+2K}\right)L_2\left(\frac{Q_2}{Q_2}\right)+2\left(\frac{1}{1-M_3}\right)\left(\frac{\boldsymbol{Q}_3}{Q_3}\right)\right]\cdot\left(\frac{\partial\phi}{\partial\boldsymbol{Q}_3}\right)$$

$$- \left(\frac{1}{\zeta+2K}\right)\left(\frac{1}{Q_3}\right)\left[-\left(\frac{1}{1-M_3}\right)\left(\frac{1}{1-M_2}\right)\left(\frac{K}{\zeta+2K}\right)^2 L_2 L_1\left(\frac{Q_1}{Q_1}\right)\right.$$

$$\left. + 2\left(\frac{1}{1-M_3}\right)\left(\frac{1}{1-M_2}\right)\left(\frac{K}{\zeta+2K}\right)L_2\left(\frac{\boldsymbol{Q}_2}{Q_2}\right)-\left(\frac{\boldsymbol{Q}_3}{Q_3}\right)\right]\cdot\left(\frac{\partial\phi}{\partial\boldsymbol{Q}_2}\right)$$

$$- \left(\frac{1}{\zeta+2K}\right)\left(\frac{1}{Q_3}\right)\left[2\left(\frac{K}{\zeta+2K}\right)^2\left(\frac{1}{1-M_3}\right)\left(\frac{1}{1-M_2}\right)L_2 L_1\left(\frac{Q_1}{Q_1}\right)\right.$$

$$\left. - \left(\frac{K}{\zeta+2K}\right)\left(\frac{1}{1-M_3}\right)\left(\frac{1}{1-M_2}\right)L_2\left(\frac{\boldsymbol{Q}_2}{Q_2}\right)\right]\cdot\left(\frac{\partial\phi}{\partial\boldsymbol{Q}_1}\right)$$

Forward substitution expression for $k = 4$:

From Eq. (B.1), we have

$$C_4 = \left(\frac{\zeta}{\zeta+2K}\right)\left(\frac{\boldsymbol{Q}_4}{Q_4^2}\right)\cdot(\boldsymbol{\kappa}\cdot\boldsymbol{Q}_4) - \left(\frac{1}{\zeta+2K}\right)\left(\frac{\boldsymbol{Q}_4}{Q_4^2}\right)\cdot\left[-\frac{\partial\phi}{\partial\boldsymbol{Q}_3}+2\frac{\partial\phi}{\partial\boldsymbol{Q}_4}-\frac{\partial\phi}{\partial\boldsymbol{Q}_5}\right] \tag{B.17}$$

$$+ \left(\frac{K}{\zeta+2K}\right)\left[C_3 L_3\left(\frac{Q_3}{Q_4}\right)+C_5 L_4\left(\frac{Q_5}{Q_4}\right)\right]$$

Multiplying Eq. (B.16) by $L_3 \left(Q_3 / Q_4 \right)$, we obtain

$$
\begin{aligned}
C_3 L_3 \left(\frac{Q_3}{Q_4} \right) &= \left(\frac{1}{1-M_3} \right) \left(\frac{K}{\zeta + 2K} \right) C_4 L_3^2 \\
&+ \left(\frac{\zeta}{\zeta + 2K} \right) \left(\frac{1}{Q_4} \right) \left[\left(\frac{1}{1-M_3} \right) L_3 \left(\frac{\boldsymbol{Q}_3}{Q_3} \right) \cdot (\boldsymbol{\kappa} \cdot \boldsymbol{Q}_3) \right. \\
&+ \left(\frac{1}{1-M_3} \right) \left(\frac{1}{1-M_2} \right) \left(\frac{K}{\zeta + 2K} \right) L_3 L_2 \left(\frac{\boldsymbol{Q}_2}{Q_2} \right) \cdot (\boldsymbol{\kappa} \cdot \boldsymbol{Q}_2) \\
&+ \left(\frac{1}{1-M_3} \right) \left(\frac{1}{1-M_2} \right) \left(\frac{K}{\zeta + 2K} \right)^2 L_3 L_2 L_1 \left(\frac{\boldsymbol{Q}_1}{Q_1} \right) \cdot (\boldsymbol{\kappa} \cdot \boldsymbol{Q}_1) \right] \\
&+ \left(\frac{1}{\zeta + 2K} \right) L_3 \left(\frac{1}{Q_4} \right) \left(\frac{\boldsymbol{Q}_3}{Q_3} \right) \cdot \left(\frac{\partial \phi}{\partial \boldsymbol{Q}_4} \right) \\
&- \left(\frac{1}{\zeta + 2K} \right) \left(\frac{1}{Q_4} \right) \left[- \left(\frac{1}{1-M_3} \right) \left(\frac{1}{1-M_2} \right) \left(\frac{K}{\zeta + 2K} \right) L_3 L_2 \left(\frac{\boldsymbol{Q}_2}{Q_2} \right) \right. \\
&+ 2 \left(\frac{1}{1-M_3} \right) L_3 \left(\frac{\boldsymbol{Q}_3}{Q_3} \right) \right] \cdot \left(\frac{\partial \phi}{\partial \boldsymbol{Q}_3} \right) \\
&- \left(\frac{1}{\zeta + 2K} \right) \left(\frac{1}{Q_4} \right) \left[- \left(\frac{1}{1-M_3} \right) \left(\frac{1}{1-M_2} \right) \left(\frac{K}{\zeta + 2K} \right)^2 L_3 L_2 L_1 \left(\frac{\boldsymbol{Q}_1}{Q_1} \right) \right. \\
&\qquad + 2 \left(\frac{1}{1-M_3} \right) \left(\frac{1}{1-M_2} \right) \left(\frac{K}{\zeta + 2K} \right) L_3 L_2 \left(\frac{\boldsymbol{Q}_2}{Q_2} \right) - L_3 \left(\frac{\boldsymbol{Q}_3}{Q_3} \right) \right] \cdot \left(\frac{\partial \phi}{\partial \boldsymbol{Q}_2} \right) \\
&- \left(\frac{1}{\zeta + 2K} \right) \left(\frac{1}{Q_4} \right) \left[2 \left(\frac{K}{\zeta + 2K} \right)^2 \left(\frac{1}{1-M_3} \right) \left(\frac{1}{1-M_2} \right) L_3 L_2 L_1 \left(\frac{\boldsymbol{Q}_1}{Q_1} \right) \right. \\
&\qquad - \left(\frac{K}{\zeta + 2K} \right) \left(\frac{1}{1-M_3} \right) \left(\frac{1}{1-M_2} \right) L_3 L_2 \left(\frac{\boldsymbol{Q}_2}{Q_2} \right) \right] \cdot \left(\frac{\partial \phi}{\partial \boldsymbol{Q}_1} \right)
\end{aligned}
\tag{B.18}
$$

Substituting Eq. (B.18) into Eq. (B.17), we obtain

$$C_4 = \left(\frac{K}{\zeta + 2K}\right)C_5 L_4 \left(\frac{Q_5}{Q_4}\right) + \left(\frac{\zeta}{\zeta + 2K}\right)\left(\frac{\boldsymbol{Q}_4}{Q_4^2}\right) \cdot (\boldsymbol{\kappa} \cdot \boldsymbol{Q}_4) \tag{B.19}$$

$$+ \left(\frac{1}{\zeta + 2K}\right)\left(\frac{1}{Q_4}\right)\left(\frac{\boldsymbol{Q}_4}{Q_4}\right) \cdot \left(\frac{\partial \phi}{\partial \boldsymbol{Q}_3}\right) - 2\left(\frac{1}{\zeta + 2K}\right)\left(\frac{1}{Q_4}\right)\left(\frac{\boldsymbol{Q}_4}{Q_4}\right) \cdot \left(\frac{\partial \phi}{\partial \boldsymbol{Q}_4}\right)$$

$$+ \left(\frac{1}{\zeta + 2K}\right)\left(\frac{1}{Q_4}\right)\left(\frac{\boldsymbol{Q}_4}{Q_4}\right) \cdot \left(\frac{\partial \phi}{\partial \boldsymbol{Q}_5}\right) + \left(\frac{1}{1 - M_3}\right)\left(\frac{K}{\zeta + 2K}\right)^2 C_4 L_3^2$$

$$+ \left(\frac{\zeta}{\zeta + 2K}\right)\left(\frac{1}{Q_4}\right)\left[\left(\frac{1}{1 - M_3}\right)\left(\frac{K}{\zeta + 2K}\right)L_3 \left(\frac{\boldsymbol{Q}_3}{Q_3}\right) \cdot (\boldsymbol{\kappa} \cdot \boldsymbol{Q}_3)\right.$$

$$+ \left(\frac{1}{1 - M_3}\right)\left(\frac{K}{\zeta + 2K}\right)^2 \left(\frac{1}{1 - M_2}\right)L_3 L_2 \left(\frac{\boldsymbol{Q}_2}{Q_2}\right) \cdot (\boldsymbol{\kappa} \cdot \boldsymbol{Q}_2)$$

$$+ \left(\frac{1}{1 - M_3}\right)\left(\frac{1}{1 - M_2}\right)\left(\frac{K}{\zeta + 2K}\right)^3 L_3 L_2 L_1 \left(\frac{\boldsymbol{Q}_1}{Q_1}\right) \cdot (\boldsymbol{\kappa} \cdot \boldsymbol{Q}_1)\Bigg]$$

$$+ \left(\frac{1}{\zeta + 2K}\right)\left(\frac{K}{\zeta + 2K}\right)L_3 \left(\frac{1}{Q_4}\right)\left(\frac{\boldsymbol{Q}_3}{Q_3}\right) \cdot \left(\frac{\partial \phi}{\partial \boldsymbol{Q}_4}\right)$$

$$- \left(\frac{1}{\zeta + 2K}\right)\left(\frac{1}{Q_4}\right)\left[-\left(\frac{1}{1 - M_3}\right)\left(\frac{1}{1 - M_2}\right)\left(\frac{K}{\zeta + 2K}\right)^2 L_3 L_2 \left(\frac{\boldsymbol{Q}_2}{Q_2}\right)\right.$$

$$+ 2\left(\frac{1}{1 - M_3}\right)\left(\frac{K}{\zeta + 2K}\right)L_3 \left(\frac{\boldsymbol{Q}_3}{Q_3}\right)\Bigg] \cdot \left(\frac{\partial \phi}{\partial \boldsymbol{Q}_3}\right)$$

$$- \left(\frac{1}{\zeta + 2K}\right)\left(\frac{1}{Q_4}\right)\left[-\left(\frac{1}{1 - M_3}\right)\left(\frac{1}{1 - M_2}\right)\left(\frac{K}{\zeta + 2K}\right)^3 L_3 L_2 L_1 \left(\frac{\boldsymbol{Q}_1}{Q_1}\right)\right.$$

$$+ 2\left(\frac{1}{1 - M_3}\right)\left(\frac{1}{1 - M_2}\right)\left(\frac{K}{\zeta + 2K}\right)^2 L_3 L_2 \left(\frac{\boldsymbol{Q}_2}{Q_2}\right) - \left(\frac{K}{\zeta + 2K}\right)L_3 \left(\frac{\boldsymbol{Q}_3}{Q_3}\right)\Bigg] \cdot \left(\frac{\partial \phi}{\partial \boldsymbol{Q}_2}\right)$$

$$- \left(\frac{1}{\zeta + 2K}\right)\left(\frac{1}{Q_4}\right)\left[2\left(\frac{K}{\zeta + 2K}\right)^3 \left(\frac{1}{1 - M_3}\right)\left(\frac{1}{1 - M_2}\right)L_3 L_2 L_1 \left(\frac{\boldsymbol{Q}_1}{Q_1}\right)\right.$$

$$- \left(\frac{K}{\zeta + 2K}\right)^2 \left(\frac{1}{1 - M_3}\right)\left(\frac{1}{1 - M_2}\right)L_3 L_2 \left(\frac{\boldsymbol{Q}_2}{Q_2}\right)\Bigg] \cdot \left(\frac{\partial \phi}{\partial \boldsymbol{Q}_1}\right)$$

Defining

$$M_4 = \left(\frac{1}{1 - M_3}\right)\left(\frac{K}{\zeta + 2K}\right)^2 L_3^2 \tag{B.20}$$

and grouping like terms together, we obtain

$$C_4 (1 - M_4) = \left(\frac{K}{\zeta + 2K}\right) C_5 L_4 \left(\frac{Q_5}{Q_4}\right) \tag{B.21}$$

$$+ \left(\frac{\zeta}{\zeta + 2K}\right)\left(\frac{1}{Q_4}\right)\left[\left(\frac{\boldsymbol{Q}_4}{Q_4}\right) \cdot (\boldsymbol{\kappa} \cdot \boldsymbol{Q}_4) + \left(\frac{1}{1 - M_3}\right)\left(\frac{K}{\zeta + 2K}\right) L_3 \left(\frac{\boldsymbol{Q}_3}{Q_3}\right) \cdot (\boldsymbol{\kappa} \cdot \boldsymbol{Q}_3)\right.$$

$$+ \left(\frac{1}{1 - M_3}\right)\left(\frac{K}{\zeta + 2K}\right)^2 \left(\frac{1}{1 - M_2}\right) L_3 L_2 \left(\frac{\boldsymbol{Q}_2}{Q_2}\right) \cdot (\boldsymbol{\kappa} \cdot \boldsymbol{Q}_2)$$

$$+ \left(\frac{1}{1 - M_3}\right)\left(\frac{1}{1 - M_2}\right)\left(\frac{K}{\zeta + 2K}\right)^3 L_3 L_2 L_1 \left(\frac{\boldsymbol{Q}_1}{Q_1}\right) \cdot (\boldsymbol{\kappa} \cdot \boldsymbol{Q}_1)\right]$$

$$+ \left(\frac{1}{\zeta + 2K}\right)\left(\frac{1}{Q_4}\right)\left(\frac{\boldsymbol{Q}_4}{Q_4}\right) \cdot \left(\frac{\partial \phi}{\partial \boldsymbol{Q}_5}\right)$$

$$- \left(\frac{1}{\zeta + 2K}\right)\left(\frac{1}{Q_4}\right)\left[-\left(\frac{K}{\zeta + 2K}\right) L_3 \left(\frac{\boldsymbol{Q}_3}{Q_3}\right) + 2\left(\frac{\boldsymbol{Q}_4}{Q_4}\right)\right] \cdot \left(\frac{\partial \phi}{\partial \boldsymbol{Q}_4}\right)$$

$$- \left(\frac{1}{\zeta + 2K}\right)\left(\frac{1}{Q_4}\right)\left[-\left(\frac{1}{1 - M_3}\right)\left(\frac{1}{1 - M_2}\right)\left(\frac{K}{\zeta + 2K}\right)^2 L_3 L_2 \left(\frac{\boldsymbol{Q}_2}{Q_2}\right)\right.$$

$$+ 2\left(\frac{1}{1 - M_3}\right)\left(\frac{K}{\zeta + 2K}\right) L_3 \left(\frac{\boldsymbol{Q}_3}{Q_3}\right) - \left(\frac{\boldsymbol{Q}_4}{Q_4}\right)\right] \cdot \left(\frac{\partial \phi}{\partial \boldsymbol{Q}_3}\right)$$

$$- \left(\frac{1}{\zeta + 2K}\right)\left(\frac{1}{Q_4}\right)\left[-\left(\frac{1}{1 - M_3}\right)\left(\frac{1}{1 - M_2}\right)\left(\frac{K}{\zeta + 2K}\right)^3 L_3 L_2 L_1 \left(\frac{\boldsymbol{Q}_1}{Q_1}\right)\right.$$

$$+ 2\left(\frac{1}{1 - M_3}\right)\left(\frac{1}{1 - M_2}\right)\left(\frac{K}{\zeta + 2K}\right)^2 L_3 L_2 \left(\frac{\boldsymbol{Q}_2}{Q_2}\right) - \left(\frac{K}{\zeta + 2K}\right) L_3 \left(\frac{\boldsymbol{Q}_3}{Q_3}\right)\right] \cdot \left(\frac{\partial \phi}{\partial \boldsymbol{Q}_2}\right)$$

$$- \left(\frac{1}{\zeta + 2K}\right)\left(\frac{1}{Q_4}\right)\left[2\left(\frac{K}{\zeta + 2K}\right)^3 \left(\frac{1}{1 - M_3}\right)\left(\frac{1}{1 - M_2}\right) L_3 L_2 L_1 \left(\frac{\boldsymbol{Q}_1}{Q_1}\right)\right.$$

$$\left.- \left(\frac{K}{\zeta + 2K}\right)^2 \left(\frac{1}{1 - M_3}\right)\left(\frac{1}{1 - M_2}\right) L_3 L_2 \left(\frac{\boldsymbol{Q}_2}{Q_2}\right)\right] \cdot \left(\frac{\partial \phi}{\partial \boldsymbol{Q}_1}\right)$$

We thus have the following final expression for C_4

$$C_4 = \left(\frac{1}{1-M_4}\right)\left(\frac{K}{\zeta+2K}\right)C_5 L_4\left(\frac{Q_5}{Q_4}\right) \tag{B.22}$$

$$+\left(\frac{\zeta}{\zeta+2K}\right)\left(\frac{1}{Q_4}\right)\left[\left(\frac{1}{1-M_4}\right)\left(\frac{\boldsymbol{Q}_4}{Q_4}\right)\cdot(\boldsymbol{\kappa}\cdot\boldsymbol{Q}_4)\right.$$

$$+\left(\frac{1}{1-M_4}\right)\left(\frac{1}{1-M_3}\right)\left(\frac{K}{\zeta+2K}\right)L_3\left(\frac{\boldsymbol{Q}_3}{Q_3}\right)\cdot(\boldsymbol{\kappa}\cdot\boldsymbol{Q}_3)$$

$$+\left(\frac{1}{1-M_4}\right)\left(\frac{1}{1-M_3}\right)\left(\frac{K}{\zeta+2K}\right)^2\left(\frac{1}{1-M_2}\right)L_3 L_2\left(\frac{\boldsymbol{Q}_2}{Q_2}\right)\cdot(\boldsymbol{\kappa}\cdot\boldsymbol{Q}_2)$$

$$+\left(\frac{1}{1-M_4}\right)\left(\frac{1}{1-M_3}\right)\left(\frac{1}{1-M_2}\right)\left(\frac{K}{\zeta+2K}\right)^3 L_3 L_2 L_1\left(\frac{\boldsymbol{Q}_1}{Q_1}\right)\cdot(\boldsymbol{\kappa}\cdot\boldsymbol{Q}_1)\right]$$

$$+\left(\frac{1}{\zeta+2K}\right)\left(\frac{1}{1-M_4}\right)\left(\frac{\boldsymbol{Q}_4}{Q_4}\right)\left(\frac{\boldsymbol{Q}_4}{Q_4}\right)\cdot\left(\frac{\partial\phi}{\partial\boldsymbol{Q}_5}\right)$$

$$-\left(\frac{1}{\zeta+2K}\right)\left(\frac{1}{Q_4}\right)\left[-\left(\frac{1}{1-M_4}\right)\left(\frac{K}{\zeta+2K}\right)L_3\left(\frac{\boldsymbol{Q}_3}{Q_3}\right)+2\left(\frac{1}{1-M_4}\right)\left(\frac{\boldsymbol{Q}_4}{Q_4}\right)\right]\cdot\left(\frac{\partial\phi}{\partial\boldsymbol{Q}_4}\right)$$

$$-\left(\frac{1}{\zeta+2K}\right)\left(\frac{1}{Q_4}\right)\left[-\left(\frac{1}{1-M_4}\right)\left(\frac{1}{1-M_3}\right)\left(\frac{1}{1-M_2}\right)\left(\frac{K}{\zeta+2K}\right)^2 L_3 L_2\left(\frac{\boldsymbol{Q}_2}{Q_2}\right)\right.$$

$$+2\left(\frac{1}{1-M_4}\right)\left(\frac{1}{1-M_3}\right)\left(\frac{K}{\zeta+2K}\right)L_3\left(\frac{\boldsymbol{Q}_3}{Q_3}\right)-\left(\frac{1}{1-M_4}\right)\left(\frac{\boldsymbol{Q}_4}{Q_4}\right)\right]\cdot\left(\frac{\partial\phi}{\partial\boldsymbol{Q}_3}\right)$$

$$-\left(\frac{1}{\zeta+2K}\right)\left(\frac{1}{Q_4}\right)\left[-\left(\frac{1}{1-M_4}\right)\left(\frac{1}{1-M_3}\right)\left(\frac{1}{1-M_2}\right)\left(\frac{K}{\zeta+2K}\right)^3 L_3 L_2 L_1\left(\frac{\boldsymbol{Q}_1}{Q_1}\right)\right.$$

$$+2\left(\frac{1}{1-M_4}\right)\left(\frac{1}{1-M_3}\right)\left(\frac{1}{1-M_2}\right)\left(\frac{K}{\zeta+2K}\right)^2 L_3 L_2\left(\frac{\boldsymbol{Q}_2}{Q_2}\right)$$

$$-\left(\frac{1}{1-M_4}\right)\left(\frac{K}{\zeta+2K}\right)L_3\left(\frac{\boldsymbol{Q}_3}{Q_3}\right)\right]\cdot\left(\frac{\partial\phi}{\partial\boldsymbol{Q}_2}\right)$$

$$-\left(\frac{1}{\zeta+2K}\right)\left(\frac{1}{Q_4}\right)\left[2\left(\frac{K}{\zeta+2K}\right)^3\left(\frac{1}{1-M_4}\right)\left(\frac{1}{1-M_3}\right)\left(\frac{1}{1-M_2}\right)L_3 L_2 L_1\left(\frac{\boldsymbol{Q}_1}{Q_1}\right)\right.$$

$$-\left(\frac{K}{\zeta+2K}\right)^2\left(\frac{1}{1-M_4}\right)\left(\frac{1}{1-M_3}\right)\left(\frac{1}{1-M_2}\right)L_3 L_2\left(\frac{\boldsymbol{Q}_2}{Q_2}\right)\right]\cdot\left(\frac{\partial\phi}{\partial\boldsymbol{Q}_1}\right)$$

Based on the pattern observed from Eqs. (B.8), (B.14), and (B.20) , a general expression for the forward susbtituition coefficients, M_k, may be written as

$$M_k = \left(\frac{K}{\zeta+2K}\right)^2\left(\frac{L_{k-1}^2}{1-M_{k-1}}\right); \quad \text{with} \quad M_1 = 0, \tag{B.23}$$

The next challenge is to prescribe a general expression for $C_k(1-M_k)$, based on the pattern discerned from Eqs. (B.9), (B.15), and (B.21). Upon careful observation and

induction, the general expression obtained at the end of the forward substitution step may be written as shown in Eq. (5.7) of Chapter 5.

B.2   Sample iterations from the backward substitution step

The backward substitution scheme involves plugging in the equation for C_k into C_{k-1}, starting with $k = N$. The step is illustrated for a series of k values, as shown below.

Backward substitution expression for $k = N$:

From Eq. (B.1), we have

$$
\begin{aligned}
C_N = {} & \left(\frac{\zeta}{\zeta + 2K}\right)\left(\frac{\boldsymbol{Q}_N}{Q_N^2}\right) \cdot (\boldsymbol{\kappa} \cdot \boldsymbol{Q}_N) - \left(\frac{k_B T}{\zeta + 2K}\right)\left(\frac{\boldsymbol{Q}_N}{Q_N^2}\right) \cdot \left[-\frac{\partial \ln \Psi}{\partial \boldsymbol{Q}_{N-1}} + 2\frac{\partial \ln \Psi}{\partial \boldsymbol{Q}_N}\right] \\
& - \left(\frac{1}{\zeta + 2K}\right)\left(\frac{\boldsymbol{Q}_N}{Q_N^2}\right) \cdot \left[-\frac{\partial \phi}{\partial \boldsymbol{Q}_{N-1}} + 2\frac{\partial \phi}{\partial \boldsymbol{Q}_N}\right] \\
& + \left(\frac{K}{\zeta + 2K}\right)\left[C_{N-1}L_{N-1}\left(\frac{Q_{N-1}}{Q_N}\right)\right]
\end{aligned}
\tag{B.24}
$$

which may be recast as

$$
\begin{aligned}
C_N = {} & \left(\frac{\zeta}{\zeta + 2K}\right)\left(\frac{\boldsymbol{Q}_N}{Q_N^2}\right) \cdot (\boldsymbol{\kappa} \cdot \boldsymbol{Q}_N) + \left(\frac{k_B T}{\zeta + 2K}\right)\left(\frac{\boldsymbol{Q}_N}{Q_N^2}\right) \cdot \left(\frac{\partial \ln \Psi}{\partial \boldsymbol{Q}_{N-1}}\right) \\
& - \left(\frac{k_B T}{\zeta + 2K}\right)\left(\frac{2\boldsymbol{Q}_N}{Q_N^2}\right) \cdot \left(\frac{\partial \ln \Psi}{\partial \boldsymbol{Q}_N}\right) \\
& + \left(\frac{1}{\zeta + 2K}\right)\left(\frac{\boldsymbol{Q}_N}{Q_N^2}\right) \cdot \left(\frac{\partial \phi}{\partial \boldsymbol{Q}_{N-1}}\right) - \left(\frac{1}{\zeta + 2K}\right)\left(\frac{2\boldsymbol{Q}_N}{Q_N^2}\right) \cdot \left(\frac{\partial \phi}{\partial \boldsymbol{Q}_N}\right) \\
& + \left(\frac{K}{\zeta + 2K}\right)\left[C_{N-1}L_{N-1}\left(\frac{Q_{N-1}}{Q_N}\right)\right]
\end{aligned}
\tag{B.25}
$$

Backward substitution expression for $k = (N - 1)$:

From Eq. (B.1), we have

$$
\begin{aligned}
C_{N-1} = {} & \left(\frac{\zeta}{\zeta + 2K}\right)\left(\frac{\boldsymbol{Q}_{N-1}}{Q_{N-1}^2}\right) \cdot (\boldsymbol{\kappa} \cdot \boldsymbol{Q}_{N-1}) - \left(\frac{k_B T}{\zeta + 2K}\right)\left(\frac{\boldsymbol{Q}_{N-1}}{Q_{N-1}^2}\right) \cdot \left[-\frac{\partial \ln \Psi}{\partial \boldsymbol{Q}_{N-2}} + 2\frac{\partial \ln \Psi}{\partial \boldsymbol{Q}_{N-1}} - \frac{\partial \ln \Psi}{\partial \boldsymbol{Q}_N}\right] \\
& - \left(\frac{1}{\zeta + 2K}\right)\left(\frac{\boldsymbol{Q}_{N-1}}{Q_{N-1}^2}\right) \cdot \left[-\frac{\partial \phi}{\partial \boldsymbol{Q}_{N-2}} + 2\frac{\partial \phi}{\partial \boldsymbol{Q}_{N-1}} - \frac{\partial \phi}{\partial \boldsymbol{Q}_N}\right] \\
& + \left(\frac{K}{\zeta + 2K}\right)\left[C_{N-2}L_{N-2}\left(\frac{Q_{N-2}}{Q_{N-1}}\right) + C_N L_{N-1}\left(\frac{Q_N}{Q_{N-1}}\right)\right]
\end{aligned}
\tag{B.26}
$$

Multiplying Eq. (B.25) by $L_{N-1}(Q_N/Q_{N-1})$,

$$C_N L_{N-1}\left(\frac{Q_N}{Q_{N-1}}\right) = \left(\frac{\zeta}{\zeta+2K}\right)\left(\frac{L_{N-1}}{Q_{N-1}}\right)\left(\frac{\boldsymbol{Q}_N}{Q_N}\right)\cdot(\boldsymbol{\kappa}\cdot\boldsymbol{Q}_N) \tag{B.27}$$

$$+\left(\frac{k_BT}{\zeta+2K}\right)\left(\frac{L_{N-1}}{Q_{N-1}}\right)\left(\frac{\boldsymbol{Q}_N}{Q_N}\right)\cdot\left(\frac{\partial\ln\Psi}{\partial\boldsymbol{Q}_{N-1}}\right) - 2\left(\frac{k_BT}{\zeta+2K}\right)\left(\frac{L_{N-1}}{Q_{N-1}}\right)\left(\frac{\boldsymbol{Q}_N}{Q_N}\right)\cdot\left(\frac{\partial\ln\Psi}{\partial\boldsymbol{Q}_N}\right)$$

$$+\left(\frac{1}{\zeta+2K}\right)\left(\frac{L_{N-1}}{Q_{N-1}}\right)\left(\frac{\boldsymbol{Q}_N}{Q_N}\right)\cdot\left(\frac{\partial\phi}{\partial\boldsymbol{Q}_{N-1}}\right) - 2\left(\frac{1}{\zeta+2K}\right)\left(\frac{L_{N-1}}{Q_{N-1}}\right)\left(\frac{\boldsymbol{Q}_N}{Q_N}\right)\cdot\left(\frac{\partial\phi}{\partial\boldsymbol{Q}_N}\right)$$

$$+\left(\frac{K}{\zeta+2K}\right)\left[C_{N-1}L_{N-1}^2\right]$$

Substituting Eq. (B.27) into Eq. (B.26), we have

$$C_{N-1} = \left(\frac{K}{\zeta+2K}\right)C_{N-2}L_{N-2}\left(\frac{Q_{N-2}}{Q_{N-1}}\right) + \left(\frac{\zeta}{\zeta+2K}\right)\left(\frac{\boldsymbol{Q}_{N-1}}{Q_{N-1}^2}\right)\cdot(\boldsymbol{\kappa}\cdot\boldsymbol{Q}_{N-1}) \tag{B.28}$$

$$+\left(\frac{k_BT}{\zeta+2K}\right)\left(\frac{1}{Q_{N-1}}\right)\left(\frac{\boldsymbol{Q}_{N-1}}{Q_{N-1}}\right)\cdot\left(\frac{\partial\ln\Psi}{\partial\boldsymbol{Q}_{N-2}}\right) - 2\left(\frac{k_BT}{\zeta+2K}\right)\left(\frac{1}{Q_{N-1}}\right)\left(\frac{\boldsymbol{Q}_{N-1}}{Q_{N-1}}\right)\cdot\left(\frac{\partial\ln\Psi}{\partial\boldsymbol{Q}_{N-1}}\right)$$

$$+\left(\frac{k_BT}{\zeta+2K}\right)\left(\frac{1}{Q_{N-1}}\right)\left(\frac{\boldsymbol{Q}_{N-1}}{Q_{N-1}}\right)\cdot\left(\frac{\partial\ln\Psi}{\partial\boldsymbol{Q}_N}\right) + \left(\frac{K}{\zeta+2K}\right)^2 C_{N-1}L_{N-1}^2$$

$$+\left(\frac{1}{\zeta+2K}\right)\left(\frac{1}{Q_{N-1}}\right)\left(\frac{\boldsymbol{Q}_{N-1}}{Q_{N-1}}\right)\cdot\left(\frac{\partial\phi}{\partial\boldsymbol{Q}_{N-2}}\right) - 2\left(\frac{1}{\zeta+2K}\right)\left(\frac{1}{Q_{N-1}}\right)\left(\frac{\boldsymbol{Q}_{N-1}}{Q_{N-1}}\right)\cdot\left(\frac{\partial\phi}{\partial\boldsymbol{Q}_{N-1}}\right)$$

$$+\left(\frac{1}{\zeta+2K}\right)\left(\frac{1}{Q_{N-1}}\right)\left(\frac{\boldsymbol{Q}_{N-1}}{Q_{N-1}}\right)\cdot\left(\frac{\partial\phi}{\partial\boldsymbol{Q}_N}\right) + \left(\frac{\zeta}{\zeta+2K}\right)\left(\frac{K}{\zeta+2K}\right)L_{N-1}\left(\frac{1}{Q_{N-1}}\right)\left(\frac{\boldsymbol{Q}_N}{Q_N}\right)\cdot(\boldsymbol{\kappa}\cdot\boldsymbol{Q}_N)$$

$$+\left(\frac{k_BT}{\zeta+2K}\right)\left(\frac{K}{\zeta+2K}\right)\left(\frac{1}{Q_{N-1}}\right)L_{N-1}\left(\frac{\boldsymbol{Q}_N}{Q_N}\right)\cdot\left(\frac{\partial\ln\Psi}{\partial\boldsymbol{Q}_{N-1}}\right)$$

$$-2\left(\frac{k_BT}{\zeta+2K}\right)\left(\frac{K}{\zeta+2K}\right)\left(\frac{1}{Q_{N-1}}\right)L_{N-1}\left(\frac{\boldsymbol{Q}_N}{Q_N}\right)\cdot\left(\frac{\partial\ln\Psi}{\partial\boldsymbol{Q}_N}\right)$$

$$+\left(\frac{1}{\zeta+2K}\right)\left(\frac{K}{\zeta+2K}\right)\left(\frac{1}{Q_{N-1}}\right)L_{N-1}\left(\frac{\boldsymbol{Q}_N}{Q_N}\right)\cdot\left(\frac{\partial\phi}{\partial\boldsymbol{Q}_{N-1}}\right)$$

$$-2\left(\frac{1}{\zeta+2K}\right)\left(\frac{K}{\zeta+2K}\right)\left(\frac{1}{Q_{N-1}}\right)L_{N-1}\left(\frac{\boldsymbol{Q}_N}{Q_N}\right)\cdot\left(\frac{\partial\phi}{\partial\boldsymbol{Q}_N}\right)$$

Defining

$$P_{N-1} = \left(\frac{K}{\zeta+2K}\right)^2 L_{N-1}^2 \tag{B.29}$$

and grouping like terms together, we have

$$C_{N-1}(1 - P_{N-1}) = \left(\frac{K}{\zeta + 2K}\right) C_{N-2} L_{N-2} \left(\frac{Q_{N-2}}{Q_{N-1}}\right) \tag{B.30}$$

$$+ \left(\frac{\zeta}{\zeta + 2K}\right) \left(\frac{1}{Q_{N-1}}\right) \left[\left(\frac{\boldsymbol{Q}_{N-1}}{Q_{N-1}}\right) \cdot (\boldsymbol{\kappa} \cdot \boldsymbol{Q}_{N-1}) + \left(\frac{K}{\zeta + 2K}\right) L_{N-1} \left(\frac{\boldsymbol{Q}_N}{Q_N}\right) \cdot (\boldsymbol{\kappa} \cdot \boldsymbol{Q}_N)\right]$$

$$+ \left(\frac{k_B T}{\zeta + 2K}\right) \left(\frac{1}{Q_{N-1}}\right) \left(\frac{\boldsymbol{Q}_{N-1}}{Q_{N-1}}\right) \cdot \left(\frac{\partial \ln \Psi}{\partial \boldsymbol{Q}_{N-2}}\right)$$

$$- \left(\frac{k_B T}{\zeta + 2K}\right) \left(\frac{1}{Q_{N-1}}\right) \left[-\left(\frac{K}{\zeta + 2K}\right) L_{N-1} \left(\frac{\boldsymbol{Q}_N}{Q_N}\right) + 2\left(\frac{\boldsymbol{Q}_{N-1}}{Q_{N-1}}\right)\right] \cdot \left(\frac{\partial \ln \Psi}{\partial \boldsymbol{Q}_{N-1}}\right)$$

$$- \left(\frac{k_B T}{\zeta + 2K}\right) \left(\frac{1}{Q_{N-1}}\right) \left[2\left(\frac{K}{\zeta + 2K}\right) L_{N-1} \left(\frac{\boldsymbol{Q}_N}{Q_N}\right) - \left(\frac{\boldsymbol{Q}_{N-1}}{Q_{N-1}}\right)\right] \cdot \left(\frac{\partial \ln \Psi}{\partial \boldsymbol{Q}_N}\right)$$

$$+ \left(\frac{1}{\zeta + 2K}\right) \left(\frac{1}{Q_{N-1}}\right) \left(\frac{\boldsymbol{Q}_{N-1}}{Q_{N-1}}\right) \cdot \left(\frac{\partial \phi}{\partial \boldsymbol{Q}_{N-2}}\right)$$

$$- \left(\frac{1}{\zeta + 2K}\right) \left(\frac{1}{Q_{N-1}}\right) \left[-\left(\frac{K}{\zeta + 2K}\right) L_{N-1} \left(\frac{\boldsymbol{Q}_N}{Q_N}\right) + 2\left(\frac{\boldsymbol{Q}_{N-1}}{Q_{N-1}}\right)\right] \cdot \left(\frac{\partial \phi}{\partial \boldsymbol{Q}_{N-1}}\right)$$

$$- \left(\frac{1}{\zeta + 2K}\right) \left(\frac{1}{Q_{N-1}}\right) \left[2\left(\frac{K}{\zeta + 2K}\right) L_{N-1} \left(\frac{\boldsymbol{Q}_N}{Q_N}\right) - \left(\frac{\boldsymbol{Q}_{N-1}}{Q_{N-1}}\right)\right] \cdot \left(\frac{\partial \phi}{\partial \boldsymbol{Q}_N}\right)$$

It is clear from the underlined terms in Eq. (B.25) and Eq. (B.30) that the coefficients for the spring force and the Brownian force terms are identical. In the forthcoming steps, therefore, only the spring force term is indicated for the sake of brevity. Once a general pattern has been identified, the final expression would contain both the Brownian and the spring force terms, multiplied by the same prefactor.

We thus have the following final expression for C_{N-1},

$$C_{N-1} = \left(\frac{1}{1-P_{N-1}}\right)\left(\frac{K}{\zeta+2K}\right)C_{N-2}L_{N-2}\left(\frac{Q_{N-2}}{Q_{N-1}}\right) \tag{B.31}$$

$$+ \left(\frac{\zeta}{\zeta+2K}\right)\left(\frac{1}{Q_{N-1}}\right)\left[\left(\frac{1}{1-P_{N-1}}\right)\left(\frac{\boldsymbol{Q}_{N-1}}{Q_{N-1}}\right)\cdot(\boldsymbol{\kappa}\cdot\boldsymbol{Q}_{N-1})\right.$$

$$+ \left(\frac{K}{\zeta+2K}\right)\left(\frac{1}{1-P_{N-1}}\right)L_{N-1}\left(\frac{\boldsymbol{Q}_N}{Q_N}\right)\cdot(\boldsymbol{\kappa}\cdot\boldsymbol{Q}_N)\right]$$

$$+ \left(\frac{1}{\zeta+2K}\right)\left(\frac{1}{1-P_{N-1}}\right)\left(\frac{1}{Q_{N-1}}\right)\left(\frac{\boldsymbol{Q}_{N-1}}{Q_{N-1}}\right)\cdot\left(\frac{\partial\phi}{\partial\boldsymbol{Q}_{N-2}}\right)$$

$$- \left(\frac{1}{\zeta+2K}\right)\left(\frac{1}{Q_{N-1}}\right)\left[-\left(\frac{1}{1-P_{N-1}}\right)\left(\frac{K}{\zeta+2K}\right)L_{N-1}\left(\frac{\boldsymbol{Q}_N}{Q_N}\right)\right.$$

$$+ 2\left(\frac{1}{1-P_{N-1}}\right)\left(\frac{\boldsymbol{Q}_{N-1}}{Q_{N-1}}\right)\right]\cdot\left(\frac{\partial\phi}{\partial\boldsymbol{Q}_{N-1}}\right)$$

$$- \left(\frac{1}{\zeta+2K}\right)\left(\frac{1}{Q_{N-1}}\right)\left[2\left(\frac{1}{1-P_{N-1}}\right)\left(\frac{K}{\zeta+2K}\right)L_{N-1}\left(\frac{\boldsymbol{Q}_N}{Q_N}\right)\right.$$

$$- \left(\frac{1}{1-P_{N-1}}\right)\left(\frac{\boldsymbol{Q}_{N-1}}{Q_{N-1}}\right)\right]\cdot\left(\frac{\partial\phi}{\partial\boldsymbol{Q}_N}\right)$$

Backward substitution expression for $k = (N-2)$:

From Eq. (B.1), we have

$$C_{N-2} = \left(\frac{\zeta}{\zeta+2K}\right)\left(\frac{\boldsymbol{Q}_{N-2}}{Q_{N-2}^2}\right)\cdot(\boldsymbol{\kappa}\cdot\boldsymbol{Q}_{N-2}) - \left(\frac{1}{\zeta+2K}\right)\left(\frac{\boldsymbol{Q}_{N-2}}{Q_{N-2}^2}\right)\cdot\left[-\frac{\partial\phi}{\partial\boldsymbol{Q}_{N-3}} + 2\frac{\partial\phi}{\partial\boldsymbol{Q}_{N-2}} - \frac{\partial\phi}{\partial\boldsymbol{Q}_{N-1}}\right]$$

$$\tag{B.32}$$

$$+ \left(\frac{K}{\zeta+2K}\right)\left[C_{N-3}L_{N-3}\left(\frac{Q_{N-3}}{Q_{N-2}}\right) + C_{N-1}L_{N-2}\left(\frac{Q_{N-1}}{Q_{N-2}}\right)\right]$$

Multiplying Eq. (B.31) by $L_{N-2}\left(Q_{N-1}/Q_{N-2}\right)$

$$C_{N-1}L_{N-2}\left(\frac{Q_{N-1}}{Q_{N-2}}\right) = \left(\frac{1}{1-P_{N-1}}\right)\left(\frac{K}{\zeta+2K}\right)C_{N-2}L_{N-2}^2 \tag{B.33}$$

$$+\left(\frac{\zeta}{\zeta+2K}\right)\left(\frac{1}{Q_{N-2}}\right)\left[\left(\frac{1}{1-P_{N-1}}\right)L_{N-2}\left(\frac{\boldsymbol{Q}_{N-1}}{Q_{N-1}}\right)\cdot(\boldsymbol{\kappa}\cdot\boldsymbol{Q}_{N-1})\right.$$

$$+\left(\frac{K}{\zeta+2K}\right)\left(\frac{1}{1-P_{N-1}}\right)L_{N-2}L_{N-1}\left(\frac{\boldsymbol{Q}_N}{Q_N}\right)\cdot(\boldsymbol{\kappa}\cdot\boldsymbol{Q}_N)\right]$$

$$+\left(\frac{1}{\zeta+2K}\right)\left(\frac{1}{1-P_{N-1}}\right)L_{N-2}\left(\frac{1}{Q_{N-2}}\right)\left(\frac{\boldsymbol{Q}_{N-1}}{Q_{N-1}}\right)\cdot\left(\frac{\partial\phi}{\partial\boldsymbol{Q}_{N-2}}\right)$$

$$-\left(\frac{1}{\zeta+2K}\right)\left(\frac{1}{Q_{N-2}}\right)\left[-\left(\frac{1}{1-P_{N-1}}\right)\left(\frac{K}{\zeta+2K}\right)L_{N-2}L_{N-1}\left(\frac{\boldsymbol{Q}_N}{Q_N}\right)\right.$$

$$+2\left(\frac{1}{1-P_{N-1}}\right)L_{N-2}\left(\frac{\boldsymbol{Q}_{N-1}}{Q_{N-1}}\right)\right]\cdot\left(\frac{\partial\phi}{\partial\boldsymbol{Q}_{N-1}}\right)$$

$$-\left(\frac{1}{\zeta+2K}\right)\left(\frac{1}{Q_{N-2}}\right)\left[2\left(\frac{1}{1-P_{N-1}}\right)\left(\frac{K}{\zeta+2K}\right)L_{N-2}L_{N-1}\left(\frac{\boldsymbol{Q}_N}{Q_N}\right)\right.$$

$$-\left(\frac{1}{1-P_{N-1}}\right)L_{N-2}\left(\frac{\boldsymbol{Q}_{N-1}}{Q_{N-1}}\right)\right]\cdot\left(\frac{\partial\phi}{\partial\boldsymbol{Q}_N}\right)$$

Substituting Eq. (B.33) into Eq. (B.32), we obtain

$$
C_{N-2} = \left(\frac{K}{\zeta + 2K}\right) C_{N-3} L_{N-3} \left(\frac{Q_{N-3}}{Q_{N-2}}\right) + \left(\frac{\zeta}{\zeta + 2K}\right) \left(\frac{\boldsymbol{Q}_{N-2}}{Q_{N-2}^2}\right) \cdot (\boldsymbol{\kappa} \cdot \boldsymbol{Q}_{N-2}) \tag{B.34}
$$

$$
+ \left(\frac{1}{\zeta + 2K}\right) \left(\frac{\boldsymbol{Q}_{N-2}}{Q_{N-2}^2}\right) \cdot \left(\frac{\partial \phi}{\partial \boldsymbol{Q}_{N-3}}\right) - 2 \left(\frac{1}{\zeta + 2K}\right) \left(\frac{\boldsymbol{Q}_{N-2}}{Q_{N-2}^2}\right) \cdot \left(\frac{\partial \phi}{\partial \boldsymbol{Q}_{N-2}}\right)
$$

$$
+ \left(\frac{1}{\zeta + 2K}\right) \left(\frac{\boldsymbol{Q}_{N-2}}{Q_{N-2}^2}\right) \cdot \left(\frac{\partial \phi}{\partial \boldsymbol{Q}_{N-1}}\right) + \left(\frac{1}{1 - P_{N-1}}\right) \left(\frac{K}{\zeta + 2K}\right)^2 C_{N-2} L_{N-2}^2
$$

$$
+ \left(\frac{\zeta}{\zeta + 2K}\right) \left(\frac{1}{Q_{N-2}}\right) \left[\left(\frac{K}{\zeta + 2K}\right) \left(\frac{1}{1 - P_{N-1}}\right) L_{N-2} \left(\frac{\boldsymbol{Q}_{N-1}}{Q_{N-1}}\right) \cdot (\boldsymbol{\kappa} \cdot \boldsymbol{Q}_{N-1})
$$

$$
+ \left(\frac{K}{\zeta + 2K}\right)^2 \left(\frac{1}{1 - P_{N-1}}\right) L_{N-2} L_{N-1} \left(\frac{\boldsymbol{Q}_N}{Q_N}\right) \cdot (\boldsymbol{\kappa} \cdot \boldsymbol{Q}_N) \right]
$$

$$
+ \left(\frac{1}{\zeta + 2K}\right) \left(\frac{K}{\zeta + 2K}\right) \left(\frac{1}{1 - P_{N-1}}\right) L_{N-2} \left(\frac{1}{Q_{N-2}}\right) \left(\frac{\boldsymbol{Q}_{N-1}}{Q_{N-1}}\right) \cdot \left(\frac{\partial \phi}{\partial \boldsymbol{Q}_{N-2}}\right)
$$

$$
- \left(\frac{1}{\zeta + 2K}\right) \left(\frac{1}{Q_{N-2}}\right) \left[-\left(\frac{1}{1 - P_{N-1}}\right) \left(\frac{K}{\zeta + 2K}\right)^2 L_{N-2} L_{N-1} \left(\frac{\boldsymbol{Q}_N}{Q_N}\right) \right.
$$

$$
+ 2 \left(\frac{1}{1 - P_{N-1}}\right) \left(\frac{K}{\zeta + 2K}\right) L_{N-2} \left(\frac{\boldsymbol{Q}_{N-1}}{Q_{N-1}}\right) \right] \cdot \left(\frac{\partial \phi}{\partial \boldsymbol{Q}_{N-1}}\right)
$$

$$
- \left(\frac{1}{\zeta + 2K}\right) \left(\frac{1}{Q_{N-2}}\right) \left[2 \left(\frac{1}{1 - P_{N-1}}\right) \left(\frac{K}{\zeta + 2K}\right)^2 L_{N-2} L_{N-1} \left(\frac{\boldsymbol{Q}_N}{Q_N}\right) \right.
$$

$$
- \left(\frac{1}{1 - P_{N-1}}\right) \left(\frac{K}{\zeta + 2K}\right) L_{N-2} \left(\frac{\boldsymbol{Q}_{N-1}}{Q_{N-1}}\right) \right] \cdot \left(\frac{\partial \phi}{\partial \boldsymbol{Q}_N}\right)
$$

Defining

$$
P_{N-2} = \left(\frac{1}{1 - P_{N-1}}\right) \left(\frac{K}{\zeta + 2K}\right)^2 L_{N-2}^2 \tag{B.35}
$$

and grouping like terms together, we have

$$C_{N-2}\left(1 - P_{N-2}\right) = \left(\frac{K}{\zeta + 2K}\right)C_{N-3}L_{N-3}\left(\frac{Q_{N-3}}{Q_{N-2}}\right) \tag{B.36}$$

$$+ \left(\frac{\zeta}{\zeta + 2K}\right)\left(\frac{1}{Q_{N-2}}\right)\left[\left(\frac{\boldsymbol{Q}_{N-2}}{Q_{N-2}}\right) \cdot \left(\boldsymbol{\kappa} \cdot \boldsymbol{Q}_{N-2}\right)\right.$$

$$+ \left(\frac{K}{\zeta + 2K}\right)\left(\frac{1}{1 - P_{N-1}}\right)L_{N-2}\left(\frac{\boldsymbol{Q}_{N-1}}{Q_{N-1}}\right) \cdot \left(\boldsymbol{\kappa} \cdot \boldsymbol{Q}_{N-1}\right)$$

$$+ \left(\frac{K}{\zeta + 2K}\right)^2\left(\frac{1}{1 - P_{N-1}}\right)L_{N-2}L_{N-1}\left(\frac{\boldsymbol{Q}_N}{Q_N}\right) \cdot \left(\boldsymbol{\kappa} \cdot \boldsymbol{Q}_N\right)\Bigg]$$

$$+ \left(\frac{1}{\zeta + 2K}\right)\left(\frac{\boldsymbol{Q}_{N-2}}{Q_{N-2}^2}\right) \cdot \left(\frac{\partial \phi}{\partial \boldsymbol{Q}_{N-3}}\right)$$

$$- \left(\frac{1}{\zeta + 2K}\right)\left(\frac{1}{Q_{N-2}}\right)\left[-\left(\frac{K}{\zeta + 2K}\right)\left(\frac{1}{1 - P_{N-1}}\right)L_{N-2}\left(\frac{\boldsymbol{Q}_{N-1}}{Q_{N-1}}\right)\right.$$

$$+ 2\left(\frac{\boldsymbol{Q}_{N-2}}{Q_{N-2}}\right)\Bigg] \cdot \left(\frac{\partial \phi}{\partial \boldsymbol{Q}_{N-2}}\right)$$

$$- \left(\frac{1}{\zeta + 2K}\right)\left(\frac{1}{Q_{N-2}}\right)\left[-\left(\frac{1}{1 - P_{N-1}}\right)\left(\frac{K}{\zeta + 2K}\right)^2 L_{N-2}L_{N-1}\left(\frac{\boldsymbol{Q}_N}{Q_N}\right)\right.$$

$$+ 2\left(\frac{1}{1 - P_{N-1}}\right)\left(\frac{K}{\zeta + 2K}\right)L_{N-2}\left(\frac{\boldsymbol{Q}_{N-1}}{Q_{N-1}}\right) - \left(\frac{\boldsymbol{Q}_{N-2}}{Q_{N-2}}\right)\Bigg] \cdot \left(\frac{\partial \phi}{\partial \boldsymbol{Q}_{N-1}}\right)$$

$$- \left(\frac{1}{\zeta + 2K}\right)\left(\frac{1}{Q_{N-2}}\right)\left[2\left(\frac{1}{1 - P_{N-1}}\right)\left(\frac{K}{\zeta + 2K}\right)^2 L_{N-2}L_{N-1}\left(\frac{\boldsymbol{Q}_N}{Q_N}\right)\right.$$

$$- \left(\frac{1}{1 - P_{N-1}}\right)\left(\frac{K}{\zeta + 2K}\right)L_{N-2}\left(\frac{\boldsymbol{Q}_{N-1}}{Q_{N-1}}\right)\Bigg] \cdot \left(\frac{\partial \phi}{\partial \boldsymbol{Q}_N}\right)$$

We thus have the following final expression for C_{N-2},

$$C_{N-2} = \left(\frac{1}{1-P_{N-2}}\right)\left(\frac{K}{\zeta+2K}\right)C_{N-3}L_{N-3}\left(\frac{Q_{N-3}}{Q_{N-2}}\right)$$

$$+\left(\frac{\zeta}{\zeta+2K}\right)\left(\frac{1}{Q_{N-2}}\right)\left[\left(\frac{1}{1-P_{N-2}}\right)\left(\frac{\boldsymbol{Q}_{N-2}}{Q_{N-2}}\right)\cdot(\boldsymbol{\kappa}\cdot\boldsymbol{Q}_{N-2})\right.$$

$$+\left(\frac{K}{\zeta+2K}\right)\left(\frac{1}{1-P_{N-2}}\right)\left(\frac{1}{1-P_{N-1}}\right)L_{N-2}\left(\frac{\boldsymbol{Q}_{N-1}}{Q_{N-1}}\right)\cdot(\boldsymbol{\kappa}\cdot\boldsymbol{Q}_{N-1})$$

$$+\left(\frac{K}{\zeta+2K}\right)^2\left(\frac{1}{1-P_{N-2}}\right)\left(\frac{1}{1-P_{N-1}}\right)L_{N-2}L_{N-1}\left(\frac{\boldsymbol{Q}_N}{Q_N}\right)\cdot(\boldsymbol{\kappa}\cdot\boldsymbol{Q}_N)\right]$$

$$+\left(\frac{1}{\zeta+2K}\right)\left(\frac{1}{1-P_{N-2}}\right)\left(\frac{\boldsymbol{Q}_{N-2}}{Q_{N-2}^2}\right)\cdot\left(\frac{\partial\phi}{\partial\boldsymbol{Q}_{N-3}}\right)$$

$$-\left(\frac{1}{\zeta+2K}\right)\left(\frac{1}{Q_{N-2}}\right)\left[-\left(\frac{K}{\zeta+2K}\right)\left(\frac{1}{1-P_{N-2}}\right)\left(\frac{1}{1-P_{N-1}}\right)L_{N-2}\left(\frac{\boldsymbol{Q}_{N-1}}{Q_{N-1}}\right)\right.$$

$$+2\left(\frac{1}{1-P_{N-2}}\right)\left(\frac{\boldsymbol{Q}_{N-2}}{Q_{N-2}}\right)\right]\cdot\left(\frac{\partial\phi}{\partial\boldsymbol{Q}_{N-2}}\right)$$

$$-\left(\frac{1}{\zeta+2K}\right)\left(\frac{1}{Q_{N-2}}\right)\left[-\left(\frac{1}{1-P_{N-2}}\right)\left(\frac{1}{1-P_{N-1}}\right)\left(\frac{K}{\zeta+2K}\right)^2 L_{N-2}L_{N-1}\left(\frac{\boldsymbol{Q}_N}{Q_N}\right)\right.$$

$$+2\left(\frac{1}{1-P_{N-2}}\right)\left(\frac{1}{1-P_{N-1}}\right)\left(\frac{K}{\zeta+2K}\right)L_{N-2}\left(\frac{\boldsymbol{Q}_{N-1}}{Q_{N-1}}\right)-\left(\frac{1}{1-P_{N-2}}\right)\left(\frac{\boldsymbol{Q}_{N-2}}{Q_{N-2}}\right)\right]\cdot\left(\frac{\partial\phi}{\partial\boldsymbol{Q}_{N-1}}\right)$$

$$-\left(\frac{1}{\zeta+2K}\right)\left(\frac{1}{Q_{N-2}}\right)\left[2\left(\frac{1}{1-P_{N-2}}\right)\left(\frac{1}{1-P_{N-1}}\right)\left(\frac{K}{\zeta+2K}\right)^2 L_{N-2}L_{N-1}\left(\frac{\boldsymbol{Q}_N}{Q_N}\right)\right.$$

$$-\left(\frac{1}{1-P_{N-2}}\right)\left(\frac{1}{1-P_{N-1}}\right)\left(\frac{K}{\zeta+2K}\right)L_{N-2}\left(\frac{\boldsymbol{Q}_{N-1}}{Q_{N-1}}\right)\right]\cdot\left(\frac{\partial\phi}{\partial\boldsymbol{Q}_N}\right) \tag{B.37}$$

Backward substitution expression for $k = (N-3)$:

From Eq. (B.1), we have

$$C_{N-3} = \left(\frac{\zeta}{\zeta+2K}\right)\left(\frac{\boldsymbol{Q}_{N-3}}{Q_{N-3}^2}\right)\cdot(\boldsymbol{\kappa}\cdot\boldsymbol{Q}_{N-3})-\left(\frac{1}{\zeta+2K}\right)\left(\frac{\boldsymbol{Q}_{N-3}}{Q_{N-3}^2}\right)\cdot\left[-\frac{\partial\phi}{\partial\boldsymbol{Q}_{N-4}}+2\frac{\partial\phi}{\partial\boldsymbol{Q}_{N-3}}-\frac{\partial\phi}{\partial\boldsymbol{Q}_{N-2}}\right]$$

$$\tag{B.38}$$

$$+\left(\frac{K}{\zeta+2K}\right)\left[C_{N-4}L_{N-4}\left(\frac{Q_{N-4}}{Q_{N-3}}\right)+C_{N-2}L_{N-3}\left(\frac{Q_{N-2}}{Q_{N-3}}\right)\right]$$

Multiplying Eq. (B.37) by $L_{N-3}(Q_{N-2}/Q_{N-3})$, we obtain

$$C_{N-2}L_{N-3}\left(\frac{Q_{N-2}}{Q_{N-3}}\right) = \left(\frac{1}{1-P_{N-2}}\right)\left(\frac{K}{\zeta+2K}\right)C_{N-3}L_{N-3}^2 \tag{B.39}$$

$$+\left(\frac{\zeta}{\zeta+2K}\right)\left(\frac{1}{Q_{N-3}}\right)\left[\left(\frac{1}{1-P_{N-2}}\right)L_{N-3}\left(\frac{\boldsymbol{Q}_{N-2}}{Q_{N-2}}\right)\cdot(\boldsymbol{\kappa}\cdot\boldsymbol{Q}_{N-2})\right.$$

$$+\left(\frac{K}{\zeta+2K}\right)\left(\frac{1}{1-P_{N-2}}\right)\left(\frac{1}{1-P_{N-1}}\right)L_{N-3}L_{N-2}\left(\frac{\boldsymbol{Q}_{N-1}}{Q_{N-1}}\right)\cdot(\boldsymbol{\kappa}\cdot\boldsymbol{Q}_{N-1})$$

$$+\left(\frac{K}{\zeta+2K}\right)^2\left(\frac{1}{1-P_{N-2}}\right)\left(\frac{1}{1-P_{N-1}}\right)L_{N-3}L_{N-2}L_{N-1}\left(\frac{\boldsymbol{Q}_N}{Q_N}\right)\cdot(\boldsymbol{\kappa}\cdot\boldsymbol{Q}_N)\Bigg]$$

$$+\left(\frac{1}{\zeta+2K}\right)\left(\frac{1}{1-P_{N-2}}\right)L_{N-3}\left(\frac{1}{Q_{N-3}}\right)\left(\frac{\boldsymbol{Q}_{N-2}}{Q_{N-2}}\right)\cdot\left(\frac{\partial\phi}{\partial\boldsymbol{Q}_{N-3}}\right)$$

$$-\left(\frac{1}{\zeta+2K}\right)\left(\frac{1}{Q_{N-3}}\right)\left[-\left(\frac{K}{\zeta+2K}\right)\left(\frac{1}{1-P_{N-2}}\right)\left(\frac{1}{1-P_{N-1}}\right)L_{N-3}L_{N-2}\left(\frac{\boldsymbol{Q}_{N-1}}{Q_{N-1}}\right)\right.$$

$$+2\left(\frac{1}{1-P_{N-2}}\right)L_{N-3}\left(\frac{\boldsymbol{Q}_{N-2}}{Q_{N-2}}\right)\Bigg]\cdot\left(\frac{\partial\phi}{\partial\boldsymbol{Q}_{N-2}}\right)$$

$$-\left(\frac{1}{\zeta+2K}\right)\left(\frac{1}{Q_{N-3}}\right)\left[-\left(\frac{1}{1-P_{N-2}}\right)\left(\frac{1}{1-P_{N-1}}\right)\left(\frac{K}{\zeta+2K}\right)^2 L_{N-3}L_{N-2}L_{N-1}\left(\frac{\boldsymbol{Q}_N}{Q_N}\right)\right.$$

$$+2\left(\frac{1}{1-P_{N-2}}\right)\left(\frac{1}{1-P_{N-1}}\right)\left(\frac{K}{\zeta+2K}\right)L_{N-3}L_{N-2}\left(\frac{\boldsymbol{Q}_{N-1}}{Q_{N-1}}\right)$$

$$-\left(\frac{1}{1-P_{N-2}}\right)L_{N-3}\left(\frac{\boldsymbol{Q}_{N-2}}{Q_{N-2}}\right)\Bigg]\cdot\left(\frac{\partial\phi}{\partial\boldsymbol{Q}_{N-1}}\right)$$

$$-\left(\frac{1}{\zeta+2K}\right)\left(\frac{1}{Q_{N-3}}\right)\left[2\left(\frac{1}{1-P_{N-2}}\right)\left(\frac{1}{1-P_{N-1}}\right)\left(\frac{K}{\zeta+2K}\right)^2 L_{N-3}L_{N-2}L_{N-1}\left(\frac{\boldsymbol{Q}_N}{Q_N}\right)\right.$$

$$-\left(\frac{1}{1-P_{N-2}}\right)\left(\frac{1}{1-P_{N-1}}\right)\left(\frac{K}{\zeta+2K}\right)L_{N-3}L_{N-2}\left(\frac{\boldsymbol{Q}_{N-1}}{Q_{N-1}}\right)\Bigg]\cdot\left(\frac{\partial\phi}{\partial\boldsymbol{Q}_N}\right)$$

Substituting Eq. (B.39) into Eq. (B.38),

$$C_{N-3} = \left(\frac{K}{\zeta + 2K}\right) C_{N-4} L_{N-4} \left(\frac{Q_{N-4}}{Q_{N-3}}\right) + \left(\frac{\zeta}{\zeta + 2K}\right)\left(\frac{\boldsymbol{Q}_{N-3}}{Q_{N-3}^2}\right) \cdot (\boldsymbol{\kappa} \cdot \boldsymbol{Q}_{N-3}) \tag{B.40}$$

$$+ \left(\frac{1}{\zeta + 2K}\right)\left(\frac{\boldsymbol{Q}_{N-3}}{Q_{N-3}^2}\right) \cdot \left(\frac{\partial \phi}{\partial \boldsymbol{Q}_{N-4}}\right) - 2\left(\frac{1}{\zeta + 2K}\right)\left(\frac{\boldsymbol{Q}_{N-3}}{Q_{N-3}^2}\right) \cdot \left(\frac{\partial \phi}{\partial \boldsymbol{Q}_{N-3}}\right)$$

$$+ \left(\frac{1}{\zeta + 2K}\right)\left(\frac{\boldsymbol{Q}_{N-3}}{Q_{N-3}^2}\right) \cdot \left(\frac{\partial \phi}{\partial \boldsymbol{Q}_{N-2}}\right) + \left(\frac{1}{1 - P_{N-2}}\right)\left(\frac{K}{\zeta + 2K}\right)^2 C_{N-3} L_{N-3}^2$$

$$+ \left(\frac{\zeta}{\zeta + 2K}\right)\left(\frac{1}{Q_{N-3}}\right)\left[\left(\frac{K}{\zeta + 2K}\right)\left(\frac{1}{1 - P_{N-2}}\right) L_{N-3} \left(\frac{\boldsymbol{Q}_{N-2}}{Q_{N-2}}\right) \cdot (\boldsymbol{\kappa} \cdot \boldsymbol{Q}_{N-2})\right.$$

$$+ \left(\frac{K}{\zeta + 2K}\right)^2 \left(\frac{1}{1 - P_{N-2}}\right)\left(\frac{1}{1 - P_{N-1}}\right) L_{N-3} L_{N-2} \left(\frac{\boldsymbol{Q}_{N-1}}{Q_{N-1}}\right) \cdot (\boldsymbol{\kappa} \cdot \boldsymbol{Q}_{N-1})$$

$$+ \left(\frac{K}{\zeta + 2K}\right)^3 \left(\frac{1}{1 - P_{N-2}}\right)\left(\frac{1}{1 - P_{N-1}}\right) L_{N-3} L_{N-2} L_{N-1} \left(\frac{\boldsymbol{Q}_N}{Q_N}\right) \cdot (\boldsymbol{\kappa} \cdot \boldsymbol{Q}_N)\right]$$

$$+ \left(\frac{1}{\zeta + 2K}\right)\left(\frac{K}{\zeta + 2K}\right)\left(\frac{1}{1 - P_{N-2}}\right)\left(\frac{1}{Q_{N-3}}\right) L_{N-3} \left(\frac{\boldsymbol{Q}_{N-2}}{Q_{N-2}}\right) \cdot \left(\frac{\partial \phi}{\partial \boldsymbol{Q}_{N-3}}\right)$$

$$- \left(\frac{1}{\zeta + 2K}\right)\left(\frac{1}{Q_{N-3}}\right)\left[-\left(\frac{K}{\zeta + 2K}\right)^2 \left(\frac{1}{1 - P_{N-2}}\right)\left(\frac{1}{1 - P_{N-1}}\right) L_{N-3} L_{N-2} \left(\frac{\boldsymbol{Q}_{N-1}}{Q_{N-1}}\right)\right.$$

$$+ 2\left(\frac{K}{\zeta + 2K}\right)\left(\frac{1}{1 - P_{N-2}}\right) L_{N-3} \left(\frac{\boldsymbol{Q}_{N-2}}{Q_{N-2}}\right)\right] \cdot \left(\frac{\partial \phi}{\partial \boldsymbol{Q}_{N-2}}\right)$$

$$- \left(\frac{1}{\zeta + 2K}\right)\left(\frac{1}{Q_{N-3}}\right)\left[-\left(\frac{1}{1 - P_{N-2}}\right)\left(\frac{1}{1 - P_{N-1}}\right)\left(\frac{K}{\zeta + 2K}\right)^3 L_{N-3} L_{N-2} L_{N-1} \left(\frac{\boldsymbol{Q}_N}{Q_N}\right)\right.$$

$$+ 2\left(\frac{1}{1 - P_{N-2}}\right)\left(\frac{1}{1 - P_{N-1}}\right)\left(\frac{K}{\zeta + 2K}\right)^2 L_{N-3} L_{N-2} \left(\frac{\boldsymbol{Q}_{N-1}}{Q_{N-1}}\right)$$

$$- \left(\frac{1}{1 - P_{N-2}}\right)\left(\frac{K}{\zeta + 2K}\right) L_{N-3} \left(\frac{\boldsymbol{Q}_{N-2}}{Q_{N-2}}\right)\right] \cdot \left(\frac{\partial \phi}{\partial \boldsymbol{Q}_{N-1}}\right)$$

$$- \left(\frac{1}{\zeta + 2K}\right)\left(\frac{1}{Q_{N-3}}\right)\left[2\left(\frac{1}{1 - P_{N-2}}\right)\left(\frac{1}{1 - P_{N-1}}\right)\left(\frac{K}{\zeta + 2K}\right)^3 L_{N-3} L_{N-2} L_{N-1} \left(\frac{\boldsymbol{Q}_N}{Q_N}\right)\right.$$

$$- \left(\frac{1}{1 - P_{N-2}}\right)\left(\frac{1}{1 - P_{N-1}}\right)\left(\frac{K}{\zeta + 2K}\right)^2 L_{N-3} L_{N-2} \left(\frac{\boldsymbol{Q}_{N-1}}{Q_{N-1}}\right)\right] \cdot \left(\frac{\partial \phi}{\partial \boldsymbol{Q}_N}\right)$$

Defining

$$P_{N-3} = \left(\frac{1}{1 - P_{N-2}}\right)\left(\frac{K}{\zeta + 2K}\right)^2 L_{N-3}^2 \tag{B.41}$$

and grouping like terms together, we obtain

$$C_{N-3}(1-P_{N-3}) = \left(\frac{K}{\zeta+2K}\right)C_{N-4}L_{N-4}\left(\frac{Q_{N-4}}{Q_{N-3}}\right) \tag{B.42}$$

$$+\left(\frac{\zeta}{\zeta+2K}\right)\left(\frac{1}{Q_{N-3}}\right)\left[\left(\frac{\boldsymbol{Q}_{N-3}}{Q_{N-3}}\right)\cdot(\boldsymbol{\kappa}\cdot\boldsymbol{Q}_{N-3})\right.$$

$$+\left(\frac{K}{\zeta+2K}\right)\left(\frac{1}{1-P_{N-2}}\right)L_{N-3}\left(\frac{\boldsymbol{Q}_{N-2}}{Q_{N-2}}\right)\cdot(\boldsymbol{\kappa}\cdot\boldsymbol{Q}_{N-2})$$

$$+\left(\frac{K}{\zeta+2K}\right)^2\left(\frac{1}{1-P_{N-2}}\right)\left(\frac{1}{1-P_{N-1}}\right)L_{N-3}L_{N-2}\left(\frac{\boldsymbol{Q}_{N-1}}{Q_{N-1}}\right)\cdot(\boldsymbol{\kappa}\cdot\boldsymbol{Q}_{N-1})$$

$$+\left(\frac{K}{\zeta+2K}\right)^3\left(\frac{1}{1-P_{N-2}}\right)\left(\frac{1}{1-P_{N-1}}\right)L_{N-3}L_{N-2}L_{N-1}\left(\frac{\boldsymbol{Q}_{N}}{Q_{N}}\right)\cdot(\boldsymbol{\kappa}\cdot\boldsymbol{Q}_{N})\Big]$$

$$+\left(\frac{1}{\zeta+2K}\right)\left(\frac{\boldsymbol{Q}_{N-3}}{Q_{N-3}^2}\right)\cdot\left(\frac{\partial\phi}{\partial\boldsymbol{Q}_{N-4}}\right)$$

$$-\left(\frac{1}{\zeta+2K}\right)\left(\frac{1}{Q_{N-3}}\right)\left[-\left(\frac{K}{\zeta+2K}\right)\left(\frac{1}{1-P_{N-2}}\right)L_{N-3}\left(\frac{\boldsymbol{Q}_{N-2}}{Q_{N-2}}\right)\right.$$

$$+2\left(\frac{\boldsymbol{Q}_{N-3}}{Q_{N-3}}\right)\Big]\cdot\left(\frac{\partial\phi}{\partial\boldsymbol{Q}_{N-3}}\right)$$

$$-\left(\frac{1}{\zeta+2K}\right)\left(\frac{1}{Q_{N-3}}\right)\left[-\left(\frac{K}{\zeta+2K}\right)^2\left(\frac{1}{1-P_{N-2}}\right)\left(\frac{1}{1-P_{N-1}}\right)L_{N-3}L_{N-2}\left(\frac{\boldsymbol{Q}_{N-1}}{Q_{N-1}}\right)\right.$$

$$+2\left(\frac{K}{\zeta+2K}\right)\left(\frac{1}{1-P_{N-2}}\right)L_{N-3}\left(\frac{\boldsymbol{Q}_{N-2}}{Q_{N-2}}\right)-\left(\frac{\boldsymbol{Q}_{N-3}}{Q_{N-3}}\right)\Big]\cdot\left(\frac{\partial\phi}{\partial\boldsymbol{Q}_{N-2}}\right)$$

$$-\left(\frac{1}{\zeta+2K}\right)\left(\frac{1}{Q_{N-3}}\right)\left[-\left(\frac{1}{1-P_{N-2}}\right)\left(\frac{1}{1-P_{N-1}}\right)\left(\frac{K}{\zeta+2K}\right)^3L_{N-3}L_{N-2}L_{N-1}\left(\frac{\boldsymbol{Q}_{N}}{Q_{N}}\right)\right.$$

$$+2\left(\frac{1}{1-P_{N-2}}\right)\left(\frac{1}{1-P_{N-1}}\right)\left(\frac{K}{\zeta+2K}\right)^2L_{N-3}L_{N-2}\left(\frac{\boldsymbol{Q}_{N-1}}{Q_{N-1}}\right)$$

$$-\left(\frac{1}{1-P_{N-2}}\right)\left(\frac{K}{\zeta+2K}\right)L_{N-3}\left(\frac{\boldsymbol{Q}_{N-2}}{Q_{N-2}}\right)\Big]\cdot\left(\frac{\partial\phi}{\partial\boldsymbol{Q}_{N-1}}\right)$$

$$-\left(\frac{1}{\zeta+2K}\right)\left(\frac{1}{Q_{N-3}}\right)\left[2\left(\frac{1}{1-P_{N-2}}\right)\left(\frac{1}{1-P_{N-1}}\right)\left(\frac{K}{\zeta+2K}\right)^3L_{N-3}L_{N-2}L_{N-1}\left(\frac{\boldsymbol{Q}_{N}}{Q_{N}}\right)\right.$$

$$-\left(\frac{1}{1-P_{N-2}}\right)\left(\frac{1}{1-P_{N-1}}\right)\left(\frac{K}{\zeta+2K}\right)^2L_{N-3}L_{N-2}\left(\frac{\boldsymbol{Q}_{N-1}}{Q_{N-1}}\right)\Big]\cdot\left(\frac{\partial\phi}{\partial\boldsymbol{Q}_{N}}\right)$$

We thus have the following final expression for C_{N-3},

$$C_{N-3} = \left(\frac{1}{1-P_{N-3}}\right)\left(\frac{K}{\zeta+2K}\right)C_{N-4}L_{N-4}\left(\frac{Q_{N-4}}{Q_{N-3}}\right) \tag{B.43}$$

$$+ \left(\frac{\zeta}{\zeta+2K}\right)\left(\frac{1}{Q_{N-3}}\right)\left[\left(\frac{1}{1-P_{N-3}}\right)\left(\frac{\boldsymbol{Q}_{N-3}}{Q_{N-3}}\right)\cdot(\boldsymbol{\kappa}\cdot\boldsymbol{Q}_{N-3})\right.$$

$$+ \left(\frac{K}{\zeta+2K}\right)\left(\frac{1}{1-P_{N-3}}\right)\left(\frac{1}{1-P_{N-2}}\right)L_{N-3}\left(\frac{\boldsymbol{Q}_{N-2}}{Q_{N-2}}\right)\cdot(\boldsymbol{\kappa}\cdot\boldsymbol{Q}_{N-2})$$

$$+ \left(\frac{K}{\zeta+2K}\right)^2\left(\frac{1}{1-P_{N-3}}\right)\left(\frac{1}{1-P_{N-2}}\right)\left(\frac{1}{1-P_{N-1}}\right)L_{N-3}L_{N-2}\left(\frac{\boldsymbol{Q}_{N-1}}{Q_{N-1}}\right)\cdot(\boldsymbol{\kappa}\cdot\boldsymbol{Q}_{N-1})$$

$$+ \left(\frac{K}{\zeta+2K}\right)^3\left(\frac{1}{1-P_{N-3}}\right)\left(\frac{1}{1-P_{N-2}}\right)\left(\frac{1}{1-P_{N-1}}\right)L_{N-3}L_{N-2}L_{N-1}\left(\frac{\boldsymbol{Q}_N}{Q_N}\right)\cdot(\boldsymbol{\kappa}\cdot\boldsymbol{Q}_N)\right]$$

$$+ \left(\frac{1}{\zeta+2K}\right)\left(\frac{1}{1-P_{N-3}}\right)\left(\frac{\boldsymbol{Q}_{N-3}}{Q_{N-3}^2}\right)\cdot\left(\frac{\partial\phi}{\partial\boldsymbol{Q}_{N-4}}\right)$$

$$- \left(\frac{1}{\zeta+2K}\right)\left(\frac{1}{Q_{N-3}}\right)\left[-\left(\frac{K}{\zeta+2K}\right)\left(\frac{1}{1-P_{N-3}}\right)\left(\frac{1}{1-P_{N-2}}\right)L_{N-3}\left(\frac{\boldsymbol{Q}_{N-2}}{Q_{N-2}}\right)\right.$$

$$+ 2\left(\frac{1}{1-P_{N-3}}\right)\left(\frac{\boldsymbol{Q}_{N-3}}{Q_{N-3}}\right)\right]\cdot\left(\frac{\partial\phi}{\partial\boldsymbol{Q}_{N-3}}\right)$$

$$- \left(\frac{1}{\zeta+2K}\right)\left(\frac{1}{Q_{N-3}}\right)\left[-\left(\frac{K}{\zeta+2K}\right)^2\left(\frac{1}{1-P_{N-3}}\right)\left(\frac{1}{1-P_{N-2}}\right)\left(\frac{1}{1-P_{N-1}}\right)L_{N-3}L_{N-2}\left(\frac{\boldsymbol{Q}_{N-1}}{Q_{N-1}}\right)\right.$$

$$+ 2\left(\frac{K}{\zeta+2K}\right)\left(\frac{1}{1-P_{N-3}}\right)\left(\frac{1}{1-P_{N-2}}\right)L_{N-3}\left(\frac{\boldsymbol{Q}_{N-2}}{Q_{N-2}}\right) - \left(\frac{1}{1-P_{N-3}}\right)\left(\frac{\boldsymbol{Q}_{N-3}}{Q_{N-3}}\right)\right]\cdot\left(\frac{\partial\phi}{\partial\boldsymbol{Q}_{N-2}}\right)$$

$$- \left(\frac{1}{\zeta+2K}\right)\left(\frac{1}{Q_{N-3}}\right)\left[-\left(\frac{1}{1-P_{N-3}}\right)\left(\frac{1}{1-P_{N-2}}\right)\left(\frac{1}{1-P_{N-1}}\right)\left(\frac{K}{\zeta+2K}\right)^3 L_{N-3}L_{N-2}L_{N-1}\left(\frac{\boldsymbol{Q}_N}{Q_N}\right)\right.$$

$$+ 2\left(\frac{1}{1-P_{N-3}}\right)\left(\frac{1}{1-P_{N-2}}\right)\left(\frac{1}{1-P_{N-1}}\right)\left(\frac{K}{\zeta+2K}\right)^2 L_{N-3}L_{N-2}\left(\frac{\boldsymbol{Q}_{N-1}}{Q_{N-1}}\right)$$

$$- \left(\frac{1}{1-P_{N-3}}\right)\left(\frac{1}{1-P_{N-2}}\right)\left(\frac{K}{\zeta+2K}\right)L_{N-3}\left(\frac{\boldsymbol{Q}_{N-2}}{Q_{N-2}}\right)\right]\cdot\left(\frac{\partial\phi}{\partial\boldsymbol{Q}_{N-1}}\right)$$

$$- \left(\frac{1}{\zeta+2K}\right)\left(\frac{1}{Q_{N-3}}\right)\left[-\left(\frac{1}{1-P_{N-3}}\right)\left(\frac{1}{1-P_{N-2}}\right)\left(\frac{1}{1-P_{N-1}}\right)\left(\frac{K}{\zeta+2K}\right)^2 L_{N-3}L_{N-2}\left(\frac{\boldsymbol{Q}_{N-1}}{Q_{N-1}}\right)\right.$$

$$+ 2\left(\frac{1}{1-P_{N-3}}\right)\left(\frac{1}{1-P_{N-2}}\right)\left(\frac{1}{1-P_{N-1}}\right)\left(\frac{K}{\zeta+2K}\right)^3 L_{N-3}L_{N-2}L_{N-1}\left(\frac{\boldsymbol{Q}_N}{Q_N}\right)\right]\cdot\left(\frac{\partial\phi}{\partial\boldsymbol{Q}_N}\right)$$

Backward substitution expression for $k = (N-4)$:

From Eq. (), we have

$$C_{N-4} = \left(\frac{\zeta}{\zeta + 2K}\right)\left(\frac{\boldsymbol{Q}_{N-4}}{Q_{N-4}^2}\right) \cdot (\boldsymbol{\kappa} \cdot \boldsymbol{Q}_{N-4}) - \left(\frac{1}{\zeta + 2K}\right)\left(\frac{\boldsymbol{Q}_{N-4}}{Q_{N-4}^2}\right) \cdot \left[-\frac{\partial \phi}{\partial \boldsymbol{Q}_{N-5}} + 2\frac{\partial \phi}{\partial \boldsymbol{Q}_{N-4}} - \frac{\partial \phi}{\partial \boldsymbol{Q}_{N-3}}\right]$$

$$\text{(B.44)}$$

$$+ \left(\frac{K}{\zeta + 2K}\right)\left[C_{N-5}L_{N-5}\left(\frac{Q_{N-5}}{Q_{N-4}}\right) + C_{N-3}L_{N-4}\left(\frac{Q_{N-3}}{Q_{N-4}}\right)\right]$$

The underlined term in Eq. (B.44) may be found by multiplying Eq. (B.43) by $L_{N-4}\left(Q_{N-3}/Q_{N-4}\right)$,

$$C_{N-3}L_{N-4}\left(\frac{Q_{N-3}}{Q_{N-4}}\right) = \left(\frac{1}{1-P_{N-3}}\right)\left(\frac{K}{\zeta+2K}\right)C_{N-4}L_{N-4}^2 \tag{B.45}$$

$$+\left(\frac{\zeta}{\zeta+2K}\right)\left(\frac{1}{Q_{N-4}}\right)\left[\left(\frac{1}{1-P_{N-3}}\right)L_{N-4}\left(\frac{\boldsymbol{Q}_{N-3}}{Q_{N-3}}\right)\cdot(\boldsymbol{\kappa}\cdot\boldsymbol{Q}_{N-3})\right.$$

$$+\left(\frac{K}{\zeta+2K}\right)\left(\frac{1}{1-P_{N-3}}\right)\left(\frac{1}{1-P_{N-2}}\right)L_{N-4}L_{N-3}\left(\frac{\boldsymbol{Q}_{N-2}}{Q_{N-2}}\right)\cdot(\boldsymbol{\kappa}\cdot\boldsymbol{Q}_{N-2})$$

$$+\left(\frac{K}{\zeta+2K}\right)^2\left(\frac{1}{1-P_{N-3}}\right)\left(\frac{1}{1-P_{N-2}}\right)\left(\frac{1}{1-P_{N-1}}\right)L_{N-4}L_{N-3}L_{N-2}\left(\frac{\boldsymbol{Q}_{N-1}}{Q_{N-1}}\right)\cdot(\boldsymbol{\kappa}\cdot\boldsymbol{Q}_{N-1})$$

$$+\left(\frac{K}{\zeta+2K}\right)^3\left(\frac{1}{1-P_{N-3}}\right)\left(\frac{1}{1-P_{N-2}}\right)\left(\frac{1}{1-P_{N-1}}\right)L_{N-4}L_{N-3}L_{N-2}L_{N-1}\left(\frac{\boldsymbol{Q}_N}{Q_N}\right)\cdot(\boldsymbol{\kappa}\cdot\boldsymbol{Q}_N)\right]$$

$$+\left(\frac{1}{\zeta+2K}\right)\left(\frac{1}{1-P_{N-3}}\right)L_{N-4}\left(\frac{1}{Q_{N-4}}\right)\left(\frac{\boldsymbol{Q}_{N-3}}{Q_{N-3}}\right)\cdot\left(\frac{\partial\phi}{\partial\boldsymbol{Q}_{N-4}}\right)$$

$$-\left(\frac{1}{\zeta+2K}\right)\left(\frac{1}{Q_{N-4}}\right)\left[-\left(\frac{K}{\zeta+2K}\right)\left(\frac{1}{1-P_{N-3}}\right)\left(\frac{1}{1-P_{N-2}}\right)L_{N-4}L_{N-3}\left(\frac{\boldsymbol{Q}_{N-2}}{Q_{N-2}}\right)\right.$$

$$+2\left(\frac{1}{1-P_{N-3}}\right)L_{N-4}\left(\frac{\boldsymbol{Q}_{N-3}}{Q_{N-3}}\right)\right]\cdot\left(\frac{\partial\phi}{\partial\boldsymbol{Q}_{N-3}}\right)$$

$$-\left(\frac{1}{\zeta+2K}\right)\left(\frac{1}{Q_{N-4}}\right)\left[-\left(\frac{K}{\zeta+2K}\right)^2\left(\frac{1}{1-P_{N-3}}\right)\left(\frac{1}{1-P_{N-2}}\right)\left(\frac{1}{1-P_{N-1}}\right)L_{N-4}L_{N-3}L_{N-2}\left(\frac{\boldsymbol{Q}_{N-1}}{Q_{N-1}}\right)\right.$$

$$+2\left(\frac{K}{\zeta+2K}\right)\left(\frac{1}{1-P_{N-3}}\right)\left(\frac{1}{1-P_{N-2}}\right)L_{N-4}L_{N-3}\left(\frac{\boldsymbol{Q}_{N-2}}{Q_{N-2}}\right)$$

$$-\left(\frac{1}{1-P_{N-3}}\right)L_{N-4}\left(\frac{\boldsymbol{Q}_{N-3}}{Q_{N-3}}\right)\right]\cdot\left(\frac{\partial\phi}{\partial\boldsymbol{Q}_{N-2}}\right)$$

$$-\left(\frac{1}{\zeta+2K}\right)\left(\frac{1}{Q_{N-4}}\right)\left[2\left(\frac{1}{1-P_{N-3}}\right)\left(\frac{1}{1-P_{N-2}}\right)\left(\frac{1}{1-P_{N-1}}\right)\left(\frac{K}{\zeta+2K}\right)^2 L_{N-4}L_{N-3}L_{N-2}\left(\frac{\boldsymbol{Q}_{N-1}}{Q_{N-1}}\right)\right.$$

$$-\left(\frac{1}{1-P_{N-3}}\right)\left(\frac{1}{1-P_{N-2}}\right)\left(\frac{1}{1-P_{N-1}}\right)\left(\frac{K}{\zeta+2K}\right)^3 L_{N-4}L_{N-3}L_{N-2}L_{N-1}\left(\frac{\boldsymbol{Q}_N}{Q_N}\right)$$

$$-\left(\frac{1}{1-P_{N-3}}\right)\left(\frac{1}{1-P_{N-2}}\right)\left(\frac{K}{\zeta+2K}\right)L_{N-4}L_{N-3}\left(\frac{\boldsymbol{Q}_{N-2}}{Q_{N-2}}\right)\right]\cdot\left(\frac{\partial\phi}{\partial\boldsymbol{Q}_{N-1}}\right)$$

$$-\left(\frac{1}{\zeta + 2K}\right)\left(\frac{1}{Q_{N-4}}\right)\times$$

$$\left[2\left(\frac{1}{1 - P_{N-3}}\right)\left(\frac{1}{1 - P_{N-2}}\right)\left(\frac{1}{1 - P_{N-1}}\right)\left(\frac{K}{\zeta + 2K}\right)^3 L_{N-4}L_{N-3}L_{N-2}L_{N-1}\left(\frac{Q_N}{Q_N}\right)\right.$$

$$\left.-\left(\frac{1}{1 - P_{N-3}}\right)\left(\frac{1}{1 - P_{N-2}}\right)\left(\frac{1}{1 - P_{N-1}}\right)\left(\frac{K}{\zeta + 2K}\right)^2 L_{N-4}L_{N-3}L_{N-2}\left(\frac{Q_{N-1}}{Q_{N-1}}\right)\right]\cdot\left(\frac{\partial \phi}{\partial Q_N}\right)$$

Based on the pattern observed from Eqs. (B.29), (B.35), and (B.41) , a general expression for the backward susbtituition coefficients, P_k, may be written as

$$P_k = \left(\frac{K}{\zeta + 2K}\right)^2 \left(\frac{L_k^2}{1 - P_{k+1}}\right); \quad \text{with} \quad P_N = 0, \tag{B.46}$$

The next challenge is to prescribe a general expression for $C_k L_{k-1}\left(Q_k/Q_{k-1}\right)$, based on the pattern discerned from Eqs. (B.27), (B.33), (B.39), and (B.45). Upon careful observation and induction, the general expression obtained at the end of the backward substitution step may be written as shown in Eq. (5.11) of Chapter 5.

Appendix C

Derivation of the stress tensor expression for bead-spring-dashpot chains with fluctuating internal friction

In the first part of this appendix, it is established that the Giesekus expression for the stress tensor, shown to be thermodynamically consistent (Schieber and Öttinger, 1994) for chains with internal friction is formally similar to the Kramers expression, provided that the force in the connector vector is redefined to account for the restoring force from the dashpot. In other words, the intermediate steps leading to Equation (5.40), starting from Eq. (5.39) [in Chapter 5] are first presented. Following this, the detailed steps for arriving at the closed-form expression for the stress tensor, as given by Eq. (5.42) in Chapter 5, are presented. Summations are indicated explicitly, and the Einstein convention is not followed.

The Giesekus expression for the stress tensor is written as follows

$$
\tau_\mathrm{p} = \frac{n_\mathrm{p}\zeta}{2} \underbrace{\left\langle \sum_{u=1}^{N} \sum_{v=1}^{N} \mathscr{C}_{uv} \boldsymbol{Q}_u \boldsymbol{Q}_v \right\rangle}_{(1)} = \frac{n_\mathrm{p}\zeta}{2} \Bigg[\frac{d}{dt} \left\langle \sum_{u,v} \mathscr{C}_{uv} \boldsymbol{Q}_u \boldsymbol{Q}_v \right\rangle - \boldsymbol{\kappa} \cdot \left\langle \sum_{u,v} \mathscr{C}_{uv} \boldsymbol{Q}_u \boldsymbol{Q}_v \right\rangle
$$
$$
- \left\langle \sum_{u,v} \mathscr{C}_{uv} \boldsymbol{Q}_u \boldsymbol{Q}_v \right\rangle \cdot \boldsymbol{\kappa}^T \Bigg]
\tag{C.1}
$$

where $\mathscr{C}_{uv}$ represents elements of the symmetric Kramers matrix (Bird *et al.*, 1987b), which is inverse to the Rouse matrix. We identify $\boldsymbol{B} \equiv \sum_{u,v=1}^{N} \mathscr{C}_{uv} \boldsymbol{Q}_u \boldsymbol{Q}_v$ in Eq. (C.1) and aim to find an expression for $\frac{d}{dt} \langle \boldsymbol{B} \rangle$, which is also referred to as the equation of change (Bird *et al.*, 1987b).

We start with the continuity equation for a bead-spring-dashpot chain in a homogeneous flow profile, which may be written as

$$\frac{\partial \psi}{\partial t} = -\sum_{j=1}^{N} \frac{\partial}{\partial \boldsymbol{Q}_j} \cdot \left\{ [\![\dot{\boldsymbol{Q}}_j]\!] \psi \right\} \tag{C.2}$$

The normalized distribution function for the internal coordinates (ψ) may be used instead of the distribution function based on all the bead positions (Ψ), due to the homogeneous flow profile being considered in the derivation of the stress tensor expression. The equation of change for the second-order tensor $\boldsymbol{B}$ may be found by multiplying both sides of Equation (C.2) and integrating over all space as follows

$$\int \boldsymbol{B} \frac{\partial \psi}{\partial t} d\boldsymbol{Q} = -\int \left(\sum_{j=1}^{N} \frac{\partial}{\partial \boldsymbol{Q}_j} \cdot \left\{ [\![\dot{\boldsymbol{Q}}_j]\!] \psi \right\} \right) \boldsymbol{B} d\boldsymbol{Q} \tag{C.3}$$

where $d\boldsymbol{Q} \equiv d\boldsymbol{Q}_1 d\boldsymbol{Q}_2 \cdots d\boldsymbol{Q}_N$ On the LHS of Eq. (C.3), since $\boldsymbol{B}$ does not depend explicitly on t, we may write

$$\int \boldsymbol{B} \frac{\partial \psi}{\partial t} d\boldsymbol{Q} = \frac{\partial}{\partial t} \int \boldsymbol{B} \psi \, d\boldsymbol{Q} = \frac{d}{dt} \langle \boldsymbol{B} \rangle \tag{C.4}$$

We represent

$$\boldsymbol{Q}_j = \sum_{\alpha} Q_j^{\alpha} \boldsymbol{e}_{\alpha}$$

$$[\![\dot{\boldsymbol{Q}}_j]\!] = \sum_{\beta} [\![\dot{Q}_k^{\beta}]\!] \boldsymbol{e}_{\beta} \tag{C.5}$$

$$\boldsymbol{B} = \sum_{m,n} B^{mn} \boldsymbol{e}_m \boldsymbol{e}_n$$

and the term within the summation on the RHS of Eq. (C.3) may be written as

$$\frac{\partial}{\partial \boldsymbol{Q}_j} \cdot \left\{ [\![\dot{\boldsymbol{Q}}_j]\!] \psi \right\} \boldsymbol{B} = \sum_{m,n,\alpha} \left[B^{mn} \frac{\partial \left([\![\dot{Q}_j^{\alpha}]\!] \psi \right)}{\partial Q_j^{\alpha}} \right] \boldsymbol{e}_m \boldsymbol{e}_n$$

$$= \sum_{m,n,\alpha} \left[\frac{\partial \left(B^{mn} [\![\dot{Q}_j^{\alpha}]\!] \psi \right)}{\partial Q_j^{\alpha}} - [\![\dot{Q}_j^{\alpha}]\!] \psi \frac{\partial \left(B^{mn} \right)}{\partial Q_j^{\alpha}} \right] \boldsymbol{e}_m \boldsymbol{e}_n \tag{C.6}$$

$$= \frac{\partial}{\partial \boldsymbol{Q}_j} \cdot \left\{ [\![\dot{\boldsymbol{Q}}_j]\!] \psi \boldsymbol{B} \right\} - \psi [\![\dot{\boldsymbol{Q}}_j]\!] \cdot \frac{\partial \boldsymbol{B}}{\partial \boldsymbol{Q}_j},$$

leading to

$$-\sum_{j=1}^{N} \left(\frac{\partial}{\partial \boldsymbol{Q}_j} \cdot \left\{ [\![\dot{\boldsymbol{Q}}_j]\!] \psi \right\} \right) \boldsymbol{B} = -\sum_{j=1}^{N} \frac{\partial}{\partial \boldsymbol{Q}_j} \cdot \left\{ [\![\dot{\boldsymbol{Q}}_j]\!] \psi \boldsymbol{B} \right\} + \sum_{j=1}^{N} \psi [\![\dot{\boldsymbol{Q}}_j]\!] \cdot \frac{\partial \boldsymbol{B}}{\partial \boldsymbol{Q}_j}, \tag{C.7}$$

and finally

$$-\int \left(\sum_{j=1}^{N} \frac{\partial}{\partial \boldsymbol{Q}_j} \cdot \left\{ [\![\dot{\boldsymbol{Q}}_j]\!] \psi \right\} \right) \boldsymbol{B} d\boldsymbol{Q} = -\int \left(\sum_{j=1}^{N} \frac{\partial}{\partial \boldsymbol{Q}_j} \cdot \left\{ [\![\dot{\boldsymbol{Q}}_j]\!] \psi \boldsymbol{B} \right\} \right) d\boldsymbol{Q} + \int \left(\sum_{j=1}^{N} \psi [\![\dot{\boldsymbol{Q}}_j]\!] \cdot \frac{\partial \boldsymbol{B}}{\partial \boldsymbol{Q}_j} \right) d\boldsymbol{Q}$$

$$\tag{C.8}$$

The first term on the RHS of Eq. (C.8) vanishes, due to the Gauss divergence theorem (Bird *et al.*, 1987b), since the configurational distribution function is expected to vanish on a surface that is infinitely large. As a result,

$$
-\int\left(\sum_{j=1}^{N}\frac{\partial}{\partial \boldsymbol{Q}_j}\cdot\left\{[\![\dot{\boldsymbol{Q}}_j]\!]\psi\right\}\right)\boldsymbol{B}d\boldsymbol{Q} = \int\left(\sum_{j=1}^{N}\psi[\![\dot{\boldsymbol{Q}}_j]\!]\cdot\frac{\partial \boldsymbol{B}}{\partial \boldsymbol{Q}_j}\right)d\boldsymbol{Q} = \left\langle\sum_{j=1}^{N}\left([\![\dot{\boldsymbol{Q}}_j]\!]\cdot\frac{\partial \boldsymbol{B}}{\partial \boldsymbol{Q}_j}\right)\right\rangle \quad \text{(C.9)}
$$

From Eqs. (C.3), C.4, and (C.9), we thus have the following simplified equation of change for $\boldsymbol{B}$,

$$
\frac{d}{dt}\langle\boldsymbol{B}\rangle = \left\langle\sum_{j=1}^{N}\left([\![\dot{\boldsymbol{Q}}_j]\!]\cdot\frac{\partial \boldsymbol{B}}{\partial \boldsymbol{Q}_j}\right)\right\rangle \quad \text{(C.10)}
$$

For the specific choice of $\boldsymbol{B}$ considered in this appendix, we have

$$
\begin{aligned}
\frac{\partial \boldsymbol{B}}{\partial \boldsymbol{Q}_j} &= \sum_{u,v}\mathscr{C}_{uv}\frac{\partial}{\partial \boldsymbol{Q}_j}\left(\boldsymbol{Q}_u\boldsymbol{Q}_v\right) \\
&= \sum_{u,v}\mathscr{C}_{uv}\sum_{\alpha,\beta,\gamma}\frac{\partial}{\partial Q_j^\alpha}\left(Q_u^\beta Q_v^\gamma\right)\boldsymbol{e}_\alpha\boldsymbol{e}_\beta\boldsymbol{e}_\gamma \\
&= \sum_{u,v}\mathscr{C}_{uv}\sum_{\alpha,\beta,\gamma}\left[Q_u^\beta\frac{\partial Q_v^\gamma}{\partial Q_j^\alpha} + Q_v^\gamma\frac{\partial Q_u^\beta}{\partial Q_j^\alpha}\right]\boldsymbol{e}_\alpha\boldsymbol{e}_\beta\boldsymbol{e}_\gamma \\
&= \sum_{u,v}\sum_{\alpha,\beta,\gamma}\mathscr{C}_{uv}\left[Q_u^\beta\delta_{vj}\delta^{\alpha\gamma}\boldsymbol{e}_\alpha\boldsymbol{e}_\beta\boldsymbol{e}_\gamma + Q_v^\gamma\delta_{uj}\delta^{\beta\gamma}\boldsymbol{e}_\alpha\boldsymbol{e}_\beta\boldsymbol{e}_\gamma\right],
\end{aligned} \quad \text{(C.11)}
$$

and obtain

$$
\frac{\partial \boldsymbol{B}}{\partial \boldsymbol{Q}_j} = \sum_{u}\sum_{\alpha,\beta}\mathscr{C}_{uj}Q_u^\beta\boldsymbol{e}_\alpha\boldsymbol{e}_\beta\boldsymbol{e}_\alpha + \sum_{v}\sum_{\alpha,\gamma}\mathscr{C}_{jv}Q_v^\gamma\boldsymbol{e}_\alpha\boldsymbol{e}_\alpha\boldsymbol{e}_\gamma \quad \text{(C.12)}
$$

The equation of motion for the connector vector velocity is written [see Chapter 5] as follows

$$
[\![\dot{\boldsymbol{Q}}_j]\!] = \boldsymbol{\kappa}\cdot\boldsymbol{Q}_j - \frac{1}{\zeta}\sum_{k=1}^{N}A_{jk}\left(k_BT\frac{\partial\ln\psi}{\partial \boldsymbol{Q}_k} + \frac{\partial\phi}{\partial \boldsymbol{Q}_k} + KC_k\boldsymbol{Q}_k\right) \quad \text{(C.13)}
$$

where A_{jk} is the Rouse matrix as defined in Eq. (2.3) of Chapter 2 and

$$
C_k = \frac{\boldsymbol{Q}_k\cdot[\![\dot{\boldsymbol{Q}}_k]\!]}{Q_k^2} \quad \text{(C.14)}
$$

The following definition holds for (Sunthar and Prakash, 2005) arbitrary spring-force laws, with the Hookean stiffness of the spring denoted by H and maximum stretched length of the spring given by Q_0

$$
\boldsymbol{F}_k^{\text{s}} \equiv \frac{\partial\phi}{\partial \boldsymbol{Q}_k} = H\boldsymbol{Q}_kf\left(Q_k/Q_0\right) \quad \text{(C.15)}
$$

The functional form of the scalar entity, $f(Q_k/Q_0)$ depends on the spring type used, and is unity for Hookean springs. The following notation is introduced $f_k \equiv f(Q_k/Q_0)$ for convenience. The underlined term in Eq. (C.1) may then be processed as

$$\frac{d}{dt} \left\langle \sum_{u,v} \mathscr{C}_{uv} \boldsymbol{Q}_u \boldsymbol{Q}_v \right\rangle \equiv \frac{d}{dt} \langle \boldsymbol{B} \rangle = \left\langle \sum_{j=1}^{N} \left([\![\dot{\boldsymbol{Q}}_j]\!] \cdot \frac{\partial \boldsymbol{B}}{\partial \boldsymbol{Q}_j} \right) \right\rangle \tag{C.16}$$

Substituting Eq. (C.13) in Eq. (C.16), we obtain

$$\begin{aligned}
\frac{d}{dt} \langle \boldsymbol{B} \rangle &= \left\langle \sum_j \left[\boldsymbol{\kappa} \cdot \boldsymbol{Q}_j \right] \cdot \frac{\partial \boldsymbol{B}}{\partial \boldsymbol{Q}_j} \right\rangle - \frac{k_B T}{\zeta} \left\langle \sum_{j,k} \left(A_{jk} \frac{\partial \ln \psi}{\partial \boldsymbol{Q}_k} \right) \cdot \frac{\partial \boldsymbol{B}}{\partial \boldsymbol{Q}_j} \right\rangle \\
&\quad - \frac{H}{\zeta} \left\langle \sum_{j,k} A_{jk} f_k \boldsymbol{Q}_k \cdot \frac{\partial \boldsymbol{B}}{\partial \boldsymbol{Q}_j} \right\rangle - \frac{K}{\zeta} \left\langle \sum_{j,k} A_{jk} C_k \boldsymbol{Q}_k \cdot \frac{\partial \boldsymbol{B}}{\partial \boldsymbol{Q}_j} \right\rangle
\end{aligned} \tag{C.17}$$

The four terms on the RHS of Eq. (C.17) are identified respectively as the flow, Brownian force, spring force, and internal viscosity force contributions. These terms are processed sequentially, as shown below. Firstly, we recognize that

$$\boldsymbol{\kappa} \cdot \boldsymbol{Q}_j = \left[\sum_{m,n} \kappa^{mn} \boldsymbol{e}_m \boldsymbol{e}_n \right] \cdot \left[\sum_{\alpha} Q_j^\alpha \boldsymbol{e}_\alpha \right] = \sum_{m,n} \kappa^{mn} Q_j^n \boldsymbol{e}_m \tag{C.18}$$

Using Eq. (C.18) and (C.12), we may write

$$\begin{aligned}
\left\langle \sum_j \left[\boldsymbol{\kappa} \cdot \boldsymbol{Q}_j \right] \cdot \frac{\partial \boldsymbol{B}}{\partial \boldsymbol{Q}_j} \right\rangle &= \left\langle \sum_j \left[\sum_{m,n} \kappa^{mn} Q_j^n \boldsymbol{e}_m \right] \cdot \left[\sum_u \sum_{\alpha,\beta} \mathscr{C}_{uj} Q_u^\beta \boldsymbol{e}_\alpha \boldsymbol{e}_\beta \boldsymbol{e}_\alpha + \sum_v \sum_{\alpha,\gamma} \mathscr{C}_{jv} Q_v^\gamma \boldsymbol{e}_\alpha \boldsymbol{e}_\alpha \boldsymbol{e}_\gamma \right] \right\rangle \\
&= \left\langle \sum_{j,u} \sum_{m,n,\alpha,\beta} \kappa^{mn} Q_j^n \mathscr{C}_{uj} Q_u^\beta \delta^{m\alpha} \boldsymbol{e}_\beta \boldsymbol{e}_\alpha \right\rangle + \left\langle \sum_{j,v} \sum_{m,n,\alpha,\beta} \kappa^{mn} Q_j^n \mathscr{C}_{jv} Q_v^\gamma \delta^{m\alpha} \boldsymbol{e}_\alpha \boldsymbol{e}_\gamma \right\rangle \\
&= \left\langle \sum_{j,u} \sum_{\alpha,\beta,n} \kappa^{\alpha n} Q_j^n \mathscr{C}_{uj} Q_u^\beta \boldsymbol{e}_\beta \boldsymbol{e}_\alpha \right\rangle + \left\langle \sum_{j,v} \sum_{\alpha,\beta,n} \kappa^{\alpha n} Q_j^n \mathscr{C}_{jv} Q_v^\gamma \boldsymbol{e}_\alpha \boldsymbol{e}_\gamma \right\rangle \\
&= \left\langle \sum_{j,u} \sum_{\alpha,\beta,n} \left(\mathscr{C}_{uj} Q_u^\beta Q_j^n \right) \kappa^{\alpha n} \boldsymbol{e}_\beta \boldsymbol{e}_\alpha \right\rangle + \left\langle \sum_{j,v} \sum_{\alpha,\beta,n} \kappa^{\alpha n} \left(\mathscr{C}_{jv} Q_j^n Q_v^\gamma \right) \boldsymbol{e}_\alpha \boldsymbol{e}_\gamma \right\rangle
\end{aligned} \tag{C.19}$$

Recognizing that

$$\begin{aligned}
\boldsymbol{\kappa} \cdot (\boldsymbol{Q}_u \boldsymbol{Q}_v) &= \sum_{m,n,r,s} \kappa^{mn} Q_u^r Q_v^s \left[(\boldsymbol{e}_m \boldsymbol{e}_n) \cdot (\boldsymbol{e}_r \boldsymbol{e}_s) \right] \\
&= \sum_{m,n,r,s} \kappa^{mn} Q_u^r Q_v^s \delta_{nr} (\boldsymbol{e}_m \boldsymbol{e}_s) \\
&= \sum_{m,r,s} \kappa^{mr} Q_u^r Q_v^s \boldsymbol{e}_m \boldsymbol{e}_s,
\end{aligned} \tag{C.20}$$

and

$$
\begin{aligned}
(\boldsymbol{Q}_u\boldsymbol{Q}_v) \cdot \boldsymbol{\kappa}^T &= \sum_{m,n,r,s} (Q_u^r Q_v^s \boldsymbol{e}_r\boldsymbol{e}_s) \cdot (\kappa^{nm}\boldsymbol{e}_m\boldsymbol{e}_n) \\
&= \sum_{m,n,r,s} \kappa^{nm} Q_u^r Q_v^s \left[(\boldsymbol{e}_r\boldsymbol{e}_s) \cdot (\boldsymbol{e}_m\boldsymbol{e}_n) \right] \\
&= \sum_{m,n,r,s} \kappa^{nm} Q_u^r Q_v^s \delta_{ms}\boldsymbol{e}_r\boldsymbol{e}_n \\
&= \sum_{m,n,r} Q_u^r Q_v^m \kappa^{nm}\boldsymbol{e}_r\boldsymbol{e}_n,
\end{aligned}
\tag{C.21}
$$

we may write

$$
\begin{aligned}
\left\langle \sum_j \left[\boldsymbol{\kappa} \cdot \boldsymbol{Q}_j \right] \cdot \frac{\partial \boldsymbol{B}}{\partial \boldsymbol{Q}_j} \right\rangle &= \left\langle \sum_{j,u} \mathscr{C}_{uj}\boldsymbol{Q}_u\boldsymbol{Q}_j \right\rangle \cdot \boldsymbol{\kappa}^T + \boldsymbol{\kappa} \cdot \left\langle \sum_{j,v} \mathscr{C}_{jv}\boldsymbol{Q}_j\boldsymbol{Q}_v \right\rangle \\
&= \left\langle \sum_{u,v} \mathscr{C}_{uv}\boldsymbol{Q}_u\boldsymbol{Q}_v \right\rangle \cdot \boldsymbol{\kappa}^T + \boldsymbol{\kappa} \cdot \left\langle \sum_{u,v} \mathscr{C}_{uv}\boldsymbol{Q}_u\boldsymbol{Q}_v \right\rangle
\end{aligned}
\tag{C.22}
$$

Next, the Brownian force term may be processed as

$$
\begin{aligned}
\left\langle \sum_{j,k} \left(A_{jk}\frac{\partial \ln \psi}{\partial \boldsymbol{Q}_k} \right) \cdot \frac{\partial \boldsymbol{B}}{\partial \boldsymbol{Q}_j} \right\rangle &= \left\langle \sum_{j,k}\sum_s \left(A_{jk}\frac{\partial \ln \psi}{\partial Q_k^s}\boldsymbol{e}_s \right) \cdot \left[\sum_u \sum_{\alpha,\beta} \mathscr{C}_{uj}Q_u^\beta \boldsymbol{e}_\alpha\boldsymbol{e}_\beta\boldsymbol{e}_\alpha \right. \right. \\
&\qquad\qquad \left. \left. + \sum_v \sum_{\alpha,\gamma} \mathscr{C}_{jv}Q_v^\gamma \boldsymbol{e}_\alpha\boldsymbol{e}_\alpha\boldsymbol{e}_\gamma \right] \right\rangle \\
&= \left\langle \left[\sum_{j,k,u} \sum_{s,\alpha,\beta} A_{jk}\frac{\partial \ln \psi}{\partial Q_k^s}\mathscr{C}_{uj}Q_u^\beta (\boldsymbol{e}_s \cdot \boldsymbol{e}_\alpha)\boldsymbol{e}_\beta\boldsymbol{e}_\alpha \right] \right\rangle \\
&\quad + \left\langle \left[\sum_{j,k,v} \sum_{s,\alpha,\gamma} A_{jk}\frac{\partial \ln \psi}{\partial Q_k^s}\mathscr{C}_{jv}Q_v^\gamma (\boldsymbol{e}_s \cdot \boldsymbol{e}_\alpha)\boldsymbol{e}_\alpha\boldsymbol{e}_\gamma \right] \right\rangle \\
&= \underline{\left\langle \left[\sum_{j,k,u} \sum_{\alpha,\beta} A_{jk}\frac{\partial \ln \psi}{\partial Q_k^\alpha}\mathscr{C}_{uj}Q_u^\beta \boldsymbol{e}_\beta\boldsymbol{e}_\alpha \right] \right\rangle} \\
&\quad + \left\langle \left[\sum_{j,k,v} \sum_{\alpha,\gamma} A_{jk}\frac{\partial \ln \psi}{\partial Q_k^\alpha}\mathscr{C}_{jv}Q_v^\gamma \boldsymbol{e}_\alpha\boldsymbol{e}_\gamma \right] \right\rangle \\
&\quad \cdots\cdots\cdots\cdots\cdots\cdots\cdots\cdots\cdots
\end{aligned}
\tag{C.23}
$$

The solid-underlined term in Eq. (C.23) may be simplified as shown below

$$
\left\langle \left[\sum_{j,k,u} \sum_{\alpha,\beta} A_{jk} \frac{\partial \ln \psi}{\partial Q_k^\alpha} \mathscr{C}_{uj} Q_u^\beta \boldsymbol{e}_\beta \boldsymbol{e}_\alpha \right] \right\rangle = \left\langle \sum_{k,u} \sum_{\alpha,\beta} \left(\sum_j A_{kj} \mathscr{C}_{ju} \right) \frac{\partial \ln \psi}{\partial Q_k^\alpha} Q_u^\beta \boldsymbol{e}_\beta \boldsymbol{e}_\alpha \right\rangle
$$

$$
= \left\langle \sum_{k,u} \sum_{\alpha,\beta} \delta_{ku} \frac{\partial \ln \psi}{\partial Q_k^\alpha} Q_u^\beta \boldsymbol{e}_\beta \boldsymbol{e}_\alpha \right\rangle
$$

$$
= \left\langle \sum_k \sum_{\alpha,\beta} \frac{\partial \ln \psi}{\partial Q_k^\alpha} Q_k^\beta \boldsymbol{e}_\beta \boldsymbol{e}_\alpha \right\rangle \tag{C.24}
$$

$$
= \sum_k \sum_{\alpha,\beta} \left[\int \left(\frac{1}{\psi} \right) \left(\frac{\partial \psi}{\partial Q_k^\alpha} \right) Q_k^\beta \psi \, d\boldsymbol{Q} \right] \boldsymbol{e}_\beta \boldsymbol{e}_\alpha
$$

The integral in Eq. (C.24) may be simplified as

$$
\int \left(\frac{\partial \psi}{\partial Q_k^\alpha} \right) Q_k^\beta \, d\boldsymbol{Q} = \int \left[\frac{\partial}{\partial Q_k^\alpha} \left(Q_k^\beta \psi \right) - \psi \frac{\partial Q_k^\beta}{\partial Q_k^\alpha} \right] d\boldsymbol{Q}
$$

$$
= \underline{\int \frac{\partial}{\partial Q_k^\alpha} \left(Q_k^\beta \psi \right) d\boldsymbol{Q}} - \delta^{\alpha\beta} \int \psi \, d\boldsymbol{Q} \tag{C.25}
$$

The underlined term in Eq. (C.25) vanishes due to the Gauss divergence theorem, and the integral in the second term is unity due to the normalization condition, and we have

$$
\int \left(\frac{\partial \psi}{\partial Q_k^\alpha} \right) Q_k^\beta \, d\boldsymbol{Q} = -\delta^{\alpha\beta} \tag{C.26}
$$

Combining Eq. (C.24) and (C.26), we may show that

$$
\left\langle \left[\sum_{j,k,u} \sum_{\alpha,\beta} A_{jk} \frac{\partial \ln \psi}{\partial Q_k^\alpha} \mathscr{C}_{uj} Q_u^\beta \boldsymbol{e}_\beta \boldsymbol{e}_\alpha \right] \right\rangle = -\sum_{k=1}^N \sum_{\alpha,\beta} \delta^{\alpha\beta} \boldsymbol{e}_\beta \boldsymbol{e}_\alpha = -N\boldsymbol{\delta} \tag{C.27}
$$

Proceeding identically to the steps outlined in Eq. (C.24) to (C.26), the dot-underlined term on the RHS of Eq. (C.23) also evaluates to be

$$
\left\langle \left[\sum_{j,k,v} \sum_{\alpha,\gamma} A_{jk} \frac{\partial \ln \psi}{\partial Q_k^\alpha} \mathscr{C}_{jv} Q_v^\gamma \boldsymbol{e}_\alpha \boldsymbol{e}_\gamma \right] \right\rangle = -N\boldsymbol{\delta} \tag{C.28}
$$

From Equations (C.23), (C.27) and (C.28), we may write

$$
\left\langle \sum_{j,k} \left(A_{jk} \frac{\partial \ln \psi}{\partial \boldsymbol{Q}_k} \right) \cdot \frac{\partial \boldsymbol{B}}{\partial \boldsymbol{Q}_j} \right\rangle = -2N\boldsymbol{\delta} \tag{C.29}
$$

The last two terms on the RHS of Equation (C.17) may be processed as follows

$$
\frac{H}{\zeta} \left\langle \sum_{j,k} A_{jk} f_k \boldsymbol{Q}_k \cdot \frac{\partial \boldsymbol{B}}{\partial \boldsymbol{Q}_j} \right\rangle + \frac{K}{\zeta} \left\langle \sum_{j,k} A_{jk} C_k \boldsymbol{Q}_k \cdot \frac{\partial \boldsymbol{B}}{\partial \boldsymbol{Q}_j} \right\rangle
$$

$$
= \frac{1}{\zeta} \left\langle \sum_{j,k} A_{jk} \left[H f_k + K C_k \right] \boldsymbol{Q}_k \cdot \frac{\partial \boldsymbol{B}}{\partial \boldsymbol{Q}_j} \right\rangle \tag{C.30}
$$

Substituting Eq. C.12 into Eq. (C.30), we write

$$
\left\langle \sum_{j,k} A_{jk} \left[Hf_k + KC_k \right] \boldsymbol{Q}_k \cdot \frac{\partial \boldsymbol{B}}{\partial \boldsymbol{Q}_j} \right\rangle = \left\langle \sum_{j,k} \sum_s A_{jk} \left[Hf_k + KC_k \right] Q_k^s \boldsymbol{e}_s \cdot \left[\sum_u \sum_{\alpha,\beta} \mathscr{C}_{uj} Q_u^\beta \boldsymbol{e}_\alpha \boldsymbol{e}_\beta \boldsymbol{e}_\alpha \right. \right.
$$
$$
\left. \left. + \sum_v \sum_{\alpha,\gamma} \mathscr{C}_{jv} Q_v^\gamma \boldsymbol{e}_\alpha \boldsymbol{e}_\alpha \boldsymbol{e}_\gamma \right] \right\rangle
$$

$$
= \left\langle \sum_{j,k,u} \sum_{s,\alpha,\beta} A_{jk} \left[Hf_k + KC_k \right] Q_k^s \mathscr{C}_{uj} Q_u^\beta \left(\boldsymbol{e}_s \cdot \boldsymbol{e}_\alpha \right) \boldsymbol{e}_\beta \boldsymbol{e}_\alpha \right.
$$
$$
\left. + \sum_{j,k,v} \sum_{s,\alpha,\gamma} A_{jk} \left[Hf_k + KC_k \right] Q_k^s \mathscr{C}_{jv} Q_v^\gamma \left(\boldsymbol{e}_s \cdot \boldsymbol{e}_\alpha \right) \boldsymbol{e}_\alpha \boldsymbol{e}_\gamma \right\rangle
$$

$$
= \left\langle \sum_{k,u} \sum_{\alpha,\beta} \left(\sum_j A_{kj} \mathscr{C}_{ju} \right) \left[Hf_k + KC_k \right] Q_k^\alpha Q_u^\beta \boldsymbol{e}_\beta \boldsymbol{e}_\alpha \right.
$$
$$
\left. + \sum_{k,v} \sum_{\alpha,\gamma} \left(\sum_j A_{kj} \mathscr{C}_{jv} \right) \left[Hf_k + KC_k \right] Q_k^\alpha Q_v^\gamma \boldsymbol{e}_\alpha \boldsymbol{e}_\gamma \right\rangle
$$

$$
= \left\langle \sum_{k,u} \sum_{\alpha,\beta} \delta_{ku} \left[Hf_k + KC_k \right] Q_k^\alpha Q_u^\beta \boldsymbol{e}_\beta \boldsymbol{e}_\alpha \right\rangle + \left\langle \sum_{k,v} \sum_{\alpha,\gamma} \delta_{kv} \left[Hf_k + KC_k \right] Q_k^\alpha Q_v^\gamma \boldsymbol{e}_\alpha \boldsymbol{e}_\gamma \right\rangle
$$

$$
= \left\langle \sum_k \sum_{\alpha,\beta} \left[Hf_k + KC_k \right] Q_k^\alpha Q_k^\beta \boldsymbol{e}_\alpha \boldsymbol{e}_\beta \right\rangle + \left\langle \sum_k \sum_{\alpha,\gamma} \left[Hf_k + KC_k \right] Q_k^\alpha Q_k^\gamma \boldsymbol{e}_\alpha \boldsymbol{e}_\gamma \right\rangle
$$

$$
= 2 \left\langle \sum_k \left[Hf_k + KC_k \right] \boldsymbol{Q}_k \boldsymbol{Q}_k \right\rangle
$$

$$
= 2 \left\langle \sum_k \left[Hf_k \boldsymbol{Q}_k + KC_k \boldsymbol{Q}_k \right] \boldsymbol{Q}_k \right\rangle
$$

$$
\tag{C.31}
$$

The underlined term in Eq. (C.31) represents the total force, $\boldsymbol{F}_k^{\text{c}}$, in the kth connector vector due to the spring and the dashpot, and may be written as

$$
\boldsymbol{F}_k^{\text{c}} = \boldsymbol{F}_k^{\text{s}} + KC_k \boldsymbol{Q}_k
\tag{C.32}
$$

where $\boldsymbol{F}_k^{\text{s}}$ is as defined in Eq. (C.15), and we finally have

$$
\left\langle \sum_{j,k} A_{jk} \left[Hf_k + KC_k \right] \boldsymbol{Q}_k \cdot \frac{\partial \boldsymbol{B}}{\partial \boldsymbol{Q}_j} \right\rangle = 2 \left\langle \sum_k \boldsymbol{F}_k^{\text{c}} \boldsymbol{Q}_k \right\rangle = 2 \left\langle \sum_k \boldsymbol{Q}_k \boldsymbol{F}_k^{\text{c}} \right\rangle
\tag{C.33}
$$

Combining Equations (C.17), (C.22), (C.29), and C.33, we may write

$$
\frac{d}{dt} \langle \boldsymbol{B} \rangle = \left\langle \sum_{u,v} \mathscr{C}_{uv} \boldsymbol{Q}_u \boldsymbol{Q}_v \right\rangle \cdot \boldsymbol{\kappa}^T + \boldsymbol{\kappa} \cdot \left\langle \sum_{u,v} \mathscr{C}_{uv} \boldsymbol{Q}_u \boldsymbol{Q}_v \right\rangle + \frac{2k_B T}{\zeta} \left(N_{\text{b}} - 1 \right) \boldsymbol{\delta} - \frac{2}{\zeta} \left\langle \sum_k \boldsymbol{Q}_k \boldsymbol{F}_k^{\text{c}} \right\rangle
$$

$$
\tag{C.34}
$$

and therefore, from Eq. (C.1),

$$\left\langle \sum_{u=1}^{N_{\rm b}-1} \sum_{v=1}^{N_{\rm b}-1} \mathscr{C}_{uv} \boldsymbol{Q}_u \boldsymbol{Q}_v \right\rangle_{(1)} = \frac{2k_BT}{\zeta} (N_{\rm b} - 1)\boldsymbol{\delta} - \frac{2}{\zeta} \left\langle \sum_{k} \boldsymbol{Q}_k \boldsymbol{F}_k^{\rm c} \right\rangle \tag{C.35}$$

with the resultant stress tensor expression given as

$$\boldsymbol{\tau}_{\rm p} = \frac{n_{\rm p}\zeta}{2} \left\langle \sum_{u=1}^{N_{\rm b}-1} \sum_{v=1}^{N_{\rm b}-1} \mathscr{C}_{uv} \boldsymbol{Q}_u \boldsymbol{Q}_v \right\rangle_{(1)} = n_{\rm p}k_BT (N_{\rm b} - 1)\boldsymbol{\delta} - n_{\rm p} \left\langle \sum_{k=1}^{N_{\rm b}-1} \boldsymbol{Q}_k \boldsymbol{F}_k^{\rm c} \right\rangle \tag{C.36}$$

It is thus established that the stress tensor expression for free-draining bead-spring-dashpot chains is formally similar to that given by the Kramers expression, with the connector vector force suitably modified to account for the contribution from the dashpot. In order to obtain a closed-form expression that may be used for the calculation of stress tensor components from BD simulations, however, it is essential that the complete expression for C_k be substituted into Eq. (C.32) and simplified.

Starting from Eq. (C.36), we have

$$\boldsymbol{\tau}_{\rm p} = n_{\rm p}k_BT (N_{\rm b} - 1)\boldsymbol{\delta} - n_{\rm p} \left\langle \sum_{k} \boldsymbol{Q}_k \boldsymbol{F}_k^{\rm s} \right\rangle - n_{\rm p}K \left\langle \sum_{k} C_k \boldsymbol{Q}_k \boldsymbol{Q}_k \right\rangle \tag{C.37}$$

From Equation (5.23) of Chapter 5, we have

$$C_k = \left(\frac{1}{1+\epsilon}\right)\left(\frac{1}{Q_k}\right) \sum_{l=1}^{N} \boldsymbol{\Lambda}_l^{(k)} \cdot (\boldsymbol{\kappa} \cdot \boldsymbol{Q}_l) - \left(\frac{k_BT}{\zeta}\right)\left(\frac{1}{1+\epsilon}\right)\left(\frac{1}{Q_k}\right) \sum_{l=1}^{N} \boldsymbol{J}_l^{(k)} \cdot \left(\frac{\partial \ln \psi}{\partial \boldsymbol{Q}_l}\right)$$
$$+ \left(\frac{1}{\zeta}\right)\left(\frac{1}{1+\epsilon}\right)\left(\frac{1}{Q_k}\right) \sum_{l=1}^{N} \boldsymbol{J}_l^{(k)} \cdot \boldsymbol{F}_l^{\rm s} \tag{C.38}$$

where $\epsilon = 2\varphi$. Multiplying both sides of Eq. (C.38) by $\boldsymbol{Q}_k$,

$$C_k \boldsymbol{Q}_k = \left(\frac{1}{1+\epsilon}\right) \sum_{l} \underline{\left(\frac{\boldsymbol{Q}_k}{Q_k}\right) \boldsymbol{\Lambda}_l^{(k)}} \cdot (\boldsymbol{\kappa} \cdot \boldsymbol{Q}_l) - \left(\frac{k_BT}{\zeta}\right)\left(\frac{1}{1+\epsilon}\right) \sum_{l} \underline{\left(\frac{\boldsymbol{Q}_k}{Q_k}\right) \boldsymbol{J}_l^{(k)}} \cdot \left(\frac{\partial \ln \psi}{\partial \boldsymbol{Q}_l}\right)$$
$$+ \left(\frac{1}{\zeta}\right)\left(\frac{1}{1+\epsilon}\right) \sum_{l} \left(\frac{\boldsymbol{Q}_k}{Q_k}\right) \boldsymbol{J}_l^{(k)} \cdot \boldsymbol{F}_l^{\rm s} \tag{C.39}$$

The dash- and dot-underlined terms in Eq. (C.39) may be replaced by $\boldsymbol{\alpha}_{kl}$ and $\boldsymbol{\mu}_{kl}$, respectively, according to Eq. (5.26) in Chapter 5, to give

$$C_k \boldsymbol{Q}_k = \left(\frac{1}{1+\epsilon}\right) \sum_{l} \boldsymbol{\alpha}_{kl} \cdot (\boldsymbol{\kappa} \cdot \boldsymbol{Q}_l) - \left(\frac{k_BT}{\zeta}\right)\left(\frac{1}{1+\epsilon}\right) \sum_{l} \boldsymbol{\mu}_{kl} \cdot \left(\frac{\partial \ln \psi}{\partial \boldsymbol{Q}_l}\right)$$
$$+ \left(\frac{1}{\zeta}\right)\left(\frac{1}{1+\epsilon}\right) \sum_{l} \boldsymbol{\mu}_{kl} \cdot \boldsymbol{F}_l^{\rm s} \tag{C.40}$$

Multiplying both sides of Eq. (C.40) by $\boldsymbol{Q}_k$ again,

$$C_k \boldsymbol{Q}_k \boldsymbol{Q}_k = \left(\frac{1}{1+\epsilon}\right) \sum_l \boldsymbol{Q}_k \boldsymbol{\alpha}_{kl} \cdot (\boldsymbol{\kappa} \cdot \boldsymbol{Q}_l) - \left(\frac{k_B T}{\zeta}\right)\left(\frac{1}{1+\epsilon}\right) \sum_l \boldsymbol{Q}_k \boldsymbol{\mu}_{kl} \cdot \left(\frac{\partial \ln \psi}{\partial \boldsymbol{Q}_l}\right)$$

$$+ \left(\frac{1}{\zeta}\right)\left(\frac{1}{1+\epsilon}\right) \sum_l \boldsymbol{Q}_k \boldsymbol{\mu}_{kl} \cdot \boldsymbol{F}_l^{\mathrm{s}} \tag{C.41}$$

Using

$$\boldsymbol{\alpha}_{kl} = \chi_l^{(k)} \left(\frac{\boldsymbol{Q}_k \boldsymbol{Q}_l}{Q_k Q_l}\right) \tag{C.42}$$

where $\chi_l^{(k)}$ is as defined in Eq. (5.27) of Chapter 5. Summing over the index k, and taking an ensemble average on both sides of Eq. (C.41), we obtain

$$\left\langle \sum_k C_k \boldsymbol{Q}_k \boldsymbol{Q}_k \right\rangle = \left(\frac{1}{1+\epsilon}\right)\left\langle \sum_{k,l} \boldsymbol{\kappa} : \frac{\chi_l^{(k)} \boldsymbol{Q}_l \boldsymbol{Q}_l \boldsymbol{Q}_k \boldsymbol{Q}_k}{Q_l Q_k} \right\rangle$$

$$- \left(\frac{k_B T}{\zeta}\right)\left(\frac{1}{1+\epsilon}\right)\left\langle \sum_{k,l} \boldsymbol{Q}_k \boldsymbol{\mu}_{kl} \cdot \left(\frac{\partial \ln \psi}{\partial \boldsymbol{Q}_l}\right) \right\rangle + \left(\frac{1}{\zeta}\right)\left(\frac{1}{1+\epsilon}\right)\left\langle \sum_{k,l} \boldsymbol{Q}_k \boldsymbol{\mu}_{kl} \cdot \boldsymbol{F}_l^{\mathrm{s}} \right\rangle \tag{C.43}$$

The second and third terms on the RHS of Eq. (C.43) are evaluated sequentially as shown below. Starting with

$$\left\langle \sum_{k,l} \boldsymbol{Q}_k \boldsymbol{\mu}_{kl} \cdot \left(\frac{\partial \ln \psi}{\partial \boldsymbol{Q}_l}\right) \right\rangle \equiv \left\langle \sum_{k,l} \sum_{s,\alpha,\beta,\gamma} Q_k^s \mu_{kl}^{\alpha\beta} \frac{\partial \ln \psi}{\partial Q_l^\gamma} \left[\boldsymbol{e}_s \boldsymbol{e}_\alpha \boldsymbol{e}_\beta \cdot \boldsymbol{e}_\gamma\right] \right\rangle$$

$$= \left\langle \sum_{k,l} \sum_{s,\alpha,\beta} Q_k^s \mu_{kl}^{\alpha\beta} \left(\frac{1}{\psi}\right) \frac{\partial \psi}{\partial Q_l^\beta} \left[\boldsymbol{e}_s \boldsymbol{e}_\alpha\right] \right\rangle \tag{C.44}$$

$$= \sum_{k,l} \sum_{s,\alpha,\beta} \left[\int Q_k^s \mu_{kl}^{\alpha\beta} \left(\frac{1}{\psi}\right) \frac{\partial \psi}{\partial Q_l^\beta} \psi \, d\boldsymbol{Q}\right] \boldsymbol{e}_s \boldsymbol{e}_\alpha$$

The integral in Eq. (C.44) is solved as

$$\int Q_k^s \mu_{kl}^{\alpha\beta} \frac{\partial \psi}{\partial Q_l^\beta} \, d\boldsymbol{Q} = \int \left\{ \left[\frac{\partial}{\partial Q_l^\beta}\left(Q_k^s \mu_{kl}^{\alpha\beta} \psi\right)\right] - (Q_k^s \psi)\frac{\partial \mu_{kl}^{\alpha\beta}}{\partial Q_l^\beta} - \left(\mu_{kl}^{\alpha\beta}\psi\right)\frac{\partial Q_k^s}{\partial Q_l^\beta} \right\} d\boldsymbol{Q}$$

$$= \underline{\int \left[\frac{\partial}{\partial Q_l^\beta}\left(Q_k^s \mu_{kl}^{\alpha\beta}\psi\right)\right] d\boldsymbol{Q}} - \int \left[Q_k^s \frac{\partial \mu_{kl}^{\alpha\beta}}{\partial Q_l^\beta}\right] \psi \, d\boldsymbol{Q} - \int \left[\mu_{kl}^{\alpha\beta} \delta_{kl}\delta^{s\beta}\right] \psi \, d\boldsymbol{Q}$$

$$\tag{C.45}$$

The underlined integral in Eq. (C.45) vanishes due to the Gauss divergence theorem, and we get

$$\int Q_k^s \mu_{kl}^{\alpha\beta} \frac{\partial \psi}{\partial Q_l^\beta} \, d\boldsymbol{Q} = -\left\langle Q_k^s \frac{\partial \mu_{kl}^{\alpha\beta}}{\partial Q_l^\beta}\right\rangle - \left\langle \mu_{kl}^{\alpha\beta}\delta_{kl}\delta^{s\beta}\right\rangle \tag{C.46}$$

Substituting Eq. (C.46) into Eq. (C.44), we obtain

$$
\left\langle \sum_{k,l} \boldsymbol{Q}_k \boldsymbol{\mu}_{kl} \cdot \left(\frac{\partial \ln \psi}{\partial \boldsymbol{Q}_l} \right) \right\rangle = - \left\langle \sum_{k,l} \sum_{s,\alpha,\beta} Q_k^s \frac{\partial \mu_{kl}^{\alpha\beta}}{\partial Q_l^{\beta}} \boldsymbol{e}_s \boldsymbol{e}_\alpha \right\rangle - \left\langle \sum_{k,l} \sum_{s,\alpha,\beta} \mu_{kl}^{\alpha\beta} \delta_{kl} \delta^{s\beta} \boldsymbol{e}_s \boldsymbol{e}_\alpha \right\rangle
$$

$$
= - \left\langle \sum_{k,l} \boldsymbol{Q}_k \frac{\partial}{\partial \boldsymbol{Q}_l} \cdot \boldsymbol{\mu}_{kl}^T \right\rangle - \left\langle \sum_{k} \boldsymbol{\mu}_{kk}^T \right\rangle \tag{C.47}
$$

With respect to the third term on the RHS of Eq. (C.43), we note that

$$
\boldsymbol{\mu}_{kl} \cdot \boldsymbol{F}_l^s = \boldsymbol{F}_l^s \cdot \boldsymbol{\mu}_{kl}^T \tag{C.48}
$$

which follows from the property of the tensor-dot product. Combining Eqs. (C.43), (C.47), and (C.48), we obtain

$$
\left\langle \sum_{k} C_k \boldsymbol{Q}_k \boldsymbol{Q}_k \right\rangle = \left(\frac{k_B T}{\zeta} \right) \left(\frac{1}{1+\epsilon} \right) \left[\left\langle \sum_{k,l} \boldsymbol{Q}_k \frac{\partial}{\partial \boldsymbol{Q}_l} \cdot \boldsymbol{\mu}_{kl}^T \right\rangle + \left\langle \sum_{k} \boldsymbol{\mu}_{kk}^T \right\rangle \right]
$$

$$
+ \left(\frac{1}{\zeta} \right) \left(\frac{1}{1+\epsilon} \right) \left\langle \sum_{k,l} \boldsymbol{Q}_k \boldsymbol{F}_l^s \cdot \boldsymbol{\mu}_{kl}^T \right\rangle + \left(\frac{1}{1+\epsilon} \right) \left\langle \sum_{k,l} \boldsymbol{\kappa} : \frac{\chi_l^{(k)} \boldsymbol{Q}_l \boldsymbol{Q}_l \boldsymbol{Q}_k \boldsymbol{Q}_k}{Q_l Q_k} \right\rangle \tag{C.49}
$$

Finally, by substituting Eq. (C.49) into Eq. (C.37), the stress tensor expression is obtained as

$$
\boldsymbol{\tau}_p = n_p k_B T (N_b - 1) \boldsymbol{\delta} - n_p \left\langle \sum_{k} \boldsymbol{Q}_k \boldsymbol{F}_k^s \right\rangle - \left(\frac{n_p k_B T}{\zeta} \right) \left(\frac{K}{1+\epsilon} \right) \left[\left\langle \sum_{k,l} \boldsymbol{Q}_k \frac{\partial}{\partial \boldsymbol{Q}_l} \cdot \boldsymbol{\mu}_{kl}^T \right\rangle
$$

$$
+ \left\langle \sum_{k} \boldsymbol{\mu}_{kk}^T \right\rangle \right] - \left(\frac{n_p}{\zeta} \right) \left(\frac{K}{1+\epsilon} \right) \left\langle \sum_{k,l} \boldsymbol{Q}_k \boldsymbol{F}_l^s \cdot \boldsymbol{\mu}_{kl}^T \right\rangle \tag{C.50}
$$

$$
- \left(\frac{n_p \zeta}{2} \right) \left(\frac{\epsilon}{1+\epsilon} \right) \left\langle \sum_{k,l} \boldsymbol{\kappa} : \frac{\chi_l^{(k)} \boldsymbol{Q}_l \boldsymbol{Q}_l \boldsymbol{Q}_k \boldsymbol{Q}_k}{Q_l Q_k} \right\rangle
$$

Upon scaling and simplification using the length- and timescales, l_H and λ_H, the dimensionless form of the stress tensor is given by

$$
\frac{\boldsymbol{\tau}_p}{n_p k_B T} = (N_b - 1) \boldsymbol{\delta} - \left\langle \sum_{k} \boldsymbol{Q}_k^* \boldsymbol{F}_k^{*s} \right\rangle - \frac{1}{2} \left(\frac{\epsilon}{1+\epsilon} \right) \left[\left\langle \sum_{k,l} (\boldsymbol{Q}_k^* \boldsymbol{F}_l^{*s}) \cdot \boldsymbol{\mu}_{kl}^T \right\rangle + \left\langle \sum_{k} \boldsymbol{\mu}_{kk}^T \right\rangle
$$

$$
+ \left\langle \sum_{k,l} \boldsymbol{Q}_k^* \frac{\partial}{\partial \boldsymbol{Q}_l^*} \cdot \boldsymbol{\mu}_{kl}^T \right\rangle \right] - \left(\frac{2\epsilon}{1+\epsilon} \right) \boldsymbol{\kappa}^* : \left\langle \sum_{k,l} \frac{\chi_l^{(k)} \boldsymbol{Q}_l^* \boldsymbol{Q}_l^* \boldsymbol{Q}_k^* \boldsymbol{Q}_k^*}{Q_l^* Q_k^*} \right\rangle \tag{C.51}
$$

which is reproduced as Eq. (5.42) in Chapter 5.

Appendix D

Recursive-function based methodology for the analytical calculation of divergence terms

This appendix is organized as follows. Section D.1 presents a route for the conversion of finite continued fractions into ratios of recursive polynomial relations: Secs. D.1.1 to D.1.3 present results for polynomial representations of continued fractions, and a list of tensor identities that is useful for the analytical calculation of the divergence terms appearing in the governing stochastic differential equation and the stress tensor expression. In Sec. D.1.4, a detailed example of the use of recursive relations is provided. In Sec. D.1.5, a comparison between the divergence calculated numerically and using recursive relations is presented. Lastly, Sec. D.2 discusses the symmetricity and positive-definiteness of the diffusion tensor.

The connector vectors and associated quantities appearing in this document are in their dimensionless form, with the asterisks omitted for the sake of notational simplicity. Summations are indicated explicitly, and the Einstein summation convention is not followed.

D.1   A recursive algorithm for the calculation of gradients of continued fractions

The discrete Euler version of the governing stochastic differential equation for bead-spring-dashpot chains with N_b beads and $N \equiv (N_b - 1)$ springs, and the stress tensor

expression, are reproduced here from Section 5.2 of Chapter 5

$$\widetilde{Q}(t_{n+1}) = \widetilde{Q}_n + \left[\mathcal{K}(t_n) \cdot \widetilde{Q}(t_n) - \left(\frac{\varphi}{1 + 2\varphi} \right) \mathcal{U}(t_n) \cdot \left(\mathcal{K}(t_n) \cdot \widetilde{Q}(t_n) \right) - \frac{1}{4} \mathcal{D}(t_n) \cdot \widetilde{F}^{\text{s}}(t_n) \right.$$

$$\left. - \left(\frac{1}{4} \right) \left(\frac{\varphi}{1 + 2\varphi} \right) \widetilde{v}(t_n) \right] \Delta t_n + \frac{1}{\sqrt{2}} \Delta \widetilde{S}_n$$

$$\text{(D.1)}$$

$$\frac{\boldsymbol{\tau}_{\text{p}}}{n_{\text{p}} k_B T} = (N_{\text{b}} - 1) \boldsymbol{\delta} - \left[\left\langle \sum_{k=1}^{N} \boldsymbol{Q}_k \boldsymbol{F}_k^{\text{s}} \right\rangle - \frac{1}{2} \left(\frac{\epsilon}{1 + \epsilon} \right) \left\langle \sum_{k,l=1}^{N} (\boldsymbol{Q}_k \boldsymbol{F}_l^{\text{s}}) \cdot \boldsymbol{\mu}_{kl}^T \right\rangle - \frac{1}{2} \left(\frac{\epsilon}{1 + \epsilon} \right) \left[\left\langle \sum_{k=1}^{N} \boldsymbol{\mu}_{kk}^T \right\rangle \right. \right.$$

$$\left. \left. + \left\langle \sum_{k,l=1}^{N} \boldsymbol{Q}_k \frac{\partial}{\partial \boldsymbol{Q}_l} \cdot \boldsymbol{\mu}_{kl}^T \right\rangle \right] - \left(\frac{2\epsilon}{1 + \epsilon} \right) \boldsymbol{\kappa} : \left\langle \sum_{k,l=1}^{N} \frac{\chi_l^{(k)} \boldsymbol{Q}_l \boldsymbol{Q}_l \boldsymbol{Q}_k \boldsymbol{Q}_k}{Q_l Q_k} \right\rangle \right.$$

$$\text{(D.2)}$$

where $\epsilon = 2\varphi$, $\widetilde{v} \equiv [\widehat{v}_1, \widehat{v}_2 ..., \widehat{v}_N]$, with $\widehat{v}_j = \sum_{k=1}^{N} (\partial/\partial \boldsymbol{Q}_k) \cdot V_{jk}^T$. Clearly, Eqs. (D.1) and (D.2) require the calculation of the divergences $(\partial/\partial \boldsymbol{Q}_k) \cdot V_{jk}^T$ and $(\partial/\partial \boldsymbol{Q}_l) \cdot \boldsymbol{\mu}_{kl}^T$ for all values of $\{j, k, l\} \in [1, N]$. It is straightforward to evaluate these divergences numerically, using the central difference approximation scheme for the calculation of gradients. In this section, an analytical route for the calculation of these gradients is presented.

It may be seen that both V_{jk}^T and $\boldsymbol{\mu}_{kl}^T$ possess essentially the same structure, i.e; they may be written as a sum of n_{t} tensors, as

$$V_{jk}^T = \boldsymbol{\pi}_1 + \boldsymbol{\pi}_2 + \cdots + \boldsymbol{\pi}_{n_{\text{t}}}$$

$$\text{(D.3)}$$

where each term on the RHS has the following general structure

$$\boldsymbol{\pi}_q = \widehat{h} \left(M_q, P_q \right) \left[\frac{\boldsymbol{Q}_i \boldsymbol{Q}_m}{Q_i Q_m} \right]$$

$$\text{(D.4)}$$

where $q \in [1, n_{\text{t}}]$, and $i, m \in [(q - 1), (q + 1)]$. In general, the quantities M_k and P_k are defined recursively as follows

$$M_k = p \left(\frac{L_{k-1}^2}{1 - M_{k-1}} \right); \quad \text{with} \quad M_1 = 0$$

$$P_k = p \left(\frac{L_k^2}{1 - P_{k+1}} \right); \quad \text{with} \quad P_N = 0$$

$$\text{(D.5)}$$

where

$$p = \left(\frac{K}{\zeta + 2K} \right)^2; \quad L_k \equiv \cos \theta_k = \frac{\boldsymbol{Q}_k \cdot \boldsymbol{Q}_{k+1}}{Q_k Q_{k+1}}$$

$$\text{(D.6)}$$

For any scalar $\widehat{h}$, and any tensor $\boldsymbol{H}$, the divergence of their product obeys the following identity,

$$\boldsymbol{\nabla} \cdot \left(\widehat{h} \boldsymbol{H} \right) = \left(\boldsymbol{\nabla} \widehat{h} \right) \cdot \boldsymbol{H} + \widehat{h} \boldsymbol{\nabla} \cdot \boldsymbol{H}$$

$$\text{(D.7)}$$

The evaluation of $(\partial/\partial \boldsymbol{Q}_k) \cdot \boldsymbol{V}_{jk}^T$ or $(\partial/\partial \boldsymbol{Q}_l) \cdot \boldsymbol{\mu}_{kl}^T$ would require knowledge of the gradient of the scalar prefactor, $\partial \widehat{h}/\partial \boldsymbol{Q}_k$. The difficulty in analytically evaluating this gradient term may be illustrated by considering a specific form of $\widehat{h}(M_q, P_q)$, say, $\widehat{h} \equiv [1 - M_6]^{-1}$, which is encountered in the calculation of $\boldsymbol{\Gamma}_6^{(7)}$, required for the construction of $\boldsymbol{\Lambda}_6^{(7)}$, and subsequently that of the elements of the block matrix, $\boldsymbol{\mathcal{U}}$, as evident from Eqs. (5.19), (5.22) and (5.26) of Chapter 5. Suppose it is desired to calculate the gradient of $\widehat{h}$ with respect to $\boldsymbol{Q}_3$. We may begin by representing $\widehat{h}$ as

$$\widehat{h} = \cfrac{1}{1 - M_6} = \cfrac{1}{1 - \cfrac{pL_5^2}{1 - \cfrac{pL_4^2}{1 - \cfrac{pL_3^2}{1 - \cfrac{pL_2^2}{1 - pL_1^2}}}}} \tag{D.8}$$

where only L_2 and L_3 are functions of $\boldsymbol{Q}_3$. Clearly, it is not trivial to apply the quotient-rule to evaluate the gradient of h with respect to $\boldsymbol{Q}_3$. Fortunately, continued fractions of the type indicated in Eq. (D.8), and finite continued products of such fractions, may be expressed as ratios of polynomials (Malila, 2014; Cretney, 2014).

Suppose we define

$$I_k = (1 - M_1)(1 - M_2)..(1 - M_{k-1})(1 - M_k) \tag{D.9}$$

It can be shown that

$$I_{k+2} = 1 - pL_1^2 - pL_2^2 - p\left[\sum_{i=3}^{k+1} L_i^2 I_{i-1}\right] \tag{D.10}$$

Similarly, defining

$$D_k = (1 - P_k)(1 - P_{k+1})..(1 - P_{N-1})(1 - P_N) \tag{D.11}$$

where N is the number of springs in the chain, it can be shown that

$$D_k = 1 - pL_{N-1}^2 - pL_{N-2}^2 - p\left[\sum_{i=k}^{N-3} L_i^2 D_{i+2}\right] \tag{D.12}$$

Note that while I_0 is not defined according to Eq. (D.9), we set $I_0 = I_1 = 1$ for programming convenience. Similarly, we set $D_{N+1} = D_N = 1$ for the same reason.

Using Eqs. (D.9)–(D.12), it can be shown that

$$\left[\prod_{i=l}^{k-1}\left(\frac{1}{1 - M_i}\right)\right] = \frac{I_{l-1}}{I_{k-1}}, \tag{D.13}$$

$$\left[\prod_{i=k+1}^{l} \left(\frac{1}{1 - P_i} \right) \right] = \frac{D_{l+1}}{D_{k+1}}, \tag{D.14}$$

$$\frac{1}{1 - M_k} = \frac{I_{k-1}}{I_k}, \tag{D.15}$$

$$\frac{1}{1 - P_k} = \frac{D_{k+1}}{D_k}, \tag{D.16}$$

and

$$\frac{1}{1 - M_i - P_k} = \frac{1}{\left(\dfrac{I_i}{I_{i-1}} \right) + \left(\dfrac{D_k}{D_{k+1}} \right) - 1} \tag{D.17}$$

Using the polynomial representations introduced above, we may concisely write

$$\frac{\widehat{\partial h}}{\partial \boldsymbol{Q}_3} = \frac{\partial}{\partial \boldsymbol{Q}_3} \left[\frac{1}{1 - M_6} \right] = \frac{\partial}{\partial \boldsymbol{Q}_3} \left(\frac{I_5}{I_6} \right) \tag{D.18}$$

The quotient rule may now be applied to the ratio of polynomials given on the RHS of Eq. (D.18). The next task is to obtain general expressions for the gradients, $\partial I_k / \partial \boldsymbol{Q}_j$, and $\partial D_k / \partial \boldsymbol{Q}_j$.

D.1.1 Forward continued product

We have seen how a recurrence relation for I_k can be obtained. We now provide an expression for I_k as a polynomial in p. Consider I_k where $1 \leq k \leq N$ is any integer. The degree, n, of the polynomial in p that expresses I_k is given by $n = \left\lfloor \dfrac{k}{2} \right\rfloor$ where $\lfloor i \rfloor$ represents the greatest integer lesser than or equal to i. We can then write

$$I_k = 1 - p \sum_{i=1}^{k-1} L_i^2 f(1, k+1, i) + p^2 \sum_{i=1}^{k-3} L_i^2 f(2, k-1, i) - p^3 \sum_{i=1}^{k-5} L_i^2 f(3, k-3, i) \cdots$$

$$+ (-1)^n p^n \sum_{i=1}^{k-(2n-1)} L_i^2 f(n, [k - (2n-3)], i) \tag{D.19}$$

where the function $f(m, l, j)$ is defined recursively as follows

$$f(m, l, j) = \sum_{s=j+2}^{l} L_s^2 f(m-1, l+2, s) \tag{D.20}$$

with

$$f(1, l, j) = 1 \qquad \forall \quad l, j \tag{D.21}$$

While Eq. (D.19) provides an expression for I_k as a polynomial in p, for the calculation of $\partial I_k / \partial Q_j$, it is desirable to obtain an expansion for I_k in terms of L_ν^2. As evident from Eq. (D.6), only L_j and L_{j-1} depend on Q_j. The calculation of $\partial I_k / \partial Q_j$ would therefore be simplified if an expansion in terms of L_ν^2 is available. This is realized in the following expression,

$$I_k = 1 + \sum_{\nu=1}^{k-1} L_\nu^2 \widetilde{q}_\nu^{(k)} \tag{D.22}$$

with

$$\widetilde{q}_\nu^{(k)} = \sum_{\mu=1}^{n} (-1)^\mu \, p^\mu \widetilde{f}\left(\mu, [k - (2\mu - 3)], -1; \widetilde{\ell}\right) \tag{D.23}$$

where $1 \le \nu < k$; $\widetilde{\ell}$ may in general be a set of numbers but $\widetilde{\ell} = \{\nu\}$ in Eq. (D.23), and the function $\widetilde{f}\left(m, l, j; \widetilde{\ell}\right)$ is defined recursively as

$$\boxed{\widetilde{f}\left(m, l, j; \widetilde{\ell}\right) = \sum_{\substack{s=j+2 \\ s \notin \widetilde{\lambda} \\ s > \min(\widetilde{\ell})}}^{l} L_s^2 \, \widetilde{f}\left(m - 1, l + 2, s; \widetilde{\ell}\right)}$$

with

$$\widetilde{f}\left(1, l, j; \widetilde{\ell}\right) = 1 \qquad \forall \quad l, j, \widetilde{\ell} \tag{D.24}$$

The set $\widetilde{\lambda}$ is related to $\widetilde{\ell}$ as follows. For the general case of $\widetilde{\ell} \equiv \{a_1, a_2, a_3, ..\}$, where the a_i represent arbitrary integers, $\widetilde{\lambda}$ is constructed as

$$\widetilde{\lambda} \equiv \{(a_1 - 1), a_1, (a_1 + 1), (a_2 - 1), a_2, (a_2 + 1), ...\}$$

For the present case of $\widetilde{\ell} = \{\nu\}$, we have $\widetilde{\lambda} = \{\nu - 1, \nu, \nu + 1\}$. The conditional summation over the index s appearing in the boxed equation above may be understood as follows. For given values of $\{m, l, j; \widetilde{\ell}\}$, the index s runs from a lower limit of $j + 2$ to an upper limit of l, with two constraints. Firstly, s must not belong to the set $\widetilde{\lambda}$, and secondly, the value of s must be larger than the smallest entry in the set $\widetilde{\ell}$. A detailed illustration of the use of the recursive relations, $f(m, l, j)$ and $\widetilde{f}\left(m, l, j; \widetilde{\ell}\right)$, has been provided below, in Sec. D.1.4.

The next task is to find a general expression for $\dfrac{\partial \widetilde{q}_\nu^{(k)}}{\partial Q_j}$. Note that

$$\frac{\partial \widetilde{q}_\nu^{(k)}}{\partial Q_j} = 0; \quad j < \nu + 2 \tag{D.25}$$

and the following equation holds when $j \geq v + 2$,

$$
\frac{\partial \widetilde{q}_v^{(k)}}{\partial \boldsymbol{Q}_j} = \widetilde{\theta}_{jv} \left[\sum_{\mu=2}^{n} (-1)^{\mu} p^{\mu} \widetilde{f}(\mu - 1, [k - (2\mu - 5)], -1; \{v, j - 1\}) \right] \frac{\partial L_{j-1}^2}{\partial \boldsymbol{Q}_j}
$$

$$
+ \widehat{\theta}_{jk} \left[\sum_{\mu=2}^{n} (-1)^{\mu} p^{\mu} \widetilde{f}(\mu - 1, [k - (2\mu - 5)], -1; \{v, j\}) \right] \frac{\partial L_j^2}{\partial \boldsymbol{Q}_j};
$$

(D.26)

where the underlined terms may be evaluated using Eq. (D.54) and Eq. (D.55) given in Sec. D.1.3, and the indicator functions, $\widetilde{\theta}_{jv}$ and $\widehat{\theta}_{jk}$ are defined as

$$
\widetilde{\theta}_{jv} = \begin{cases} 0; & j \leq v + 2 \\ \\ 1; & j > v + 2 \end{cases}
$$

(D.27)

and

$$
\widehat{\theta}_{jk} = \begin{cases} 0; & j = k \\ \\ 1; & j \neq k \end{cases}
$$

(D.28)

which enables us to write

$$
\frac{\partial I_k}{\partial \boldsymbol{Q}_j} = \begin{cases} 0; & j > k \\ \\ \sum_{i=1}^{j-2} L_i^2 \frac{\partial \widetilde{q}_i^{(k)}}{\partial \boldsymbol{Q}_j} + \widetilde{q}_{j-1}^{(k)} \frac{\partial L_{j-1}^2}{\partial \boldsymbol{Q}_j} + \widetilde{q}_j^{(k)} \frac{\partial L_j^2}{\partial \boldsymbol{Q}_j}; & j \leq k \end{cases}
$$

(D.29)

In Fig. D.1, the derivative of the polynomial I_k, with respect to the $y-$th component of $\boldsymbol{Q}_j$, is plotted for arbitrarily chosen values of $k = 14$, $j = 7$, and the chain length, $N = 20$. There is an excellent agreement between the derivative calculated numerically, and that obtained analytically using Eq. (D.29).

D.1.2 Backward continued product

The backward continued product defined in Eq. (D.11) may be expressed as a polynomial in p. Consider D_k where $1 \leq k \leq N$ is any integer. The degree, n, of the polynomial in p that expresses D_k is given by $n = \left\lceil \dfrac{N - k}{2} \right\rceil$ where $\lceil i \rceil$ represents the smallest integer greater than or equal to i. We write

$$
D_k = 1 - p \sum_{i=k}^{N-1} L_i^2 g(1, k - 2, i) + p^2 \sum_{i=k+2}^{N-1} L_i^2 g(2, k, i) - p^3 \sum_{i=k+4}^{N-1} L_i^2 g(3, k + 2, i) \cdots
$$

$$
+ (-1)^n p^n \sum_{i=k+2(n-1)}^{N-1} L_i^2 g(n, [k + 2(n - 2)], i)
$$

(D.30)
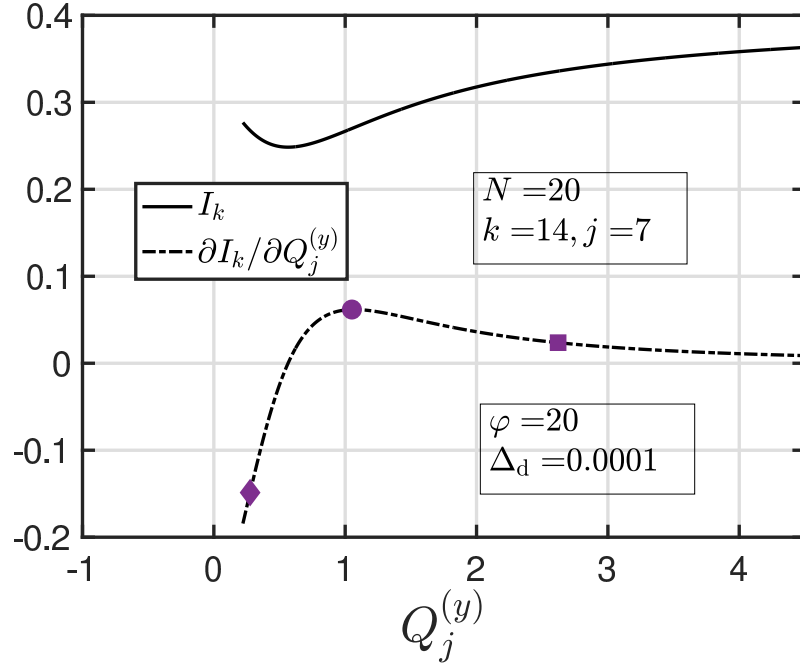
Figure D.1: Plot of I_k [solid line, from Eq. (D.19)] and its gradient in the $y-$direction [broken line, from Eq. (D.29)]. Symbols indicate derivatives calculated using central-difference scheme, with a spatial discretization width of Δ_{d}.

where the function $g(m, l, j)$ is written recursively as

$$g(m, l, j) = \sum_{s=l}^{j-2} L_s^2 \, g(m-1, l-2, s)$$

with

$$g(1, l, j) = 1 \qquad \forall \quad l, j \tag{D.31}$$

A polynomial expansion for D_k in terms of L_ν may be written as

$$D_k = 1 + \sum_{\nu=k}^{N-1} L_\nu^2 \widetilde{w}_\nu^{(k)} \tag{D.32}$$

where

$$\widetilde{w}_\nu^{(k)} = \sum_{\mu=1}^{n} (-1)^\mu \, p^\mu \widetilde{g}(\mu, [k + 2(\mu - 2)], (N + 1); \widetilde{\ell}) \tag{D.33}$$

where $k \leq \nu < N$, and the function $\widetilde{g}(m, l, j; \widetilde{\ell})$ is written recursively as follows

$$\widetilde{g}(m, l, j; \widetilde{\ell}) = \sum_{\substack{s=l \\ s \notin \widetilde{\lambda} \\ s > \min(\widetilde{\ell})}}^{j-2} L_s^2 \widetilde{g}(m-1, l-2, s; \widetilde{\ell})$$

with

$$\widetilde{g}\left(1, l, j; \widetilde{\ell}\right) = 1 \qquad \forall \quad l, j, \widetilde{\ell} \tag{D.34}$$

In the expansion given by Eq. (D.33), $\widetilde{\ell} = \{v\}$, and $\widetilde{\lambda} = \{(v-1), v, (v+1)\}$.

The next task is to find a general expression for $\dfrac{\partial \widetilde{w}_v^{(k)}}{\partial \boldsymbol{Q}_j}$. Note that

$$\frac{\partial \widetilde{w}_v^{(k)}}{\partial \boldsymbol{Q}_j} = 0; \quad j < v+2 \tag{D.35}$$

and the following equation holds when $j \geq v+2$,

$$\begin{aligned}
\frac{\partial \widetilde{w}_v^{(k)}}{\partial \boldsymbol{Q}_j} &= \widetilde{\theta}_{jv} \left[\sum_{\mu=2}^{n} (-1)^\mu \, p^\mu \widetilde{g}(\mu-1, [k+2(\mu-3)], (N+1); \{v, j-1\}) \right] \frac{\partial L_{j-1}^2}{\partial \boldsymbol{Q}_j} \\
&+ \widehat{\theta}_{jN} \left[\sum_{\mu=2}^{n} (-1)^\mu \, p^\mu \widetilde{g}(\mu-1, [k+2(\mu-3)], (N+1); \{v, j\}) \right] \frac{\partial L_j^2}{\partial \boldsymbol{Q}_j};
\end{aligned} \tag{D.36}$$

which enables us to write

$$\frac{\partial D_k}{\partial \boldsymbol{Q}_j} = \begin{cases} 0; & j < k \\ \sum_{i=k}^{j-2} L_i^2 \frac{\partial \widetilde{w}_i^{(k)}}{\partial \boldsymbol{Q}_j} + \widetilde{w}_{j-1}^{(k)} \frac{\partial L_{j-1}^2}{\partial \boldsymbol{Q}_j} + \widetilde{w}_j^{(k)} \frac{\partial L_j^2}{\partial \boldsymbol{Q}_j}; & j \geq k \end{cases} \tag{D.37}$$

In Fig. D.2, the derivative of the polynomial D_k, with respect to the x−th component of $\boldsymbol{Q}_j$, is plotted for arbitrarily chosen values of $k = 5$, $j = 10$, and the chain length, $N = 20$. There is an excellent agreement between the derivative calculated numerically, and that obtained analytically using Eq. (D.37).

D.1.3   List of tensor identities

We first present the derivation of the following identity,

$$\frac{\partial}{\partial \boldsymbol{Q}_j} \cdot \boldsymbol{\Xi}_{jl} \cdot \frac{\partial \widehat{f}}{\partial \boldsymbol{Q}_l} = \frac{\partial}{\partial \boldsymbol{Q}_j} \frac{\partial}{\partial \boldsymbol{Q}_l} : \left[\boldsymbol{\Xi}_{jl}^T \widehat{f} \right] - \frac{\partial}{\partial \boldsymbol{Q}_j} \cdot \left[\widehat{f} \frac{\partial}{\partial \boldsymbol{Q}_l} \cdot \boldsymbol{\Xi}_{jl}^T \right] \tag{D.38}$$

where $\boldsymbol{\Xi}_{jl}$ is a configuration-dependent tensor, defined as

$$\boldsymbol{\Xi}_{jl} = \sum_{m,n} \Xi_{jl}^{mn} \boldsymbol{e}_m \boldsymbol{e}_n, \tag{D.39}$$

and $\widehat{f}$ is a scalar. This identity is useful for converting the second order partial derivative in the Fokker-Planck equation, also called the "diffusion term", into a form more suitable for the application of the Itô interpretation.
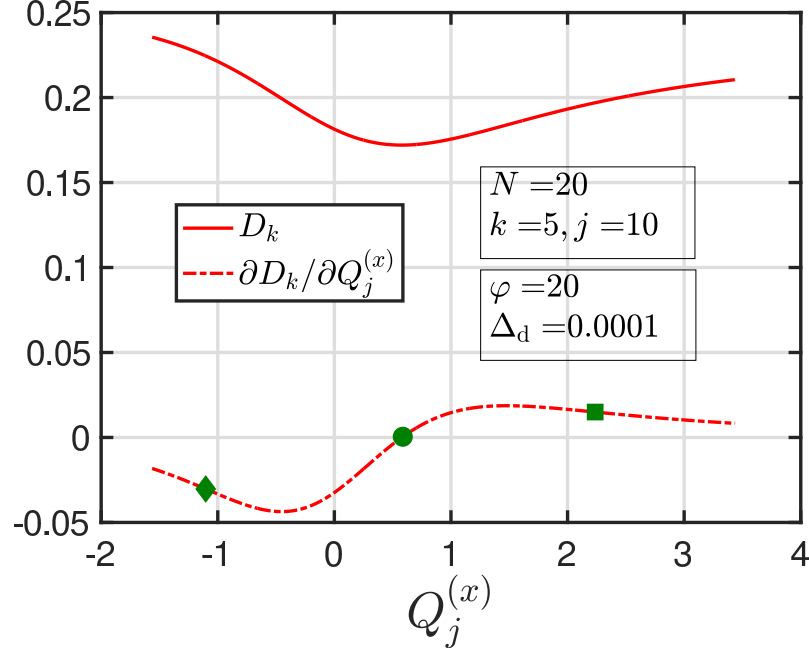
Figure D.2: Plot of D_k [solid line, from Eq. (D.30)] and its gradient in the $x-$direction [broken line, from Eq. (D.37)]. Symbols indicate derivatives calculated using central-difference scheme, with a spatial discretization width of Δ_d.

Starting from

$$
\frac{\partial}{\partial \boldsymbol{Q}_j} \frac{\partial}{\partial \boldsymbol{Q}_l} : \left[\boldsymbol{\Xi}_{jl}^T \widehat{f} \right] \equiv \sum_{r,p,m,n} \left(\frac{\partial}{\partial Q_j^r} \boldsymbol{e}_r \right) \left(\frac{\partial}{\partial Q_l^p} \boldsymbol{e}_p \right) : \left[\left(\boldsymbol{\Xi}_{jl}^{mn} \boldsymbol{e}_m \boldsymbol{e}_n \right)^T \widehat{f} \right]
$$

$$
= \sum_{r,p,m,n} \left(\frac{\partial}{\partial Q_j^r} \boldsymbol{e}_r \right) \left(\frac{\partial}{\partial Q_l^p} \boldsymbol{e}_p \right) : \left[\boldsymbol{\Xi}_{jl}^{nm} \boldsymbol{e}_m \boldsymbol{e}_n \widehat{f} \right] \tag{D.40}
$$

$$
= \sum_{r,p,m,n} \frac{\partial}{\partial Q_j^r} \frac{\partial}{\partial Q_l^p} \left(\boldsymbol{\Xi}_{jl}^{nm} \widehat{f} \right) \left[\boldsymbol{e}_r \boldsymbol{e}_p : \boldsymbol{e}_m \boldsymbol{e}_n \right] = \frac{\partial}{\partial Q_j^r} \frac{\partial}{\partial Q_l^p} \left(\boldsymbol{\Xi}_{jl}^{nm} \widehat{f} \right) \left[\delta_{rn} \delta_{pm} \right]
$$

$$
= \sum_{r,p} \frac{\partial}{\partial Q_j^r} \left[\frac{\partial}{\partial Q_l^p} \left(\boldsymbol{\Xi}_{jl}^{rp} \widehat{f} \right) \right]
$$

$$
= \sum_{r,p} \frac{\partial}{\partial Q_j^r} \left[\boldsymbol{\Xi}_{jl}^{rp} \frac{\partial \widehat{f}}{\partial Q_l^p} + \widehat{f} \frac{\partial \boldsymbol{\Xi}_{jl}^{rp}}{\partial Q_l^p} \right]
$$

we have

$$
\frac{\partial}{\partial \boldsymbol{Q}_j} \frac{\partial}{\partial \boldsymbol{Q}_l} : \left[\boldsymbol{\Xi}_{jl}^T \widehat{f} \right] = \sum_{r,p} \frac{\partial}{\partial Q_j^r} \boldsymbol{\Xi}_{jl}^{rp} \frac{\partial \widehat{f}}{\partial Q_l^p} + \sum_{r,p} \frac{\partial}{\partial Q_j^r} \widehat{f} \frac{\partial \boldsymbol{\Xi}_{jl}^{rp}}{\partial Q_l^p} \tag{D.41}
$$

Next, we examine

$$\frac{\partial}{\partial \boldsymbol{Q}_j} \cdot \boldsymbol{\Xi}_{jl} \cdot \frac{\partial \widehat{f}}{\partial \boldsymbol{Q}_l} \equiv \sum_{r,p,m,n} \left(\frac{\partial}{\partial Q_j^r} \boldsymbol{e}_r \right) \cdot \left(\Xi_{jl}^{mn} \boldsymbol{e}_m \boldsymbol{e}_n \right) \cdot \left(\frac{\partial \widehat{f}}{\partial Q_l^p} \boldsymbol{e}_p \right)$$

$$= \sum_{r,p,m,n} \frac{\partial}{\partial Q_j^r} \Xi_{jl}^{mn} \frac{\partial \widehat{f}}{\partial Q_l^p} \left[\boldsymbol{e}_r \cdot (\boldsymbol{e}_m \boldsymbol{e}_n) \cdot \boldsymbol{e}_p \right] \qquad (D.42)$$

$$= \sum_{r,p,m,n} \frac{\partial}{\partial Q_j^r} \Xi_{jl}^{mn} \frac{\partial \widehat{f}}{\partial Q_l^p} \delta_{rm} \delta_{np}$$

Thus we have

$$\frac{\partial}{\partial \boldsymbol{Q}_j} \cdot \boldsymbol{\Xi}_{jl} \cdot \frac{\partial \widehat{f}}{\partial \boldsymbol{Q}_l} = \sum_{r,p} \frac{\partial}{\partial Q_j^r} \Xi_{jl}^{rp} \frac{\partial \widehat{f}}{\partial Q_l^p} \qquad (D.43)$$

Finally, we examine

$$\frac{\partial}{\partial \boldsymbol{Q}_j} \cdot \left[\widehat{f} \frac{\partial}{\partial \boldsymbol{Q}_l} \cdot \boldsymbol{\Xi}_{jl}^T \right] \sum_{r,p,m,n} \equiv \left(\frac{\partial}{\partial Q_j^r} \boldsymbol{e}_r \right) \cdot \left[\widehat{f} \left(\frac{\partial}{\partial Q_l^p} \boldsymbol{e}_p \right) \cdot \left(\Xi_{jl}^{mn} \boldsymbol{e}_m \boldsymbol{e}_n \right)^T \right]$$

$$= \sum_{r,p,m,n} \left(\frac{\partial}{\partial Q_j^r} \boldsymbol{e}_r \right) \cdot \left[\widehat{f} \frac{\partial \Xi_{jl}^{nm}}{\partial Q_l^p} \delta_{pm} \boldsymbol{e}_n \right] \qquad (D.44)$$

$$= \sum_{r,p,n} \frac{\partial}{\partial Q_j^r} \widehat{f} \frac{\partial \Xi_{jl}^{np}}{\partial Q_l^p} (\boldsymbol{e}_r \cdot \boldsymbol{e}_n) = \sum_{r,p} \frac{\partial}{\partial Q_j^r} \widehat{f} \frac{\partial \Xi_{jl}^{np}}{\partial Q_l^p} \delta_{rn}$$

Thus we have

$$\frac{\partial}{\partial \boldsymbol{Q}_j} \cdot \left[\widehat{f} \frac{\partial}{\partial \boldsymbol{Q}_l} \cdot \boldsymbol{\Xi}_{jl}^T \right] = \sum_{r,p} \frac{\partial}{\partial Q_j^r} \widehat{f} \frac{\partial \Xi_{jl}^{rp}}{\partial Q_l^p} \qquad (D.45)$$

From Eqs. (D.41), (D.43), and (D.45), we can write

$$\frac{\partial}{\partial \boldsymbol{Q}_j} \frac{\partial}{\partial \boldsymbol{Q}_l} : \left[\boldsymbol{\Xi}_{jl}^T \widehat{f} \right] = \frac{\partial}{\partial \boldsymbol{Q}_j} \cdot \boldsymbol{\Xi}_{jl} \cdot \frac{\partial \widehat{f}}{\partial \boldsymbol{Q}_l} + \frac{\partial}{\partial \boldsymbol{Q}_j} \cdot \left[\widehat{f} \frac{\partial}{\partial \boldsymbol{Q}_l} \cdot \boldsymbol{\Xi}_{jl}^T \right], \qquad (D.46)$$

which may then be rearranged to give Eq. (D.38)

The following identities, useful in the numerical calculation of divergence, are stated without proof:

$$\frac{\partial Q_i^2}{\partial \boldsymbol{Q}_k} = 2\boldsymbol{Q}_i \delta_{ki} \qquad (D.47)$$

$$\frac{\partial}{\partial \boldsymbol{Q}_k} \left(\frac{\boldsymbol{Q}_i}{Q_i} \right) = \frac{1}{Q_k} \left[\boldsymbol{\delta} - \frac{\boldsymbol{Q}_k \boldsymbol{Q}_k}{Q_k^2} \right] \delta_{ki} \qquad (D.48)$$

$$\frac{\partial}{\partial \boldsymbol{Q}_k} \cdot \left[\frac{\boldsymbol{Q}_i \boldsymbol{Q}_j}{Q_i Q_j} \right] = \left(\frac{1}{Q_i Q_j} \right) \left[\boldsymbol{Q}_i - \left(\frac{\boldsymbol{Q}_j \boldsymbol{Q}_j}{Q_j^2} \right) \cdot \boldsymbol{Q}_i \right] \delta_{kj} + 2 \left(\frac{\boldsymbol{Q}_j}{Q_j Q_i} \right) \delta_{ki} \tag{D.49}$$

$$\frac{\partial L_i}{\partial \boldsymbol{Q}_k} = \left\{ \left(\frac{1}{Q_i} \right) \left[\left(\frac{\boldsymbol{Q}_{i+1}}{Q_{i+1}} \right) - L_i \left(\frac{\boldsymbol{Q}_i}{Q_i} \right) \right] \right\} \delta_{ki} + \left\{ \left(\frac{1}{Q_{i+1}} \right) \left[\left(\frac{\boldsymbol{Q}_i}{Q_i} \right) - L_i \left(\frac{\boldsymbol{Q}_{i+1}}{Q_{i+1}} \right) \right] \right\} \delta_{k,i+1} \tag{D.50}$$

Setting $i = (j - 1)$, $k = j$ in Eq. (D.50),

$$\frac{\partial L_{j-1}}{\partial \boldsymbol{Q}_j} = \frac{1}{Q_j} \left[\left(\frac{\boldsymbol{Q}_{j-1}}{\boldsymbol{Q}_{j-1}} \right) - L_{j-1} \left(\frac{\boldsymbol{Q}_j}{Q_j} \right) \right] \tag{D.51}$$

Setting $i = k = j$ in Eq. (D.50),

$$\frac{\partial L_j}{\partial \boldsymbol{Q}_j} = \frac{1}{Q_j} \left[\left(\frac{\boldsymbol{Q}_{j+1}}{\boldsymbol{Q}_{j+1}} \right) - L_j \left(\frac{\boldsymbol{Q}_j}{Q_j} \right) \right] \tag{D.52}$$

$$\frac{\partial L_i^2}{\partial \boldsymbol{Q}_k} = \left\{ \left(\frac{2L_i}{Q_i} \right) \left[\left(\frac{\boldsymbol{Q}_{i+1}}{Q_{i+1}} \right) - L_i \left(\frac{\boldsymbol{Q}_i}{Q_i} \right) \right] \right\} \delta_{ki} + \left\{ \left(\frac{2L_i}{Q_{i+1}} \right) \left[\left(\frac{\boldsymbol{Q}_i}{Q_i} \right) - L_i \left(\frac{\boldsymbol{Q}_{i+1}}{Q_{i+1}} \right) \right] \right\} \delta_{k,i+1} \tag{D.53}$$

Setting $i = (j - 1)$, $k = j$ in Eq. (D.53) and simplifying,

$$\frac{\partial L_{j-1}^2}{\partial \boldsymbol{Q}_j} = \frac{2L_{j-1}}{Q_{j-1} Q_j^2} \left[Q_j \boldsymbol{Q}_{j-1} - L_{j-1} Q_{j-1} \boldsymbol{Q}_j \right] \tag{D.54}$$

Setting $i = k = j$ in Eq. (D.53) and simplifying,

$$\frac{\partial L_j^2}{\partial \boldsymbol{Q}_j} = \frac{2L_j}{Q_{j+1} Q_j^2} \left[Q_j \boldsymbol{Q}_{j+1} - L_j Q_{j+1} \boldsymbol{Q}_j \right] \tag{D.55}$$

$$\frac{\partial}{\partial \boldsymbol{Q}_k} \left[L_i L_j \right] = \left(\frac{L_i}{Q_j} \right) \left[\left(\frac{\boldsymbol{Q}_{j+1}}{Q_{j+1}} \right) - L_j \left(\frac{\boldsymbol{Q}_j}{Q_j} \right) \right] \delta_{kj} + \left(\frac{L_i}{Q_{j+1}} \right) \left[\left(\frac{\boldsymbol{Q}_j}{Q_j} \right) - L_j \left(\frac{\boldsymbol{Q}_{j+1}}{Q_{j+1}} \right) \right] \delta_{k,j+1}$$
$$+ \left(\frac{L_j}{Q_i} \right) \left[\left(\frac{\boldsymbol{Q}_{i+1}}{Q_{i+1}} \right) - L_i \left(\frac{\boldsymbol{Q}_i}{Q_i} \right) \right] \delta_{ki} + \left(\frac{L_j}{Q_{i+1}} \right) \left[\left(\frac{\boldsymbol{Q}_i}{Q_i} \right) - L_i \left(\frac{\boldsymbol{Q}_{i+1}}{Q_{i+1}} \right) \right] \delta_{k,i+1} \tag{D.56}$$

Setting $i = (k - 1)$, $j = k$ in Eq. (D.56) and simplifying,

$$\frac{\partial}{\partial \boldsymbol{Q}_k} \left[L_{k-1} L_k \right] = \frac{1}{Q_{k-1} Q_k^2 Q_{k+1}} \left\{ Q_{k-1} Q_k L_{k-1} \boldsymbol{Q}_{k+1} - 2 Q_{k-1} Q_{k+1} L_{k-1} L_k \boldsymbol{Q}_k + Q_k Q_{k+1} L_k \boldsymbol{Q}_{k-1} \right\}$$

$$\tag{D.57}$$

D.1.4   Illustrative example for algorithmic approach to gradient calculation of forward continued product

The application of a recursive-function-based route for the calculation of I_k and $\dfrac{\partial I_k}{\partial \boldsymbol{Q}_j}$ will be made clear in this section using an illustrative example, for $k = 8$, $j = 4$ in a chain with $N = 10$ springs. Note that the exact value of N is immaterial for calculations of

derivatives involving the forward continued product. The degree, n, of the polynomial in p that expresses I_8 is given by

$$n = \left\lfloor \frac{8}{2} \right\rfloor = 4 \tag{D.58}$$

Using Eq. (D.19), we have

$$I_8 = 1 - p \sum_{i=1}^{8-1} L_i^2 f(1, [8+1], i) + p^2 \sum_{i=1}^{8-3} L_i^2 f(2, [8-1], i)$$

$$- p^3 \sum_{i=1}^{8-5} L_i^2 f(3, [8-3], i) + (-1)^4 p^4 \sum_{i=1}^{8-7} L_i^2 f(4, [8-5], i)$$

$$= 1 - p \sum_{i=1}^{7} L_i^2 \underline{f(1, 9, i)} + p^2 \sum_{i=1}^{5} L_i^2 f(2, 7, i) - p^3 \sum_{i=1}^{3} L_i^2 f(3, 5, i) + p^4 \sum_{i=1}^{1} L_i^2 f(4, 3, i) \tag{D.59}$$

From Eq. (D.21), the above underlined term is just unity, and Eq. (D.59) may be simplified as

$$I_8 = 1 - p \sum_{i=1}^{7} L_i^2 + p^2 \left[L_1^2 f(2, 7, 1) + L_2^2 f(2, 7, 2) + L_3^2 f(2, 7, 3) + L_4^2 f(2, 7, 4) \right.$$

$$\left. + L_5^2 f(2, 7, 5) \right] - p^3 \left[L_1^2 \underline{f(3, 5, 1)} + L_2^2 f(3, 5, 2) + L_3^2 f(3, 5, 3) \right] + p^4 L_1^2 f(4, 3, 1) \tag{D.60}$$

The underlined term in Eq. (D.60) will be evaluated as an example. Using Eq. (D.20)

$$f(3, 5, 1) = \sum_{s=1+2}^{5} L_s^2 f([3-1], [5+2], s) = \sum_{s=3}^{5} L_s^2 f(2, 7, s)$$

$$= L_3^2 f(2, 7, 3) + L_4^2 f(2, 7, 4) + L_5^2 f(2, 7, 5)$$

$$= L_3^2 \left[\sum_{s=3+2}^{7} L_s^2 f([2-1], [7+2], s) \right] + L_4^2 \left[\sum_{s=4+2}^{7} L_s^2 f([2-1], [7+2], s) \right]$$

$$+ L_5^2 \left[\sum_{s=5+2}^{7} L_s^2 f([2-1], [7+2], s) \right]$$

$$= L_3^2 \left[L_5^2 + L_6^2 + L_7^2 \right] + L_4^2 \left[L_6^2 + L_7^2 \right] + L_5^2 L_7^2 \tag{D.61}$$

Following a similar procedure, the complete expression for I_8 may be obtained as

$$
\begin{aligned}
I_8 = {} & 1 - p\left(L_1^2 + L_2^2 + L_3^2 + L_4^2 + L_5^2 + L_6^2 + L_7^2\right) + p^2\Big[L_1^2\left(L_3^2 + L_4^2 + L_5^2 + L_6^2 + L_7^2\right) + \\
& + L_2^2\left(L_4^2 + L_5^2 + L_6^2 + L_7^2\right) + L_3^2\left(L_5^2 + L_6^2 + L_7^2\right) + L_4^2\left(L_6^2 + L_7^2\right) + L_5^2 L_7^2\Big] \\
& - p^3 L_1^2\Big[L_3^2\left(L_5^2 + L_6^2 + L_7^2\right) + L_4^2\left(L_6^2 + L_7^2\right) + L_5^2 L_7^2\Big] - p^3 L_2^2\Big[L_4^2\left(L_6^2 + L_7^2\right) + L_5^2 L_7^2\Big] \\
& - p^3 L_3^2 L_5^2 L_7^2 p^4 L_1^2 L_3^2 L_5^2 L_7^2
\end{aligned}
$$

$$(D.62)$$

It is now desired to take the gradient of I_8 with respect to $\mathbf{Q}_4$. From Eq. (D.6), it is clear that only L_3 and L_4 are functions of $\mathbf{Q}_4$. By grouping together the relevant terms on the RHS of Eq. (D.62), the expression for $\dfrac{\partial I_8}{\partial \mathbf{Q}_4}$ may then be written as

$$
\begin{aligned}
\frac{\partial I_8}{\partial \mathbf{Q}_4} = {} & \left\{-p + p^2\left(L_1^2 + L_5^2 + L_6^2 + L_7^2\right) - p^3 L_5^2 L_7^2 - p^3 L_1^2\left(L_5^2 + L_6^2 + L_7^2\right) + p^4 L_1^2 L_5^2 L_7^2\right\}\frac{\partial L_3^2}{\partial \mathbf{Q}_4} \\
& + \left\{-p + p^2\left(L_1^2 + L_2^2 + L_6^2 + L_7^2\right) - p^3\left(L_1^2 + L_2^2\right)\left(L_6^2 + L_7^2\right)\right\}\frac{\partial L_4^2}{\partial \mathbf{Q}_4}
\end{aligned}
$$

$$(D.63)$$

where the underlined terms may be evaluated using Eq. (D.54) and Eq. (D.55) given in Sec. D.1.3. Equation (D.63) has been obtained using a bruteforce approach, by individually examining terms on the RHS of Eq. (D.62) and retaining the ones that do not vanish when a gradient with respect to $\mathbf{Q}_4$ is taken. An algorithmic approach for obtaining an expression for $\dfrac{\partial I_8}{\partial \mathbf{Q}_4}$ is illustrated next. Starting with Eq. (D.29),

$$
\begin{aligned}
\frac{\partial I_8}{\partial \mathbf{Q}_4} &= \sum_{i=1}^{2} L_i^2 \frac{\partial \widetilde{q}_i^{(8)}}{\partial \mathbf{Q}_4} + \widetilde{q}_3^{(8)} \frac{\partial L_3^2}{\partial \mathbf{Q}_4} + \widetilde{q}_4^{(8)} \frac{\partial L_4^2}{\partial \mathbf{Q}_4} \\
&= L_1^2 \frac{\partial \widetilde{q}_1^{(8)}}{\partial \mathbf{Q}_4} + L_2^2 \frac{\partial \widetilde{q}_2^{(8)}}{\partial \mathbf{Q}_4} + \widetilde{q}_3^{(8)} \frac{\partial L_3^2}{\partial \mathbf{Q}_4} + \widetilde{q}_4^{(8)} \frac{\partial L_4^2}{\partial \mathbf{Q}_4}
\end{aligned}
$$

$$(D.64)$$

The steps for the construction of $\dfrac{\partial \widetilde{q}_1^{(8)}}{\partial \mathbf{Q}_4}$, using Eq. (D.26), may be written as

$$
\begin{aligned}
\frac{\partial \widetilde{q}_1^{(8)}}{\partial \mathbf{Q}_4} = {} & \widetilde{\theta}_{41}\left[\sum_{\mu=2}^{4}(-1)^\mu\, p^\mu \widetilde{f}(\mu-1, [8-(2\mu-5)], -1; \{1,3\})\right]\frac{\partial L_3^2}{\partial \mathbf{Q}_4} \\
& + \widehat{\theta}_{48}\left[\sum_{\mu=2}^{4}(-1)^\mu\, p^\mu \widetilde{f}(\mu-1, [8-(2\mu-5)], -1; \{1,4\})\right]\frac{\partial L_4^2}{\partial \mathbf{Q}_4};
\end{aligned}
$$

$$(D.65)$$

recognizing that $v = 1$, $\widetilde{\ell} = \{v, j - 1\} = \{1, 3\}$ for the first term on the RHS of Eq. (D.65), and $\widetilde{\ell} = \{v, j\} = \{1, 4\}$ for the second term on the RHS. Upon simplifying Eq. (D.65) using the indicator functions defined in Eqs. (D.27) and (D.28), we obtain

$$\frac{\partial \widetilde{q}_1^{(8)}}{\partial \boldsymbol{Q}_4} = \underbrace{\left[\sum_{\mu=2}^{4} (-1)^\mu p^\mu \widetilde{f}(\mu - 1, [8 - (2\mu - 5)], -1; \{1, 3\}) \right]}_{\cdots\cdots\cdots\cdots\cdots\cdots\cdots\cdots\cdots\cdots\cdots\cdots\cdots\cdots\cdots\cdots\cdots\cdots} \frac{\partial L_3^2}{\partial \boldsymbol{Q}_4}$$

$$+ \left[\sum_{\mu=2}^{4} (-1)^\mu p^\mu \widetilde{f}(\mu - 1, [8 - (2\mu - 5)], -1; \{1, 4\}) \right] \frac{\partial L_4^2}{\partial \boldsymbol{Q}_4}; \quad \text{(D.66)}$$

The contents within the square braces, underlined as shown above, will be evaluated explicitly next.

$$\sum_{\mu=2}^{4} (-1)^\mu p^\mu \widetilde{f}(\mu - 1, [8 - (2\mu - 5)], -1; \{1, 3\}) = p^2 \widetilde{f}(1, 9, -1; \{1, 3\}) - p^3 \widetilde{f}(2, 7, -1; \{1, 3\})$$

$$+ p^4 \widetilde{f}(3, 5, -1; \{1, 3\})$$

$$\text{(D.67)}$$

Now

$$\widetilde{f}(1, 9, -1; \{1, 3\}) = 1 \quad \text{(D.68)}$$

which follows from Eq. (D.24). The $\widetilde{f}$ appearing in the second term on the RHS of Eq. (D.67) is evaluated as

$$\widetilde{f}(2, 7, -1; \{1, 3\}) = \sum_{\substack{s=-1+2 \\ s \notin \widetilde{\lambda} \\ s > \min(\{1,3\})}}^{7} L_s^2 \widetilde{f}(1, 9, s; \{1, 3\})$$

where $\widetilde{\ell} = \{1, 3\}$, and $\widetilde{\lambda} \equiv \{(1 - 1), 1, (1 + 1), (3 - 1), 3, (3 + 1)\} = \{0, 1, 2, 3, 4\}$, with duplicate entries in the set $\widetilde{\lambda}$ discarded. We therefore obtain

$$\widetilde{f}(2, 7, -1; \{1, 3\}) = \sum_{\substack{s=1 \\ s \notin \{0,1,2,3,4\} \\ s > 1}}^{7} L_s^2 \widetilde{f}(1, 9, s; \{1, 3\})$$

i.e.,

$$\widetilde{f}(2, 7, -1; \{1, 3\}) = L_5^2 \underline{\widetilde{f}(1, 9, 5; \{1, 3\})} + L_6^2 \underline{\widetilde{f}(1, 9, 6; \{1, 3\})} + L_7^2 \underline{\widetilde{f}(1, 9, 7; \{1, 3\})}$$

Eq. (D.24) implies that each of the underlined terms in the above equation is unity, allowing us to write

$$\widetilde{f}(2, 7, -1; \{1, 3\}) = L_5^2 + L_6^2 + L_7^2 \quad \text{(D.69)}$$

Similarly,

$$\widetilde{f}(3, 5, -1; \{1, 3\}) = \sum_{\substack{s=1 \\ s \notin \{0,1,2,3,4\} \\ s>1}}^{5} L_s^2 \, \widetilde{f}(2, 7, s; \{1, 3\}) = L_5^2 \, \widetilde{f}(2, 7, 5; \{1, 3\})$$

We then have

$$\widetilde{f}(2, 7, 5; \{1, 3\}) = \sum_{\substack{s=7 \\ s \notin \{0,1,2,3,4\} \\ s>1}}^{7} L_s^2 \, \widetilde{f}(1, 9, s; \{1, 3\}) = L_7^2$$

and may write

$$\widetilde{f}(3, 5, -1; \{1, 3\}) = L_5^2 L_7^2 \tag{D.70}$$

Using Eqs. (D.68), (D.69), and (D.70), Eq. (D.67) may be rewritten as

$$\sum_{\mu=2}^{4} (-1)^\mu \, p^\mu \widetilde{f}(\mu - 1, [8 - (2\mu - 5)], -1; \{1, 3\}) = p^2 - p^3 \left(L_5^2 + L_6^2 + L_7^2 \right) + p^4 L_5^2 L_7^2 \tag{D.71}$$

Following along similar lines, the contents of the square braces in the second term on the RHS of Eq. (D.65) may be evaluated to be

$$\sum_{\mu=2}^{4} (-1)^\mu \, p^\mu \widetilde{f}(\mu - 1, [8 - (2\mu - 5)], -1; \{1, 4\}) = p^2 \widetilde{f}(1, 9, -1; \{1, 4\}) - p^3 \widetilde{f}(2, 7, -1; \{1, 4\})$$
$$+ p^4 \widetilde{f}(3, 5, -1; \{1, 4\})$$
$$= p^2 - p^3 \left(L_6^2 + L_7^2 \right) \tag{D.72}$$

From Eqs. (D.71) and (D.72), Eq. (D.66) may be rewritten as

$$\frac{\partial \widetilde{q}_1^{(8)}}{\partial \boldsymbol{Q}_4} = \left[p^2 - p^3 \left(L_5^2 + L_6^2 + L_7^2 \right) + p^4 L_5^2 L_7^2 \right] \frac{\partial L_3^2}{\partial \boldsymbol{Q}_4} + \left[p^2 - p^3 \left(L_6^2 + L_7^2 \right) \right] \frac{\partial L_4^2}{\partial \boldsymbol{Q}_4} \tag{D.73}$$

Following along similar lines, we obtain

$$\frac{\partial \widetilde{q}_2^{(8)}}{\partial \boldsymbol{Q}_4} = \left[p^2 - p^3 \left(L_6^2 + L_7^2 \right) \right] \frac{\partial L_4^2}{\partial \boldsymbol{Q}_4} \tag{D.74}$$

The steps for the construction of $\widetilde{q}_4^{(8)}$ are given next. Starting from Eq. (D.23),

$$\widetilde{q}_4^{(8)} = \sum_{\mu=1}^{4} (-1)^\mu \, p^\mu \widetilde{f}(\mu, [8 - (2\mu - 3)], -1; \{4\})$$

$$= -p \widetilde{f}(1, 9, -1; \{4\}) + p^2 \widetilde{f}(2, 7, -1; \{4\}) - p^3 \widetilde{f}(3, 5, -1; \{4\}) + p^4 \widetilde{f}(4, 3, -1; \{4\}) \tag{D.75}$$

Now

$$\widetilde{f}(1, 9, -1; \{4\}) = 1 \tag{D.76}$$

which follows from Eq. (D.24). The $\widetilde{f}$ appearing in the second term on the RHS of Eq. (D.75) is evaluated as

$$\widetilde{f}(2, 7, -1; \{4\}) = \sum_{\substack{s=-1+2 \\ s \notin \widetilde{\lambda} \\ s > \min(\{4\})}}^{7} L_s^2 \, \widetilde{f}(1, 9, s; \{4\})$$

where $\widetilde{\lambda} \equiv \{(4-1), 4, (4+1)\} = \{3, 4, 5\}$. We therefore obtain

$$\widetilde{f}(2, 7, -1; \{4\}) = \sum_{\substack{s=1 \\ s \notin \{3,4,5\} \\ s > 4}}^{7} L_s^2 \, \widetilde{f}(1, 9, s; \{4\}) = L_6^2 \, \underline{\widetilde{f}(1, 9, 6; \{4\})} + L_7^2 \, \underline{\widetilde{f}(1, 9, 7; \{4\})}$$

Eq. (D.24) implies that each of the underlined terms in the above equation is unity, allowing us to write

$$\widetilde{f}(2, 7, -1; \{4\}) = L_6^2 + L_7^2 \tag{D.77}$$

Processing the next term,

$$\widetilde{f}(3, 5, -1; \{4\}) = \sum_{\substack{s=1 \\ s \notin \{3,4,5\} \\ s > 4}}^{5} L_s^2 \, \widetilde{f}(2, 7, s; \{4\}) = 0$$

and similarly

$$\widetilde{f}(4, 3, -1; \{4\}) = \sum_{\substack{s=1 \\ s \notin \{3,4,5\} \\ s > 4}}^{3} L_s^2 \, \widetilde{f}(3, 5, s; \{4\}) = 0$$

Using Eqs. (D.76) and (D.77), Eq. (D.75) may be rewritten as

$$\widetilde{q}_4^{(8)} = -p + p^2 \left(L_6^2 + L_7^2 \right) \tag{D.78}$$

Following along similar lines, we obtain

$$\widetilde{q}_3^{(8)} = -p + p^2 \left(L_5^2 + L_6^2 + L_7^2 \right) - p^3 L_5^2 L_7^2 \tag{D.79}$$

Using Eqs. (D.73), (D.74), (D.78) and (D.79), Eq. (D.64) may be rewritten as

$$
\begin{aligned}
\frac{\partial I_8}{\partial \boldsymbol{Q}_4} &= L_1^2\left\{\left[p^2 - p^3\left(L_5^2 + L_6^2 + L_7^2\right) + p^4 L_5^2 L_7^2\right]\frac{\partial L_3^2}{\partial \boldsymbol{Q}_4} + \left[p^2 - p^3\left(L_6^2 + L_7^2\right)\right]\frac{\partial L_4^2}{\partial \boldsymbol{Q}_4}\right\} \\
&\quad + L_2^2\left\{\left[p^2 - p^3\left(L_6^2 + L_7^2\right)\right]\frac{\partial L_4^2}{\partial \boldsymbol{Q}_4}\right\} + \left\{-p + p^2\left(L_5^2 + L_6^2 + L_7^2\right) - p^3 L_5^2 L_7^2\right\}\frac{\partial L_3^2}{\partial \boldsymbol{Q}_4} \\
&\quad + \left\{-p + p^2\left(L_6^2 + L_7^2\right)\right\}\frac{\partial L_4^2}{\partial \boldsymbol{Q}_4} \\
&= \left\{-p + p^2\left(L_5^2 + L_6^2 + L_7^2\right) - p^3 L_5^2 L_7^2 + L_1^2\left[p^2 - p^3\left(L_5^2 + L_6^2 + L_7^2\right) + p^4 L_5^2 L_7^2\right]\right\}\frac{\partial L_3^2}{\partial \boldsymbol{Q}_4} \\
&\quad + \left\{-p + p^2\left(L_6^2 + L_7^2\right) + L_1^2\left[p^2 - p^3\left(L_6^2 + L_7^2\right)\right] + L_2^2\left[p^2 - p^3\left(L_6^2 + L_7^2\right)\right]\right\}\frac{\partial L_4^2}{\partial \boldsymbol{Q}_4}
\end{aligned}
$$
(D.80)

which, upon simplification, yields

$$
\begin{aligned}
\frac{\partial I_8}{\partial \boldsymbol{Q}_4} &= \left\{-p + p^2\left(L_1^2 + L_5^2 + L_6^2 + L_7^2\right) - p^3 L_5^2 L_7^2 - p^3 L_1^2\left(L_5^2 + L_6^2 + L_7^2\right) + p^4 L_1^2 L_5^2 L_7^2\right\}\frac{\partial L_3^2}{\partial \boldsymbol{Q}_4} \\
&\quad + \left\{-p + p^2\left(L_1^2 + L_2^2 + L_6^2 + L_7^2\right) - p^3\left(L_1^2 + L_2^2\right)\left(L_6^2 + L_7^2\right)\right\}\frac{\partial L_4^2}{\partial \boldsymbol{Q}_4}
\end{aligned}
$$
(D.81)

It is thus observed that Eq. (D.81), which has been obtained using the recursive-function-based route for the algorithmic calculation of the gradient, is identical to the expression for the gradient written using a bruteforce approach, given by Eq. (D.63).

D.1.5   Calculation of divergence terms in SDE and stress tensor expression

As the first step, it is desired to examine the effect of the spatial discretization width, Δ_{d}, on the accuracy of the numerical calculation of the gradient. As an example, the gradient of $[1/(1 - M_k - P_k)]$, evaluated with respect to the connector vector $\boldsymbol{Q}_j$ for different values of $j, k,$ and N, using the central-difference approximation [Eq. (19) of the main paper], is compared against the solution obtained using the recursive algorithm detailed in Secs. D.1.1- D.1.3.

The error in the gradient evaluated using the central-difference approximation is calculated as

$$
\% \text{ error} = \frac{|\boldsymbol{d}_{\mathrm{num}} - \boldsymbol{d}_{\mathrm{recursive}}|}{|\boldsymbol{d}_{\mathrm{recursive}}|} \times 100
$$
(D.82)

where $\boldsymbol{d} \equiv \left(\partial/\partial \boldsymbol{Q}_j\right)[1/(1 - M_k - P_k)]$, and $|\boldsymbol{d}| = \sqrt{d_x^2 + d_y^2 + d_z^2}$.
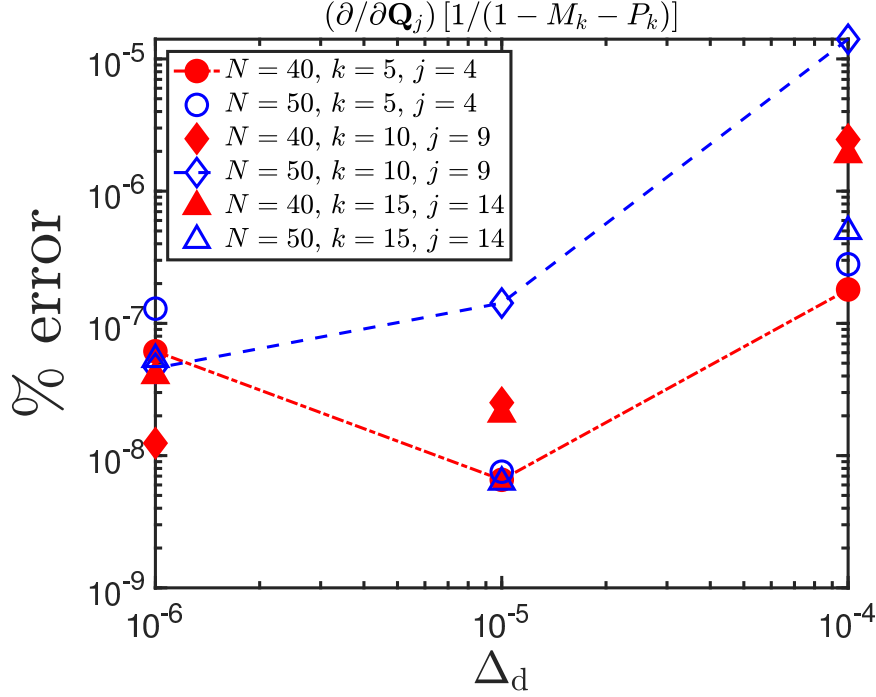
Figure D.3: Variation of error in the calculation of gradient [Eq. (D.82)], as a function of the spatial discretization width, for two different chain lengths. An internal friction parameter of $\varphi = 200$ is used for all the data points.

In Fig. D.3, the variation of this error is plotted as a function of the discretization width, Δ_d, for several test cases. For the data set denoted by empty diamond symbols, the error is seen to decrease nearly monotonically with the decrease in the spatial discretization width. However, for several other data sets, the error varies non-monotonically as the spatial discretization width is changed. Since the minima in the error, where it exists, is observed to occur in the neighbourhood of $\Delta_d = 10^{-5}$, this value of the discretization width has been used in all our calculations. It is noted that the time required for the numerical calculation of the gradient is practically independent of the discretization width.

In Fig. D.4, the error in the calculation of divergence terms, which appear in the governing stochastic differential equation and the stress tensor expression, is plotted as a function of the chain length. The error is calculated as

$$\% \text{ error} = \frac{|z_{\text{num}} - z_{\text{recursive}}|}{|z_{\text{recursive}}|} \times 100 \tag{D.83}$$

where $z \equiv (\partial/\partial\mathbf{Q}_k) \cdot \mathbf{V}_{jk}^T$ or $(\partial/\partial\mathbf{Q}_l) \cdot \boldsymbol{\mu}_{kl}^T$, and various values of $j, k,$ and l have been considered. The error in all the cases is seen to be $\sim 10^{-7}\%$.

In Fig. D.5, the execution time needed for calculating the divergence is plotted as a function of chain length. At lower values of the chain length, the execution times
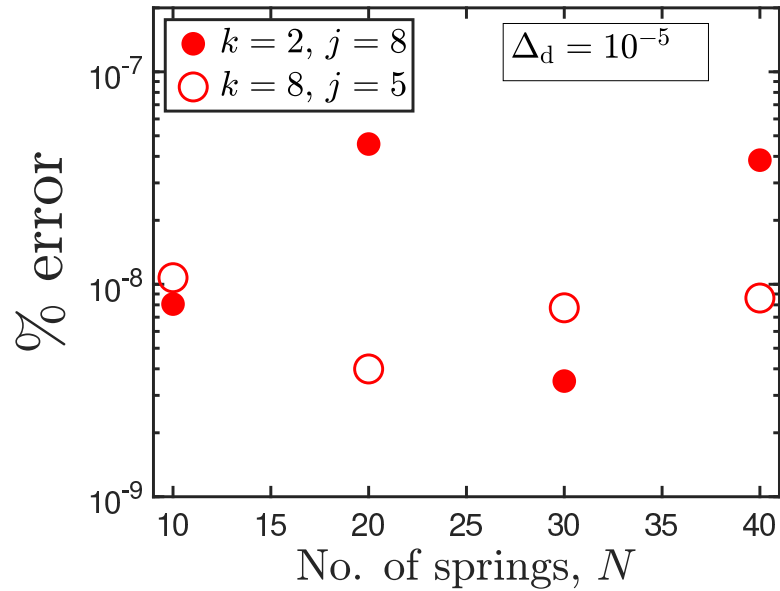
(a)
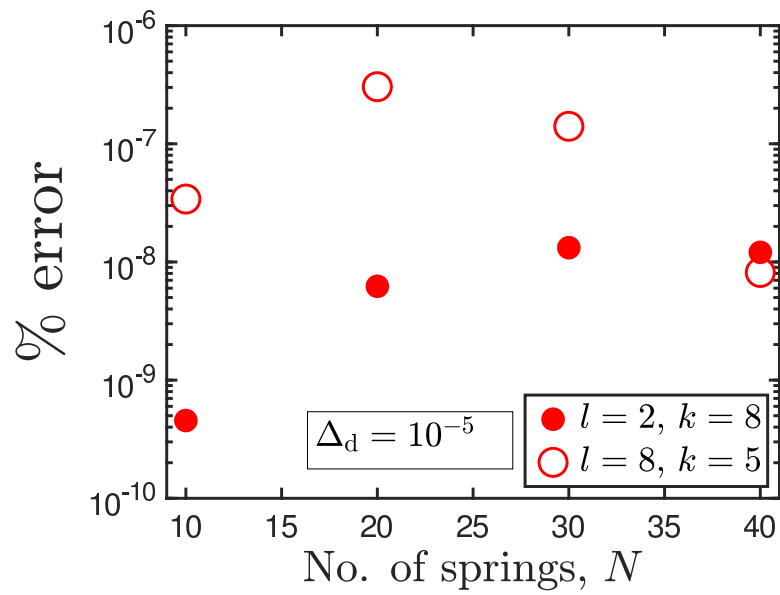
(b)

Figure D.4: Error in the calculation of (a) $(\partial/\partial\boldsymbol{Q}_k)\cdot\boldsymbol{V}_{jk}^T$ and (b) $(\partial/\partial\boldsymbol{Q}_l)\cdot\boldsymbol{\mu}_{kl}^T$, as a function of chain length. An internal friction parameter of $\varphi = 200$ is used for all the data points.
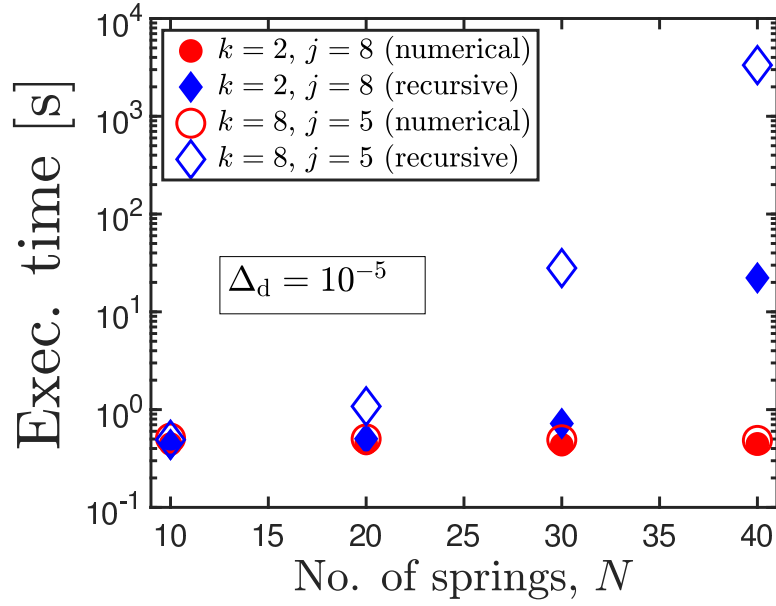
(a)
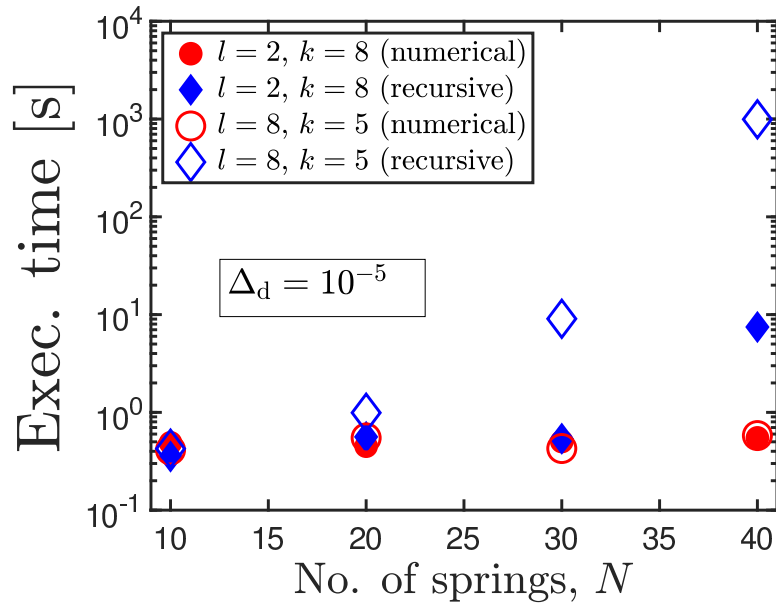
(b)

Figure D.5: Execution time, in seconds, for the calculation of (a) $(\partial/\partial\mathbf{Q}_k) \cdot \boldsymbol{V}_{jk}^T$ and (b) $(\partial/\partial\mathbf{Q}_l) \cdot \boldsymbol{\mu}_{kl}^T$, using two different methods, as a function of chain length. An internal friction parameter of $\varphi = 200$ is used for all the data points. All the runs were executed on on MonARCH, the HPC hosted at Monash University, on the same type of processor [16 core Xeon-E5-2667-v3 @ 3.20GHz servers with 100550MB usable memory].
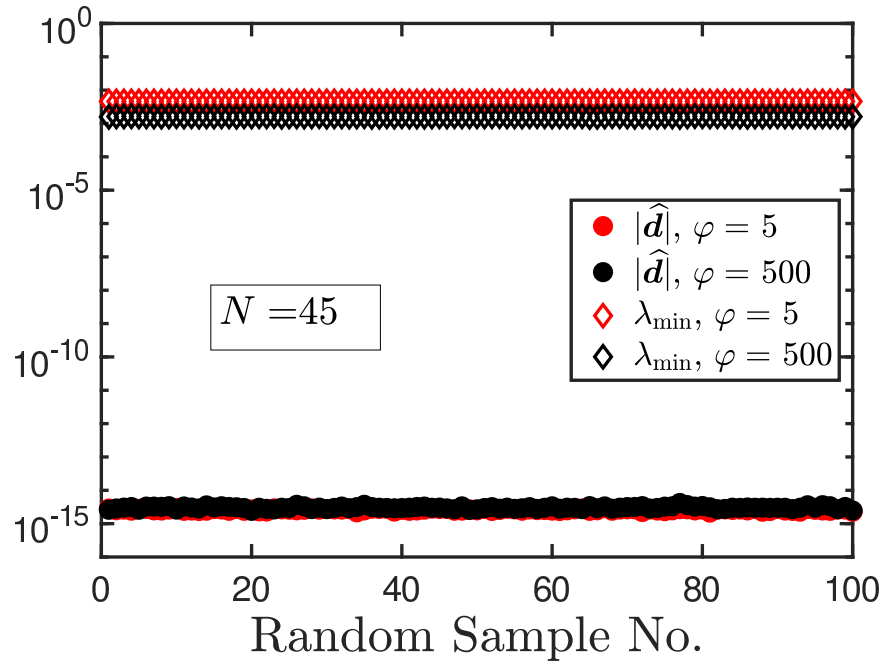
Figure D.6: Test for symmetricity, and smallest eigenvalue of the diffusion tensor, for a hundred randomly chosen initial values of the chain configuration for a forty-five spring chain.

using the two approaches are comparable. With the increase in chain length, however, the time needed for recursive calculation is vastly greater than that for the numerical route. Furthermore, while the execution time using the direct route is nearly independent of the chain length, the time needed for the recursive route increases precipitously at higher chain lengths, due to the larger number of polynomial evaluations. In view of its faster execution execution time, and excellent accuracy ($\sim 10^{-7}\%$), the numerical method for divergence calculation has been used in all our simulations.

D.2   Symmetricity and positive-definiteness of the diffusion tensor

A pre-requisite to the use of the Cholesky decomposition method is that the matrix be positive-definite (Press *et al.*, 2007). We are not able to prove analytically that the diffusion tensor, $\mathcal{D}$, appearing in Equation (5.37) of Chapter 5 is positive-definite. However, we checked for a hundred different random initial configurations of a forty-five spring chain that the eigenvalues of the diffusion matrix are real and positive.

In Fig. D.6, the smallest eigenvalue for each sample configuration, and difference between the diffusion matrix and its transpose, are plotted for two different values of the

internal friction parameter. The difference is computed as follows: firstly, the diffusion matrix and its transpose are subtracted, to generate a $3N \times 3N$ matrix. This matrix is then unwrapped to give an array, $\widehat{\boldsymbol{d}}$, of $9N^2$ elements. Finally, the $2-$norm of this array is computed, and taken to be a numerical measure of the difference between the diffusion matrix and its transpose, as

$$\|\mathcal{D}^T - \mathcal{D}\| \equiv |\widehat{\boldsymbol{d}}| = \sqrt{\left(\widehat{d_1}\right)^2 + \left(\widehat{d_2}\right)^2 + \cdots + \left(\widehat{d_{9N^2}}\right)^2} \tag{D.84}$$

The difference computed in this manner is $O(10^{-14})$, meaning that the diffusion matrix may be considered symmetric for all practical purposes.

Appendix E

Solution of bead-spring-dashpot chain model with preaveraged internal friction

This appendix is organized as follows. Section E.1 presents the discrete version of the Rouse model with internal friction (RIF), which is a finite-bead representation of the model introduced by McLeish and coworkers (Khatri and McLeish, 2007), and accounts for the presence of a flow term. Using normal mode analysis, an expression for the time evolution of the mean-squared end-to-end distance in shear flow has been derived. In Sec. E.2, the governing Langevin equation for a bead-spring-dashpot chain with preaveraged internal friction is solved semi-analytically using normal mode analysis, in order to derive expressions for observables at equilibrium [Sec. E.2.1] and in simple shear flow [Sec. E.2.2]. The stress tensor expression for bead-spring-dashpot chains with preaveraged internal friction is derived in Sec. E.2.3, and an analytical expression for the time-evolution of the shear viscosity is presented. Summations are indicated explicitly, and the Einstein convention is not followed.

E.1 Discrete version of Rouse model with internal friction subjected to shear flow

The Langevin equation for the μth bead of a discrete Rouse chain with internal friction (Khatri and McLeish, 2007) is given by

$$\frac{d\boldsymbol{r}_\mu}{dt} = -\left(\frac{H}{\zeta} + \frac{K}{3\zeta}\frac{d}{dt}\right)\sum_{\nu=1}^{N_{\text{b}}} A_{\mu\nu}^{(\text{R})}\boldsymbol{r}_\nu + \boldsymbol{\kappa}\cdot\boldsymbol{r}_\mu + \boldsymbol{\xi}_\mu \qquad (\text{E.1})$$

where H is the Hookean spring constant, $(K/3)$ is the dashpot coefficient, ζ is the monomeric friction coefficient, κ indicates the flow-field, ξ_μ represents the noise term, and $A_{\mu\nu}^{(R)}$ are elements of the connectivity matrix of size $N_b \times N_b$, which has the form (Verdier, 1966)

$$A^{(R)} = \begin{pmatrix} 1 & -1 & 0 & \cdots & & 0 \\ -1 & 2 & -1 & 0 & \cdots & 0 \\ 0 & -1 & 2 & -1 & \cdots & \\ \vdots & \vdots & \vdots & & & \\ 0 & 0 & \cdots & -1 & 2 & -1 \\ 0 & 0 & \cdots & 0 & -1 & 1 \end{pmatrix} \tag{E.2}$$

The elements of the orthogonal matrix $\boldsymbol{\Omega}$ which project the bead-positions into normal-mode space are given by (Verdier, 1966; Kopf *et al.*, 1997)

$$\Omega_{\mu n} = \left(\frac{2 - \delta_{n0}}{N_b}\right)^{1/2} \cos\left[\left(\mu - \frac{1}{2}\right)\frac{n\pi}{N_b}\right] \tag{E.3}$$

where $\mu = 1, 2, 3, ...N_b$ and $n = 0, 1, 2, ...(N_b - 1)$. The columns of $\boldsymbol{\Omega}$ are eigenvectors of $A^{(R)}$, which means

$$\sum_\mu \Omega_{\mu m}\Omega_{\mu n} = \delta_{mn}$$

$$\sum_n \Omega_{\mu n}\Omega_{\nu n} = \delta_{\mu\nu} \tag{E.4}$$

$$\sum_\mu \sum_\nu \Omega_{\mu n}A_{\mu\nu}\Omega_{\nu m} = a_m\delta_{nm}$$

where a_m refers to the eigenvalues of $A^{(R)}$, given by

$$a_m = 4\sin^2\left(\frac{m\pi}{2N_b}\right); \quad m = 0, 1, 2, ..., (N_b - 1) \tag{E.5}$$

The internal friction coefficient is given by $\varphi = K/\zeta$, and we additionally define $\theta = (K/3\zeta) = \varphi/3$. The derivation for the time evolution of mean-squared end-to-end distance of this model in simple shear flow may be found by first setting

$$\kappa = \begin{pmatrix} 0 & \dot{\gamma} & 0 \\ 0 & 0 & 0 \\ 0 & 0 & 0 \end{pmatrix} \tag{E.6}$$

in Eq. (E.1), where $\dot{\gamma}$ denotes the shear rate. Transforming Eq. (E.1) into normal-mode coordinates using $X_j = \sum_\mu \Omega_{\mu j}r_\mu$, we obtain

$$\frac{dX_p}{dt} = -\frac{Ha_p}{\zeta\left(1 + \theta a_p\right)}X_p + \left(\frac{1}{1 + \theta a_p}\right)\kappa \cdot X_p + g_p(t) \tag{E.7}$$

where the moments of the noise vector, $\boldsymbol{g}_p(t)$, are

$$\left\langle g_p^\alpha \right\rangle = 0; \quad \left\langle g_p^\alpha(t) g_q^\beta(t') \right\rangle = \frac{2k_B T}{\zeta_p} \delta_{pq} \delta^{\alpha\beta} \delta(t - t') \tag{E.8}$$

The governing equation may be written in terms of the cartesian components of $\boldsymbol{X}_p \equiv [x_p, y_p, z_p]^T$, and $\boldsymbol{g}_p \equiv \left[g_p^{(x)}, g_p^{(y)}, g_p^{(z)} \right]^T$ as

$$\frac{d}{dt} \begin{bmatrix} x_p \\ y_p \\ z_p \end{bmatrix} = -\left(\frac{1}{\tau_p}\right) \begin{bmatrix} x_p \\ y_p \\ z_p \end{bmatrix} + \left(\frac{1}{1 + \theta a_p}\right) \begin{bmatrix} \dot{\gamma} y_p \\ 0 \\ 0 \end{bmatrix} + \begin{bmatrix} g_p^{(x)} \\ g_p^{(y)} \\ g_p^{(z)} \end{bmatrix} \tag{E.9}$$

Recognizing that Eq. (E.9) represents a system of three linear stochastic differential equations, we write

$$\frac{dx_p}{dt} + \left(\frac{1}{\tau_p}\right) x_p = \left(\frac{\dot{\gamma}}{1 + \theta a_p}\right) y_p + g_p^{(x)} \tag{E.10}$$

$$\frac{dy_p}{dt} + \left(\frac{1}{\tau_p}\right) y_p = g_p^{(y)} \tag{E.11}$$

$$\frac{dz_p}{dt} + \left(\frac{1}{\tau_p}\right) z_p = g_p^{(z)} \tag{E.12}$$

The equation for x_p depends explicitly on y_p, but y_p is not coupled to x_p. Furthermore, z_p evolves independently of x_p and y_p. The methodology to solve for $y_p(t)$ is identical to that of solving for $z_p(t)$, and consequently, only the steps for the solution of $y_p(t)$ are given. The solution for $x_p(t)$ is dealt with subsequently. In the solution of these three equations [Eqs. (E.10)-(E.12)], we closely follow the framework described in detail in Howard and Milner (2011).

We note that

$$\begin{aligned} \left\langle \boldsymbol{X}_p(t) \cdot \boldsymbol{X}_q(t) \right\rangle &= \left\langle \left[x_p(t)\boldsymbol{e}_x + y_p(t)\boldsymbol{e}_y + z_p(t)\boldsymbol{e}_z \right] \cdot \left[x_q(t)\boldsymbol{e}_x + y_q(t)\boldsymbol{e}_y + z_q(t)\boldsymbol{e}_z \right] \right\rangle \\ &= \left\langle x_p(t)x_q(t) \right\rangle + \left\langle y_p(t)y_q(t) \right\rangle + \left\langle z_p(t)z_q(t) \right\rangle \end{aligned} \tag{E.13}$$

and our task now involves the computation of the three ensemble-averaged quantities on the RHS of Eq. (E.13). Starting from Eq. (E.11), the formal solution for $y_p(t)$ is written as

$$\begin{aligned} y_p(t) &= y_p(0)e^{-t/\tau_p} + \int_0^t dt_1 g_p^{(y)}(t_1) e^{-(t-t_1)/\tau_p} \\ &= y_p(0)e^{-t/\tau_p} + \Delta \mathcal{Y}_p(t) \end{aligned} \tag{E.14}$$

The moments of $\Delta \mathcal{Y}_p(t)$ are

$$\left\langle \Delta \mathcal{Y}_p(t) \right\rangle \equiv \left\langle \int_0^t dt_1 g_p^{(y)}(t_1) e^{-(t-t_1)/\tau_p} \right\rangle = \int_0^t dt_1 \left\langle g_p^{(y)}(t_1) \right\rangle e^{-(t-t_1)/\tau_p} = 0 \qquad \text{(E.15)}$$

and

$$\left\langle \Delta \mathcal{Y}_p(t) \Delta \mathcal{Y}_q(t) \right\rangle = \frac{k_B T}{H_p} \delta_{pq} \left[1 - e^{-2t/\tau_p} \right] \qquad \text{(E.16)}$$

The equal-time correlations of the $y-$ and $z-$ components are identical, and can be derived to be

$$\left\langle y_p(t) y_q(t) \right\rangle = \left\langle z_p(t) z_q(t) \right\rangle = \frac{k_B T}{H_p} \delta_{pq} \qquad \text{(E.17)}$$

Starting from Eq. (E.10), the formal solution for $x_p(t)$ is written as

$$x_p(t) = x_p(0) e^{-t/\tau_p} + \int_0^t dt_1 \, g_p^{(x)}(t_1) e^{-(t-t_1)/\tau_p} + \left(\frac{\dot{\gamma}}{1+\theta a_p} \right) \underline{\int_0^t dt_2 \, y_p(t_2) e^{-(t-t_2)/\tau_p}} \qquad \text{(E.18)}$$

The underlined integral is evaluated as

$$\int_0^t dt_2 \, y_p(t_2) e^{-(t-t_2)/\tau_p} = t y_p(0) e^{-t/\tau_p} + \int_0^t dt_2 \int_0^{t_2} dt_3 \, g_p^{(y)}(t_3) e^{-(t-t_3)/\tau_p} \qquad \text{(E.19)}$$

with the double-integral solved using the Cauchy formula for repeated integration (Oldham and Spanier, 1974),

$$\int_0^t dt_2 \int_0^{t_2} dt_3 \, g_p^{(y)}(t_3) e^{-(t-t_3)/\tau_p} = \frac{1}{(2-1)!} \int_0^t dt' \, (t-t') \, g_p^{(y)}(t') e^{-(t-t')/\tau_p}, \qquad \text{(E.20)}$$

to obtain the following expression for $x_p(t)$,

$$x_p(t) = e^{-t/\tau_p} \left[x_p(0) + \left(\frac{\dot{\gamma}}{1+\theta a_p} \right) t y_p(0) \right] + \Delta \mathcal{X}_p^{(x)}(t) + \left(\frac{\dot{\gamma}}{1+\theta a_p} \right) \Delta \mathcal{X}_p^{(y)}(t) \qquad \text{(E.21)}$$

where

$$\Delta \mathcal{X}_p^{(x)}(t) = \int_0^t dt_1 g_p^{(x)}(t_1) e^{-(t-t_1)/\tau_p}$$

$$\Delta \mathcal{X}_p^{(y)}(t) = \int_0^t dt' \, (t-t') \, g_p^{(y)}(t') e^{-(t-t')/\tau_p} \qquad \text{(E.22)}$$

The equal-time correlation of the $x-$ component is obtained as

$$\left\langle x_p(t) x_q(t) \right\rangle = \left(\frac{k_B T}{H_p} \right) \delta_{pq} e^{-2t/\tau_p} + \underline{\left\langle \Delta \mathcal{X}_p^{(x)}(t) \Delta \mathcal{X}_q^{(x)}(t) \right\rangle} + \left(\frac{\dot{\gamma} \tau_p}{1+\theta a_p} \right)^2 \left(\frac{2t}{\tau_p} \right)^2 \left(\frac{k_B T}{4 H_p} \right) \delta_{pq} e^{-2t/\tau_p}$$

$$+ \left(\frac{\dot{\gamma}}{1+\theta a_p} \right) \left(\frac{\dot{\gamma}}{1+\theta a_q} \right) \underline{\left\langle \Delta \mathcal{X}_p^{(y)}(t) \Delta \mathcal{X}_q^{(y)}(t) \right\rangle}$$

$$\text{(E.23)}$$

The solid-underlined term is identical to $\langle \Delta \mathcal{Y}_p(t) \Delta \mathcal{Y}_q(t) \rangle$, and may be obtained from Eq. (E.16). The dashed underlined term may be simplified as

$$
\begin{aligned}
\langle \Delta \mathcal{X}_p^{(y)}(t) \Delta \mathcal{X}_q^{(y)}(t) \rangle &= \left\langle \int_0^t dt' \, (t-t') \, g_p^{(y)}(t') e^{-(t-t')/\tau_p} \int_0^t dt'' \, (t-t'') \, g_p^{(y)}(t'') e^{-(t-t'')/\tau_q} \right\rangle \\
&= \frac{2k_BT}{\zeta_p} \delta_{pq} \int_0^t dt' \, (t-t')^2 \, e^{-2(t-t')/\tau_p} \\
&= -\left(\frac{\tau_p}{2}\right) t^2 e^{-2t/\tau_p} + \int_0^t \tau_p(t-t') e^{-2(t-t')/\tau_p} dt' \\
&= -\left(\frac{\tau_p}{2}\right) t^2 e^{-2t/\tau_p} + \left(\frac{\tau_p^2}{2}\right) \int_0^t (t-t') \frac{d}{dt'}\left[e^{-2(t-t')/\tau_p} \right] dt' \\
&= \left(\frac{k_BT}{4H_p}\right) \tau_p^2 \delta_{pq} \left\{ 2 - \left[2 + 2\left(\frac{2t}{\tau_p}\right) + \left(\frac{2t}{\tau_p}\right)^2 \right] e^{-2t/\tau_p} \right\}
\end{aligned}
$$

(E.24)

to give

$$
\langle x_p(t) x_q(t) \rangle = \left(\frac{k_BT}{H_p}\right) \delta_{pq} + 8\left(\frac{k_BT}{H_p a_p^2}\right) \delta_{pq} \, (\lambda_H \dot{\gamma})^2 \left\{ 1 - \left[1 + \left(\frac{2t}{\tau_p}\right) \right] e^{-2t/\tau_p} \right\}
$$

(E.25)

Plugging Eqs. (E.17) and (E.25) into Eq. (E.13), the equal-time correlation for the modes is obtained as

$$
\langle \boldsymbol{X}_p(t) \cdot \boldsymbol{X}_q(t) \rangle = \left(\frac{3k_BT}{H}\right)\left(\frac{1}{a_p}\right) \delta_{pq} \left\{ 1 + \frac{8(\lambda_H\dot{\gamma})^2}{3a_p^2}\left[1 - \left(e^{-2t/\tau_p}\left[1 + \left(\frac{2t}{\tau_p}\right) \right] \right) \right] \right\}
$$

(E.26)

Recognizing that the end-to-end vector is given by

$$
\boldsymbol{R}_{\mathrm{E}}(t) = -2\sqrt{\frac{2}{N_{\mathrm{b}}}} \sum_{q:\text{odd}}^{N_{\mathrm{b}}-1} \cos\left(\frac{q\pi}{2N_{\mathrm{b}}}\right) \boldsymbol{X}_q(t),
$$

(E.27)

the expression for $\langle \boldsymbol{R}_{\mathrm{E}}^2(t) \rangle$ may be written as

$$
\langle \boldsymbol{R}_{\mathrm{E}}^2(t) \rangle = \left(\frac{8}{N_{\mathrm{b}}}\right) \sum_{q:\text{odd}}^{N_{\mathrm{b}}-1} \sum_{p:\text{odd}}^{N_{\mathrm{b}}-1} \cos\left(\frac{p\pi}{2N_{\mathrm{b}}}\right) \cos\left(\frac{q\pi}{2N_{\mathrm{b}}}\right) \langle \boldsymbol{X}_p(t) \cdot \boldsymbol{X}_q(t) \rangle
$$

(E.28)

Using Eqs. (E.26) and (E.28), we get

$$
\langle \boldsymbol{R}_{\mathrm{E}}^2(t) \rangle = \left(\frac{8}{N_{\mathrm{b}}}\right)\left(\frac{3k_BT}{H}\right) \sum_{p:\text{odd}}^{N_{\mathrm{b}}-1} \left(\frac{1}{a_p}\right) \cos^2\left(\frac{p\pi}{2N_{\mathrm{b}}}\right) \left\{ 1 + \frac{8(\lambda_H\dot{\gamma})^2}{3a_p^2}\left[1 - \left(e^{-2t/\tau_p}\left[1 + \left(\frac{2t}{\tau_p}\right) \right] \right) \right] \right\},
$$

(E.29)

Upon using the following scheme for scaling the time variable,

$$
\frac{t}{\tau_p} \equiv \frac{H_p t}{\zeta_p} = \left(\frac{Ha_p t}{\zeta(1+\theta a_p)}\right) = \left(\frac{Ha_p t}{4H\lambda_H(1+\theta a_p)}\right) = \left(\frac{1}{4}\right)\left(\frac{a_p}{1+\theta a_p}\right)\left(\frac{t}{\lambda_H}\right) = \left(\frac{a_p}{1+\theta a_p}\right)\frac{t^*}{4},
$$

(E.30)

the dimensionless form of Eq. (E.29) becomes

$$\left\langle R_{\rm E}^{*2}(t^*) \right\rangle = \left(\frac{24}{N_{\rm b}}\right) \sum_{p:\text{odd}}^{N_{\rm b}-1} \left(\frac{1}{a_p}\right) \cos^2\left(\frac{p\pi}{2N_{\rm b}}\right) \left\{ 1 + \frac{8\left(\lambda_{\rm H}\dot\gamma\right)^2}{3a_p^2}\left[1 - \left(\exp\left[-\left(\frac{a_p}{1+\theta a_p}\right)\frac{t^*}{2}\right]\right.\right.$$
$$\left.\left.\times\left[1 + \left(\frac{a_p}{1+\theta a_p}\right)\frac{t^*}{2}\right]\right)\right]\right\} \tag{E.31}$$

The steady-state result is obtained by taking the limit $t^* \to \infty$ in Eq. (E.31), to give

$$\left\langle R_{\rm E}^{*2} \right\rangle \equiv \left\langle R_{\rm E}^{*2}(t^* \to \infty) \right\rangle = \left(\frac{24}{N_{\rm b}}\right) \sum_{p:\text{odd}}^{N_{\rm b}-1} \left(\frac{1}{a_p}\right) \cos^2\left(\frac{p\pi}{2N_{\rm b}}\right) \left\{ 1 + \frac{8\left(\lambda_{\rm H}\dot\gamma\right)^2}{3a_p^2}\right\} \tag{E.32}$$

In the limit of large $N_{\rm b}$, Eq. (E.32) is found to agree with Eq. (10) of Bhattacharyya and Cherayil (2012), which is the result for a continuum model of a Rouse chain in shear flow. Scaling Eq. (E.31) by the mean-squared end-to-end vector gives

$$\frac{\left\langle R_{\rm E}^{*2}(t^*) \right\rangle}{\left\langle R_{\rm E}^{*2} \right\rangle_{\rm eq}} = \left[\frac{8}{N_{\rm b}(N_{\rm b}-1)}\right] \sum_{p:\text{odd}}^{N_{\rm b}-1} \left(\frac{1}{a_p}\right) \cos^2\left(\frac{p\pi}{2N_{\rm b}}\right)$$
$$\times \left\{ 1 + \frac{8\left(\lambda_{\rm H}\dot\gamma\right)^2}{3a_p^2}\left[1 - \left(\exp\left[-\left(\frac{a_p}{1+\theta a_p}\right)\frac{t^*}{2}\right]\left[1 + \left(\frac{a_p}{1+\theta a_p}\right)\frac{t^*}{2}\right]\right)\right]\right\} \tag{E.33}$$

Additionally, it is of utility to compute the correlation, $\left\langle x_p(t)y_q(t) \right\rangle$, for subsequent use in the derivation of an analytical expression for the transient variation of the shear viscosity, as discussed later in Sec. E.2.3. Note that this correlation is zero in the absence of flow, by virtue of the noise being white in normal mode space [See Eq. 6.8]. From Eq. (E.14) and (E.21), we can write, after some algebra

$$\left\langle x_p(t)y_q(t) \right\rangle = \left(\frac{\dot\gamma}{1+\theta a_p}\right)\delta_{pq}\left(\frac{k_BT}{H_p}\right)te^{-2t/\tau_p} + \left(\frac{\dot\gamma}{1+\theta a_p}\right)\underline{\left\langle \Delta\mathcal{X}_p^{(y)}(t)\Delta\mathcal{Y}_q(t) \right\rangle} \tag{E.34}$$

The underlined term is evaluated to be

$$\left\langle \Delta\mathcal{X}_p^{(y)}(t)\Delta\mathcal{Y}_q(t) \right\rangle = \left(\frac{k_BT}{H_p}\right)\left(\frac{\tau_p}{2}\right)\delta_{pq}\left[1 - e^{-2t/\tau_p}\left(1 + \left(\frac{2t}{\tau_p}\right)\right)\right] \tag{E.35}$$

Plugging Eq. (E.35) into Eq. (E.34), we obtain

$$\left\langle x_p(t)y_q(t) \right\rangle = \delta_{pq}\left(\frac{\dot\gamma}{1+\theta a_p}\right)\left(\frac{\tau_p}{2}\right)\left[1 - e^{-2t/\tau_p}\right] \tag{E.36}$$

E.2 Semi-analytical solution to the bead-spring-dashpot chain with preaveraged internal friction

The Langevin equation corresponding to the stochastic differential equation governing the dynamics of a bead-spring-dashpot chain with preaveraged internal friction [Eq. (6.47) of

Chapter 6 is given by

$$\frac{d\boldsymbol{Q}_k}{dt} = \left(\frac{1}{1+2\theta}\right)\left[\sum_{l=1}^{N}\Lambda_{kl}\left(\boldsymbol{\kappa}\cdot\boldsymbol{Q}_l\right) - \left(\frac{H}{\zeta}\right)\sum_{l=1}^{N}J_{kl}\boldsymbol{Q}_l\right] + \sqrt{\frac{2k_BT}{\zeta(1+2\theta)}}\sum_{l=1}^{N}B_{kl}\boldsymbol{f}_l(t) \quad \text{(E.37)}$$

where

$$\sum_{j=1}^{N}B_{kj}B_{lj} = J_{kl} \qquad \text{(E.38)}$$

and

$$\langle\boldsymbol{f}_l(t)\rangle = 0$$

$$\langle\boldsymbol{f}_l(t)\boldsymbol{f}_m(t')\rangle = \delta_{ml}\boldsymbol{\delta}\delta(t-t') \qquad \text{(E.39)}$$

$$\langle\boldsymbol{f}_l(t)\cdot\boldsymbol{f}_m(t')\rangle = 3\,\delta_{ml}\,\delta(t-t')$$

The quantities Λ_{kl} and J_{kl} result from the decoupling procedure used to obtain the governing equation for the system, and their precise definitions have been given in Sec. 6.3 of Chapter 6. Notably, Λ_{kl} and J_{kl} are functions only of the internal friction parameter θ, and depend neither on the chain reconfiguration, nor on the flow strength. In the absence of internal friction, $\Lambda_{kl} = \delta_{kl}$, and $J_{kl} = A_{kl}$, where A_{kl} is the Rouse matrix defined as in Equation (2.3). The notations $\boldsymbol{\Lambda}$ and $\boldsymbol{J}$ are introduced to indicate $N \times N$ matrices whose elements are given by Λ_{kl} and J_{kl}, respectively

Semi-analytical solutions to Eq. (E.37) at equilibrium and in the presence of shear flow are presented below.

E.2.1   Normal mode analysis at equilibrium

To obtain the correlation of the end-to-end vector for a Rouse chain with preaveraged internal friction, we set $\boldsymbol{\kappa} = 0$ in Eq. (E.37) and obtain the governing Langevin equation as

$$\frac{d\boldsymbol{Q}_k}{dt} = -\left[\frac{H}{\zeta(1+2\theta)}\right]\sum_{l=1}^{N}J_{kl}\boldsymbol{Q}_l + \sqrt{\frac{2k_BT}{\zeta(1+2\theta)}}\sum_{l=1}^{N}B_{kl}\boldsymbol{f}_l(t) \qquad \text{(E.40)}$$

This equation is converted into normal mode coordinates by means of the transformation $\boldsymbol{Q}'_j = \sum_m \Pi_{mj}\boldsymbol{Q}_m$, where the orthogonalizing matrix $\boldsymbol{\Pi}$ satisfies the following properties

$$\sum_{k=1}^{N}\Pi_{kj}\Pi_{kl} = \delta_{jl} = \sum_{n=1}^{N}\Pi_{jn}\Pi_{ln}$$

$$\sum_{l=1}^{N}\sum_{n=1}^{N}\Pi_{lj}J_{ln}\Pi_{nk} = \widetilde{a}_j\delta_{jk}$$

$$\text{(E.41)}$$
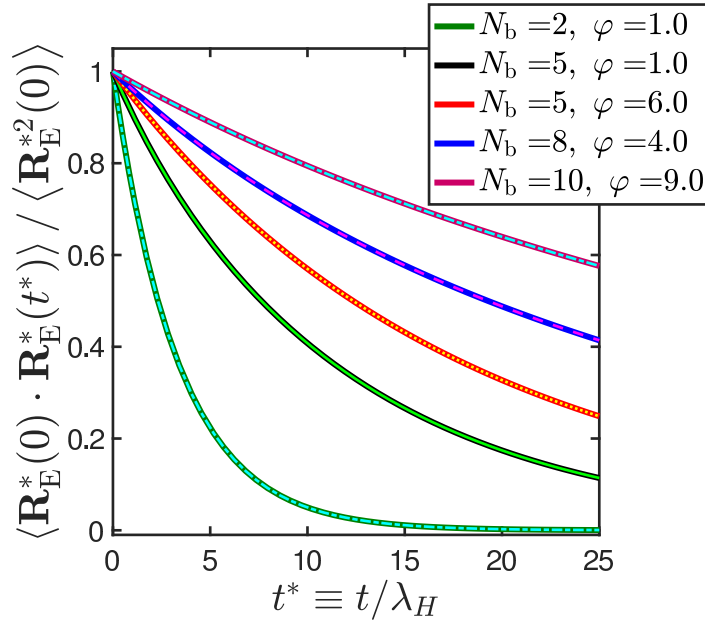
(a)
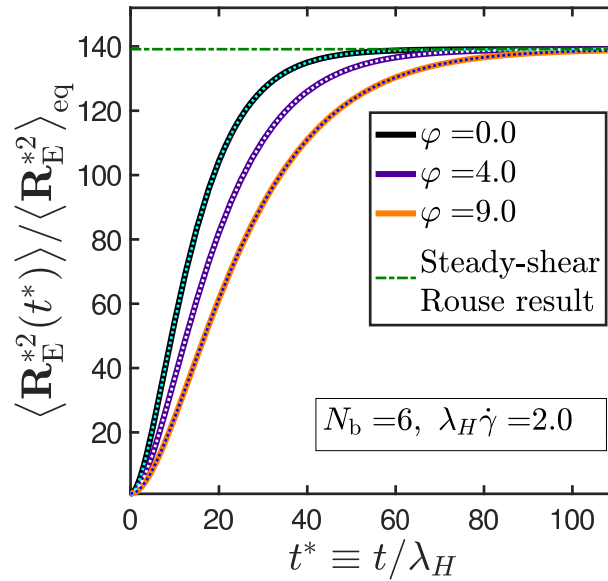
(b)

Figure E.1: A comparison of the results for the (a) normalized autocorrelation and (b) transient evolution of the mean-squared end-to-end vector predicted by the discrete RIF model and the preaveraged IV model derived using the principles of polymer kinetic theory. Each legend entry corresponds to two lines: the thicker lines represents the discrete RIF results [Eq. 6.19 in (a) and Eq. (E.33) in (b)], while the thinner lines represents semi-analytical soutions for the preaveraged IV model [Eq. E.47 in (a) and Eq. (E.54) in (b)].

and must be determined numerically. In Eq. (E.41), the $\widetilde{a}_j$ represent the eigenvalues of $\boldsymbol{J}$.

The governing equation for the normal coordinates is given as

$$\frac{d\boldsymbol{Q}'_m}{dt} = -\left[\frac{H\widetilde{a}_m}{\zeta(1 + 2\theta)}\right]\boldsymbol{Q}'_m + \sqrt{\frac{2k_BT}{\zeta(1 + 2\theta)}}\sum_k\sum_l \Pi_{km}B_{kl}\boldsymbol{f}_l(t) \tag{E.42}$$

whose formal solution may be written as

$$\boldsymbol{Q}'_m(t) = \boldsymbol{Q}'_m(0)e^{-t/\widehat{\tau}_m} + \sqrt{\frac{2k_BT}{\zeta(1 + 2\theta)}}\int_0^t dt_1\left[\sum_k\sum_l \Pi_{km}B_{kl}\boldsymbol{f}_l(t_1)\right]e^{-(t-t_1)/\widehat{\tau}_m} \tag{E.43}$$

where $\widehat{\tau}_m = \zeta(1 + 2\theta)/H\widetilde{a}_m$. The autocorrelation of the normal modes may be derived to be

$$\left\langle\boldsymbol{Q}'_p(0)\cdot\boldsymbol{Q}'_m(t)\right\rangle = \frac{3k_BT}{H}\delta_{pm}e^{-t/\widehat{\tau}_p} \tag{E.44}$$

Recognizing that

$$\langle\boldsymbol{R}_{\mathrm{E}}(0)\cdot\boldsymbol{R}_{\mathrm{E}}(t)\rangle = \sum_{i,m,j,p}\Pi_{im}\Pi_{jp}\left\langle\boldsymbol{Q}'_p(0)\cdot\boldsymbol{Q}'_m(t)\right\rangle \tag{E.45}$$

and

$$\frac{t}{\widehat{\tau}_p} \equiv \left[\frac{H\widetilde{a}_pt}{\zeta(1 + 2\theta)}\right] = \left[\frac{H\widetilde{a}_pt}{4H\lambda_H(1 + 2\theta)}\right] = \left(\frac{1}{4}\right)\left(\frac{\widetilde{a}_p}{1 + 2\theta}\right)\left(\frac{t}{\lambda_H}\right) = \left(\frac{\widetilde{a}_p}{1 + 2\theta}\right)\frac{t^*}{4} \tag{E.46}$$

the normalized autocorrelation of the end-to-end vector in dimensionless time units may be written as

$$\frac{\langle\boldsymbol{R}_{\mathrm{E}}^*(0)\cdot\boldsymbol{R}_{\mathrm{E}}^*(t^*)\rangle}{\left\langle\boldsymbol{R}_{\mathrm{E}}^{*2}(0)\right\rangle} = \left[\frac{1}{N_{\mathrm{b}} - 1}\right]\sum_{i,j,p}^{N_{\mathrm{b}}-1}\Pi_{ip}\Pi_{jp}\exp\left[-\left(\frac{\widetilde{a}_p}{1 + 2\theta}\right)\frac{t^*}{4}\right] \tag{E.47}$$

E.2.2   Normal mode analysis in shear flow

The governing Langevin equation for a Rouse chain with preaveraged internal friction in shear flow is written as

$$\frac{d\boldsymbol{Q}_k}{dt} = \left(\frac{1}{1 + 2\theta}\right)\left[\sum_{l=1}^N \Lambda_{kl}(\boldsymbol{\kappa}\cdot\boldsymbol{Q}_l) - \frac{H}{\zeta}J_{kl}\boldsymbol{Q}_l\right] + \sqrt{\frac{2k_BT}{\zeta(1 + 2\theta)}}\sum_{l=1}^N B_{kl}\boldsymbol{f}_l(t) \tag{E.48}$$

Eq. (E.48) is transformed into normal coordinates using the orthogonalizing matrix introduced in Eq. (E.41). It is assumed that the same matrix also orthogonalizes Λ_{kl}, such that

$$\sum_{l=1}^N\sum_{k=1}^N \Pi_{km}\Lambda_{kl}\Pi_{lq} = \widetilde{b}_m\delta_{mq} \tag{E.49}$$

The quality of this assumption is found to be excellent, based on several test cases. The governing equation in normal coordinates is derived to be

$$\frac{d\boldsymbol{Q}'_m}{dt} = \left(\frac{\widetilde{b}_m}{1 + 2\theta}\right)\boldsymbol{\kappa}\cdot\boldsymbol{Q}'_m - \left[\frac{H\widetilde{a}_m}{\zeta(1 + 2\theta)}\right]\boldsymbol{Q}'_m + \sqrt{\frac{2k_BT}{\zeta(1 + 2\theta)}}\sum_k\sum_l \Pi_{km}B_{kl}\boldsymbol{f}_l(t) \tag{E.50}$$

Following a procedure identical to that described in Sec. E.1, the correlation between the Cartesian components of the normal modes can be derived to be

$$\left\langle Q_p^{\prime(x)}(t)Q_q^{\prime(x)}(t)\right\rangle = \left(\frac{k_BT}{H}\right)\delta_{pq} + 8\left(\frac{k_BT}{H}\right)\delta_{pq}\left(\frac{\widetilde{b}_q}{\widetilde{a}_q}\right)^2 (\lambda_H\dot{\gamma})^2\left[1 - \left(e^{-2t/\widehat{\tau}_q}\left[1 + \left(\frac{2t}{\widehat{\tau}_q}\right)\right]\right)\right]$$

$$\left\langle Q_p^{\prime(y)}(t)Q_q^{\prime(y)}(t)\right\rangle = \left\langle Q_p^{\prime(z)}(t)Q_q^{\prime(z)}(t)\right\rangle = \left(\frac{k_BT}{H}\right)\delta_{pq}$$

$$\left\langle Q_p^{\prime(x)}(t)Q_q^{\prime(y)}(t)\right\rangle = \left(\frac{k_BT}{H}\right)\delta_{pq}(\lambda_H\dot{\gamma})\,I_q(t)$$

$$\text{(E.51)}$$

where

$$I_q(t) = 2\left(\frac{\widetilde{b}_q}{\widetilde{a}_q}\right)\left[1 - e^{-2t/\widehat{\tau}_q}\right].\tag{E.52}$$

The equal-time correlation of the normal modes is subsequently obtained as

$$\left\langle \boldsymbol{Q}_p'(t)\cdot\boldsymbol{Q}_q'(t)\right\rangle = \left(\frac{3k_BT}{H}\right)\delta_{pq}\left\{1 + \frac{8\,(\lambda_H\dot{\gamma})^2}{3}\left(\frac{\widetilde{b}_p}{\widetilde{a}_p}\right)^2\left[1 - \left(e^{-2t/\widehat{\tau}_p}\left[1 + \left(\frac{2t}{\widehat{\tau}_p}\right)\right]\right)\right]\right\},\quad\text{(E.53)}$$

and the time evolution of the normalized mean-squared end-to-end distance may then be derived to be

$$\frac{\left\langle \boldsymbol{R}_E^{*2}(t^*)\right\rangle}{\left\langle \boldsymbol{R}_E^{*2}\right\rangle_{eq}} = \left[\frac{1}{N_b - 1}\right]\sum_{i,j,p}^{N_b-1}\Pi_{ip}\Pi_{jp}\left\{1 + \frac{8\,(\lambda_H\dot{\gamma})^2}{3}\left(\frac{\widetilde{b}_p}{\widetilde{a}_p}\right)^2\left[1 - \left(\exp\left[-\left(\frac{\widetilde{a}_p}{1+2\theta}\right)\frac{t^*}{2}\right]\right.\right.$$
$$\left.\left.\times\left[1 + \left(\frac{\widetilde{a}_p}{1+2\theta}\right)\frac{t^*}{2}\right]\right)\right]\right\}$$

$$\text{(E.54)}$$

In Fig. (6.4) of Chapter 6, the equivalence between the discrete RIF model and the preaveraged IV model is established by comparison of the analytical predictions of the discrete RIF model against BD simulation data obtained by numerically integrating the stochastic differential equation for the preaveraged IV model [Eq. (6.47)]. In Fig. E.1, predictions of the discrete RIF model are compared against the semi-analytical solutions for the preaveraged IV model, and an excellent agreement is observed.

We have therefore established that: (a) the discrete RIF model and the preaveraged IV model are equivalent, and (b) the preaveraged model may be solved for observables at equilibrium and in simple shear flow using either BD simulations to integrate the governing stochastic differential equation [Eq. (6.47)] or a semi-analytical approach involving the normal-mode decomposition of the governing Langevin equation [Eq. (E.37)].

E.2.3   Derivation of stress tensor expression

As discussed in Chapter 5 and Appendix C, the Kramers expression for the stress tensor is thermodynamically inconsistent (Schieber and Öttinger, 1994) for chains with fluctuating internal friction, and the use of the Giesekus expression is recommended instead. In the absence of any discussion surrounding the viscometric functions of chains with preaveraged internal friction, we have used the Giesekus expression (Bird *et al.*, 1987b), as follows

$$\boldsymbol{\tau}_{\mathrm{p}} = \frac{n_{\mathrm{p}}\zeta}{2}\left\langle\sum_{u=1}^{N}\sum_{v=1}^{N}\mathscr{C}_{uv}\boldsymbol{Q}_u\boldsymbol{Q}_v\right\rangle_{(1)} = \frac{n_{\mathrm{p}}\zeta}{2}\left[\frac{d}{dt}\left\langle\sum_{u,v}\mathscr{C}_{uv}\boldsymbol{Q}_u\boldsymbol{Q}_v\right\rangle - \boldsymbol{\kappa}\cdot\left\langle\sum_{u,v}\mathscr{C}_{uv}\boldsymbol{Q}_u\boldsymbol{Q}_v\right\rangle\right.$$
$$\left.- \left\langle\sum_{u,v}\mathscr{C}_{uv}\boldsymbol{Q}_u\boldsymbol{Q}_v\right\rangle\cdot\boldsymbol{\kappa}^T\right]$$

(E.55)

with $\mathscr{C}_{jk}$ denoting the elements of the symmetric Kramers matrix defined as follows (Bird *et al.*, 1987b)

$$\mathscr{C}_{jk} = \begin{cases} j(N_{\mathrm{b}} - k)/N_{\mathrm{b}}; & j \le k \\ \\ k(N_{\mathrm{b}} - j)/N_{\mathrm{b}}; & k \le j \end{cases}$$

(E.56)

We identify $\boldsymbol{B} \equiv \sum_{u,v=1}^{N}\mathscr{C}_{uv}\boldsymbol{Q}_u\boldsymbol{Q}_v$ and note that a simplified, closed-form expression for the stress tensor in the present case may be found by following the steps detailed in Appendix C. Only the salient intermediate steps of the derivation are therefore shown below. We start with the expression for the equation of change,

$$\frac{d}{dt}\langle\boldsymbol{B}\rangle = \left\langle\sum_{j=1}^{N}\left(\llbracket\dot{\boldsymbol{Q}}_j\rrbracket\cdot\frac{\partial\boldsymbol{B}}{\partial\boldsymbol{Q}_j}\right)\right\rangle$$

(E.57)

and substitute into it the expression for $\llbracket\dot{\boldsymbol{Q}}_j\rrbracket$ given in Eq. (6.41) of Chapter 6, to obtain

$$\frac{d}{dt}\langle\boldsymbol{B}\rangle = \left(\frac{1}{1+2\theta}\right)\left\langle\sum_{j,k}\Lambda_{jk}\left(\boldsymbol{\kappa}\cdot\boldsymbol{Q}_k\right)\cdot\frac{\partial\boldsymbol{B}}{\partial\boldsymbol{Q}_j}\right\rangle - \left(\frac{k_BT}{\zeta}\right)\left(\frac{1}{1+2\theta}\right)\left\langle\sum_{j,k}J_{jk}\frac{\partial\ln\psi}{\partial\boldsymbol{Q}_k}\cdot\frac{\partial\boldsymbol{B}}{\partial\boldsymbol{Q}_j}\right\rangle$$
$$- \left(\frac{H}{\zeta}\right)\left(\frac{1}{1+2\theta}\right)\left\langle\sum_{j,k}J_{jk}\boldsymbol{Q}_k\cdot\frac{\partial\boldsymbol{B}}{\partial\boldsymbol{Q}_j}\right\rangle$$

(E.58)

where we have used the choice of $\partial\phi/\partial\boldsymbol{Q}_l \equiv H\boldsymbol{Q}_l$ to focus our attention on Rouse chains. Also, the distribution function for the internal coordinates (ψ) has been used instead of (Ψ), due to the homogeneous flow field under consideration. The expression for $\dfrac{\partial\boldsymbol{B}}{\partial\boldsymbol{Q}_j}$

remains unchanged from Eq. (C.12) in Appendix C The three terms on the RHS of Eq. (E.58) may be processed as shown below.

$$\left\langle \sum_{j,k} \Lambda_{jk} \left(\boldsymbol{\kappa} \cdot \boldsymbol{Q}_k \right) \cdot \frac{\partial \boldsymbol{B}}{\partial \boldsymbol{Q}_j} \right\rangle = \left\langle \sum_{k,u} \sum_{\beta,m,s} \left(\sum_j \Lambda_{kj} \mathscr{C}_{ju} \right) \kappa^{ms} Q_k^s Q_u^\beta \boldsymbol{e}_\beta \boldsymbol{e}_m \right\rangle$$
$$+ \left\langle \sum_{k,v} \sum_{m,\gamma,s} \left(\sum_j \Lambda_{kj} \mathscr{C}_{jv} \right) \kappa^{ms} Q_k^s Q_v^\gamma \boldsymbol{e}_m \boldsymbol{e}_\gamma \right\rangle \tag{E.59}$$

Defining the symmetric matrix $\boldsymbol{\mathcal{S}} = \boldsymbol{\Lambda} \cdot \boldsymbol{C}$, i.e., $\mathcal{S}_{ku} = \sum_j \Lambda_{kj} \mathscr{C}_{ju}$, Eq. (E.59) may be simplified to give

$$\left\langle \sum_{j,k} \Lambda_{jk} \left(\boldsymbol{\kappa} \cdot \boldsymbol{Q}_k \right) \cdot \frac{\partial \boldsymbol{B}}{\partial \boldsymbol{Q}_j} \right\rangle = \sum_{k,u} \mathcal{S}_{ku} \left[\langle \boldsymbol{Q}_u \boldsymbol{Q}_k \rangle \cdot \boldsymbol{\kappa}^T + \boldsymbol{\kappa} \cdot \langle \boldsymbol{Q}_u \boldsymbol{Q}_k \rangle^T \right] \tag{E.60}$$

Next,

$$\left\langle \sum_{j,k} J_{jk} \frac{\partial \ln \psi}{\partial \boldsymbol{Q}_k} \cdot \frac{\partial \boldsymbol{B}}{\partial \boldsymbol{Q}_j} \right\rangle = \left\langle \sum_{k,u} \sum_{\alpha,\beta} \left(\sum_j J_{kj} \mathscr{C}_{ju} \right) \frac{\partial \ln \psi}{\partial Q_k^\alpha} Q_u^\beta \boldsymbol{e}_\beta \boldsymbol{e}_\alpha \right\rangle$$
$$+ \left\langle \sum_{k,v} \sum_{\alpha,\gamma} \left(\sum_j J_{kj} \mathscr{C}_{jv} \right) \frac{\partial \ln \psi}{\partial Q_k^\alpha} Q_v^\gamma \boldsymbol{e}_\alpha \boldsymbol{e}_\gamma \right\rangle \tag{E.61}$$

Defining the symmetric matrix $\boldsymbol{\mathcal{L}} = \boldsymbol{J} \cdot \boldsymbol{C}$, i.e., $\mathcal{L}_{ku} = \sum_j J_{kj} \mathscr{C}_{ju}$, the first term on the RHS of Eq. (E.61) may be simplified to give

$$\left\langle \sum_{k,u} \sum_{\alpha,\beta} \mathcal{L}_{ku} \frac{\partial \ln \psi}{\partial Q_k^\alpha} Q_u^\beta \boldsymbol{e}_\beta \boldsymbol{e}_\alpha \right\rangle = \sum_{k,u} \mathcal{L}_{ku} \sum_{\alpha,\beta} \int \left[\frac{\partial \psi}{\partial Q_k^\alpha} Q_u^\beta d\boldsymbol{Q} \right] \boldsymbol{e}_\beta \boldsymbol{e}_\alpha$$
$$= - \sum_{k,u} \mathcal{L}_{ku} \delta_{ku} \sum_{\alpha,\beta} \delta^{\alpha\beta} \boldsymbol{e}_\beta \boldsymbol{e}_\alpha \tag{E.62}$$
$$= -\text{tr}\left(\boldsymbol{\mathcal{L}} \right) \boldsymbol{\delta}$$

Therefore,

$$\left\langle \sum_{j,k} J_{jk} \frac{\partial \ln \psi}{\partial \boldsymbol{Q}_k} \cdot \frac{\partial \boldsymbol{B}}{\partial \boldsymbol{Q}_j} \right\rangle = -2\text{tr}\left(\boldsymbol{\mathcal{L}} \right) \boldsymbol{\delta} \tag{E.63}$$

Lastly, the third term on the RHS of Eq. (E.58) may be simplified as

$$\left\langle \sum_{j,k} J_{jk} \boldsymbol{Q}_k \cdot \frac{\partial \boldsymbol{B}}{\partial \boldsymbol{Q}_j} \right\rangle = \left\langle \sum_{k,u} \sum_{\alpha,\beta} \left(\sum_j J_{kj} \mathscr{C}_{ju} \right) Q_k^\alpha Q_u^\beta \boldsymbol{e}_\beta \boldsymbol{e}_\alpha \right\rangle$$
$$+ \left\langle \sum_{k,v} \sum_{\alpha,\gamma} \left(\sum_j J_{kj} \mathscr{C}_{jv} \right) Q_k^\alpha Q_v^\gamma \boldsymbol{e}_\alpha \boldsymbol{e}_\gamma \right\rangle \tag{E.64}$$
$$= \sum_{k,u} \mathcal{L}_{ku} \left[\langle \boldsymbol{Q}_k \boldsymbol{Q}_u \rangle + \langle \boldsymbol{Q}_k \boldsymbol{Q}_u \rangle^T \right]$$
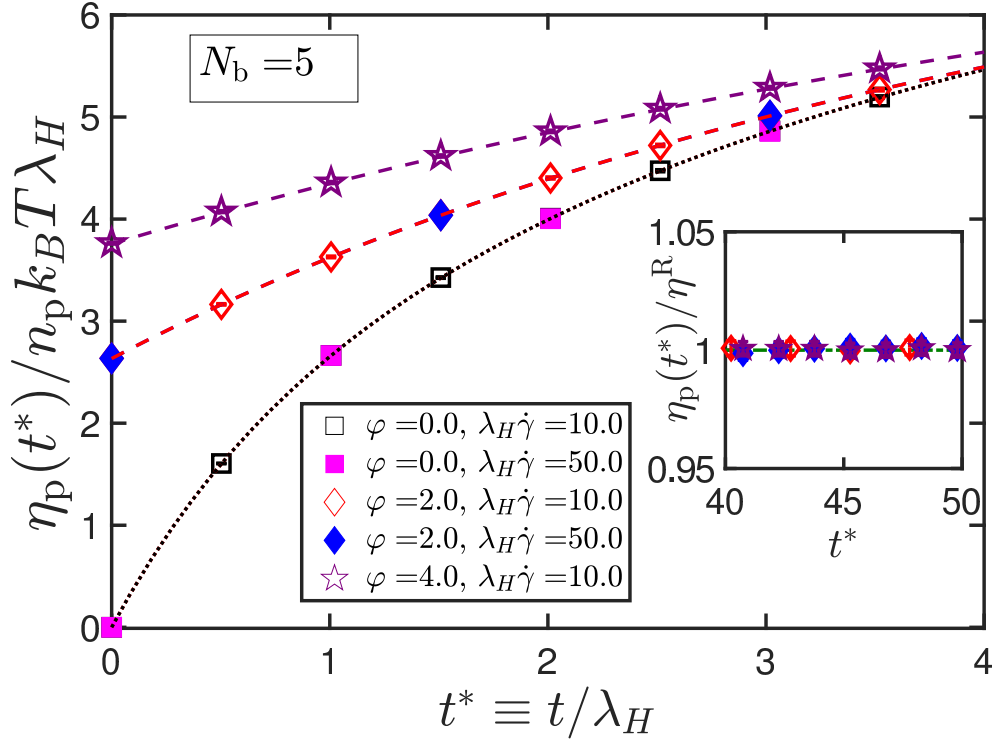
Figure E.2: Validating the expression for the transient evolution of shear viscosity for a five-bead Rouse chain with preaveraged internal friction for various values of the dimensionless shear rate ($\lambda_H\dot{\gamma}$) and internal friction parameter (φ). Lines represent Eq. (E.69) and symbols are BD simulations results. Inset shows the steady-state values of viscosity for the various cases.

From Equations (E.55), (E.60), (E.63), and (E.64), we have

$$\left\langle \sum_{u=1}^{N}\sum_{v=1}^{N}\mathscr{C}_{uv}\boldsymbol{Q}_u\boldsymbol{Q}_v \right\rangle_{(1)} = \left(\frac{1}{1+2\theta}\right)\sum_{k,u}\mathcal{S}_{ku}\left[\langle\boldsymbol{Q}_u\boldsymbol{Q}_k\rangle\cdot\boldsymbol{\kappa}^T + \boldsymbol{\kappa}\cdot\langle\boldsymbol{Q}_u\boldsymbol{Q}_k\rangle^T\right]$$

$$+\left(\frac{2k_BT}{\zeta}\right)\left(\frac{1}{1+2\theta}\right)\mathrm{tr}\left(\mathcal{L}\right) + \sum_{k,u}\mathcal{L}_{ku}\left[\langle\boldsymbol{Q}_k\boldsymbol{Q}_u\rangle + \langle\boldsymbol{Q}_k\boldsymbol{Q}_u\rangle^T\right]\boldsymbol{\delta} \quad \text{(E.65)}$$

$$-\boldsymbol{\kappa}\cdot\left\langle\sum_{u,v}\mathscr{C}_{uv}\boldsymbol{Q}_u\boldsymbol{Q}_v\right\rangle - \left\langle\sum_{u,v}\mathscr{C}_{uv}\boldsymbol{Q}_u\boldsymbol{Q}_v\right\rangle\cdot\boldsymbol{\kappa}^T$$

Substituting Eq. (E.65) into Eq. (E.55) and simplifying, the following expression for the stress tensor is obtained

$$\boldsymbol{\tau}_p = n_pk_BT\left[\left(\frac{1}{1+2\theta}\right)\mathrm{tr}\left(\mathcal{L}\right)\right]\boldsymbol{\delta} - \frac{n_pH}{2}\left[\left(\frac{1}{1+2\theta}\right)\sum_{m,n}\mathcal{L}_{mn}\left[\langle\boldsymbol{Q}_m\boldsymbol{Q}_n\rangle + \langle\boldsymbol{Q}_n\boldsymbol{Q}_m\rangle\right]\right]$$

$$-\frac{n_p\zeta}{2}\left\{\sum_{m,n}\left(\mathscr{C}_{mn} - \frac{1}{1+2\theta}\mathcal{S}_{mn}\right)\left[\langle\boldsymbol{\kappa}\cdot(\boldsymbol{Q}_m\boldsymbol{Q}_n)\rangle + \langle(\boldsymbol{Q}_m\boldsymbol{Q}_n)\cdot\boldsymbol{\kappa}^T\rangle\right]\right\} \quad \text{(E.66)}$$

The $xy-$ component of the stress tensor is written as

$$\tau_{\text{p},xy} = -n_{\text{p}}H\left[\left(\frac{1}{1+2\theta}\right)\sum_{m,n}\mathcal{L}_{mn}\left\langle Q_m^{(x)}Q_n^{(y)}\right\rangle\right] - \frac{n_{\text{p}}\zeta\dot\gamma}{2}\left\{\sum_{m,n}\left(\mathscr{C}_{mn} - \frac{1}{1+2\theta}\mathcal{S}_{mn}\right)\left[\left\langle Q_m^{(y)}Q_n^{(y)}\right\rangle\right]\right\}$$
(E.67)

The first term on the RHS of Eq. (E.67) represents the elastic component to the total shear stress, while the second term represents the viscous or dissipative contribution. Following a procedure identical to that described in Sec. E.1, the underlined terms are evaluated to be

$$\left\langle Q_m^{(x)}Q_n^{(y)}\right\rangle = \left(\frac{k_BT}{H}\right)(\lambda_H\dot\gamma)\sum_q \Pi_{mq}\Pi_{nq}I_q(t)$$

$$\left\langle Q_m^{(y)}Q_n^{(y)}\right\rangle = \left(\frac{k_BT}{H}\right)\delta_{mn}$$
(E.68)

from which the expression for the dimensionless shear viscosity may be obtained as

$$\frac{\eta_{\text{p}}(t^*)}{n_{\text{p}}k_BT\lambda_H} \equiv -\frac{\tau_{\text{p},xy}}{n_{\text{p}}k_BT\lambda_H\dot\gamma}$$

$$= \left(\frac{1}{1+2\theta}\right)\sum_{m,n,q}\Pi_{mq}\mathcal{L}_{mn}\Pi_{nq}I_q(t^*) + 2\,\text{tr}\left[\mathcal{C} - \frac{1}{1+2\theta}\mathcal{S}\right]$$
(E.69)

with

$$I_q(t^*) = 2\left(\frac{\widetilde{b}_q}{\widetilde{a}_q}\right)\left\{1 - \exp\left[-\left(\frac{\widetilde{a}_q}{1+2\theta}\right)\frac{t^*}{2}\right]\right\},$$
(E.70)

In Fig. E.2, the solution given by Eq. (E.69) is compared against BD simulation data for the preaveraged IV model, obtained by numerically integrating the governing stochastic differential equation [Eq. (6.47)] and using the stress tensor expression given by Eq. (E.66), for a variety of internal friction parameters and shear rates. An excellent agreement is observed between the results obtained using the two approaches.

Appendix F

Stress tensor components at the inception of simple shear flow

This appendix presents an explanation, using a pedagogical example of a free-draining Hookean dumbbell with internal viscosity, for the fact that an instantaneous jump at the inception of shear flow is predicted only in the viscosity, but not in the normal stress coefficients.

The stress tensor expression for a free-draining Hookean dumbbell with IV is given by

$$
\begin{aligned}
\boldsymbol{\tau}_{\mathrm{p}} = n_{\mathrm{p}} k_B T \boldsymbol{\delta} - \left(\frac{1}{1+\epsilon} \right) n_{\mathrm{p}} H \left\langle \boldsymbol{QQ} \right\rangle - 3 n_{\mathrm{p}} k_B T \left(\frac{\epsilon}{1+\epsilon} \right) \left\langle \frac{\boldsymbol{QQ}}{Q^2} \right\rangle \\
- \frac{n_{\mathrm{p}} \zeta}{2} \left(\frac{\epsilon}{1+\epsilon} \right) \left[\boldsymbol{\kappa} : \left\langle \frac{\boldsymbol{QQQQ}}{Q^2} \right\rangle \right]
\end{aligned}
\tag{F.1}
$$

The equilibrium configurational distribution function for a Hookean dumbbell is given by

$$
\psi_{\mathrm{eq}}(\boldsymbol{Q}) = \left(\frac{H}{2\pi \, k_B T} \right)^{3/2} \exp\left[-\frac{1}{2} H Q^2 \right]
\tag{F.2}
$$

and is unaffected by internal friction. The stress tensor components at the inception of shear flow may be found by evaluating the moments in Eq. (F.1) with respect to the distribution function given by Eq. (F.2), as follows

$$
\left\langle \boldsymbol{QQ} \right\rangle_{\mathrm{eq}} \equiv \int \boldsymbol{QQ} \psi_{\mathrm{eq}} d\boldsymbol{Q} = \left(\frac{k_B T}{H} \right) \boldsymbol{\delta}
\tag{F.3}
$$

$$
\left\langle \frac{\boldsymbol{QQ}}{Q^2} \right\rangle_{\mathrm{eq}} = \left(\frac{1}{3} \right) \boldsymbol{\delta}
\tag{F.4}
$$

The identity (E.3-5) from Bird *et al.* (1987b) has been used in evaluating the integral in Eq. (F.3), while the result given by Eq. (F.4) is taken from Eq. (4.47) of Doi and Edwards

(1986). Denoting

$$S \equiv \boldsymbol{\kappa} : \left\langle \frac{\boldsymbol{QQQQ}}{Q^2} \right\rangle_{\text{eq}} \tag{F.5}$$

it may be shown, using polar spherical coordinates (Manke and Williams, 1988), that, in shear flow,

$$S_{xy} \equiv \dot{\gamma} \left\langle \frac{Q_x^2 Q_y^2}{Q^2} \right\rangle_{\text{eq}} = \left(\frac{k_B T}{5H} \right) \tag{F.6}$$

and

$$S_{xx} \equiv \dot{\gamma} \left\langle \frac{Q_x^3 Q_y}{Q^2} \right\rangle_{\text{eq}} = 0$$

$$S_{yy} \equiv \dot{\gamma} \left\langle \frac{Q_x Q_y^3}{Q^2} \right\rangle_{\text{eq}} = 0 \tag{F.7}$$

$$S_{zz} \equiv \dot{\gamma} \left\langle \frac{Q_x Q_y Q_z^2}{Q^2} \right\rangle_{\text{eq}} = 0$$

From equations (F.3)—(F.7), and the definitions of the material functions in simple shear flow [Eq. (2.14) of Chapter 2], it is clear that only the viscosity has a stress jump at the inception of flow, while the two normal stress coefficients, Ψ_1 and Ψ_2, remain jump-free.

References

Abramowitz, M., and Stegun, I., 1972, *Handbook of Mathematical Functions with Formulas, Graphs, and Mathematical Tables (Partially Mathcad-enabled)* (U.S. Department of Commerce, NIST).

Alexander-Katz, A., Wada, H., and Netz, R. R., 2009, "Internal friction and nonequilibrium unfolding of polymeric globules," *Phys. Rev. Lett.* **103**, 028102.

Ameseder, F., Radulescu, A., Holderer, O., Falus, P., Richter, D., and Stadler, A. M., 2018, "Relevance of Internal Friction and Structural Constraints for the Dynamics of Denatured Bovine Serum Albumin," *J. Phys. Chem. Lett.* **9**, 2469–2473.

Ansari, A., Jones, C. M., Henry, E. R., Hofrichter, J., and Eaton, W. A., 1992, "The Role of Solvent Viscosity in the Dynamics of Protein Conformational Changes," *Science* **256**, 1796–1798.

Avdoshenko, S. M., Das, A., Satija, R., Papoian, G. A., and Makarov, D. E., 2017, "Theoretical and computational validation of the Kuhn barrier friction mechanism in unfolded proteins," *Sci. Rep.* **7**, 269.

Bazúa, E. R., and Williams, M. C., 1974, "Rheological Properties of Internal Viscosity Models with Stress Symmetry," *J. Polym. Sci. Polym. Phys. Ed.* **12**, 825–848.

Bekard, I. B., Asimakis, P., Bertolini, J., and Dunstan, D. E., 2011, "The effects of shear flow on protein structure and function," *Biopolymers* **95**, 733–745.

Bhattacharyya, P., and Cherayil, B. J., 2012, "Chain extension of a confined polymer in steady shear flow," *J. Chem. Phys.* **137**

Bieri, O., Wirz, J., Hellrung, B., Schutkowski, M., Drewello, M., and Kiefhaber, T., 1999, "The speed limit for protein folding measured by triplet-triplet energy transfer," *Proc. Natl. Acad. Sci. U.S.A.* **96**, 9597–9601.

Bird, R. B., 1989, "Attempts to find a molecular theory for which the high-frequency dynamic viscosity is less than the solvent viscosity," *Rheol. Acta* **28**, 457–463.

Bird, R. B., Curtiss, C. F., Armstrong, R. C., and Hassager, O., 1987a, *Dynamics of Polymeric Liquids - Volume 1 : Fluid Mechanics* (John Wiley and Sons, New York).

Bird, R. B., Curtiss, C. F., Armstrong, R. C., and Hassager, O., 1987b, *Dynamics of Polymeric Liquids - Volume 2 : Kinetic Theory* (John Wiley and Sons, New York).

Black, J. W., Kamenetska, M., and Ganim, Z., 2017, "An Optical Tweezers Platform for Single Molecule Force Spectroscopy in Organic Solvents," *Nano Lett.* **17**, 6598–6605.

Booij, H. C., and van Wiechen, P. H., 1970, "Effect of Internal Viscosity on the Deformation of a Linear Macromolecule in a Sheared Solution," *J. Chem. Phys.* **52**, 5056–5068.

Callen, H. B., 1985, *Thermodynamics and an Introduction to Thermostatics* (John Wiley and Sons, New York).

Cellmer, T., Henry, E. R., Hofrichter, J., and Eaton, W. A., 2008, "Measuring internal friction of an ultrafast-folding protein," *Proc. Natl. Acad. Sci. U.S.A.* **105**, 18320–18325.

Cerf, R., 1951, "Recherches théoriques et expérimentales sur l'effet maxwell des solutions de macromolécules déformables - ii. application de la théorie de la sphère élastique aux solutions de macromolécules en chaînes," *J. Chim. Phys.* **48**, 85–105.

Cerf, R., 1957, "La macromol6cule en chahe dans un champ hydrodynamique. Th6orie g6nkrale. Propri6tks dynamo-optiques," *J. Polym. Sci.* **23**, 125–150.

Chaki, S., and Chakrabarti, R., 2018, "Entropy production and work fluctuation relations for a single particle in active bath," *Physica A* **511**, 302–315.

Cheng, R. R., Hawk, A. T., and Makarov, D. E., 2013, "Exploring the role of internal friction in the dynamics of unfolded proteins using simple polymer models," *J. Chem. Phys.* **138**, 074112.

Christiansen, R. L., and Bird, R. B., 1977, "Dilute solution rheology: experimental results and finitely extensible nonlinear elastic dumbbell theory," *J. Non-Newtonian Fluid Mech.* **3**, 161–177.

Chung, H. S., and Eaton, W. A., 2013, "Single-molecule fluorescence probes dynamics of barrier crossing," *Nature* **502**, 685–688.

Chung, H. S., Piana-Agostinetti, S., Shaw, D. E., and Eaton, W. A., 2015, "Structural origin of slow diffusion in protein folding," *Science* **349**, 1504–1510.

Cretney, R., 2014, "The origins of Euler's early work on continued fractions," *Historia Mathematica* **41**, 139–156.

Daldrop, J. O., Kappler, J., Brunig, F. N., and Netz, R. R., 2018, "Butane dihedral angle dynamics in water is dominated by internal friction," *Proc. Natl. Acad. Sci. U.S.A.* **115**, 5169–5174.

Dasbach, T. P., Manke, C. W., and Williams, M. C., 1992, "Complex viscosity for the rigorous formulation of the multibead internal viscosity model with hydrodynamic interaction," *J. Phys. Chem.* **96**, 4118–4125.

de Gennes, P.-G., 1979, *Scaling Concepts in Polymer Physics* (Cornell University Press, Ithaca).

Des Cloizeaux, J., 1980, "Short range correlation between elements of a long polymer in a good solvent," *J. Phys. France* **10**, 223–238.

Dhar, A., 2005, "Work distribution functions in polymer stretching experiments," *Phys. Rev. E* **71**, 036126.

Doi, M., and Edwards, S. F., 1986, *The Theory of Polymer Dynamics* (Clarendon, Oxford).

Echeverria, I., Makarov, D. E., and Papoian, G. A., 2014, "Concerted dihedral rotations give rise to internal friction in unfolded proteins," *J. Am. Chem. Soc.* **136**, 8708–8713.

Fixman, M., 1988, "Dynamics of stiff polymer chains," *J. Chem. Phys.* **89**, 2442.

Fixman, M., 1986, "Construction of Langevin forces in the simulation of hydrodynamic interaction," *Macromolecules* **19**, 1204–1207.

Gerhardt, L. J., and Manke, C. W., 1994, "Relationships among shear stress jumps and high-frequency dynamic viscosity of viscoelastic fluids," *J. Rheol.* **38**, 1227–1234.

Gupta, A. N., Vincent, A., Neupane, K., Yu, H., Wang, F., and Woodside, M. T., 2011, "Experimental validation of free-energy-landscape reconstruction from non-equilibrium single-molecule force spectroscopy measurements," *Nat. Phys.* **7**, 631–634.

Hagen, S. J., 2010, "Solvent viscosity and friction in protein folding dynamics," *Curr. Protein Pept. Sci.* **11**, 385–395.

Harris, N. C., Song, Y., and Kiang, C.-H., 2007, "Experimental Free Energy Surface Reconstruction from Single-Molecule Force Spectroscopy using Jarzynski's Equality," *Phys. Rev. Lett.* **99**, 068101.

Hodges, E., Cooke, B. M., Sevick, E. M., Searles, D. J., Dünweg, B., and Prakash, J. R., 2016, "Equilibrium binding energies from fluctuation theorems and force spectroscopy simulations," *Soft Matter* **12**, 9803–9820.

Howard, M. P., and Milner, S. T., 2011, "Numerical simulation methods for the Rouse model in flow," *Phys. Rev. E* **84**, 051804.

Hua, C. C., and Schieber, J. D., 1995, "Nonequilibrium Brownian dynamics simulations of Hookean and FENE dumbbells with internal viscosity," *J. Non-Newtonian Fluid Mech.* **56**, 307–332.

Hua, C. C., and Schieber, J. D., 1996, "Application of kinetic theory models in spatiotemporal flows for polymer solutions, liquid crystals and polymer melts using the connffessit approach," *Chem. Eng. Sci.* **51**, 1473–1485.

Hua, C. C., Schieber, J. D., and Manke, C. W., 1996, "Linear viscoelastic behavior of the Hookean dumbbell with internal viscosity," *Rheol. Acta* **35**, 225–232.

Hummer, G., and Szabo, A., 2010, "Free energy profiles from single-molecule pulling experiments," *Proc. Natl. Acad. Sci. U.S.A.* **107**, 21441–21446.

Huppler, J. D., MacDonald, I. F., Ashare, E., Spriggs, T. W., Bird, R. B., and Holmes, L. A., 1967, "Rheological properties of three solutions. Part II. Relaxation and growth of shear and normal stresses," *Trans. Soc. Rheol.* **11**, 181–204.

Jain, N., Narang, D., Bhasne, K., Dalal, V., Arya, S., Bhattacharya, M., and Mukhopadhyay, S., 2016, "Direct Observation of the Intrinsic Backbone Torsional Mobility of Disordered Proteins," *Biophys. J.* **111**, 768–774.

Jarzynski, C., 1997, "Nonequilibrium Equality for Free Energy Differences," *Phys. Rev. Lett.* **78**, 2690–2693.

Jarzynski, C., 2006, "Rare events and the convergence of exponentially averaged work values," *Phys. Rev. E* **73**, 046105.

Jarzynski, C., 2007, "Comparison of far-from-equilibrium work relations," *C. R. Phys.* **8**, 495–506.

Jas, G. S., Eaton, W. A., and Hofrichter, J., 2001, "Effect of Viscosity on the Kinetics of α-Helix and β-Hairpin Formation," *J. Phys. Chem. B* **105**, 261–272.

Jendrejack, R. M., Graham, M. D., and De Pablo, J. J., 2000, "Hydrodynamic interactions in long chain polymers: Application of the Chebyshev polynomial approximation in stochastic simulations," *J. Chem. Phys.* **113**, 2894–2900.

Kailasham, R., Chakrabarti, R., and Prakash, J. R., 2018, "Rheological consequences of wet and dry friction in a dumbbell model with hydrodynamic interactions and internal viscosity," *J. Chem. Phys.* **149**, 094903.

Kailasham, R., Chakrabarti, R., and Prakash, J. R., 2020, "Wet and dry internal friction can be measured with the Jarzynski equality," *Phys. Rev. Res.* **2**, 013331.

Kailasham, R., Chakrabarti, R., and Prakash, J. R., 2021a, "How important are fluctuations in the treatment of internal friction in polymers?."

Kailasham, R., Chakrabarti, R., and Prakash, J. R., 2021b, "Rouse model with fluctuating internal friction,"

Khatri, B. S., Kawakami, M., Byrne, K., Smith, D. A., and McLeish, T. C. B., 2007, "Entropy and barrier-controlled fluctuations determine conformational viscoelasticity of single biomolecules," *Biophys. J.* **92**, 1825–1835.

Khatri, B. S., and McLeish, T. C. B., 2007, "Rouse model with internal friction: A coarse grained framework for single biopolymer dynamics," *Macromolecules* **40**, 6770–6777.

Kishbaugh, A. J., and McHugh, A. J., 1990, "A discussion of shear-thickening in bead-spring models," *J. Non-Newtonian Fluid Mech.* **34**, 181–206.

Kopf, A., Dünweg, B., and Paul, W., 1997, "Dynamics of polymer "isotope" mixtures: Molecular dynamics simulation and Rouse model analysis," *J. Chem. Phys.* **107**, 6945–6955.

Kröger, M., Alba-Perez, A., Laso, M., and Öttinger, H. C., 2000, "Variance reduced Brownian simulation of a bead-spring chain under steady shear flow considering hydrodynamic interaction effects," *J. Chem. Phys.* **113**, 4767–4773.

Kuhn, W., and Kuhn, H., 1945, "Bedeutung beschränkt freier Drehbarkeit für die Viskosität und Strömungsdoppelbrechung von Fadenmolekellösungen I," *Helv. Chim. Acta* **28**, 1533–1579.

Kumari, K., Duenweg, B., Padinhateeri, R., and Prakash, J. R., 2020, "Computing 3D Chromatin Configurations from Contact Probability Maps by Inverse Brownian Dynamics," *Biophys. J.* **118**, 2193–2208.

Kumari, K., Prakash, J. R., and Padinhateeri, R., 2021, "Spatiotemporal organization of chromatin domains: role of interaction energy and polymer entropy,"

Lamb, J., and Matheson, A. J., 1964, "The Viscoelastic Properties of Polystyrene Solutions," *Proc. Royal So. A* **281**, 207–222.

Larson, R., 1988, *Constitutive Equations for Polymer Melts and Solutions* (Butterworths, Boston).

Larson, R. G., 2005, "The rheology of dilute solutions of flexible polymers: Progress and problems," *J. Rheol.* **49**, 1–70.

Latinwo, F., Hsiao, K.-W., and Schroeder, C. M., 2014, "Nonequilibrium thermodynamics of dilute polymer solutions in flow," *J. Chem. Phys.* **141**, 174903.

Lesage, A., Dahirel, V., Victor, J. M., and Barbi, M., 2019, "Polymer coil-globule phase transition is a universal folding principle of Drosophila epigenetic domains," *Epigenetics Chromatin* **12**, 28.

Liang, C.-H., and Mackay, M. E., 1993, "The stress jump of a semirigid macromolecule after shear: Steady-state results," *J. Rheol.* **37**, 149–174.

Liphardt, J., Dumont, S., Smith, S. B., Tinoco Jr., I., and Bustamante, C., 2002, "Equilibrium Information from in an Experimental Test of Jarzynski's Equality," *Science* **296**, 1832–1835.

Lodge, T. P., 1993, "Solvent dynamics, local friction, and the viscoelastic properties of polymer solutions," *J. Phys. Chem.* **97**, 1480–1487.

Mackay, M. E., Liang, C. H., and Halley, P. J., 1992, "Instrument effects on stress jump measurements," *Rheol. Acta* **31**, 481–489.

Malila, J., 2014, "The Derivative of a finite continued fraction," *Appl. Math. E-notes* **14**, 13–19.

Manke, C. W., and Williams, M. C., 1989, "Transient stress and strain responses predicted by the internal viscosity model in shear flow," *J. Rheol.* **33**, 949–978.

Manke, C. W., and Williams, M. C., 1991, "Transient stress responses predicted by the internal viscosity model in elongational flow," *Rheol. Acta* **30**, 316–328.

Manke, C. W., and Williams, M. C., 1985, "Internal Viscosity of Polymers and the Role of Solvent Resistance," *Macromolecules* **18**, 2045–2051.

Manke, C. W., and Williams, M. C., 1986, "The Internal-Viscosity Dumbbell in the High-IV Limit : Implications for Rheological Modeling," *J. Rheol.* **30**, 19–28.

Manke, C. W., and Williams, M. C., 1988, "Stress Jump at the Inception of Shear and Elongational Flows of Dilute Polymer Solutions, Due to Internal Viscosity," *J. Rheol.* **31**, 495–510.

Manke, C. W., and Williams, M. C., 1992, "Stress jumps predicted by the internal viscosity model with hydrodynamic interaction," *J. Rheol.* **36**, 1261–1274.

Manke, C. W., and Williams, M. C., 1993, "Comparison of a new internal viscosity model with other constrained-connector theories of dilute polymer solution rheology," *Rheol. Acta* **32**, 418–421.

Marko, J. F., and Siggia, E. D., 1995, "Stretching DNA," *Macromolecules* **28**, 8759–8770.

Massa, D. J., Schrag, J. L., and Ferry, J. D., 1971, "Dynamic Viscoelastic Properties of Polystyrene in High-Viscosity Solvents. Extrapolation to Infinite Dilution and High-Frequency Behavior," *Macromolecules* **4**, 210–214.

Mochimaru, Y., 1981, "Further comments on the FENE-P dumbbell model," *J. Non-Newtonian Fluid Mech.* **9**, 179–184.

Mondal, D., Adhikari, R., and Sharma, P., 2020, "Internal friction controls active ciliary oscillations near the instability threshold," *Sci. Adv.* **6**, eabb0503.

Morris, R. L., Amelar, S., and Lodge, T. P., 1988, "Solvent friction in polymer solutions and its relation to the high frequency limiting viscosity," *J. Chem. Phys.* **89**, 6523–6537.

Murayama, Y., Wada, H., and Sano, M., 2007, "Dynamic force spectroscopy of a single condensed DNA," *Eur. Phys. Lett.* **79**, 58001.

Nandagiri, A., Gaikwad, A. S., Potter, D. L., Nosrati, R., Soria, J., O'Bryan, M. K., Jadhav, S., and Prabhakar, R., 2020, "Flagellar energetics from high-resolution imaging of beating patterns in tethered mouse sperm,"

Neuman, K. C., and Nagy, A., 2008, "Single-molecule force spectroscopy: optical tweezers, magnetic tweezers and atomic force microscopy," *Nat. Methods.* **5**, 491–505.

Neupane, K., Foster, D. A. N., Dee, D. R., Hao Yu, F. W., and Woodside, M. T., 2016, "Direct observation of transition paths during the folding of proteins and nucleic acids," *Science* **352**, 239–243.

Neupane, K., Hoffer, N. Q., and Woodside, M. T., 2018, "Measuring the Local Velocity along Transition Paths during the Folding of Single Biological Molecules," *Phys. Rev. Lett.* **121**, 18102.

Neupane, K., Wang, F., and Woodside, M. T., 2017, "Direct measurement of sequence-dependent transition path times and conformational diffusion in DNA duplex formation," *Proc. Natl. Acad. Sci. U.S.A.* **114**, 1329–1334.

Oldham, K. B., and Spanier, J., 1974, *The Fractional Calculus*, Mathematics in Science and Engineering, Vol. 111 (Elsevier).

Onuchic, J. N., Luthey-Schulten, Z., and Wolynes, P. G., 1997, "Theory of protein folding: the energy landscape perspective," *Annu. Rev. Phys. Chem* **48**, 545–600.

Orr, N. V., and Sridhar, T., 1996, "Stress relaxation in uniaxial extension," *J. Non-Newtonian Fluid Mech.* **67**, 77–103.

Öttinger, H. C., 1996, *Stochastic Processes in Polymeric Fluids* (Springer, Berlin).

Pabit, S. A., Roder, H., and Hagen, S. J., 2004, "Internal friction controls the speed of protein folding from a compact configuration," *Biochemistry* **43**, 12532–12538.

Petera, D., and Muthukumar, M., 1999, "Brownian dynamics simulation of bead-rod chains under shear with hydrodynamic interaction," *J. Chem. Phys.* **111**, 7614–7623.

Peterlin, A., 1967, "Frequency Dependence of Intrinsic Viscosity of Macromolecules with Finite Internal Viscosity," *J. Polym. Sci. A-2 Polym. Phys.* **5**, 179–193.

Peterlin, A., and Reinhold, C., 1967, "Dynamic Intrinsic Viscosity of Macromolecules with Internal Viscosity. III. Effect of Molecular Weight, Excluded Volume, and Hydrodynamic Interaction," *Trans. Soc. Rheol.* **11**, 15–37.

Pham, T. T., Sunthar, P., and Prakash, J. R., 2008, "An alternative to the bead-rod model: bead-spring chains with successive fine graining," *J. Non-Newt. Fluid Mech.* **149**, 9–19.

Philippoff, W., 1964, "Dynamic Investigations of Polymer Solutions in an Extended Range of Frequencies," *Trans. Soc. Rheol.* **8**, 117–135.

Poirier, M. G., and Marko, J. F., 2002, "Effect of Internal Friction on Biofilament Dynamics," *Phys. Rev. Lett.* **88**, 228103.

Prabhakar, R., and Prakash, J. R., 2002, "Viscometric functions for Hookean dumbbells with excluded volume and hydrodynamic interactions," *J. Rheol.* **46**, 1191–1220.

Prabhakar, R., and Prakash, J. R., 2004, "Multiplicative separation of the influences of excluded volume, hydrodynamic interactions and finite extensibility on the rheological properties of dilute polymer solutions," *J. Non-Newtonian Fluid Mech.* **116**, 163–182.

Prabhakar, R., and Prakash, J. R., 2006, "Gaussian approximation for finitely extensible bead-spring chains with hydrodynamic interaction," *J. Rheol.* **50**, 561–593.

Prakash, J. R., 1999, "The kinetic theory of dilute solutions of flexible polymers: Hydrodynamic interaction," in *Rheology Series*, Vol. 8, edited by Siginer, D. A., De Kee, D., and Chhabra, R. P. (Elsevier). pp. 467–517.

Prakash, J. R., 2019, "Universal dynamics of dilute and semidilute solutions of flexible linear polymers," *Curr. Opin. Colloid Interface Sci.* **43**, 63–79.

Prakash, J. R., and Öttinger, H. C., 1999, "Viscometric functions for a dilute solution of polymers in a good solvent," *Macromolecules* **32**, 2028–2043.

Press, W., Teukolsky, S., Vetterling, W., and Flannery, B., 2007, *Numerical Recipes 3rd Edition: The Art of Scientific Computing* (Cambridge University Press).

Qiu, L., and Hagen, S. J., 2004a, "A Limiting Speed for Protein Folding at Low Solvent Viscosity," *J. Am. Chem. Soc.* **126**, 3398–3399.

Qiu, L., and Hagen, S. J., 2004b, "A Limiting Speed for Protein Folding at Low Solvent Viscosity," *J. Am. Chem. Soc.* **126**, 3398–3399.

Qiu, L., Pabit, S. A., Roitberg, A. E., and Hagen, S. J., 2002, "Smaller and faster: The 20-residue Trp-cage protein folds in 4 μs," *J. Am. Chem. Soc.* **124**, 12952–12953.

R. Cerf, 1969, "Sur la théorie des propriétés hydrodynamiques des solutions de macromolécules en chaines," *J. Chim. Phys.* **66**, 479–488.

Raman, S., Utzig, T., Baimpos, T., Ratna Shrestha, B., and Valtiner, M., 2014, "Deciphering the scaling of single-molecule interactions using Jarzynski's equality," *Nat. Commun.* **5**, 1–7.

Ritort, F., Bustamante, C., and Tinoco, I., 2002, "A two-state kinetic model for the unfolding of single molecules by mechanical force," *Proc. Natl. Acad. Sci. U.S.A.* **99**, 13544–13548.

Rotne, J., and Prager, S., 1969, "Variational treatment of hydrodynamic interaction in polymers," *J. Chem. Phys.* **50**, 4831–4837.

Rouse, P. E., 1953, "A Theory of the Linear Viscoelastic Properties of Dilute Solutions of Coiling Polymers," *J. Chem. Phys.* **21**, 1272–1280.

Rubinstein, M., and Colby, R. H., 2003, *Polymer Physics* (Oxford University Press).

Sagnella, D. E., Straub, J. E., and Thirumalai, D., 2000, "Time scales and pathways for kinetic energy relaxation in solvated proteins: Application to carbonmonoxy myoglobin," *J. Chem. Phys.* **113**, 7702–7711.

Samanta, N., and Chakrabarti, R., 2013, "End to end loop formation in a single polymer chain with internal friction," *Chem. Phys. Lett.* **582**, 71–77.

Samanta, N., and Chakrabarti, R., 2016, "Reconfiguration dynamics in folded and intrinsically disordered protein with internal friction: Effect of solvent quality and denaturant," *Physica A* **450**, 165–179.

Samanta, N., Ghosh, J., and Chakrabarti, R., 2014, "Looping and reconfiguration dynamics of a flexible chain with internal friction," *AIP Adv.* **4**, 067102.

de Sancho, D., Sirur, A., and Best, R. B., 2014, "Molecular origins of internal friction effects on protein-folding rates.." *Nat. Commun.* **5**, 4307.

Santra, A., Kumari, K., Padinhateeri, R., Dünweg, B., and Prakash, J. R., 2019, "Universality of the collapse transition of sticky polymers," *Soft Matter* **15**, 7876–7887.

Sashi, P., Ramakrishna, D., and Bhuyan, A. K., 2016, "Dispersion Forces and the Molecular Origin of Internal Friction in Protein," *Biochemistry* **55**, 4595–4602.

Sasmal, C., Hsiao, K.-W., Schroeder, C. M., and Prakash, J. R., 2017, "Parameter-free prediction of DNA dynamics in planar extensional flow of semidilute solutions," *J. Rheol.* **61**, 169.

Schieber, J. D., 1993, "Internal Viscosity Dumbbell Model with A Gaussian Approximation," *J. Rheol.* **37**, 1003–1027.

Schieber, J. D., and Öttinger, H. C., 1994, "On consistency criteria for stress theory models tensors in kinetic," *J. Rheol.* **38**, 1909.

Schroeder, C. M., 2018, "Single Polymer Dynamics for Molecular Rheology," *J. Rheol.* **62**, 371–403.

Schulz, J. C. F., Miettinen, M. S., and Netz, R. R., 2015a, "Unfolding and Folding Internal Friction of β-Hairpins Is Smaller than That of α-Helices," *J. Phys. Chem. B* **119**, 4565–4574.

Schulz, J. C. F., Miettinen, M. S., and Netz, R. R., 2015b, "Unfolding and Folding Internal Friction of β-Hairpins Is Smaller than That of α-Helices," *J. Phys. Chem. B* **119**, 4565–4574.

Schulz, J. C. F., Schmidt, L., Best, R. B., Dzubiella, J., and Netz, R. R., 2012, "Peptide Chain Dynamics in Light and Heavy Water: Zooming in on Internal Friction," *J. Am. Chem. Soc.* **134**, 6273–6279.

Seki, K., and Bagchi, B., 2015, "Relationship between entropy and diffusion: A statistical mechanical derivation of Rosenfeld expression for a rugged energy landscape," *J. Chem. Phys.* **143**, 194110.

Seki, K., Bagchi, K., and Bagchi, B., 2016, "Anomalous dimensionality dependence of diffusion in a rugged energy landscape: How pathological is one dimension?." *J. Chem. Phys.* **144**, 194106.

Smith, S. B., Bustamante, C., Wen, J.-D., Manosas, M., Li, P. T., Tinoco, I., and Ritort, F., 2007, "Force Unfolding Kinetics of RNA Using Optical Tweezers. I. Effects of Experimental Variables on Measured Results," *Biophys. J.* **92**, 2996–3009.

Socol, M., Wang, R., Jost, D., Carrivain, P., Vaillant, C., Le Cam, E., Dahirel, V., Normand, C., Bystricky, K., Victor, J. M., Gadal, O., and Bancaud, A., 2019, "Rouse model with transient intramolecular contacts on a timescale of seconds recapitulates folding and fluctuation of yeast chromosomes," *Nucleic Acids Res* **47**, 6195–6207.

Soddemann, T., Dünweg, B., and Kremer, K., 2001, "A generic computer model for amphiphilic systems," *Eur. Phys. J. E* **6**, 409–419.

Soranno, A., Buchli, B., Nettels, D., Cheng, R. R., Müller-Späth, S., Pfeil, S. H., Hoffmann, A., Lipman, E. A., Makarov, D. E., and Schuler, B., 2012, "Quantifying internal friction in unfolded and intrinsically disordered proteins with single-molecule spectroscopy," *Proc. Natl. Acad. Sci. U.S.A.* **109**, 17800–17806.

Soranno, A., Holla, A., Dingfelder, F., Nettels, D., Makarov, D. E., and Schuler, B., 2017, "Integrated view of internal friction in unfolded proteins from single-molecule FRET, contact quenching, theory, and simulations," *Proc. Natl. Acad. Sci. U.S.A.* **114**, E1833–E1839.

Soranno, A., Zosel, F., and Hofmann, H., 2018, "Internal friction in an intrinsically disordered protein—Comparing Rouse-like models with experiments," *J. Chem. Phys.* **148**, 123326.

Speck, T., and Seifert, U., 2005, "Dissipated work in driven harmonic diffusive systems: General solution and application to stretching Rouse polymers," *Eur. Phys. J. B* **43**, 521–527.

Speck, T., 2017, "Geometric view of stochastic thermodynamics for non-equilibrium steady states,"

Speck, T., and Seifert, U., 2004, "Distribution of work in isothermal nonequilibrium processes," *Phys. Rev. E* **70**, 066112.

Stewart, W. E., and Sorensen, J. P., 1972, "Hydrodynamic Interaction Effects in Rigid Dumbbell Suspensions. II. Computations for Steady Shear Flow," *Trans. Soc. Rheol.* **16**, 1.

Sunthar, P., and Prakash, J. R., 2005, "Parameter-free prediction of DNA conformations in elongational flow by successive fine graining," *Macromolecules* **38**, 617–640.

Sureshkumar, R., and Beris, A. N., 1995, " Uniformly valid approximations for the conformational integrals resulting from Gaussian closure in the Hookean dumbbell model with internal viscosity a) ," *J. Rheol.* **39**, 1361–1384.

Thurston, G. B., and Morrison, J. D., 1969, "Eigenvalues and the intrinsic viscosity of short Gaussian chains," *Polymer* **10**, 421–438.

Toan, N. M., Morrison, G., Hyeon, C., and Thirumalai, D., 2008, "Kinetics of loop formation in polymer chains," *J. Phys. Chem. B* **112**, 6094–6106.

Trepagnier, E. H., Jarzynski, C., Ritort, F., Crooks, G. E., Bustamante, C. J., and Liphardt, J., 2004, "Experimental test of Hatano and Sasa's nonequilibrium steady-state equality," *Proc. Natl. Acad. Sci. U.S.A.* **101**, 15038–15041.

Underhill, P. T., and Doyle, P. S., 2004, "On the coarse-graining of polymers into bead-spring chains," *J. Non-Newt. Fluid.Mech* **122**, 3–31.

Varghese, A., Vemparala, S., and Rajesh, R., 2013, "Force fluctuations in stretching a tethered polymer," *Phys. Rev. E* **88**, 022134.

Verdier, P. H., 1966, "Monte carlo studies of lattice-model polymer chains. i. correlation functions in the statistical-bead model," *J. Chem. Phys.* **45**, 2118–2121.

Vincenzi, D., 2021, "Effect of internal friction on the coil–stretch transition in turbulent flows," *Soft Matter* **17**, 2421–2428.

Wagner, N. J., and Öttinger, H. C., 1997, "Accurate simulation of linear viscoelastic properties by variance reduction through the use of control variates," *J. Rheol.* **41**, 757–768.

Waldauer, S. A., Bakajin, O., and Lapidus, L. J., 2010, "Extremely slow intramolecular diffusion in unfolded protein L," *Proc. Natl. Acad. Sci. U.S.A.* **107**, 13713–13717.

Warner, H. R., 1972, "Kinetic Theory and Rheology of Dilute Suspensions of Finitely Extendible Dumbbells," *Ind. Eng. Chem. Fundam.* **11**, 379–387.

Wedgewood, L. E., 1993, "Internal viscosity in polymer kinetic theory: shear flows," *Rheologica Acta* **32**, 405–417.

Wedgewood, L. E., and Öttinger, H. C., 1988, "A Model of Dilute Polymer-Solutions with Hydrodynamic Interaction and Finite Extensibility .2. Shear Flows," *J. Non-Newtonian Fluid Mech.* **27**, 245–264.

Wensley, B. G., Batey, S., Bone, F. A. C., Chan, Z. M., Tumelty, N. R., Steward, A., Kwa, L. G., Borgia, A., and Clarke, J., 2010, "Experimental evidence for a frustrated energy landscape in a three-helix-bundle protein family," *Nature* **463**, 685–688.

Yamakawa, H., 1971, *Modern Theory of Polymer Solutions* (Harper and Row).

Young, P., 2015, *Everything You Wanted to Know About Data Analysis and Fitting but Were Afraid to Ask* (Springer, Berlin).

Yu, S., Wang, S., and Larson, R. G., 2013, "Proteins searching for their target on DNA by one-dimensional diffusion: Overcoming the "speed-stability" paradox," *J. Biol. Phys.* **39**, 565–586.

Yunger Halpern, N., and Jarzynski, C., 2016, "Number of trials required to estimate a free-energy difference, using fluctuation relations," *Phys. Rev. E* **93**, 052144.

Zheng, W., Hofmann, H., Schuler, B., and Best, R. B., 2018, "Origin of Internal Friction in Disordered Proteins Depends on Solvent Quality," *J. Phys. Chem. B* **122**, 11478–11487.

Zimm, B. H., 1956, "Dynamics of Polymer Molecules in Dilute Solution: Viscoelasticity, Flow Birefringence and Dielectric Loss," *J. Chem. Phys.* **24**, 269–278.

Zwanzig, R., 1988, "Diffusion in a rough potential.." *Proc. Natl. Acad. Sci. U.S.A.* **85**, 2029–2030.

Zylka, W., 1991, "Gaussian approximation and Brownian dynamics simulations for Rouse chains with hydrodynamic interaction undergoing simple shear flow," *J. Chem. Phys.* **94**, 4628–4636.

Zylka, W., and Öttinger, H. C., 1989, "A comparison between simulations and various approximations for Hookean dumbbells with hydrodynamic interaction," *J. Chem. Phys.* **90**, 474.

List of Publications

Papers in Refereed Journals

1. **Kailasham, R.**, Chakrabarti, R., and Prakash, J. R., 2018, "Rheological consequences of wet and dry friction in a dumbbell model with hydrodynamic interactions and internal viscosity," *J. Chem. Phys.* **149**, 094903.

2. **Kailasham, R.**, Chakrabarti, R., and Prakash, J. R., 2020, "Wet and dry internal friction can be measured with the Jarzynski equality," *Phys. Rev. Res.* **2**, 013331.

3. **Kailasham, R.**, Chakrabarti, R., and Prakash, J. R., 2021b, "Rouse model with fluctuating internal friction," *J. Rheol.* **65**, 903.

4. **Kailasham, R.**, Chakrabarti, R., and Prakash, J. R., 2021a, "How important are fluctuations in the treatment of internal friction?," *Soft Matter* **17**, 7133.

Contributed Conference Abstracts/Conference Presentations

1. **Kailasham, R.**, Chakrabarti, R., and Prakash, J. R., 2021, "Rouse model with fluctuating internal friction", Statistical Mechanics in Chemistry and Biology Conference 2021, organized by IIT Tirupati, IIT Goa, and IISER Tirupati, held online from January 23-26th, 2021.

2. **Kailasham, R.**, Chakrabarti, R., and Prakash, J. R., 2020, "Coarse-grained models for the effects of internal friction on dilute polymer solution rheology", 18th International Congress on Rheology, realized virtually from December 14-17th, 2020.

3. **Kailasham, R.**, Chakrabarti, R., and Prakash, J. R., 2020, "Wet and Dry Internal Friction can be measured with the Jarzynski equality", 18th International Congress on Rheology, realized virtually from December 14-17th, 2020.

4. **Kailasham, R.**, Chakrabarti, R., and Prakash, J. R., 2020, "Rouse model with fluctuating internal friction", Statistical Mechanics of Soft Matter 2020, hosted by

Griffith University and University of Queensland, held online from December 14-15th, 2020.

5. **Kailasham, R.**, Chakrabarti, R., and Prakash, J. R., 2020, "Rouse model with fluctuating internal friction", Complex Fluids Symposium 2020, organized by IIT Bombay and the Indian Society of Rheology, held online from December 10-12th, 2020.

6. **Kailasham, R.**, Chakrabarti, R., and Prakash, J. R., 2019, "Wet and Dry Internal Friction can be measured with the Jarzynski equality", In House Symposium 2019 (Department of Chemistry), held at IIT Bombay on 28th September 2019.

7. **Kailasham, R.**, Chakrabarti, R., and Prakash, J. R., 2019, "Wet and dry friction in a dumbbell model for a polymer", Soft Matter and Statistical Mechanics Conference 2019, at IISER Pune from January 4-5th, 2019.

8. **Kailasham, R.**, Chakrabarti, R., and Prakash, J. R., 2018, "Wet and dry friction in a dumbbell model for a polymer", IUTAM Symposium on Dynamics of Complex Fluids and Interfaces 2018, at IIT Kanpur from December 17-20th, 2018.

9. **Kailasham, R.**, Chakrabarti, R., and Prakash, J. R., 2017, "Non-Equilibrium Conformational Dynamics of a coarse-grained polymer model with internal friction and hydrodynamic interactions", 7th Annual Monash University Chemical Engineering Conference, at Monash University on October 26th, 2017.